Nanocharacterization of Functional Materials for Biomagnetic Sensing and Breath Analysis

Dissertation

submitted to obtain the degree of

Doctor of Engineering (Dr.-Ing.)

at

Faculty of Engineering - Kiel University
Institute for Material Science

Niklas Wolff

Kiel

2020

First supervisor: Prof. Dr. Lorenz Kienle
Faculty of Engineering - Kiel University

Second reviewer: Prof Dr. Rainer Adelung
Faculty of Engineering - Kiel University

Third reviewer: Prof. Dr. David Johnson
Department of Chemistry and Biochemistry - University of Oregon

Date of oral examination: 16th June 2020
Permission for publication: 16th June 2020

Abstract

The presented thesis is covering materials aspects for the development of magnetoelectric sensors for biomagnetic sensing and solid state sensors for breath monitoring. The electrophysiological signals of the human body and especially their irregularities provide extremely valuable information about the heart, brain or nerve malfunction in medical diagnostics. Similar and even more detailed information is contained in the generated biomagnetic fields which measurement offers improved diagnostics and treatment of the patients. A new type of room temperature operable magnetoelectric composite sensors is developed in the framework of the CRC1261 *Magnetoelectric Sensors: From Composite Materials to Biomagnetic Diagnostics*. This thesis focuses on the individual materials structure-property relations and their combination in magnetoelectric composite sensors studied by electron beam based techniques, at lengths scales ranging from micrometers to atomic resolution. The first part of this thesis highlights selected studies on the structural and analytic aspects of single phase materials and their composites using TEM as the primary method of investigation. With respect to the piezoelectric phase, alternatives to AlN have been thoroughly investigated to seek for improvement of specific sensor approaches. In this context, the alloying of Sc into the AlN matrix has been demonstrated to yield high quality films with improved piezoelectric and unprecedented ferroelectric properties grown under the control of deposition parameters. Lead-free titanate films with large piezo-coefficients at the verge of the morphotropic phase boundary as alternative to PZT films have been investigated in terms of crystal symmetry, defect structure and domains of cation ordering. New morphologies of ZnO and GaN semiconductors envisioned for a piezotronic-based sensor approach were subject of in-depth defect and analytical studies describing intrinsic defects and lattice strains upon deposition as well as hollow composite structures. When the dimensions of a materials are reduced, novel exciting properties such as in-plane piezoelectricity can arise in planar transition-metal dichalcogenides. Here, the turbostratic disorder in a few-layered $MoSe_2$ film has been investigated by nanobeam electron diffraction and Fast Fourier Transformations. From the perspective of magnetic materials, the atomic structure of magnetostrictive multilayers of FeCo/TiN showing stability up to elevated temperatures has been analyzed in detail regarding the crystallographic relationship of heteroepitaxy in multilayer composites exhibiting individual layer thicknesses below 1 nm. Further, magnetic hard layers have been investigated in the context of exchange spring concepts and ME composites based on shape memory alloy substrates have been studied regarding structural changes implied by different annealing processes. The second part of this thesis introduces materials aspects and sensor studies on gas detection in the clinical context of breath analysis. The detection of specific vapors in the human breath is of medical relevance, since certain species can be enriched depending on the conditions and processes within the human body. Hence, they can be regarded as biomarkers for the patients condition of health. The selection of suitable materials and the gas measurement working principle are considered and selected studies on solid state sensors with different surface functionalization or targeted application on basis of ZnO or CuO-oxide and Fe-oxide species are presented.

Kurzfassung

Die vorliegende Dissertationsschrift gliedert sich in zwei thematische Bereiche. Im ersten Teil wird über die aktuelle Entwicklung magnetoelektrischer Sensoren für biomagnetische Anwendungen berichtet. Der Schwerpunkt liegt dabei auf den verwendeten Materialien und deren Strukturanalytik. Im zweiten Teil liegt der Fokus auf Festkörpersensoren für die Atemanalyse in der medizinischen Diagnostik. Die elektrophysiologischen Signale des menschlichen Körpers stellen in der medizinischen Diagnostik eine extrem wertvolle Informationsquelle über dessen Funktion dar. Insbesondere können so eine vorliegende Arrhythmie, neurologische Erkrankungen sowie Schädigungen am zentralen Nervensystem schnell und sicher diagnostiziert und untersucht werden. Darüber hinaus verfügt die Messung der gleichsam induzierten biomagnetischen Felder über vergleichbare und teilweise detailgenauere Informationen und eröffnen der Medizin eine verbesserte Diagnostik und Behandlung des Patienten. Neuartige Sensortypen auf Basis magnetoelektrischer Komposite stellen die Raumtemperaturanwendung biomagnetischer Messungen in den Vordergrund und werden innerhalb des Sonderforschungsbereichs 1261 "Magnetoelektrische Sensoren: Von Kompositmaterialien zur biomagnetischen Diagnostik" untersucht. Die in dieser Arbeit vorgestellten Studien fokussieren sich dabei auf die Untersuchung von Struktur-Eigenschaftsbeziehungen der einzelnen Sensorkomponenten und deren Zusammenspiel in magnetoelektrischen Kompositen mit Elekronenstrahl basierten Techniken auf Längenskalen von einigen Mikrometern bis zur atomaren Auflösung. In dieser zusammenfassenden Arbeit werden nun ausgewählte eigene Studien unter dem Gesichtspunkt der strukturellen und analytischen Charakterisierung möglicher Sensormaterialen und deren Komposite mit Methoden der Transmissionselektronenmikroskopie vorgestellt. In Bezug auf die Verbesserung von Materialeigenschaften der piezoelektrischen Phase wurden verschiedene Alternativen zu Aluminiumnitrid (AlN) Dünnfilmen untersucht. Insbesondere wurde gezeigt, dass durch die Zugabe von Scandium in die AlN Matrix strukturell qualitative Dünnfilme mit verbesserten piezoelektrischen und unvorhergesehenen ferroelektrischen Eigenschaften hergestellt werden können. Als Alternative zu bleihaltigen Piezoelektrika, wie dem Bleizirkontitanat (PZT), wurden Dünnfilme der bleifreien Phase Bariumcalciumzirkontitanat (BCZT) hergestellt, die hohe Piezokoeffizienten am Rande der morphotropen Phasengrenze aufweist. Diese Dünnfilme wurden auf ihre Kristallstruktur, vorhandene Kristallsymmetrie und Defektstruktur untersucht. Dabei wurde lokal eine Ausordnung der Kation-Teilstruktur beobachtet. Weiterhin wurden im Hinblick auf piezotronische Bauelemente Strukturen mit neuartiger Morphologie der Zinkoxid (ZnO) und Galliumnitrid (GaN) Halbleiter auf ihre Defekte und chemische Zusammensetzung untersucht. Dabei wurden intrinsische Fehlordnung wie Zwillingsdefekte oder plastische Deformation als Resultat der Abscheideparameter beobachtet, sowie dreidimensionale röhrenförmige Kompositstrukturen tomographisch dargestellt. Materialien mit zweidimensionaler Morphologie aus der Gruppe der Übergangsmetall-Dichalkogenide weisen neue Materialeigenschaften auf, wie das Auftreten von Piezoelektrizität parallel zu den Netzebenen. Exemplarisch für diese Materialklasse wurde die Rotationsfehlordnung innerhalb und zwischen einzelnen Schichten am Beispiel von achtlagigen Molybdän-Diselenid ($MoSe_2$) Strukturen mithilfe spezieller lokal aufgelöster Elektronenbeugungsmethoden und einer Fouriertransformationsanalyse untersucht. Im Kontext der magnetostriktiven Phase wurde die atomare Struktur von ultra-dünnen Schichtsystemen aus Eisen-Kobalt/Titannitrid (FeCo/TiN), die Aufgrund des TiN eine erhöhte Temperaturwiderstandsfestigkeit aufweisen, analysiert und im Detail die kristallographischen Beziehungen des

heteroepitaktischen Systems beschrieben. Weiterhin wurde die Struktur hartmagnetischer Komposit-Dünnfilme beschrieben, wie sie in magnetisch gekoppelten Schichtkonzepten Anwendung finden könnten. Ebenso wurde die Herstellung neuartiger ME Sensorkonzepte begleitet, die auf Basis der eingestellten Phasenanteile in einer Formgedächtnislegierung ihre Resonanzfrequenz verändern und untersucht, wie sich einzelne Temperaturbehandlungen bei der Herstellung auf die Mikrostruktur auswirken. In einem zweiten Teil dieser Arbeit werden Materialaspekte und Sensorstudien zur Gasdetektion mittels Festkörpersensoren im klinischen Kontext der Atemanalyse betrachtet. Die Detektion und Quantifizierung einzelner Komponenten des menschlichen Atems ist von medizinscher Bedeutung, da einzelne Gase unter bestimmten Bedingungen und Vorgänge im Körper erhöht sein können und als Biomarker für den Gesundheitszustand des Patienten dienen können. Die Auswahl geeigneter Materialien und das Messprinzip werden theoretisch erläutert und einzelne Studien zu Festkörpersensoren mit unterschiedlich funktionalisierten Oberflächen und Anwendungsbereichen auf Basis von ZnO oder Kupfer- und Eisenoxiden präsentiert.

Declaration of Authorship

I hereby declare that this thesis was independently composed and authored by myself. All content and ideas drawn directly or indirectly from external sources are indicated as such. All sources and materials that have been used are referred to in this thesis.

The thesis has not been submitted to any other examining body and has not been published.

The thesis was conducted following the guidelines of excellent scientific practice of the German Research Foundation.

No academic degree have been withdrawn.

Place, date

Signed: Niklas Wolff

Acknowledgements / Danksagungen

Meine Disseration ist in einem konstruktiven und motivierenden sozialen Arbeitsumfeld des SFB1261 entstanden. Nun ist Platz hier auf formelle Weise meinen tiefsten Dank auszudrücken: Dank für mir entgegengebrachtes Vertrauen; Dank für die vielfältigen Forschungsmöglichkeiten; Dank meinen Horizont auf zahlreichen Messreisen, Konferenzen und Forschungsaufenthalten zu erweitern; Dank für die fachlichen sowie freundschaftlichen Diskussionen; Dank für die Freundschaften; Dank für die gegenseitige Unterstützung über die Grenzen der eigenen Arbeitsgruppe und Arbeitszeit hinaus; Dank für gemeinsame Zeit bei Döner, Kaffee, Kuchen und Eis; Dank fürs Zuhören; Dank fürs Dasein und Dank für die allgegenwärtige Liebe meiner Familie.

Mein Dank gebührt namentlich...

aktuellen und ehemaligen Mitgliedern der Arbeitsgruppe Synthese und Realstruktur, allen voran meinem Doktorvater *Lorenz Kienle*, sowie *Ulrich Schürmann, Katrin Brandenburg, Christin Szillus, Viktor Hrkac, Grit Köppel, Torben Dankwort, Julian Strobel, Marius Kamp, Ole Gronenberg, Henrik Groß, Irina Plesco und Niklas Kohlmann,*

allen Mitgliedern des Sonderforschungsbereichs 1261 "Magnetoelectric Sensors: From Composite Materials to Biomagnetic Diagnostics", insbesondere meiner Kollegen: *Dirk Meyners, Sören Kaps, Philipp Jordt, Bridget Murphy, Lars Thormählen, Matic Klug, Simon Fichtner, Sabrina Curtis und Jeffrey McCord,*

meinen weiteren Kooperationspartnern: *Andriy Lotnky, Viola Duppel, Ion Tiginyanu, Tudor Braniste, Oleg Lupan und Dave Johnson,*

meinen Kollegen und Freunden aus Studienzeiten: *Anne Kittmann, Justin Jetter, Fabian Schütt, Daria Smazna, Alexander Vahl.*

den Mitgliedern der Prüfungskommission, die sich der Bewertung dieser Disseration angenommen haben, sowie der Deutschen Forschungsgemeinschaft, die meine Arbeit an dieser Promotion finanziert hat.

Zuletzt danke ich meinen liebevollen Eltern *Martina und Ingo*, meinem Bruder *Felix*, die mir jederzeit eine moralische Unterstützung sind.

Publications

During my time as PhD student I took part in a plethora of material studies providing detailed nanoscale structural and chemical analysis. Up to date, their majority led to publication in international scientific journals with the scope of materials research. In the following, a full list of these contributions, divided into First Author and Co-Author publications is presented in inverse chronological order. These articles were selected for discussion with respect to the scope of this manuscript and are included as full articles referring to their original journal publication. Publications which are not in the scope of this manuscript are listed as "other".

First author contributions

[1] **N. Wolff**, P. Jordt, J. Jetter, H. Vogt, A. Lotnyk, K. Seemann, S. Ulrich, E. Quandt, B. M. Murphy, L. Kienle: Heteroepitaxy in ultra-thin FeCo/TiN Nanolayer Films", sent to review by *Materials Characterization* (02.02.2020).

[2] **N.Wolff**, V. Ciobanu, M. Enachi, M. Kamp, T. Braniste, V. Duppel, S. Shree, S. Raevchi, M. Medina-Sánchez, R. Adelung, O. Schmidt, I. Tiginyanu, L. Kienle: Advanced Hybrid GaN/ZnO nano-Architectured Microtubes for fluorescent Micromotors driven by UV-light, *Small* 16, 1905141 (2019).

[3] **N. Wolff**, V. Hrkac, J. J. Ditto, V. Duppel, Y. K. Mishra, D. C. Johnson, R. Adelung, L. Kienle: Crystallography at the nanoscale, planar defects in ZnO nanospikes. *J. Appl. Cryst.* 52, 1009-1015 (2019).

[4] **N. Wolff**, P. Jordt, T. Braniste, V. Popa, E. Monaico, V. Ursaki, A. Petraru, R. Adelung, B. M. Murphy, L. Kienle, I. Tiginyanu: Modulation of Electrical Conductivity and Lattice Distortions in Bulk HVPE-Grown GaN, *ECS J. Solid State Sci. Technol.* 8, 141–146 (2019).

Co-author contributions

[1] S. Curtis, **N. Wolff**, D. Dengiz, H. Lewitz, J. Jetter, L. Bumke, E. Yarar, L. Thormählen, L. Kienle, D. Meyners, E. Quandt: Magnetoelectric Composites on Ultra-Low Fatigue TiNiCu Shape Memory Alloy Thin-Films, *Journal of Materials Research* 35, 1298-1306 (2020).

[2] L. Siebert, **N. Wolff**, N. Ababii, M.-I. Teresa, O. Lupan, A. Vahl, V. Duppel, H. Qiu, M. Tienken, M. Mirabelli, V. Sontea, F. Faupel, L. Kienle, R. Adelung: Facile Fabrication of Semiconducting Oxide Nanostructures by Direct Ink Writing of Readily Available Metal Microparticles and their Application as Low Power Acetone Gas Sensors, *Nano Energy* 70, 104420 (2020).

[3] E. C. Hadland, H. Jang, **N. Wolff**, R. Fischer, A. C. Lygo, G. Mitchson, D. Li, L. Kienle, D. G. Cahill, D. C. Johnson, Ultralow Thermal Conductivity of Turbostratically Disordered $MoSe_2$ Ultra-thin Films and Implications for Heterostructures, *Nanotechnology* 30, 285401 (2019).

[4] S. Fichtner, **N. Wolff**, F. Lofink, L. Kienle, B. Wagner, AlScN: A III-V Semiconductor based Ferroelectric, *Journal of Applied Physics* 125, 114103 (2019).

[5] O. Lupan, V. Postica, **N. Wolff**, J. Su, F. Labat, I. Ciofini, H. Cavers, R. Adelung, O. Polonskyi, F. Faupel, L. Kienle, B. Viana, T. Pauporté: Low-Temperature Solution Synthesis of Au-Modified ZnO Nanowires for Highly Efficient Hydrogen Nanosensors, *ACS Appl. Mater. Interfaces* 11, 32115–32126 (2019).

[6] A. Piorra, V. Hrkac, **N. Wolff**, C. Zamponi, V. Duppel, J. Hadermann, L. Kienle, E. Quandt: $(Ba_{0.85}Ca_{0.15})(Ti_{0.9}Zr_{0.1})O_3$ Thin Films prepared by PLD: Relaxor Properties and Complex Microstructure, *Journal of Applied Physics* 125, 244103 (2019).

[7] M. Hoppe, O. Lupan, V. Postica, **N. Wolff**, V. Duppel, L. Kienle, I. Tiginyanu, R. Adelung: $ZnAl_2O_4$-Functionalized Zinc Oxide Microstructures for Highly Selective Hydrogen Gas Sensing Applications, *physica status solidi (a)* 215, 1700772 (2018).

[8] O. Lupan, V. Postica, **N. Wolff**, O. Polonskyi, V. Duppel, V. Kaidas, E. Lazari, N. Ababii, F. Faupel, L. Kienle, R. Adelung: Localized Synthesis of Iron Oxide Nanowires and Fabrication of High Performance Nanosensors Based on a Single Fe_2O_3 Nanowire, *Small* 13, 1602868 (2017).

[9] S. Fichtner, **N. Wolff**, G. Krishnamurthy, A. Petraru, S. Bohse, F. Lofink, S. Chemnitz, H. Kohlstedt, L. Kienle, B. Wagner: Identifying and Overcoming the Interface Originating C-Axis Instability in Highly Sc Enhanced AlN for Piezoelectric Micro-Electromechanical Systems, *Journal of Applied Physics* 122, 035301 (2017).

[10] D. Smazna, **N. Wolff**, S. Shree, F. Schuett, Y. K. Mishra, L. Kienle, R. Adelung: Enhancing the Conductivity of ZnO Micro- and Nanowire Networks with Gallium Oxide, *in Proceedings of the 2017 IEEE 7th International Conference Nanomaterials: Application & Properties (nap), A. D. Pogrebnjak, V. Novosad, P. Zukowski, S. I. Protsenko, Y. Shabelnyk, Eds. (IEEE, New York, 2017)*, p. UNSP 01FNC07 (2017).

[11] U. Schürmann, C. Chluba, **N. Wolff**, D. Smazna, R. Lima de Miranda, P. Junker, R. Adelung, E. Quandt, L. Kienle: Functional NiTi grids for *in situ* straining in the TEM, *Ultramicroscopy* 182, 10–16 (2017).

Others

[1] A. Vahl, O. Lupan, D. Santos-Carballal, V. Postica, S. Hansen, H. Cavers, **N. Wolff**, M.-I. Terasa, M. Hoppe, A. Cadi-Essadek, T Dankwort, L. Kienle, N. H. de Leeuw, R. Adelung, F. Faupel, Journal of Materials Chemistry A. (2020). doi: 10.1039/D0TA03224G

[2] I. Plesco, T. Braniste, **N. Wolff**, L. Gorceac, V. Duppel, B. Cinic, Y. K. Mishra, A. Sarua, R. Adelung, L. Kienle, I. Tiginyanu: Aero-ZnS Architectures with dual Hydrophilic-Hydrophobic Properties for Microfluidic Applications, *APL Materials* 8, 061105 (2020).

[3] J. Rodrigues, M. Hoppe, N. B. Sedrine, **N. Wolff**, V. Duppel, L. Kienle, R. Adelung, Y. K. Mishra, M. R. Correia, T. Monteiro: $ZnAl_2O_4$ decorated Al-doped ZnO tetrapodal 3D Network: Microstructure, Raman and Detailed Temperature Dependent Photoluminescence Analysis, *Nanoscale Advances* 2, 2114-2126 (2020).

[4] X. Tao, H. Jin, M. Mintken, **N. Wolff**, Y. Wang, R. Tao, Y. Li, H. Torun, J. Xie, J. Luo, J. Zhou, Q. Wu, S. Dong, J. Luo, L. Kienle, R. Adelung, Y. K. Mishra, Y. Q. Fu: Three-Dimensional Tetrapodal ZnO Microstructured Network Based Flexible Surface Acoustic Wave Device for Ultraviolet and Respiration Monitoring Applications, *ACS Applied Nano Materials* 3, 1468-1478 (2020).

[5] F. Schütt, M. Zapf, S. Signetti, J. Strobel, H. Krüger, R. Roeder, J. Carstensen, **N. Wolff**, J. Marx, T. Carey, M. Schweichelt, M. Terasa, L. Siebert, H.-K. Hong, S. Kaps, B. Fiedler, Y. Mishra, Z. Lee, N. Pugno, L. Kienle, A. Ferrari, F. Torrisi, C. Ronning, R. Adelung: Conversionless Efficient and Broadband Laser Light Diffusers for High Brightness Illumination Applications, *Nature Communications* 11, 1437 (2020).

[6] C. T. Koops, S. B. Hrkac, M. Abes, P. Jordt, J. Stettner, A. Petraru, H. Kohlstedt, V. Hrkac, **N. Wolff**, L. Kienle, O. H. Seeck, G. Nisbet, O. M. Magnussen, B. M. Murphy: Elastic Coupling at Epitaxial Multiferroic Interfaces: in situ X-ray Studies of Electric Field Induced Strain, *in 4th International Conference on Nanotechnologies and Biomedical Engineering, I. Tiginyanu, V. Sontea, S. Railean, Eds. (Springer International Publishing, 2020), IFMBE Proceedings*, 187–191 (2020).

[7] V. Postica, I. Paulowicz, O. Lupan, F. Schütt, **N. Wolff**, A. Cojocaru, Y.K. Mishra, L. Kienle, R. Adelung: The Effect of Morphology and Functionalization on UV Detection Properties of ZnO Networked Tetrapods and Single Nanowires, *Vacuum* 166, 39-398 (2019).

[8] V. Hrkac, **N. Wolff**, V. Duppel, I. Paulowicz, R. Adelung, Y. K. Mishra, L. Kienle: Atomic Structure and Crystallography of Joints in SnO_2 Nanowire Networks, *Appl. Microsc* 49, 1 (2019).

[9] O. Lupan, V. Postica, M. Hoppe, **N. Wolff**, O. Polonskyi, T. Pauporté, B. Viana, O. Majérus, L. Kienle, F. Faupel, R. Adelung: PdO/PdO_2 Functionalized ZnO: Pd Films for Lower Operating Temperature H_2 Gas Sensing, *Nanoscale* 10, 14107–14127 (2018).

[10] I. Paulowicz, V. Postica, O. Lupan, **N. Wolff**, S. Shree, A. Cojocaru, M. Deng, Y. K. Mishra, I. Tiginyanu, L. Kienle, R. Adelung: Zinc Oxide Nanotetrapods with Four Different Arm Morphologies for Versatile Nanosensors, *Sensors and Actuators B: Chemical* 262, 425–435 (2018).

[11] O. Lupan, **N. Wolff**, V. Postica, T. Braniste, I. Paulowicz, V. Hrkac, Y. K. Mishra, I. Tiginyanu, L. Kienle, R. Adelung: Properties of a Single $SnO_2 : Zn_2SnO_4$ – Functionalized Nanowire Based Nanosensor, *Ceramics International* 44, 4859–4867 (2018).

[12] R. A. Henning, T. Leichtweiss, D. Dorow-Gerspach, R. Schmidt, **N. Wolff**, U. Schürmann, Y. Decker, L. Kienle, M. Wuttig, J. Janek: Phase Formation and Stability in TiO_x and ZrO_x thin films: Extremely Sub-Stoichiometric Functional Oxides for Electrical and TCO Applications, *Zeitschrift für Kristallographie - Crystalline Materials* 232, 161–183 (2017).

[13] M. Krengel, A.-L. Hansen, M. Kaus, S. Indris, **N. Wolff**, L. Kienle, D. Westfal, W. Bensch: CuV_2S_4: A High Rate Capacity and Stable Anode Material for Sodium Ion Batteries, *ACS Appl. Mater. Interfaces* 9, 21283-21291 (2017).

[14] N. Faraji, C. Ulrich, **N. Wolff**, L. Kienle, R. Adelung, Y. K. Mishra, J. Seidel: Visible-Light Driven Nanoscale Photoconductivity of Grain Boundaries in Self-Supported ZnO Nano- and Microstructured Platelets, *Advanced Electronic Materials* 2, 1600138 (2016).

[15] M. Abes, C. T. Koops, S. B. Hrkac, J. McCord, N. O. Urs, **N. Wolff**, L. Kienle, W. J. Ren, L. Bouchenoire, B. M. Murphy, O. M. Magnussen: Domain Structure and Reorientation in $CoFe_2O_4$, *Phys. Rev. B* 93, 195427 (2016).

[16] M. Deng, V. Hrkac, U. Schürmann, B. Erkartal, **N. Wolff**, K. Gerwien, B. Hesseler, F. Beiroth, W. Bensch, V. Duppel, L. Kienle: Nanocomposite CdSe/Cr_2Se_3: Synthesis, Characterization, and *in situ* Transformation Study, *Zeitschrift für anorganische und allgemeine Chemie* 641, 214–220 (2015).

Contents

Chapter 1

Introduction

The presented thesis is thematically divided into two parts. The first part reports about the development of magnetoelectric sensors in context of biomagnetic sensing. Here, the emphasis is put on material studies and their nanoanalytical characterization. The second part focuses on solid state gas sensors in the context of breath monitoring for medical applications.

Medical analysis and diagnostics in the clinical environment is often sensed tedious and uncomfortable, at least in the patients' perspective. For the clinician, the monitoring and diagnostic tools shall be designed to their convenience, regarding physical handling or and reliability with minor tolerances. That is especially true for standard tools such as electrocardiography (ECG), which is used for more than 100 years, despite its cumbersome application on the patient body.[1], [2] ECG is recording the electric potentials by connecting electrodes to the human skin in order to retrieve information on the electrophysiological signals of cardiac activity. The similar electroencephalograpy (EEG), in which electrodes are adhered to the human scalp is commonly used to monitor brain activity in case of neuronal diseases. Alternatively, biomagnetic fields can provide richer diagnostic information of physiological activity and improves spatial diagnostics for targeted treatments, e.g. deep brain stimulation (DBS). The first measurements of biomagnetic fields inherent to physiological cardiac activity was sufficiently achieved in 1970 with the innovation of a Superconducting Quantum Interference Device (SQUID).[3] These SQUID based magnetometers operate superconducting materials cooled down to cryogenic temperatures by a liquid Helium ($T = 4\,K$). The working principle uses a constant driving current through a discontinuous superconductive ring and the change of electrical potentials induced by compensating currents as result of quantized changes of the external magnetic flux. This development enabled the first reliable contactless magnetocardiographic (MCG) measurements with comparable quality to ECG recordings.[4] Two years later, in 1972, also magnetic recordings of the human brain activity by magnetoencephalography (MEG) were demonstrated to be comparable in quality with EEG measurements.[5] In general, the measurement of biomagnetic fields requires magnetometers with high sensitivity in the order of $1\,fT/\sqrt{Hz}$ - $1\,pT/\sqrt{Hz}$ in the frequency range of 0.1-1000 Hz. Further, the sensors shall allow for a vector field analysis of the magnetic flux to compute 3D models and allow for measurements under ambient conditions. The SQUID technology greatly succeeds in sensitivity but requires specially designed rooms with magnetic shielding against the earth magnetic field and a liquid helium cooling system, which is associated with extremely high costs. However, it took more than 40 years of development to get the first stationary SQUID based system installed in Germany in 2013, up to 20 systems are installed all over Germany in the present. Despite these technological advances, the development of cost effective and portable diagnostic tools as alternatives for SQUID systems without magnetic shielding are highly demanded for future convenient and effective treatments.

In this respect, tremendous research efforts are conducted on new types of magnetometers, since fluxgate (FG)[6] or search coil (SC)[7] magnetometers do not display the required sensitivity or frequency bandwidth. The sensitivity and frequency bandwidth of biomagnetic signals demanded for individual medical application are displayed in Figure 1.1 showing the characteristics of different magnetometers. From Figure 1.1 it is apparent that only SQUID systems and the recently developed atomic magnetometers show the sensitivity and bandwidth for the desired application in MCG and MEG diagnostics. Atomic magnetometers measure the magnetic field through a direct relation between the magnetic field and the orientation of atomic spins. One prominent example providing comparable sensitivity to SQUIDs are optically pumped magnetometers (OPM).[8] So- called Spin Exchange Relaxation-Free (SERF) magnetometers operate with a high density alkali-metal vapor and have a fundamental sensitivity limit of $10^{-17}\,\mathrm{T}$ which is superior to SQUID sensors.[9] However, theoretical calculation demonstrated a trade-off between sensitivity and bandwidth, exemplary resulting in $10\,\mathrm{fT}/\sqrt{\mathrm{Hz}}$ for 1-100 Hz bandwidth in case of a Rb vapor and the OPM's vapor-cell dimensions. The OPMs provide a portable alternative measurement setup only requiring medium operation temperatures $< 200\,^{\circ}\mathrm{C}$. The working principle of these sensors exploit the optical transparency of an alkali-metal vapor with respect to the alkali-atom energy state and an external magnetic field. These vapor cells work in a local magnetically shielded environment by placing the ferrite coils within the MEMS device resulting in a tremendous benefit to sensor noise reaching $0.75\,\mathrm{fT}/\sqrt{\mathrm{Hz}}$[10]. However, complementary measurements have been demonstrated to be capable to detect $12\,\mathrm{pT}/\sqrt{\mathrm{Hz}}$ without magnetic shielding.[11] Further, the OPM technology exhibits the potential to perform vector measurements with a single cell setup.[12] Despite these first efforts, this technique is still under development and also requires reliable data processing software for the clinician to be conveniently used in the future.

The development of an alternative sensor concept has been pursued by researchers in Kiel throughout the last decade to provide a cost effective platform for biomagnetic measurements with high convenience for both clinicians and patients. The anticipated new sensor technology must be highly sensitive to biomagnetic fields with a limit of detection (LOD) of the order of $< 1\,\mathrm{pT}/\sqrt{\mathrm{Hz}}$ in accordance to allow the targeted low and high frequency medical applications such as MCG and DBS. Ideally, the new sensor fulfills a variety of requirements which are a small size, consistent with standard MEMS (microelectromechanical system) fabrication processes, room temperature operation, measuring outside a magnetic shielded chamber and allow for vectorized monitoring without physical contact. In a simple explanation, these sensors exploit the physical coupling between a magnetostrictive and a piezoelectric material forming a magnetoelectric (ME) composite. The ME effect describes the magnetoelastic coupling of magnetically induced strain into a strain sensitive material which responds with a measurable output voltage; a mechanism which will be further outlined in Chapter 2 *Sensor Concepts*. The materials development is substantial to these goals as the materials properties are strongly related to the crystal and defect structure, chemical composition, electronic structure, lattice strains and order/disorder phenomena. It is therefore of tremendous importance to investigate suitable materials and their coupling by analytical methods from macro- to nanoscale by X-ray diffraction and electron microscopy. Especially, techniques of transmission electron microscopy (TEM) offer sub-atomic resolution with sharp and high contrast even in atomic imaging modes. The ability to analyze cross-section through the composite allows for a unique imaging opportunity to investigate all functional layers. The studies

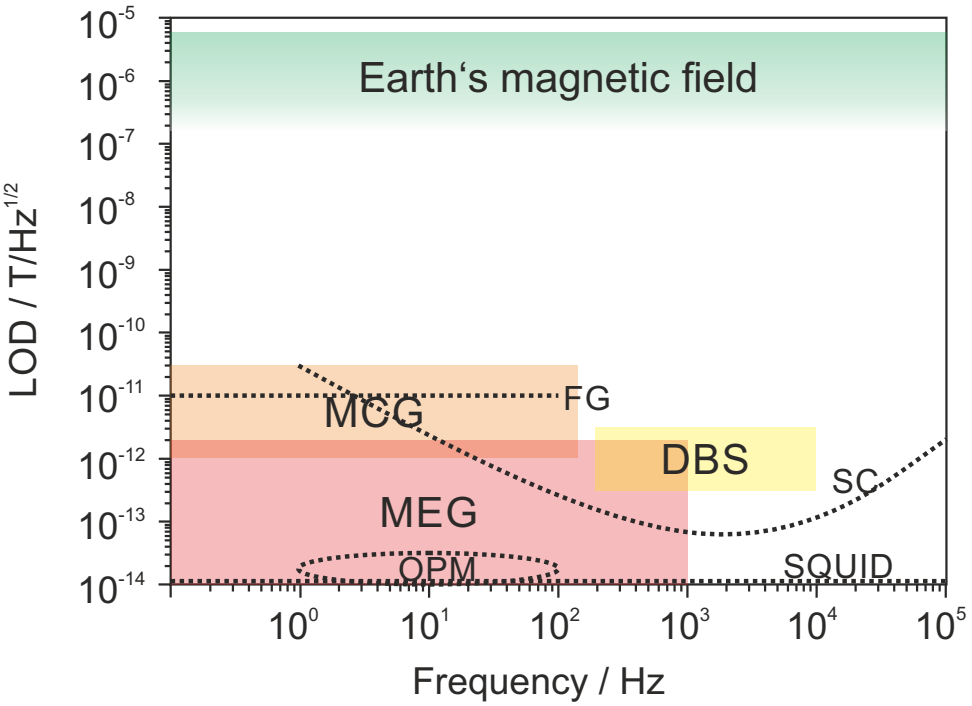

FIGURE 1.1: Schematic illustration showing the required magnetic sensitivity (Limit of detection, LOD) as a function of frequency for various biomedical applications and the detection limits of common magnetometers. (Biomedical application: *MCG = magnetocardiography, MEG = magnetoencephalography, DBS = deep brain stimulation.* Magnetometers: *FG = fluxgate,[6] SC = search coil,[7] OPM = optically pumped magnetometer,[8] SQUID = superconducting quantum interference devices.[13]*)

presented in this thesis have been conducted in the framework of the CRC1261- *Magnetoelectric Sensors: From Composite Materials to Biomagnetic Diagnostics* funded by the *Deutsche Forschungsgemeinschaft*. Therein, I focused on the nanoscale analysis of single materials for the piezoelectric and ferromagnetic phases and their composites using dedicated methods of TEM.
In the following chapters, I will introduce into the required materials properties (Section 2.1) for ME sensing and exemplary outline specific sensor concepts (Section 2.2). The applied methods and special techniques of TEM will be described in Chapter 3 *Advanced Methods* providing special discussions on techniques to measure atomic displacements in crystalline materials (Section 3.2) and atomic near-range order in amorphous materials (Section 3.3) on the nanoscale. The results of these TEM studies have been published in scientific and peer reviewed journals and are highlighted in Chapter 4 *Materials for Magnetoelectric Sensors* (Sections 4.1 - 4.3).

In the second part of this thesis, I will discuss the important development of breath sensing as non-invasive method to monitor the patients health condition, e.g. in case of diabetes. The desired materials properties and their function will be reviewed in Section 2.3 and the conducted materials and sensor studies are highlighted in context of hydrogen and acetone breath sensing in Chapter 5 *Sensors for Breath Monitoring*.

The thesis closes on a summary of the published results and concludes on the current status of ME sensor development in outlook to future strategies in the perspective to materials

studies.

Chapter 2

Sensor Concepts

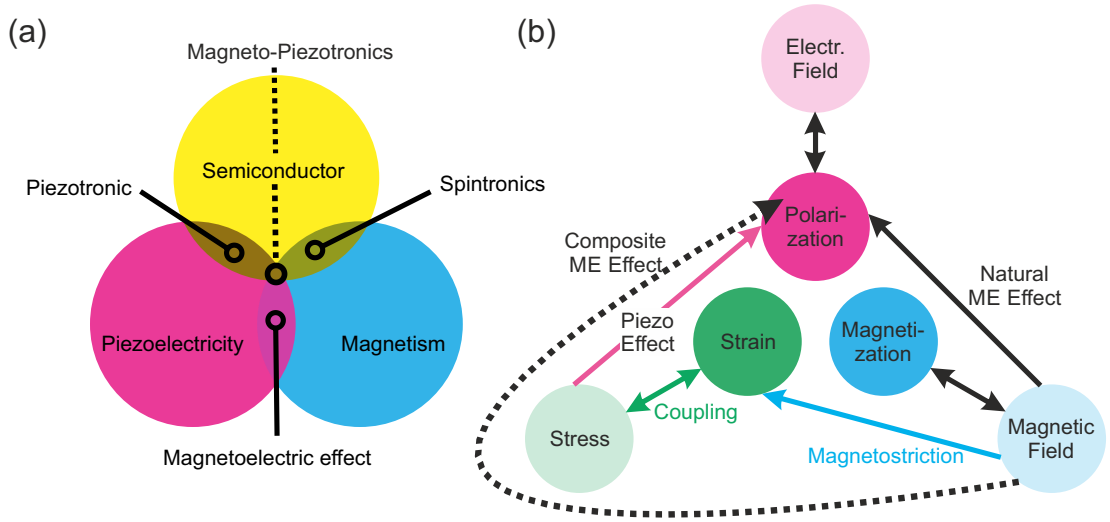

FIGURE 2.1: (a) Three-phase-coupling among the electronic structure of semiconductors, magnetism and piezoelectricity results in new material properties grouped into the fields of piezotronics, spintronics, magnetoelectrics and magneto-piezotronics. [Adapted from [14].] (b) The schematic representation of the ME effect displays the natural ME coupling between a magnetic field and the polarization as well as the composite effect, where the magnetostrictive strain is coupled to the piezoelectric phase.

The combination of physical material properties is highly interesting for the development of future micro- and nanoelectronics. The key objective is the interplay between magnetism, piezoelectricity and semiconductor properties in single material or material composites, which is schematically depicted in Figure 2.1(a). The coupling between semiconductor and piezoelectric properties is described as *Piezotronics* and the magnetoelastic coupling between piezoelectricity and magnetism is described by the magnetoelectric (ME) effect. The natural and composite ME effects are illustrated in Figure 2.1(b). The underlying mechanism of the composite effect uses the effect of magnetostriction to induce a piezoelectric voltage in a piezoelectric material via the transfer of stress. The natural ME effect describes a material property of small magnitude compared to the composite effect and can be generally neglected for technical relevant applications.[15], [16] Hence, magnetic materials which respond to small magnetic fields via a large change of dimensions and piezoelectric materials in which a prominent polarization is induced by a change of dimensions have to be identified. Both research areas will be introduced in the following sections in context of the development of magnetoelectric sensors.

2.1 Materials for ME Sensors

Piezoelectric Materials

The ability to induce an electric dipole moment in a crystalline material by the application of strain is described via the piezoelectric effect. Piezoelectricity is an inherent material property of crystal structures without inversion symmetry, which is further specified by the point group. This is true for 21[1] of the total of 32 point groups.[17] In the CRC, the identification and tailoring of piezoelectric properties of thin film piezoelectrics with respect to the desired ME sensor is pursued. Specifically, piezoelectric thin films with a large out of plane polarization P related to large effective (clamped film) longitudinal $d_{33,f}$, or transversal $e_{31,f}$ coefficients, which are representing the effect size in parallel and perpendicular polarization direction are desired. These coefficients are not constant material properties but can be manipulated, e.g. by film thickness.[18]–[22] High $d_{33,f}$ coefficients are realized in ferroelectric thin films of $BaTiO_3$ (BTO) (30-100 pm/V)[23], [24] or $Pb[Zr_xTi_{1-x}]O_3$ (PZT) (100-170 pm/V)[25], [26]. However, their applicability for ME sensors is limited by their high dielectric loss tanδ (PZT: 2.4-3.6 %)[25] and deposition processes which require high temperatures and which are not suitable for standard MEMS process chains. The dielectric loss tanδ is a measure of the dissipated energy during on polarization cycle, i.e. the area of the ferroelectric hysteresis P-E. With this in mind, non-ferroelectric materials with wurtzite-type structure such as ZnO, GaN or AlN still exhibit a decent polarization $d_{33,f}(AlN) = 5.5\,pm/V$ but show far smaller dielectric losses $tan\delta = 0.025\,\%$.[22] The implementation of AlN thin films is advantageous from an engineering perspective, since they can be grown by sputter deposition which is a commonly available standard MEMS fabrication process.[27] Further, the substitution of AlN with ScN demonstrated the potential for a nearly fivefold improvement of the longitudinal piezoelectric coefficient.[28] Moreover, a variety of piezoelectric materials such as $(Ba_{1-x}Ca_x)(Ti_{0.9}Zr_{0.1})O_3$ (BCZT), $Pb(Mg_{1/3}Nb_{2/3})O_3$–$PbTiO_3$ (PMN-PT), PZT or ZnO have been studied within the past years and their application for ME sensors was evaluated.[29]–[34] Studies using TEM on piezoelectric materials have been conducted within this thesis on AlScN, BCZT, ZnO, GaN and $MoSe_2$ and are discussed in Chapter 4 and Section 4.1.

Magnetostrictive Materials

Sensing biomagnetic fields reaching from the pT to fT regime requires special attention to the quality and properties of the magnetostrictive component. The transducer function of the MS phase is converting the sensing magnetic field input into a measurable sensor voltage output via the coupling to the piezoelectric phase, but also determines the sensor noise, which is especially relevant for low frequency application.[35], [36]
Magnetostriction is an inherent material property of ferromagnetic materials in which a direct exchange coupling between magnetic and mechanical energies is present via spin-orbit interactions, resulting in a change in physical dimensions under the influence of an external magnetic field. In context of magnetic field sensing, the piezomagnetic coefficient $\frac{\partial\lambda}{\partial H}$ describes the length change ΔL of the magnetostrictive phase in a magnetic field and must be as large as possible (saturation magnetostriction: λ_s). In an idealized model for application in ME sensors, the largest effect size of magnetostriction should be achieved at magnetic saturation using only small excitation fields H_s.

[1] Materials with point group 432 are non-centrosymmetric, but do not exhibit the piezoelectric effect.

Potential ferromagnetic materials which partially meet these requirements are rare earth compounds RFe_2 (R: rare earth metal) and amorphous metallic glasses containing atoms of ferromagnetic iron and cobalt or nickel, with essentially no magnetocrystalline anisotropy energy contribution making them magnetically soft. With respect to an increased piezomagnetic response, polycrystalline films of alloy $TbFe_2$ yield a giant saturation magnetostriction of $\lambda_s = 2630$ ppm with the remedy of having a high $H_s > 25$ kOe[37] or 280 ppm in amorphous films showing saturation over 15 kOe.[38] Adding $DyFe_2$ to $TbFe_2$ was shown to magnetically soften the material under the expense of $\lambda_s = 500$ ppm and $H_s = 500$ Oe.[39] Alternative approaches exploit multilayers of TbFe and FeCo or FeCoSiB to realize a decent magnetostriction and high saturation magnetization paired with low saturation field strength reaching 200 Oe.[40] That was enabled by the FeCo-based amorphous glass $(Fe_{90}Co_{10})_{78}Si_{12}B_{10}$, which shows an acceptable magnetostriction of $\lambda_s = 158$ ppm and a very small H_s of 20 Oe.[41] In comparison, FeNi-based alloys exhibit decreased magnetostriction λ_s compared to FeCo-based glasses, making them rather unattractive for ME field sensing application.[42] A promising alternative to FeCoSiB was demonstrated by adding boron to FeGa leading to amorphization at 9-21 at% content. The magnetoelastic properties of these FeGaB thin films show comparable values of $\lambda_s = 45$-70 ppm and $H_s = 15$-30 Oe and $H_c = 0.4$-1 Oe.[43] Thus, the application of FeCoSiB[41] and FeGaB[44], [45] thin films for ME sensors with ultra-high sensitivity has been selected because of their high strain sensitivity.

Concerning the magnetic noise, the magnetic phase must be tailored with respect to its magnetic domain structure and domain wall movement. Pursued strategies involve the incorporation of an exchange-bias system into the magnetic phase[35], [46] and compensating edge-effects by geometrical features. These topics are outlined in detail in the thesis of Matic Jovivcevic Klug "Methodological Reduction of Magnetically Induced Noise in Magnetic Multilayers for Sensor".[47]
TEM studies on magnetostrictive materials such as FeCoSiB thin films and alternative concepts of the magnetostrictive component including high temperature stable FeCo/TiN multilayer thin films or exchange spring concepts of FeNi/MnIr multilayers are discussed in Sections 3.3 and 4.2.

2.2 ME Sensor Concepts

The typical ME sensor consists of sputtered thin films of a magnetostrictive FeCoSiB and the piezoelectric AlN on a Si cantilever substrate enabling the measurement of magnetic fields as depicted in Figure 2.2. The operation in a magnetic field $\vec{H}$ generates a measurable polarization $\vec{P}$ ($\rightarrow$electric field: $\vec{E}$) by magnetoelastic coupling from the MS phase to the piezoelectric phase. The magnetoelectric coefficient specifying the size of the ME effect is given by

$$\alpha_{ME} = \frac{\partial \vec{E}}{\partial \vec{H}} = \frac{\partial \vec{E}}{\partial \sigma} \frac{\partial \sigma}{\partial \lambda} \frac{\partial \lambda}{\partial \vec{H}} = g_{ij}\, k_c\, d_{kl}^{m},$$

where $\frac{\partial \lambda}{\partial \vec{H}}$ describes the strain ε induced by the magnetic field. The partial derivative $\frac{\partial \vec{E}}{\partial \sigma}$ describes the piezoelectric effect in the piezoelectric phase and $\frac{\partial \sigma}{\partial \lambda}$ the transduction of the magnetostrictive strain σ to a stress in the piezoelectric material. Thus, g_{ij}, k_c, and d_{kl}^{m} represent the piezoelectric voltage coefficient ($g_{ij} = (d_{ij}/\varepsilon_{ij})$, here ε_{ij} is the permittivity of the piezoelectric component), an elastic coupling coefficient and the piezomagnetic coefficient, respectively. In order to achieve large magnetoelectric coefficients the piezoelectric phase and

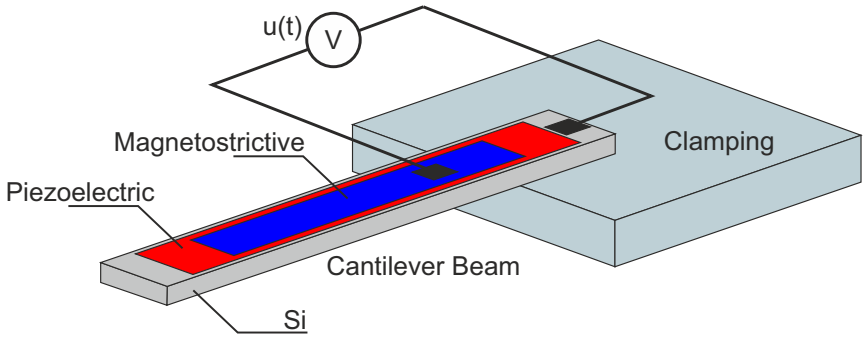

FIGURE 2.2: Schematic illustration of a typical composite ME sensor with a piezoelectric and magnetostrictive phase.

the magnetostrictive phase have to be optimized with respect to these coefficients as well as the elastic-elastic coupling between both phases. In this respect, the combination of AlN and FeCoSiB phases was demonstrated to yield a giant ME coefficient α_{ME} in resonance of 737 V/cm Oe @753 Hz[41] and 5 kV/cm Oe @867 Hz.[48] In comparison, α_{ME} measured in resonance of various other thin film laminates such as AlN/NiMnIn (99 V/cm Oe @5 kHz),[49] polyvinylidene fluoride/FeBSiC (7.2 V/cm Oe @1 kHz),[50] PZT/platinized nickel-zinc ferrite (140 mV/cm Oe @1 kHz)[51] or PZT/$TbDyFe_2$ (4.68 V/cm Oe)[33] and PZT/$TbDyFe_2$ thin films (150 mV/cm Oe @100 Hz)[52] are substantially smaller.

The output voltage amplitude is strongly dependent on the cantilever mechanical resonance frequency f_r based on the cantilever design, enabling the direct detection of magnetic fields with high sensitivity close to f_r. This restriction to the mechanical resonance limits the available bandwidth and suffers from a dramatic reduction in signal amplitude aside f_r and an increased noise level with *1/f* dependence at low biomedical relevant frequencies 1-100 Hz. However, significant sensor improvement at low magnetic field frequencies is achieved by an frequency-conversion approach in which the low frequency signal is up-converted to the sensor's mechanical resonance by a magnetic modulation field.[53]

Besides direct detection, strategies to up-convert off-resonance signals have been developed which actively modulate the ME composite by magnetic bias fields[53], electric fields[54], [55] or utilizing the delta-E effect,[56], [57] which describes the softening of the elastic modulus E in a magnetic field. A completely different approach of using the delta-E effect for magnetic field sensing employs the phase change between Love waves, which are horizontally polarized surface waves traveling in a SiO_2 guiding layer. The phase shift is generated, when a mechanically coupled ferromagnetic film (e.g. FeCoSiB) changes its elastic properties in an external magnetic field. This design concentrates not only on the change of E but moreover the shear modulus G and has the potential of a magnetic sensitivity 100 $\mathrm{pT}/\sqrt{\mathrm{Hz}}$.[58] These approaches benefit from mechanical resonances and are sensitive to small magnetic fields in the low frequency regime < 1 kHz, but with large bandwidth. Further discussion on the recent development of these magnetometer ME sensors is provided in a joined review by colleagues from Boston and Kiel University.[59] An alternative concept exploits the phenomenon that the magnetoelastic strain induces an energy band bending in piezoelectric semiconductors when interfaced to a metal of higher work function leading to dramatic changes in the charge carrier transport properties. This piezotronic effect describes a change in the overall current,

which is easily measurable as a piezotronic current.[60], [61] Further approaches pursue generator/transducer concepts based on the capacitive modulation between an electret material and an magnetostrictive film on a cantilever beam.[61] The current state of the achieved sensitivity of these sensor concepts are summarized in Table 2.1. In the following, the delta-*E* effect sensor concept as well as the alternative piezotronic concept will be briefly discussed to point out the relevant material aspects.

Delta-*E* Effect Sensor Concept

The concept of the delta-*E* effect sensor is based on the mechanical softening of a magnetostrictive material subjected to a magnetic modulation field. The contribution of the magnetostriction to this magnetic modulation field $H_{ac}(t)$ in the small strain regime decreases the young's modulus E_H of the magnetic material:

$$\Delta E = E_M - E_H,$$

where E_M is the Young's modulus at a fixed magnetization and considering pure elastic strain. The change in mechanical stiffness of the magnetostrictive phase, thus, gives rise to a shift in mechanical resonance frequency using magnetic thin film coated Si substrates in the presence of $H_{ac}(t)$, with

$$f_0 \propto \sqrt{E_{eff}},$$

where $\sqrt{E_{eff}}$ is the effective Young's modulus of the coated cantilever, the shift in resonance frequency refers to

$$\Delta f(t) = f_0(E_{eff,M}) - f_0(E_{eff,H}).$$

The change in resonance frequency can be read-out optically via the change in oscillation amplitude[57], [62] or electrically in combination with a piezoelectric phase.[56] In order to improve the sensitivity of delta-*E* effect sensors, researchers from Kiel identified and described a few major factors: (1) The quality of the piezoelectric phase can increase the sensitivity of the sensor since the frequency dependence of *E(f)* is related to the piezoelectric coefficients which are further interrelated with signal to noise ratio and dielectric losses $\tan\delta$.
(2) The quality factor *Q* of the sensor which describes the damping of a resonator and is determined by its design or operation environment, e.g. vacuum.[56], [63] Theoretical modeling of experimental results proposed, that the quality factor has direct influence on the signal-to-noise ratio and that the LOD can be improved with a scaling factor proportional to $Q^{3/2}$. This is argued to be valid if thermal-mechanical noise is the dominant noise source and electric and magnetic noise are sufficiently suppressed.[63], [64]
(3) The quality of the magnetic material: First, the magnitude of the delta-*E* effect in the magnetoelastic material is highest at maximum magnetostrictive susceptibility, which is achieved by a large saturation magnetostriction λ_s at small magnetic field needed for saturation H_s.[62] Second, magnetic noise contributions arise e.g. when magnetic domain walls move, coalesce and become pinned and released at defects in the magnetic structure, a phenomenon called *Barkhausen* noise.[65], [66] Therefore, strategies to reduce the magnetic noise by magnetic domain control or introduction of single domain states are pursued on the basis of exchange-bias concepts.[35], [46] The exchange-bias also introduces a bias magnetic field inside the sensor to reduce the impact of external stimuli to operate the sensor close to its ferromagnetic resonance.

(4) The frequency dependence of the delta-E effect of the Young's modulus and the magnetic sensitivity can be described as a function of the dynamic differential susceptibility χ of magnetization.[62], [67] The magnitude of the delta-E effect is dependent on a damping factor and decreases with increasing frequency if the damping is large or results in a maximum effect magnitude close to the ferromagnetic resonance if the damping is small. The same argument holds true for the sensitivity, which is an argument for reducing the effect of the magnetic susceptibility meaning a low damping and hence the requirement of very soft magnetic properties.[67]
(5) The delta-E effect significantly depends on the resonance mode shape of the cantilever beam excited at different vibration frequencies which depend on the beam geometry. Analytical mean-field modeling was conducted and compared to experimental data on cantilever beams with specific electrode placement and demonstrated that the magnetic sensitivity can be increased by using the second-order bending modes compared to first-order modes.[68], [69] However, it was reported that the shear mode is advantageous over bending by a factor of 6 in sensitivity if the easy axis of the magnetic thin film is aligned perfectly by 90° with respect to the applied magnetic field. Any deviation by more than 5° results in a significant reduction of ΔE.

In conclusion the delta-E effect approach is highly sensitive to low frequency magnetic fields with no need for an external magnetic bias field. The fully integrable sensor concept works at room temperature, offers a high band width and possesses vector field capability.[57]

The analysis of the single piezoelectric and magnetostrictive materials for ME composites therein plays a decisive role in order to support the process of sensor development at the earliest stage of material deposition and sample annealing. To do so, the manifold analytic capabilities offered by sophisticated methods of transmission electron microscopy with respect to the chemistry and structure as well as the characterization of strain in composites are exploited in the studies outlined in this manuscript. For instance, the piezoelectric properties of AlN or AlScN films strongly depend on the quality of the c-axis texture and oxygen impurities; information which is easily accessed by electron diffraction techniques or analysis of X-ray spectroscopy. Further, the identification of micro- and nanoscale defects such as inversion domain boundaries, misoriented grains, twin defects, voids, chemical segregation or breakdown of magnetic layered structures which determine the quality of the materials are within reach by TEM.

(Magneto-) Piezotronic Sensor Concept

Another promising sensor concept for the detection of low frequency magnetic fields in the low pT to fT range is based on the piezotronic effect arising in semiconducting piezoelectrics in contact with a noble metal having a higher work function. The basic concept behind piezotronics is described in "Fundamental theory of piezotronics" by Yan Zhang, Ying Liu and Zhong Lin Wang: *"Due to polarization of ions in crystals with noncentral symmetry, such as ZnO, GaN, and InN, a piezoelectric potential (piezopotential) is created in the crystal when stress is applied. Electronics fabricated using the inner-crystal piezopotential as a gate voltage to tune or control the charge transport behavior across a metal/semiconductor interface or a p–n junction are called piezotronics."* [70] Basically, any piezoelectric semiconductor can be used for magnetic field sensing in a ME composite geometry applying the piezotronic readout

mechanism. However, the size of the bandgap influences the sensor noise (see Section 4.1.3). In combination with a magnetostrictive material which translates a magnetic field induced strain to the semiconductor, the charge transport over the Schottky barrier is modulated and depends on the sign of strain. In this way a linear relationship between the measurement current and the applied magnetic field is exploited and the applicability of this effect for ME sensor readout has been proven. A simple and not optimized approach using a ZnO needle-shaped crystal showed sensitivity to magnetic fields as low as 380 $\mathrm{pT}/\sqrt{\mathrm{Hz}}$ @ 79.4 Hz [60], AlN thin films on cantilever geometry sensors showed 63 $\mathrm{pT}/\sqrt{\mathrm{Hz}}$ @ 1 kHz and magnetic-induced-piezopotential gated MoS_2 transistors demonstrated to work fine with mT fields.[14] A schematic energy-band diagram depicting the piezotronic effect is shown in Figure 2.3. Here, the strain-induced band bending leads to a modulation of charge transport over a metal-semiconductor (n-type) Schottky contact. Piezoelectric charges accumulate at the interface causing a space-charge region by building up a piezopotential which is related to band bending. The height and width of this Schottky contact are closely interrelated with the charge transport which can be tuned directly by the magnitude and sign of the applied strain. The principal advantage of the piezotronic approach is the internal signal amplification at the Schottky-contact to a metal electrode which can effectively limit capacitive noise sources of wiring. A further discussion about the intrinsic noise sources is included in Chapter 4 Section 4.1.3.

In this context, crystal structure analysis including the investigation of defect states and the quantification of intrinsic and externally induced lattice strains requires sophisticated TEM methods to support the fundamental understanding of the electronic processes at the semiconductor-metal interface. When the materials are doped with foreign atoms to influence their electronic parameters, chemical analysis on the atomic scale is able to visualize the doping atoms distribution and to identify dopant atoms which can cluster at defects, for example.[71], [72] In addition, hollow morphologies of semiconductor GaN are envisioned as component of piezotronic-based sensors. Those materials exhibit nanometer thin crystalline walls and are ideal samples for TEM due to their intrinsic electron transparency.[73]

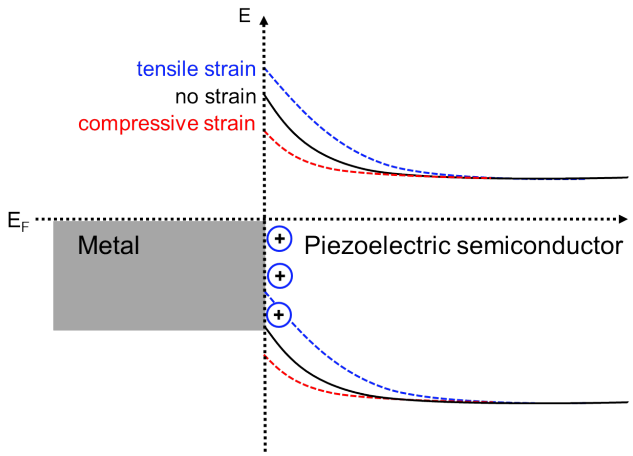

FIGURE 2.3: Schematic illustration of the piezotronic effect at the metal-(n-type) semiconductor interface (Schottky contact). The height of the Schottky contact in dependency of strain is shown for tensile strain (blue) including the accumulation of positive charges at the interface, no strain (black) and compressive strain (red).

TABLE 2.1: Characteristics of ME sensor approaches.

Sensor Concept	**LOD** /pT/$\sqrt{\text{Hz}}$	**Frequency Bandwidth**	**Comments**
Direct ME	300[74] @ 152 Hz	narrow	1/f-noise limits high sensitivity at low f
Magnetic Modulation	60[36]-120[35] @ 10 Hz	large	high power consumption of $B_{ac,mod}$
Electric Modulation	70[54] @ 10 Hz, 30* @ 10 Hz	large	no magnetic bias field is required
Δ-E Effect	100[68] @ 10-100 Hz	large	electric and magnetic biasing needed
SAW	250[58] @ 10 Hz, 70* @ 10 Hz	very large	very large dynamic range of B
Piezotronic Effect	380[60] @ 79.4 Hz	-	-
Soft Hybrid Electret-based Sensor	73* @ 321 Hz	-	-

*not published

2.3 Materials for Breath Sensors

Solid-state gas sensors offer low cost, high sensitivity, good accuracy, stability and durability and are easy to integrate into electronic circuits to advance their application in new generations of smart sensors e.g. capable to detect gaseous species in the human breath for health monitoring. This section will briefly cover the desired physical properties which are prerequisites for solid-state gas sensing and determine the choice of material according to the review by Korotcenkov.[75] Herein, the focus is on semiconducting metal-oxide materials (SMO) to be consistent to the case studies presented in Chapter 5 on *Sensors for Breath Monitoring*. Accordingly, the main mechanism of gas sensing with SMO will be introduced.

The basic sensing mechanism of solid-state gas sensors describes the reversible interaction of gas molecules with the surface states of the solid-state material, leading to a change in conductivity of the material and other physical quantities such as capacitance, work function, mass or optical characteristics. This rather general description of chemical processes which detect gas by a selective chemical reaction using solid-state chemical detection principles is common for all sensors putting no limitations to the materials design, physical, chemical, structural or electrical properties. Hence, it is the materials researchers task to identify the most suitable material with a specific combination of physical-chemical properties to be used in practice for a specified task, location and condition of sensor operation.
Solid-state sensors based on SMO are typically chemiresistive-type sensors with a high surface-to-volume ratio, where the SMO is operated on a heated insulating substrate between metallic electrodes to manipulate the sensor performance stimulating desired chemical reactions and its kinetics thereby changing the density of available charge carriers. The significant changes in the electrical resistance under exposure to reducing or oxidizing gas species can be easily observed and used for detection of changes in the atmospheric composition. Hence, the material of choice strongly influences the sensor properties by the electronic structure of bulk and solid surface and should consider a variety of key properties such as adsorption ability, electrophysical and chemical properties, catalytic activity, thermodynamic stability, crystallographic structure, interface state and compatibility to materials used in gas sensor fabrication. Numerous materials studies pointed out that the operating characteristics are controlled by three distinct factors which are describing the sensors receptor function, representing the ability of the oxide surface to react with the target gas, the transducer function, describing the ability to convert the chemical reaction on the surface to an electric signals and the sensor design and construction.[76]–[79]

The receptor function of SMO is essentially determined by five parameters: the density of charged surface states, the electronic structure, the adsorption/desorption parameters, the catalytic activity of the oxide surface and of course the geometry as smaller structures provide more surface atoms which can participate in the reaction. On the other hand, the transducer function is related to the bandgap, the electroconductivity, the type of conductivity and oxygen diffusion kinetics.
For instance, the density of native charged surface states is an important parameter for the sensitivity threshold of the sensor and should be minimized. The surface potential is a function of the amount of these charged surface states and the partial pressure of the analyte gas in the atmosphere. If the amount of free surface states in the oxide material is too high, the induced surface potential pins the surface Fermi level which reduces the flexibility of the sensor to respond to changes in the gas concentration. Moreover, if the native surface charge is sufficiently

low, the charge of the chemisorbed particles on the surface dominates and the sensitivity to changes in the concentration of gas is high if the semiconductors electronic properties correlate well to the state of its surface. This correlation is found to be strong in semiconductors and SMOs with predominantly ionic bonding, for example SnO_2, ZnO, SiO_2, Ga_2O_3, Al_2O_3 or ZnS. [80]

The electronic structure of the gas-sensing metal oxide is of particular importance since the symmetry of available valence orbitals strongly determines the adsorption properties. In this respect, transition-metal oxides feature d-orbitals resulting in variable oxidation states, crystal field splitting and high defect concentration in contrast to non-transition-metal oxides with d^0 or d^{10} configuration which have mostly *s*- or *p*-symmetry valence orbitals.[81] The oxidation state also controls the type of chemisorption and the formation of defects by oxidation or reduction mechanisms. Pre-transition-metal oxides with d^0 often possess a large bandgap and cannot be reduced or oxidized easily, making those insulating materials not promising for conductometric gas sensors. For transition-metal oxides, only those with d^0 or d^{10} electronic configuration find real gas sensor application due to issues of structural instabilities, a small bandgap and electroconductivity if the *d*-band is partially filled. Hence, post-transition-metal oxides with cations having a filled d^{10} configuration such as ZnO or SnO_2, or transition-metal oxides with empty d^0 configuration such as TiO_2, V_2O_5, WO_3 are practically available.

The adsorption and desorption parameters describe the dynamics of molecules on the metal oxide surface. In the adsorption process, gas molecules can adsorb physically onto the surface in a neutral process or react chemically with the surface charges or already ionosorbed surface species under charge transfer mechansims. Only the latter process of chemisorption controls the change of surface charge and the related potential of metal oxides when exposed to a gas containing atmosphere. With respect to the adsorption/desorption dynamics this means that the material of choice should have a small activation energy of adsorption and a considerably high activation energy of desorption, but keeping the recovery time within practicable limits. In normal atmosphere, the metal oxide surface is covered with adsorbed species of oxygen and water, their adsorption/desorption parameters are critically determining the sensors conductivity response. A simple strategy to reduce the response and recovery time of the sensor is to increase the operating temperature to about 300 °C for which temperature an activation energy of oxygen desorption of 1 eV is optimal.[82] Further improvement of these dynamics and hence the sensor response can be achieved by enhancing the materials conductivity and change of surface potential after exposure to the analyte gas. Such can be achieved for instance by changing the composition of the metal oxide or surface doping adding metal catalyst particles.[83] Surface doping or functionalization by catalysts can lead to a decrease of the activation energy of detected gas adsorption changing the maximum sensor response to lower temperatures.[84]

A high catalytic reactivity of the metal oxide surface to a selective gas is beneficial, since in many gas sensors chemical reactions involving surface oxygen change the surface potential and concentration of point defects. Thereby, the catalytic activity is a function of temperature and is used to determine the sensors operating temperature with maximum sensor response which correlates with the catalytic conversion of detected gas at a certain temperature. Since temperature is also a selective factor for the catalytic reactions taking place on the surface, the operating temperature can be used for selective sensing of targeted gas molecules. However, the catalytic activity of the metal oxide itself is not the predominant factor for a materials

choice, but is often paired with catalytic metal particles providing the desired functions. So, operating temperatures can be reduced with respect to power dissipation, optimization of gas response and improvement of reliability, durability and safety.

In conclusion to the receptor functions, the material of choice should be a semiconducting metal oxide with strong contribution of ionic bonding which is offering a low density of native charged surface states. In terms of the electronic configuration, only transition-metal oxides and post-transition-metal oxides with cations having either empty (d^0) or filled (d^{10}) d-orbitals find real gas sensor application. Attention has to be paid to the dynamics of adsorption and desorption which could be altered by surface doping with noble metal particles or metal oxides to lower activation energies and serving as catalytic materials to channel charge transfer processes coupled to specific chemical reactions with gas molecules to detect.

In order to have good transducer capabilities of the gas sensor material a fairly large bandgap higher than 2.5 eV and a small activation energy for oxygen conductivity is necessary to avoid operation in the region of self-conductance and to reduce the influence of ambient stimuli such as temperature. For room temperature application, of course, a material with smaller bang gap can be used and might be even favourable, however at lower temperature the influence of air humidity to the sensitivity of the sensor's parameters has to be taken into account. The influence of humidity on the sensor response will be elaborated further in Chapter 5.
The electroconductivity and the type of conductivity are also important parameters for the sensor response. For example, for the chemisorptional conductometric gas sensors the conductivity should not exceed 10^{-2} to 10^{1} Sm/cm which can be achieved by a high number of point defects. For SMO materials also n-type or p-type conductivity is a relevant parameter for the direction of conductivity change upon interaction with the same gas. In this example, the conductivity increases with rising oxygen partial pressure in p-type and decreases with n-type oxide materials. Materials with n-type conductivity are used for the design of the most effectively working gas sensors based on adsorption of oxygen and charge transfer reactions with reducing gases leading to a decrease in resistance of n-type oxides. The most prominent n-type SMOs are SnO_2, TiO_2, WO_3, ZnO and In_2O_3 which are all thermally stable. P-type CuO and iron oxides are suitable for adsorption type gas sensors as well since oxygen can be adsorbed superior than in n-type oxides, where the negative charges have to be compensated by ionized donors in a space charge layer.

The benefit of TEM is the detailed analysis of crystal defects in microstructures of semiconducting oxide materials such as SnO_2 or ZnO.[85], [86] Also, the distribution and size of metallic particles used for surface functionalization can be efficiently analyzed by TEM and their chemical composition can be determined and mapped out. Doing so, oxidation of metallic particles or the formation of ternary phases during functionalization are typical tasks for the microscopist.[87], [88] For example, the oxidation state of metal oxides can be investigated by recording energy shifts in electron energy-loss spectra.[89]

2.4 Gas Sensing Mechanism

The gas-sensing mechanism of chemiresistive gas sensors is based on the gas/semi-conductor surface interactions featuring reduction/oxidation processes, chemisorption of chemical species

and adsorption by the reaction with surface states which are associated with pre-adsorbed ambient oxygen. On the electronic level, electronic transfer of delocalized conduction-band electrons to localized surface states and vice versa is the main mechanism of a conduction change accompanied by catalytic effects and in general complex surface chemical reactions between the different adsorbed chemical species. These complex mechanisms will be addressed in more detail regarding energy band diagrams, schematics and typical measurement curves in the following explanations on the example of a Pd-doped ZnO (ZnO:Pd) thin film exposed to hydrogen gas.[87]

The situation of exposure to air and hydrogen gas is schematically illustrated in Figure 2.4. In the presence of air atmosphere, oxygen molecules are adsorbed on the metal oxide surface and occupy previously formed oxygen vacancies. There the molecular oxygen takes an electron from the conduction band and forms negatively charged molecular or atomic species dependent on the operating temperature.

$$O_2 + e^- \xrightarrow{T < 150\,^\circ C} O_2^-$$

$$O_2 \xrightarrow{T > 150\,^\circ C} 2\,O + n\,e^- \xrightarrow{T > 150\,^\circ C} O^- \text{or} O^{2-}$$

The adsorption process captures negative charges from the metal oxide surface causing the formation of an electron depletion region and band bending at ZnO grain boundaries reducing the conductivity across the grains (see Fig. 2.4(a)+(c)). This is why the diameter of the SMO nanostructures is utmost important for the magnitude of the current change. According to this oxygen adsorption/desorption model, the band bending can be reversed meaning the width of this space-charge layer can be minimized in the presence of a reducing gas leading to chemical reaction with the trapped and charged oxygen species or by a competitive adsorption and replacement of adsorbed oxygen by other molecules.[90] In the presence of hydrogen gas in the ambient atmosphere, the H_2 molecules are oxidized at the charged oxygen species by releasing negative charge which reduces the width of the depletion layer and lowers the height of the potential barrier (see Fig. 2.4(b)).

$$\frac{1}{2}\,O_2^- + H_2 \rightarrow H_2O + e^-$$

$$2\,O^- + 2\,H_2 \rightarrow 2\,H_2O + 2\,e^-$$

Despite the reaction with adsorbed oxygen species H_2 is known to adsorb also chemically directly on the surface, which is associated with an even larger electron transfer reaction.[91] Hence, the conductivity and the sensor response are increased in the presence of a reducing gas being dependent on the modulation of the barrier height. The sensors gas response curves to different gases measured with increasing operating temperature are depicted in Figure 2.4(d). The measured current output signal displays different magnitude after exposure to ammonium, acetone and ethanol gas and exhibit increased response with higher temperature demonstrating selectivity of the sensor to different molecules according to its receptor function principles. The typical shape of these measurement curves can be also explained by the adsorption/desorption dynamics at the SMO surface determining the steepness to the sides of the current profile, whereas the height of profile is determined by the transducer functions to the specific molecule. The response curve to ethanol gas resembles apparent differences concerning the sensor gas response and the response/recovery behaviour, i.e. the gas response increases and the total slope $\mathrm{d}I/\mathrm{d}t$ increases with T after exposure to ethanol

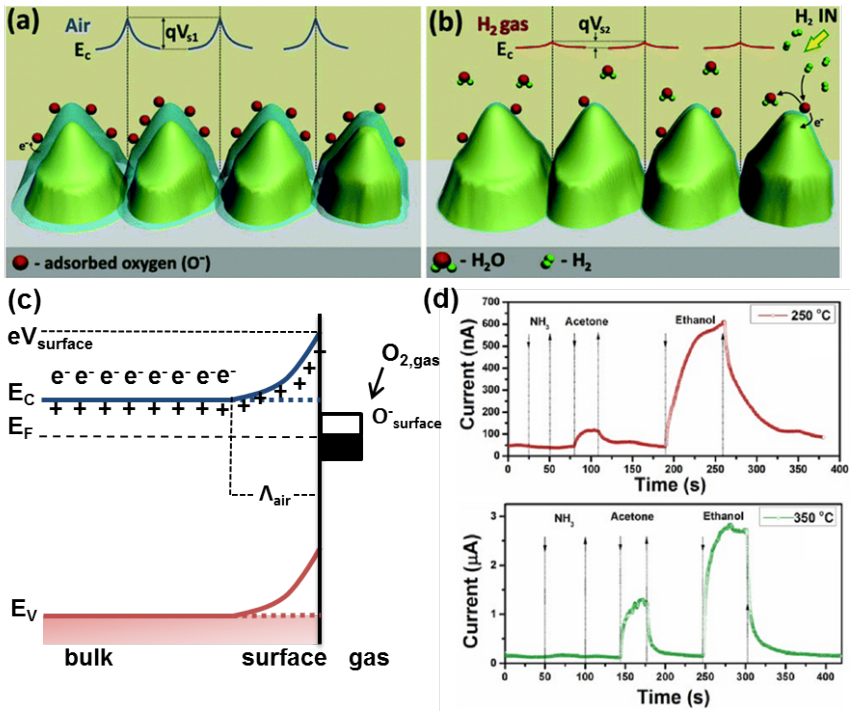

FIGURE 2.4: (a) Schematic illustration of the tentatively proposed gas sensing mechanism of ZnO:Pd grains upon exposure to ambient air at temperatures $> 200\,^{\circ}C$ (b) and upon exposure to H_2 gas. (c) Schematic energy band diagram showing the band bending at the surface resulting in a depletion region with depth Λ_{air} from the surface. (adapted from [92]) (d) Measurement current response of ZnO:Pd films exposed to different gases ammonium, acetone and ethanol at temperatures of $250\,^{\circ}C$ and $350\,^{\circ}C$. |(a,b,d) reused from [Nanoscale 10, 14107 (2018)[87]]. Reproduced by permission of The Royal Society of Chemistry.

gas and subsequent flushing with atmosphere. This is related to the accelerated dynamics of the adsorption/desorption processes of oxygen and gas molecules on the surface by temperature. First, elevated temperatures introduce a higher amount of oxygen vacancies on the SMO surface which is easily occupied by oxygen species.[93], [94] As a result, the width of the conduction channel decreases related to stronger band bending. Hence, the ratio in the current signal of the base state and sensing state increases. In addition, an increase in temperature shifts the equilibrium of charge transfer processes towards the reduction of adsorbed oxygen species by the gas molecules. By this not only the maximum gas response is reached in a smaller amount of time, but temperature can also act as a selective factor by favouring the reaction with different gas molecules.[95] Maximum sensor response is reached when oxidation of new oxygen adsorbing on the surface and reduction of the charged oxygen species by hydrogen or ethanol gas molecules as well as chemisorption are in equilibrium. When gas supply is switched off, first oxygen is again adsorbed at free oxygen vacancies rapidly increasing the resistance and second chemisorbed species and water molecules are released from the surface. The latter process happens on larger time scale and is represented by the slowly running out tail in the measurement curves, a process which can be accelerated by temperature. However, these desorption processes of chemisorbed species can be relatively inert, so external stimuli such as UV-light[96] or bias voltage[87] in case of self-heating is used to release those species and to retain the sensors baseline state.

Chapter 3

Advanced Methods

This chapter aims to introduce into the applied methods of transmission electron microscopy (TEM) and providing a full list of microscopes involved in the presented studies. However, for a full discussion of conventional imaging and diffraction theory as well as analytical techniques connected to TEM the reader is referred to a standard textbook, e.g. the book of Williams & Carter "Transmission Electron Microscopy: A Textbook for Materials Science"[97], [98] or the book by Fultz & Howe "Transmission Electron Microscopy and Diffractometry of Materials"[99]. Nevertheless, the most common techniques shall be shortly described in the following paragraphs and are explained in further detail in the presented publications if needed. The chapter closes with discussions on strain measurement and strain imaging techniques in the TEM and highlights a new approach to generate and visualize localized data on structural ordering phenomena in amorphous solids via electron diffraction and data processing. These methods display key analysis techniques for state-of-the-art electron microscopy in materials science and have been applied to materials investigated in this work and their use will be extended in future investigations.
TEM is a direct imaging technique in which an high-energetic electron beam is transmitted through electron transparent material. The kinetic interactions with the atomic structure results in manifold detectable signals which are exploited for imaging down to the atomic scale or further enhanced characterization of the micro- or nanostructure together with chemical features. The commonly available and applied techniques involve:

- Conventional TEM (CTEM): Image formation includes all elastically and inelastically scattered electrons creating a mass-thickness contrast.
- Dark-field TEM (DF): Only one set elastically scattered electrons diffracted at a specific lattice plane are used for imaging creating pure diffraction contrast to visualize either defects or specific crystal orientations.
- High-Resolution TEM (HRTEM): The image is formed by the superposition of electron wave-functions of the transmitted and diffracted beams generating a phase-contrast according to a contrast transfer function which is dependent on microscope and experimental parameters.
- Scanning TEM (STEM): STEM exploits an highly parallel and spatially confined electron probe which is scanned over the sample to detect the results of forward scattering (Rutherford scattering). The forward scattered electrons are processed by annular detectors which provides an image with a relative intensity according to a power-law dependence Z^{α}.
- High-Resolution STEM (HRSTEM): HRSTEM is the extension of conventional STEM to high-resolution down to the atomic scale with sub-angstrom resolution. To achieve

the smallest information limit, HRSTEM benefits from the correction of spherical aberrations subjected to the electron probe.

- Selected-Area Electron Diffraction (SAED): This standard diffraction method for crystal structure analysis uses a virtual aperture (actual aperture is inserted into the back focal plane below the sample) to limit the illuminated area of a specimen and hence the diffraction volume to create an intensity pattern in reciprocal space.
- Precession Electron Diffraction (PED): PED uses a slightly tilted electron beam which is rotated in circular motion (precessing) around the optical axis to create a set of ED patterns which are integrated resulting in a highly kinematic diffraction pattern and enhanced information limit reaching into higher order Laue zones.
- Nanobeam Electron Diffraction (NBED): NBED uses a strongly confined and parallel electron probe to perform diffraction experiments on small scale objects or local regions of interest. Paired with STEM, this powerful technique provides four dimensional data cubes with each pixel containing one diffraction pattern for further strain or pair-correlation analysis.
- Convergent Beam Electron Diffraction (CBED): In this electron microdiffraction technique, the electron beam is focused directly onto the sample using a large beam-convergence angle. The convergent beam features a probe size of a few nanometers, hence providing highly localized information. The typical spot pattern is enlarged by the convergence angle, producing diffraction disks in which the central transmission disk is crossed by a pattern of high-order Laue zone (HOLZ) lines. The positions of the HOLZ lines are highly sensitive to strain within the nanometer-sized electron probe. Further the contribution of HOLZ to the contrast in the surrounding diffraction disks allows for enhanced symmetry determination of point or space groups compared to SAED.
- STEM Tomography: A method which is used to compute a 3D model of the morphological features of nanomaterials such as layers, tubes or particles. To do so multiple STEM images are stepwise recorded under a large-angle tilt range.
- Energy-Dispersive X-ray Spectroscopy (EDS): Analytical method collecting characteristic and element specific X-rays excited during the inelastic scattering processes in the atomic shells yielding both qualitative and quantitative information on the present elements in a sample. Combined with STEM or HRSTEM, also local distribution imaging of element specific X-rays down to the atomic scale is enabled.
- Electron Energy-Loss Spectroscopy (EELS): EELS is a technique which can be applied both in TEM and STEM mode to collect inelastic scattered electrons with specific energy-loss according to the inelastic scattering process. Thereby, not only the present elements (preferable for light/small Z elements) can be identified both qualitatively and quantitatively but the local chemical coordination environment e.g. the orbital bonding state and oxidation number.
- Energy-filtered TEM (EFTEM): Direct element distribution imaging method using only electrons with a specified energy-loss for image formation in TEM mode by selecting defined energy windows.

3.1 Instrumentation

The TEM studies presented in this work have been conducted on microscopes installed in research facilities all around the world. Some of them provided probe or image correction systems for the spherical aberrations (C_s). For these C_s-corrected microscopes, the point resolution and information limit are similar under ideal conditions. Therefore, no artifacts or delocalization effects are observed in phase contrast imaging of non periodic regions of the specimen. This enables also a quantitative interpretation of HRTEM electron micrographs, whereas HRSTEM benefits from increased image resolution and direct quantification from scattering contrasts. The list of involved instruments is tabulated below:

- **FEI Tecnai F30 G^2 STwin** TEM/STEM with a field emission gun (FEG) operated at 300 kV and no C_s correction system ($C_s = 1.2$ mm). Spectroscopic analysis in TEM/STEM mode is supported by an EDAX EDX detector for analysis of emitted X-ray energies and a Gatan Tridiem spectrometer model 863 for electron energy-loss spectroscopy (EELS) with a typical energy resolution of ∼1 eV. Various Gatan sample holders used during the studies enabled: (a) double-tilt experiments by controlling the tilt axis of the goniometer α which is along the long axis of the sample holder but also the tilt axis β which is perpendicular to the sample holder axis, (b) tomography experiments in a high-angle single tilt holder, (c) local heating of a TEM sample up to 1000 °C. [This microscope is installed at the Christian-Albrechts-Universität zu Kiel, Technical Faculty, Kiel, Germany]
- **JEOL JEM2100** TEM/STEM with a LaB_6 thermionic gun operated at 200 kV. [This microscope is installed at the Christian-Albrechts-Universität zu Kiel, Technical Faculty, Kiel, Germany]
- **Phillips CM30** ST TEM running on a LaB_6 thermionic gun at 300 kV and $C_s = 1.15$ mm. The microscope is equipped with a Digistar (NANOMEGAS) device to conduct electron diffraction in precession mode. [This microscope is installed at the Max-Planck-Institute for solid state research, Nanochemistry, Stuttgart, Germany, and is operated by Viola Duppel]
- **FEI Titan 80-300** TEM/STEM operated at 300 kV with C_s image corrector system. In hexapole image corrector systems the aberrations of the objective lens can be tuned to their elimination up to the 5^{th} order.[100] [Center for Advanced Materials Characterization in Oregon (CAMCOR) at the University of Oregon, Eugene/Oregon, United States of America]
- **FEI Titan^3 G^2 60-300** TEM/STEM operated at 300 kV with probe-correction system enabling high-resolution STEM imaging with minimal aberrations. A four-sector EDX geometry is used to collect sample geometry independent high dose of X-rays without the need to tilt the specimen stage towards the detector (data was acquired by Dr. Andriy Lotnyk). [Leibniz Institute of Surface Engineering, IOM, Leipzig, Germany]
- **FEI Titan 80-300** TEM/STEM with C_s image corrector operated at 300 kV. The microscope can be equipped with the MerlinEM (Quantum Detectors), which is a Hybrid Pixel Detector for direct detection of electrons and rapid readout at low noise level enabling ultrafast measurements for diffraction and 4D-STEM experiments (data was acquired by Dr. Di Wang and Dr. Xiaoke Mu in collaboration with KNMF proposals).[Karlsruhe Institute of Technology, Institute of Nanotechnology, Karlsruhe, Germany]

- **FEI TitanX 60-300** TEM/STEM with $C_s = 1.2\,\text{mm}$ [National Center for Electron Microscopy at Lawrence Berkeley National Lab, Berkely/California, United States of America]
- **JEOL JEM-ARM200F 30-200** TEM/STEM with cold FEG and ASCOR probe correction system operated at 200 kV for probe aberration corrected HRSTEM and EDS (data was acquired in the process of test measurements by a JEOL operator).
- **ThermoFisher Themis Z 30-300** TEM/STEM with C_s-probe correction operated at 300 kV for probe aberration corrected HRSTEM and EDS (data was acquired in the process of test measurements by a ThermoFisher operator).

3.2 Strain Mapping on the Nanoscale

The physical properties of a material are strongly influenced by the crystal structure and modifications of the crystal lattice, especially with the continuous reduction of device dimensions and complexity. With respect to the ideal lattice, a modification is easily induced by doping with foreign atoms being placed on interstitial or substitute lattice positions, by structural defects such as stacking faults or dislocations and interfaces within the material, to other material or to the environment, all introducing some sort of lattice reconstruction as a direct result of local stress and strain fields.[101]–[103] Hence, the detailed knowledge about the present stress and strain in a device and the resulting effects are important for further physical understanding and strain-property engineering. For instance, strain in semiconductors such as Si or Ge is known since the 50's to significantly affect the electronic transport properties and its re-discovery was boosting the performance of metal-oxide-semiconductor field-effect transistors (MOSFET) in the early 80's.[104], [105]
Strain dependent energy-band-gap shifts in III-V heterostructures are also of high importance for optical applications.[106] For instance, a strain compensation approach to grow GaN films with reduced defect density for LED lighting onto a thin GaN buffer layer enabled the development of blue and white light emitting diodes which is regarded as milestone for the development of solid state lighting technology.[107] Also the development of high-power optical lasers intensively facilitates strain engineering approaches of the active region. For example the performance of quantum well heterostructure lasers containing multiple lattice mismatch interfaces are strongly influenced by the precise control of a net strain by tuning growth parameters or strain-balancing [108]–[110], since extensive strain is known to result in rapid degradation of device performance.[111]
Further, the emerging research field of piezotronics for future everyday devices is exploiting a strain-based local deformation of the electronic energy landscape to manipulate the electron transport characteristics. Recently, the piezotronic approach has been demonstrated for a strain-gated field-effect transistor[112] and is adapted for sensing ultra-small biomagnetic fields generated in the human heart or brain.[60]

The given summary of the evolution of elastic strain engineering in nanostructures and devices motivates the development of dedicated characterization methods facilitating the electron microscope. Those should be capable of both observation and quantification of the actual strain in a sample. In this regard, TEM is a particularly powerful tool due to its ability to spatially resolve strain with high precision and spatial resolution. Other techniques such as μ–Raman spectroscopy or X-ray diffraction both provide non-destructive tools for measuring strain with high precision but are lacking in spatial resolution and imaging capabilities. To the benefit of the latter, synchrotron-based methods using a strongly confined nanometer X-ray beam offer spatially resolved 3D data from coherent X-ray diffraction imaging (CXDI)[113] or X-ray ptychography (XPT).[114] On the electron microscope numerous techniques for strain data acquisition have been developed which can be divided into direct imaging and probe-related techniques, all of these have their strengths and weaknesses.[115] Strained Si/SiGe gate electrodes used in MOSFET devices display a representative specimen for the quantitative analysis of strain and is employed as comparable standard for methodical development. A direct comparison of the available strain precision and spatial resolution reported about the different methods is presented in Table 3.1. The concept of geometric phase analysis (GPA) was first derived from direct imaging techniques and was first introduced to the materials science community. The GPA exploits the phase component by post-processing of HRTEM

Table 3.1: Strain measurement and 2D imaging techniques used on the TEM

Method	Strain precision	Spatial resolution	Ref.
HRTEM/HRSTEM GPA	10^{-3}	1-4 nm	[116], [117]
SMF	10^{-3}	1-4 nm	[127]
DFEH	$2x10^{-4}$	4 nm	[121]
CBED	10^{-4}	1-10 nm	[123]
NBED	$6x10^{-4}$	2.7 nm	[124]
NPED	$2x10^{-4}$	1 nm	[125]

and HRSTEM micrographs to determine lattice displacements with a precision of 10^{-3} and a spatial resolution between 1-4 nm.[116], [117] Direct strain imaging methods closing the gap between low spatial resolution but large field of view (XRD) and high spatial resolution but small field of view (HRTEM/HRSTEM) modes are scanning moiré fringe imaging (SMF)[118], [119] and dark-field electron holography (DFEH)[120]–[122] both capable of measuring strains with high precision, nanometer resolution and a large field of view. In the SMF method, moiré fringes are generated due to an harmonic interference artefact in conventional HAADF-STEM images in the middle range of magnification. These SMFs appear when the scanning grating and the lattice spacing are similar and lattice strains can be easily obtained in quantitative maps via a GPA algorithm. DFEH combines the SMF technique with off-axis holography to exploit the interference of two diffracted beams being in diffraction condition in an unstrained reference crystal and a strained thin layer with the help of a electrostatic biprism. The phase difference is extracted directly from the holographic fringes being dependent on dynamical elastic scattering and the geometric phase, which encodes the strain information through phase gradients.

Probe-related methods using electron diffraction techniques with nanometer resolution can also be applied to measure strain efficiently. In combination with scanning the electron beam across the sample similar strain maps to the direct imaging techniques can be recorded, but are suffering from increased complexity and time consumption. These methods include the analysis of HOLZ line shifts in CBED pattern[123] or evaluating the position of discrete intensities in spot pattern recorded in NBED[124] and nanobeam precession electron diffraction (NPED)[125] experiments increasing the quality and robustness of nanoscale strain analysis. However, it has to be noted that the accuracy of strain analysis in ultrathin-specimens using TEM is affected by strain relaxation effects from two surfaces created during sample preparation. In addition, the focused ion beam (FIB) technique facilitates the implantation of Ga-ions during ion milling which is adding a source of strain to the material. [126]

3.2.1 Geometric Phase Analysis

The measurement of lattice strains by the straightforward geometric phase analysis algorithm evolved into a standard technique for analysis of nanoscale strain distributions. Since GPA is based on the Fourier analysis of the phase components of HRTEM micrographs, aberration-correction on the microscope is necessary to minimize phase contributions from the contrast transfer function implied by the objective lens system. This technique is especially attractive

for aberration-corrected TEM images that resolve every atomic column and was performed within the studies presented in Section 4.2.

The GPA technique is based on the analysis of spatial frequency components of HRTEM lattice images converted to its Fourier transform.[128]. The strong Bragg-reflections correspond to the two dimensional unit cell of the projected crystalline structure. Two non-colinear reciprocal lattice vectors are selected by apertures in Fourier space which serve as Bragg filter. The size of this aperture determines the spatial resolution achievable in the strain map. Those Bragg reflections display sharply peaked frequency components of the ideal lattice and smear out with lattice distortion inducing a net phase shift of the local wave function leaving the crystal. These variation in phase shift with respect to an supposed unstrained reference lattice can be used to calculate the displacement fields whose gradient is the strain tensor. The math is implemented into a plug-in[1] for the DigitalMicrograph software package and can be conveniently used to calculate strain maps.

Following the mathematical treatment provided by Hytch et al. the Fourier components $\mathrm{H_g}$ of the image of a perfect crystal are expressed in terms of amplitude $\mathrm{A_g}$ and phase $\mathrm{P_g}$ of the corresponding set of lattice fringes $\mathbf{g}$.[128]

$$\mathrm{H_g} = \mathrm{A_g} \cdot \exp\{\mathrm{iP_g}\}$$

The local intensity of the image I(r) can be expressed as the sum of the local Fourier components g(r)in the image.

$$\mathrm{I(r)} = \sum_{\mathrm{g}} \mathrm{H_g(r)} \cdot \exp\{2\pi \mathrm{i}\mathbf{g} \cdot \mathrm{r}\}.$$

Hence, the real image is a function of its Fourier amplitude and phase components. By using a Brillouin zone mask around one Bragg reflection in the Fourier space, the image of a particular set of lattice fringes g(r)is therefore given by

$$\mathrm{B_g(r)} = 2\mathrm{A_g} \cos\{2\pi\mathbf{g} \cdot \mathrm{r} + \mathrm{P_g}\}.$$

A displacement of the reciprocal lattice vector to $\mathbf{g} \rightarrow \mathbf{g} + \Delta\mathbf{g}$ leads to the transformation of the above expression into

$$\mathrm{B_g(r)} = 2\mathrm{A_g} \cos\{2\pi\mathbf{g} \cdot \mathrm{r} + 2\pi\Delta\mathbf{g} \cdot \mathrm{r} + \mathrm{P_g}\},$$

from which the gradient of the phase $\nabla\mathrm{P_g(r)} = 2\pi\Delta\mathbf{g}$ as a function of position gives the local deviation of the reciprocal lattice vector of the reference lattice vector of which the phase images can be derived. A displacement field $\mathbf{u}(\mathrm{r})$ acting on the position dependent phase component $\mathrm{P_g(r)}$ leads to a displacement of the maximum fringe positions in the direction of the reciprocal lattice vector $\mathbf{g}$. Using two non-colinear vectors $\mathrm{g_1}$ and $\mathrm{g_2}$ the vectorial displacement field can be calculated using the matrix

$$\begin{pmatrix} \mathrm{u_x} \\ \mathrm{u_y} \end{pmatrix} = -\frac{1}{2\pi} \begin{pmatrix} \mathrm{g_{1x}} & \mathrm{g_{1y}} \\ \mathrm{g_{2x}} & \mathrm{g_{2y}} \end{pmatrix}^{-1} \begin{pmatrix} \mathrm{P_{g1}} \\ \mathrm{P_{g2}} \end{pmatrix}.$$

[1] FRWRtools plug-in, open accessible and provided by Christoph T. Koch, HU Berlin, Institute of Physics

The real space lattice vectors a_1 and a_2 are derived from the reciprocal lattice vectors by taking the transponent $G^T = A^{-1}$ with

$$A = \begin{pmatrix} a_{1x} & a_{2x} \\ a_{1y} & a_{2y} \end{pmatrix} \text{ and } \quad G = \begin{pmatrix} g_{1x} & g_{2x} \\ g_{1y} & g_{2y} \end{pmatrix}$$

obtaining the expression for the displacement field

$$\begin{pmatrix} u_x \\ u_y \end{pmatrix} = -\frac{1}{2\pi} \begin{pmatrix} a_{1x} & a_{2x} \\ a_{1y} & a_{2y} \end{pmatrix}^{-1} \begin{pmatrix} P_{g1} \\ P_{g2} \end{pmatrix}.$$

The strain field giving the local distortion is derived as the gradient of the displacement field $\nabla \mathbf{u}$ and is defined as follows:

$$e = \begin{pmatrix} e_{xx} & e_{xy} \\ e_{yx} & e_{yy} \end{pmatrix} = \begin{pmatrix} \frac{\partial u_x}{\partial x} & \frac{\partial u_x}{\partial y} \\ \frac{\partial u_y}{\partial x} & \frac{\partial u_y}{\partial y} \end{pmatrix}$$

results

$$e = -\frac{1}{2\pi} \begin{pmatrix} a_{1x} & a_{2x} \\ a_{1y} & a_{2y} \end{pmatrix} \begin{pmatrix} \frac{\partial P_{g1}}{\partial x} & \frac{\partial P_{g1}}{\partial y} \\ \frac{\partial P_{g2}}{\partial x} & \frac{\partial P_{g2}}{\partial y} \end{pmatrix}.$$

Application example: Strain at the ZnO/Au interface

In the following the application example, GPA is applied to characterize lattice strains at the ZnO interface between an ZnO microneedle and Au nanodots which have been grown by sputter deposition of a thin Au film and subsequent heating. The SEM images depicted in Figure 3.1 provide an overview of the sample morphology of a ZnO microwire decorated by Au crystals. The cross-section view through one Au crystal and the ZnO wire depicts clean interfaces and suggests that the Au crystals are partially embedded by wetting during the annealing. Further, elemental distribution maps obtained by EDS on the SEM are depicted.

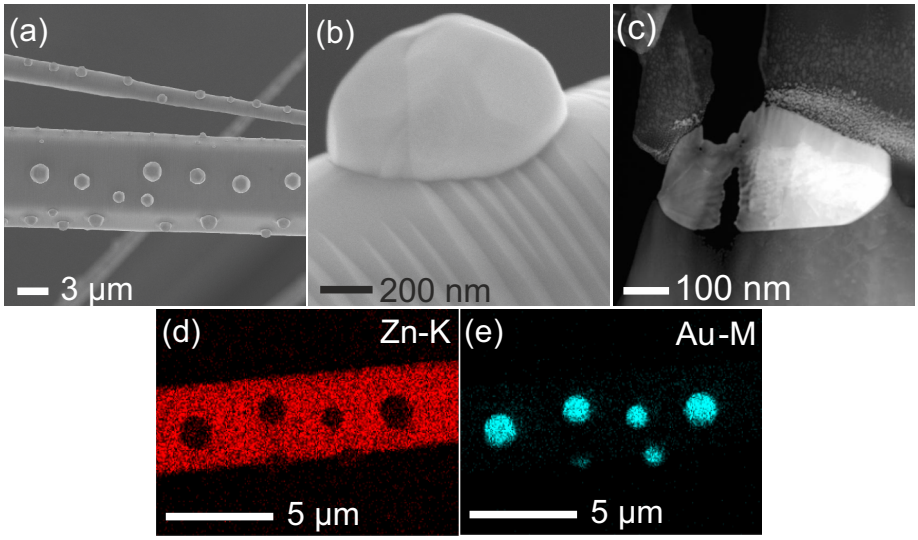

FIGURE 3.1: (a) SEM image of Au nanodots on ZnO microwires. (b) High magnification SEM image of a Au nanodot on the ZnO surface showing ripples. (c) STEM cross-section image of a Au nanodot sitting on ZnO surface. (d,e) SEM/EDS maps of Zn-K and Au-M excitation.

The GPA analysis was conducted on C_s-corrected HRTEM micrographs depicted in Figure 3.2. Both presented examples (a) and (b) show the ZnO lattice located at the bottom of the image and the Au nanocrystal at the top. For the computation two non-colinear vectors of the ZnO reflections $\mathbf{g}_a$ $(01\bar{1}0)$ and $\mathbf{g}_b$ $(10\bar{1}0)$ were defined in the Fourier space and masked by a Brillouin zone mask, its size determines the strain resolution to 2.0 nm. The diffractograms shown in represent crystal orientation along the growth direction of the microwire (hexagonal-pole). The individual phase images $P_g(r)$ and the resulting strain maps showing the individual components of the strain tensor, the in-plane component ε_{xx}, out-of-plane component ε_{yy} and shear strain component ε_{xy}. The phase maps, especially the P_a maps show good correlation with the in-plane strain component being the most prominent for both examples. Here, alternating compressive as well as tensile strain is evidenced, but on a scale which is less then 1% of the reference lattice. The ε_{xx} component of (b) shows mostly compressive strain at the interface which inverses in shorter parts of about 2 nm having tensile strain. Further, small hotspots are observed in the bottom region of ZnO indicating some lattice defect.

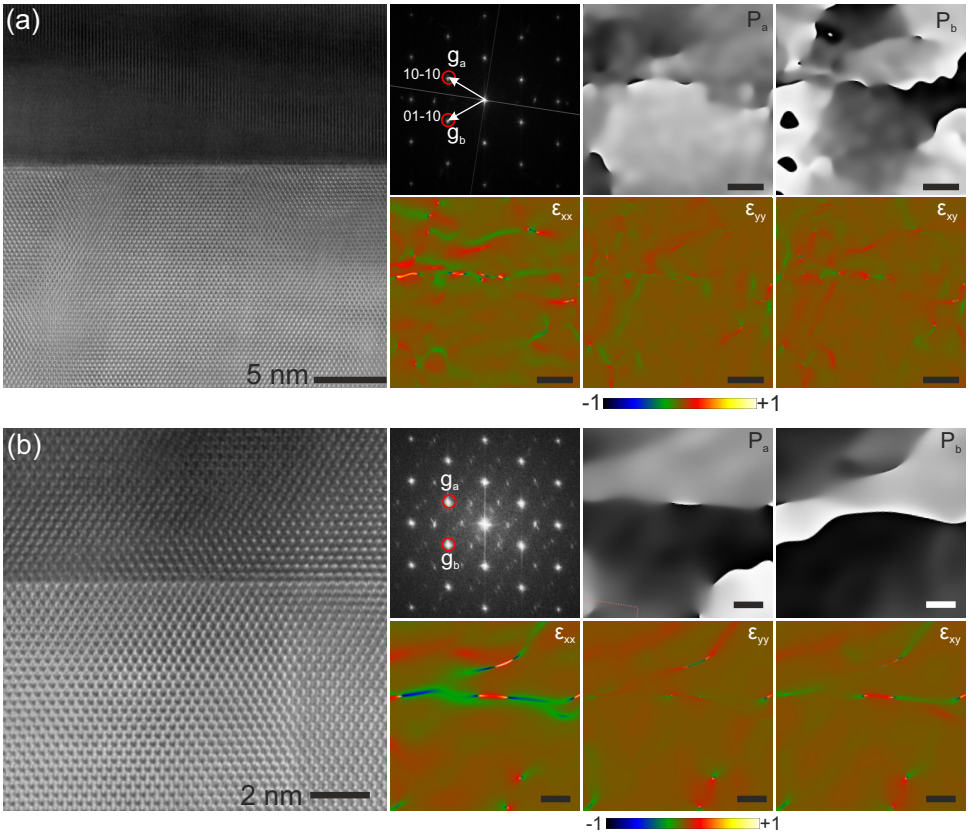

FIGURE 3.2: Example of GPA analysis on a ZnO/Au (bottom/top) interface showing the HRTEM micrograph, diffractogram with indication of Brillouin zone masks, phase images P_a and P_b, and maps of the strain tensor components. An area of the ZnO crystal far away from the interface was chosen as reference lattice assuming unstrained conditions. For both examples (a) and (b) only small in-plane strain <1% with respect to the reference lattice can be detected at the interface.

3.3 4D STEM Radial Distribution Function Imaging

The magnetic properties of amorphous metallic glasses are critically determined by their amorphous structure classified by a distinct short-range order and the lack of long-range order.[129] Therefore the analysis of the radial distribution function (RDF) or pair correlation function in amorphous glasses prior to crystallization might be an indispensable tool to explain discrepancies in magnetic characteristics.[130], [131] In such intermediate stages at the onset of crystallization (paracrystalline state) the atoms are locally rearranged but dot not yet form a regular periodic lattice. The speckle intensity distribution of nanobeam electron diffraction pattern can be an efficient measure of nanoscale fluctuations of the atomic order with nanometer resolution,[132] which is comparable to the methodological approach to extract strain in crystalline materials by NBED analysis.[124] As an alternative, it was demonstrated that one can retrieve the reduced density function *G(r)* also by an numerical approach by extracting diffraction data from the complex-valued exit-face wave function obtained by HRTEM focal series reconstruction or electron holography.[133] The nowadays capabilities of 4D STEM allow for recording two dimensional nets of NBED pattern according to the HAADF STEM image. In particular, the resolution of such NBED nets which is determined by the nanoprobe size could be enhanced by the development of D-STEM creating a highly parallel probe with 1-2 nm in diameter for diffraction experiments.[134] The diffraction information gathered from such small volumes contains information on the atomic arrangement of heterogeneous amorphous materials and is capable to resolve changes of the near-range order. The developed technique is based on the calculation of the spot RDF from single D-STEM pattern and subsequent imaging of the RDF's collected within an amorphous layer by hyperspectral analysis.[135]
The RDF describes in principle a probability to find certain atomic pairs at a distance r. The evaluation of D-STEM pattern with respect to the spot RDFs with nanometer resolution gains new insight into cluster formation, mixing at interfaces or chemical segregation both in the purely amorphous or paracrystalline state with extreme sensitivity to small atomic packing variations.

The experimental settings and data analysis procedures of the RDF imaging are described within the works of X. Mu [135], [136] and are theoretically based on the descriptions of electron scattering from amorphous materials.[137], [138] In the following, these procedures will be shortly explained on the basis of the referred publications[135] at hand of an amorphous FeCoSiB film showing a broadened magnetic hysteresis. The aspect of magnetic hardening is an indication of structural rearrangement of the amorphous phase. Indeed, structural peculiarities in the amorphous phase are related to chemical variations which might be indicated by the HAADF STEM contrast.

To perform such an experiment a quasi-parallel nanobeam condition is set up providing a nano-sized probe using the STEM microprobe operation and choosing a semi-convergence angle i.e. 0.6 mrad or 0.8 mrad to focus on either spatial resolution or RDF resolution. Further, the GunLens parameter was set to 6 and the spotsize to 7. The experimental setup comprises a direct electron detector (MerlinEM, Quantum Detectors) to record an array of high intensity NBED pattern with millisecond acquisition time by stepwise (0.6 nm) scanning the electron probe across the sample (diffraction (D)-STEM). The generated 4D-STEM data cube contains the HAADF STEM information including one NBED pattern collected at each pixel of that image. The diffraction information contains data of high scattering angles

where the high frequency structural information is encoded which endorses the calculation of the RDF. The RDF of each diffraction pattern is being calculated by first generating the diffraction intensity profile. From there, the structure factor is obtained by subtracting and normalizing with single atomic scattering factors of the analyzed material, which elements have to be known. The Debye formula describes the diffraction intensity generated by the interference of scattered electron waves taking into account the number of atoms N in the investigated material, the electron scattering factor $\mathrm{f_m}$ of the specified atom m, the scattering vector $\mathrm{s} = 2\vartheta/\lambda$ being relation of half the scattering angle ϑ and the incident wavelength λ, the pair distance $\mathrm{r_{mn}} = |\hat{\mathrm{r}}_\mathrm{m} - \hat{\mathrm{r}}_\mathrm{n}|$ between atoms m and n and the position $\hat{\mathrm{r}}_\mathrm{n}$ of atom n.

$$\mathrm{I(s)} = \sum_{\mathrm{m}}^{\mathrm{N}} \mathrm{f_m(s)}^2 + \sum_{\mathrm{m}}^{\mathrm{N}} \sum_{\mathrm{n}\neq\mathrm{m}} \mathrm{f_m(s) f_n(s)} \frac{\sin(2\pi\,\mathrm{i\,s\,r_{mn}})}{2\pi \mathrm{s\,r_{mn}}}$$

The structure factor φ of the experimentally measured diffraction intensity is calculated by subtracting and normalizing with single atomic scattering factors.

$$\varphi(\mathrm{s}) = \frac{\mathrm{I(s)} - \mathrm{N}\langle \mathrm{f(s)}^2 \rangle}{\mathrm{N}\langle \mathrm{f(s)} \rangle^2} \mathrm{s}$$

Herein, f(s) are the parametric elemental scattering factors, $\langle \mathrm{f(s)} \rangle = \sum_\mathrm{i} \mathrm{C_i f_i(s)/N}$ denotes an average of elemental atomic scattering factors $\mathrm{f_i(s)}$ over all elements i weighted by the atomic percentages $\mathrm{C_i}$. Accordingly, the RDF (G(r)) is calculated by a sine Fourier transformation of the structure factor

$$\mathrm{G(r)} = \int_0^{\mathrm{s_{max}}} \varphi(\mathrm{s}) \sin(2\pi\,\mathrm{s\,r})\,\mathrm{ds}.$$

The obtained RDF cube is further processed by hyperspectral techniques such as multiple linear least squares (MLLS)[139] to fit the data cube with linear combinations of reference spectra. The dimensions of the data cube are effectively reduced to 2D images of the respective fitting coefficients of the reference spectra by the MLLS fitting routine.

Application Example: RDF imaging of amorphous FeCoSiB

The method of RDF imaging is exemplary applied to a thin film of FeCoSiB with a film thickness of 50 nm. FeCoSiB is the standard magnetic material commonly used for the ME sensors in this research center. This particular sample was chosen to investigate the structure-property relation between the magnetic properties and the short-range order in the amorphous structure, since the magnetic coercive field of this thin film was fairly larger than measured for standard FeCoSiB films.[41] An overview of the sample is depicted in Figure 3.3 showing (a) a TEM image of the film sandwiched in between Ta electrodes, (b) a HRTEM micrograph with FFT inset and (c) elemental distribution maps obtained by EDS. The overall film composition was measured by EDS and quantified to atomic percent of $Fe_{70.4} : Co_{8.2} : Si_{21.4}$ which is close to the standard film composition of $Fe_{78} : Co_{8.6} : Si_{13.4}$ in $(Fe_{90}Co_{10})_{78}Si_{12}B_{10}$ films despite the higher amount of Si. Note, the detecion of B is not available with the EDAX EDS system. A filament-like contrast variation can be observed from the TEM and HRTEM images which is apparent both vertical and horizontal about 5 nm away from the Ta layer. However, the FFT resembles that of a complete amorphous material. The contrast variations within the film might indicate chemical fluctuation on the nanoscale; an assumption which is supported by STEM EDS maps. Here, Fe-poor and complementary Si-rich regions are identified having differences in atomic composition in the range of $Fe_{26.1} : Co_{3.7} : Si_{70.2}$ to the surrounding local matrix $Fe_{45.3} : Co_{2.7} : Si_{52.0}$. It is apparent, that the local film composition does not at all display the overall film composition.

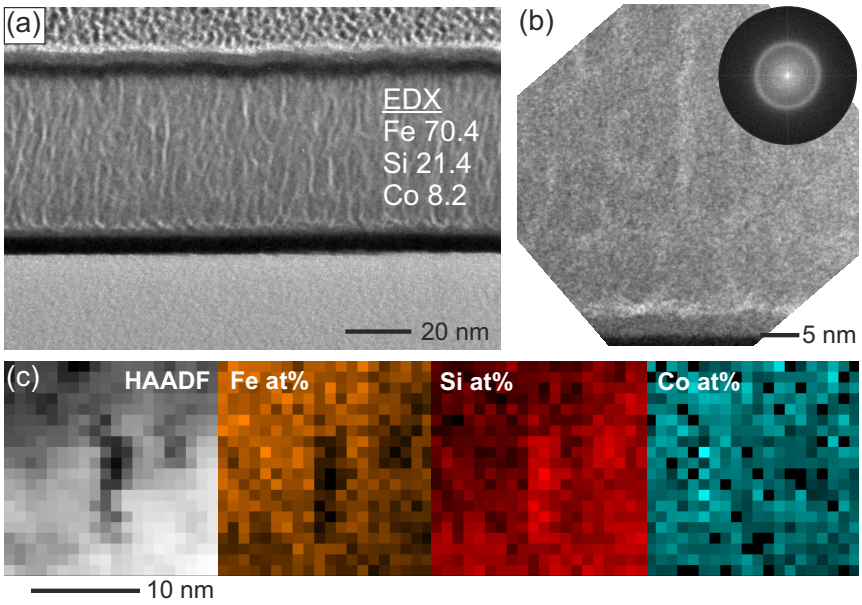

FIGURE 3.3: Morphology and chemical composition analysis of amorphous FeCoSiB thin films. (a) TEM overview image of a 50 nm FeCoSiB thin film sandwiched between Ta electrodes and average chemical composition obtained by EDX spectroscopy. (b) HRTEM micrograph with contrast variations parallel and vertical to the Ta electrode and FFT depicting a pattern of an amorphous phase. (c) Elemental mapping provides evidence of local chemical variations.

The 4D-STEM data cube was acquired using a NanoMegas software for performing ultra-fast scanning of the electron beam. The diffraction patterns were recorded and evaluated following the procedures described above which have been implemented into a MatLab script

by X. Mu at the Karlsruhe Institute of Technology. The evaluated data cube is further analyzed by choosing reference RDFs for the hyperspectral analysis, comparing the references to each individual RDF by the MLLS routine. The obtained data is presented in Figure 3.4 showing the RDF cube including the positions of the selected reference RDFs, the diffraction intensity image resembling a HAADF STEM image and the RDF images of the individual references (1-5) and the MLLS residual function. The reference RDFs were locally selected for the SiO_2 substrate (1), the FeCoSiB film (2,3), the Ta electrodes (4) and on average for the FeCoSiB film (5) to check for missing regions with different short-range order. The diffraction intensity image displays intensity variations in the FeCoSiB film which are comparable to the observations made in the TEM images of Figure 3.3. Two RDFs with apparent difference have been selected within the FeCoSiB film, indeed indicating variation in short-range order which is possibly due to the observed chemical variation. The spatial distribution of both RDFs (2) and (3) show inverted intensity at some instances which is the case in the upper left corner of the film for example, supporting the observation of chemical fluctuations in the film. The residual function of the MLLS fit however shows larger fitting errors close to the Ta interfaces, which could be evidence of a third structural arrangement in the FeCoSiB film. In comparison with the TEM images, this third RDF component could match to the contrast variations observed directly at the Ta interface.

A colored superposition image showing the distribution of all reference RDFs is shown in Figure 3.5(a) also indicating missing intensity at the bottom Ta/FeCoSiB and Ta/SiO_2 interfaces pointing to distinct variation in short-range order. The normalized reference RDFs are plotted and displayed in Figure 3.5(b) for comparison, showing the relative atomic density versus the radial distance. Figure 3.5(c,d) display the experimentally obtained reference RDFs with largest differences selected from the RDF cube and intensity image. The two reference RDF of FeCoSiB exhibit a minute variation in magnitude and position of the first and second maxima. The radius of this first coordination sphere shows different values of 2.52 Å(RDF 2) and 2.56 Å(RDF 3). This first coordination volume contains the distances of Fe-Fe pairs and short-range coordination of Fe-Co and Fe-Si.[140], [141] The position of the second and smaller maximum is given by values of r being 4.26 Å(RDF 2) and 4.16 Å(RDF 3) and can be referred to the second coordination distances of Fe-Si and Si-Si pairs.[141]. The differences between the position of the first coordination distance r might be correlated with an percentage increase of Fe-Fe distances in RDF(3) with respect to RDF(2) where Fe-Si pairs are more dominant. These conclusions stem from comparison with calculated single pair distribution functions of FeSiB.[141]. In conclusion, the differences in the positions of the first and second coordination radii displayed by the maxima of atomic density in the FeCoSiB material could be related to small fluctuations of the chemical environment in the FeCoSiB film showing either stronger influence of Fe-Fe or Fe-Si pairs. In perspective, the proven capability of the RDF analysis to identify and to map out local variations in short-range order might be a valuable method to explain e.g. unexpected deterioration of the magnetic properties.

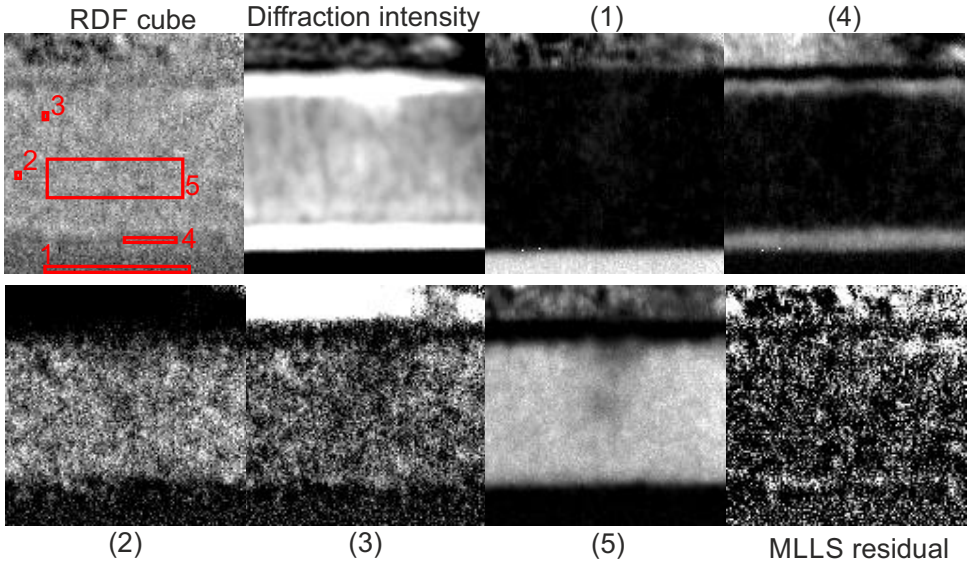

FIGURE 3.4: Presentation of the 4D-STEM RDF imaging data cube containing one single RDF in each pixel (roughly 1x1 nm). The position of the reference RDFs (1-5) used for mapping is shown in the RDF cube image. The diffraction intensity image is showing the intensity of higher scattering angles from the nanoscale NBED patterns.The MLLS residual image displays intensity wherever there is larger deviation to the reference function.

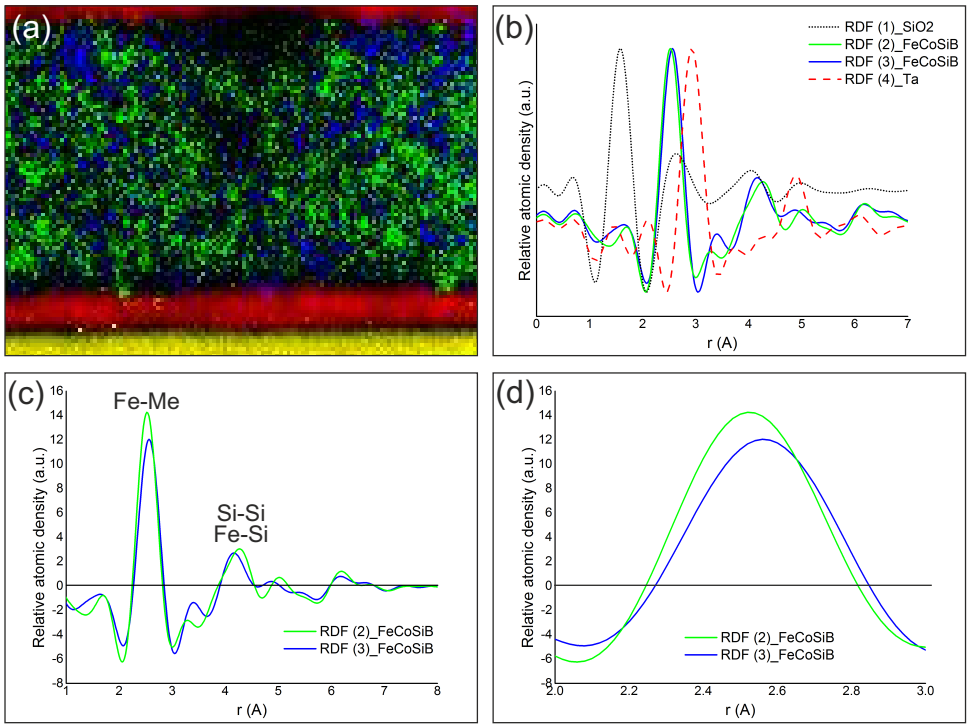

FIGURE 3.5: (a) Distribution map of reference RDFs for SiO_2, Ta, and FeCoSiB. (b) Normalized plots of the reference RDFs showing the relative atomic density versus the coordination radius. (c) Plot of the RDFs identified in FeCoSiB indicating coordination spheres of Fe-Metal (Fe, Co, Si) as well as Fe-Si and Si-Si, compare [141].(d) Difference of position of the first atomic density maximum.

3.4 Functional Grids: An *in situ* TEM straining Platform

With proceeding miniaturization of device components to the microscale or even down to the nanoscale, gaining knowledge about the mechanics on these length scales is inevitable for long time device operation. In this respect, precisely designed deformation experiments in the TEM or SEM *in situ* allow to identify underlying mechanisms of strain mediation by plastic deformation and failure, e.g. via direct imaging of dislocation movement on the micro- to nanoscale under load.[142], [143] Further, the mechanical data can be combined with 3D information for implementation in large-scale molecular dynamics simulation to create better understanding of the role of strain localization and predominant defect processes. [144] To this purpose, special deformation platforms in push-to-pull geometry have been developed based on MEMS technology or 3D-printed spring structures and their function is demonstrated on a variety of metallic and ceramic materials inside the limited space of a TEM.[145]–[149] Despite the deformation mechanics, tremendous interest lies on investigating structure-property relations *in situ* which is the simultaneous measurement of a physical property under load.[150]–[152] In this regard the study of electromechanical characteristics of 1D or 2D piezoelectric materials such as ZnO or TMD materials would be of large interest.

In the light of these developments which often require specialized TEM sample holders to operate, **functional NiTi grids for *in situ* straining in the TEM**[2][153] were developed[3] with temperature regulated device functions based on the shape memory effect.[154], [155] These devices have the advantage that they can be used in a conventional heating holder (if applicable). This shape memory effect describes the cyclic transformation between the tetragonal lower temperature phase martensite to the cubic higher temperature phase austenite by a specific temperature change. The working principle was demonstrated by pre-straining experiments of the NiTi grids in twinned martensite resulting in a reversible strain deformation by detwinning of martensite variants and is supported by finite element simulation. The device function was tested inside the TEM using an entangled tetrapodal ZnO network for an *in situ* tensile test experiment.

In a second experiment the functional grid platform was used for straining a nanocrystalline (nc) Au film. The Au film was magnetron sputtered onto a cleaved face of a NaCl crystal, which was dissolved in water to detach the Au film and loaded to the functional grid by simple uptake from the water surface. The grids have to be pre-strained before, which is performed on a flat surface and gentle pulling on the spring with a tip of tweezers placed into the sample stage orifice. The experimental images demonstrate unfolding, folding and rupture processes via crack propagation upon straining the Au film. The micromechanical evolution is presented in Figure 3.6 for different temperatures and resulting gap distance. Initially, the Au film is not flat but shows highly wrinkled regions which are unfolded with increasing gap size. In this process, additional folds are introduced and the large strain forces lead to intergranular crack propagation of the nc grain structure until complete rupture, described in analogy by tearing a sheet of paper. The mechanism of brittle and intergranular fracture is related to grain boundary porosity in nc sputtered films.[156] Electron diffraction pattern recorded before and after the experiment show differences of the radial intensity distribution of the diffraction rings depicted in Figure 3.7. Here, the radial intensity distribution

[2]Reprinted with permission from Ultramicroscopy 182, 10-16 published by ©2017 Elsevier, https://doi.org/10.1016/j.ultramic.2017.06.003

[3]work denoted to Christoph Chluba and Rodrigo Lima de Miranda

of the {111}, {002} and {022} reflections was analyzed and is presented in radial plots. All three diffraction rings show an increased accumulation of diffraction intensity according to the reflection position present in a single crystalline material. For the {111} reflections, the radial intensity distribution shows a "X"-shaped pattern with 60° between adjacent and 120° between opposing intensity maxima. Both, the {002} and {022} intensity maxima depict clear defined "+"-shaped pattern with 90° between their intensity maxima. Together, the intensity distribution within the analyzed diffraction rings resembles the geometry of reflections in {100} and {110} zone axis orientation in the ED pattern recorded after the straining experiment.

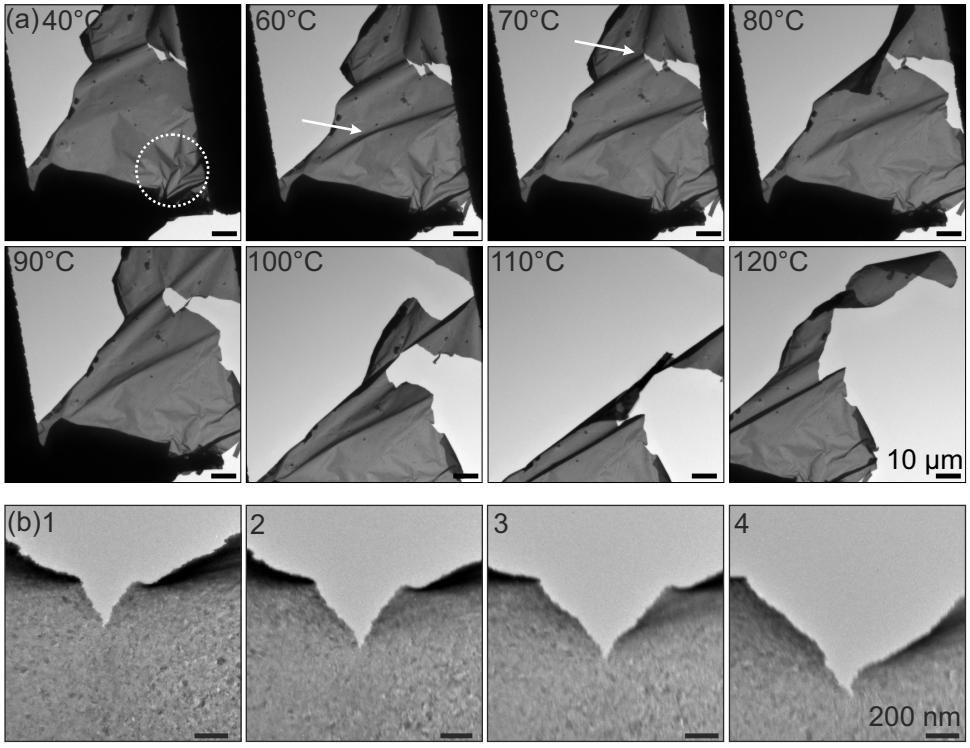

FIGURE 3.6: *In situ* straining experiment using a nano-polycrystalline Au foil on the functional grid technology platform. (a) Stages of straining and rupturing in the temperature interval 40 °C-120 °C. Upon heating the densely folded area in the right lower corner is extended until 80 °C and is folded upwards (indicated by the arrow in the 60 °C image). An other feature is crack propagation of the already semi-ruptured film starting from the crack indicated by the arrow in the image at 70 °C leading to a complete rupture. (b) Magnified view showing crack propagation during tensile testing.

These results can be compared with similar *in situ* TEM studies reporting on the mechanics of sputter deposited nc Au films under tensile load by the advanced combination of STEM and ACOM.[157], [158] The typical mechanisms of plastic deformation in nc Au film observed are described as: (1) local twinning/detwinning processes, (2) anomalous grain growth to the benefit of larger grains and shrinkage of smaller grains in their vicinity also resulting in merging of grains, by (3) distinct grain rotation and (4) a minor strain-induced strengthening of the {110} texture. This slight increase of texture is in agreement with the observations on the nc Au film strained with the functional grid platform in this study.

However, following a direct interpretation has to be taken with care, considering if the

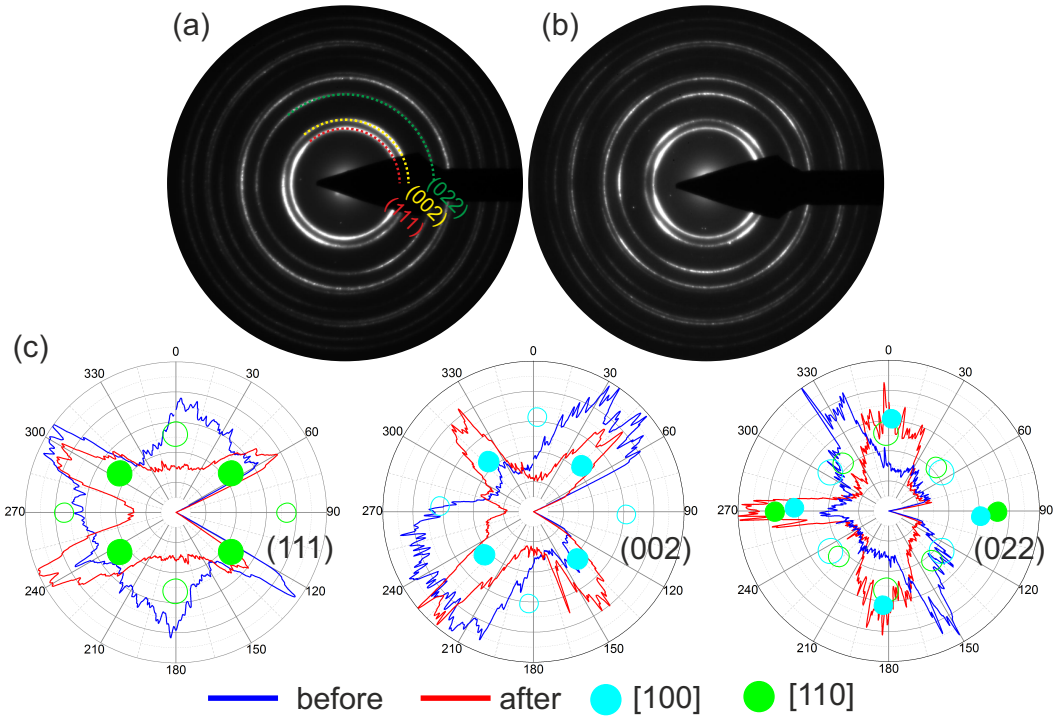

FIGURE 3.7: Analysis of texture in nanocrystalline Au films before and after *in situ* tensile straining. (a) ED pattern recorded on the Au film before the experiment. The {111}, {002}, {022} diffraction rings are highlighted. (b) ED pattern recorded after the experiment. (c) Plots of the radial intensity distribution confined to the highlighted diffraction rings. A strengthening of the pristine film texture is observed, which is related to grain rotation effects. blue: before straining, red: after straining, turquoise: [100], green: [110], the filled circles represent the respective reflections of each figure (111), (002) and (022), not to scale to avoid overlap.

evolution of nc texture observed in this experiment is a definite result of the applied strain, e.g. by strain-induced grain rotation and anomalous growth of grains in the favourable orientation, by unfolding of the wrinkled film, or if this effect is just arising due to possibly illuminating non-identical sample positions in the diffraction experiment.

In context of experimental reliability it has to be stressed that no direct measurement of applied stress to the sample is available and further mechanoelectrical characterization requires intense design improvement and a sample holder with heating capabilities plus wiring and electrical contacts. In addition, handling of the functional grid platform exhibits currently several major issues: (1) Manual pre-straining of the grids as described above often results in broken spring-elements (depending on design) and inclined spring deformation leading to asymmetric straining in the experiment. For improving the pre-straining process, an improved sample stage with an acting piezo-driven force motor as shown in [153] has to be designed, but on flat surface, since pre-straining without stabilizing support results in bending of the spring and uneven leveling of device structures at the gap. (2) Loading and fixation of suitable electron transparent samples onto the grid platform is challenging. Macroscopic samples such as the demonstrated ZnO networks and Au films can be placed and glued manually, but certain specimens would require the handling with micro-manipulators inside a FIB/SEM. In principal, it should be possible to transfer an ion-milled sample to the grid platform. However, state of the art grid designs are not suitable for the standard small dimensions (15x10 m) of a FIB prepared specimen. In addition, poor manipulation of specimens with the *Omniprobe*

manipulator results in misaligned samples with respect to the loading axis or sample damage prior to testing. Also Ga-ion implantation is known as an additional source of sample modification [159] and Pt-deposits acting as clamps do not always provide the desired stiffness needed during tensile testing.[160] (3) The most challenging is the mechanical instability of the flexible spring structure when transferring the loaded grid to the Gatan$^{\text{Inc}}$ heating holder available in Kiel. This holder uses a screw-based clamping system to fixate a TEM grid between platelets of Beryllium. The screwing fixation exposes the grid to large shearing forces which result in high probability for sample detachment by deformation of the spring stage.
To overcome these limitations, a more rigid grid design or heating holder geometry could enable more reliable use of the functional grid platform in practical application to study potential morphological changes, phase transformations, defect propagation or other mechanical induced phenomena.[153]
With the development of more robust designs, the functional grid platform could potentially offer the flexibility to perform cyclic loading tests outperforming existing chips. But, for a high-quality multipurpose experiment, such as measuring the strain-dependent current flow over a Schottky-barrier through a piezoelectric material, an experiment describing the piezotronic effect, conventional chip-based approaches might be more favourable.

Ultramicroscopy 182 (2017) 10–16

Contents lists available at ScienceDirect

Ultramicroscopy

journal homepage: www.elsevier.com/locate/ultramic

Functional NiTi grids for *in situ* straining in the TEM

U. Schürmann[a,1], C. Chluba[b,1], N. Wolff[a], D. Smazna[c], R. Lima de Miranda[e], P. Junker[d], R. Adelung[c], E. Quandt[b], L. Kienle[a,*]

[a] Institute for Materials Science, Synthesis and Real Structure, Christian Albrechts University, Kaiserstraße 2, Kiel D-24143, Germany
[b] Institute for Materials Science, Inorganic Functional Materials, Christian Albrechts University, Kaiserstraße 2, Kiel D-24143, Germany
[c] Institute for Materials Science, Functional Nanomaterials, Christian Albrechts University, Kaiserstraße 2, Kiel D-24143, Germany
[d] Institute of Mechanics, University of Wuppertal, Gaußstraße 20, Wuppertal D-42119, Germany
[e] Acquandas GmbH, Kaiserstraße 2, Kiel D-24143, Germany

ARTICLE INFO

Article history:
Received 6 October 2016
Revised 19 May 2017
Accepted 1 June 2017
Available online 9 June 2017

Keywords:
In situ straining
Transmission electron microscopy
Shape memory alloys
ZnO
Finite element simulations

ABSTRACT

In situ measurements are a pivotal extension of conventional transmission electron microscopy (TEM). By means of the shape memory alloy NiTi thin film Functional Grids were produced for *in situ* straining as alternative or at least complement of expensive commercial holders. Due to the martensite-austenite transition temperature straining effects can be observed by use of customary heating holders in the range of 50 to 100 °C. The grids can be produced in diversified designs to fit for different strain situations. Micro tensile tests were performed and compared with finite element simulations to estimate the applied forces on the sample and to predict the functionality of different grid designs. As a first example of this Functional Grid technology, we demonstrate the impact of applying a strain to a network of ZnO tetrapods.

1. Introduction

In the last years, the increasing necessity for *in situ* observations in analytical methods becomes apparent. In the field of transmission electron microscopy a wide range of parameters have been altered inside the instrument. Next to the examination of temperature dependent properties where *in situ* heating holders are widely-used also electrical biasing, electrochemical reactions, electron beam irradiation as well as mechanical and tensile testing were examined [1–6]. Even for novel and sophisticated setups using TEM-compatible MEMS devices one drawback of all these methods is often the need for dedicated and expensive devices and holders [7,8].

In this work we present a new approach for *in situ* straining of samples by using a Functional TEM Grid composed of shape memory alloy (SMA) Nickel-Titanium thin films which can be utilized inside a common TEM heating holder at moderate temperatures. Morphological changes, phase transformations, straining effects, defect propagation and other mechanical induced phenomena are intended to be observed with this technique.

The shape memory effect of NiTi alloys depends on the martensitic phase transformation between the cubic high temperature phase austenite and the tetragonal low temperature phase martensite. This well-known effect is described in detail in the literature [9–11]. Cooling from the austenite phase results in a twinned martensite, which keeps the macroscopic shape of the austenite phase. The twinned martensite consists of three twin variants with different c-axis orientation. Deformation occurs via detwinning of this martensite leading to a macroscopic shape change with up to 8% strain. Application of moderate heating initiates back transformation into the austenite phase and as a result the material recovers its original shape.

These austenitic transformation temperatures strongly depend on the alloys composition with marginal variations and can be tailored precisely by variation of fractions of an atomic percent. The composition of the alloy used in this study was chosen to provide an austenite start temperature well below 100 °C to avoid side effects on the sample during straining like undesired phase transitions.

To achieve an effect on the material to be tested, a sufficiently high force has to be applied on the sample. This force can be determined directly by tensile test measurements or estimated indirectly by finite elements methods (FEM). Both methods were combined to draw conclusions about the utility of the Functional Grids. Furthermore the feasibility of FEM on the presented design shows the possibility to predict the suitability of other and more complex designs in order to conduct variable kinds of deformation experiments in TEM.

* Corresponding author.
E-mail address: lk@tf.uni-kiel.de (L. Kienle).
[1] U. Schürmann and C. Chluba contributed equally to this work.

http://dx.doi.org/10.1016/j.ultramic.2017.06.003
0304-3991/

Table 1
Used model parameters. Details on the model and the respective meaning can be found in [16,17].

Transformation strain η	0.051 [-]	Poisson's ratio for transformation ν_T	0.45 [-]
Elasticity module austenite E_A	60 [GPa]	Poisson's ratio for austenite ν_A	0.35 [-]
Elasticity module martensite E_M	40 [GPa]	Poisson's ratio for austenite ν_M	0.35 [-]
Enthalpy constant a	5.5 [MPa]	Entropy constant b	0.23 [MPa/K]
Dissipation parameter r	4.1 [MPa/s]		

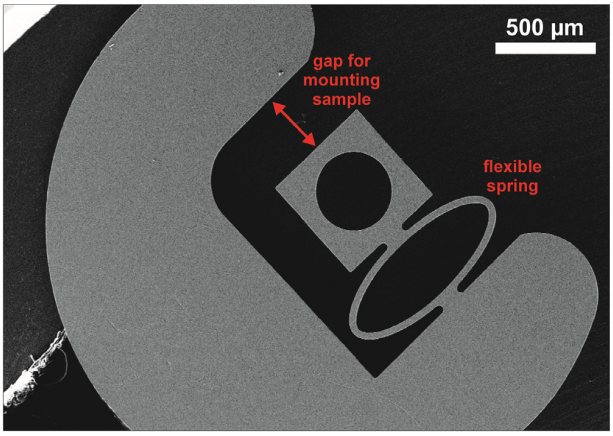

Fig. 1. SEM image of a NiTi grid in relaxed martensitic state at ambient temperature.

We demonstrate the effectiveness of the Functional Grid on a ZnO tetrapod network produced within the recently introduced flame transport synthesis (FTS) [12,13].

2. Experimental

The Functional Grid device fabrication was performed by cleanroom technology following a flow chart described in detail elsewhere [14,15]. The relevant steps to obtain freestanding structured NiTi films comprise sputter deposition onto pre-structured sacrificial layers followed by chemical wet-etching. Two different setups were investigated: the as-obtained amorphous films possess a composition of $Ti_{51}Ni_{49}$ and thickness of ~50 µm and ~40 µm, respectively. Crystallization and adjustment of the transformation temperatures is conducted by a sequential heat treatment at 650 °C for 10 min using rapid thermal annealing. Diversified designs can be realized with respect to individual application. *In situ* straining experiments were carried out in a TEM Tecnai F30 STwin microscope (300 kV, field emission gun (FEG) cathode, spherical aberration coefficient $C_s = 1.2$ mm) using a double-tilt heating holder (Gatan). A Zeiss Gemini Ultra55Plus was applied for scanning electron microscopy (SEM).

To determine the force displacement curve of the Functional Grid during application a combination of micro tensile tests and simulation was utilized. Tensile tests have been performed using a self-built micro tensile test setup consisting of an actuator (PI M-229.26S) and a load cell (ME KD24s 10 N). During testing the grid deformation was observed using an optical microscope. For the mechanical tests grids with two different strut widths of 50 µm and 40 µm are used.

Along with the experimental investigations, numerical simulations of the 50 µm grid based on a variational material model for shape memory alloys were performed. The model solely relies on energetic material parameters, i.e. for the dissipated energy due to phase transformations. This allows for one single model calibration. It has been shown in [16] and [17] that the model can be calibrated using either tensile tests at two different temperatures or one single digital scattering calorimetry (DSC) measurement. This unique property of the model ensures a huge reliability of the numerical results. The model was implemented into the finite element code FEAP and the parameters according to Table 1 were used.

The numerical simulations provide assistance to understand the evolving phase transitions and indicate the parts of the specimen under maximum stress/load. Furthermore, an investigation of the interplay between geometry and mechanical / thermal loading can be employed.

For the visualization of a straining experiment a small amount of ZnO network (macroscopically appearing as "wool") was fixed to the pre-strained Functional Grid across the gap by using UV hardened, commercially available glue. The ZnO wool consists of a variety of micron-sized crystal morphologies including wires, tetrapods and flakes, which are interconnected and forming in such a manner a 3D network.

The ZnO 3D network was prepared by a modified flame transport synthesis (FTS). During the FTS that is introduced in our previous publications [12,13] the Zn particles get oxidized in normal atmosphere of the furnace and a polyvinyl butyral (PVB) component is burned creating a defined oxygen atmosphere. When the temperature has reached 900 °C the vaporized Zn oxidizes and is deposited on the walls of the ceramic crucible where the precursors are placed initially. In a new modified approach no polymer precursor is used, but the small amount of Zn (covering less than

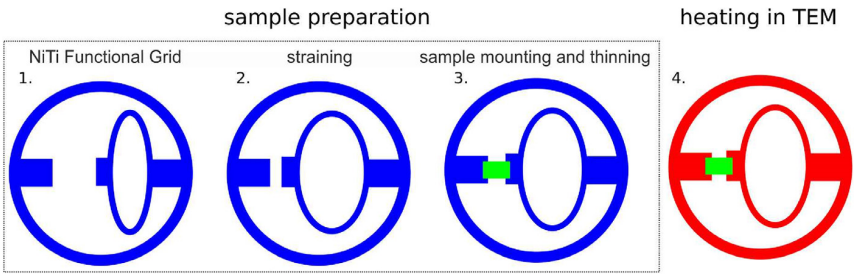

Fig. 2. Schematic of the Functional Grid concept: sample preparation at room temperature and TEM analysis by using a heating holder. 1. Sketch of the Functional Grid in the relaxed martensitic state, 2. Pre-straining of the grid introduces deformation and local detwinning of the martensite. 3. Sample (green) mounting 4. Afterwards, the grid is transfered to a TEM heating holder. During analysis the temperature of the grid is increased and force acting on the specimen is built up during the martensite-to-austenite transformation process recovering its original shape as depicted in I. (For interpretation of the references to colour in this figure legend, the reader is referred to the web version of this article.)

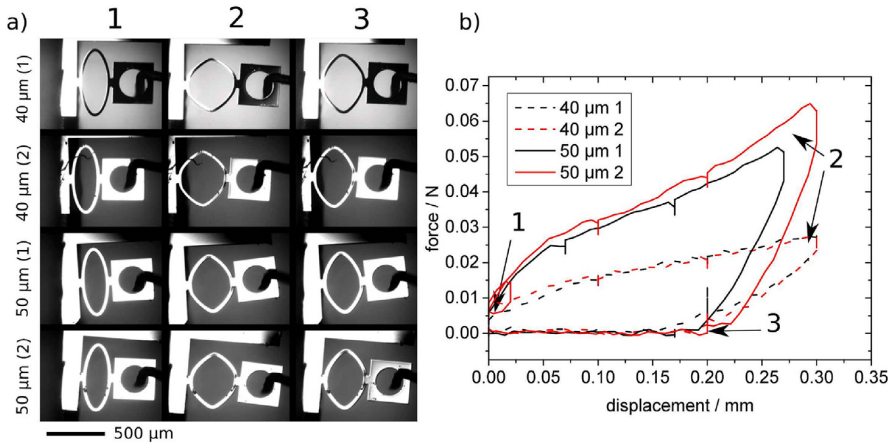

Fig. 3. Pre-straining experiments of four grids with 40 µm and 50 µm spring width, respectively. a) shows the deformation at three stages 1 (undeformed), 2 (stressed), and 3 (unloaded/deformed) denoted in the corresponding stress strain curve b). The drop-off in the force at several reading points are caused by the interruption of the measurement due to image capturing.

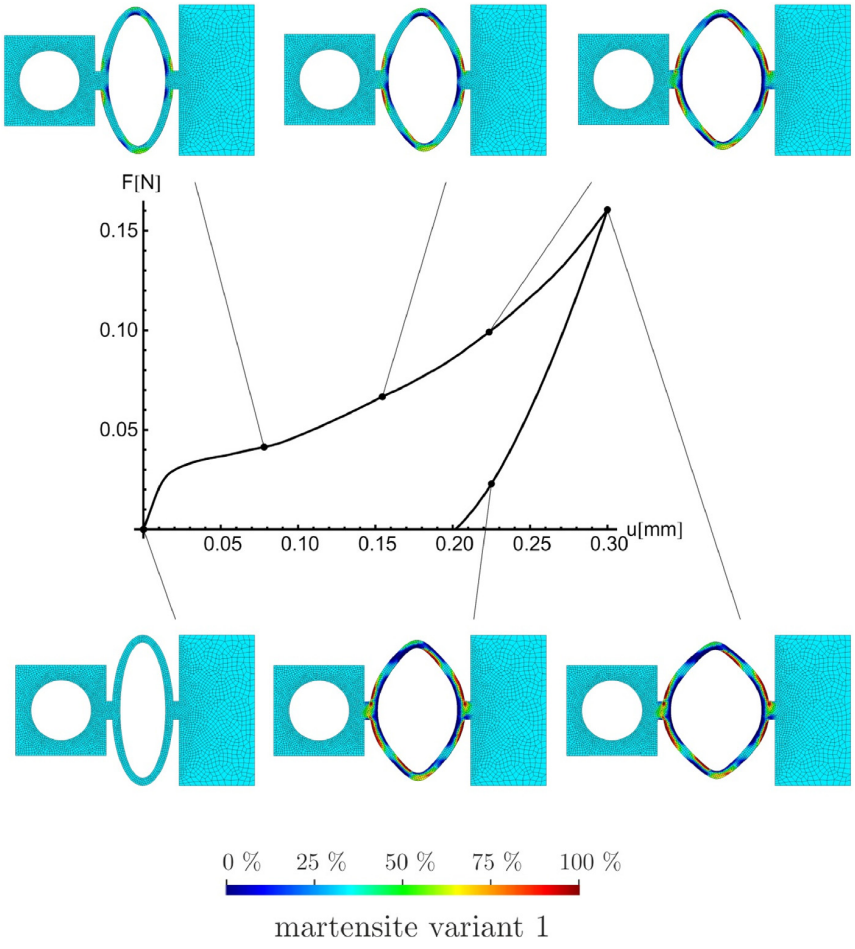

Fig. 4. Calculated stress strain curve by FEM and distribution of one martensite variant over the Functional Grid during six states of the pre-straining process (exact description see text).

10% of the ceramic crucible) is placed into the furnace preheated to 900 °C and containing of 90% nitrogen atmosphere. When the Zn is converted to vapor after 7 minutes, nitrogen flow is changed to pressured air and the reaction of Zn oxidation takes place creating a 3D interconnected network of ZnO structures.

3. Results

The functionality of the thin film Functional Grids relies on a compact semi-opened ring ending up in spring-like flexible parts where the grid can be pre-strained upon introducing the de-twinned martensitic phase. An SEM image showing one of the

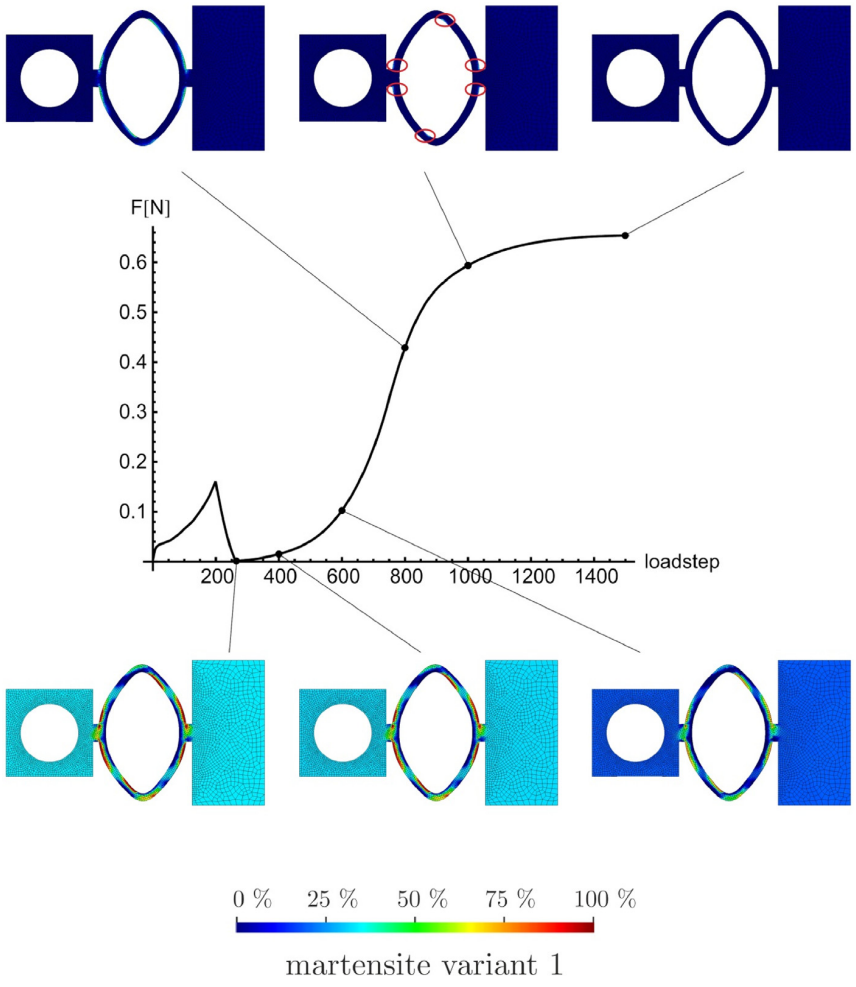

Fig. 5. Force/displacement curve of the specimen over the loadsteps during pre-straining (up to load step 265) and subsequent heating. The increasing amount of blue areas is an indication of the propagating austenitic phase. The red circles emphasize very small martensitic zones, where remarkable higher temperature is needed for the back transformation, responsible for the decreasing slope of the curve. (For interpretation of the references to colour in this figure legend, the reader is referred to the web version of this article.)

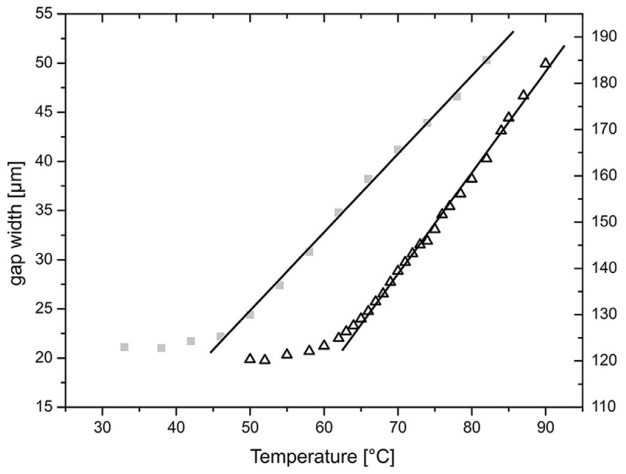

Fig. 6. Temperature dependence of the gap width of two Functional Grids with different designs and starting width after pre-straining. Squares representing design with starting width of 20 µm (left axis), triangles representing design with starting width of 120 µm (right axis). Linear fits are given starting at the austenite starting temperature.

tested designs is depicted in Fig. 1. The active region is assumed to be located inside edges of the filigree arms of the spring. At this flexible component pre-straining is necessary to minimize the gap where the actual sample should be mounted. During heat treatment above the austenite starting temperature, e.g. inside TEM, the spring arms re-transform into the austenitic phase retaining its original shape, thereby applying strain onto a mounted sample. The process sequence is depicted schematically in Fig. 2 on the basis of a principle Functional Grid design.

3.1. Micro tensile testing

Micro tensile testing experiments were performed to determine the forces at the pre-straining and to measure the forces applied during the *in situ* TEM experiments. Two designs with a structure thickness of 40 µm and 50 µm were tested, in which two grids of each design were used for reproducibility. The deformation states (1. undeformed, 2. stressed and 3. unloaded/deformed) as well as the stress-displacment curves are shown in Fig. 3. The required force for pre-straining is twice the value of the 50 µm compared to the 40 µm structure size but the remaining deformation after unloading is with ~200 µm comparable for both. Reproducibility derivations of the deformation micrographs and the stress-

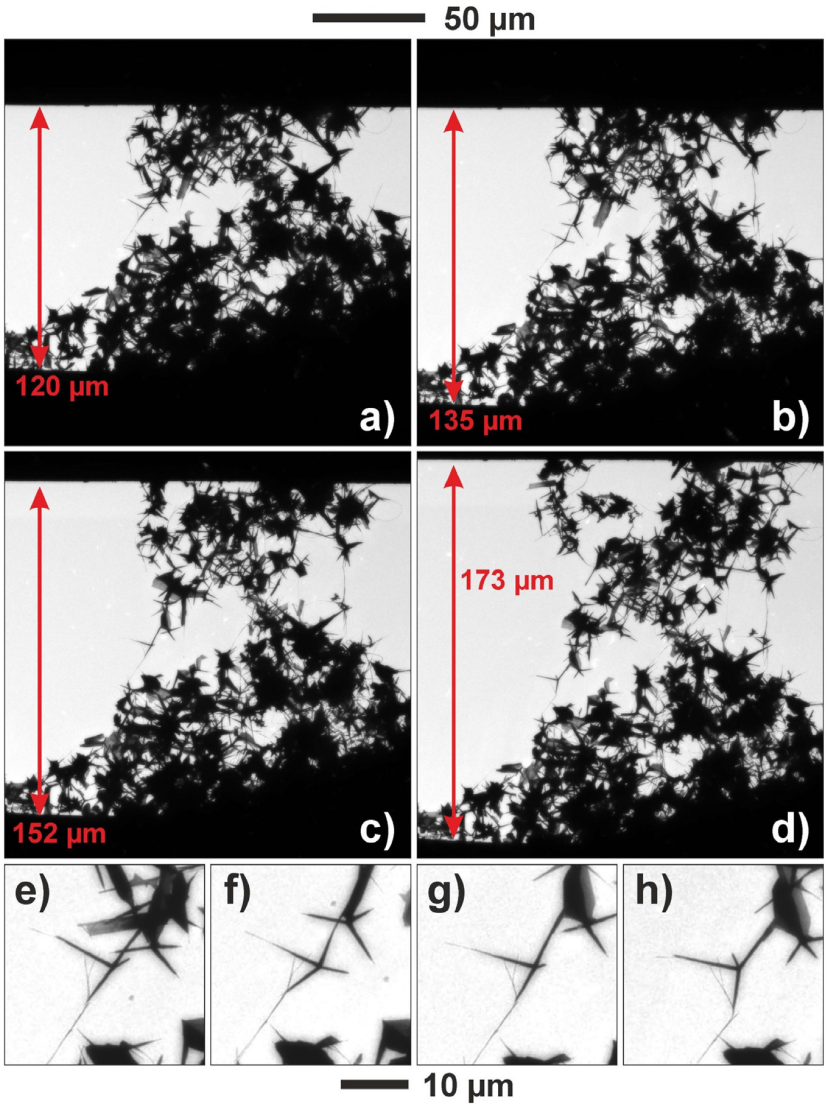

Fig. 7. First *in situ* straining experiments via Functional Grids. TEM Images at low magnification showing the gap of a grid loaded with a ZnO network at different temperatures: a) 50 °C, b) 68 °C, c) 76 °C and d) 85 °C. An enlargement of a detail showing a rotating tetrapod at the same temperatures is given in e–h).

displacement results are considered to be caused by the sample mounting and not by the structure itself. This problem is likely to be solved by using more advanced handling and mounting techniques which can be easily implemented by additional structuring.

3.2. Finite elements simulation

Finite elements methods were applied for more exact determination of the transition process of the Functional Grids. Questions to be addressed are the magnitude of the martensitic-austenitic transformation zone, the prediction which design may fulfil best the requirements of particular applications, and the estimation of the applied forces to the sample.

Fig. 4 shows the martensitic material behaviour of the specimen. After a linear elastic increase of forces over prescribed displacement, phase transformation is initialized. This microstructural rearrangement (detwinning) is accompanied by a highly non-linear material reaction. Due to geometric reasons, inhomogeneous bending states are predominant in the specimen which prevents a flat plateau. However, the onset of the transformation process can easily be identified ($u = 0.014$ mm). The uploading process simulation is also given in a video sequence (link video2). For a more detailed investigation, the distribution of the martensitic configuration is plotted for various load steps. The initial state is given as a homogeneous distribution of the martensite variant. Since the model calculates three variants (each with a transformation strain in the respective Cartesian direction), the initial value is 1/3. As expected, the focal points of the ellipse transform first, while the rest of the elliptic part of the specimen transforms at larger loads.

Fig. 5 shows the force/displacement curve of the specimen over the loadsteps during the pre-straining and the following heat treatment. This curve is identical to the one presented in Fig. 4 up to a resultant force of zero Newton (load step 265) during the mechanical loading and unloading. After mechanical unloading, temperature is increased linearly with fixed displacements at the left and right hand side of the boundary value problem. While the material transforms temperature-driven from the martensitic composition to the austenite state, the resultant force increases due to the fixed boundary conditions. Small variations of the microstructure induce large forces (load steps 400 and 600). The back transforma-

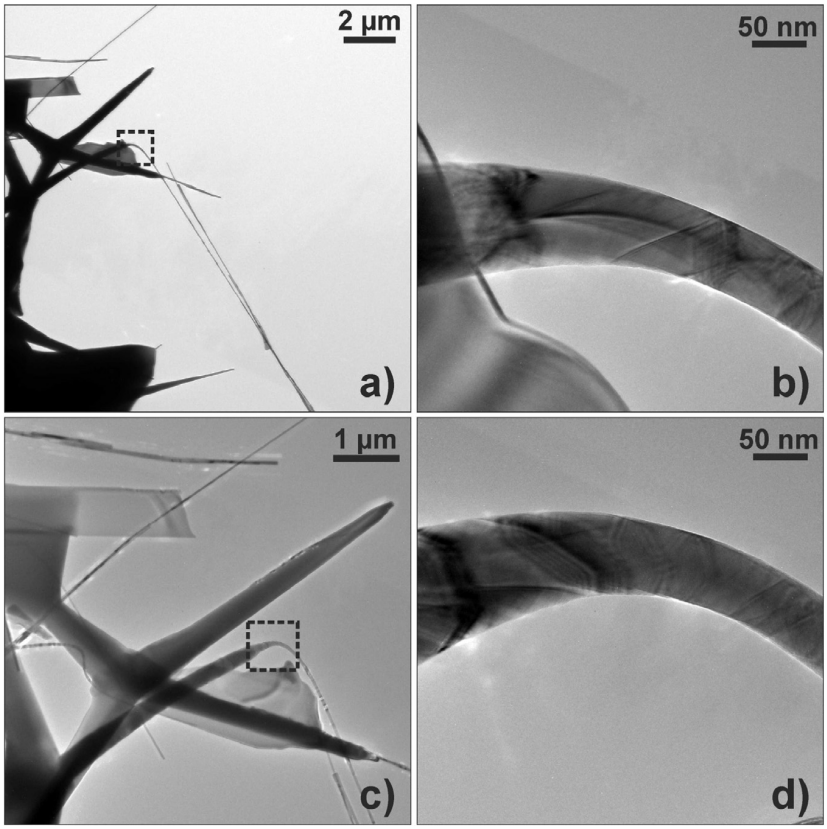

Fig. 8. TEM Images presenting a bent wire as part of the ZnO network at different temperatures: a)+b) 71 °C, c)+d) 90 °C.

tion of very small martensitic zones (load step 1000, red circles) requires a remarkably higher temperature increase as compared to the beginning (load step 400). This effect decreases the slope of the curve. Finally, the force converges since the specimen has completely transformed to austenite.

Due to the geometry, large distortions may be expected during mechanical loading. This would require formulating the model in the context of large deformation. This topic is beyond the scope of the present contribution. We therefore emphasize here that some derivations between experimental and numerical force/displacement relations may be expected which we have to neglect during the further discussion. Details on the implementation of the model into a finite element routine are given in [18].

The numerical simulations allow investigating the distribution of the martensitic variants and thus detect the most loaded zones. Furthermore, the thermo-mechanically coupled structure behaviour can be studied.

3.3. *TEM* in situ *experiments*

In situ TEM heating experiments show the linearity of the temperature dependence of the gap width for an unloaded as well as for a loaded grid. Starting at room temperature with a gap width of ca. 20 µm for an unloaded grid this width increased initially slowly with 200 nm/K up to the austenite starting temperature at almost 50 °C. From this temperature the underlying function of the grid started and the gap width extended at a rate of 800 nm/K (Fig. 6, square symbols). For a grid loaded with a ZnO network another design was used where the starting gap width was already 120 µm. For this grid an extended linear rate of 2.2 µm/K is given at temperatures above 60 °C due to the modified design (Fig. 6, triangle symbols). The heating rate of the holder was set to 1.5 K/min. For recording images the heating ramp was paused. During this time the increase of gap distance was not proceeding demonstrating high mechanical reliability of the Functional Grid. Experiments with several designs show that the velocity of gap broadening is strongly dependent on the grid design.

Fig. 7 and a video sequence (link video1) illustrate the influence of the straining on the 3-dimensional ZnO network using the Functional Grid. During the experiment the gap width is increasing from initially 120 µm to more than 180 µm. The individual building blocks of the ZnO network are interconnected through entangled wires and tetrapods. These links are stretched during the increase of gap distance. As a result crystalline wires which are fixed on static parts of the network are progressively bent reaching angles beyond 90° with increasing temperature (cf. Fig. 8). Tetrapods as integral part are connected via two of its arms to the rest of the network. Under straining the tetrapods are observed to rotate, as shown in the detail enlargements in Fig. 7e–h).

4. Discussion

The results of the micro tensile tests and the finite elements simulations are similar within certain limits. The shape of the curves corresponds and the remaining displacement at a force of 0 N is 0.2 mm. This correlation argues for the assumption that the simulated forces for the *in situ* heating experiment inside the TEM (up to 0.6 N) are also reliable. This maximum applicable force is large enough to treat samples with a small cross-sectional area like TEM samples which has to be electron transparent. The agreement between the tensile tests and the simulations is a prerequisite for the prediction of suitable grid designs.

The exemplification of the Functional Grids with 3D ZnO network samples shows the observability of changes in the morphology during the *in situ* straining experiment. Until now we have confined on the observation of morphology changes but due to the possibility to controllably terminate and to resume again the heating process it should also be possible to perform electron diffraction on proper samples sequentially *in situ*.

Our future work should exceed the present proof of principle. Besides network samples also thin film samples, e.g. polymer / nanoparticle composites, are intended to be strained with the Functional Grids, although the mounting and required thinning via focussed ion beam milling is yet very sophisticated.

Other mechanical modes like compression or torsion should be accessible with modified grid designs. It is conceivable to design grids which have more than one spring so one can cycle proper samples with these Functional Grids. Even the allocation of electrical contacts seems feasible to monitor the alteration of electrical properties during sample straining.

5. Conclusion

In this work we have shown the possibility to produce Functional Grids out of NiTi shape memory thin films for *in situ* straining of samples in the TEM using customary heating holders. The functionality was demonstrated at 3D ZnO networks where single wires were bent and tetrapods as part of the network were distorted.

Finite elements methods have shown that the elliptic spring is loaded most and all mechanically induced phase transformations are confined. Furthermore, numerical simulations have revealed that the increase of temperature results in a remarkable large force which once again shows the potential of shape memory alloys for actuator systems. The values at the pre-straining process were verified with a micro tensile testing device.

Acknowledgements

This work was funded by the German Research Foundation (DFG) as part of the Collaborative Research Center 1261–Magnetoelectric sensors from composite materials to biomagnetic diagnostics (SFB 1261). The authors want to thank Christin Szillus, Matthias Frank, Niko Carstens and Christiane Zamponi for sample preparation. We thank Dustin R. Jantos for the creation of the finite element mesh.

Supplementary materials

Supplementary material associated with this article can be found, in the online version, at doi:10.1016/j.ultramic.2017.06.003.

References

[1] F.M. Ross, In situ transmission electron microscopy, in: P.W. Hawkes, J.C.H. Spence (Eds.), Science of Microscopy, Springer, New York, 2007, pp. 445–534.
[2] U. Schürmann, M. Winkler, J.D. König, X. Liu, V. Duppel, W. Bensch, H. Böttner, L. Kienle, In Situ TEM investigations on thermoelectric Bi_2Te_3/Sb_2Te_3 multilayers, Adv. Eng. Mater. 14 (3) (2012) 139–143.
[3] A. Asthana, K. Momeni, A. Prasad, Y.K. Yap, R.S. Yassar, In situ probing of electromechanical properties of an individual ZnO nanobelt, Appl. Phys. Lett. 95 (17) (2009) 172106.
[4] S. Yang, L. Wang, X. Tian, Z. Xu, W. Wang, X. Bai, E. Wang, The piezotronic effect of zinc oxide nanowires studied by in situ TEM, Adv. Mater. 24 (34) (2012) 4676–4682.
[5] T. Yokota, M. Murayama, J.M. Howe, In situ transmission-electron-microscopy investigation of melting in submicron Al-Si alloy particles under electron-beam irradiation, Phys. Rev. Lett. 91 (26) (2003) 265504.
[6] M. Deng, V. Hrkac, U. Schürmann, B. Erkartal, N. Wolff, K. Gerwien, B. Hesseler, F. Beiroth, W. Bensch, V. Duppel, L. Kienle, Nanocomposite $CdSe/Cr_2Se_3$: synthesis, characterization, and in situ transformation study, Z. Anorg. Allg. Chem. 641 (2) (2015) 214–220.
[7] D.C. Bufford, D. Stauffer, W.M. Mook, S.A.S. Asif, B.L. Boyce, K. Hattar, Combining orientation mapping and in situ TEM to investigate high-cycle fatigue and failure, Microsc. Microanal. 22 (S3) (2016) 1736–1737.
[8] E. Izadi, A. Darbal, P. Peralta, J. Rajagopalan, In situ TEM Straining of ultrafine–grained aluminum films of different textures using automated crystal orientation mapping, Microsc. Microanal. 22 (S3) (2016) 1950–1951.
[9] K. Otsuka, X. Ren, Physical metallurgy of Ti–Ni-based shape memory alloys, Prog. Mater. Sci. 50 (5) (2005) 511–678.
[10] J. Frenzel, A. Wieczorek, I. Opahle, B. Maaß, R. Drautz, G. Eggeler, On the effect of alloy composition on martensite start temperatures and latent heats in Ni–Ti-based shape memory alloys, Acta Mater. 90 (2015) 213–231.
[11] C. Chluba, W. Ge, R.L. de Miranda, J. Strobel, L. Kienle, E. Quandt, M. Wuttig, Ultralow-fatigue shape memory alloy films, Science 348 (6238) (2015) 1004–1007.
[12] Y.K. Mishra, S. Kaps, A. Schuchardt, I. Paulowicz, X. Jin, D. Gedamu, S. Freitag, M. Claus, S. Wille, A. Kovalev, S.N. Gorb, R. Adelung, Fabrication of macroscopically flexible and highly porous 3d semiconductor networks from interpenetrating nanostructures by a simple flame transport approach, Part. Part. Syst. Charact. 30 (9) (2013) 775–783.
[13] Y.K. Mishra, G. Modi, V. Cretu, V. Postica, O. Lupan, T. Reimer, I. Paulowicz, V. Hrkac, W. Benecke, L. Kienle, R. Adelung, Direct growth of freestanding ZnO tetrapod networks for multifunctional applications in photocatalysis, UV photodetection, and gas sensing, ACS Appl. Mater. Interfaces 7 (26) (2015) 14303–14316.
[14] R. Lima de Miranda, C. Zamponi, E. Quandt, Micropatterned freestanding superelastic TiNi films, Adv. Eng. Mater. 15 (1–2) (2013) 66–69.
[15] E. Quandt, C. Zamponi, R. Lima de Miranda, Method for producing a medical functional element comprising a selfsupporting lattice structure, US8758636 B2 (2014).
[16] P. Junker, S. Jaeger, O. Kastner, G. Eggeler, K. Hackl, Variational prediction of the mechanical behavior of shape memory alloys based on thermal experiments, J. Mech. Phys. Solids 80 (2015) 86–102.
[17] P. Junker, An accurate, fast and stable material model for shape memory alloys, Smart Mater. Struct. 23 (11) (2014) 115010.
[18] P. Junker, K. Hackl, Calibration and finite element implementation of an energy-based material model for shape memory alloys, Shape Mem. Superelasticity (2016) 1–7.

Chapter 4

Materials for Magnetoelectric Sensors

4.1 Piezoelectric Materials

Piezoelectric materials display one key component for the development of highly sensitive ME composite sensors (Figure 4.1) in which the piezoelectric phase translates a magnetic field dependent strain input into an easily measurable ME voltage or piezotronic current output signal. To achieve high piezoelectric performance the piezoelectric phase has to be tailored with respect to the individual application regarding the materials choice, morphological aspects and the specific crystallographic orientation. Furthermore, the use of environmental toxic or rare earth elements such as Pb or Sc have to be considered with care. In addition, the deposition process should be straight forward and compatible with standard process chains used e.g. for microelectromechanical systems (MEMS).

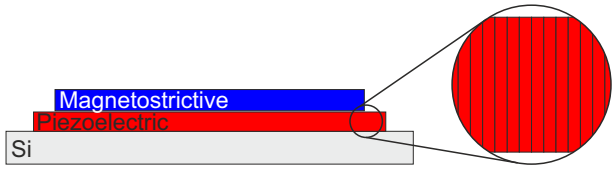

FIGURE 4.1: Cross-section of a typical ME sensor geometry with focus on the piezoelectric material, which can be grown highly textured in case of AlN.

The following sections each give a short theoretical insight into the current status of materials research and highlight the structural and analytical examinations by advanced methods of TEM, which were performed on these materials as the main subject of this thesis. These studies cover a variety of piezoelectric materials suggested for ME sensors. The investigated materials contain group III-nitrides such as Sc-alloyed AlN and different morphologies of GaN as well as oxide materials such as ZnO and $(Ba_{1-x}Ca_x)(Ti_{0.9}Zr_{0.1})O_3$. Section 4.1 closes with a discussion on 2D-layered $MoSe_2$ being an "hot topic" example of materials which gain new interesting properties such as piezoelectricity by the reduction of its dimensions.

4.1.1 AlScN Thin Films

The material selection is most important for the magnetic field sensor since high piezocoefficients and low dielectric losses are linked to the sensor noise performance providing a good signal to noise ratio (SNR). Aluminum nitride (AlN) is up to date the most important thin film piezoelectric for the fabrication of magnetoelectric composite sensors. Despite having a relatively low effective longitudinal piezocoefficient $d_{33,f} = 5.6\,pm/V$, lead free AlN benefits from low dielectric losses as low as $\tan\delta = 0.025\,\%$, when compared to oxide piezoelectrics such as $Pb[Zr_xTi_{1-x})O_3$ (PZT). [22], [161] Plus, for the implementation into common processes micrometer thick layers of [0001]-oriented AlN can be easily grown using sputter-deposition at low temperature compared to 700 °C needed to crystallize PZT.
Due to this high potential of AlN thin films for MEMS application and especially for biomagnetic sensors the enhancement of the piezoelectric performance is of special interest. The manipulation of the wurtzite-type unit cell by the addition of scandium (Sc) ($Sc_xAl_{1-x}N$) was reported resulting in a giant increase in the effective piezoelectric coefficient $d_{33,f}$ by a maximum 500% measured at x = 0.43.[28] The giant improvement of piezoelectricity is explained by a hybridization of covalency onto ionic bonding by alloying with Sc atoms which induces lattice distortions. The lower electronegativity of Sc compared to Al is expected to render the alloys more electrovalent, meaning the strengthening of the ionic character of the covalent bonds.[28], [162] In dependence of the Sc concentration the piezoelectric coefficients monotonically increase until reaching a plateau describing the phase transition to the non-polar rocksalt-type structure beyond x = 43 at%.[163], [164] However, even larger enhancement up to d_{33}=100 pm/V could be potentially achieved in non-equilibrium alloys at even higher Sc amount according to *ab initio* calculations, if phase separation can be kinetically prevented.[165] The large mixing enthalpies and alloy interaction parameters display both high barriers to realize a high crystal quality in $Sc_xAl_{1-x}N$ alloys with $x > 0.2$.

Alternative strategies to enhance the electromechanical coupling of AlN pursue the addition of bivalent and tetravelent elements to substitute the trivalent rare earth element Sc. One of these studies reports about MgNbAlN films achieving a comparable high $d_{33} = 22\,pm/V$.[166] Besides their promising application in ME sensors, AlScN has high potential for implementation in various disruptive technologies because of its excellent compatibility to already existing devices and the recent discovery of ferroelectricity in AlScN films.[167] Such fields of future technology include optoelectronics, energy harvesting, mobile communication or data storage.[168]

The process parameters for implementation of high quality $Sc_xAl_{1-x}N$ thin films with $x > 0.2$ into existing technology platforms and the evolution of piezocoefficients with the Sc content as well as dielectric losses has been investigated and presented in the article: **Identifying and overcoming the interface originating c-axis instability in highly Sc enhanced AlN for piezoelectric micro-electromechanical systems**[1].[169] Without optimization of the deposition parameters, the microstructure of these films was characterized by misoriented grains, which out-of-plane oriented c-axis reduced the overall piezoelectric properties of these films. This investigation was further supported by TEM studies using SAED and dark-field imaging. The results report about the incipient formation of (100) oriented grains in a (001) matrix. Further, analytical studies by TEM EDS proved the chemical homogeneity of

[1]Reproduced from Journal of Applied Physics 122, 035301 (2017), with the permission of AIP Publishing.

disoriented grains with the matrix and a transformation of the Wurzite-$Sc_{0.27}Al_{0.77}N$ crystal structure could be excluded as well for being the reason for this instability. These results supported the optimization of parameter studied resulting into the stabilization of exclusive *c*-axis orientation up to high Sc concentration of $x = 0.43$. In conclusion, engineering of the electrode material by plasma etching and optimization the sputter geometry resulted in a significant improvement of the $d_{33,f}$ coefficients.

A second publication on high Sc content $Sc_{0.43}Al_{0.57}N$ alloys was focusing on the onset of the wurtzite-rocksalt phase transition. Accordingly, ferroelectric switching was demonstrated for the first time for wurtzite-type nitride materials as described in **AlScN A III-V semiconductor based ferroelectric**[2].[167] The ferroelectric switching can be explained on unit cell level by the transition from a N-polar to a metal-polar configuration crossing a metastable layered hexagonal regime. It has been demonstrated that the energy barrier between the polarization states of the wurtzite structure can be sufficiently lowered by strain engineering or incorporation of non-III metals individually to tune the switching voltage for a desired application. However, the mechanism behind the ferroelectric switching is not well understood. TEM electron diffraction demonstrated that the wurtzite-type structure was conserved after switching and that no unconsidered phases are induced by the high power electric fields. As a result of composition, small structural variations in the form of potential cubic grains were occasionally observed.

Future investigations demand for the detailed analysis of the ferroelectric switching mechanism and atomic structure as well as strain analysis at domain boundaries separating opposite polarization states. Among TEM techniques, the ferroelectric domains polarization state can be identified using convergent beam electron diffraction (CBED) as was demonstrated for domains in perovskite-structure ferroelectrics.[24], [123] In CBED the violation of Friedel's rule in ferroelectric domains origins in minute contrast variations in the fringe pattern of (00l) and (00$\bar{\text{l}}$) diffraction disks. The observable fringes in the diffraction disks arise as a result of dynamic scattering processes only provided by a certain sample thickness. However, for serial investigations using complementary methods such as CBED + HRSTEM, the different needs of sample thickness are critical. The thinning by ion beam milling has the potential to change the morphology of the sample and is known to degrade the electronic properties by Ga-implantation and amorphization. Hence, the scientific integrity of such serial investigations is questionable.[170] Different strategies to image the polarization direction in ferroelectric domains rely on electron holography techniques[171] or evaluation of atomic positions in ultra-high resolution Z-contrast images.[172], [173]. Also the investigation of the transition to a paraelectric intermediate state which is supposed to be an unpolar layered hexagonal phase is of high interest. Further, the phase transitions from hexagonal to cubic accompanied with the loss of piezo/ferroelectricity at high Sc concentrations and possible involved intermediate phases and their evolution under temperature influence has to be examined in more detail.

[2]Reproduced from Journal of Applied Physics 125, 114103 (2019) with the permission of AIP Publishing.

JOURNAL OF APPLIED PHYSICS **122**, 035301 (2017)

Identifying and overcoming the interface originating c-axis instability in highly Sc enhanced AlN for piezoelectric micro-electromechanical systems

Simon Fichtner,[1,2,a)] Niklas Wolff,[3] Gnanavel Krishnamurthy,[1] Adrian Petraru,[4] Sascha Bohse,[2] Fabian Lofink,[2] Steffen Chemnitz,[1,2] Hermann Kohlstedt,[4] Lorenz Kienle,[3] and Bernhard Wagner[1,2]

[1]*Materials and Processes for Nanosystem Technologies, Institute for Material Science, Christian-Albrechts-Universität, Kaiserstr. 2, 24143 Kiel, Germany*
[2]*Fraunhofer Institute for Silicon Technology, Fraunhoferstr. 1, 25524 Itzehoe, Germany*
[3]*Synthesis and Real Structure, Institute for Material Science, Christian-Albrechts-Universität, Kaiserstr. 2, 24143 Kiel, Germany*
[4]*Nanoelectronics, Institute of Electrical and Information Engineering, Christian-Albrechts-Universität, Kaiserstr. 2, 24143 Kiel, Germany*

(Received 28 April 2017; accepted 1 July 2017; published online 18 July 2017)

Enhancing the piezoelectric activity of AlN by partially substituting Al with Sc to form $Al_{1-x}Sc_xN$ is a promising approach to improve the performance of piezoelectric micro-electromechanical systems. Here, we present evidence of an instability in the morphology of $Al_{1-x}Sc_xN$, which originates at, or close to, the substrate/$Al_{1-x}Sc_xN$ interface and becomes more pronounced as the Sc content is increased. Based on Transmission electron microscopy, piezoresponse force microscopy, X-ray diffraction, and SEM analysis, it is identified to be the incipient formation of (100) oriented grains. Approaches to successfully reestablish exclusive c-axis orientation up to $x = 0.43$ are revealed, with electrode pre-treatment and cathode-substrate distance found to exert significant influence. This allows us to present first measurements of the transversal thin film piezoelectric coefficient $e_{31,f}$ and dielectric loss tangent tan δ beyond $x = 0.3$. *Published by AIP Publishing.*
[http://dx.doi.org/10.1063/1.4993908]

I. INTRODUCTION

Aluminium nitride (AlN) has attracted widespread attention as a piezoelectric material for micro-electromechanical systems (MEMS) applications in recent years.[1] Due to its advantageous dielectric properties, chemical stability, and robust deposition processes, AlN is now used not only for sensing devices but also for applications such as piezoelectric thin film ultrasound transducers and energy harvesters, which were often envisioned based on ferroelectrics.[2–4] To further advance the potential of such applications, enhancing the comparably low piezoelectric coefficients of pure AlN is of great importance.

The piezoelectricity of AlN is a direct result of its polar wurtzite-type unit cell (w-AlN) with a dipole moment parallel to the c-axis. Thus, unlike in ferroelectric materials, the piezoelectric response of polycrystalline AlN thin films is dependent on a deposition process which guarantees a dominating, or ideally exclusive, c-axis direction. In the past, either (pulsed) DC or RF sputter deposition was employed successfully to produce pure AlN thin films with almost ideal piezoelectric response.[5–7] Beyond this, the addition of Sc to form $Al_{1-x}Sc_xN$ was shown to monotonically increase the measured piezoelectric coefficients with Sc content, until reaching a phase transition to the non-polar rocksalt-type structure.[8,9] A maximal increase in d_{33} and d_{31} by more than 400% was reported at $x = 0.43$.[8,10] In spite of this tremendous increase, most publications since then were focusing on w-$Al_{1-x}Sc_xN$ with less than 30% of Al atoms substituted by Sc and correspondingly lower piezoelectric coefficients.[11–14] Often, loss of c-axis orientation was observed at higher Sc contents, before reaching the wurtzite- to rocksalt-type phase transition, and the effect of sputter gas composition and substrate temperature was investigated.[13,15]

This paper provides compelling evidence of a growing instability of c-axis orientation with the Sc content, which originates at, or close to, the electrode/$Al_{1-x}Sc_xN$ interface. In consequence, factors such as electrode material and pre-deposition treatment become increasingly important to conserve a net-piezoelectric effect in films with higher Sc content and the general susceptibility to process parameters becomes more pronounced. A detailed insight into the changes in $Al_{1-x}Sc_xN$ morphology during the initial loss of substrate-normal polar orientation is given, based on X-ray diffraction (XRD), SEM, Transmission electron microscopy (TEM), and piezoresponse force microscopy (PFM) analysis.

The distance between cathodes and substrate during deposition was found to have a decisive impact on the degree of overall polarity. Based on an improved electrode/$Al_{1-x}Sc_xN$ interface, a suitable distance could then be determined, which resulted in exclusively c-axis oriented films grown beyond $x = 0.4$. This allowed first measurements of the dielectric loss tangent tan δ and transversal thin film piezoelectric coefficient $e_{31,f}$ at Sc contents beyond $x = 0.3$.

[a)]sif@tf.uni-kiel.de

II. EXPERIMENTAL DETAILS

Based on a process described in a previous paper,[14] $Al_{1-x}Sc_xN$ films were grown by reactive pulsed DC co-sputtering from pure Al (5 N) and Sc (3 N) targets. The Sc content was adjusted by varying the ratio of power applied to the individual targets, while keeping the total power constant. The gas flow during deposition was set to 5.3 sccm of Ar and 15 sccm of N_2. These flows resulted in films with low residual stress (±100 MPa) at $x = 0.27$.[14] As substrates, 6″ (100) c-Si wafers with 2 μm and 8″ (100) c-Si Wafer with 650 nm of oxide were used, with no significant difference in $Al_{1-x}Sc_xN$ film quality observed in direct comparisons between the two. As the bottom electrode, two different configurations were investigated: Pt (100 nm) based (with 20 nm AlN as the adhesion promoter) and Mo (100 nm) based (with 100 nm AlN below to promote textured growth). Pt was chosen due to its chemical inertness and suitability as a seed layer for pure AlN.[16] For comparison, Mo was chosen, due to its prevalence in MEMS process flows based on selective wet etching of the electrode and AlN. The full width at half maximum (FWHM) of the (111) Pt and (110) Mo XRD rocking curve was kept below 2°, ensuring decent electrode crystallinity. Prior to deposition, facultative etching of the electrode surface in an Ar/O_2-plasma in a Sentech SI100 reactor was carried out for 7 min at 200 W. The effect of this treatment will be discussed in the following. In general, the Mo electrode was also rinsed with H_2O to dissolve any native or plasma induced surface oxide.

X-ray diffraction (XRD) Θ-2Θ patterns and rocking curves were measured using Kα radiation in a Seifert XRD 3000 PTS system. Additional Θ-2Θ scans with reduced noise floor and pole figures were obtained in a Panalytical X'Pert Pro MPD system.

The nanoscale piezoelectric properties of our $Al_{1-x}Sc_xN$ thin films were investigated by piezoresponse force microscopy (PFM). Here, a SmartSPM 1000 Scanning Probe Microscope from AIST-NT was used.

Transmission electron microscopy (TEM) analysis using dark field imaging, selected area electron diffraction (SAED), and scanning (S)TEM energy-dispersive X-ray (EDX) analysis were performed on two microscopes, a JEOL JEM-2100 (200 kV, LaB6 cathode) and a Tecnai F30 STwin microscope (300 kV, field emission cathode) equipped with a Si/Li detector (EDAX System). The cross-section sample was prepared by focused ion beam (FIB) milling using a standard lift-out method with a FEI Helios Nanolab system. The electron diffraction data were evaluated by correlating the experimental Miller plane distances with an expanded AlN wurtzite-type unit cell.

The piezoelectric response $e_{31,f}$ was characterized via an aixACCT 4-point bending probe,[17] using only the electrode area and substrate specific quantities to determine the piezoelectric coefficient independently of additional $Al_{1-x}Sc_xN$ material parameters. The dielectric permittivity and loss tangent were measured using a HP 4284A precision LCR meter at 10 kHz and 1 V peak-to-peak.

III. RESULTS AND DISCUSSION

A. Loss of exclusive c-axis orientation

Previously,[14] we reported on the fabrication and piezoelectric performance of 400 nm $Al_{1-x}Sc_xN$ films with $x \leq 0.33$. Excellent $e_{31,f}$ values were measured up to $x = 0.27$. For higher Sc concentrations, a decline in piezoelectric performance was observed. It was speculated that this was due to the appearance of the reported phase transition of the w-$Al_{1-x}Sc_xN$ unit cell to rocksalt-type.[8] This was supported by the appearance of a second type of crystallite with distinct topography in SEM imaging [Fig. 1(b)], at $x = 0.29$. A further increase in the Sc content leads to a complete loss of polar orientation. However, no additional reflections were observed in the measured XRD patterns [Fig. 2] and the FWHM of the (002)-reflection rocking curve was still excellent at $x = 0.29$, with 1.7°.

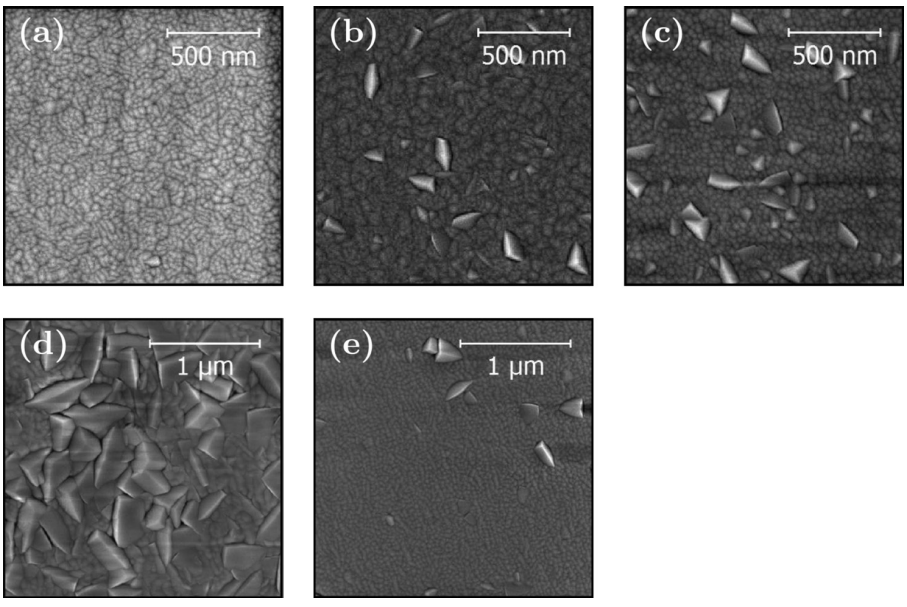

FIG. 1. Comparative SEM top views of $Al_{1-x}Sc_xN$ films deposited on either a Pt or Mo bottom electrode. (a) $Al_{0.73}Sc_{0.27}N$ (400 nm) on Pt, (b) $Al_{0.71}Sc_{0.29}N$ (400 nm) on Pt, (c) $Al_{0.73}Sc_{0.27}N$ (400 nm) on Mo, (d) $Al_{0.73}Sc_{0.27}N$ (2 μm) on Mo, and (e) $Al_{0.73}Sc_{0.27}N$ (2 μm) on a plasma etched Mo electrode.

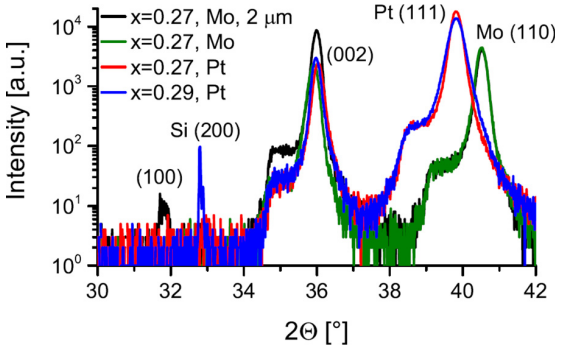

FIG. 2. XRD Θ-2Θ scans of the samples (a)–(d) depicted by SEM in Fig. 1.

Subsequently, a similar effect was observed for $Al_{0.73}Sc_{0.27}N$ films on Mo electrodes. In this case, $e_{31,f}$ dropped by 20% compared to films deposited under the same conditions on Pt. The XRD patterns [Fig. 2] still indicated good c-axis orientation, but SEM images revealed a significant change in sample topography [Figs. 1(c) and 1(d)].

We note that for pure AlN, the combination of seemingly excellent c-axis orientation but reduced piezoelectric response was previously investigated.[18] A correlation with the appearance of traces of secondary w-AlN XRD reflections could be established. The reason for the reduction of piezoelectric coefficients was assumed to be the formation of domains with inverse out-of-plane polarization, but no definite proof was given.

Only after increasing the film thickness of $Al_{0.73}Sc_{0.27}N$ films deposited on untreated Mo to 2 μm, also in our XRD patterns traces of an additional reflection appeared at $2\Theta = 31.7^\circ$ [Fig. 1(d)]. This reflection matches with the (100) peak of $Al_{0.73}Sc_{0.27}N$, taking into account the expansion of the w-$Al_{1-x}Sc_xN$ lattice parameter a upon increasing the Sc content.[8]

Simultaneously, the surface area covered by the new type of crystallite increased significantly [Fig. 1(d)], and $e_{31,f}$ dropped by 40% compared to a film deposited on Pt and dielectric losses increased by a factor of three. This is however not attributed to the appearance of additional grains. Instead, their growth rate surpasses that of the surrounding matrix, giving rise to protruding, cone-like crystallites originating at, or close to, the electrode/$Al_{1-x}Sc_xN$ interface [Fig. 3]. This, and the profound change upon shifting from a deposition on Pt to a deposition on Mo, suggests that the phenomenon itself is influenced by the electrode/$Al_{1-x}Sc_xN$ interface. We also note that no change in crystal morphology was observed in SEM when depositing pure AlN on either Pt or Mo electrodes, with both stacks appearing to be homogeneous. Together with the degradation observed when depositing $Al_{1-x}Sc_xN$ with $x \geq 0.29$ on Pt, this supports that the effect is itself dependent on the Sc content. Thus, a Sc content dependent, interface originating c-axis instability in $Al_{1-x}Sc_xN$ is revealed. This instability makes the fabrication of exclusively c-axis oriented w-$Al_{1-x}Sc_xN$ thin films more challenging as the Sc content is increased.

To provide a more definite understanding with regard to the nature and consequences of the protruding crystallites,

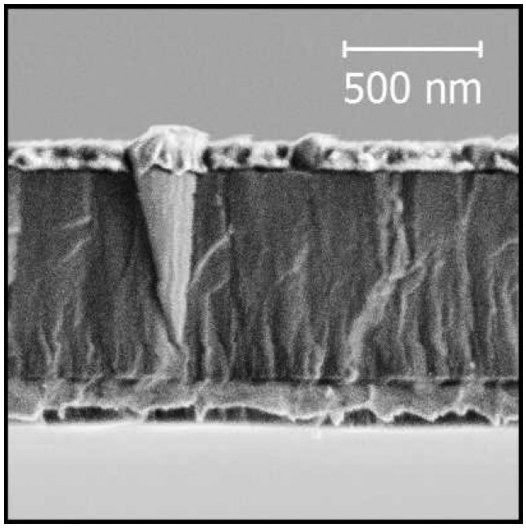

FIG. 3. SEM side view of a 1 μm thick $Al_{0.73}Sc_{0.27}N$ film deposited on plasma etched Mo with protruding, cone-like crystallite present at the line of fracture.

and thus this instability, we performed a study combining PFM and TEM in addition to SEM and XRD on a sample with 2 μm of $Al_{0.73}Sc_{0.27}N$ on a plasma treated Mo surface. As an effect of this treatment, the presence of protruding crystallites was significantly reduced, albeit not eliminated [Figs. 1(d) and 1(e)]. This, however, has to be seen as additional proof that the observed instability is indeed interface related.

As the existence of inversion domains has frequently been observed[6,19–21] in c-axis oriented AlN thin films and could explain the observed drop in the piezoelectric response, PFM was employed to investigate our samples. A sinusoidal excitation voltage of 5 V peak-to-peak amplitude and a frequency of 168 kHz (out-of-resonance) were applied between the conductive AFM tip and the base electrode during the PFM scan. The magnitude and phase of the out-of-plane and in-plane piezoresponse were acquired together with the topographic images, as presented in Fig. 4. Grains similar to the ones depicted by SEM can easily be observed in the topographic image (they are about 50 nm protruding from the surrounding matrix). No evidence for out-of-plane polarization reversal was observed in the out-of-plane phase of the piezoresponse [Figs. 4(c) and 4(e)]. However, the protruding grains do possess a distinct fingerprint in the other components of the piezoresponse. Thus, the in-plane magnitude and phase images suggest that the protruding grains have a different crystal structure or orientation with respect to the surrounding matrix. Moreover, while there are no inversion domains with respect to the out-of-plane polarization, the in-plane phase images reveal an inner structure of the grains. This structure can consist of 180° rotated, anti-parallel domains (sub-grains). A single grain is imaged in Figs. 4(f)–4(j) for more details.

In order to reveal the crystal structure of an individual protruding grain, a TEM study was performed on an electron transparent cross-sectional $Al_{0.73}Sc_{0.27}N$ lamella prepared by focused ion beam milling. Exclusive c-axis orientation normal to the substrate was confirmed for the matrix by electron

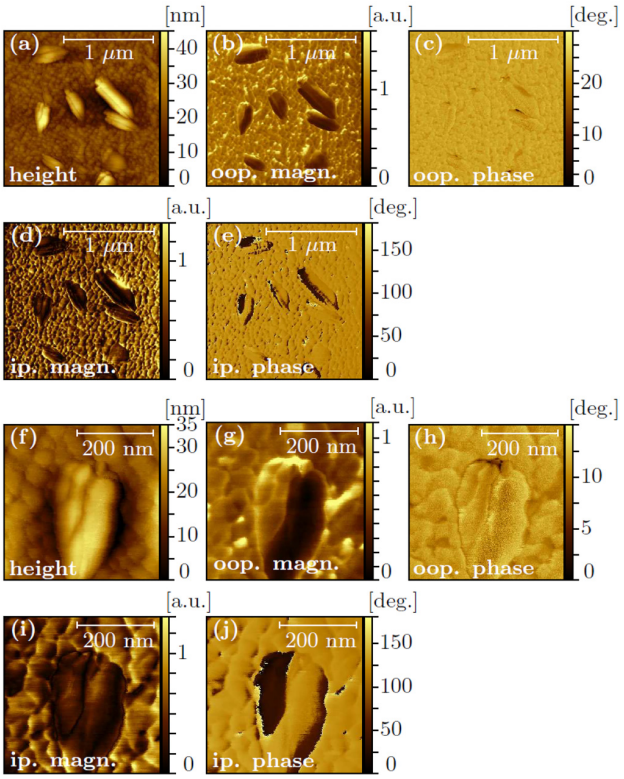

FIG. 4. PFM measurements of $Al_{0.73}Sc_{0.27}N$ on Mo (plasma etched). (a)–(e) 1.7 μm scan. (f)–(j) Single grain scan (oop.: out-of-plane, ip.: in-plane).

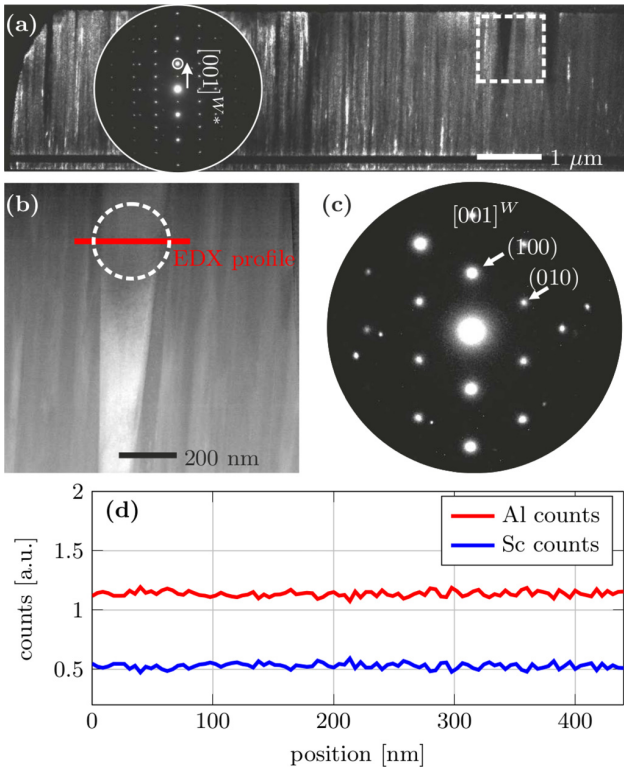

FIG. 5. TEM study of 2 μm $Al_{0.73}Sc_{0.27}N$ on plasma etched Mo: (a) TEM dark field image over the full height of the $Al_{0.73}Sc_{0.27}N$ layer. The inset shows the electron diffraction pattern of the matrix used to gain the contrast displayed. (b) STEM image of a protruding, cone-like, crystallite. (c) SAED pattern along the [001] zone axis of the crystallite indicated in (b). Recorded at a sample tilt of 21° in-plane and 2° out-of-plane. (d) Sc and Al associated intensity as obtained by TEM-EDX linescan over a surface parallel profile including the crystallite shown in (b).

diffraction. The free azimuthal rotation of columnar grains around the c-axis results in the appearance of additional reflections from related zone axes [see supplementary material]. The lattice parameter a of w-$Al_{0.73}Sc_{0.27}N$ was estimated to increase from 3.05 Å in pure AlN to = 3.25 ± 0.02 Å while c remained virtually unchanged. This matches well with the (002) and the suspected (100) orientation observed by XRD [Fig. 3], with the latter resulting in a lattice parameter of $a = 3.26$ Å. TEM dark field images based on the (002) w-$Al_{0.73}Sc_{0.27}N$ diffraction peak revealed strong contrast in cone-like structures corresponding to the protruding grains observed in SEM and PFM before. By choosing an appropriately dimensioned aperture, selected area electron diffraction (SAED) patterns were recorded from an area containing exclusively parts of a cone-like grain. The sample was tilted with respect to the incident beam, until aligned with a low order zone axis. At a sample in-plane tilt of 21°, a pattern matching the [001] w-$Al_{0.73}Sc_{0.27}N$ orientation was obtained. This confirmed a grain with in-plane c-axis alignment—and thus with a vanishing contribution to the piezoelectric out-of-plane response. Nonetheless, the wurtzite-type structure of the unit cell remains. To verify that, in addition, also the chemical composition of the cone-like grains and the surrounding matrix is invariant, EDX spectroscopy was performed in the scanning TEM mode [Fig. 5(d)]. For this, a surface parallel profile centered around the same grain as investigated before was chosen. Over this profile, no significant variation of the respective Al and Sc intensity and thus x in $Al_{1-x}Sc_xN$ was recorded. TEM therefore confirmed the homogeneity and preservation of the w-$Al_{1-x}Sc_xN$ crystal structure at x = 0.27—albeit with the potential of a sizable population of grains with in-plane c-axis orientation.

XRD pole figures of the (002) reflection were recorded in order to investigate a possible correlation between the appearance of protruding crystallites and other secondary orientations aside from the (100) orientation. No such correlation was found. However, pole figures of the (100) orientation at $2\Theta = 31.7°$ (Fig. 6) can illustrate why even a high density of misaligned crystallites still resulted in only a trace of (100) w-$Al_{1-x}Sc_xN$ intensity in Θ-2Θ scans. Measurements of a 2 μm $Al_{0.73}Sc_{0.27}N$ film on Mo without improved electrode treatment, and thus a surface almost covered in (100) oriented crystallites [Fig. 1(d)], revealed a broad center peak with a FWHM of about 19°. In contrast, the FWHM of the (002) reflection in this sample is 1.6°. Taking into account the size dependency $\sim \sin\psi$ of an area element on colatitude ψ allows for an estimation of the total intensity associated with the (100) and (002) lattice planes parallel to the substrate. Assuming a Gaussian distribution symmetric with respect to longitude ϕ gives an intensity-ratio of approximately 1:2 for (100) vs. (002). The fact that the incipient formation of secondary orientations in Al(Sc)N can be hard to identify from XRD patterns is therefore attributed to the diffuse orientation of misaligned grains.

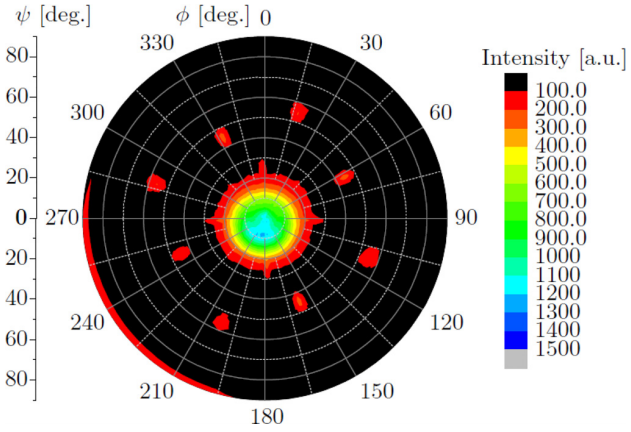

FIG. 6. Pole figure of the $Al_{0.73}Sc_{0.27}N$ (100) reflection at $2\Theta = 31.7°$ of the sample depicted in Fig. 1(d): $Al_{0.73}Sc_{0.27}N$ on untreated Mo (high density of protruding crystallites).

Nonetheless, they are still found to obey a preferential (100) direction. The literature[18,22] discussing the morphology of pure AlN suggest that differences in process conditions and/or substrate can also result in the formation of other secondary orientations besides (100), which might manifest in a similar manner. In consequence, complementary SEM imaging of Al(Sc)N film surfaces is deemed advisable.

While the (100) orientation is thus only loosely aligned when out-of-plane, the [001] direction of the affected grains appears not to reverse, its rotation being limited to a maximum of 90°. This can be deduced from a comparison with the PFM measurements. Here, no signs of out-of-plane polarization reversal were observed on any of the protruding grains, which should be the case, if the [001] direction started to point towards the substrate. In contrast to samples with the presence of protruding crystallites, a sample of $Al_{0.73}Sc_{0.27}N$ deposited on Pt (with no protruding crystallites appearing in SEM) showed no trace of elevated intensity in the center of its (100) pole-figure.

To conclude, an interface originating instability of the c-axis orientation exists in w-$Al_{1-x}Sc_xN$ thin films and becomes more pronounced as the Sc content is increased. The instability manifests in an increased tendency to seed (100)-oriented, cone-like, protruding crystallites. These crystallites nucleate at, or close to, the electrode/$Al_{1-x}Sc_xN$ interface. In the following, approaches for reestablishing an exclusive c-axis orientation normal to the substrate will be discussed.

B. The impact of the electrode/AlScN interface and cathode/substrate distance on c-axis orientation

Both the electrode/AlScN interface and the cathode/substrate distance were found to have a potential impact on the c-axis orientation in w-$Al_{1-x}Sc_xN$ films. Taking into account the results presented above, which indicated the nucleation of (100) oriented grains at, or close to, the electrode/$Al_{1-x}Sc_xN$ interface, it appeared likely that the electrode itself exerts a (de-)stabilizing effect on the $Al_{1-x}Sc_xN$ layer during the initial phase of film growth. The effect of a change in the electrode material (Pt to Mo) was already depicted in Figs. 1(b) and 1(d), with a profound effect on the piezoelectric response of the samples.

We note that, while a certain quality of orientation of the electrode (either (111) Pt or (110) Mo) as expressed by the FWHM of the respective XRD rocking curves is likely required, we find no reason to assume that it is a limiting factor in our experimental setup.

In the context of sputter deposition of pure AlN, previous authors found that treatments by physical ablative methods (e.g., simple sputter etching) of the interface prior to deposition of AlN lead to significantly improved c-axis orientation.[7,23,24] While no definite explanation of the mechanism behind the observed improvement exists, a clear correlation between a plasma pre-treatment of the electrode and the reduction of secondary AlN orientations was confirmed.

We therefore investigated the feasibility of improving the c-axis orientation, first of $Al_{0.73}Sc_{0.27}N$ on Mo, by sputter etching the electrode surface in an Ar/O_2 plasma immediately prior to deposition. This was followed by a rinse in H_2O to dissolve any native or plasma-induced oxide. SEM images of the resulting films reveal a significant reduction of protruding crystallites [Figs. 1(d) and 1(e)]. As no traces of (100) orientation could be detected in the Seifert XRD Setup for the treated film, additional scans in a Panalytical X'Pert Pro MPD setup, offering a lower noise floor, were carried out. Here, traces of (100) orientation could be detected again, albeit with greatly reduced intensity compared to the untreated sample [Fig. 7]. No traces could be detected in an $Al_{0.73}Sc_{0.27}N$ sample on Pt. The piezoelectric coefficient $e_{31,f}$ on plasma etched Mo however was improved close to the level of $Al_{0.73}Sc_{0.27}N$ deposited on Pt with exclusive c-axis orientation. A major reduction of the dielectric loss tangent from 0.51% to 0.15% was also measured. It is therefore concluded that the level of (100)-orientation observed for the sample discussed is sufficiently low to result in very good piezoelectric performance. On Pt, the same etch process resulted in a reduction of protruding grains in $Al_{1-x}Sc_xN$ with $x > 0.27$ as well. This reduction was however not sufficient to allow fabrication of films with $x > 0.3$ and exclusive c-axis orientation.

The previously reported approach to stabilize the c-axis orientation by adapting the Ar/N_2 ratio[13] was not found to result in significant changes in sample topography. As a consequence, controlling the residual stress in $Al_{1-x}Sc_xN$ via this ratio[14] remains feasible.

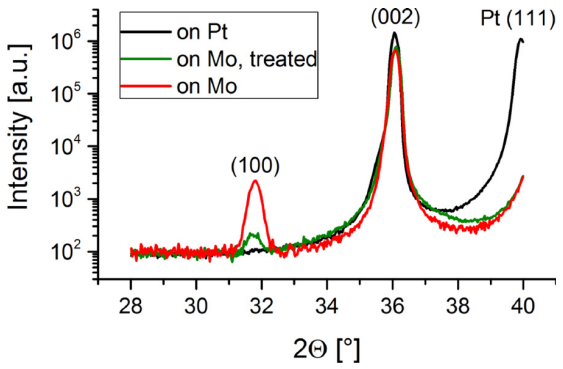

FIG. 7. XRD patterns with reduced noise floor of 2 μm thick $Al_{0.73}Sc_{0.27}N$ films on Pt (no protruding crystallites), on plasma etched Mo (medium density), and untreated Mo (surface almost covered).

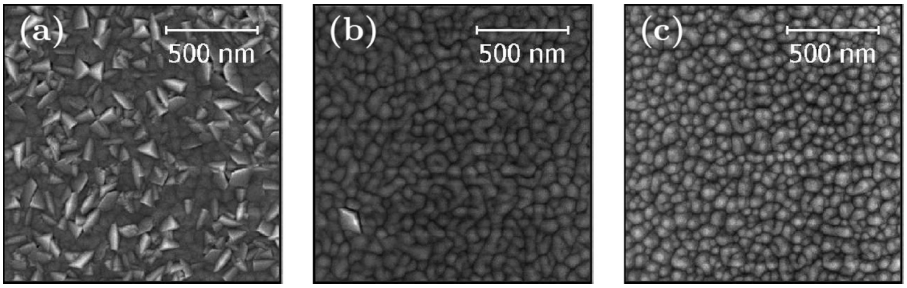

FIG. 8. SEM top view of $Al_{1-x}Sc_xN$ samples deposited on plasma etched Pt electrodes with adapted cathode-substrate distance. (a) 400 nm $Al_{0.64}Sc_{0.36}N$ deposited after increasing the distance by 20 mm, (b) 1 μm $Al_{0.64}Sc_{0.36}N$ deposited after increasing the distance by 30 mm, and (c) 1 μm $Al_{0.57}Sc_{0.43}N$ deposited after increasing the distance by 30 mm.

As an alternative approach to alter the influx of particles on the substrate during sputter deposition, the effect of adapting the cathode/substrate distance was investigated for $Al_{1-x}Sc_xN$ with $x > 0.27$. Initially, the distance was increased by 20 mm. This allowed fabrication of films on plasma treated Pt without traces of (100) orientation up to $x = 0.34$. For values of x exceeding 0.36, the formation of (100) oriented crystallites was observed again [Fig. 8(a)]. Increasing the distance between the cathode and the substrate by another 10 mm then allowed us to increase the Sc content to $x = 0.43$, with virtually no protruding crystallites observable in SEM [Figs. 8(b) and 8(c)] and no trace of (100) orientation recorded in XRD. Pure AlN and $Al_{0.73}Sc_{0.27}N$ films deposited on Pt with any of the three distances investigated were found to be free of (100) oriented grains as well. This again highlights the correlation between the increasing Sc-content and decreasing c-axis stability normal to the substrate. Thus, providing process parameters resulting in exclusive c-axis orientation becomes more challenging when increasing the Sc content but remains feasible.

C. Piezo- and dielectric properties with stabilized c-axis orientation

Based on the improved process described above, films with x up to 0.43 were fabricated, and their transversal thin film coefficient $e_{31,f}$ [Fig. 9] and permittivity and dielectric loss [Fig. 10] were measured. Asides from the electrode area (16 mm^2), substrate thickness, and Poisson ratio ($\nu_{Si,\langle 110\rangle} = 0.065$), no further input or correction was used in the measurement procedure for $e_{31,f}$. This can be seen as an improvement over e.g., the wafer flexure method,[10,27] where the resulting d_{31} depends also on the film's Young's modulus—the latter being strongly dependent on Sc content as well.[10]

$$e_{31,f} = e_{31} - e_{33}\frac{c_{13}}{c_{33}}, \tag{1}$$

$$e_{31,f} = d_{31}\left(c_{11} + c_{12} - 2\frac{c_{13}^2}{c_{33}}\right). \tag{2}$$

Up to $x = 0.43$, $e_{31,f}$ was found to increase monotonically from 1.08 C/m^2 (pure AlN) to 3.16 C/m^2. The slope of $e_{31,f}$ over the Sc content however started to decline above $x = 0.36$. The experimental values nonetheless exceeded values calculated via Eq. (1) from purely theoretical predictions for the variation of the piezoelectric and stiffness tensor e_{ij} and c_{ij} with the Sc content.[25] Experimental values of the stiffness tensor in $Al_{1-x}Sc_xN$ can so far only be found at $x = 0.4$,[26] for samples with less than optimal piezoelectric response.[26] A comparison with purely experimental data on $e_{31,f}$ above $x = 0.17$ (Ref. 11) is therefore limited. Still, $e_{31,f}$ can be determined via Eq. (2), either based on purely experimental[10,26] data or combined with supplementary theoretical[25] predictions for c_{ij} and d_{31}. The thus obtained references however show

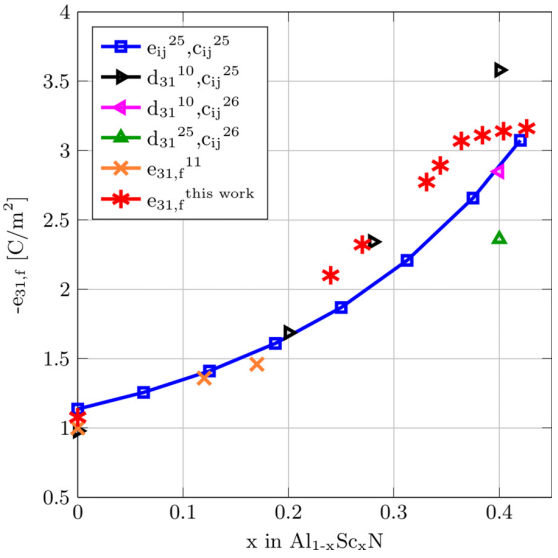

FIG. 9. Transverse thin film piezoelectric coefficient $e_{31,f}$ over percentage of Al atoms substituted by Sc. The values shown are either directly measured,[11] calculated based on Eq. (1) from theoretical data,[25] or calculated based on Eq. (2) using combinations of theoretical[25] and experimental[10,26] data.

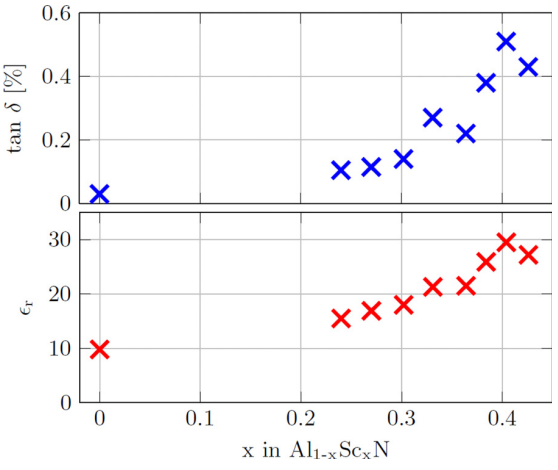

FIG. 10. Relative dielectric permittivity and loss tangent over percentage of Al atoms substituted by Sc.

strong divergence with respect to the particular combination of data at $x = 0.4$ [Fig. 9], with the average $e_{31,f} = 2.92\,C/m^2$.

In the entire range of Sc contents displayed, we observed no traces of additional w-$Al_{1-x}Sc_xN$ reflections in XRD and SEM imaging revealed no distinct second type of crystallite [Fig. 8(c)]. The reduced slope observed for $x > 0.36$ is therefore possibly due to a gradual dissolution of the wurtzite-type $Al_{1-x}Sc_xN$ phase, though no XRD reflections clearly assignable to the material's cubic phase were detected.

The relative dielectric permittivity was found to gradually increase up to a maximum of 29.5 at $x = 0.4$. This exceeds the experimental values published before by Akiyama *et al.*[10] by more than 80% but is in line with measurements reported by Yanagitani and Suzuki.[28]

Reports regarding the dielectric loss of $Al_{1-x}Sc_xN$ with higher Sc contents are still scarce—we found that in selected samples of pure AlN, the dielectric loss tangent $\tan\delta$ could be below 0.04% and was regularly below 0.1%. Up to $x = 0.27$, $\tan\delta$ increased moderately to 0.11%. This was followed by a sharp rise, with $\tan\delta = 0.5\%$ at $x = 0.4$. In the case of MEMS applications which are limited by dielectric noise or other issues arising from energy dissipation within their piezoelectric layer, this deterioration will potentially outcompete the benefits of an increased piezoelectric coefficient beyond $x = 0.3$. Nonetheless, the dielectric losses of the samples investigated remained well below the typically values reported for ferroelectrics.[29,30]

IV. CONCLUSION

In this paper, we presented evidence of an interface originating instability in the morphology of w-$Al_{1-x}Sc_xN$, which becomes more pronounced at higher Sc contents. This instability manifested in protruding, cone-like crystallites, nucleating at, or close to, the electrode/$Al_{1-x}Sc_xN$ interface. Their appearance was correlated with reduced piezoelectric activity. By employing TEM, PFM, and XRD, it was conclusively shown that these crystallites preserve the piezoelectric wurtzite-type structure but obey a diffuse (100) preferential orientation normal to the substrate. This diffuse alignment makes the identification of the incipient formation of this secondary orientation via XRD more challenging. Complementary SEM imaging of film surfaces thus becomes advisable. After confirming an inhomogeneous c-axis orientation, approaches to reestablish an exclusive direction were investigated. Plasma etching of the electrode surface prior to deposition was found to have a significant effect on the population of misaligned grains. The distance between the cathode and the substrate was proven to be another decisive parameter. A combination of the two approaches allowed fabrication of w-$Al_{1-x}Sc_xN$ films with exclusive c-axis orientation up to $x = 0.43$. First measurements of the material's transversal piezoelectric thin film coefficient $e_{31,f}$ and dielectric loss $\tan\delta$ beyond $x = 0.3$ were presented. The latter increased significantly beyond $x = 0.3$ but remained well below 1%. The piezoelectric coefficient $e_{31,f}$ was measured to be above theoretical predictions up to $x = 0.41$. The fabrication of highly piezoelectric w-$Al_{1-x}Sc_xN$ films thus becomes more challenging at higher Sc contents but remains feasible.

SUPPLEMENTARY MATERIAL

See supplementary material for more detailed TEM analysis of the c-axis oriented matrix of $Al_{0.73}Sc_{0.27}N$ on Mo.

ACKNOWLEDGMENTS

The authors thank C. Szillus for the preparation of the TEM specimen and M. Dietze for additional XRD measurements with reduced noise floor.

[1]G. Piazza, V. Felmetsger, P. Muralt, R. H. Olsson, and R. Ruby, MRS Bull. **37**, 1051 (2012).
[2]R. Elfrink, T. Kamel, M. Goedbloed, D. Matova, S. Hohlfeld, Y. van Andel, and R. van Schaijk, J. Micromech. Microeng. **19**, 094005 (2009).
[3]F. Stoppel, C. Schröder, F. Senger, B. Wagner, and W. Benecke, Procedia Eng. **25**, 721 (2011).
[4]Y. Lu, A. Heidari, and D. A. Horsley, J. Microelectromech. Syst. **24**, 904 (2015).
[5]F. Martin, P. Muralt, M.-A. Dubois, and A. Pezous, J. Vac. Sci. Technol. A: Vacuum, Surf., Films **22**, 361 (2004).
[6]M. Akiyama, T. Kamohara, K. Kano, A. Teshigahara, and N. Kawahara, Appl. Phys. Lett. **93**, 021903 (2008).
[7]E. Yarar, V. Hrkac, C. Zamponi, A. Piorra, L. Kienle, and E. Quandt, AIP Adv. **6**, 075115 (2016).
[8]M. Akiyama, T. Kamohara, K. Kano, A. Teshigahara, Y. Takeuchi, and N. Kawahara, Adv. Mater. **21**, 593 (2009).
[9]S. Zhang, D. Holec, W. Y. Fu, C. J. Humphreys, and M. A. Moram, J. Appl. Phys. **114**, 133510 (2013).
[10]M. Akiyama, K. Umeda, A. Honda, and T. Nagase, Appl. Phys. Lett. **102**, 021915 (2013).
[11]R. Matloub, M. Hadad, A. Mazzalai, N. Chidambaram, G. Moulard, C. S. Sandu, T. Metzger, and P. Muralt, Appl. Phys. Lett. **102**, 152903 (2013).
[12]A. Zukauskaite, G. Wingqvist, J. Palisaitis, J. Jensen, P. O. A. Persson, R. Matloub, P. Muralt, Y. Kim, J. Birch, and L. Hultman, J. Appl. Phys. **111**, 093527 (2012).
[13]P. M. Mayrhofer, C. Eisenmenger-Sitter, M. Stöger-Pollach, H. Euchner, A. Bittner, and U. Schmid, J. Appl. Phys. **115**, 193505 (2014).
[14]S. Fichtner, T. Reimer, S. Chemnitz, F. Lofink, and B. Wagner, APL Mater. **3**, 116102 (2015).
[15]M. Akiyama, K. Kano, and A. Teshigahara, Appl. Phys. Lett. **95**, 162107 (2009).
[16]M.-A. Dubois and P. Muralt, J. Appl. Phys. **89**, 6389 (2001).
[17]K. Prume, P. Muralt, F. Calame, T. Schmitz-Kempen, and S. Tiedke, J. Electroceram. **19**, 407 (2007).
[18]A. Sanz-Hervás, M. Clement, E. Iborra, L. Vergara, J. Olivares, and J. Sangrador, Appl. Phys. Lett. **88**, 161915 (2006).
[19]J. Jasinski, Z. Liliental-Weber, Q. S. Paduano, and D. W. Weyburne, Appl. Phys. Lett. **83**, 2811 (2003).
[20]E. Milyutin, S. Harada, D. Martin, J. F. Carlin, N. Grandjean, V. Savu, O. Vaszquez-Mena, J. Brugger, and P. Muralt, J. Vac. Sci. Technol. B **28**, L61 (2010).
[21]V. Hrkac, A. Kobler, S. Marauska, A. Petraru, U. Schürmann, V. S. K. Chakravadhanula, V. Duppel, H. Kohlstedt, B. Wagner, B. V. Lotsch, C. Kübel, and L. Kienle, J. Appl. Phys. **117**, 014301 (2015).
[22]M. Reusch, K. Holc, W. Pletschen, L. Kirste, A. Zukauskaite, T. Yoshikawa, D. Iankov, O. Ambacher, and V. Lebedev, J. Vac. Sci. Technol. B **34**, 052001 (2016).
[23]M. Schneider, A. Bittner, F. Patocka, M. Stöger-Pollach, E. Halwax, and U. Schmid, Appl. Phys. Lett. **101**, 221602 (2012).
[24]B. Paci, A. Generosi, V. R. Albertini, M. Benetti, D. Cannatà, F. D. Pietrantonio, and E. Verona, Sens. Actuators, A **137**, 279 (2007).
[25]M. A. Caro, S. Zhang, M. Ylilammi, T. Riekkinen, M. A. Moram, O. Lopez-Acevedo, J. Molarius, and T. Laurila, J. Phys.: Condens. Matter **27**, 279602 (2015).
[26]A. Konno, M. Kadota, J. I. Kushibiki, Y. Ohashi, M. Esashi, Y. Yamamoto, and S. Tanaka, in *2014 IEEE International Ultrasonics Symposium* (2014) pp. 273–276.
[27]A. L. Kholkin, C. Wütchrich, D. V. Taylor, and N. Setter, Rev. Sci. Instrum. **67**, 1935 (1996).
[28]T. Yanagitani and M. Suzuki, Appl. Phys. Lett. **105**, 122907 (2014).
[29]S. Trolier-McKinstry and P. Muralt, J. Electroceram. **12**, 7 (2004).
[30]T. R. Shrout and S. J. Zhang, J. Electroceram. **19**, 113 (2007).

Journal of Applied Physics ARTICLE scitation.org/journal/jap

AlScN: A III-V semiconductor based ferroelectric

Cite as: J. Appl. Phys. **125**, 114103 (2019); doi: 10.1063/1.5084945
Submitted: 7 December 2018 · Accepted: 28 February 2019 ·
Published Online: 18 March 2019

Simon Fichtner,[1,2,a)] Niklas Wolff,[3] Fabian Lofink,[2] Lorenz Kienle,[3] and Bernhard Wagner[1,2]

AFFILIATIONS

[1]Materials and Processes for Micro/Nanosystem Technologies, Institute for Material Science, University of Kiel, Kaiserstr. 2, 24143 Kiel, Germany
[2]Fraunhofer Institute for Silicon Technology (ISIT), Fraunhoferstr. 1, 25524 Itzehoe, Germany
[3]Synthesis and Real Structure, Institute for Material Science, University of Kiel, Kaiserstr. 2, 24143 Kiel, Germany

[a)]**E-mail:** sif@tf.uni-kiel.de

ABSTRACT

Ferroelectric switching is unambiguously demonstrated for the first time in a III-V semiconductor based material: $Al_{1-x}Sc_xN$—A discovery which could help to satisfy the urgent demand for thin film ferroelectrics with high performance and good technological compatibility with generic semiconductor technology which arises from a multitude of memory, micro/nano-actuator, and emerging applications based on controlling electrical polarization. The appearance of ferroelectricity in $Al_{1-x}Sc_xN$ can be related to the continuous distortion of the original wurtzite-type crystal structure towards a layered-hexagonal structure with increasing Sc content and tensile strain, which is expected to be extendable to other III-nitride based solid solutions. Coercive fields which are systematically adjustable by more than 3 MV/cm, high remnant polarizations in excess of 100 μC/cm^2—which constitute the first experimental estimate of the previously inaccessible spontaneous polarization in a III-nitride based material, an almost ideally square-like hysteresis resulting in excellent piezoelectric linearity over a wide strain interval from −0.3% to + 0.4% and a paraelectric transition temperature in excess of 600 °C are confirmed. This intriguing combination of properties is to our knowledge as of now unprecedented in the field of polycrystalline ferroelectric thin films and promises to significantly advance the commencing integration of ferroelectric functionality to micro- and nanotechnology, while at the same time providing substantial insight to one of the central open questions of the III-nitride semiconductors—that of their spontaneous polarization.

INTRODUCTION

Ferroelectrics possess a unit-cell originating spontaneous electrical polarization with a spatial orientation that can be altered from one stable direction to another under an applied electric field. This makes them a distinct class with increased functionality among the piezoelectric materials. The drive towards miniaturization of piezoelectric sensors and actuators (microelectromechanical systems, MEMS), the introduction of ferroelectric functionality into integrated circuit (IC-) technology, and numerous emerging applications based on polarization control have led to substantial scientific and commercial interest in ferroelectric thin films.[1–5] Many of the more important ferroelectrics are oxide perovskites, with typical disadvantages such as low paraelectric transition temperatures, non-linear displacements, or limited compatibility with, e.g., complementary metal-oxide-semiconductor (CMOS) or III-nitride technology—issues which so far impede the universal availability of ferroelectric functionality in microtechnology.[2,6]

In the wurtzite-type structure (space group $P6_3mc$), the III-V semiconductors AlN, GaN, and InN possess a spontaneous polarization along their *c*-axis, which originates in the separation of the group-III and nitrogen atoms in individual planes.[7] Therefore, two antiparallel polarization directions exist: N-polar and metal-polar (e.g., Ga- or Al-polar) [Fig. 1(a)]. The pure wurtzite-type III-nitrides are thus pyroelectric materials, but not ferroelectric, as it is accepted that their polarization direction cannot be switched with electric fields below their individual dielectric breakdown limit.[2] Due to the higher piezoelectric coefficients of AlN compared to GaN or InN, AlN is generally preferred for piezoelectric applications.[7,8] Akiyama *et al.* demonstrated that the piezoelectric response of solid solutions constituted from AlN and ScN increases monotonously with Sc content, as long as the wurtzite structure is maintained.[9,10] This can be related to a highly metastable layered-hexagonal phase (space group $P6_3/mmc$) in ScN,[11,12] which in turn flattens the ionic potential energy landscape of, e.g., wurtzite-type

Journal of Applied Physics ARTICLE scitation.org/journal/jap

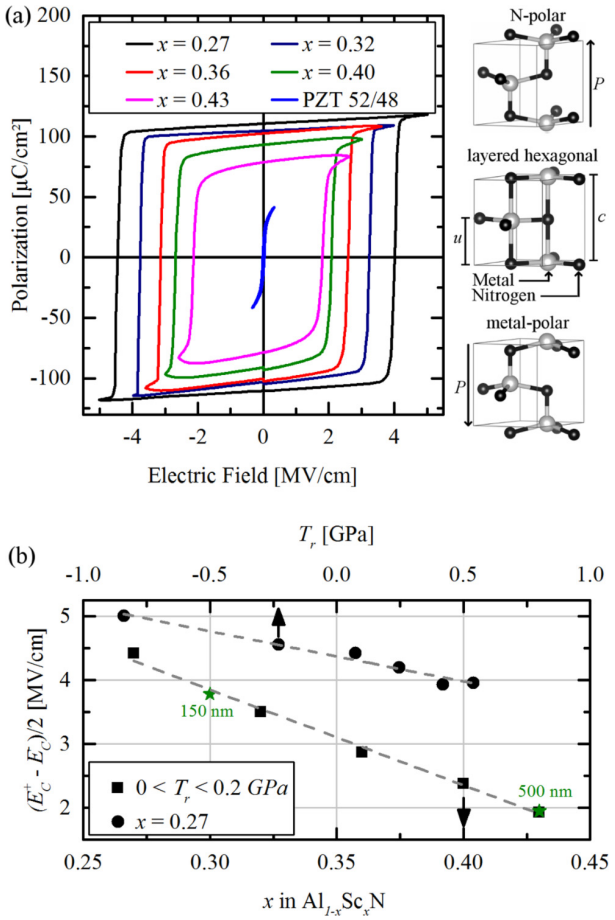

FIG. 1. (a) P-E loops of ferroelectric $Al_{1-x}Sc_xN$ with Sc contents of $x = 0.27$, 0.30, 0.32, 0.36, 0.40, and 0.43 as well as of PZT 52/48. To the right, the structures associated with the respective polarization states are displayed. (b) Dependence of the mean coercive field on the residual stress T_r and the Sc content of the $Al_{1-x}Sc_xN$ films. Sc content and T_r were varied independently.

$Al_{1-x}Sc_xN$. Consequently, the wurtzite basal plane as well as the internal parameter u (the length of the metal-nitrogen bond parallel to the c-axis relative to the lattice parameter c) increases, i.e., the layered hexagonal phase is approached, particularly at the Sc sites.[11,13,14] While the layered hexagonal structure itself is non-polar, it can be seen as a transition state ($u = ½$) between the two polarization orientations of the wurtzite structure [Fig. 1(a)]. The sign of the polarization switches once u passes ½. Due to the flattening of the ionic potential towards the hexagonal structure, the energy barrier which is associated with $u = ½$ is set to decrease as the Sc content is increased. Strain engineering of the wurtzite basal plane should enable a further decrease of this barrier, as was predicted by Zhang *et al.* for $Ga_{0.625}Sc_{0.375}N$.[13] In the same case, the electric field necessary to achieve ferroelectric polarization switching was also calculated to be potentially below the dielectric breakdown limit of pure GaN.[13] Aside from the incorporation of ScN into AlN, GaN, or InN, other metal nitrides such as YN or MgN-NbN were predicted and/or found to lead to a similar softening, increased a/c-lattice parameter ratio, or improved piezoelectric response.[12,13,15–17] The key to ferroelectric switching, however, remains that the energy barrier between the two polarization states of the wurtzite structure can be lowered sufficiently—either by increasing the ratio of the non-III metal or via strain engineering, while to some extent preserving the dielectric breakdown resistance of the pure III-nitride. In spite of this theoretical motivation, no experimental evidence of ferroelectric III-nitride semiconductors has been reported to date.

EXPERIMENTAL DETAILS

Polycrystalline $Al_{1-x}Sc_xN$ films were prepared by reactive sputter deposition on oxidized 200 mm (100) Si wafers covered with an AlN/Pt bottom electrode. The relevant process parameters for the $Al_{1-x}Sc_xN$ films deposited from dual targets (all except $Al_{0.64}Sc_{0.36}N$) were previously published.[18] $Al_{0.64}Sc_{0.36}N$ was deposited from a single alloy AlSc target with a nominal Sc content of 43 at. % and a purity of 99.9 at. %. Here, the DC power was set to 600 W, the gas flows into the chamber to 7.5 sccm of Ar and 15 sccm of N_2, while the substrate was kept at 400 °C during deposition. The film thickness was set to 400 nm (all films with $x = 0.27$), 600 nm ($x = 0.32$; 0.36; 0.40), or 1 μm ($x = 0.43$), unless stated explicitly. The lead zirconate titanate (PZT) film with a thickness of 600 nm was derived via solgel deposition with previously published process details.[19] (Piezo-) Electrical characterization took place on parallel plate capacitors with Pt top electrodes structured by lift-off. A commercially available aixACCT double beam laser interferometer (*P-E* loops, inverse piezoelectric effect, square 0.25 mm^2 top electrodes for *P-E* Loops, square 1 mm^2 top electrode for strain measurements) and a 4-point bending probe (direct piezoelectric effect, 16 mm^2 top electrodes) were used for the (piezo-) electric characterization.[20,21] P-E loops were measured with a triangular voltage input at 711 Hz and 411 Hz (for correction only, see the supplementary material). The inverse piezoelectric effect was measured with a triangular voltage input at 211 Hz. Due to systematic errors arising from non-neglectable substrate deformation during measurements of the inverse piezoelectric effect,[22] a correction factor of 0.85 was multiplied with the measured strain response (see the supplementary material). Permanent polarization inversion was initiated through a unipolar 0.1 Hz sine wave with a peak value of −200 V over 60 s. The residual stress was calculated via Stoney's equation based on capacitive measurements (E + H MX 203) and profilometer line scans (Ambios XP2) to extract the substrate curvature on the wafer level.[23] Temperature treatments were performed in consecutive steps of 5 min each under an ambient atmosphere. Etching experiments to resolve the polarity distribution in the $Al_{1-x}Sc_xN$ films were carried out in 85% phosphoric acid (H_3PO_4) and 25% potassium hydroxide (KOH) aqueous solutions at 80 °C. To remove the top electrodes after *ex situ* polarization inversion, ion beam etching (IBE, Oxford Instruments Ionfab 300) was employed. For the characterization of the micro- and nanostructure, transmission electron microscopy

Journal of Applied Physics ARTICLE scitation.org/journal/jap

was performed on three different microscopes during this investigation: Dark-field imaging was performed on a JEOL JEM-2100 (200 kV, LaB_6 cathode) while high-resolution TEM imaging was performed on a Tecnai F30 STwin microscope (300 kV, field emission cathode, $C_S = 1.2$ mm) and a Philips CM 30 ST (300 kV, LaB_6 cathode, CS = 1.15 mm). The cross-section sample was prepared by focused ion beam (FIB) milling using a standard lift-out method with a FEI Helios Nanolab system. The Sc content was measured by scanning electron microscopy energy dispersive x-ray spectroscopy (SEM-EDX) (Oxford x-act, 10 kV).

FERROELECTRIC PROPERTIES: POLARIZATION HYSTERESIS, DIRECT AND INDIRECT PIEZOELECTRIC EFFECT

Depending on the Sc content and the planar mechanical stress of the $Al_{1-x}Sc_xN$ films, it was possible to demonstrate not only that ferroelectric switching can indeed be achieved in wurtzite-type III-nitride based solid solutions—but also that the material has exceptional properties of relevance to the core-applications of ferroelectric thin films. The studied $Al_{1-x}Sc_xN$ layers generally exhibited good *c*-axis orientation normal to the substrate,[18] although grains with secondary orientations/phases were observed for Sc contents with $x \geq 0.4$ (see the supplementary material).

Distinct ferroelectric polarization inversion was measured starting at Sc contents of $x = 0.27$. Below $x = 0.22$, dielectric breakdown occurred before reaching the coercive field E_C. *P-E* (polarization over electric field) hysteresis loops of $Al_{1-x}Sc_xN$ with $x = 0.27$, 0.30, 0.32, 0.36, 0.40, and 0.43 are given in Fig. 1(a).

For comparison, the P-E loop of a $PbZr_{0.52}Ti_{0.48}O_3$ (PZT 52/48) film measured with the same parameters is displayed as well. To (at least partially) compensate the *P-E* loops with respect to the non-negligible leakage currents at higher electric fields, a modified dynamic leakage current compensation was employed (see the supplementary material).[24] In general, we observed very large coercive fields (close to 5 MV/cm at $x = 0.27$), almost undiminished polarization between the coercive fields and high remnant polarizations ($110\,\mu C/cm^2$ at $x = 0.27$). The latter is significantly above most theoretical predictions of the spontaneous polarization in both pure AlN ($\approx 10\,\mu C/cm^2$) and $Al_{1-x}Sc_xN$ ($\approx 30\,\mu C/cm^2$ at $x = 0.5$), which were made using the zincblende structure as the reference.[7,25,26] The polarization and its trend to decrease with increasing Sc content (which in turn increases *u* and leads to approaching the non-polar layered hexagonal structure) are, however, in line with a more recent prediction made in reference to the layered hexagonal structure by Dreyer *et al.*[8] As such, it is a welcome side-effect of ferroelectricity in $Al_{1-x}Ax_xN$ that the previously experimentally virtually inaccessible spontaneous polarization of AlN can therefore projected to be indeed above $100\,\mu C/cm^2$, rather than below $10\,\mu C/cm^2$—thus providing an answer with regard to the uncertainty associated with the polarization constant of the III-nitrides and confirming the approach by Dreyer *et al.*

In addition to this theoretical prediction, the comparably large spontaneous polarization of AlN and $Al_{1-x}Sc_xN$ can also be motived based on its Born effective charge and ionic displacement. The Born effective charge Z^B of AlN is around 2.5 e,[7,14] while the ionic displacement Δd upon ferroelectric switching is twice the nearest neighbour distance between metal and N-planes, i.e., $\Delta d = c(1-2u) = 1.2$ Å with $c = 5$ Å and $u = 0.38$.[9,13] While Z^B reportedly increases with increasing Sc content, Δd decreases due to an increasing internal parameter *u*—however, both values do not change dramatically until being energetically very close to the layered hexagonal phase (i.e., around x = 0.50).[13,14] While the effective ionic charge in $Al_{1-x}Sc_xN$ is thus not particularly large, the ionic displacement is 5-15 times above that of classical ferroelectric oxide perovskites like Barium- and Lead-Titanate.[27,28]

The polarization constant of AlN itself can be roughly approximated by

$$P = \frac{1}{2V} Z^B \Delta d = 126\,\mu C/cm^2, \quad (1)$$

where *V* is the volume per metal-nitrogen pair.[28] The so derived spontaneous polarization is close to the density functional theory-derived value of $135\,\mu C/cm^2$ for pure AlN[8] and motivates that, in spite of modest effective ionic charges, the large ionic displacements in ferroelectric $Al_{1-x}Sc_xN$ imply a spontaneous polarization above that of most other ferroelectrics.

The almost ideal box-like shape of the polarization hysteresis and the large coercive fields can be related to a still sizeable energy barrier associated with the hexagonal phase, good compositional homogeneity, and the wurtzite structure itself, which allows only 180° domain rotations. In terms of shape and polarization magnitude, the *P-E* loops of $Al_{1-x}Sc_xN$ remind of certain measurements on epitaxial ferroelectric thin films,[29–31] albeit without the need for a specific template to facilitate epitaxy and therefore with increased compatibility and ease of fabrication.

The gradual lowering of the switching barrier ($u = ½$) with increasing Sc content results in a linear decline of the coercive field [Fig. 1(b)], from about 5 MV/cm ($Al_{0.73}Sc_{0.27}N$) to less than 2 MV/cm ($Al_{0.57}Sc_{0.43}N$). Just as the Sc content distorts the wurtzite-type crystal structure by expanding its basal plane and increasing *u*, lateral mechanical straining of the films can be used to the same end. Similar to what has been reported for pure AlN, permanent lateral mechanical stress of a well-defined magnitude was induced to the $Al_{1-x}Sc_xN$ films by varying the Ar partial pressure of the sputter gas.[32,33] Adjusting the mechanical stress T_r in $Al_{0.73}Sc_{0.27}N$ films from about −0.8 GPa to +0.5 GPa resulted in a linear decline of the coercive field by more than 1 MV/cm. Therefore, a high degree of flexibility exists to systematically adjust the switching voltage towards a value favoured for the intended application by independent variation of the residual stress or the Sc content. The range of achievable switching voltages is further extended by the observation that polycrystalline Al(Sc)N can possess a preferential c-axis orientation already on the first 10 nm from the substrate (see the supplementary material) and functional films of corresponding thicknesses are therefore feasible.[34] Thus, both high switching voltages (>100 V) of advantage to linear piezoelectric excitation and low switching voltages in ranges of relevance for memory applications (<10 V) could be realized.

Measurements of the direct and inverse piezoelectric effect in ferroelectric $Al_{0.64}Sc_{0.36}N$ are given in Figs. 2(a) and 2(b), respectively. Both directions imply the possibility for virtually complete

Journal of Applied Physics ARTICLE scitation.org/journal/jap

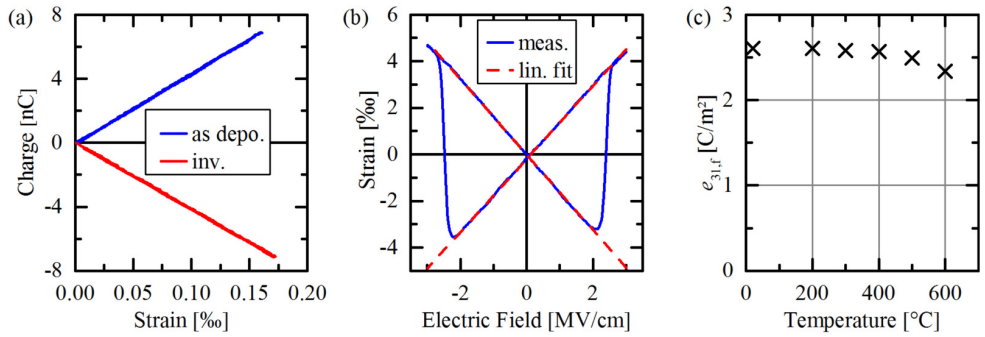

FIG. 2. (a) Direct piezoelectric effect: Charge-strain curves of $Al_{0.64}Sc_{0.36}N$ as deposited and after ferroelectric polarization inversion. (b) Converse piezoelectric effect: Longitudinal strain response of $Al_{0.64}Sc_{0.36}N$. (c) Transverse piezoelectric coefficient after polarization inversion and successive temperature treatments at the indicated temperatures without subsequent repolarization.

polarization inversion during ferroelectric switching. For measurements of the direct piezoelectric effect on an inverted sample, a simple 1-min poling procedure at room temperature was used to switch between the polarization states. Under this procedure, the effective transverse piezoelectric coefficient $e_{31,f}$ was inverted from an as-deposited $-2.90\ C/m^2$ to $2.76\ C/m^2$. Both values can be considered high for an AlN-based solid solution.[18,35] Repeated measurements of the piezoelectric response up to 30 weeks after polarization inversion did not show measurable degradation.

Moreover, the polarization inversion was conserved up to at least 600 °C: $e_{31,f}$ declined only slightly during the temperature treatment steps [Fig. 2(c)]. Consequently, 600 °C can be seen as a lower limit for the paraelectric transition temperature of $Al_{0.64}Sc_{0.36}N$. Beyond 600 °C, a degradation of the electrodes prohibited further electrical characterization of the capacitors.

The longitudinal displacement butterfly curve [Fig. 2(b)] of the inverse piezoelectric effect has broad linear regimes with almost equal slopes which correspond to an effective longitudinal piezoelectric coefficient $d_{33,f}$ of 15.7 pm/V and −16.2 pm/V. Compared to state of the art polycrystalline ferroelectric thin-films, both the width of the linear strain regime of 0.7% and its symmetry around the field axis are outstanding.[36]

ADDITIONAL EVIDENCE FOR GENUINE FERROELECTRICITY ASSOCIATED WITH THE WURTZITE CRYSTAL STRUCTURE

It is long known that not only true ferroelectricity results in P-E hysteresis loops, but also electrets, finite conductance, or p-n and Schottky junctions can lead to P-E measurements which resemble ferroelectricity.[3,37–40] In contrast to these spurious effects, which are connected with charge migration on length scales up to the film thickness, ferroelectricity is based on a stable and repeatable polarization reorientation on unit-cell level. The ultimate evidence for ferroelectric switching would therefore be the *in situ* observation of the underlying atomic displacement under and after the application of an external electric field. While such experiments were performed in the past,[41] the high coercive fields of AlScN would add additional challenge to an already demanding investigation. Alternatively, *ex situ* polarization inversion could be used with methods where the contrast specific for the unit-cell orientation can be obtained between pristine regions and switched regions. For the case of the wurtzite semiconductors GaN, AlN, InN, and ZnO, a standard method which provides such unit-cell orientation specific contrast is wet-etching in both acid (H_3PO_4) and bases like aqueous KOH and tetramethyl ammonium hydroxide (TMAH).[42–48] While N-polar surfaces etch readily and with distinct residues, metal polar surfaces do barely etch at all and initially remain smooth, with the exception of local defects and inversion domains.

To investigate whether this anisotropy can be observed in $Al_{1-x}Sc_xN$, samples from the same wafer as used for the piezoelectric characterization above had some of their capacitors switched, while others were kept as deposited. Subsequently, their top electrode was removed via IBE with an intentional 50 nm overetch into the $Al_{0.64}Sc_{0.36}N$ film [Fig. 3(a)]. This overetch was chosen in order to, on the one hand, rule out masking due to residues of the top electrode and, on the other hand, remove the interface region of the $Al_{0.64}S_{0.36}N$ film, as charge injection and ionic migration typically manifest around the electrodes.[38,39] Afterwards, the samples were etched in H_3PO_4 and KOH until not more than residues remained on the bottom electrode outside the capacitor areas. After wet etching, polarization inverted structures were conserved with close to their full height (ca. 500 nm), having a smooth surface intermitted by deep holes due to either defects or non-switching inversion domains [Fig. 3(b)] [the presence of the latter can be assumed due to the slightly lower inverted piezoelectric coefficient of the samples, Fig. 2(a)], which merged after longer etching times in H_3PO_4 or when etching in KOH, because of generally more rapid etching in the latter case. Due to this lateral etching, even small defect regions can account for the observed pits on the metal-polar surface. Asides from the metal polar-surface, the rest of the film etched readily and with the characteristic, cone like residues [Fig. 3(c)]. Due to the comprehensive investigation of the same effect in pure wurtzite semiconductors, this result provides conclusive evidence that polarization switching on unit-cell level does indeed take place in $Al_{1-x}Sc_xN$ and that, therefore, the material is a genuine ferroelectric.

Journal of Applied Physics ARTICLE scitation.org/journal/jap

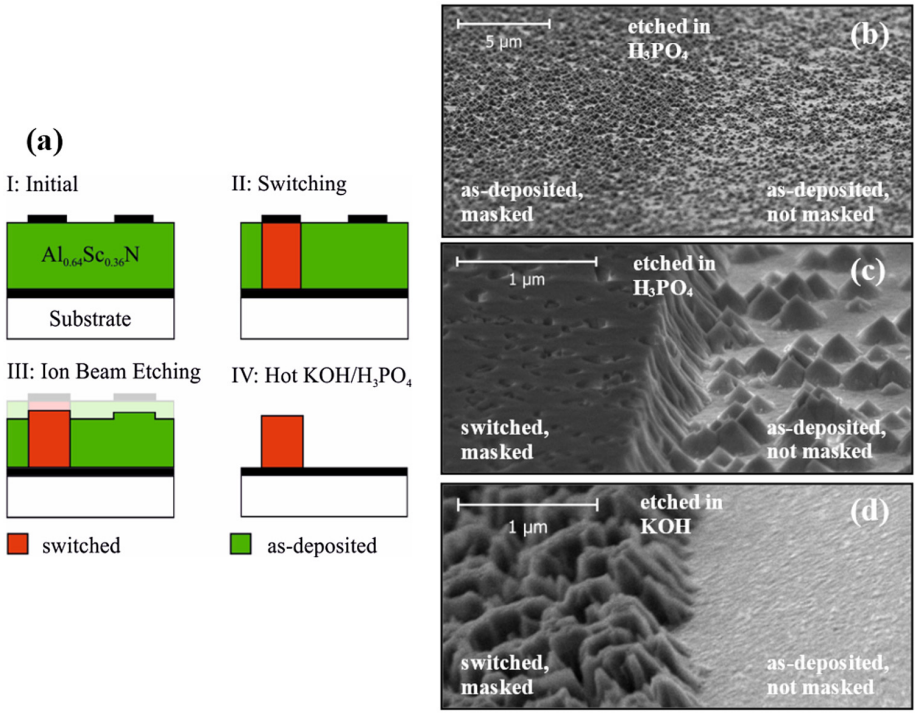

FIG. 3. (a) Sketch of the experimental procedure to determine the polarity of $Al_{0.64}Sc_{0.36}N$ via wet etching. (b) SEM image of the step from a masked, as deposited, region to an unmasked as-deposited region (faintly visible as a line through the center of the image) after etching in H_3PO_4 for 5 min. (c) Step from a switched region to an as-deposited region after etching in H_3PO_4 for 5 min. (d) Step from a switched region to an as-deposited region after etching in KOH for 15 s.

Additional evidence for ferroelectricity in $Al_{1-x}Sc_xN$ can be obtained from retention and frequency dependent measurements of the electrical polarization. Unlike the measured coercive field, the measured switching polarization of a true ferroelectric material should be largely independent of the measurement frequency. Due to $\Delta P \sim \int I(t)\,dt$, where I(t) is the measured current during sweeping of the electric field, the extrema of the former have to be approximately proportional to frequency (or more precisely, the area under its peaks has to be). This is typically not the case for currents due to charge injection/leakage, which either stay constant or decrease for increasing frequencies.[24,38] For $Al_{1-x}Sc_xN$, the area associated with the switching current peaks does scale proportionally with frequency over more than two orders of magnitude and the measured switching polarization consequently is constant (see the supplementary material)—as one would expect of a proper ferroelectric.

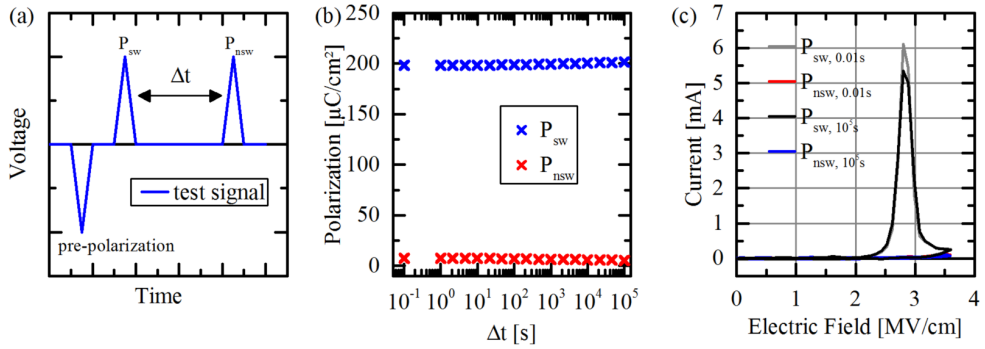

FIG. 4. (a) Pulse sequence to determine the retention behaviour of $Al_{1-x}Sc_xN$ via switching and non-switching polarization measurements (P_{sw}, P_{nsw}) separated by a time Δt during which the capacitor was shortened. The pulse width is 2 ms. (b) Switching and non-switching polarization over retention time Δt. (c) Initial and final current measurements, from which P_{sw} and P_{nsw} were extracted—a slight increase due to leakage current can be observed in the non-switching current for high electric fields, contributing to the non-zero non-switching polarization which is therefore not due to true polarization switching.

Journal of Applied Physics ARTICLE scitation.org/journal/jap

Furthermore, the stability of the polarization in electrets due to injected charges over time has the tendency to be lower than those of ferroelectrics (although there are exceptions).[37] The retention behavior of $Al_{0.64}Sc_{0.36}N$ was therefore determined by using the voltage pulse sequence given in Fig. 4(a). In between the read pulses for the switching (P_{sw}) and non-switching polarization (P_{nsw}), the capacitor was shortened. Over 10^5s, no polarization loss that could be attributed to polarization back switching was observed [Fig. 4(b)]. The fact that P_{nsw} is still not exactly zero appears to be rather due to purely dielectric effects [leakage and polarization magnitude, Fig. 4(c)]. The typical linear loss of polarization after ferroelectric switching which was observed over a logarithmic time scale in other materials[37,49] could not be observed in $Al_{1-x}Sc_xN$, although orders of magnitude longer measurements would be necessary to give a more definite understanding of the polarization retention in $Al_{1-x}Sc_xN$. It is, however, straightforward to motivate an exceptionally long retention time in $Al_{1-x}Sc_xN$, based not only on the current retention measurements but also on the fact that in its parent material, AlN, polarization is considered to be permanently aligned.

Asides from providing evidence that actual ferroelectric switching on unit-cell level does take place, transmission electron microscopy (TEM) was employed to confirm that the wurtzite structure is indeed conserved during the application of a switching field and no previously unconsidered phase is induced. In this context, an $Al_{0.57}Sc_{0.43}N$ TEM sample was prepared such that it contains two regions: one being sandwiched by Pt electrodes and subjected to ferroelectric polarization inversion and an unaltered region to allow for a structural comparison. An illustration of stitched TEM dark field images mapping out the intensity of the wurtzite-type $Al_{0.57}Sc_{0.43}N$ (0002) reflection is given in Fig. 5(a) with the precession electron diffraction (PED) pattern of the wurtzite structure in Fig. 5(b). No significant difference in contrast between crystal columns below the Pt top electrode used for polarization inversion and crystal columns not subjected to the switching electric field was observed.

From electron diffraction experiments, the majority of the film was identified as (0002) textured $Al_{1-x}Sc_xN$, in both the pristine and the polarization-inverted regions. Therefore, ferroelectricity in $Al_{1-x}Sc_xN$ can indeed be related to the wurtzite-type structure. However, owned to the high Sc content of the particular sample, a number of misoriented wurtzite grains were identified, some of which are marked by asterisks in Fig. 5(a). Moreover, small structural variations in the form of potential cubic grains and an unidentified phase were occasionally observed. Although being of high interest, the transition towards a layered hexagonal structure itself cannot be retrieved from precession electron diffraction data alone—kinematic simulations suggest that the contrast between the polar and non-polar phases can hardly be differentiated at a Sc content of $x = 0.43$. These aspects are discussed in more detail within the supplementary material.

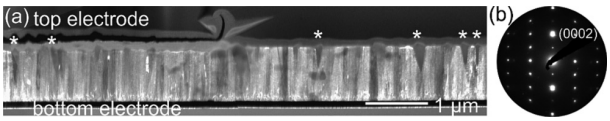

FIG. 5. (a) TEM darkfield image mapping out the intensity of the (0002) reflection indicated in the PED pattern (b). Misoriented crystals that do not exhibit the wurtzite-type (0002) texture of the matrix are displayed with a darker contrast in the brighter crystal matrix and are partially indicated by (*).

CONCLUSION

In summary, ferroelectric switching could be demonstrated in $Al_{1-x}Sc_xN$, beginning at Sc concentrations of $x = 0.27$. We expect that this material is only the first of a new group of ferroelectric wurtzite-type III-nitride based solid solutions, with likely additional candidates for this class being, e.g., $Ga_{1-x}Sc_xN$, $Al_{1-x}Y_xN$, or $Al_{1-x-y}Mg_xNb_yN$. Ferroelectric switching allowed the first direct experimental observation of the switching spontaneous polarization in an AlN based material and confirmed that, contrary to most prior theoretical publications, it can reach values larger than 100 μC/cm^2. The unique combination of ferroelectric properties of $Al_{1-x}Sc_xN$ in concert with the excellent compatibility to existing technology platforms should make the material highly relevant for both the classical applications of ferroelectrics, like piezoelectric multilayer actuator stacks or non-volatile memory cells and for novel approaches based on controlling electrical polarization, e.g., in the fields of optoelectronics, multiferroic composites, and III-nitride technology.[1,4,5,25]

SUPPLEMENTARY MATERIAL

See the supplementary material for a discussion of the leakage current as well as longitudinal strain correction, frequency dependent measurements of the switching current, additional SEM images illustrating the sample morphology, and a more in-depth TEM analysis of the microstructure of $Al_{0.57}Sc_{0.43}N$.

ACKNOWLEDGMENTS

The authors thank Viola Duppel from the Max Planck Institute for Solid State Research for additional TEM analyses and Professor Bettina Lotsch for enabling these experiments. Christin Szillus is acknowledged for TEM sample preparation, Dr. Andre Piorra for the fabrication of the PZT reference, and Professor Hermann Kohlstedt for discussion and encouragement.

Also, the authors thank the German Research Foundation (DFG) (No. CRC 1261, subprojects A3, A6, and Z1), the German Federal Ministry of Education and Research (BMBF) (Grant No. 16ES0632), and the Federal State of Schleswig-Holstein (Competence Center for Nanosystem-Technology) for funding part of this work.

REFERENCES

[1] N. Setter, D. Damjanovic, L. Eng, G. Fox, S. Gevorgian, S. Hong, A. Kingon, H. Kohlstedt, N. Y. Park, G. B. Stephenson, I. Stolitchnov, A. K. Taganstev, D. V. Taylor, T. Yamada, and S. Streiffer, J. Appl. Phys. **100**, 51606 (2006).
[2] P. Muralt, R. G. Polcawich, and S. Trolier-Mckinstry, MRS Bull. **35**, 658 (2009).
[3] M. Dawber, K. M. Rabe, and J. F. Scott, Rev. Mod. Phys. **77**, 1083 (2005).
[4] Y. Zhang, W. Jie, P. Chen, W. Liu, and J. Hao, Adv. Mater. **30**, 1707007 (2018).
[5] J. Ma, J. Hu, Z. Li, and C. W. Nan, Adv. Mater. **23**, 1062 (2011).
[6] S. Zhang, R. Xia, L. Lebrun, D. Anderson, and T. R. Shrout, Mater. Lett. **59**, 3471 (2005).

Journal of Applied Physics ARTICLE scitation.org/journal/jap

[7]F. Bernardini, V. Fiorentini, and D. Vanderbilt, Phys. Rev. B **56**, R10 024 (1997).
[8]C. E. Dreyer, A. Janotti, C. G. Van de Walle, and D. Vanderbilt, Phys. Rev. X **6**, 021038 (2016).
[9]M. Akiyama, T. Kamohara, K. Kano, A. Teshigahara, Y. Takeuchi, and N. Kawahara, Adv. Mater. **21**, 593 (2009).
[10]M. Akiyama, K. Kano, and A. Teshigahara, Appl. Phys. Lett. **95**, 162107 (2009).
[11]F. Tasnadi, B. Alling, C. Höglund, G. Wingqvist, J. Birch, L. Hultman, and I. A. Abrikosov, Phys. Rev. Lett. **104**, 137601 (2010).
[12]N. Farrer and L. Bellaiche, Phys. Rev. B **66**, 2012031 (2002).
[13]S. Zhang, D. Holec, W. Y. Fu, C. J. Humphreys, and M. Moram, J. Appl. Phys. **114**, 133510 (2013).
[14]R. Deng, K. Jiang, and D. Gall, J. Appl. Phys. **115**, 13506 (2014).
[15]C. Tholander, J. Birch, F. Tasnádi, L. Hultman, J. Pališaitis, P. O. Å. Persson, J. Jensen, P. Sandström, B. Alling, and A. Žukauskaitė, Acta Mater. **105**, 199 (2016).
[16]P. M. Mayrhofer, H. Riedl, H. Euchner, M. Stöger-Pollach, P. H. Mayrhofer, A. Bittner, and U. Schmid, Acta Mater. **100**, 81 (2015).
[17]M. Uehara, H. Shigemoto, Y. Fujio, T. Nagase, Y. Aida, K. Umeda, and M. Akiyama, Appl. Phys. Lett. **111**, 112901 (2017).
[18]S. Fichtner, N. Wolff, G. Krishnamurthy, A. Petraru, S. Bohse, F. Lofink, S. Chemnitz, H. Kohlstedt, L. Kienle, and B. Wagner, J. Appl. Phys. **122**, 35301 (2017).
[19]A. Piorra, R. Jahns, I. Teliban, J. L. Gugat, M. Gerken, R. Knöchel, and E. Quandt, Appl. Phys. Lett. **103**, 32902 (2013).
[20]K. Prume, P. Muralt, F. Calame, T. Schmitz-Kempen, and S. Tiedke, IEEE Trans. Ultrason. Ferroelectr. Freq. Control **54**, 8 (2007).
[21]P. Gerber, A. Roelofs, O. Lohse, C. Kügeler, S. Tiedke, U. Böttger, and R. Waser, Rev. Sci. Instrum. **74**, 2613 (2003).
[22]S. Sivaramakrishnan, P. Mardilovich, T. Schmitz-Kempen, and S. Tiedke, J. Appl. Phys. **123**, 14103 (2018).
[23]G. C. A. M. Janssen, M. M. Abdalla, F. van Keulen, B. R. Pujada, and B. van Venrooy, Thin Solid Films **517**, 1858 (2009).
[24]R. Meyer, R. Waser, K. Prume, T. Schmitz, and S. Tiedke, Appl. Phys. Lett. **86**, 142907 (2005).
[25]O. Ambacher, J. Smart, J. R. Shealy, N. G. Weimann, K. Chu, M. Murphy, W. J. Schaff, L. F. Eastman, R. Dimitrov, L. Wittmer, M. Stutzmann, W. Rieger, and J. Hilsenbeck, J. Appl. Phys. **85**, 3222 (1999).
[26]M. Caro, S. Zhang, T. Riekkinen, M. Ylilammi, M. Moram, O. Lopez-Acevedo, J. Molarius, and T. Laurila, J. Phys. Condens. Matter **27**, 245901 (2015).
[27]R. E. Cohen, Nature **358**, 136 (1993).
[28]P. Ghosez, J. Michenaud, and X. Gonze, Phys. Rev. B **58**, 6224 (1998).
[29]H. W. Jang, S. H. Baek, D. Ortiz, C. M. Folkman, C. B. Eom, Y. H. Chu, P. Shafer, R. Ramesh, V. Vaithyanathan, and D. G. Schlom, Appl. Phys. Lett. **92**, 062910 (2008).
[30]I. Vrejoiu, G. Le Rhun, L. Pintilie, D. Hesse, M. Alexe, and U. Gösele, Adv. Mater. **18**, 1657 (2006).
[31]J. Karthik, A. R. Damodaran, and L. W. Martin, Adv. Mater. **24**, 1610 (2012).
[32]S. Fichtner, T. Reimer, S. Chemnitz, F. Lofink, and B. Wagner, APL Mater. **3**, 116102 (2015).
[33]M.-A. Dubois and P. Muralt, J. Appl. Phys. **89**, 6389 (2001).
[34]U. Zaghloul and G. Piazza, Appl. Phys. Lett. **104**, 253101 (2014).
[35]S. Mertin, B. Heinz, O. Rattunde, G. Christmann, M.-A. Dubois, S. Nicolay, and P. Muralt, Surf. Coat. Technol. **343**, 2–6 (2018).
[36]B. Narayan, J. S. Malhotra, R. Pandey, K. Yaddanapudi, P. Nukala, B. Dkhil, A. Senyshyn, and R. Ranjan, Nat. Mater. **17**, 427 (2018).
[37]J. F. Scott, C. A. Araujo, H. B. Meadows, L. D. McMillan, and A. Shawabkeh, J. Appl. Phys. **66**, 1444 (1989).
[38]L. Pintilie and M. Alexe, Appl. Phys. Lett. **87**, 112903 (2005).
[39]J. F. Scott and P. Zubko, in *12th International Symposium on Electrets*, Salvador, Brazil, 11-14 September 2005 (IEEE, New York, 2005), p. 113.
[40]J. F. Scott, J. Phys. Condens. Matter **20**, 21001 (2008).
[41]P. Gao, C. T. Nelson, J. R. Jokisaari, S. H. Baek, C. W. Bark, Y. Zhang, E. Wang, D. G. Schlom, C. B. Eom, and X. Pan, Nat. Commun. **2**, 591 (2011).
[42]P. Visconti, D. Huang, M. A. Reshchikov, F. Yun, R. Cingolani, D. J. Smith, J. Jasinski, W. Swider, Z. Liliental-Weber, and H. Morkoç, Mater. Sci. Eng. B **93**, 229 (2002).
[43]J. Jasinski, Z. Liliental-Weber, Q. S. Paduano, and D. W. Weyburne, Appl. Phys. Lett. **83**, 2811 (2003).
[44]M. Bickermann, S. Schmidt, B. M. Epelbaum, P. Heimann, S. Nagata, and A. Winnacker, J. Cryst. Growth **300**, 299 (2007).
[45]D. Zhuang and J. H. Edgar, Mater. Sci. Eng. R Reports **48**, 1 (2005).
[46]A. N. Mariano and R. E. Hanneman, J. Appl. Phys. **34**, 384 (1963).
[47]E. S. Hellman, MRS Internet J. Nitride Semicond. Res. **3**, 1 (1998).
[48]E. Milyutin, S. Harada, D. Martin, J. F. Carlin, N. Grandjean, V. Savu, O. Vaszquez-Mena, J. Brugger, and P. Muralt, J. Vac. Sci. Technol. B **28**, L61 (2010).
[49]X. J. Lou, J. Appl. Phys. **105**, 024101 (2009).

Morphology of the $Al_{1-x}Sc_xN$ films

SEM imaging is a convenient tool in order to detect the incipient formation of secondary orientations in $Al_{1-x}Sc_xN$ thin films. These secondary orientations typically manifest in an additional elevated type of grain surrounded by a c-axis oriented matrix and can be visualized in SEM before their respective diffraction peaks appear in a standard XRD Θ-2Θ scan [4,5]. Figure S5 therefore shows SEM-top views of films with the five Sc concentrations investigated in this work. Starting at x = 0.40, elevated grains associated with secondary orientations appear. The main difference in the processes used for depositing these films, compared to the ones shown in our previous work without traces of secondary orientations was a variation in Ar flow to adjust the residual stress in the $Al_{1-x}Sc_xN$ layers – which was made necessary by the correlation between residual stress and the coercive fields [4]. While our previous films had increasing compressive stress with increasing Sc content, films in this work where adjusted to be under low tensile stress (T_r in [0 200 MPa]).

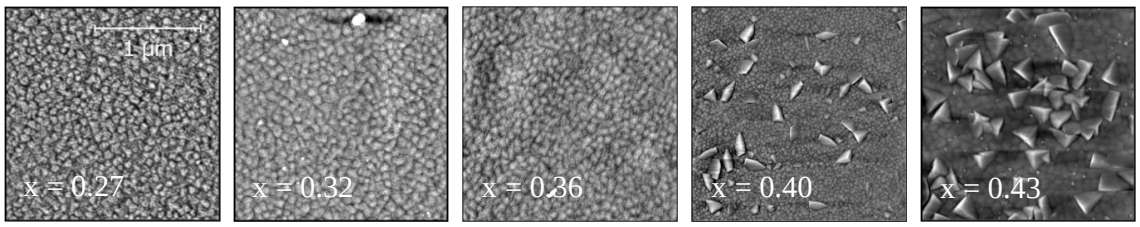

Figure S5: SEM surface images of the 5 films used to study the effect of Sc content on the coercive field in this work. Film thicknesses from left to right are: 400 nm, 600 nm, 600 nm, 600 nm and 1 µm.

TEM Analysis of $Al_{0.57}Sc_{0.43}N$

The wurtzite-type $Al_{0.57}Sc_{0.43}N$ film matrix in this investigation consists of highly crystalline and columnar shaped grains growing along the [0001] direction with lateral size of about 80-100 nm. Electron diffraction experiments (see figure S6 (a)) indicate the systematic rotation of the single crystalline columns around their joined rotation axis [0001] following the description of the wurtzite crystal structure of AlN [6]. The c/a ratio of ≈1.44-1.46 was determined from

the ED experiments and agrees very well with the observations of Akiyama *et al*. [7] for Sc rich alloys. The c-axis instability [4] of columnar shaped grains which appears with higher degree of alloying leads to a number of misoriented grains with sustained wurtzite structure. Direct information about the misorientation of the c-axis with respect to the (0002) film texture can be deduced from superposition selected-area (SA)ED pattern figure S5 (b), (c)) and precession (P)ED pattern (figure S6 (d)). For visualization, each ED pattern is combined with a structural model in the respective zone axis orientation. The rather random in-plane and out-of-plane rotation of the polar axis adds a reduced contribution to the overall piezoelectric response.

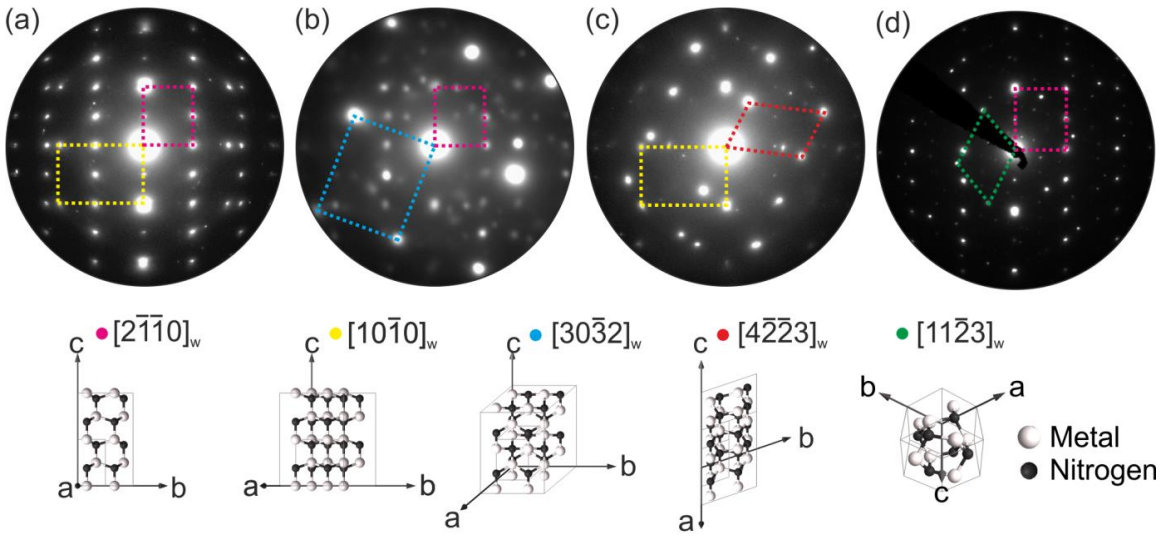

Figure S6: Selected area electron diffraction (SAED) pattern (a-c) and precession electron diffraction pattern (d) of the *w*-$Al_{0.57}Sc_{0.43}N$ film with a structural representation of the observed orientations. (a) The crystal matrix is composed of columns rotated around their c-axis, showing the superposition of the $[2\bar{1}\bar{1}0]_w$ and $[10\bar{1}0]_w$ zone axis reflections. (b-d) Superposition ED pattern of misoriented crystals (blue, red, green) in the matrix as indicated.

The stoichiometry of the Sc alloy is set in the mixed phase microstructure intermediate region described by Akiyama *et al.*,reflecting the transition zone from the wurtzite structure for $x < 0.41$ to the rocksalt phase for $x > 0.46$ in $Al_{1-x}Sc_xN$ [7,8]. Indeed this wurtzite instability is supported by high-resolution TEM images and their respecting fast Fourier transforms (FFTs) depicted in figure S7. The intermittent microstructural variations from the wurtzite structure are reflected in: a) the appearance of a polycrystalline character (red dashed) close to the bottom electrode with lattice plane distances not consistent with the superimposed $[2\bar{1}\bar{1}0]_w$ pattern, but

congruent with the description of Akiyama *et al*. and Höglund *et al*. for the appearance of a c-$Al_{0.60}Sc_{0.40}N$ phase with 4.25 Å lattice parameter; b) an entire crystal with its FFT showing a typical [110] pattern of a cubic structure, however, the lattice parameter of 3.94 Å fits very well to the metastable (at ambient pressures) high-pressure phase of AlN [9], rather than to the description of rocksalt structure alloy films discussed by Höglund *et al*. [8] and Saha *et al*. [10]; c) a grain boundary between a $[2\bar{1}\bar{1}0]_w$ oriented crystal (i) and one crystal with a non-identified structure (ii), but with lattice plane distances partially coinciding with the neighbouring grain. Both crystals share the position of the *w*-(0002) reflection, which would systematically hide these grains in the respective dark-field images.

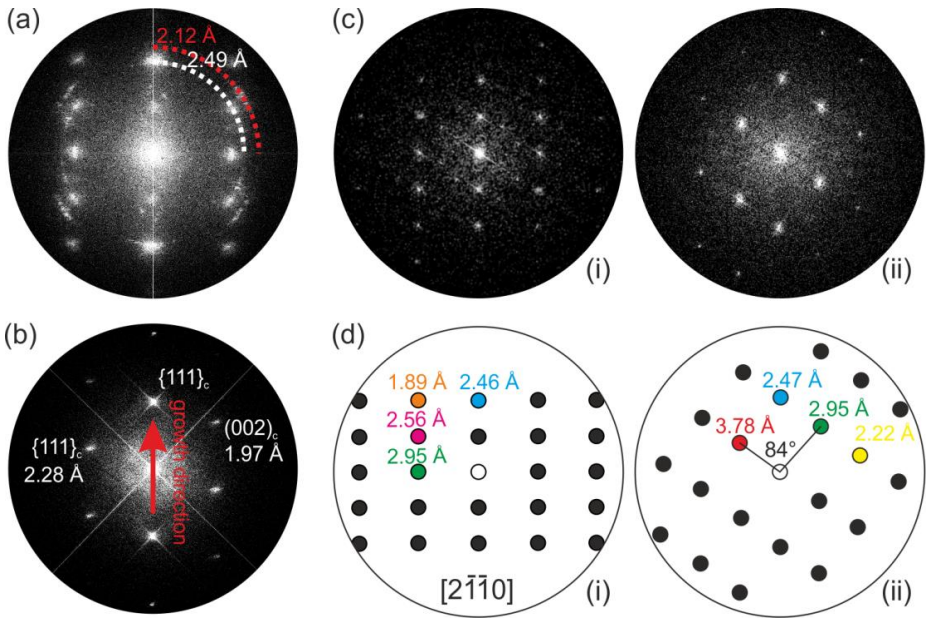

Figure S7: FFT study from HRTEM micrographs on the structural variations present in the AlScN film. (a) Intensities with polycrystalline character appear close to the bottom electrode. Intensities along the red circle line might indicate the formation of nano-precipitates of a cubic phase with lattice parameters different to the modified wurtzite-type structure. (b) FFT of a single grain showing a cubic [110] pattern and interplanar distances matching with a high-pressure AlN phase from literature. (c) FFTs from two neighbouring grains and (d) a graphical representation: The grain in (i) shows the $[2\bar{1}\bar{1}0]$ orientation of the wurtzite-type structure, whereas (ii) depicts a grain of different orientation but coinciding reflections along the direction of growth according to the matching interplanar distances along *w*-[000l] (d~2.47Å). However, the determined d-values and angles could not be attributed to the wurtzite-type structure of hexagonal AlScN.

Further studies will concentrate on the structure at the onset of wurtzite-rocksalt phase transition region, and the direct observation of the polarization inversion itself by convergent beam electron diffraction (CBED). In addition to dark-field imaging in specific diffraction

conditions [11] , the CBED method was proven to be able to identify the polarization direction in wurtzite GaN [12] and AlN crystals [13,14].

A HRTEM image of the $Al_{0.57}Sc_{0.43}N$/electrode interface with corresponding FFT patterns is given infFigure S8. In spite of the less than perfect crystal structure and morphology of the sample and its general polycrystalline character, c-axis alignement in the oriented parts of the sample can be observed down the first few nanometers of film growth.

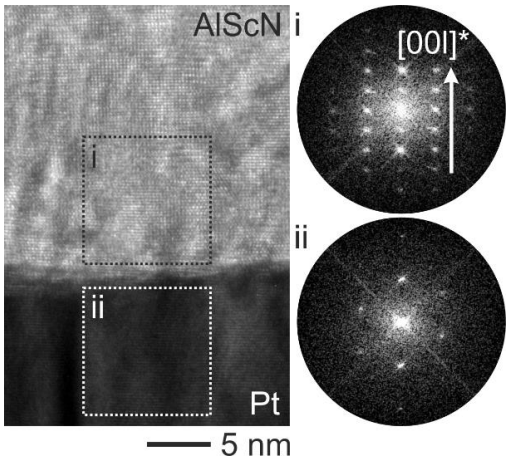

Figure S8: HRTEM image of the $Al_{0.57}Sc_{0.43}N$/electrode interface and corresponding FFTs.

Kinematic simulations (Emap Version 1.0, AnaliTEX) of ED pattern demonstrate the intensity variations with increasing internal parameter *u* up to *u*=1/2 c (figure S9), meaning a transition from the polar wurtzite-type into a non-polar configuration and increasing Sc concentration in the alloy. In the extreme cases the parent AlN phase shows identifiable variations in diffracted intensities of type (0,k,-k,l+1) in the depicted $[2\bar{1}\bar{1}0]$ pattern. However, the incorporation of Sc atoms on Al lattice positions increases electron scattering, giving rise to higher intensity (with Sc concentration) and a less pronounced intensity variation with increasing *u* on these lattice positions. On the onset of the proposed transition from the polar to non-polar phase (at x = 0.43) we demonstrate, that the intensity variations are hardly differentiable in the simulations even for low indexed reflections, e.g. $(01\bar{1}1)$. Therefore we reason that a reliable identification

of polar and non-polar configurations of the wurtzite-type structure is not feasible using conventional and precession electron diffraction techniques.

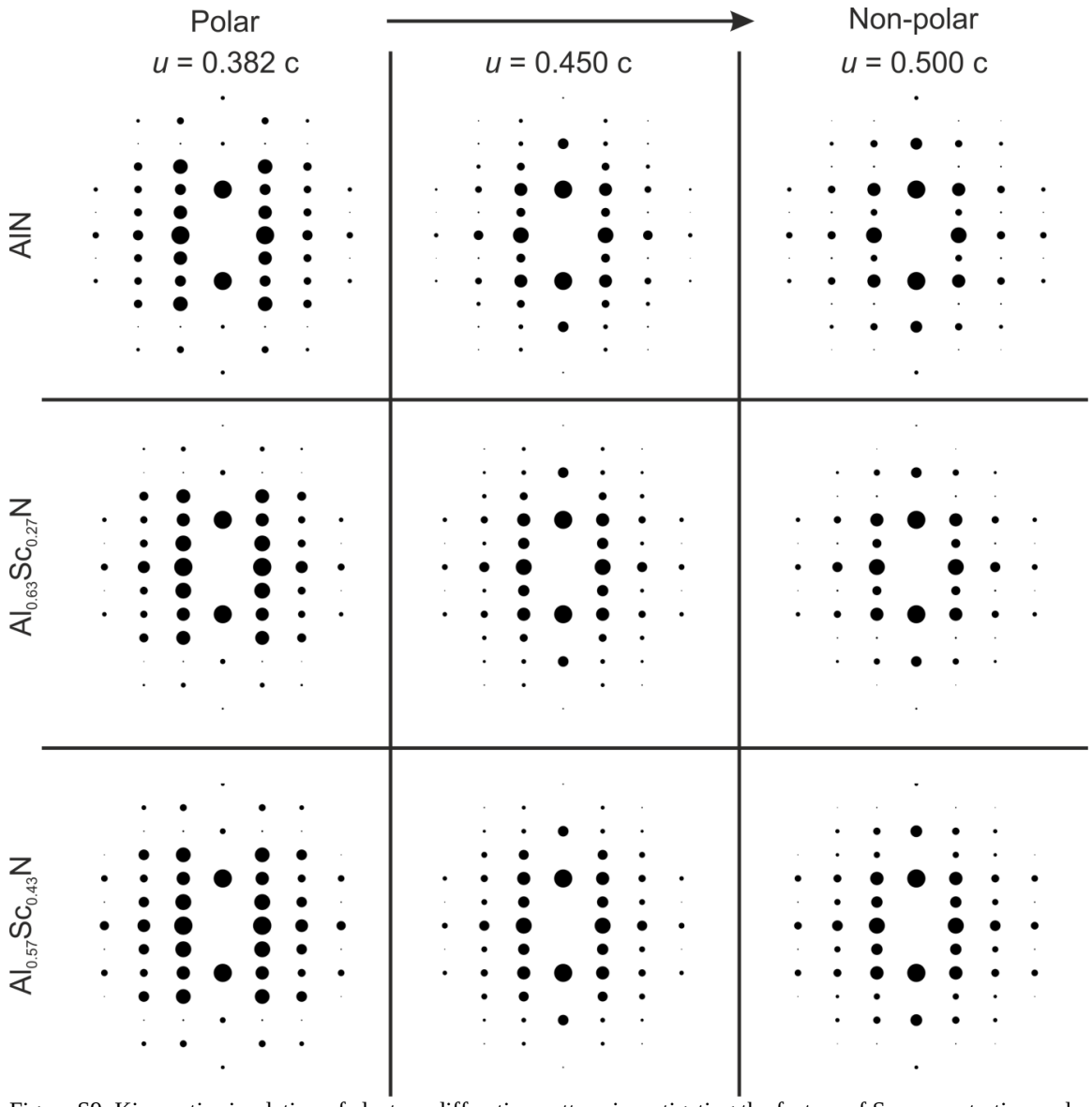

Figure S9: Kinematic simulation of electron diffraction pattern investigating the factors of Sc concentration and the internal parameter *u* on the reflection intensities.

[1] J. F. Scott, J. Phys. Condens. Matter **20**, 21001 (2008).

[2] R. Meyer, R. Waser, K. Prume, T. Schmitz, and S. Tiedke, Appl. Phys. Lett. **86**, 142907 (2005).

[3] S. Sivaramakrishnan, P. Mardilovich, T. Schmitz-Kempen, and S. Tiedke, J. Appl. Phys. **123**, 14103 (2018).

[4] S. Fichtner, N. Wolff, G. Krishnamurthy, A. Petraru, S. Bohse, F. Lofink, S. Chemnitz, H. Kohlstedt, L. Kienle, and B. Wagner, J. Appl. Phys. **122**, 35301 (2017).

[5] M. Reusch, K. Holc, W. Pletschen, L. Kirste, A. Žukauskaitė, T. Yoshikawa, D. Iankov, O. Ambacher, and V. Lebedev, J. Vac. Sci. Technol. B **34**, 52001 (2016).

[6] V. Hrkac, A. Kobler, S. Marauska, A. Petraru, U. Schürmann, V. S. Kiran Chakravadhanula, V. Duppel, H. Kohlstedt, B. Wagner, B. V. Lotsch, C. Kübel, and L. Kienle, J. Appl. Phys. **117**, 14301 (2015).

[7] M. Akiyama, T. Kamohara, K. Kano, A. Teshigahara, Y. Takeuchi, and N. Kawahara, Adv. Mater. **21**, 593 (2009).

[8] C. Höglund, J. Bareo, J. Birch, B. Alling, Z. Czigány, and L. Hultman, J. Appl. Phys. **105**, 113517 (2009).

[9] Q. Xia, H. Xia, and A. L. Ruoff, J. Appl. Phys. **73**, 8198 (1993).

[10] B. Saha, S. Saber, G. V. Naik, A. Boltasseva, E. A. Stach, E. P. Kvam, and T. D. Sands, Phys. Status Solidi Basic Res. **252**, 251 (2015).

[11] R. Serneels, M. Snykers, P. Delavignette, R. Gevers, and S. Amelinckx, Phys. Status Solidi **58**, 277 (1973).

[12] B. Daudin, J. L. Rouvière, and M. Arlery, Appl. Phys. Lett. **69**, 2480 (1996).

[13] S. Dasgupta, F. Wu, J. S. Speck, and U. K. Mishra, Appl. Phys. Lett. **94**, 151906 (2009).

[14] J. Jasinski, Z. Liliental-Weber, Q. S. Paduano, and D. W. Weyburne, Appl. Phys. Lett. **83**, 2811 (2003).

4.1.2 $(Ba_{1-x}Ca_x)(Ti_{0.9}Zr_{0.1})O_3$ Thin Films

Nontoxic lead-free and high performing ferroelectric materials as a replacement of $Pb(Zr_xTi_{1-x})O_3$ (PZT) are urgently demanded. The increasing research effort resulted in numerous Pb-free alternatives, some of them focusing on the cation exchange and co-doping of ABO_3-type $BaTiO_3$(BTO).[174]

The versatile applications of Pb-based and Pb-free ferroelectric titanate materials origins in the structural peculiarities of the perovskite-structure. Unlike the mineral, the perovskite-structure favours a cubic symmetry where the cation positions are described by anion-terminated coordination polyhedra, i.e. corner-sharing $[BO_6]$ octahedral coordination of B-site cations and cuboctahedral coordination of A-site cations. Ferroelectric behaviour in perovskites is generated by the competition of long-range Coulomb forces (favouring ferroelectricity) between ionic charges and short-range repulsion forces (stabilizing the non-polar cubic symmetry). The resulting average off-center displacements of the B-site cation (e.g. Ti) is denoted to a covalent softening by the hybridization between the titanium *3d* states and oxygen *2p* states which creates a net polarization which is stabilized up to the Curie-Temperature.[175] The piezoelectric behaviour of ferroelectrics is an immediate result of the coupling of polarization, hence the displacement-vector of the B-site cation to applied electric fields promotes large piezoelectric, dielectric, and electromechanical coefficients. The selection of A- and B-site cations places emphasis on the ionic radii and the electronic structure which both affect temperature dependent polymorphic phase transformations (PPT) in a material. The PPT describe the phase transitions e.g. from a tetragonal to a cubic structure, which is promoted by the interaction between the A-site cation and oxygen anion, where the type of cation is the determinant on the structure of the stabilized phase. In the case of $PbTiO_3$, the strong hybridization of Pb *s* states and oxygen *2p* states result in large lattice strains which stabilize the tetragonal phase, whereas in $BaTiO_3$ the interaction between Ba *p* and O *2p* states is purely ionic, favouring a rhombohedral structure.[175]

The science-based benefits of co-doping in PZT or other ferroelectrics resulting in giant electromechanical performance are related to the structural degeneracy of ferroelectric polymorphs coexisting at a morphotropic phase boundary (MPB) and the increased amount of possible polarization vectors within. In PZT, the tetragonal to rhombohedral transition is known to be mediated by intermediate phases of monoclinic symmetry[176] which is accompanied by a large property enhancement in the MPB regime because of symmetry-allowed free polarization rotation.[177] Interestingly, the existence of MPBs is not only proven for variations of the atomic composition but also in single crystals of pure ferroelectrics under high pressure in the case of $PbTiO_3$, giving rise to speculation that the formation of a solid solution only tunes the $PbTiO_3$ MPB to ambient pressure.[178]

One of the most promising candidates with respect to the piezoelectric and dielectric properties leveling up to PZT is the compound $(Ba_{1-x}Ca_x)(Ti_{0.9}Zr_{0.1})O_3$, which performance can be efficiently tuned by stoichiometric regulation and doping. In this respect, a Ca content x within the MPB regime ($0.14 \leqslant x \leqslant 0.18$) where rhombohedral and orthorhombic phases coexist at room temperature is favourable [179] and doping with e.g. Zn was reported to improve the dielectric and piezoelectric properties.[180]

A second class of ferroelectric materials showing super-high electromechanical coupling

are relaxor ferroelectrics. These are solid solutions between a relaxor material such as $PbMg_{1/3}Nb_{2/3}O_3$ and a ferroelectric such as $PbTiO_3$. What is so special about relaxor ferroelectrics is that they do not posses a polar ground state but disordered polarization concentrated into small and ordered polar nanoregions.[181] These are individually polarized below a temperature known as the Burns temperature.[182]–[184]

In the publication on **$(Ba_{0.85}Ca_{0.15})(Ti_{0.9}Zr_{0.1})O_3$ thin films prepared by PLD: Relaxor properties and complex microstructure**[3] we report about the dielectric and piezoelectric properties of BCZT thin films with a composition in the vicinity of the MPB.[185] In the attached study, we demonstrate the combination of CBED and HRTEM/HRSTEM imaging to determine the symmetry of the present structural polymorphs and to analyze structural peculiarities such as twinning and structural modulations with the assistance of suitable supercell models. The diffraction disks intensity distribution of CBED patterns are evident of symmetry operation along a specific viewing direction, enabling a more reliable identification of slight variations from the cubic structure than conventional electron diffraction. Complex nanostructural modulations close to the Pt seed layer have been imaged by HRSTEM Z-contrast with atomic resolution and speculatively assigned to cation segregation. Unfortunately, analytical methods such as EDS and EELS have not been capable to identify specific cations due to the partial overlap of the electron energy levels in Ti and Ba.

[3]Reproduced from Journal of Applied Physics 125, 244103 (2019) with the permission of AIP Publishing.

Journal of Applied Physics ARTICLE scitation.org/journal/jap

$(Ba_{0.85}Ca_{0.15})(Ti_{0.9}Zr_{0.1})O_3$ thin films prepared by PLD: Relaxor properties and complex microstructure

Cite as: J. Appl. Phys. **125**, 244103 (2019); doi: 10.1063/1.5063428
Submitted: 27 September 2018 · Accepted: 6 June 2019 ·
Published Online: 25 June 2019

André Piorra,[1] Viktor Hrkac,[2] Niklas Wolff,[2] Christiane Zamponi,[1] Viola Duppel,[3] Joke Hadermann,[4] Lorenz Kienle,[2] and Eckhard Quandt[1,a)]

AFFILIATIONS

[1]Inorganic Functional Materials, Faculty of Engineering, Kiel University, 24143 Kiel, Germany
[2]Synthesis and Real Structure, Faculty of Engineering, Kiel University, 24143 Kiel, Germany
[3]Max Planck Institute for Solid State Research, 70569 Stuttgart, Germany
[4]EMAT, Department of Physics, University of Antwerp, 2020 Antwerpen, Belgium

[a)]**Electronic mail:** eq@tf.uni-kiel.de

ABSTRACT

Ferroelectric lead-free thin films of the composition $(Ba_{0.85}Ca_{0.15})(Ti_{0.9}Zr_{0.1})O_3$ (BCZT) were deposited by pulsed laser deposition on $Pt/TiO_2/SiO_2/Si$ substrates using a ceramic BCZT target prepared by a conventional solid state reaction. The target material itself shows a piezoelectric coefficient of $d_{33} = 640$ pm/V. The (111) textured thin films possess a thickness of up to 1.1 μm and exhibit a clamped piezoelectric response $d_{33,f}$ of up to 190 pm/V, a dielectric coefficient of $\varepsilon_r = 2000$ at room temperature, and a pronounced relaxor behavior. As indicated by transmission electron microscopy, the thin films are composed of longitudinal micrometersized columns with ~100 nm lateral dimension that are separated at twin- and antiphase boundaries. The superposition phenomena according to this columnar growth were simulated based on suitable supercells. The major structural component is described as a tetragonal distorted variant of the perovskite parent type; however, frequently coherently intergrown nanodomains were observed indicating a much more complex structure that is characterized by a 7-layer modulation along the growth direction of the films.

INTRODUCTION

Ferroelectric thin films with high piezoelectric coefficients are attractive for many sensor and actuator applications.[1–3] Despite the toxicity of lead containing compounds, most of these applications are based on the excellent piezoelectric properties of lead zirconate titanate (PZT) and its compounds.[4] Legal restrictions to replace lead by nontoxic materials have led to significant achievements in the preparation of high performance lead-free ferroelectric and especially piezoelectric materials in recent years.[5–7] Despite the great variety of promising lead-free materials, thin films made of lead-free ferroelectric materials still show a comparable lower piezoelectric response. Effective piezoelectric coefficients in the range of around $d_{33,f} = 60$ pm/V were found for films of tantalum substituted $K_{0.5}Na_{0.5}NbO_3$ or $Bi_{3.15}Dy_{0.85}Ti_3O_{12}$ being thus around two times lower than for state of the art thin films of PZT.[8–10] A more promising candidate was recently identified to be the compound $(Ba_{0.85}Ca_{0.15})(Ti_{0.9}Zr_{0.1})O_3$ (BCZT). The piezoelectric coefficient of $d_{33} = 620$ pC/N for BCZT bulk ceramics was reported to be close to the one of PZT.[11] However, the piezoelectric constant d_{33} of bulk ceramics is significantly higher than the effective $d_{33,f}$ of thin films due to the clamping of the film by the substrate.[12] The effective piezoelectric constant $d_{33,f}$ of a clamped thin film on a substrate can be estimated based on the following formula:[13]

$$d_{33,f} = d_{33} - \frac{2\,S_{13}^E}{S_{11}^E + S_{12}^E} \cdot d_{31}, \tag{1}$$

with d_{31} and d_{33} the piezoelectric coefficients and S_{ij}^E of the bulk material.

Journal of Applied Physics ARTICLE scitation.org/journal/jap

TABLE I. Piezoelectric and elastic constants for BCZT[11,15] and PZT.[16]

	d_{31}/pC/N	d_{33}/pC/N	d_{33}/pm/V	$S_{11}^E/10^{-12}$ Pa^{-1}	$S_{12}^E/10^{-12}$ Pa^{-1}	$S_{13}^E/10^{-12}$ Pa^{-1}
BCZT	−231	546	1140	15.5	−5.5	−7.4
PZT	−93.5	223	900	13.8	−4.01	−5.8

Following Eq. (1) and using the materials constants of BCZT given in Table I, one can assume an effective piezoelectric constant $d_{33,f} = 203$ pm/V for thin films. This would be a considerably higher piezoelectric constant compared to the expected value for PZT ($d_{33,f} = 168$ pm/V).[14] Calculations based on the piezoelectric coefficient of the converse effect and under the assumption that the d_{31} scales with the same ratio provide a theoretical coefficient of $d_{33,f} = 427$ pm/V and demonstrate the enormous potential of BCZT films.

Published experimental values of the piezoelectric coefficient for films of BCZT are indeed promising.

Thin films prepared by a chemical solution deposition process show piezoelectric coefficients of $d_{33,f} = 1.1$ pm/V,[17] a $d_{33,f} = 104$ pm/V,[18] or a $d_{33,f} = 141$ pm/V.[19] Reported values for films prepared by other deposition methods, like magnetron sputtering ($d_{33,f} = 94$ pm/V[20]) and pulsed laser deposition ($d_{33,f} = 80$ pm/V[21]), show similar piezoelectric response.

Ferroelectric BCZT bulk ceramics exhibit a sharp transition from the ferroelectric tetragonal phase to the paraelectric cubic phase with a Curie temperature, $T_C = 93\,^{\circ}$C.[11] However, several reports on thin films of BCZT give the presumption of a relaxor behavior.[22,23] In general, the substitution of Ti ions by Zr ions is seen as a key factor for a transition from a ferroelectric phase transition to a relaxor state.[24,25] The main characteristic of a relaxor is the pronounced diffuse change in permittivity ε at temperatures near transition,[26,27] whereby the maximum of the dielectric constant ε_M at T_m shows a dependence of frequency f according to the Vogel-Fulcher relationship following the equation:[28]

$$f = f_0 \cdot \exp\left(\frac{-E_A}{k_B(T_m - T_f)}\right), \tag{2}$$

where E_A is the activation energy, k_B is the Boltzmann constant, T_f is the Vogel-Fulcher temperature, and f_0 an attempt frequency.

Similar to ferroelectrics, relaxor materials show a paraelectric phase at high temperatures. Ferroelectrics transform at the Curie temperature T_C into the paraelectric phase near the maximum of the dielectric constant ε_M associated with a structural change. A relaxor material possesses a polarization unequal to zero above ε_M until the Burns temperature T_B is reached, where the polarization becomes zero and the material will be in a paraelectric state without a change in the crystal structure.[29] Between ε_M and T_B, the dielectric constant ε follows a modified Curie-Weiss law in dependence of the temperature proposed by Uchino *et al.*,[30]

$$\frac{1}{\varepsilon} - \frac{1}{\varepsilon_M} = \frac{(T - T_M)^{\gamma}}{C'}, \tag{3}$$

with γ and C' being constants. The parameter γ describes the diffuse character of the transition and ranges between 1 and 2; for $\gamma = 1$, a normal ferroelectric material is observed, and for $\gamma = 2$, a complete diffuse transition is seen.[31,32]

Closely related to the appearance of relaxor behavior is the existence of polar nanoregions (polar nanodomains). By cooling, they transform from the nonpolar paraelectric phase at the Burns temperature, T_B, to nanometer scale polar regions with randomly oriented dipole moments. The relaxor exists in the ergodic state, where external forces (electrical fields or mechanical stress) could transform it reversely into a ferroelectric state. With decreasing temperature, the mobility of the polar nanodomains decreases. At the temperature T_f, the nanodomains are frozen in and the relaxor is transformed into a nonergodic state. In this state, the relaxor can irreversibly be transformed into a ferroelectric state by applying sufficiently strong external fields.[25,29]

Despite first studies on the nanostructure of bulk samples from BCZT,[33] a lack of in-depth analyses of BCZT thin film samples must be stated. In this work, we discuss the di- and piezoelectric properties of BCZT thin films, which are associated with the characteristics of a relaxor. Nanostructural features have been investigated by methods of transmission electron microscopy (TEM) and evaluated using computational approaches.

EXPERIMENTAL

Thin film fabrication

A ceramic target of BCZT was prepared by a conventional solid state reaction starting from pure powders followed by sintering to solid targets (size: 20 mm in diameter). More details of the preparation of the target material can be found in Ref. 21. A pulsed laser deposition workstation manufactured by Surface System & Technology GmbH & Co. KG was used to prepare the BCZT thin films utilizing a KrF laser with a wavelength of 248 nm and energy of 350 mW. The platinized silicon substrates were prepared by sputtering (von Ardenne CS730S sputtering system) a 150 nm thick platinum film on thermally oxidized silicon wafers [Si (100)] with a power of 20 W without additional heating. A 10 nm thick sputter deposited titanium film was used as diffusion barrier. Deposition of ~900 nm thick BCZT thin films was carried out at a laser frequency of 10 Hz and an oxygen partial pressure of 0.14 mbar on 10 mm by 10 mm pieces of platinized silicon at a deposition temperature of 800 °C. The target to substrate distance was set to 50 mm and 40 mm. Subsequently, the films were cooled down to room temperature at an oxygen partial pressure of 3 mbar. The deposition rate was determined to be 0.12 nm/pulse.

Thin film characterization

The microstructures of the thin films were characterized by X-ray diffraction (XRD) (Seifert XRD 3003 PTS). The structuring

Journal of Applied Physics ARTICLE scitation.org/journal/jap

of Au electrodes for measuring the piezo- and ferroelectric properties was done via sputtering and photolithographic etching followed by a lift-off process. Thin films and bulk ceramics were characterized with a double beam laser interferometer (DBLI) (aixDBLI, Aixacct).

TEM investigations

The structural analysis on samples deposited at a substrate to a target distance of 50 mm was carried out using three different TEMs: (1) a FEI Tecnai F30 G^2 STwin operated at 300 kV [field emission gun (FEG), spherical aberration coefficient $C_S = 1.2$ mm] and (2) a Philips CM 30 ST microscope (LaB_6 cathode, 300 kV, $C_S = 1.15$ mm) were used for electron diffraction analysis, (3) a FEI Titan 80–300 "cubed" microscope equipped with a Super-X EDX detector and operated at 200 kV was used for high resolution scanning transmission electron microscopy (HRSTEM) images and STEM-EDX elemental maps. A thin lamella of BCZT was prepared by focused ion beam (FIB) milling using a lift-out method with an FEI Helios Nanolab system. Selected area electron diffraction (SAED) patterns were obtained using a radial aperture, which limited the diffraction to an area of 250 nm (Tecnai F30) and 100 nm (Philips) in diameter. All high resolution (HR)TEM micrographs and ED pattern were evaluated with the program Digital Micrograph 3.6.1 (Gatan, Inc.) (DM). Simulations of SAED patterns were calculated using the JEMS program package.[34] For contrast enhancement of HRTEM micrographs, the HRTEM filter plug-in for DM was applied.[35] Due to the small variations in the lattice parameters of BCZT for the possible phases[9,36] and to simplify the discussion of crystallographic orientations, cubic metrics (labeled by "C") will be used for the notation of the presented miller indices. An exception is the symmetry discussion for the convergent beam electron diffraction (CBED) studies.

RESULTS AND DISCUSSION

Morphology and real structure of major component

Experimentally obtained XRD patterns (see Fig. 1) exhibit a strong $(111)_c$ texture of BCZT films (FWHM of 1.3°) on a preferably (111) oriented Pt seed layer (FWHM of 1.4°). Only marginal intensity is observed for other planes as $(100)_c$ and $(110)_c$. This result proves the absence of secondary crystalline phases; however, the precise determination of metrics and symmetry is not feasible by XRD. The highly oriented growth represents a clear improvement compared to the previous work.[21] The strongly textured $(111)_c$ growth on (111) oriented Pt films on silicon is well known for $BaTiO_3$ (BTO) films prepared by pulsed laser deposition due to the small lattice mismatch of Pt and BTO.[37]

Dielectric and piezoelectric properties

The (111) orientation of the BTO films is favorable for a maximum piezoelectric coefficient as shown by calculations from Davis *et al.*[38] and Ouyang *et al.*[39] These calculations where confirmed by Li *et al.* via investigations on $Ba_{0.98}Ca_{0.02}Ti_{0.96}Sn_{0.04}O_3$ thin films with different preferred orientations. For (111) and (100) oriented films, the authors found a piezoelectric coefficient of $d_{33,f} = 78$ pm/V and $d_{33,f} = 36$ pm/V,[40] respectively. As BCZT is based on BTO it is thus assumed that the (111) orientation is also the most favorable orientation in BCZT.

The dielectric and piezoelectric properties of the BCZT film are depicted in Fig. 2. A narrow ferroelectric hysteresis is observed [Fig. 2(a)] with low coercive fields and only a small coercivity in the C(apacitance)-V(oltage) curves. Additionally, a maximum dielectric permittivity of $\varepsilon = 2000$ at 5 kHz and room temperature was measured being within the broad range of reference values reaching from $\varepsilon = 259$[18] to $\varepsilon = 2913$[17] reported for BCZT thin films [Fig. 2(b)]. The dielectric measurements demonstrate a shift of the field characteristics, which was already noted in previous studies[21] as imprint. A preference of one polarization state over the other leading to a shift of the ferroelectric hysteresis on the voltage axes.[41,42] Oxygen loss gradients inside the film arising during preparation or mechanical stress inside the film could be responsible for this imprint behavior.[43–45] Besides this, extrinsic effects due to different electrode materials, on bottom, we use Platinum, on top, Chromium and Gold could also lead to this behavior due to the different work functions.[46,47]

Furthermore, the BCZT films exhibit a giant piezoelectric response with respect to other lead-free ferroelectric thin films,[21] possessing a maximum effective piezoelectric constant of more than $d_{33,f} = 190$ pm/V [Fig. 2(c)], exceeding the PZT value, but showing a discontinuous variation across the entire film. Areas with an effective piezoelectric constant of $d_{33,f} = 190$ pm/V and

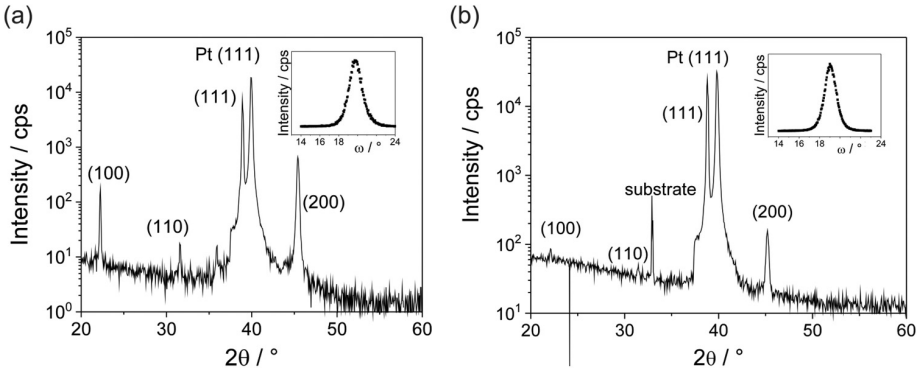

FIG. 1. XRD scans of BCZT thin films deposited at a substrate to target distance of (a) 50 mm and (b) 40 mm. The full width-at-half maxima of the (111) intensities are 1.55° and 1.3° and show the strong texture of the films, respectively.

Journal of Applied Physics ARTICLE scitation.org/journal/jap

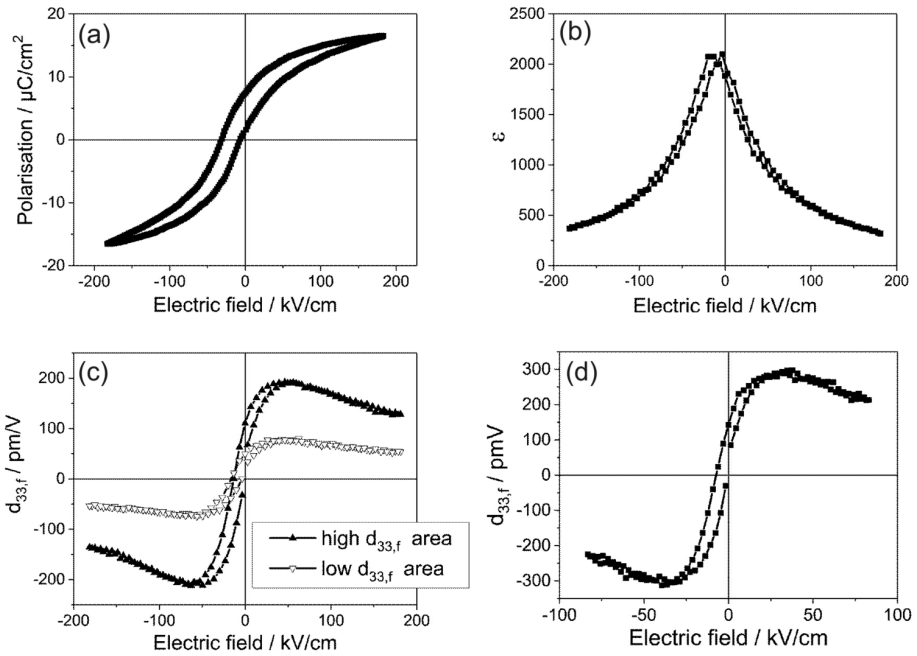

FIG. 2. Di- and piezoelectric properties of BCZT thin films. (a) Ferroelectric hysteresis, (b) dielectric permittivity vs voltage, (c) piezoelectric coefficient $d_{33,f}$ vs voltage of different positions on the sample at 50 mm substrate to target distance and (d) piezoelectric coefficient $d_{33,f}$ vs voltage for 40 mm substrate to target distance.

with $d_{33,f} = 80\,\mathrm{pm/V}$ in maximum were detected; please note that the $d_{33,f}$ values within a given area are constantly high or low. Interestingly, by decreasing the substrate to target distance from 50 mm to 40 mm, the maximum effective piezoelectric coefficient could be increased up to $d_{33,f} = 300\,\mathrm{pm/V}$ in maximum [Fig. 2(d)], marking one of the highest values reported for lead-free piezoelectric films. However, the origin of the discontinuous variation and higher piezoelectric coefficient is highly speculative up to date and is a topic for future research. Multiple factors which were reported to influence the piezoelectric coefficients concern the quality of the microstructure, e.g., crystal orientation,[18] crystal structure and chemical composition around the morphotropic phase boundary,[11,48,49] the grain size,[50] interfacial strain and dislocation density,[51] film thickness,[52] as well as speculations about the density of polar nanodomains responsible for the relaxor effect seems reasonable.[53]

BCZT ceramics introduced as the ferroelectric material show a sharp transition from the ferroelectric tetragonal phase to the paraelectric cubic phase.[11] The temperature dependence of the dielectric permittivity within a frequency range from kilohertz to megahertz is investigated for the BCZT films with a substrate target distance of 50 mm, [cf. Fig. 3(a)]. The recorded curves are characterized by a broad peak and thus do not express a clear defined maximum. From these data, the characteristic transition is, therefore, hard to identify, which is contrary to the distinct phase transition of the bulk ceramic. Indeed, own investigations on BCZT bulk ceramics show clear ferroelectric characteristics as depicted in Fig. S2 of the supplementary material.

Furthermore, BCZT films show a temperature shift of the maximum value for the dielectric constant ε_M when applying different frequencies during the respective measurements [cf. Fig. 3(a)]. For the performed experiments, the peak temperature values T_M corresponding to $\varepsilon_M(f)$ are in the range from 326 K (53 °C) to 334 K 61 °C. Such findings serve as an indication for a relaxor behavior. Additional validation for this hypothesis is deducible from the deviation of the linear Curie-Weiss law near and above ε_M at 10 kHz as presented in Fig. 3(b). Starting from 360 K (87 °C), a linear behavior according to the Curie-Weiss law is visible. The diffuse region below the paraelectric part and above ε_M can be described by using the modified Curie-Weiss law [Eq. (3)]. Replotting the same data within modified axes $\{y = \ln\left(\frac{1}{\varepsilon} - \frac{1}{\varepsilon_M}\right)$ and $x = \ln(T - T_M)$ [Fig. 3(c)]$\}$, the degree of diffuseness γ is determined to be $\gamma = 2$, confirming an ideal relaxor behavior.[30] Following the phenomenology of a relaxor material, the temperature of 360 K sets the Burns temperature T_B, i.e., the transition from the high temperature paraelectric phase to the state of an ergodic relaxor. A particularity at T_B is the appearance of mobile polar nanodomains and the decrease of this mobility during a cooling process. At a certain temperature, the nanodomains are frozen. According to the Vogel-Fulcher-law, this freezing temperature can be calculated by fitting the temperature dependent maxima of the dielectric permittivity in dependence of the frequency.[25,29] Additionally, the implementation of the Vogel-Fulcher law is a criterion for the complete crossover from a ferroelectric to a relaxor state.[25] Figure 3(d) shows $\ln f$ as a function of T_M and the fitted values using the Vogel-Fulcher relationship [Eq. (2)]. A Vogel-Fulcher temperature as expression for the freezing of polar nanodomains was identified at $T_{V-F} = 303$ K.

Similar relaxor behavior of BCZT thin films was observed in other studies. For instance, Bhardwaj *et al.* reported about the relaxor behavior of BCZT films prepared by pulsed laser deposition. A diffuseness parameter of $\gamma = 1.88$ and a dependence of the maximum

Journal of Applied Physics ARTICLE scitation.org/journal/jap

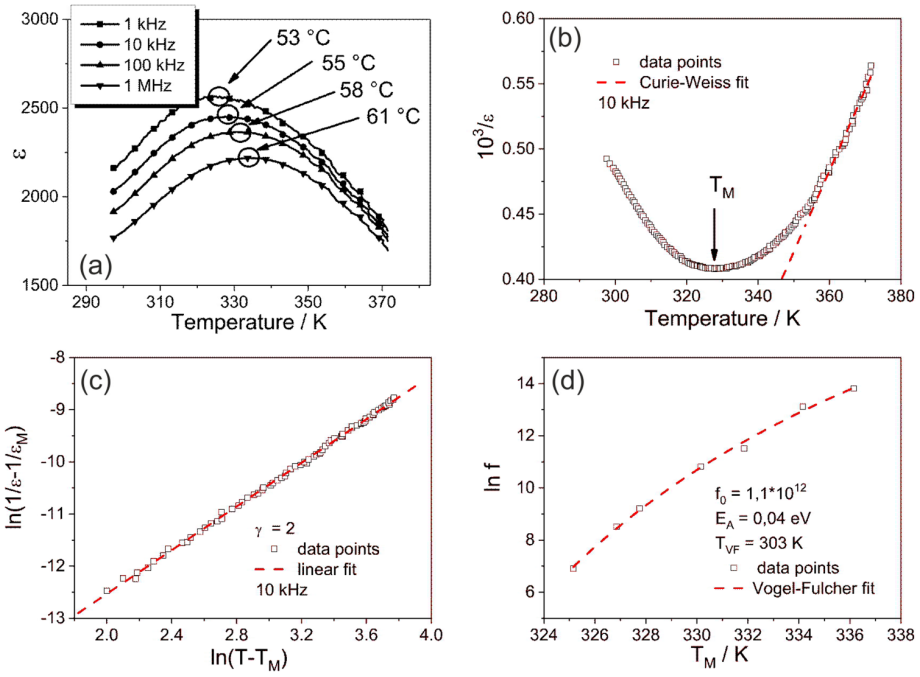

FIG. 3. Relaxor properties of BCZT thin films. (a) Temperature dependence of dielectric constant at different frequencies, (b) reciprocal dielectric constant as function of the temperature at 10 kHz, fits shows the range of validity of the Curie-Weiss law, (c) modified Curie-Weiss law fit of values, and (d) fit of measured values according to Vogel-Fulcher relation shift.

of the dielectric constant ε_M according to the Vogel-Fulcher law was found, and a Vogel-Fulcher temperature of $T_{V-F} = 329.7$ K was determined.[22] For sol-gel prepared thin films with the discussed composition of BCZT, Lin *et al.* found a matching of the Vogel-Fulcher relationship with a Vogel-Fulcher temperature of $T_{V-F} = 315$ K and a diffuseness parameter of $\gamma = 1.98$.[23]

In these cases, the origin of the relaxor behavior was explained by the simultaneous substitution of Ca^{2+} on Ba^{2+} sites and Zr^{4+} on Ti^{4+} sites of the $BaTiO_3$ host lattice.[22,23]

However, the simultaneous substitution is only one possible option of the four. The second and third options are the homovalent substitution of Zr^{4+} ions on Ti^{4+} sites or either Ca^{2+} ions on Ba^{2+} sites. The fourth option describes the heterovalent substitution of Ca^{2+} ions on Ti^{4+} sites. Each option leads to structural and charge inhomogeneities. These structural and charge inhomogeneities cause the appearance of polar nanodomains and are closely related to a relaxor behavior.

In classical relaxor materials such as PMN these inhomogeneities result from the coexistence of the two B-site ions Mg^{2+} and Nb^{5+}. These heterovalent cations are inhomogeneously distributed and form chemically ordered regions which are surrounded by disordered regions and act as sources for random electric fields.[25] These fields are proposed to be the origin of a relaxor behavior.[54]

The origin of random fields and by that the explanation of a ferroelectric-relaxor crossover in homovalent substituted compositions like in $BaTi_{1-x}Zr_xO_3$ differs from the heterovalent case due to the absence of any charge disorder. The ferroelectric polarization in pure BTO results mainly from the off-centre shifts of the Ti^{4+} ions.[25] That is, Zr^{4+} ions on Ti^{4+} sites cannot go off-centre due to their larger radius, thus breaking of the cooperative displacement of the Ti-O-Ti-O chains.[40] Such a broken-bond-type state changes in the course of a higher degree of substitution into a predominately random-field-type disorder.[25] This disorder is due to the distortion around Zr^{4+} ions and interrelated redistributions of charges and local formation of charged centres.

The substitution of Zr^{4+} on Ti^{4+} positions of BTO leads indeed to a complete crossover from a ferroelectric to a relaxor state, as reported for bulk ceramics[24,29] and thin films.[55] However, the critical concentration of Zr for a ferroelectric-relaxor crossover in $BaTi_{1-x}Zr_xO_3$ substituted ceramics is found to be $x = 30$ at. %.[25] Dixit *et al.* investigated thin films of $BaTi_{1-x}Zr_xO_3$ in the range $0.3 \leq x \leq 0.7$ and found a maximum of the diffusivity for the composition $BaZr_{0.40}Ti_{0.60}O_3$ with $\gamma = 1.8$ at the fulfilment of the Vogel-Fulcher law simultaneously.[31]

The above discussed BCZT composition contains 10 at. % of Zr. Thus, the role of substituent Ca^{2+} attaches high importance. A homovalent substitution of Ca^{2+} ions on B-sites could also generate random electric fields. Ca^{2+} ions are smaller than Ba^{2+} ions and are able to occupy off-centre positions on the A-site. Additionally, Ca^{2+} ions can substitute B-site positions.[56] Victor *et al.* found that films of $Ba_{1-x}Ca_xTiO_3$ which were prepared by pulsed laser deposition on platinized silicon substrates exhibit a relaxorlike behavior with increasing Ca^{2+} ion content.[57] For a concentration $x = 12$ at. % of Ca^{2+}, a behavior according to the Vogel-Fulcher law was obtained, and the parameter γ was determined to be $\gamma = 1.78$. The effect was explained by the substitution of Ca^{2+} ions on Ti^{4+} sites. The substitution of Ca^{2+} on Ti^{4+}-sites was demonstrated by Park *et al.* and Krishna *et al.*[58,59] A substitution can occur for compositions with a

Journal of Applied Physics ARTICLE scitation.org/journal/jap

molar ratio (Ba + Ca) / Ti = 1 and not only for compositions with a molar ratio (Ba + Ca)/Ti > 1 with an excess of Ca.[59] A solubility limit of 3 mol. % was found at a temperature 1450 °C for the BTO ceramic.[60] Due to the substitution of Ca^{2+} on Ti^{4+} sites, a neighboring O^{2-} ion forms a vacancy to balance the charge misfit and Ca^{2+}-V_O dipoles result.[56]

A homovalent substitution leads to weaker random fields than a heterovalent substitution.[54] Due to the relatively low substituent content of the investigated BCZT films in comparison to pure Zr substituted BTO based relaxor materials, one can argue that the substitution of Ca^{2+} ions on Ti^{4+} sites, which has the character of a heterovalent substitution, leads to the observed pronounced relaxor behavior. Additionally, first-principle calculations on homovalent substituted compositions of $BaTi_{0.74}Zr_{0.26}O_3$ by Laulhé *et al.* have shown that the displacement of Ti^{4+} ions is not only restricted to the ⟨111⟩directions but also does appear for the ⟨100⟩ and ⟨110⟩directions. The authors argued that these findings are also applicable for other BTO based homovalent substituted relaxors.[61] The higher degree of polarization directions links not only the formation of polar nanodomains[61] but could also give an explanation for the excellent piezoelectric properties of the investigated BCZT films.

TEM investigations

Thin films of BCZT were studied in the following. The morphology [Fig. 4(a)] is characterized by columnar BCZT grains (~150 nm in lateral dimension) which are extended perpendicularly to the substrate-BCZT interface with a more or less pronounced wedge shape of these columns. A preferred growing direction of the columns was observed along the $[111]_c$ direction using electron diffraction and Fourier transformations of HRTEM micrographs, confirming the XRD results. Applying CBED, a more reliable identification of the slight deviations from the cubic symmetry of the structure is possible by carefully analyzing the intensity of the diffraction disks, which revealed symmetry with the two

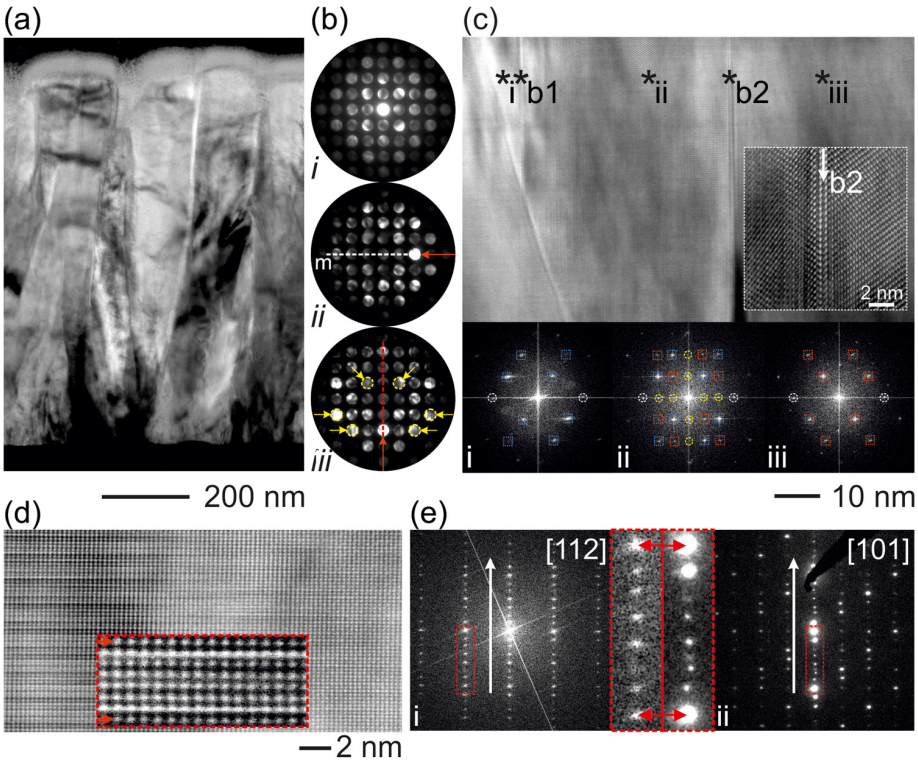

FIG. 4. Structural observations of the BCZT layer. (a) TEM bright field image of a cross-sectional view of BCZT. (b) Representative CBED symmetry study of a single grain: CBED pattern along the $[100]_C$ zone axis (b-i) and after a deliberate tilting away from pattern center following the red arrows (b-ii and b-iii). Marks (b): (expected) mirror planes (dashed lines), m—mirror plane, yellow circles emphasize absent mirror plane. (c) HRTEM micrograph of two domains oriented along the $[110]_C$ zone axis forming a superposition region separated by boundaries of superposition contrast (b1 and b2). Regions: (c-i, c-iii) Single crystalline domains, (c-ii) superposition. Marks: single domains (blue and red), the common intergrowth plane $\{111\}_C$ (dashed white line); fundamental reflections (white) and superposition reflections (yellow). (d) Overview HRSTEM micrograph with modulated (left) and unmodulated structure (right) along the $[112]_C$ zone axis, inset: magnified view of a 7L periodicity. (e) Reciprocal data set demonstrating a 1/7 $[111]_C$ modulation vector for the FFT pattern of the HRTEM micrograph (e-i) and a SAED pattern along the $[101]_C$ zone axis (e-ii) inset: magnified view of the periodicity. Marks: Growing direction along $[111]_C$ (white arrows), 7L periodicity (red arrows).

Journal of Applied Physics ARTICLE scitation.org/journal/jap

dimensional space group *pm*, [cf. Fig. 4(b-i)]. The pattern is oriented along the $[100]_c$ zone axis containing a single mirror plane assignable to $(001)_c$ or $(010)_c$. A verification of this finding was obtained by a deliberate tilt into perpendicular directions, respectively. Only in the tilt position of Fig. 4(b-ii) a mirror plane is detectable; in the other direction, a clear breakdown of the mirror symmetry becomes even more clearly [cf. marks in Fig. 4(b-iii)]. Consequently, several of the $\{110\}_c$ mirror planes were excluded analogously. The experimental findings allow the assumption of the space group *P*4 *mm* as an adequate candidate for the structure. On closer inspection, the expected symmetry of the CBED pattern is marginally violated. An interpretation of similar observations was provided by Tsuda *et al.* for BTO.[62] In these studies, CBED examinations indicated the presence of nanosized domains with different symmetries, e.g., local contributions of a coexisting trigonal (rhombohedral) phase.[37] Note that the experimental findings and the suggested presence of a morphotropic phase boundary (MPB)[33,63] can also be reasonably interpreted as a monoclinic symmetry (space group *Pm*). The recorded patterns, including mirror planes $(001)_c$ or $(010)_c$, would then be assigned to the monoclinic zone axes $[h0l]$ or $[0h\bar{l}]$. However, in the present investigations, clear evidence is missing for a monoclinic or trigonal symmetry.

The wedge shaped columns contain a complex substructure differentiating into twinned domains, cf. the HRTEM micrograph of Fig. 4(c) and the ED pattern in Fig. S4 of the supplementary material. In this special case, the corresponding Fourier transforms show two single crystalline domains oriented along $[110]_c$, which are mirrored along the $\{111\}_c$ planes, cf. domains (i) and (iii) of Fig. 4(c). Both domains are separated by boundaries b1 and b2, and these twinned domains seem to be superimposed along the viewing direction in region (ii) according to a three-dimensional inclined defect boundary model discussed in Fig. S2 of the supplementary material. Hence, b1 and b2 represent boundaries of superposition contrast. The FFT pattern of region (ii) appears as a superposition of the pattern from regions (i) and (iii), with Bragg intensities from pattern (iii) less pronounced and, thus, as minority component. Due to the superposition and the interrelated double diffraction phenomena, another group of intensities is observable, which is not assignable to one of the single domain patterns [see yellow marks in Fig. 4(c)]. The interpretation of these intensities and simulations of TEM data are based on supercells of superimposed twin domains.[64–66] Construction details of the supercell (Fig. S3 in the supplementary material) and respective experimental data with simulations for two experimentally observed scenarios, the edge-on view and special superposition case are provided in the supplementary material and are compared with each other (Fig. S4 in the supplementary material): (1) An experimental SAED pattern recorded on two adjacent single domains shows no indication of superposition contrast, thus, no superposition area is present. Only fundamental Bragg reflections of the respective single domains are visible matching excellently with the arrangement of the reflections in a kinematical simulation based on a supercell. Note, additional reflections seen in Fig. 4(c-ii) are absent. (2) Assuming a superposition of two $[110]_c$ oriented domains in a dynamical simulation, additional Bragg reflections can be generated agreeing with the experimental FFT pattern (Fig. S4 in the supplementary material). Thus, the additional Bragg intensities in the FFT are superposition introduced features and are located on commensurable lattice positions of this pattern. The formation of polysynthetic {111} growth twins is a well-known characteristic of the BTO bulk and thin films with a cubic or tetragonal symmetry.[67–69] Following the interpretation of previous studies the edge-on {111}-defect structure can be described as $\sum = 3$ twin boundary with coinciding (111) and $(\bar{1}12)$ reflections in ED patterns along the zone axis $[1\bar{1}0]$.[70–72] In the case of tetragonal BTO, the local arrangement of TiO_6 octahedra at the twin interface varies with respect to the bulk structure, i.e., corner-sharing TiO_6 ocatahedra are replaced by face-sharing Ti_2O_9-dimers. Such a local structure variation is supposed to accommodate for local oxygen deficiency.[73] These results can be analogously transferred to BCZT in many instances. However, to obtain in-depth information about the atomic configuration directly at the interface region, further aberration corrected HRTEM investigations are essential.

In some instances, lamellar fringes are detected propagating parallel to the Pt surface, which is expressed by an alternating bright-dark contrast. Preliminary EDX nanoprobe measurements excluded the diffusion of Pt into the fringe dominated areas and also variations of the composition on a larger scale. A high-resolution inspection of the fringed areas reveals a periodic arrangement of a seven layer (7L) sequence, cf. Fig. 4(d), featuring disturbances of locally different repetition schemes. By evaluating the corresponding FFT [Fig. 4(e-i)] and a correlated SAED pattern [Fig. 4(e-ii)], satellite intensities were observed, referring to a structural modulation[74] of the ideal pseudocubic structure. The modulation vector is close to 1/7 $[111]_c$ as observed along different viewing directions, cf. the respective insets Fig. 4(e). Further, the magnified views of the diffraction pattern reveal an incommensurate arrangement of the satellite reflections, which is particularly visible in the SAED pattern indicating high order satellites. A polytypism[75] could serve as possible basis for the interpretation of the experimental findings and is discussed further in Fig. S5 in the supplementary material. In the literature, stoichiometric and oxygen-deficient polytypes were discussed for several perovskites or perovskite-related oxides.[76–78] A first set of experiments with a transmission electron microscope equipped with a Super-X EDX system for atomic resolution EDX was carried out to study the chemical composition with atomic resolution (see Fig. S6 in the supplementary material). However, a clear interpretation of the layer sequence of BCZT and the polytype was impossible from EDX data due to the overlap of the Ti-K and Ba-L peaks. *In situ* annealing experiments were performed exhibiting no significant change to the modulated structure during the entire process. Consequently, we assume that the modulated structure is not based on oxygen deficiency but homovalent cationic ordering on A- and B-sites. With respect to further investigations, the capabilities of aberration-corrected microscopy allow precise determination of the atomic configuration in PZT at the nanoscale.[79] Hence, an aberration-corrected HRTEM micrograph of BCZT is depicted in Fig. S7 in the supplementary material displaying pronounced contrast intensity variations on the cationic positions indicating the presence of cationic disordering compared to high-resolution simulations (Fig. S7-i in the supplementary material) based on the tetragonal (*P*4 *mm*) structure model (ii). Despite such ordering scheme, well known for relaxor materials, these structural domains

Journal of Applied Physics ARTICLE scitation.org/journal/jap

are not expected to produce the randomly oriented dipoles since their density is too low.

SUMMARY AND CONCLUSIONS

Ferroelectric lead-free thin films of the composition $(Ba_{0.85}Ca_{0.15})(Ti_{0.9}Zr_{0.1})O_3$ (BCZT) were deposited by pulsed laser deposition (PLD). The BCZT thin films are composed of columnar grains with preferred $[111]_C$ growth. We report a maximum of the dielectric permittivity of $\varepsilon = 2000$ at 5 khZ and a maximum effective piezoelectric constant of $d_{33,f} = 190\,\mathrm{pm/V}$, which could be improved to 300 pm/V. The temperature dependence of the permittivity on the frequency and deviation from the Curie-Weiss law indicates a relaxor behavior for the present thin films. CBED studies on single domains are consistent with a noncubic but tetragonal $P4mm$ symmetry. Additionally, inside the columns several microstructural characteristics were observed: (1) The presence of a modulation along the $[111]_C$ direction, and, a polytype with pronounced cation segregation was assumed as a potential interpretation. (2) Twinned domains with varying interconnection of the octahedral structural units. Transmitted areas with twinned domains show additional reflections which were proven to be excited by dynamical scattering and not by a potentially lower symmetry. All these characteristics are not interconnected with the microstructural origin of the relaxor effect, however, their presence complicate the identification of potential polar nanodomains.

SUPPLEMENTARY MATERIAL

See the supplementary material for additional information on physical and structural investigations performed during the study and referred to in the text.

ACKNOWLEDGMENTS

The authors want to thank Dr. Martina Luysberg and Dr. Lothar Houben from the Ernst Ruska Centre in Jülich for discussion and C_S-corrected microscopy. Funding of this work via the DFG (No. CRC1261) "Magnetoelectric Sensors: From Composite Materials to Biomagnetic Diagnostics" and the PAK902 is gratefully acknowledged.

REFERENCES

[1]P. Muralt, J. Am. Ceram. Soc. **91**, 1385 (2008).
[2]R. G. Polcawich, J. S. Pulskamp, S. Bedair, G. Smith, R. Kaul, C. Kroninger, E. Wetzel, H. Chandrahalim, and S. A. Bhave, in *2010 IEEE Sensors* (New York, 2010), pp. 2193–2196.
[3]C.-B. Eom and S. Trolier-McKinstry, MRS Bull. **37**, 1007 (2012).
[4]S. Trolier-McKinstry and P. Muralt, J. Electroceram. **12**, 7 (2004).
[5]M. D. Maeder, D. Damjanovic, and N. Setter, J. Electroceram. **13**, 385 (2004).
[6]J. Rödel, W. Jo, K. T. P. Seifert, E.-M. Anton, T. Granzow, and D. Damjanovic, J. Am. Ceram. Soc. **92**, 1153 (2009).
[7]E. Aksel and J. L. Jones, Sensors **10**, 1935 (2010).
[8]S. Y. Lee, C. W. Ahn, J. S. Kim, A. Ullah, H. J. Lee, H.-I. Hwang, J. S. Choi, B. H. Park, and I. W. Kim, J. Alloys Compd. **509**, L194 (2011).
[9]X. J. Zheng, Y. F. Rong, D. Z. Zhang, T. Zhang, L. He, and X. Feng, Mater. Lett. **64**, 618 (2010).
[10]N. Ledermann, P. Muralt, J. Baborowski, S. Gentil, K. Mukati, M. Cantoni, A. Seifert, and N. Setter, Sens. Actuators A **105**, 162 (2003).
[11]W. Liu and X. Ren, Phys. Rev. Lett. **103**, 257602 (2009).
[12]P. Muralt, Integr. Ferroelectr. **17**, 297 (1997).
[13]K. Lefki and G. J. M. Dormans, J. Appl. Phys. **76**, 1764 (1994).
[14]N. Sama, C. Soyer, D. Remiens, C. Verrue, and R. Bouregba, Sens. Actuators A **158**, 99 (2010).
[15]D. Xue, Y. Zhou, H. Bao, C. Zhou, J. Gao, and X. Ren, J. Appl. Phys. **109**, 054110 (2011).
[16]E. A. Neppiras, J. Sound Vib. **20**, 562 (1972).
[17]G. Kang, K. Yao, and J. Wang, J. Am. Ceram. Soc. **95**, 986 (2012).
[18]Q. G. Chi, H. F. Zhu, J. C. Xu, X. Wang, J. Q. Lin, Z. Sun, Y. Chen, and Q. Q. Lei, Ceram. Int. **39**, 8195 (2013).
[19]A. Jalalian, A. M. Grishin, X. L. Wang, Z. X. Cheng, and S. X. Dou, Appl. Phys. Lett. **104**, 103112 (2014).
[20]B. C. Luo, D. Y. Wang, M. M. Duan, and S. Li, Appl. Phys. Lett. **103**, 122903 (2013).
[21]A. Piorra, A. Petraru, H. Kohlstedt, M. Wuttig, and E. Quandt, J. Appl. Phys. **109**, 104101 (2011).
[22]C. Bhardwaj and D. Kaur, Curr. Appl. Phys. **12**, 1239 (2012).
[23]Y. Lin, N. Qin, G. Wu, T. Sa, and D. Bao, Appl. Phys. A **109**, 743 (2012).
[24]T. Maiti, R. Guo, and A. S. Bhalla, Ferroelectrics **425**, 4 (2011).
[25]V. V. Shvartsman and D. C. Lupascu, J. Am. Ceram. Soc. **95**, 1 (2012).
[26]L. E. Cross, Ferroelectrics **76**, 241 (1987).
[27]A. J. Moulson and J. M. Herbert, *Electroceramics* (John Wiley & Sons, Ltd, Chichester, UK, 2003).
[28]D. Viehland, S. J. Jang, L. E. Cross, and M. Wuttig, J. Appl. Phys. **68**, 2916 (1990).
[29]A. A. Bokov and Z.-G. Ye, in *Frontiers of Ferroelectricity* (Berlin, 2006), pp. 31–52.
[30]K. Uchino and S. Nomura, Ferroelectrics **44**, 55 (1982).
[31]A. Dixit, S. B. Majumder, R. S. Katiyar, and A. S. Bhalla, J. Mater. Sci. **41**, 87 (2006).
[32]X. G. Tang, K.-H. Chew, and H. L. W. Chan, Acta Mater. **52**, 5177 (2004).
[33]J. Gao, D. Xue, Y. Wang, D. Wang, L. Zhang, H. Wu, S. Guo, H. Bao, C. Zhou, W. Liu, S. Hou, G. Xiao, and X. Ren, Appl. Phys. Lett. **99**, 092901 (2011).
[34]P. A. Stadelmann, Ultramicroscopy **21**, 131 (1987).
[35]R. Kilaas, J. Microsc. **190**, 45 (1998).
[36]D. S. Keeble, F. Benabdallah, P. A. Thomas, M. Maglione, and J. Kreisel, Appl. Phys. Lett. **102**, 092903 (2013).
[37]Y. Yang, Z. Wang, J.-F. Li, and D. Viehland, J. Nanomater. **2010**, e756319 (2010).
[38]M. Davis, M. Budimir, D. Damjanovic, and N. Setter, J. Appl. Phys. **101**, 054112 (2007).
[39]J. Ouyang, R. Ramesh, and A. L. Roytburd, Appl. Surf. Sci. **252**, 3394 (2006).
[40]W. Li, J. Hao, W. Bai, and J. Zhai, J. Solgel Sci. Technol. **66**, 220 (2013).
[41]N. Abt, R. Moazzami, and Y. Nissan-Cohen, Integr. Ferroelectr. **2**, 121 (1992).
[42]W. L. Warren, B. A. Tuttle, D. Dimos, G. Pike E, H. N. Al-Shareef, R. Ramesh, and J. T. J. Evans, Jpn. J. Appl. Phys. **35**, 1521 (1996).
[43]J. Lee, R. Ramesh, V. G. Keramidas, W. L. Warren, G. E. Pike, and J. T. Evans, Appl. Phys. Lett. **66**, 1337 (1995).
[44]G. E. Pike, W. L. Warren, D. Dimos, B. A. Tuttle, R. Ramesh, J. Lee, V. G. Keramidas, and J. T. Evans, Appl. Phys. Lett. **66**, 484 (1995).
[45]A. Gruverman, B. J. Rodriguez, A. I. Kingon, R. J. Nemanich, A. K. Tagantsev, J. S. Cross, and M. Tsukada, Appl. Phys. Lett. **83**, 728 (2003).
[46]A. K. Tagantsev and G. Gerra, J. Appl. Phys. **100**, 051607 (2006).
[47]Y. Liu, Z. Wang, A. S. Thind, T. Orvis, D. Sarkar, R. Kapadia, A. Y. Borisevich, R. Mishra, A. I. Khan, and J. Ravichandran, J. Vac. Sci. Technol. A **37**, 011502 (2019).
[48]H. Bao, C. Zhou, D. Xue, J. Gao, and X. Ren, J. Phys. D Appl. Phys. **43**, 465401 (2010).
[49]K. Prabahar, R. Ranjith, A. Srinivas, S. V. Kamat, B. Mallesham, V. L. Niranjani, J. P. Praveen, and D. Das, Ceram. Int. **43**, 5356 (2017).
[50]X.-G. Tang and H. L.-W. Chan, J. Appl. Phys. **97**, 034109 (2005).
[51]N. D. Scarisoreanu, F. Craciun, A. Moldovan, V. Ion, R. Birjega, C. Ghica, R. F. Negrea, and M. Dinescu, ACS Appl. Mater. Interfaces **7**, 23984 (2015).

Journal of Applied Physics ARTICLE scitation.org/journal/jap

[52]V. Ion, F. Craciun, N. D. Scarisoreanu, A. Moldovan, A. Andrei, R. Birjega, C. Ghica, F. Di Pietrantonio, D. Cannata, M. Benetti, and M. Dinescu, Sci. Rep. **8**, 2056 (2018).
[53]X. Dai, Z. Xu, J.-F. Li, and D. Viehland, J. Mater. Res. **11**, 618 (1996).
[54]W. Kleemann, J. Adv. Dielect. **02**, 1241001 (2012).
[55]A. Dixit, S. B. Majumder, R. S. Katiyar, and A. S. Bhalla, Appl. Phys. Lett. **82**, 2679 (2003).
[56]S. Yun, X. Wang, B. Li, and D. Xu, Solid State Commun. **143**, 461 (2007).
[57]P. Victor, R. Ranjith, and S. B. Krupanidhi, J. Appl. Phys. **94**, 7702 (2003).
[58]J. G. Park, T. S. Oh, and Y. H. Kim, J. Mater. Sci. **27**, 5713 (1992).
[59]P. S. R. Krishna, D. Pandey, V. S. Tiwari, R. Chakravarthy, and B. A. Dasannacharya, Appl. Phys. Lett. **62**, 231 (1993).
[60]M. Čeh and D. Kolar, Mater. Res. Bull. **29**, 269 (1994).
[61]C. Laulhé, A. Pasturel, F. Hippert, and J. Kreisel, Phys. Rev. B **82**, 132102 (2010).
[62]K. Tsuda, R. Sano, and M. Tanaka, Phys. Rev. B **86**, 214106 (2012).
[63]H. Wang, J. Zhu, N. Lu, A. A. Bokov, Z.-G. Ye, and X. W. Zhang, Appl. Phys. Lett. **89**, 042908 (2006).
[64]V. Hrkac, L. Kienle, S. Kaps, A. Lotnyk, Y. K. Mishra, U. Schürmann, V. Duppel, B. V. Lotsch, and R. Adelung, J. Appl. Crystallogr. **46**, 396 (2013).
[65]L. Kienle and A. Simon, J. Solid State Chem. **167**, 214 (2002).
[66]H.-J. Deiseroth, C. Reiner, K. Xhaxhiu, M. Schlosser, and L. Kienle, Z. Anorg. Allg. Chem. **630**, 2319 (2004).
[67]O. Eibl, P. Pongratz, and P. Skalicky, Philos. Mag. B **57**, 521 (1988).
[68]A. Rečnik, J. Bruley, W. Mader, D. Kolar, and M. Rühle, Philos. Mag. B **70**, 1021 (1994).
[69]C. L. Jia, Philos. Mag. Lett. **79**, 99 (1999).
[70]M. Fujimoto, J. Cryst. Growth **237–239**, 430 (2002).
[71]C. L. Jia, K. Urban, M. Mertin, S. Hoffmann, and R. Waser, Philos. Mag. A **77**, 923 (1998).
[72]C. L. Jia and A. Thust, Phys. Rev. Lett. **82**, 5052 (1999).
[73]C. L. Jia and K. Urban, Science **303**, 2001 (2004).
[74]G. King, S. Garcia-Martin, P. M. and Woodward, Acta Crystallogr. B **65**, 676 (2009).
[75]A. Guinier, G. B. Bokij, K. Boll-Dornberger, J. M. Cowley, S. Ďurovič, H. Jagodzinski, P. Krishna, P. M. de Wolff, B. B. Zvyagin, D. E. Cox, P. Goodman, T. Hahn, K. Kuchitsu, and S. C. Abrahams, Acta Crystallogr. **40**, 399 (1984).
[76]E. García-González, M. Parras, and J. M. González-Calbet, Chem. Mater. **11**, 433 (1999).
[77]H. Yang, Y. K. Tang, L. D. Yao, W. Zhang, Q. A. Li, F. Y. Li, C. Q. Jin, and R. C. Yu, J. Alloys Compd. **432**, 283 (2007).
[78]J.-G. Cheng, J. A. Alonso, E. Suard, J.-S. Zhou, and J. B. Goodenough, J. Am. Chem. Soc. **131**, 7461 (2009).
[79]K. W. Urban, Science **321**, 506 (2008).

Supporting Material

$(Ba_{0.85}Ca_{0.15})(Ti_{0.9}Zr_{0.1})O_3$ thin films prepared by PLD: relaxor properties and complex microstructure

André Piorra[1], Viktor Hrkac[2], Niklas Wolff[2], Christiane Zamponi[1], Joke Hadermann[3], Viola Duppel[4], Lorenz Kienle[2] and Eckhard Quandt[1]

[1]Inorganic Functional Materials, Faculty of Engineering, Kiel University, Germany

[2]Synthesis and Real Structure, Faculty of Engineering, Kiel University, Germany

[3]EMAT, Department of Physics, University of Antwerp, Belgium

[4]Max Planck Institute for Solid State Research, Heisenbergstr. 1, D-70569 Stuttgart, Germany

I. Ferroelectric nature of bulk BCZT

The piezoelectric hysteresis of the BCZT bulk phase depicted in Fig. S1 a) shows the typical characteristic of a ferroelectric material. A piezoelectric constant d_{33} of 700 pm/V can be calculated. This value is comparable to the published piezoelectric constant (d_{33} = 620 pc/N) of the material[1]. The temperature dependence of the dielectric permittivity ε is shown in Fig. S1 b) for frequencies between the kHz to MHz regime. The results clearly indicate a sharp and frequency independent ferroelectric to paraelectric transition with a Curie temperature T_C of 78 °C which also correlates with published data of this composition[11]. A dielectric permittivity of ε = 4500 at 1000 Hz at room temperature has also to be noted. Finally, the existence of ferroelectric regions (Fig. S1 c) denote the proof of the ferroelectric nature of the BCZT bulk ceramic.

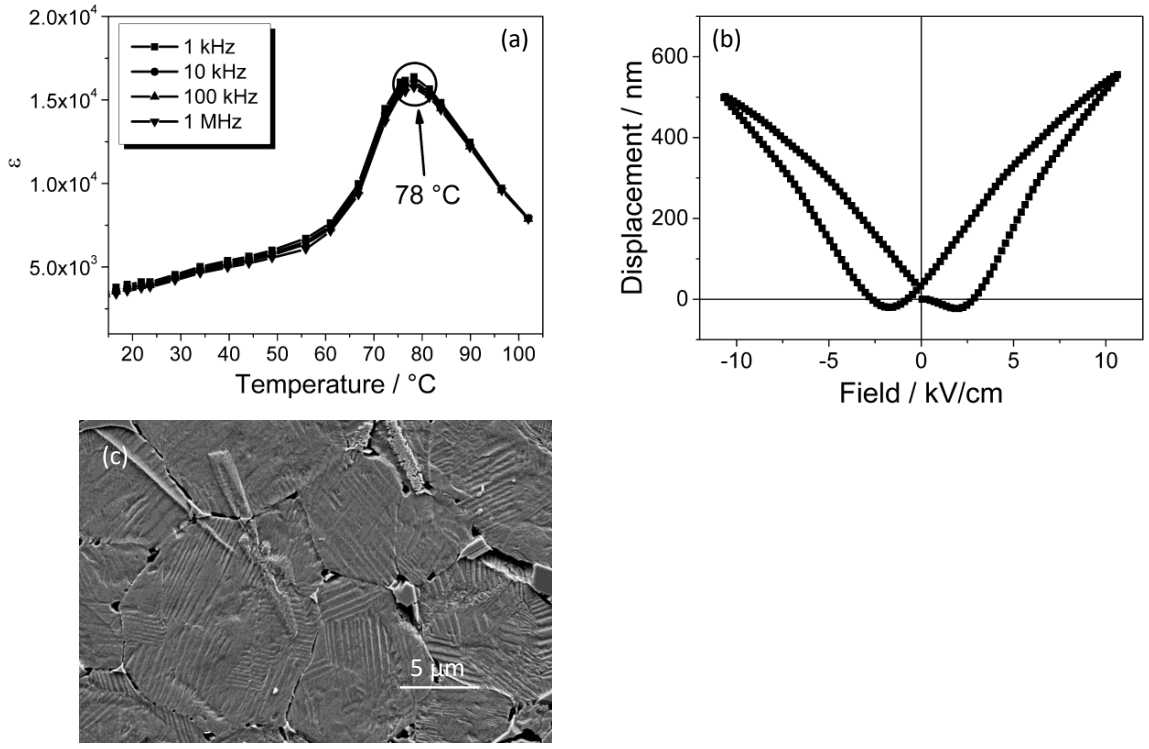

Figure S1: Properties of sintered BCZT bulk. (a) Piezoelectric displacement as function of an applied electric field, (b) temperature dependence of the dielectric constant at different frequencies, (c) SEM micrograph of microstructure of BCZT bulk. To visualize the domain structure the surface was etched by a mixture of hydrochloric and hydrofluoric acid.

[1] W. Liu and X. Ren, Physical Review Letters **103**, 257602 (2009).

II. Description of a superposition defect

The 3d defect situation is sketched in Figure S2 showing domains i and iii separated by a defect plane (yellow) as suggested previously. In image **A** we depict the situation very close to the [-110] viewing direction exemplary showing one vertical (11-1) plane in green color which belongs to the boundary of superposition contrast mistakenly suggested as an edge-on twin boundary in Figure 4c of the manuscript.
To retrieve the nature of the inclined defect plane we tilt the model by 90° into a [112] viewing direction. The situation is depicted in **B** where a second plane (-110, blue) is shown to prove the 90° rotation. According to geometrical considerations possible defect planes are parallel to [112]. One of these low indexed planes is the (0-21) plane (yellow plane in **C**), which is inclined by ~ 40° to (11-1). However, we cannot definitely denominate the (0-21) plane to be the present defect plane due to projection. But, from the experimental spacing between the boundaries b1 and b2, which is 50-60 nm, and assumed specimen thickness in the same magnitude, we can argue that the inclination angle shall not deviate much from 45°. Hence, the (0-21) plane seems to be a feasible candidate as defect plane.

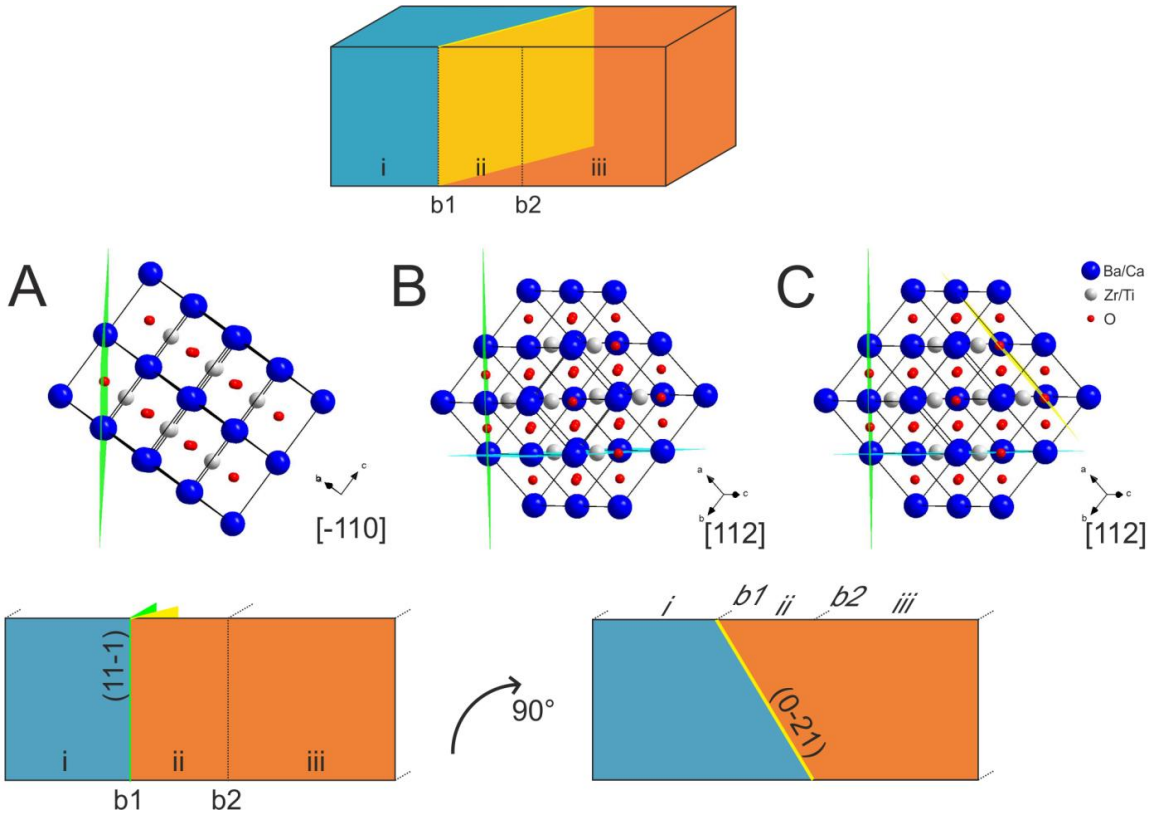

Figure S2: Scenario of two twinned domains with an inclined defect boundary.

III. Details of the supercell approach for the $\{111\}^{PC}$/ $[110]^{PC}$ twin interface observed in BCZT:

(1) In a preliminary step, the viewing direction $[110]^{PC}$ is transformed into a principle axis for the supercell. In this case a two-step symmetry reduction is performed from $Pm\bar{3}m$ (a = 4.0191 Å) to the t (translationsgleiche)-subgroup $P4/mnm$ (c/a = 1) and afterwards to $C2/mmm$ (a-b, a+b, c) (also t-subgroup). In the orthorhombic $C2/mmm$ unit cell the $\{111\}^{PC}$ twin plane is transformed to $\{101\}^{Supercell}$.

(2) A straightforward realization of a rectangular supercell can be achieved using the transformation matrices P in accordance with the transformation conventions[2],

$$P=\begin{pmatrix} 2 & 0 & -2 \\ 0 & 1 & 0 \\ 2 & 0 & 4 \end{pmatrix}$$

The lattice parameters for the supercell are a = 13.9226 Å, b = 5.6839 Å, c = 19.6895 Å with α, β, γ = 90°. The a-axis of the supercell coincides with the twin plane $(111)^{PC}$ of the pseudocubic structure.

(3) Generating a second supercell with inverted x-parameters and superimposing it with the former supercell a superposition structure (SPS) is created with the experimentally observed twinning/ superposition features as incorporated features. Note, that a conventional separation step is omitted as the main emphasis lies on the investigations of the Bragg intensities.

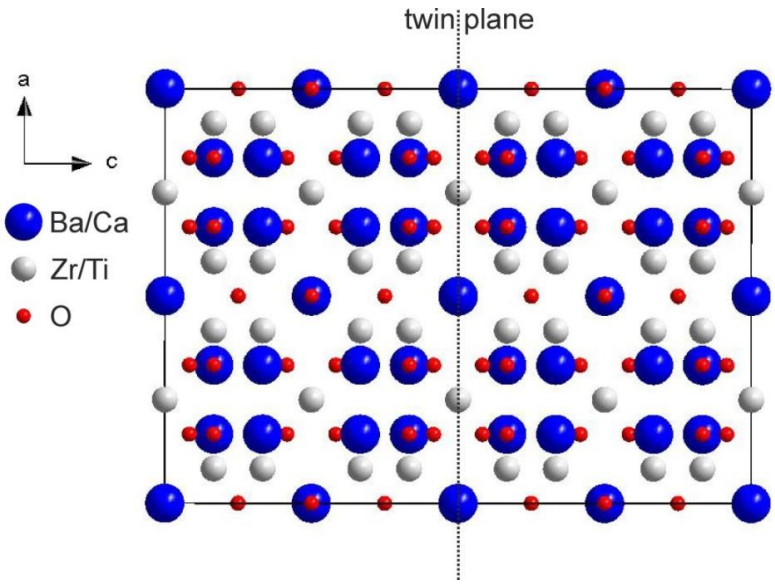

Figure S3: Superposition structure of the twin interface used for the simulation of ED pattern in Fig. S4.

[2] Hahn, T. (2002). Editor. International Tables for Crystallography, Vol. A. Dordrecht: Kluwer Academic Publishers.

IV. Simulation of electron diffraction data for the twinned domains

Two respective ED pattern were simulated based on a kinematical and dynamical approach for the pseudocubic zone axis [110] and compared with the experimental findings in Fig. S3.

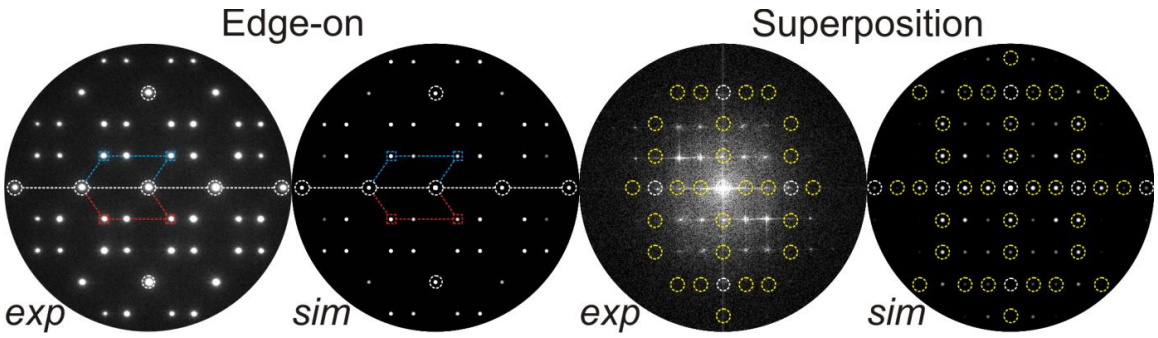

Figure S4: Reciprocal data set along the $[110]_C$ zone axis: (Edge-on) experimental SAED vs. simulated ED pattern. (Superposition) experimental FFT vs. simulated ED pattern. Marks: single domains (blue and red), the twin plane $\{111\}_C$ (dashed white line); fundamental reflections (white) and superposition reflections (yellow)

V. Comparision of 7L-structure with a 7H-polytype model

In order to rationalize the further similarities between the experimentally obtained 7L-structure with a 7H-polytype model (7H-$Ba_7Nb_4MoO_{20}$ polytype[3]), electron diffraction patterns were simulated based on the latter model. The zone axes [1 0-1 0] and [2 -1 -1 0] of the trigonal setting correspond with the (pseudo)cubic [1 1 2] and [1 0 1] directions, respectively, and were compared with the experimental data, see Figure 3c. Although a good match between the modulation vectors is observable, the intensities of the reflections show significant differences. In the 7H model the Bragg reflections are commensurable. Apparently, the atomic species differ, but a variation of the modulated layer sequence must also be considered in the BCZT thin film system with respect to the 7H model.

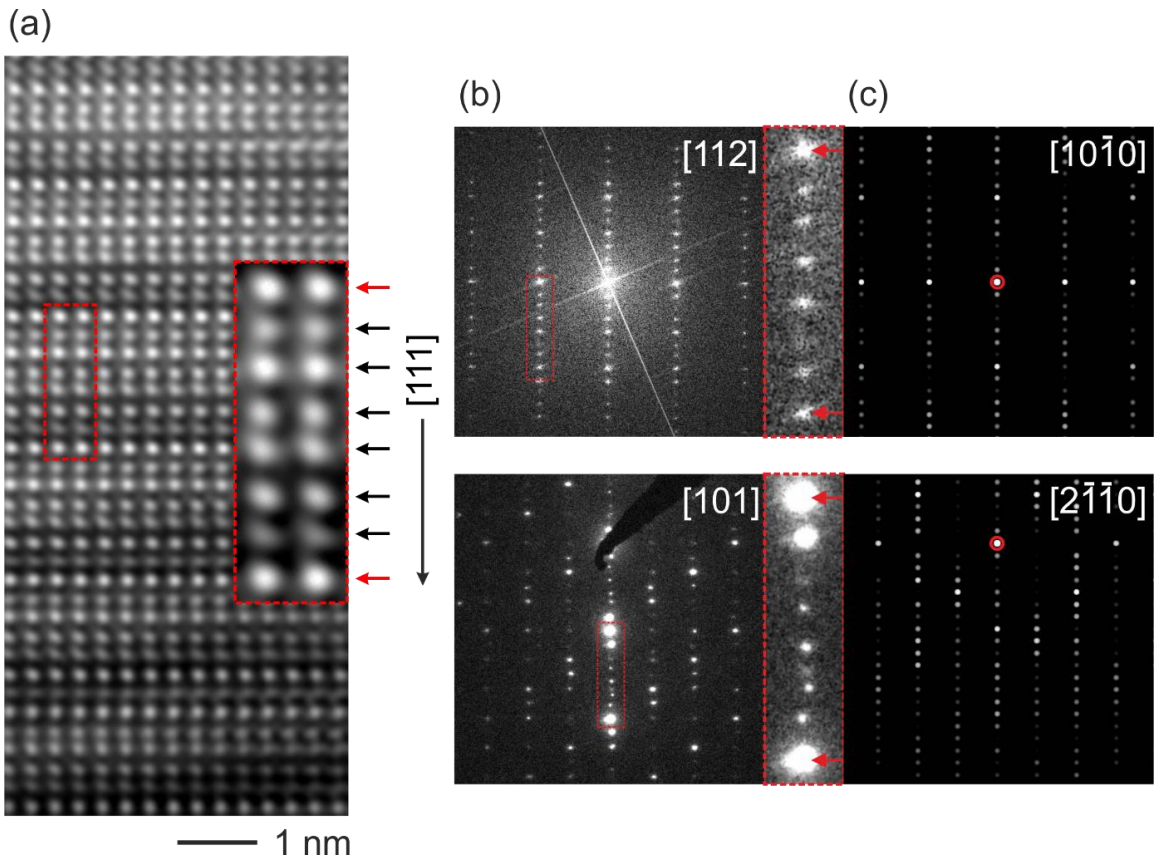

Figure S5: BCZT thin film: (a) HRTEM micrograph of a potential polytype structure, the read box exhibits a 7L periodicity along the zone axis [1 1 2]. The red arrows mark repeating layers, the further black arrows emphasize the other single layers. (b) Observation of the modulated BCZT structure along (top) [1 1 2] in a FFT pattern and (bottom) [1 1 0] in a SAED pattern. The modulation vector is identified as 1/7 <1 1 1> using pseudocubic notation. The red arrows mark the fundamental {1 1 1} Bragg intensities in the respective pattern. (c) For rationalization of the modulation, a comparison is provided with simulated electron diffraction pattern of a 7H-Ba7Nb4MoO20 polytype. The structure is set in the trigonal P-3m1 space group; the zone axis [1 0-1 0] corresponds to the pseudocubic [1 1 2] direction and [2-1 -1 0] to [1 0 1]. The red rings mark the center of the simulated patterns.

[3] E. Garcia-Gonzalez, M. Parras, and J. M. Gonzalez-Calbet. Crystal structure of an unusual polytype:7H-Ba7Nb4MoO20. Chemistry of Materials, 11(2):433-437, 1999.

VI. Chemical Analysis with EDX

Atomic resolved EDX experiments were conducted to study the chemical composition within the modulated structure with a transmission electron microscope equipped with a Super-X EDX system.

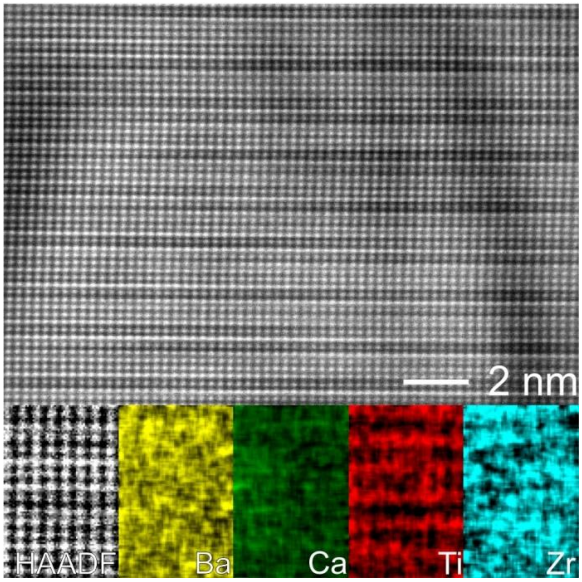

Figure S6: Atomic resolution STEM EDX mapping of the modulated structure. The overlap of Ti-K and Ba-L peaks avoid a clear interpretation the chemical composition of atomic columns.

VII. Aberration corrected HRTEM

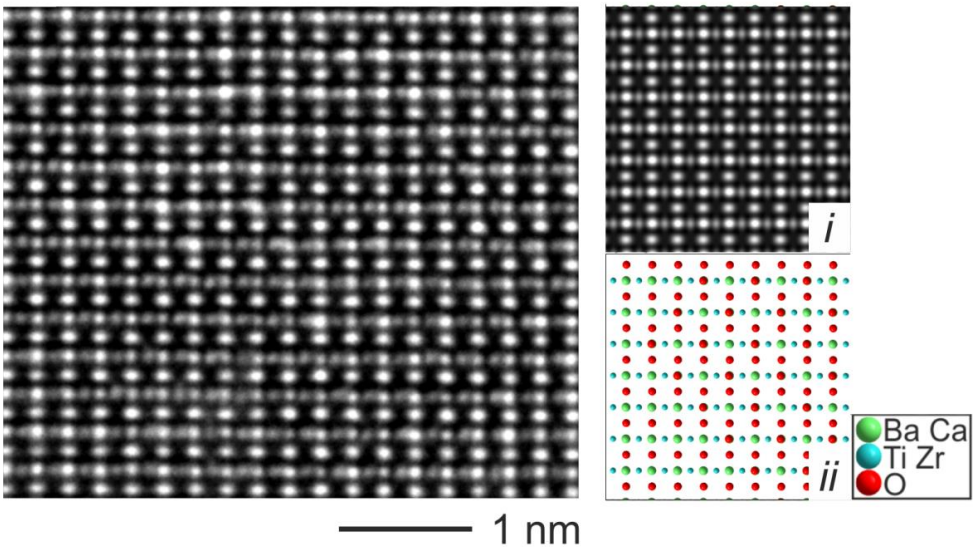

Figure S7: Experimental data of BCZT: aberration corrected HRTEM micrograph of a thin film specimen indicating cationic disordering with respect to the simulation shown in the simulated data of BCZT: (i) aberration corrected HRTEM contrast (Δf = 9 nm | specimen thickness ca. 4 nm), (ii) structural model. , For all panels the viewing direction is along the pseudocubic [112] direction.

4.1.3 ZnO Microstructures and Functionalization

Zinc oxide micro- and nanostructures, especially single crystalline (hexagonal-wurtzite) ZnO microneedles display one of the most investigated materials of the last decade in the field of piezotronic and related piezo-phototronic applications including strain sensors, nanogenerators, solar cells or light emitting diodes.[186]–[188] This tremendous research interest is not only derived by easy synthesis processes enabling also large scale production of high crystal quality ZnO in unique and large structural variety[189], [190] but also by the electronic properties offering a wide direct band gap of 3.37 eV.[191] The non-centrosymmetric crystal structure of ZnO facilitates the generation of a piezopotential along the c-axis under tensile or compressive load which can be efficiently exploited at a metal-semiconductor(M-S) interface to drive a strain dependent piezotronic current over the Schottky-contact. This effect has been translated to single 1D ZnO nano- and microrod based ME sensing devices and the novel piezotronic measurement principle has been demonstrated in the realization of a first piezotronic ME sensor.[60]

The performance of the piezotronic sensor was analyzed for different materials and electrode designs and highlighted the possibility to outperform piezoelectric ME sensors in terms of sensitivity by the integrated signal amplification. In this respect, a high piezotronic current output and hence a high sensitivity to ultra-low magnetic field strengths is limited by noise sources arising in the space charge region (SCR).[61] These noise sources can be principally discussed referring to a diode equation describing the amplified current signal I(t) as a Boltzmann term including the modulation voltage at the working point U_{wp}, the sum of the piezopotential induced in the bulk and in the SCR U(t) and the voltage noise $N_U(t)$ multiplied with a prefactor including the intrinsic current $I_{0,intrinsic}$, the intrinsically generated leakage current $N_{0,intrinsic}$ and additional defect leakage currents $I_{0,defects}$ with its respective noise term $N_{0,defects}$:[4]

$$I(t) = [I_{0,intrinsic} + N_{0,intrinsic}(t) + I_{0,defects} + N_{0,defects}(t)] \exp\left(\frac{q[U_{wp} + U(t) + N_U(t)]}{nkT}\right)$$

The intrinsic leakage current describes the elevation of electrons from the valence band to the conduction band by thermal excitation or by the Fermi-distribution function and can be minimized by choosing a material with a suitable high band gap $< 3\,eV$ such as ZnO or GaN. Defect currents are generated by electronic defect states in the bandgap or close to the conduction band, enhancing the probability of thermal excitation from these states. Hence, the crystal and M-S interface quality require to be free of defects in order to eliminate these noise sources. In conclusion, the quality of the SCR is the most demanding part in terms of a high sensitivity and low noise piezotronic ME sensor which is strongly affected by structural imperfections and the resulting modulation of the electronic structure, e.g. also by doping.[192]

In this regard, the capabilities of TEM can be exploited to analyze these requirements by identifying structural defects as well as the effects of doping, e.g. the homogeneity of the doping agent distribution.

[4] This theoretical discussion of noise in piezotronic sensors belongs to work of Dr. Jürgen Carstensen.

A simple strategy for **enhancing the conductivity of ZnO micro- and nanowire networks with gallium oxides**[5] is reported in the work of Smazna, Wolff *et al.*[193] describing the electronic properties and structural changes to the ZnO lattice after surface hybridization of microneedles by thermal annealing in the presence of organic Ga-salts. The modified surface of ZnO needles was observed to favor an high amount of lattice defects such as stacking faults and nano-inclusions of gallium oxide species after the treatment, which transfer strain to the ZnO lattice. Dependent on the annealing atmosphere the surface hybridization was evidenced to increase the ZnO conductivity by a factor of 200 in the presence of argon gas.

The second feature article concentrates on the crystallographic characterization of hidden **planar defects in ZnO nanospikes**,[194] which are masked from direct observation by their special morphology. The application of a special sample preparation method to yield high quality cross-section specimens of freestanding and highly anisotropic structures is presented. Defect analysis was carried out by correlating the phase contrast of HRTEM micrographs to model based simulations of the defect structure.
Other studies concentrated on the influence of ZnO morphology on the response of exposed crystal facets or decorative surface functionalization by metal or metal oxide nanoparticles on external stimuli, which are also partially discussed in Chapter 5.[87], [88], [195]–[198]

Essential knowledge on the defect structure in various ZnO morphologies could be gained and strategies to improve the charge transport over the Schottky-barrier in ZnO microneedles was demonstrated. However, the high amount of defects accompanied with the surface hybridization and the intrinsic defect structure of the ZnO nanospikes is eliminating these structures for consideration in piezotronic ME sensors in terms of noise reduction. These studies are pivotal extensions on the development of biomagnetic field ME sensors based on the piezotronic effect.

[5]Reprinted with permission, from [D. Smazna, N. Wolff, S. Shree, F. Schütt, Y.K. Mishra, L. Kienle, R. Adelung, Enhancing the Conductivity of ZnO Micro- and Nanowire Networks with Gallium Oxide, IEEE 7th International Conference on Nanomaterials: Applications and Properties (NAP), 12/2017], not included in the online version of this thesis.

NAP-2017, 2017 IEEE 7th International Conference on Nanomaterials: Applications and Properties (NAP)

Enhancing the Conductivity of ZnO Micro- and Nanowire Networks with Gallium Oxide

D. Smazna, N. Wolff, S. Shree, F. Schütt, Y.K. Mishra, L. Kienle, R. Adelung
Institute for Materials Science, Kiel University
Kaiserstr.2, 24143,
Kiel, Germany
dasm@tf.uni-kiel.de

***Abstract*— In this work a successful hybridization strategy for ZnO micro- and nanowire's surface with Ga_2O_3 nano-networks is presented and briefly discussed. The ZnO micro- and nanowires are grown by an upgraded flame transport synthesis (FTS) approach. The ZnO wires have been coated with gallium acetylacetonate ($Ga(acac)_3$) organic solution followed by subsequent annealing in air and argon atmospheres. Depending on the annealing conditions, distinct impacts on the electrical properties of individual hybridized ZnO microwires are observed which demonstrate a remarkable increase in conductivity (factor of 20 for air and 200 for argon environments). Scanning transmission electron microscopy (STEM) in combination with energy-dispersive X-ray spectroscopy (EDX) confirmed that the gallium oxide nanoparticles form, alter the ZnO surface features and might effect a doping in such a way. High-resolution transmission electron microscopy (HRTEM) studies of the hybridized ZnO surface reveal that both the β-/γ-Ga_2O_3 phases are present as nanoinclusions in the top layer. These investigations confirmed noticeable modifications in the ZnO lattice caused by the hybridization with gallium oxide. Moreover, the structural changes in the ZnO surface were traced via Raman spectroscopy examinations revealing an increase in the scattering peaks intensity at 569 cm^{-1} and 646 cm^{-1} which are responsible for the native oxygen vacancies in ZnO and a corresponding blue shift for the E_2(high) peak indicates an introduction of strain into ZnO lattice.**

Keywords— ZnO; hybridization; microwires; nanoparticles.

I. INTRODUCTION

ZnO micro- and nanostructuring has received significant research focus due to its large number of applications ranging from conventional nanoelectronics to advanced biomedical technologies [1]. The wide and direct band gap ~ 3.37 eV, n-type conductivity, versatile growth nature, and high robustness make ZnO suitable for a large variety of applications [2–4]. Most of the ZnO structural variants are obtained via kinetic growth along the c-axis because of its hexagonal-wurtzite type crystal structure. As ZnO is a quite thermally stable, non-toxic and optically very active material, it is utilized in a broad range of applications, e.g., photovoltaic cells, field effect transistor, UV-, chemical-, gas-, or biosensors, etc. [5, 6]. In addition to various applications, the ZnO nano- and microstructures can be used as sacrificial templates to fabricate new micro- and nanostructures from different materials. After the deposition of a desired material, the ZnO template underneath can be easily removed, either by a simple chemical vapor deposition process or by wet chemistry, e.g., using HCl. The sacrificial nature of ZnO offers a large number of nanostructuring opportunities and structures extending from individual hollow nanotubes to porous interconnected tetrapodal networks have been successfully fabricated [7–9] .

Although pristine ZnO exhibits n-type conductivity (due to its defects) which is rather small with respect to many desired electronic applications (e.g., for piezotronic devices[10, 11] or in transparent conductive thin films coatings [12, 13]). Hence enhancing its conductivity has always been an issue which has been achieved by adopting several strategies, for example, doping, alloying, or hybridization of ZnO micro- or nanostructures with other inorganic and carbon materials [10, 12–16]. These methods are always accompanied by an increase in the amount of defects in the metal oxide semiconductor [17–19] and the large doping amounts could easily disturb the crystalline stoichiometry of ZnO. In this respect, a detailed research on the change in the material's structure is quite important for the understanding the phenomenon of increased conductivity in doped ZnO structures. Some studies have reported about the visible change in ZnO lattice due to doping by HRTEM- or electron diffraction studies [20–22]. But a detailed study about nano-analysis of the ZnO-dopant interface in hybridized ZnO materials is rather hard to find to the best of our literature knowledge.

Furthermore, most of the ZnO synthesis methods require a complicated procedure, having a very slow growth rate [2,17,23]. Here, we utilize a quite simple method for a rapid synthesis of 1D ZnO micro- and nanowires and their large microstructural family including 3D interconnected networks. Starting with a flame transport approach introduced by Mishra *et al.* [4,24,25], the synthesis was further modified until a rapid, non-toxic approach was elaborated. As a result of this synthesis, the surface of ZnO contains an abundant number of oxygen vacancies that promotes the interactions with ions in the coating solution. Important morphological characterizations including Raman and scanning electron microscopy are utilized to investigate the produced ZnO 1D structures and the effects of hybridization via Ga_xO_y nano structures.

II. MATERIALS AND METHODS

A. Synthesis of ZnO micro- and nanowires

For the synthesis a Zn wire (purity 99.9% purchased at *Alpha Aesar*, diameter of ~ 3 mm) was placed in a metal

NAP-2017, 2017 IEEE 7th International Conference on Nanomaterials: Applications and Properties (NAP)

crucible and rapidly heated in a simple muffle furnace to 950 °C. After the temperature was reached an oxygen flow was established and a rapid growth of ZnO crystals took place. The duration of the synthesis process was varied from 15 to 30 minutes. A controlled growth of 1D ZnO micro- and nanostructures was achieved via placing several ceramic platelets at the top of the crucible to limit the oxygen flow.

B. Post-synthesis hybridization of ZnO micro- and nanowires

For the hybridization of the nanowires, a solution of Ga acetylacetonate ($Ga(acac)_3$) in chloroform of 0.3 mg/ml was prepared and the as grown ZnO wires were directly immersed into the solution under stirring and UV illumination for 12 hours, followed by simple drying in air. The post annealing was carried out under air or argon (Ar) atmosphere at 600 °C for 1 h.

C. Electrical characterizations of 1D nanowires

Current-voltage (I-V) characteristics were measured with a Keithley source meter (model 2400) utilizing a two-wire sensing method (due to the relatively high resistance of the material). The individual ZnO 1D wire was contacted with a conductive silver paste and dried on a hot plate at 150 °C. The heating leads to a fast evaporation of the solvents in the conductive paste and thus, to a better adhesion between single Ag platelets by that increasing the contact properties to ZnO [26].

D. Scanning electron microscopy (SEM), Raman and Transmission electron microscopy (TEM)

Structural characterization of the samples was done by using a SEM Zeiss Ultra Plus (acceleration voltage 10-20 kV), TEM Tecnai F30 STwin, and a Raman alpha 300 RA (with a triple grating spectrometer and a CCD detector) and WITec instruments software for the spectra analysis.

III. Results

A. Electrical characterization

In Fig.1. the measured IV curves for three investigated sample types (i.e. pristine ZnO microwires and ZnO microwires functionalized and annealead in air or argon for one hour at 600 °C) are presented (the inset figure corresponds to I-V for pure ZnO wires).

The silver paste contacts resulted in a Schottky contact on one side and an ohmic contact on the other side of the 1D ZnO microwire (recognisable from the shape of the I-V curve, a bahaviour know from [1]).

For all the I-V curves, a slope was measured in the region [-3,-2] V in order to compare the electrical resistivities (ρ) of 1D microstructures in this work. The specific resistivity for the pristine ZnO microwires is in the range of 7-1 MΩ·cm, for the nanowires coated and annealed in air ρ=190-120 kΩ·cm and the for the coated and annealed in argon atmosphere ρ=73-11 kΩ·cm, respectively.

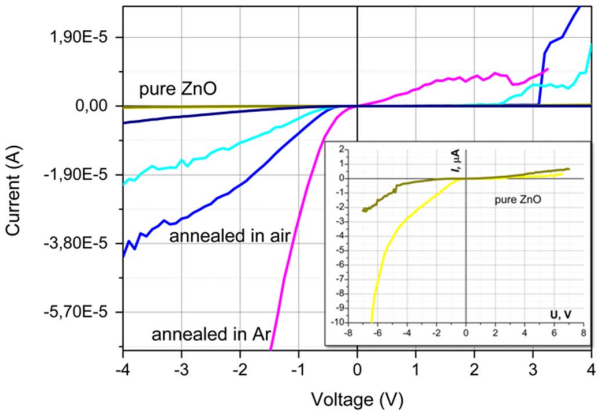

Fig. 1. I-V curves of flame synthesized 1D ZnO nano-microwires based devices: as synthesized *(yellow and brown)*, functionalized and annealed in air *(cyan and blue)* and annealed in argon *(pink)*. Only few curves are shown per sample type for the sake of simplicity. The inset figure shows simple I-V curves for pristine ZnO nano- and microwires.

This corresponds to an improvement of a factor of ~ 20 in electrical conductivity for the wires coated and annealed in air and of a factor of ~ 200 for the samples coated and annealed in argon. In order to understand the changes and the impacts of annealing conditions on the electrical conductivity of the hybridized ZnO micro- and nanowires, a detailed structural analysis was performed.

B. Surface morphology of hybridized ZnO wires

The surface of ZnO microwires before and after hybridization is shown in Fig.2. The macroscopic length of a single wire is in the range of few mm, allowing for a comfortable handling. The cross-section of a single wire is ranging from 15 μm to 80 μm.

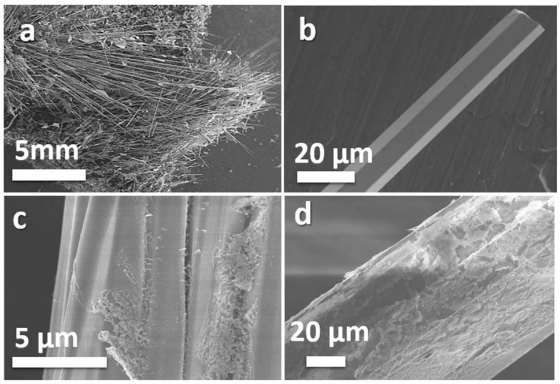

Fig. 2. SEM images of the as grown ZnO micro- and nanowires *(a)* and *(b)*, ZnO microwires annealed in at 600 °C for 1 hour in: air *(c)* and in argon atmosphere*(d)*.

The hexagonal facets of the micro- and nanowires, which are an evidence of the hexagonal ZnO lattice structure, are distinctly visible in the SEM images shown in Fig.2.d.

NAP-2017, 2017 IEEE 7th International Conference on Nanomaterials: Applications and Properties (NAP)

By comparing the surface of the microwires from the batch annealed in air and those from the batch annealed under inert conditions a higher nanoparticle coverage could be observed for the latter case. Examples of such surfaces are presented in Fig. 2c and d.

C. Raman studies

Raman scattering spectra corresponding to all the specimen types are presented in Fig. 3. For the pristine and hybridized ZnO wires, Raman peaks at 99, 203, 330, 380, 438 and 1150 cm^{-1} were recorded and peak positions corresponds to pure ZnO [27,28]. Under the influence of hybridization a shift in the E_2(high) peak position to higher frequencies (from 438 cm^{-1} to 441 cm^{-1}) could be observed.

Furthermore, the pristine ZnO peak at 203 cm^{-1} gets less distinguishable, as a peak at 213 cm^{-1} (that is related to the β-Ga_2O_3 phase [29]) becomes more dominant. The peaks in the region between 530-650 cm^{-1} that represent A1(LO) and TA+LO modes in ZnO are more pronounced (the region is indicated with a green dotted frame for the upper two spectra, Fig.3).

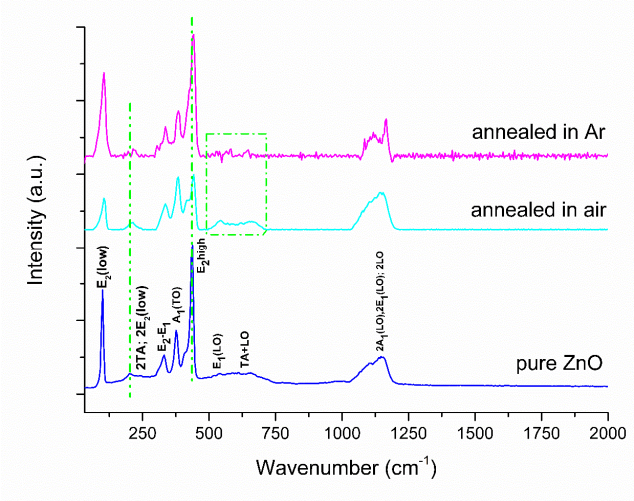

Fig. 3. Raman measurements of ZnO 1D structures as synthesized *(blue)*, functionalized and annealed in air *(cyan)* and annealed in argon *(pink)*. Green dotted lines indicate the peaks were shifts are observed. Green dotted window marks the region of (TA+LO) modes that are more pronounced for the hybridized samples.

D. Transmission electron microscopy analysis

Single ZnO microwires annealed under inert Ar gas atmosphere were characterized with localized STEM EDX measurements with respect to the amount of Ga. From the STEM image in Fig.4 no Ga_2O_3 networks could be observed which are clearly visible if present for both annealing procedures, see Fig.5 for comparision. The quantified EDX data is listed in Tab.1 for the K-peaks of Zn, O and Ga. The reduced oxygen signal stems most possibly from absorption phenomena of low energy X-rays at the vicinity of large crystals close to the region of interest. The intensity of the Ga K-peaks shown in Fig.4 is above background and gives results around 1 at% which seems to be a reasonable doping concentration in comparision with [30,31]. However, due to the large diameter of the microwire, we can not exclude contributions from residual Ga_2O_3 phases on the rear side of the structure.

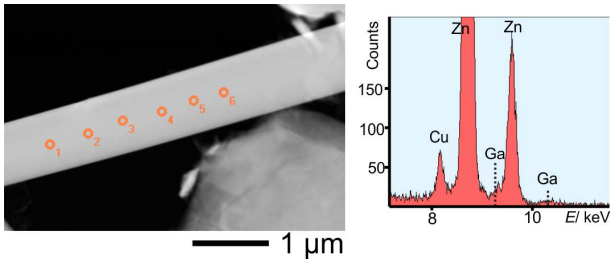

Fig. 4. Single position STEM EDX measurement on a microwire previously annealed in argon atmosphere for 1hour at 600 °C. O_x mark the positions where the EDX spectra (see rigth: extract of spectrum #6) were taken.

TABLE I. EDX DATA

Position number	*Detected Elements (at%)*		
	Zn	***O***	***Ga***
1	69,16	30,32	0,5
2	68,76	30,44	0,79
3	67,43	31,55	1,01
4	73,34	25,85	0,79
5	69,54	29,42	1,03
6	72,4	26,76	0,82

A chemical map of samples annealed under normal atmosphere conditions is presented in Fig.5. In comparison to Fig.4 a distinct modification of the ZnO surface in form of a shell layer is apparent. The STEM EDX data for the Ga signal is evaluated to be below 1.5 at% and shows larger content at the bright green area which can be attributed to a pure Ga_2O_3 network on the hybridized ZnO/Ga_2O_3 surface shell.

The hybridized shell surface found for both annealing cases was further examined by high-resolution TEM given in Fig.6. In relation to the low-defect ZnO micro and nanostructures obtained by the FTS the hybridized and annealed ZnO surface shows a high defect density as indicated by the arrows in Fig.6a. Planar defects such as stacking faults, inversion domain boundaries and superlattices were also reported for similar metal(oxide)-doped ZnO crystals [32–35] and indicate the strong influence of the hybridization by a GaO_x phase on the nanostructure. With respect to gallium oxide phases present, crystals of the monoclinic β-Ga_2O_3 and oxygen deficient spinel γ-Ga_2O_3 (Ga_6O_{11}) phase could be observed as polyrystalline networks on top of the shell regions or as nanoinclusions. A nanoinclusion of the γ-Ga_2O_3 phase in the defect-rich ZnO structure is shown in Fig. 6b and fast fourier transformation (FFT) images.

IV. Discussion

The observed enhanced value of electrical conductivity (in case of annealing in inert atmosphere) is accompanied by a pronounced coverage of the ZnO microwire surface with Ga_2O_3 networks. The improved conductivity might be attributed to two different mechanisms.

NAP-2017, 2017 IEEE 7th International Conference on Nanomaterials: Applications and Properties (NAP)

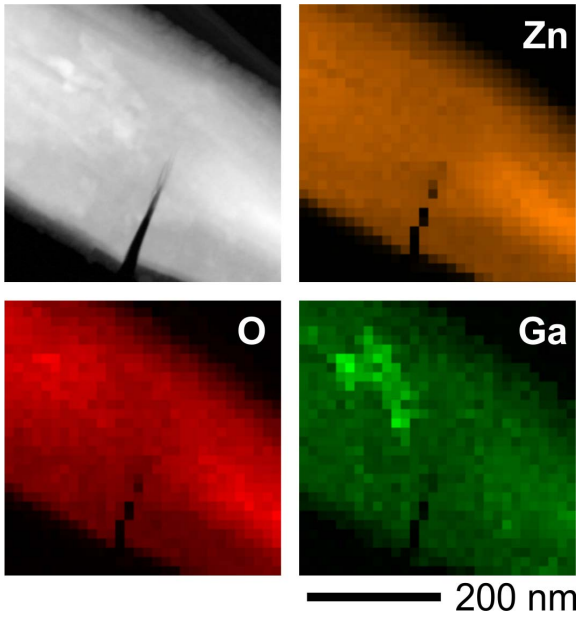

Fig. 5. STEM image and EDX maps for ZnO microstructures annealed at 600 °C for 1 hour in air.

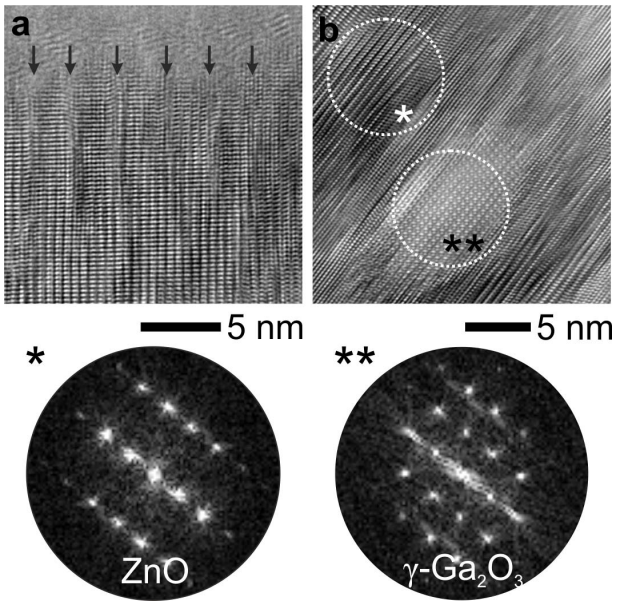

Fig. 6. HRTEM micrographs of the hybridized ZnO microwire surface. (a) A high density of planar defects and (b) nanoinclusions of γ-Ga_2O_3 phase are observed.

First, it may be explained by Ga_2O_3 nanonetworks being formed in a more oxygen deficient atmosphere during annealing, resulting in a β-phase of Ga_2O_3 containing more oxygen vacancies that has been reported to be more conductive [18,19,36].

Second, raman analysis performed on the pristine and functionalized ZnO microwires revealed several indications of the structural changes occurring after the hybridization. The shift in the spectral position observed for the E_2(high) peak can be attributed to the tensile strain in the ZnO lattice structure [27]. Moreover, more pronounced character of the A1(LO) and TA+LO peaks at 530-650 cm^{-1} is mainly caused by an increase in the oxygen vacancies in ZnO, meaning the Ga_2O_3 causes an oxygen deplition in ZnO. Alternatively, this, on the other hand, is often interpreted as incorporation of Ga atoms into the ZnO lattice [31,37,38].

V. CONCLUSION

In summary, a successful hybridization of ZnO surface with gallium oxide nanonetworks was successfully achieved by using a simple flame based synthesis technique. The structural intactness of the hybrid samples were confirmed via TEM, STEM and EDX. Likewise, the increased conductivity of single 1D ZnO nano- and microwires is a strong indication for the changes occurred on the ZnO surface. Raman shifts and occurrence of new peaks related to Ga_2O_3 phase lead to a conclusion that there is some lattice distortion (confirmed by HRTEM as well) and an interaction between ZnO and Ga_2O_3 phases. The simple interpretation that the addition of Ga-atoms to the synthesis leads to a Ga doping might be wrong without the detailed microanalysis. In our case, the interpretation of defects induced in the ZnO causing further n-doping appears more likely.

ACKNOWLEDGMENT

Authors from Kiel University acknowledge the support from German Research Foundation (DFG) under the scheme SFB 1261, TP {(A05, RA) & (A06, LK)}.

REFERENCES

[1] Z.L. Wang, “Piezopotential gated nanowire devices: Piezotronics and piezo-phototronics,” Nano Today, vol. 5, pp. 540–552, 2010.

[2] B.-C. Lin, C.-S. Ku, H.-Y. Lee, and A.T. Wu, “Epitaxial growth of ZnO nanorod arrays via a self-assembled microspheres lithography,” Appl. Surface Sci., vol. 414, pp. 212–217, 2017.

[3] J. Liu, S. Li, B. Zhang, Y. Xiao, Y. Gao, Q. Yang, Y. Wang, and G. Lu, “Ultrasensitive and low detection limit of nitrogen dioxide gas sensor based on flower-like ZnO hierarchical nanostructure modified by reduced graphene oxide,” Sensor. Actuat. B: Chem., vol. 249, pp. 715–724, 2017.

[4] Y.K. Mishra, S. Kaps, A. Schuchardt, I. Paulowicz, X. Jin, D. Gedamu, S. Wille, O. Lupan, and R. Adelung, “Versatile Fabrication of Complex Shaped Metal Oxide Nano-Microstructures and Their Interconnected Networks for Multifunctional Applications,” KONA, vol. 31, pp. 92–110, 2014.

[5] S. Ben Dkhil, M. Gaceur, A.K. Diallo, Y. Didane, X. Liu, M. Fahlman, O. Margeat, J. Ackermann, and C. Videlot-Ackermann, “Reduction of Charge-Carrier Recombination at ZnO-Polymer Blend Interfaces in PTB7-Based Bulk Heterojunction Solar Cells Using Regular Device Structure: Impact of ZnO Nanoparticle Size and Surfactant,” ACS Appl. Mater. Interface., vol. 9, pp. 17256–17264, 2017.

[6] Y.K. Mishra, G. Modi, V. Cretu, V. Postica, O. Lupan, T. Reimer, I. Paulowicz, V. Hrkac, W. Benecke, L. Kienle, and R. Adelung, “Direct Growth of Freestanding ZnO Tetrapod Networks for Multifunctional Applications in Photocatalysis, UV Photodetection, and Gas Sensing,” ACS Appl. Mater. Interface., vol 7, pp. 14303–14316, 2015.

[7] R. Meija, S. Signetti, A. Schuchardt, K. Meurisch, D. Smazna, M. Mecklenburg, K. Schulte, D. Erts, O. Lupan, B. Fiedler, Y.K. Mishra, R. Adelung, and N.M. Pugno, “Nanomechanics of individual aerographite tetrapods,” Nat. Commun., vol. 8, pp. 14982, 2017.

[8] I. Hölken, G. Neubüser, V. Postica, L. Bumke, O. Lupan, M. Baum, Y.K. Mishra, L. Kienle, and R. Adelung, "Sacrificial Template Synthesis and Properties of 3D Hollow-Silicon Nano- and Microstructures," ACS Appl. Mater. Interface., vol. 8, pp. 20491–20498, 2016.

[9] S. Chandrasekaran, W.V. Liebig, M. Mecklenburg, B. Fiedler, D. Smazna, R. Adelung, and K. Schulte, "Fracture, failure and compression behaviour of a 3D interconnected carbon aerogel (Aerographite) epoxy composite," Compos. Sci. Technol., vol. 122, pp. 50–58, 2016.

[10] C.-L. Hsu, I.-L. Su, and T.-J. Hsueh, "Tunable Schottky contact humidity sensor based on S-doped ZnO nanowires on flexible PET substrate with piezotronic effect," J. Alloy. Compd., vol. 705, pp. 722–733, 2017.

[11] S. Liu, L. Wang, X. Feng, Z. Wang, Q. Xu, S. Bai, Y. Qin, and Z.L. Wang, "Ultrasensitive 2D ZnO Piezotronic Transistor Array for High Resolution Tactile Imaging," Adv. Mater. (Deerfield Beach, Fla.), vol. 29, 2017.

[12] K. Cheng, J. Liu, R. Jin, J. Liu, X. Liu, Z. Lu, Y. Liu, X. Liu, and Z. Du, "Surface microstructure evolution of highly transparent and conductive Al-doped ZnO thin films and its application in CIGS solar cells," Appl. Surface Sci. vol. 409, pp. 124–131, 2017.

[13] L. Gong, Y. Liu, L. Jiang, and F. Liu, "Study on the adhesive mechanism between the Ga doped ZnO thin film and the polycarbonate substrate," Mater. Sci. Semiconductor Proc., vol. 66, pp. 105–108, 2017.

[14] J. Gröttrup, V. Postica, D. Smazna, M. Hoppe, V. Kaidas, Y.K. Mishra, O. Lupan, and R. Adelung, "UV detection properties of hybrid ZnO tetrapod 3-D networks," Vacuum, 2017.

[15] O. Lupan, V. Postica, J. Gröttrup, A.K. Mishra, N.H. de Leeuw, J.F.C. Carreira, J. Rodrigues, N. Ben Sedrine, M.R. Correia, T. Monteiro, V. Cretu, I. Tiginyanu, D. Smazna, Y.K. Mishra, and R. Adelung, "Hybridization of Zinc Oxide Tetrapods for Selective Gas Sensing Applications," ACS Appl. Mater. Interfaces, vol. 9, pp. 4084–4099, 2017.

[16] L. He, S. Mei, Q. Chen, W. Zhang, J. Zhang, J. Zhu, G. Chen, and R. Guo, "Two-step synthesis of highly emissive C/ZnO hybridized quantum dots with a broad visible photoluminescence," Appl. Surface Sci., vol. 364, pp. 710–717, 2016.

[17] B. Chouchene, T.B. Chaabane, K. Mozet, E. Girot, S. Corbel, L. Balan, G. Medjahdi, and R. Schneider, "Porous Al-doped ZnO rods with selective adsorption properties," Appl. Surface Sci., vol. 409, pp. 102–110, 2017.

[18] W. Mu, Z. Jia, Y. Yin, Q. Hu, Y. Li, B. Wu, J. Zhang, and X. Tao, "High quality crystal growth and anisotropic physical characterization of Ga 2 O 3 single crystals grown by EFG method," J. Alloy. Compd., vol 714, pp. 453–458, 2017.

[19] S. Müller, H. von Wenckstern, D. Splith, F. Schmidt, and M. Grundmann, "Control of the conductivity of Si-doped β-Ga 2 O 3 thin films via growth temperature and pressure," Phys. Status Solidi A, vol. 211, pp. 34–39, 2014.

[20] C.S. Spanjers, R.S. Sim, N.P. Sturgis, B. Kabius, and R.M. Rioux, "In Situ Spectroscopic Characterization of Ni 1– x Zn x /ZnO Catalysts and Their Selectivity for Acetylene Semihydrogenation in Excess Ethylene," ACS Catal., vol. 5, pp. 3304–3315, 2015.

[21] L. Umaralikhan, and M.J.M. Jaffar, "Green synthesis of ZnO and Mg doped ZnO nanoparticles, and its optical properties," J. Mater. Sci.: Mater. Electron., vol. 28, pp. 7677–7685, 2017.

[22] Y. Zhang, C. Liu, J. Liu, J. Xiong, J. Liu, K. Zhang, Y. Liu, M. Peng, A. Yu, A. Zhang, Y. Zhang, Z. Wang, J. Zhai, and Z.L. Wang, "Lattice Strain Induced Remarkable Enhancement in Piezoelectric Performance of ZnO-Based Flexible Nanogenerators," ACS Appl. Mater. Interfaces, vol. 8, pp. 1381–1387, 2016.

[23] Y.N. Rane, D.A. Shende, M.G. Raghuwanshi, A.V. Ghule, V.L. Patil, P.S. Patil, S.R. Gosavi, and N.G. Deshpande, "Synthesis of flower shaped ZnO thin films for resistive sensing of NO2 gas," Microchim Acta, vol. 184, pp. 2455–2463, 2017.

[24] Y.K. Mishra, S. Kaps, A. Schuchardt, I. Paulowicz, X. Jin, D. Gedamu, S. Freitag, M. Claus, S. Wille, A. Kovalev, S.N. Gorb, and R. Adelung, "Fabrication of Macroscopically Flexible and Highly Porous 3D Semiconductor Networks from Interpenetrating Nanostructures by a Simple Flame Transport Approach," Part. Part. Syst. Charact., vol. 30, pp. 775–783, 2013.

[25] S. Kaps, S. Bhowmick, J. Grttrup, V. Hrkac, D. Stauffer, H. Guo, O.L. Warren, J. Adam, L. Kienle, A.M. Minor, R. Adelung, and Y.K. Mishra, "Piezoresistive Response of Quasi-One-Dimensional ZnO Nanowires Using an in Situ Electromechanical Device," ACS Omega, vol. 2, pp. 2985–2993, 2017.

[26] J.H. Kim, H.-S. Chung, K.H. Oh, T.-S. Bae, and W.-K. Hong, "Influence of the contact interface on the electrical characteristics of a ZnO microwire with silver paste electrodes," J. Alloy. Compd., vol. 681, pp. 75–80, 2016.

[27] M. Šćepanović, M. Grujić-Brojčin, K. Vojisavljević, S. Bernik, and T. Srećković, "Raman study of structural disorder in ZnO nanopowders," J. Raman Spectrosc., vol. 41, pp. 914–921, 2010.

[28] A. Souissi, C. Sartel, G. Amiri, A. Meftah, A. Lusson, P. Galtier, V. Sallet, and M. Oueslati, "Raman study of activated quasi-modes due to misorientation of ZnO nanowires," Solid State Commun., vol. 152, pp. 1729–1733, 2012.

[29] Y. Zhao, J. Yang, and R.L. Frost, "Raman spectroscopy of the transition of gallium oxyhydroxide to gallium oxide nanorods," J. Raman Spectrosc., vol. 39, pp. 1327–1331, 2008.

[30] S.K. Pandey, S.K. Pandey, S. Verma, M. Gupta, V. Sathe, and S. Mukherjee, "Investigation of dual ion beam sputtered transparent conductive Ga-doped ZnO films," J. Mater. Sci: Mater. Electron., vol. 24, pp. 4919–4924, 2013.

[31] R. Jothi Ramalingam, and G.S. Chung, "Polymer assisted Ga doped ZnO nanodisk/nanorod structures prepared by a low temperature one-pot hydrothermal method," Mater. Lett., vol. 68, pp. 247–250, 2012.

[32] J.H. Lim, S.M. Lee, H.-S. Kim, H.Y. Kim, J. Park, S.-B. Jung, G.C. Park, J. Kim, and J. Joo, "Synergistic effect of Indium and Gallium co-doping on growth behavior and physical properties of hydrothermally grown ZnO nanorods," Sci. Rep., vol. 7, pp. 41992, 2017.

[33] H. Takemoto, K. Fugane, P. Yan, J. Drennan, M. Saito, T. Mori, and H. Yamamura, "Reduction of thermal conductivity in dually doped ZnO by design of three-dimensional stacking faults," RSC Adv., vol. 4, pp. 2661–2672, 2014.

[34] H.-B. Wang, F. Ma, Q.-Q. Li, C.-Z. Dong, D.-Y. Ma, H.-T. Wang, and K.-W. Xu, "Synthesis and stress relaxation of ZnO/Al-doped ZnO core-shell nanowires," Nanoscale, vol. 5, pp. 2857–2863, 2013.

[35] Q. Yang, L. Lou, and G. Wang, "Optical properties of indium doped ZnO planar superlattice nanoribbons," Physica E, vol. 89, pp. 124–129, 2017.

[36] Y. Huang, S. Yue, Z. Wang, Q. Wang, C. Shi, Z. Xu, X.D. Bai, C. Tang, and C. Gu, "Preparation and electrical properties of ultrafine Ga2O3 nanowires," J. Phys. Chem. B, vol. 110, pp. 796–800, 2006.

[37] H. Mahdhi, S. Alaya, J.L. Gauffier, K. Djessas, and Z. Ben Ayadi, "Influence of thickness on the structural, optical and electrical properties of Ga-doped ZnO thin films deposited by sputtering magnetron," J. Alloy. Compd., vol. 695, pp. 697–703, 2017.

[38] S.K. Pandey, S.K. Pandey, S. Verma, M. Gupta, V. Sathe, and S. Mukherjee, "Investigation of dual ion beam sputtered transparent conductive Ga-doped ZnO films," J. Mater. Sci.: Mater. Electron., vol. 24, pp. 4919–4924, 2013.

research papers

JOURNAL OF APPLIED CRYSTALLOGRAPHY

ISSN 1600-5767

Received 12 April 2019
Accepted 1 July 2019

Edited by G. Kostorz, ETH Zurich, Switzerland

Keywords: cross-section specimen preparation; high-resolution transmission electron microscopy; 3D defect reconstruction; anisotropic nanostructures.

Crystallography at the nanoscale: planar defects in ZnO nanospikes

Niklas Wolff,[a] Viktor Hrkac,[a] Jeffrey J. Ditto,[b] Viola Duppel,[c] Yogendra K. Mishra,[d] David C. Johnson,[b] Rainer Adelung[d] and Lorenz Kienle[a]*

[a]Synthesis and Real Structure and Institute for Material Science, Kiel University, Kaiserstrasse 2, Kiel 24143, Germany, [b]Department of Chemistry and Biochemistry and Materials Science Institute, University of Oregon, Eugene, OR 97403, USA, [c]Nanochemistry, Max Planck Institute for Solid State Research, Heisenbergstrasse 1, Stuttgart 70569, Germany, and [d]Functional Nanomaterials and Institute for Material Science, Kiel University, Kaiserstrasse 2, Kiel 24143, Germany. *Correspondence e-mail: lk@tf.uni-kiel.de

The examination of anisotropic nanostructures, such as wires, platelets or spikes, inside a transmission electron microscope is normally performed only in plan view. However, intrinsic defects such as growth twin interfaces could occasionally be concealed from direct observation for geometric reasons, leading to superposition. This article presents the shadow-focused ion-beam technique to prepare multiple electron-beam-transparent cross-section specimens of ZnO nanospikes, via a procedure which could be readily extended to other anisotropic structures. In contrast with plan-view data of the same nanospikes, here the viewing direction allows the examination of defects without superposition. By this method, the coexistence of two twin configurations inside the wurtzite-type structure is observed, namely $[2\bar{1}\bar{1}0]^{W}/(01\bar{1}1)$ and $[2\bar{1}\bar{1}0]^{W}/(01\bar{1}3)$, which were not identified during the plan-view observations owing to superposition of the domains. The defect arrangement could be the result of coalescence twinning of crystalline nuclei formed on the partially molten Zn substrate during the flame-transport synthesis. Three-dimensional defect models of the twin interface structures have been derived and are correlated with the plan-view investigations by simulation.

1. Introduction

Nanostructured zinc oxide (ZnO) semiconductors have attracted much research interest over recent decades owing to their diversity of chemical and physical properties (Özgür *et al.*, 2005; Meyer *et al.*, 2004; Pearton, 2005; Yang *et al.*, 2002; Djurišić & Leung, 2006; Li *et al.*, 2008). Due to the characteristic of a wurtzite-type structure (denoted by a superscript W; space group $P6_3mc$), *i.e.* the absence of inversion symmetry, the piezoelectric effect is present in ZnO. With a direct bandgap of 3.37 eV and an exciton binding energy of 60 meV at room temperature, ZnO nanostructures are promoted for applications in the fields of electronic materials (Jebril *et al.*, 2010; Gupta, 1990), opto-electronics (Keis *et al.*, 2002; Könenkamp *et al.*, 2000), sensor devices (Liu *et al.*, 2016; Chai *et al.*, 2012; Lupan *et al.*, 2008) and field emitters (Wang *et al.*, 2005; Li *et al.*, 2004), among other sensor systems based on piezotronics (Wang, 2007). Many of these reports relied on anisotropic ZnO nanostructures, *e.g.* nanospikes, which can be synthesized by manifold approaches (Singh, 2010), one of which is by flame transport (Mishra *et al.*, 2013).

A fundamental understanding of functional nanomaterials requires in-depth analysis procedures to determine morphology, defects (Kienle & Simon, 2002), interfaces (Wen *et al.*, 2013), doping (Lu *et al.*, 2015), band structure (Shi *et al.*,

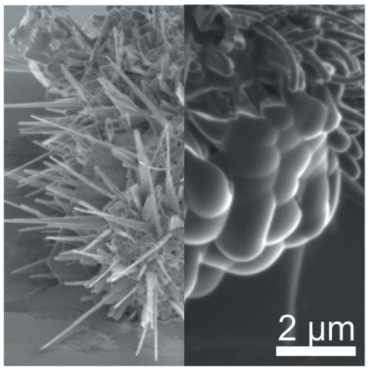

2012) and local deformation behaviour, as all of these aspects contribute to and affect the final device properties. In this pursuit, transmission electron microscopy (TEM) offers a variety of techniques from structure determination up to nanoscale chemical analysis. Optimized sample preparation is perhaps the most critical and challenging prerequisite for these TEM techniques, and the sample preparation must be tailored to the specific task and scientific issue (Jia *et al.*, 2011). Site-specific sectioning along selective crystal orientations is critical for structure–property investigations of anisotropic nanostructures including buried defects (Hrkac *et al.*, 2013), and strain and chemical integrity at interfaces (Abes *et al.*, 2013; Hrkac *et al.*, 2013; Huang *et al.*, 2014). In preparing these sections, filler materials, such as epoxy resins (Müller & Krumeich, 2000; Lenrick *et al.*, 2014), platinum (Giannuzzi & Stevie, 1999), carbon (Leer *et al.*, 2009; Baram & Kaplan, 2008) or aluminium oxide (Stiegler *et al.*, 2012), are often used as stabilizing matrix materials or protective coatings against ion bombardment.

Electron-transparent slices of matrices containing nanostructures are typically prepared by ion-beam etching techniques such as precision ion polishing and focused ion-beam (FIB) milling or by ultramicrotomy (Huang *et al.*, 2014; Chen *et al.*, 2004). Limiting possible modifications to the sample during the preparation procedure is critical for quality high-resolution (HR)TEM investigations. This is particularly true when dealing with very sensitive nanostructures such as wires or hollow tubes. Possible sources of damage include shrinking of epoxy resins during the solidification and curing process (Cairney & Munroe, 2001), and the introduction of residual stresses and knock-on damage (Egerton *et al.*, 2010; Bowden & Brandon, 1963) during the deposition of protective coatings or ion bombardment. Even diamond-knife ultramicrotomy can lead to mechanically damaged cross sections and increase the likelihood of coating delamination (Lipomi *et al.*, 2010). In the case of targeting special orientations, FIB preparation offers unique and diverse approaches to keep sample modifications to a minimum. Examples include a 'direct lift-out' procedure (Li *et al.*, 2006, 2003), and milling under small grazing angles and lower energies during the final milling steps.

Particularly when working with very fragile nanostructures, a new approach, the shadow-FIB method introduced by Welz *et al.* (2005), enables nearly artefact-free TEM specimen preparation by using the substrate as protection during heavy-ion milling. Thus, the shadow-FIB method circumvents the deposition of metal protective layers and keeps modifications and contaminations to a low level. The shadow-FIB procedure has enabled site- and orientation-specific sectioning of fragile specimens such as layered crystals (Spiecker *et al.*, 2006), organic films (Kim *et al.*, 2009; Mor *et al.*, 2014) and in particular anisotropic nanostructures (Tessarek *et al.*, 2013; Vieweg *et al.*, 2012).

Here we have prepared ZnO nanospike cross sections using the geometric shadow-FIB technique. The ZnO nanospikes were embedded in an amorphous carbon matrix by electron-beam-induced decomposition of an organic precursor. Several regions of the lamella were thinned to expose different nanospikes for HRTEM investigations. This enabled the direct observation and identification of two types of twin boundary in the ZnO nanospikes which were not observed during plan-view examination.

2. Experimental

Synthesis of ZnO nanospikes was conducted following the flame-transport approach (Mishra *et al.*, 2013), in which Zn microparticles with typical diameters of 10 µm are mixed homogenously into a slurry of polyvinyl butyral (PVB) powder and ethanol. A typical weight ratio for Zn:PVB:ethanol is 1:2:6, which can be varied depending upon the requirements for morphology and specific applications. Further steps involve coating of Si substrates via a slip-casting technique and subsequent heating inside a simple muffle-type box furnace to 873 K for 1 h with a ramp rate of 100 K min^{-1}. The PVB–ethanol mixture thereby acts as a sacrificial spacing layer between the particles which decomposes completely at elevated temperatures.

HRTEM was carried out on an FEI Tecnai F30 G^2 STwin microscope (FEG, 300 kV, spherical aberration C_S = 1.2 mm) and low-resolution scanning transmission electron microscopy (STEM) imaging on a TITAN 80-300 (image corrector). Precession electron diffraction (PED) was conducted on a Philips CM 30 ST microscope (LaB_6, 300 kV) equipped with a spinning star device (NanoMEGAS). HRTEM micrographs were obtained by tilting the individual specimens into the $[2\overline{1}\overline{1}0]^W$ zone-axis orientation, which allowed for visualizing planar defects without superposition.

For the simulation of HRTEM micrographs and fast Fourier transforms (FFTs) the software *eMAP* (Version 1.0) by AnaliTEX (Oleynikov, 2011), the *JEMS* program package (Stadelmann, 1987) and the *Diamond* software (Version 3.2) for crystal and molecular structure visualization (Pennington, 1999) to assist with crystallographic computing were applied. Data evaluation was conducted with the Gatan Microscopy Suite *DigitalMicrograph* (Version 2.32) software.

An FEI Helios 600 dual-beam scanning electron microscope with focused ion beam and Omniprobe micromanipulators for *in situ* sample manipulation was used for TEM sample preparation. The gas injection system was equipped with precursors for platinum and carbon deposition.

3. Results and discussion

3.1. Specimen preparation

After synthesis with the flame-transport approach, ZnO nanospikes were found to grow out of the Zn spheres (see the scanning electron images in Fig. 1), forming an interconnected network of particle–spike structures. Their morphology, in particular their length, can be adjusted from the nano- to the micrometre range by controlling the temperature and heating time (Mishra *et al.*, 2013). The nanospikes show tapered and plate-like morphologies with dimensions of 2–10 µm in length

and *ca* 200 nm laterally. Individual nanospikes feature multiple tips, which indicate the coalescence of crystalline precipitates during growth.

For TEM sample preparation from freestanding ZnO nanospikes, the geometric shadow-FIB technique enabled the preparation of several cross-section specimens in one FIB lamella. The individual preparation steps are displayed in Fig. 2. Experimental problems with charging effects and the support material were circumvented by embedding the ZnO nanospikes in amorphous carbon by decomposing a naphthalene precursor with the electron beam [Fig. 2(*a*)]. To achieve conformal coating during the deposition process, a high voltage of 10 kV was applied to produce secondary electrons on all surfaces of the spikes evenly. Note that at this high voltage (the optimum is ∼2 kV) the deposition rate is much lower, so this step took about 45 min. After cutting trenches to either side [Fig. 2(*b*)] and lifting the lamella out, the sample was mounted on a needle followed by an *ex situ* 180° flip and attachment to the TEM grid, as demonstrated in Fig. 2(*c*). The top Si substrate now served as the protection layer during ion milling, since direct milling of the carbon matrix would lead to immediate destruction of the specimen. To ensure mechanical stability of the final lamella [Fig. 2(*d*)], the silicon and the edges on either side were left relatively thick.

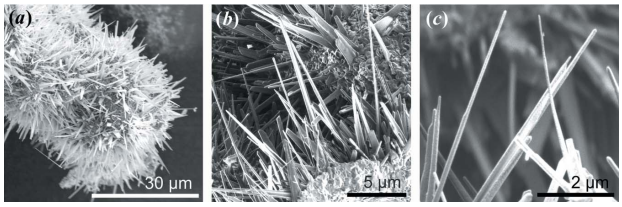

Figure 1
(*a*) ZnO nanospikes grown from Zn spheres via the flame-transport synthesis approach. (*b*), (*c*) The nanospikes feature a plate-like shape and show coalescence, forming spikes with multiple tips during the growth process.

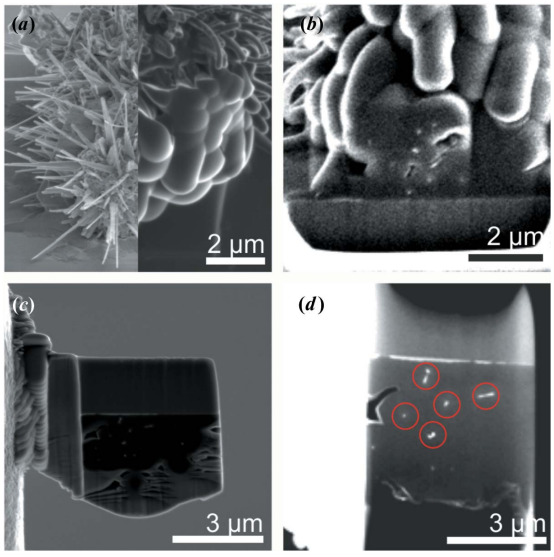

Figure 2
The preparation steps of ZnO nanospike cross-sections using the geometric shadow-FIB technique. (*a*) (Left) As-grown ZnO nanospikes from a Zn spherical particle. (Right) Amorphous carbon was deposited via electron-beam-induced decomposition to embed the spikes in a matrix material. (*b*) The first step of FIB trench milling and the lift-out process. (*c*) The rotated (180°) specimen was milled with a Ga ion beam using the silicon substrate as protection against severe damage to the carbon matrix. (*d*) An ion-milled lamella with electron-beam-transparent cross-section specimens (red circles).

3.2. Real-structure analysis

A representative HRTEM micrograph of a ZnO nanospike tip with characteristic superposition fringe contrast is shown in Fig. 3. Previous TEM studies of ZnO nanospikes (Hrkac *et al.*, 2013; Huang *et al.*, 2009) with tapered growth morphology revealed a similar contrast phenomenon in high-resolution imaging, which was rationalized as the 2D superposition of individual 3D domains in a systematically twinned microstructure. The fringe contrast can be correlated with the superposition of two twinned domains by the PED pattern depicting the superposition of two mirrored $[2\bar{1}\bar{1}3]$ oriented patterns. The inspection of several cross-section specimens in the same lamella allowed for a detailed structural characterization using HRTEM and subsequent defect modelling.

The embedded cross sections of ZnO nanospikes were analysed by HRTEM by tilting the specimens into the nearest zone axis $[2\bar{1}\bar{1}0]^{W}$, being the direction of the electron beam orthogonal on the specimen with respect to all cross sections observed. The recorded micrographs are presented in Fig. 4 and confirm the multiple twinned morphology. Two types of twin boundary are classified via the formalism [zone-axis orientation]/(twin plane) and identified by inspection of the FFTs given in Fig. 4: $[2\bar{1}\bar{1}0]^{W}/(01\bar{1}1)$ and $[2\bar{1}\bar{1}0]^{W}/(1\bar{1}3)$. Therefore, the growth direction of these ZnO nanospikes is rationalized to be along $2\bar{1}\bar{1}0$ as well. For crystals with hexagonal symmetry having the wurtzite-type structure, unidirectional crystal growth along the {0001} planes is promoted under a broad range of process conditions, as this growth direction minimizes the electrostatic energy between Zn^{2+} and

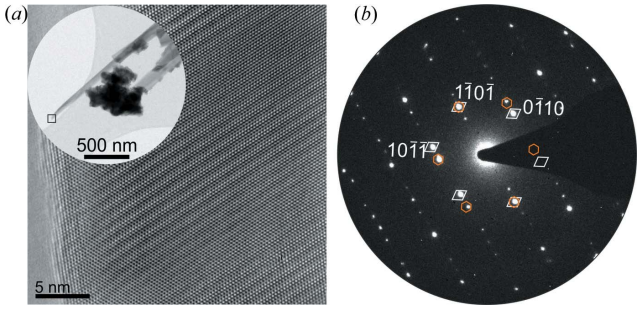

Figure 3
(*a*) HRTEM micrograph of a ZnO nanospike tip, showing the characteristic superposition fringe contrast as a feature of twinning. (Inset) A TEM image of the ZnO nanospike. (*b*) A precession electron diffraction pattern showing the superposition of two mirrored single-crystal patterns in $[2\bar{1}\bar{1}3]$ orientation. The reflections of the individual twin components are indicated by the diamond and hexagon markers.

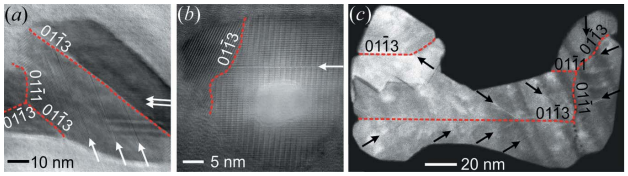

Figure 4
(*a*), (*b*) HRTEM and (*c*) low-resolution STEM micrographs of ZnO nanospike cross sections along their growth direction, which is $[2\bar{1}\bar{1}0]^{W}$. The spikes contain a high density of twinned domains (red dashed lines represent twin boundaries) and basal-plane stacking-mismatch defects (arrows). Often, twin boundaries of type $(01\bar{1}3)$ split the crystal into larger domains.

O^{2-} terminated surfaces. However, the introduction of planar defects parallel to the polar surfaces can decrease the surface energy and stabilize different crystal morphologies, as has already been described for nanobelts (Ding *et al.*, 2004) and whiskers (Huang *et al.*, 2008, 2009). Owing to the observed multiple twin defects, this explanation might also be applicable to the nanospikes investigated herein. A growth model for ZnO nanospikes from a partially molten Zn source including such mosaic and multiple twinning has been proposed by Huang *et al.* (2009). They described the initial twinning of condensate seeds and further coalescence and intergrowth of individual spikes, resulting in a mosaic twinned structure with a tapered shape. Very similar growth conditions are believed to apply during the flame-transport process.

A large population of basal-plane stacking faults is observed in the specimen cross sections, as indicated by arrows in Fig. 4. Note that the observation of this defect type is exclusively enabled by the cross-section view. Twinning on the $(01\bar{1}3)$ planes was observed more frequently than on the $(01\bar{1}1)$ planes and often appeared to divide the nanospikes into smaller domains. In addition, shorter boundaries were observed featuring both types of twin. This is in agreement with theoretical energy calculations for twin defects in wurtzite structures (Béré & Serra, 2003), which predict the population of the $(01\bar{1}3)$ twin to be dominant over $(01\bar{1}1)$.

During the HRTEM investigation, severe beam-damage effects under observation with an unmodified electron dose led to dissipation of the carbon matrix and subsequent release of the specimen into the microscope. Further, the very thin specimens suffered rapid material loss due to electron knock-on damage, as demonstrated by the large void in the centre of the cross section depicted in Fig. 4(*b*). Therefore, working with a reduced electron dose is highly recommended for cross sections embedded in a carbon matrix.

3.3. Structure modelling

Models based on a supercell approach were designed for both twin boundary structures, $[2\bar{1}\bar{1}0]^{W}/(01\bar{1}3)$ and $[2\bar{1}\bar{1}0]^{W}/(01\bar{1}1)$, on the basis of previous studies (Hrkac *et al.*, 2013; Paulowicz *et al.*, 2015).

The supercell approach involved the following three steps, which are displayed in Fig. 5.

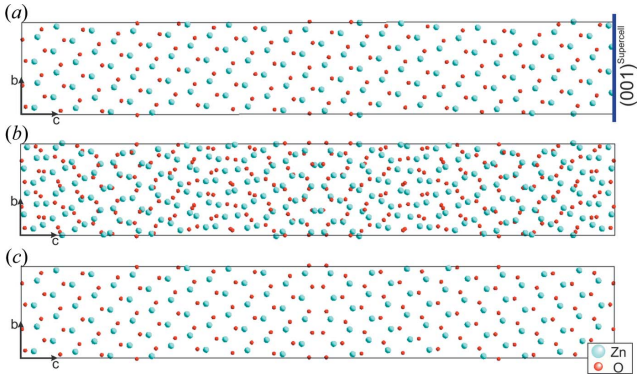

Figure 5
The construction of a supercell following the individual steps (i)–(iii) described in the text. (*a*) The triclinic supercell including the defect plane as one of its rectangular faces. (*b*) A superposition structure is created by mirroring the *P*1 cell at its defect plane. (*c*) The separation model containing the defect structure in the centre.

(i) The initial wurtzite-type (superscript W; hexagonal cell, $P6_3mc$) was transformed into an orthohexagonal cell. Following the conventions described by Arnold (Hahn, 2002, pp. 78–89), the unit-cell transformation of the ideal structure into a triclinic (*P*1) structure is given mathematically by

$$(\mathbf{a}', \mathbf{b}', \mathbf{c}') = (\mathbf{a}, \mathbf{b}, \mathbf{c})\mathbf{P},$$
$$\begin{pmatrix} u' \\ v' \\ w' \end{pmatrix} = \mathbf{Q}\begin{pmatrix} u \\ v \\ w \end{pmatrix},$$
$$\mathbf{Q} = \mathbf{P}^{-1},$$

with $(\mathbf{a}, \mathbf{b}, \mathbf{c})$ as the base vectors of direct space and (u, v, w) as the indices of a direction in direct space; primes ($'$) mark the parameters for the *P*1 cell. $\mathbf{P}$ and $\mathbf{Q}$ are (3×3) square matrices, linear parts of an affine transformation.

A suitable supercell for the respective defect structure is obtained by applying the transformation matrices $\mathbf{P}_1$ and $\mathbf{Q}_1$ [for the twin $(01\bar{1}1)$],

$$\mathbf{P}_1 = \begin{pmatrix} 1 & 0 & 0 \\ 0 & 3 & -2 \\ 0 & 4 & 7 \end{pmatrix}, \qquad \mathbf{Q}_1 = \begin{pmatrix} 1 & 0 & 0 \\ 0 & 7/29 & 2/29 \\ 0 & -4/29 & 3/29 \end{pmatrix},$$

and the transformation matrices $\mathbf{P}_2$ and $\mathbf{Q}_2$ [for the twin $(01\bar{1}3)$],

$$\mathbf{P}_2 = \begin{pmatrix} 1 & 0 & 0 \\ 0 & 1 & -2 \\ 0 & 12 & 7 \end{pmatrix}, \qquad \mathbf{Q}_2 = \begin{pmatrix} 1 & 0 & 0 \\ 0 & 7/31 & 2/31 \\ 0 & -12/31 & 1/31 \end{pmatrix},$$

The lattice parameters for the respective supercells are $a_1 = 3.249$, $b_1 = 11.835$, $c_1 = 76.740$, $a_2 = 3.249$, $b_2 = 19.836$ and $c_2 = 42.831$ Å. All angles were set to 90° as the deviation from exact rectangularity is <0.1% and the resulting errors in the atom positions are marginal. The resulting supercells are rectangular and possess triclinic *P*1 symmetry.

(ii) A superposition structure (SPS) was created by adding the atomic coordinates from an unmodified supercell from

step (i) to its mirrored version. The appropriate mirroring of the supercell was accomplished by the inversion of the c parameter, corresponding to a mirror plane at $(0\,0\,1)^{\text{Supercell}}$. Note this procedure is analogous for both supercells.

(iii) A separation model is obtained by the deliberate reduction of the atoms in the respective SPS. In this manner unit cells are generated containing two single domains separated by a twin plane. To generate a good agreement between the experimental and simulated data, the separation models were adjusted in an iterative approach by shifting the atomic parameters to achieve matching contrast between simulated and experimental images.

3.4. Simulation

The superposition structures [step (ii)] of each twin model were used for the simulation of electron diffraction (ED) patterns rendered possible by the translational invariance of the reciprocal lattice. The simulated ED pattern and FFT images calculated from experimental HRTEM micrographs of the two twin boundaries are compared qualitatively in Fig. 6. Both the FFT images and the simulated ED pattern from the structure models match on a qualitative basis, indicating the quality of the superposition structure. However, owing to the impact of the contrast transfer function on HRTEM micrographs, an exact match between the FFT and the pure kinematic simulation is not possible.

To approximate the atomic interface structures, the separation models were used for HRTEM simulations. The atomic positions at the interface of the separation models were adjusted iteratively to optimize the simulation pattern in agreement with the experiment. The results of this process are presented in Fig. 7, showing the HRTEM micrographs together with the simulations and interface structure models. The simulation parameters for the $(01\bar{1}1)$ twin are defocus value $\Delta f = -24$ nm and thickness $t = 3.9$ nm. The simulation parameters for the $(01\bar{1}3)$ twin are $\Delta f = -58$ nm and $t = 2.6$ nm. In the case of the $(01\bar{1}1)$ twin boundary, the model best fitting the experiment contains a single plane of oxygen atoms formed by the direct coalescence of two $(01\bar{1}1)$ planes. This atomic configuration results in a conformation of ZnO_4 tetrahedra that are connected by common edges and surfaces at the boundary. For such a configuration the electrostatic repulsion energies are expected to be quite large. For the $(01\bar{1}3)$ twin boundary, an atomic configuration with slightly distorted tetrahedra connected via common corners yielded excellent agreement with the experimental high-resolution contrast.

After verification with the experimental data, the designed structure models were compared with energy-minimizing computer calculations based on the work by Béré & Serra (2003). For the twin defects presented here they calculated the energetically most favourable atomic boundary structures for GaN in its wurtzite-type structure using an empirical interatomic potential of the Stillinger–Weber type and the quench–molecular dynamic method. The formation energies for different atomic boundary structures have been discussed for both types of twin boundary. According to this work, a related atomic boundary structure for the $(01\bar{1}1)$ twin was calculated, exhibiting a single plane of atoms formed by the head-to-head coalescence of two $(01\bar{1}1)$ planes. This head-to-head junction possesses the highest calculated formation energy of

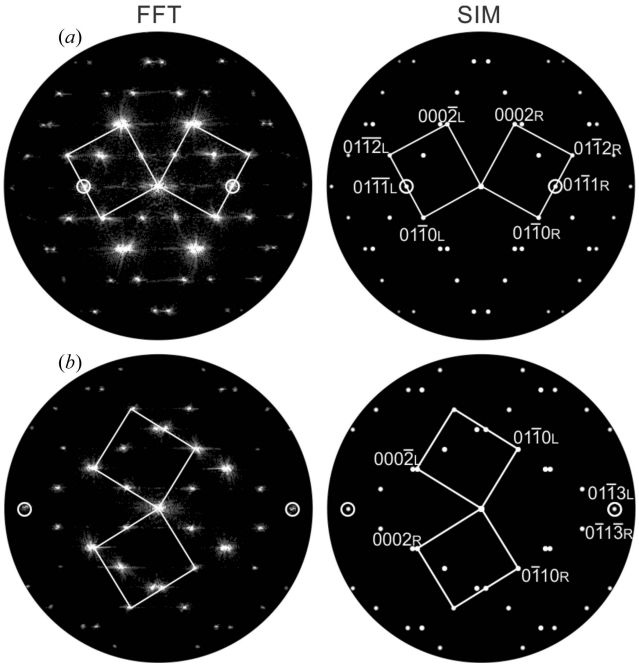

Figure 6
Qualitative comparisons of (left) experimental FFT images recorded at two twin boundaries and (right) simulations based on kinematic scattering using the superposition structure models. (*a*) $(01\bar{1}1)$ and (*b*) $(01\bar{1}3)$. The indices L and R denote reflections from the left and right twin component, respectively.

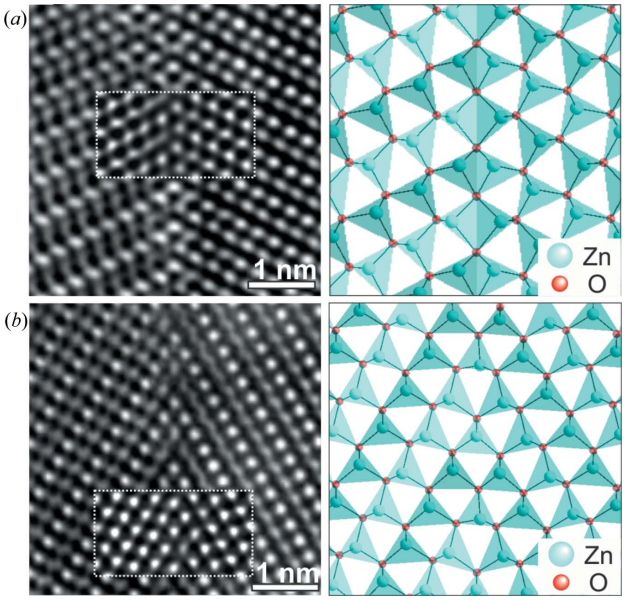

Figure 7
(Left) HRTEM images of the twin interfaces and (right) simulations of the inset panels for (*a*) the $(01\bar{1}1)$ boundary and (*b*) the $(01\bar{1}3)$ boundary using appropriate models from the supercell approach.

$\sim$3.5 J m^{-2} in GaN, which is about 0.8 J m^{-2} larger than for boundary structures with a corrugated or head-to-tail interface. Furthermore, first-principles density-functional total-energy calculations by Yan *et al.* (2005) showed, in principle, that the same twin boundary structures are formed in ZnO as in wurtzite group III nitrides but with $\sim$1/3 of the GaN twin boundary energy. Hence, the above considerations can be expected to hold qualitatively true in ZnO and can explain the small number of these head-to-head $(01\bar{1}1)$ type of junctions in the nanospikes compared with the corrugated conformations observed. For some of the most common and energy-reduced twin junctions in ZnO nanowires, Shan *et al.* (2009) calculated the boundary energies to be 0.67 J m^{-2} for the head-to-tail $(01\bar{1}1)$ twin and 0.53 J m^{-2} for the head-to-head $(01\bar{1}3)$ twin boundary. These numbers validate the larger population of $(01\bar{1}3)$ boundaries observed in the nanospikes, also acting as a structural feature in the growth process. Relaxed structure models of the latter congruent with the model presented here are reported in the literature (Ding & Wang, 2009; Shan *et al.*, 2009). Hence, we conclude that our models provide reasonable approximations for twin boundary structures of the described type in ZnO nanospikes.

This direct observation and identification of two types of twin boundary in ZnO nanospikes presented herein provides complementary information to previous plan-view studies by Hrkac *et al.* (2013). Those authors presented an in-depth discussion of the origin of HRTEM superposition contrasts, as well as identification of twin planes $\{\bar{1}101\}$ observed in the $[2\bar{1}\bar{1}3]^{W}$ viewing direction using suitable supercell models. Since similar samples containing nanospikes grown from Zn particles were investigated in our studies, it is not surprising that the same twin planes were observed. The congruent

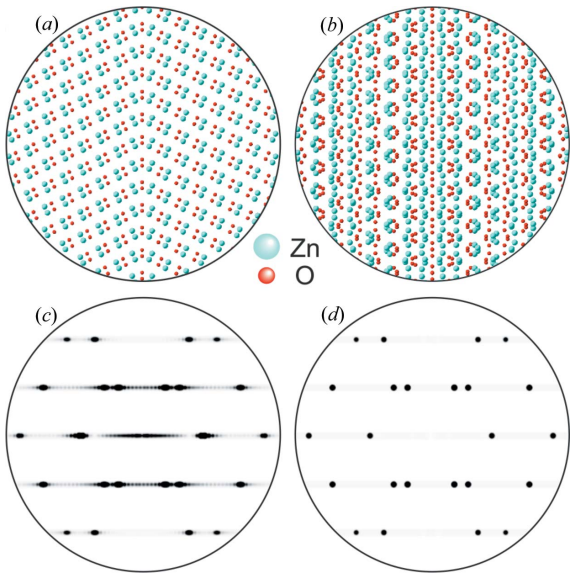

Figure 8
(*a*) The new model for the atomic $[2\bar{1}\bar{1}0]^{W}/(01\bar{1}1)$ twin interface was tilted into a viewing direction congruent with $[2\bar{1}\bar{1}3]^{W}$. (*b*) A superposition structure was constructed by introducing mirror symmetry. (*c*), (*d*) Simulated electron diffraction data for the $[2\bar{1}\bar{1}3]^{W}$ zone axis using an SPS with (*c*) and without (*d*) the twin, see text.

results are demonstrated by tilting the $[2\bar{1}\bar{1}0]^{W}/(01\bar{1}1)$ structure model into a direction equal to $[2\bar{1}\bar{1}3]^{W}$ as shown in Fig. 8. In addition, an SPS is generated by introducing mirror symmetry. The tilted *P*1 model and the superposition structure are presented in Figs. 8(*a*) and 8(*b*), respectively. The simulated diffraction pattern of this SPS (space group *P*1*m*) and the SPS constructed by Hrkac *et al.* are depicted in Figs. 8(*c*) and 8(*d*) for comparison. Both simulated ED patterns depict qualitatively the same arrangement of spot pattern. The evident superstructure reflections [looking like diffuse streaks in Fig. 8(*c*)] arise because of the implementation of the single planar twin defect in the model which introduces additional lattice periodicity.

4. Conclusions

In this work, the cross-sectional investigation of twin defects in ZnO nanospikes complements previous plan-view studies and more generally opens up the fundamental characterization of complex and highly anisotropic nanostructures containing structural defects. The preparation of multiple cross-section specimens of nanospikes attached to a substrate particle to achieve electron transparency was established using the shadow-FIB geometry. Intrinsic and multiple twinning was observed to be a main structural feature and is assumed to reduce the surface energy during the growth process along an energetically more unfavourable $[2\bar{1}\bar{1}0]^{W}$ direction. Two types of twin boundary could be identified and simulated on the basis of structure models from a supercell approach. The phase-contrast simulations revealed the nature of the approximate twin boundary configurations and a direct link to plan-view investigations could be demonstrated.

In conclusion, the combination of both plan-view and cross-section analysis allows for an unambiguous determination of structural defects which are not directly accessible with a simple plan-view experiment. This combined 3D crystallographic examination approach proved to be extremely valuable and could be extended to a variety of anisotropic nanostructures.

Acknowledgements

The authors thank Professor Dr Bettina Lotsch for enabling additional TEM investigation. JJD and DCJ acknowledge the use of equipment in the Center for Advanced Materials Characterization in Oregon (CAMCOR) at the University of Oregon.

Funding information

The following funding is acknowledged: Deutsche Forschungsgemeinschaft (grant No. CRC1261 P06); National Science Foundation (grant No. DMR-1710214).

References

Abes, M., Koops, C. T., Hrkac, S. B., Greve, H., Quandt, E., Collins, S. P., Murphy, B. M. & Magnussen, O. M. (2013). *Appl. Phys. Lett.* **102**, 011601.

Baram, M. & Kaplan, W. (2008). *J. Microsc.* **232**, 395–405.
Béré, A. & Serra, A. (2003). *Phys. Rev. B*, **68**, 033305.
Bowden, P. & Brandon, D. G. (1963). *J. Nucl. Mater.* **9**, 348–354.
Cairney, J. M. & Munroe, P. R. (2001). *Mater. Charact.* **46**, 297–304.
Chai, G. Y., Lupan, O., Rusu, E. V., Stratan, G. I., Ursaki, V. V., Şontea, V., Khallaf, H. & Chow, L. (2012). *Sens. Actuators A Phys.* **176**, 64–71.
Chen, H., Gao, Y., Yu, H., Zhang, H., Liu, L., Shi, Y., Tian, H., Xie, S. & Li, J. (2004). *Micron*, **35**, 469–474.
Ding, Y., Kong, X. Y. & Wang, Z. L. (2004). *Phys. Rev. B*, **70**, 235408.
Ding, Y. & Wang, Z. L. (2009). *Micron*, **40**, 335–342.
Djurišić, A. B. & Leung, Y. H. (2006). *Small*, **2**, 944–961.
Egerton, R. F., McLeod, R., Wang, F. & Malac, M. (2010). *Ultramicroscopy*, **110**, 991–997.
Giannuzzi, L. A. & Stevie, F. A. (1999). *Micron*, **30**, 197–204.
Gupta, T. K. (1990). *J. Am. Ceram. Soc.* **73**, 1817–1840.
Hahn, Th. (2002). Editor. *International Tables for Crystallography*, Vol. A, *Space-Group Symmetry*, 5th ed. Dordrecht: Kluwer Academic Publishers.
Hrkac, V., Kienle, L., Kaps, S., Lotnyk, A., Mishra, Y. K., Schürmann, U., Duppel, V., Lotsch, B. V. & Adelung, R. (2013). *J. Appl. Cryst.* **46**, 396–403.
Huang, B.-H., Chen, S.-Y. & Shen, P. (2008). *J. Phys. Chem. C*, **112**, 1064–1071.
Huang, B.-H., Shen, P. & Chen, S.-Y. (2009). *Nanoscale Res. Lett.* **4**, 503–512.
Huang, X., Willinger, M.-G., Fan, H., Xie, Z., Wang, L., Klein-Hoffmann, A., Girgsdies, F., Lee, C.-S. & Meng, X.-M. (2014). *Nanoscale*, **6**, 8787–8795.
Jebril, S., Kuhlmann, H., Müller, S., Ronning, C., Kienle, L., Duppel, V., Mishra, Y. K. & Adelung, R. (2010). *Cryst. Growth Des.* **10**, 2842–2846.
Jia, C.-L., Urban, K. W., Alexe, M., Hesse, D. & Vrejoiu, I. (2011). *Science*, **331**, 1420–1423.
Keis, K., Bauer, C., Boschloo, G., Hagfeldt, A., Westermark, K., Rensmo, H. & Siegbahn, H. (2002). *J. Photochem. Photobiol. Chem.* **148**, 57–64.
Kienle, L. & Simon, A. (2002). *J. Solid State Chem.* **167**, 214–225.
Kim, S., Liu, G. & Minor, A. M. (2009). *Microsc. Today*, **17**, 20–23.
Könenkamp, R., Boedecker, K., Lux-Steiner, M. C., Poschenrieder, M., Zenia, F., Levy-Clement, C. & Wagner, S. (2000). *Appl. Phys. Lett.* **77**, 2575–2577.
Leer, B. V., Giannuzzi, L. & Wang, Y.-C. (2009). *Microsc. Microanal.* **15**, 336–337.
Lenrick, F., Ek, M., Jacobsson, D., Borgström, M. T. & Wallenberg, L. R. (2014). *Microsc. Microanal.* **20**, 133–140.
Li, J., Gertsman, V. Y. & Lo, J. (2003). *Microsc. Microanal.* **9**, 888–889.
Li, J., Malis, T. & Dionne, S. (2006). *Mater. Charact.* **57**, 64–70.
Li, Q., Mahendra, S., Lyon, D. Y., Brunet, L., Liga, M. V., Li, D. & Alvarez, P. J. J. (2008). *Water Res.* **42**, 4591–4602.
Li, Y. B., Bando, Y. & Golberg, D. (2004). *Appl. Phys. Lett.* **84**, 3603–3605.
Lipomi, D. J., Martinez, R. V., Rioux, R. M., Cademartiri, L., Reus, W. F. & Whitesides, G. M. (2010). *ACS Appl. Mater. Interfaces*, **2**, 2503–2514.
Liu, J., Huang, H., Zhao, H., Yan, X., Wu, S., Li, Y., Wu, M., Chen, L., Yang, X. & Su, B.-L. (2016). *ACS Appl. Mater. Interfaces*, **8**, 8583–8590.
Lu, S., Qi, J., Gu, Y., Liu, S., Xu, Q., Wang, Z., Liang, Q. & Zhang, Y. (2015). *Nanoscale*, **7**, 4461–4467.
Lupan, O., Shishiyanu, S., Chow, L. & Shishiyanu, T. (2008). *Thin Solid Films*, **516**, 3338–3345.
Meyer, B. K., Alves, H., Hofmann, D. M., Kriegseis, W., Forster, D., Bertram, F., Christen, J., Hoffmann, A., Straßburg, M., Dworzak, M., Haboeck, U. & Rodina, A. V. (2004). *Phys. Status Solidi B*, **241**, 231–260.
Mishra, Y. K., Kaps, S., Schuchardt, A., Paulowicz, I., Jin, X., Gedamu, D., Freitag, S., Claus, M., Wille, S., Kovalev, A., Gorb, S. N. & Adelung, R. (2013). *Part. Part. Syst. Charact.* **30**, 775–783.
Mor, G. K., Le, T. P., Vakhshouri, K., Kozub, D. R. & Gomez, E. D. (2014). *ACS Appl. Mater. Interfaces*, **6**, 19638–19643.
Müller, E. & Krumeich, F. (2000). *Ultramicroscopy*, **84**, 143–147.
Oleynikov, P. (2011). *Cryst. Res. Technol.* **46**, 569–579.
Özgür, Ü., Alivov, Y. I., Liu, C., Teke, A., Reshchikov, M. A., Doğan, S., Avrutin, V., Cho, S.-J. & Morkoç, H. (2005). *J. Appl. Phys.* **98**, 041301.
Paulowicz, I., Hrkac, V., Kaps, S., Cretu, V., Lupan, O., Braniste, T., Duppel, V., Tiginyanu, I., Kienle, L., Adelung, R. & Mishra, Y. K. (2015). *Adv. Electron. Mater.* **1**, 1500081.
Pearton, S. J. (2005). *Prog. Mater. Sci.* **50**, 293–340.
Pennington, W. T. (1999). *J. Appl. Cryst.* **32**, 1028–1029.
Shan, X., Zhang, X., Gao, J., You, L., Xu, H., Xu, J., Yu, D. & Ye, H. (2009). *J. Phys. Chem. C*, **113**, 18014–18019.
Shi, J., Starr, M. B. & Wang, X. (2012). *Adv. Mater.* **24**, 4683–4691.
Singh, D. P. (2010). *Sci. Adv. Mater.* **2**, 245–272.
Spiecker, E., Schmid, A. K., Minor, A. M., Dahmen, U., Hollensteiner, S. & Jäger, W. (2006). *Phys. Rev. Lett.* **96**, 086401.
Stadelmann, P. A. (1987). *Ultramicroscopy*, **21**, 131–145.
Stiegler, J. M., Tena-Zaera, R., Idigoras, O., Chuvilin, A. & Hillenbrand, R. (2012). *Nat. Commun.* **3**, 1131.
Tessarek, C., Bashouti, M., Heilmann, M., Dieker, C., Knoke, I., Spiecker, E. & Christiansen, S. (2013). *J. Appl. Phys.* **114**, 144304.
Vieweg, B. F., Butz, B., Peukert, W., Klupp Taylor, R. N. & Spiecker, E. (2012). *Ultramicroscopy*, **113**, 165–170.
Wang, R. C., Liu, C. P., Huang, J. L., Chen, S.-J., Tseng, Y.-K. & Kung, S.-C. (2005). *Appl. Phys. Lett.* **87**, 013110.
Wang, Z. L. (2007). *Adv. Mater.* **19**, 889–892.
Welz, S., Browning, N. & Minor, A. M. (2005). *Microsc. Microanal.* **11**, 834–835.
Wen, X., Wu, W., Ding, Y. & Wang, Z. L. (2013). *Adv. Mater.* **25**, 3371–3379.
Yan, Y., Al-Jassim, M. M., Chisholm, M. F., Boatner, L. A., Pennycook, S. J. & Oxley, M. (2005). *Phys. Rev. B*, **71**, 041309.
Yang, P., Yan, H., Mao, S., Russo, R., Johnson, J., Saykally, R., Morris, N., Pham, J., He, R. & Choi, H.-J. (2002). *Adv. Funct. Mater.* **12**, 323–331.

4.1.4 Advanced Morphologies of GaN

High-quality GaN thin films became technological available for the first time with controlling epitaxy on sapphire substrates by Nakamura in 1991.[107] Since then, the III-V wurtzite-structure semiconductor GaN (bandgap of 3.44 eV) displays high relevance for nowadays and future technological application in optoelectronics[199], power electronics and high frequency applications[200], [201] as well as piezotronics and related fields.[202], [203] However, since almost all GaN thin films are grown on substrates, the properties of the heteroepitaxy strongly influence the GaN film quality, such as surface roughness, threading dislocations, impurities, polarity and strain. [204] The perfect substrate for GaN is of course GaN itself which eliminates the difficulties associated with poor heteroepitaxy. In this respect, homoepitaxial films deposited onto GaN wafers with high crystal and optical quality could exhibit superior properties than the substrate itself offering significant progress in the development of several optoelectronic and high-power devices.[205], [206] There are several technological methods available for the production of bulk GaN freestanding single crystalline substrates, one of them is hydride vapor phase epitaxy (HVPE).[207] The HVPE growth method relies on high growth rates up to 100 µm/h of GaN films onto a substrate crystal and its easy removal by lattice mismatch strains accumulating with increasing film thickness. However, the different thermal expansion behaviours of substrate and GaN film induces a bowing of the final GaN crystal and large-scale surface morphologies or intrinsic conductivity modulations may be present, related to overgrown defects.[208]

In this respect, we investigated the **modulation of electrical conductivity and lattice distortions in bulk HVPE-grown GaN** single crystalline wafers.[209] The combination of TEM and XRD methods evidenced that inelastic strain manifests in distortions between the c-axis and the basal plane of the wurtzite structure. In general, the investigation of intrinsic strains and structural distortions is highly relevant for fundamental research on piezotronic based ME sensors, since strain transfer between the magnetic material and the GaN crystal could be significantly impeded and a direct influence on the intrinsic electronic structure may result.[210], [211]

In comparison to ZnO based piezotronic devices, anisotropic nanostructures such as membranes,[212] single nanowires,[213] nanowire arrays[214] or nanobelts[215] of GaN are investigated for piezotronic logic-devices or nanogenerators. Recently, also the synthesis of novel hollow GaN tetrapod structures has been demonstrated by epitaxial templating of ZnO. [73] These and more **advanced hybrid GaN/ZnO nano-architectured microtubes**[6] have been studied in detail by TEM.[216] The method of STEM tomography was conducted in cooperation with Marius Kamp to compute a 3D model of the hierarchical nanoarchitecture. These hollow frameworks could potentially be employed for piezotronic strain or ME sensors.

[6] Reproduced from small 16, article 1905141 (2019)

ECS Journal of Solid State Science and Technology, **8** (8) Q141-Q146 (2019) Q141

Modulation of Electrical Conductivity and Lattice Distortions in Bulk HVPE-Grown GaN

Niklas Wolff,[1] Philipp Jordt,[2] Tudor Braniste,[3] Veaceslav Popa,[3] Eduard Monaico,[3] Veaceslav Ursaki,[3] Adrian Petraru,[4] Rainer Adelung,[5] Bridget M. Murphy,[2,6,z] Lorenz Kienle,[1,z] and Ion Tiginyanu[3,7,*,z]

[1]*Synthesis and Real Structure, Institute for Materials Science, Kiel University, 24143 Kiel, Germany*
[2]*Institute for Experimental and Applied Physics, Kiel University, 24118 Kiel, Germany*
[3]*National Center for Materials Study and Testing, Technical University of Moldova, MD-2004 Chisinau, Republic of Moldova*
[4]*Nanoelectronics, Institute for Materials Science, Kiel University, 24143 Kiel, Germany*
[5]*Functional Nanomaterials, Institute for Materials Science, Kiel University, 24143 Kiel, Germany*
[6]*Ruprecht-Haensel Laboratory, Kiel University, 24118 Kiel, Germany*
[7]*Academy of Sciences of Moldova, MD-2001 Chisinau, Republic of Moldova*

The nature of self-organized three-dimensional structured architectures with spatially modulated electrical conductivity emerging in the process of hydride vapor phase epitaxial growth of single crystalline n-GaN wafers is revealed by photoelectrochemical etching. The amplitude of the carrier concentration modulation throughout the sample is derived from photoluminescence analysis and the localized heterogeneous piezoelectric response is demonstrated. The formation of such architectures is rationalized based on the generation of V-shaped pits and their subsequent overgrowth in variable direction. Detailed structure analysis with respect to X-ray diffraction and transmission electron microscopy gives striking evidence for inelastic strain to manifest in distortions of the $P6_3mc$ wurtzite-type structure. The deviation from hexagonal symmetry by angular distortions of the β angle between the basal plane and c-axis is found to be of around 1°. It is concluded that the lattice distortions are generated by the misfit strains originating during crystal growth, which are slightly relaxed upon photoelectrochemical etching.
 [DOI: 10.1149/2.0041908jss]

Manuscript submitted May 21, 2019; revised manuscript received June 28, 2019. Published July 10, 2019.

Over the last 20 years GaN has become one of the most important semiconductor materials and may replace Si in many electronic applications. Particularly, it is already replacing Si in LDMOS radio-frequency devices used in base stations for mobile communication as well as GaAs for radar applications.[1–7] The highly advantageous properties of GaN-based semiconductors such as high electron mobility and saturation velocity, high sheet carrier concentration at heterojunction interfaces, high breakdown field, and low thermal impedance make them extremely promising for high-power high-temperature microwave applications, as evidenced by their high Johnson's figure of merit.[8–10] Exemplary, solid-state lighting optoelectronic devices assembled from white LEDs based on GaN are replacing conventional light sources such as incandescent bulbs and fluorescent lamps nowadays. This is due to their high efficiency, long operational lifetime, compact form factor, no emission of harmful ultraviolet (UV) or infrared radiation, and low maintenance cost. A recent review also highlights the prospects of GaN LEDs for visible light communications (VLC) in both fiber and free-space embodiments.[11] The state-of-the-art technology enabling bandwidth of GaN LEDs in the range of >400 MHz has been explored and multi-gigabit-per-second VLC has been demonstrated.

Better performance characteristics than those of Si power devices make also GaN power devices promising for automotive applications.[12] These electronic applications are based on using primarily silicon or silicon carbide substrates, since from a synthesis point of view thick GaN substrates are commercially unavailable. In spite of considerable progress in addressing the challenges related to significant mismatches between crystal lattices and thermal expansion coefficients, as well as silicon thermal stability when using Si substrates,[13] GaN-on-Si, GaN-on-SiC, and GaN-on-Sapphire remain costly solutions. In fact, GaN remains the most costly electronic material among the wide bandgap compounds (excluding single crystalline diamond).

For a long time, GaN has been grown by Metalorganic Chemical Vapor Deposition (MOCVD) on sapphire, Si, or SiC for research and device applications. However, challenges related to the growth of high-performance films remain, still hampering their utilization in devices.[14] Therefore, single crystalline GaN substrates are essential for future high-performance devices.

Nowadays, there are three main technologies used for GaN crystal growth: hydride vapor phase epitaxy (HVPE), sodium flux, and ammonothermal growth.[15] The last two approaches belong to the group of solution growth methods. High structural quality and high purity have been demonstrated by using the sodium flux growth method. However, it is supposed that this method is a perfect technology for fabricating seeds for further growth of gallium nitride but not for mass production of crystalline wafers, because this technological process is quite expensive and complicated.[15] On the other hand, the ammonothermal growth seems to be appropriate for mass production of GaN crystals, high structural quality substrates with 2-inch diameters and various electrical properties being successfully grown.[16] However, the main problem of this technology is the low growth rate of up to a few micrometers per hour. Apart from that, despite the high crystalline quality, the properties of ammonothermal GaN crystals and substrates are affected by the presence of impurities and other defects that hinder their use for device applications.[17] Therefore, the most appropriate approach for manufacturing GaN substrates is considered HVPE, due to the relatively high growth rate (>100 μm/h) and crystallization of high-purity material.[15] In spite of important advantages of this technology, however, achieving a good crystalline quality is still challenging, because of the formation of V-shaped defects or pits, which lead to the formation of extended inhomogeneous structures upon subsequent overgrowth (see for example Refs. 18,19). Self-organized 3D nanostructured architectures including quasi-ordered concentric hexagonal structures generated during the growth of single crystalline *n*-GaN substrates by HVPE have been revealed by subjecting the samples to electrochemical or photoelectrochemical (PEC) etching.[18] It was supposed that these architectures are produced due to a fine modulation of doping related to the spatial distribution of impurities in the volume of samples generated by some peculiarities of the HVPE growth.

In this paper, we demonstrate by means of transmission electron microscopy (TEM) that the self-organized nanostructured architectures disclosed by photoelectrochemical etching are not related to systematic variations of the crystal structure but by the modulation

*Electrochemical Society Member.
[z]E-mail: murphy@physik.uni-kiel.de; lk@tf.uni-kiel.de; ion.tighineanu@cnstm.utm.md

Q142 ECS Journal of Solid State Science and Technology, 8 (8) Q141-Q146 (2019)

of electrical parameters, e.g. by zero and one dimensional defects. Furthermore, we disclose a monoclinic or triclinic lattice distortion of the wurtzite structure by the combination of electron diffraction (ED) and X-ray diffraction (XRD) techniques. We estimate the amplitude of modulation of the free carrier concentration by making use of photoluminescence spectroscopy. The prospects of employing the fine modulation of electrical conductivity for the purpose of nanostructuring by design of GaN and related materials are also discussed. We suggest that the lattice distortion is kinetically induced and measure residual misfit strains of the crystal which relax upon photoelectrochemical etching.

Experimental

The experiments have been realized on 2-inch diameter HVPE-grown *n*-GaN single crystalline templates acquired from SAINT-GOBAIN Crystals. The 300 μm thick wurtzite-phase GaN substrates were of (0001)-orientation with virgin Ga-face and polished N-face. The density of threading dislocations in the substrates was in the range of (1–2) × 10^7 cm^{-2}. PEC etching was carried out in a stirred 0.1 mol. aqueous solution of KOH for periods up to 30 min under in-situ ultraviolet (UV) illumination provided by focusing the radiation of a 350 W Hg lamp to a spot of about 3.5 mm in diameter on the sample surface. No bias field was applied to the sample during etching, the electrical circuit being closed with a platinum electrode in the electrolyte and an electrical contact made on the back side of the sample using a conductive silver paste. The morphology of as-grown and PEC-etched GaN samples was studied using Zeiss Ultra Plus and VEGA TESCAN TS 5130MM scanning electron microscopes equipped with an INCA Energy 200 EDX System (Oxford Instruments) for chemical composition microanalysis, as well as using a NANOSTATION Atomic Force Microscope (AFM) from Surface Imaging Systems. The local piezoelectric response has been monitored by the piezoresponse force microscopy techniques (PFM) on a SmartSPM 1000 scanning probe microscope from AIST-NT. A sinusoidal modulation voltage of 10 V peak-to-peak at a resonance frequency of 247 kHz was applied between the conductive tip and the sample. The scan was performed in contact mode acquiring the topographic image simultaneously to the vertical piezoresponse amplitude and phase. The photoluminescence (PL) spectra were measured in a temperature interval from 10 to 300 K under excitation by radiation from a He-Cd laser with a wavelength of 325 nm operating in a continuous-wave (CW) mode.

The transmission electron microscopy investigation was carried out on a FEI Tecnai F30 STwin instrument operating at 300 kV (spherical aberration constant $C_S = 1.2$) to determine the structural features of as-grown HVPE single crystalline templates as well as PEC-etched GaN samples using electron diffraction and high-resolution transmission electron microscopy (HRTEM). Electron transparent cross-sectional specimens (~12 × 8 μm) were prepared via a dual beam scanning electron microscope FEI Helios Nanolab system performing a standard focused ion beam (FIB) technique. To account for the high surface roughness and to achieve a more homogenous covering of samples subjected to PEC etching we deposited a layer of carbon using the E-beam prior to the deposition of platinum protection layers to fill up the concentrically etched trenches. For the high-resolution X-ray diffraction (HRXRD) investigations, we used a Rigaku Micromax rotating anode with the characteristic Cu-K_α X-ray energy, at a wavelength of 1.54 Å. The beam size was 1 × 1 mm^2 ($h \times v$) with a resolution of 2 × 10^{-4} $Å^{-1}$.

Results and Discussion

SEM images demonstrate some quasi-periodical modulation of the physical properties of as-grown HVPE samples both on the top surface (Figure 1a, upper part) and in the bulk (a cross-sectional view is illustrated in the lower part of Figure 1a). We suggest that these features are related to the modulation of the electrical conductivity across the sample volume, as SEM is sensitive to electrical parameters of the material. A model describing the occurrence of such modulations during the HVPE crystal growth has been proposed previously.[18,19]

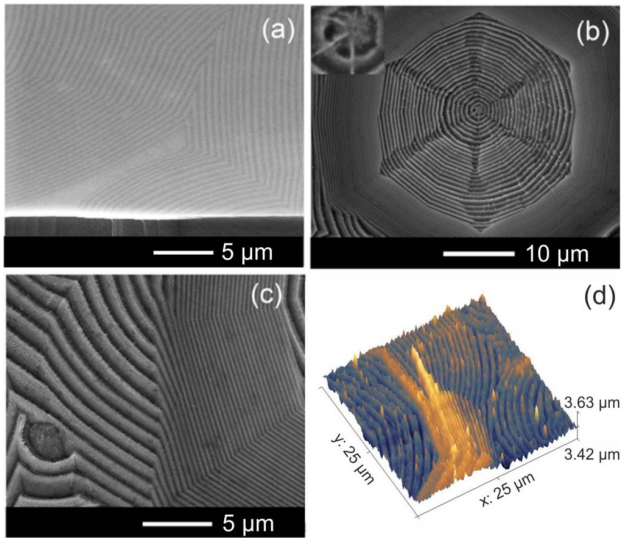

Figure 1. Oblique SEM view (a) of a cleaved as-grown HVPE GaN sample revealing an alternating bright-dark pattern. SEM (b,c) and AFM (d) images of nanostructured regions showing the micrometer deep etched trenches produced in a HVPE GaN sample subjected to PEC etching.

The morphology of a GaN sample subjected to PEC etching as revealed by SEM and AFM is illustrated in Figures 1b–1d which discloses concentric rings forming hexagonal patterned domains on the surface of the sample with the average density of approximately 10^4 cm^{-2}. In PEC etched samples, the pattern in SEM images arises due to differences in the rates of electrochemical dissolution of regions exhibiting different values of electrical conductivity, while in as-grown samples the light-dark pattern is caused by the modulation of the electrical conductivity. So, PEC etching proves to be a versatile tool for disclosing patterns of electrical parameters in inhomogeneous semiconductors. One can see from Figure 1b that the formation of nanostructured domains starts at certain points at early stages of the crystal growth, and these domains develop further according to the previously proposed model.[18] The insert in Figure 1b suggests that these nucleation points are genetically related to sites with a high density of dislocations, which are evidenced by PEC etching, since it is well established that the dislocations in GaN are resistant against PEC attack.[20–22] The morphology of regions where differently nanostructured domains intersect each other is illustrated in Figures 1c, 1d. The 3D spatial architecture of these porous domains can be described as hollow cones which are concentrically stacked into each other as exemplified in Figure S1 (Supplementary Information) by a SEM image taken from an electrochemically etched sample.

Note that there is a difference in the mechanisms of electrochemical and PEC etching of GaN. In an electrochemical process, the regions possessing higher electrical conductivity usually are characterized by a higher degree of porosity. In contrast to that, the etch rate during PEC etching decreases linearly with the logarithm of the carrier concentration, i.e. the regions with lower carrier concentration are etched faster than surrounding regions, which leads to the formation of concentric rings along the surface subjected to etching.[22] Further images of the photoelectrochemically etched GaN surface can be found in Figure S2, illustrating the clear modulation of electrical conductivity.

An interesting issue is the estimation of the amplitude of modulation of electrical parameters across the material as a result of peculiarities of the HVPE growth. Qualitative PFM measurements revealed a modulation of the local piezoresponse within hexagonal patterned domains and boundary regions in between, further named “islands”, a phenomenon which can be correlated with the presence of inversion

ECS Journal of Solid State Science and Technology, 8 (8) Q141-Q146 (2019) Q143

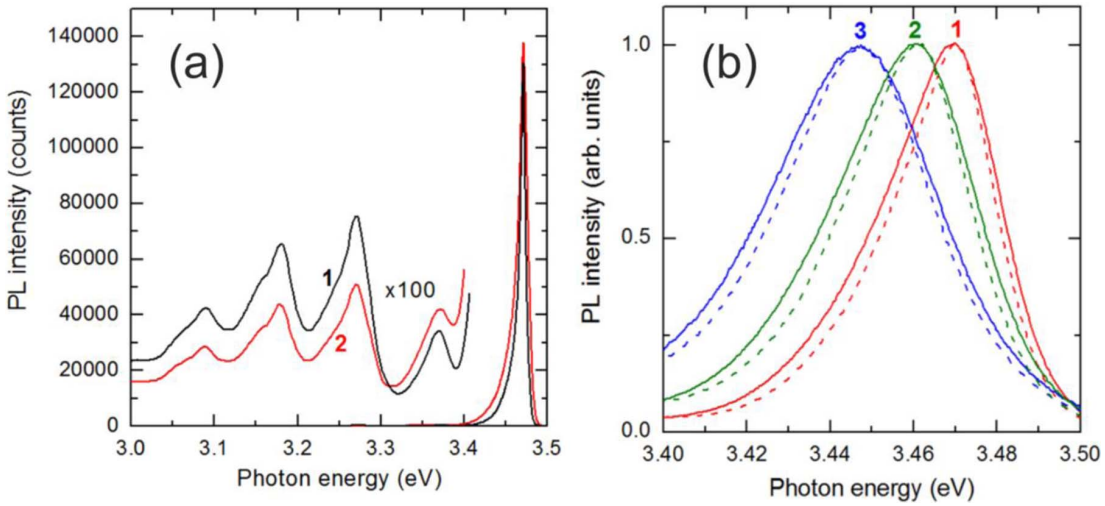

Figure 2. (a) PL spectrum of as-grown (curve 1) and PEC etched (curve 2) GaN samples measured at 10 K. (b) The NBG PL band measured at 75 K (curves 1), 100 K (curves 2), and 150 K (curves 3) in the as-grown (dashed line) and PEC etched (solid line) samples.

domains.[23] The results are presented and discussed in Figure S3. Further, in a previous study by means of Kelvin Probe Force Microscopy,[18] it was suggested that the fine modulation of doping is related to the spatial distribution of impurities. It is difficult, however, to estimate the amplitude of modulation by means of this methodology. In this paper, we make use of PL spectroscopy for the purpose of evaluating the amplitude of spatial modulation of the free carrier concentration in the specimen.

According to a semi-classical model regarding the broadening of impurity bands in heavily doped semiconductors developed by Morgan,[24] the carrier concentration can be estimated from the dependence of the photoluminescence full width at half maximum (FWHM) on the carrier concentration. This model has been previously applied to explain the broadening of near-band-gap (NBG) photoluminescence in *n*-GaN films.[25] It was shown that the model can be reliably applied to GaN samples with an electron concentration higher than 10^{18} cm^{-3}, and a calibration curve has been deduced for the relation between the FWHM of the NBG photoluminescence measured at 77 K and the electron concentration in the GaN material.

The PL spectra measured at 10 K for both the as-grown and the PEC etched samples (Figure 2a) are typical for GaN according to samples grown previously by using various techniques. Apart from the NBG PL band with the maximum at 3.471 eV, a series of PL bands with an intensity more than two orders of magnitude lower are observed in the spectral range from 3.0 to 3.4 eV. Note also the presence of a broad green PL band with nearly the same intensity in the visible spectral range (not shown in this figure). The band located at 3.37 eV could be attributed to a free-to-bound transition, while several bands in the spectral range of 3.2 – 3.3 eV followed by one- and two-phonon replicas are usually associated with donor-acceptor pair (DAP) transitions.[26,27] The origin of the 3.27 eV PL band as a DAP recombination has been well documented in the literature through its shift to higher photon energies with increasing the excitation power density and a transition from a DAP recombination to conduction band-acceptor recombination at an elevated temperature. The PL band at 3.27 eV with two shoulders at 3.29 eV and 3.24 eV suggests the presence of different impurities in our samples. However, additional investigations are needed to identify the chemical nature of the respective impurities.

The analysis of the NBG PL band (Figure 2b) discloses its slight broadening in the PEC etched sample as compared to the as-grown one: the FWHM increases from 29 to 33 meV at 75 K, from 35 to 40 meV at 100 K, and from 42 to 47 meV at 150 K. By using the calibration curve from Ref. 25, one can estimate that at 75 K the carrier concentration increases from 1.0×10^{18} cm^{-3} in the as-grown sample to 1.6×10^{18} cm^{-3} in the PEC etched sample, i.e. the carrier concentration increases by ca. 60%. These data corroborate the previous findings that PEC etching removes basically the material with low conductivity and leaves areas with higher carrier concentration. On the other hand, the as-grown material contains nanorings with both low and high carrier concentration, i.e. the NBG PL band comes as a superposition of a narrow band from rings with low carrier concentration and a broader band from rings with higher carrier concentration. This means that the NBG PL band from areas with low carrier concentration should be even narrower, which would give a carrier concentration lower than the deduced value of 1.0×10^{18} cm^{-3}. In this context, it is clear that the amplitude of modulation of the electrical conductivity in the HVPE samples is even higher than 60%.

The results of TEM investigations show that the self-organized nanostructured electrical architectures produced during HVPE growth seem not to be related to regions of structural variation with respect to a single crystal material. Moreover, the comparison of the as-grown and PEC-etched samples demonstrates a high density of defects such as stacking faults and dislocations close to the surface serving as possible attack sites for the PEC-etch. For the as-grown (0001) nanostructured GaN (see Figures 3a, 3b) dislocation networks originating at the (0001) GaN surface have been observed to extend 200–300 nm deep into the crystal. For the etched sample, a TEM lamella has been cut from the center of the circular formations. Dislocation networks were evidenced to be concentrated at the center of these hexagonal domains, developing along the polar direction throughout the prepared crystal lamella (Figures 3d, 3e). This observation is in congruence to previous investigations of pits at the center of the nanostructured architectures which are related to pile up of screw or mixed-type dislocations using AFM.[18] These defects were visualized by exploiting the diffraction contrast in the scanning TEM (STEM) high-angle annular dark-field mode after tilting away from the [2-1-10] diffraction condition of the crystal to enhance electron scattering processes at defects. Further, we report that after etching, neither dislocation networks nor stacking faults could be observed beneath the (0001) surface, indicating that defect rich regions of the crystal lattice have been preferentially under attack by the PEC-etch, which is especially active for regions with low carrier concentration. Indeed, several reports exist about the influence of crystal defects in GaN on the electric conductivity[27] especially related to threading dislocations and gallium vacancies by e.g. the existence of deep level trapping states[28] in the yellow luminescence band, the reduction of the minority carrier concentration at dislocations acting as non-radiative recombination centers[29] and low transverse mobility by scattering of electrons at charged dislocation lines.[30] However, the dislocation network observed at the center of nanostructured architectures has not been subjected to the

Q144 ECS Journal of Solid State Science and Technology, 8 (8) Q141-Q146 (2019)

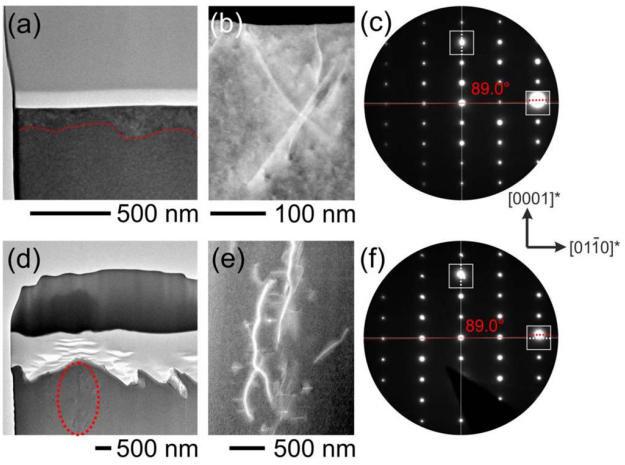

Figure 3. TEM cross-section investigation of the as-grown (a-c) and PEC etched GaN bulk films (d-f). (a) As-grown GaN films show low surface roughness. The red line indicates a change in contrast between the upper and lower part of the crystal, which is related to a high density of near-surface defects such as stacking faults and threading dislocations as depicted in the STEM image in (b). (c) Selected area electron diffraction pattern in [2-1-10] zone axis showing the *c*-axis oriented film growth and a distortion of the reciprocal $\beta \approx 89°$ angle of the wurtzite-type crystal structure ($\alpha° = \beta° = 90°$). (d) Surface etched GaN crystal cut through the center of one hexagonal microdomain (marked with the red ellipse), where dislocation networks were observed in the STEM mode (e). (f) SAED pattern showing the deviation of the reciprocal β angle. The red dashed lines display the angular deviation of the intensities with respect to 90°, white dashed line.

PEC attack as evidenced by the STEM images and described in literature.[20]

The mediation of stress due to crystal lattice mismatch and differences in the thermal lattice expansion coefficients during growth introduce high defect densities of the family of screw, edge, and mixed-type dislocations and have been shown to be concentrated at the substrate/film interface of ~6 mm thick HVPE grown GaN crystals, decreasing in density with the growth direction.[31] Strategies to reduce the generation of high defect densities comprise the initiation of cracks in the sapphire substrate and homoepitaxial growth onto thin GaN seed layers.[32] However, with substantial thickness the large stresses generated lead to the self-separation of substrate and film and could manifest in lattice distortions.[33,34] The results of crystal structure investigations disclose a clear deviation from the $P6_3mc$ wurtzite-type structure in the as-grown and PEC etched samples. A detailed electron diffraction (SAED) study from multiple selected areas revealed a slight deviation of the reciprocal unit-cell angle $\beta \approx 89°$ from rectangularity. The angle β is observed between the [0001]* and [01-10]* directions in the [2-1-10] zone axis pattern (we refer to the magnified insets, in which the red dashed lines display the angular deviation of the intensities with respect to 90°, white dashed line), as depicted in Figures 3c, 3f. The lattice distortion was observed in several selected areas as evidenced from SAED experiments on the as-grown GaN sample (Figure S4). The reduction of symmetry was apparent irrespective of the slight bending of the lamella itself indicated by the increasing amount of out-of-zone axis orientation when moving from i) to iv) in Figure S4(a). Whereas SAED collects more averaged information from a relatively large sample area of 0.785 μm^2 in this experiment, the β distortion was also locally observed at the nanoscale by high resolution imaging. HRTEM micrographs and their Fast Fourier Transforms (FFTs) (see Figure 4) taken from different areas of the patterned PEC etched sample show the defect-free nanostructures of the hillocks depicted in Figure 3d. Whereas the analysis of this selected area by FFT (Figures 4a, 4b) does not show any deviation from the 90° angle an even larger distortion of 88° could be observed in neighboring areas (see Figures 4c, 4d). This finding indicates local lattice relaxation potentially due to the increase in free surface upon etching. The variation of the reciprocal angle according to the bulk wurtzite unit cell alters the angle β between the basal plane and the *c* axis. This angular distortion from 90° depending on the direction and the magnitude of strain results in a symmetry reduction in respect to the wurtzite aristotype. The symmetry of the deformed structure may be assigned to a maximum subgroup of $P6_3mc$, e.g. with monoclinic ($Cm11$ or $C1c1$) or triclinic symmetry. Due to missing superstructure reflections in the diffraction patterns, the symmetry reduction has to be assigned to as the t-type[35] (for *translationengleich*).

Indeed, structural distortions of $\beta \approx 89.05°$ have been described by Rao et al. as triclinic lattice distortion in wurtzite-type gallium nitride films grown by metal organic vapor-phase epitaxy on sapphire substrates.[36] There, a triclinic distortion was investigated by electron diffraction studies using convergent beam electron diffraction (CBED) and SAED near the film/substrate interface. The large misfit strain during crystal growth was reasoned to be the origin for the lattice distortion and was observed to relax within 1 μm distance from the substrate interface.

In case of rapid growth conditions of a few hundred μm/h present in HVPE it seems apparent that the large film stresses due to the initial substrate/film misfit strain can introduce lattice distortions which are then unable to relax in the limited amount of time. Since the lamellae observed in TEM only represent a small fraction of the entire sample volume, high-resolution X-ray diffraction has been applied as a complimentary technique to TEM to probe a larger volume of the sample. This offers quantitative information about the average bulk-like 3D lattice structure and residual strains in the sample with very high resolution.

The experimental setup of the high-resolution X-ray diffraction experiments is depicted schematically in Figure 5a displaying the 2*theta (2θ) measurement geometry. The β-distortion observed in the TEM was tracked down by measuring the angle omega ω, which is the equivalent deviation parameter between the *c*-axis and the surface normal, $\omega = 90° - \beta$. Here, the two examples of a single crystal with a $P6_3mc$ wurtzite-type structure with perfect $\omega = 0$ geometry and a lattice distortion $\omega > 0$ are presented. This offset angle ω is measured by performing rocking scans at several azimuthal positions achieved by a rotation (phi φ) horizontal to the surface normal and monitoring

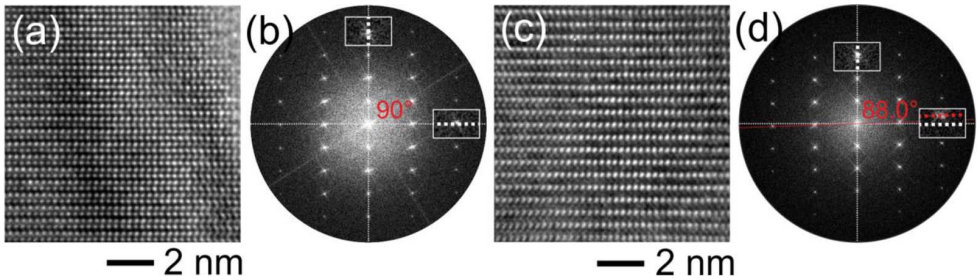

Figure 4. Local high resolution TEM study with corresponding FFT images on PEC etched samples showing areas with apparently no lattice distortion $\beta = 90°$ (a-b) and a stronger distortion of the crystal metrics $\beta = 88°$ (c-d) in GaN films.

ECS Journal of Solid State Science and Technology, **8** (8) Q141-Q146 (2019) Q145

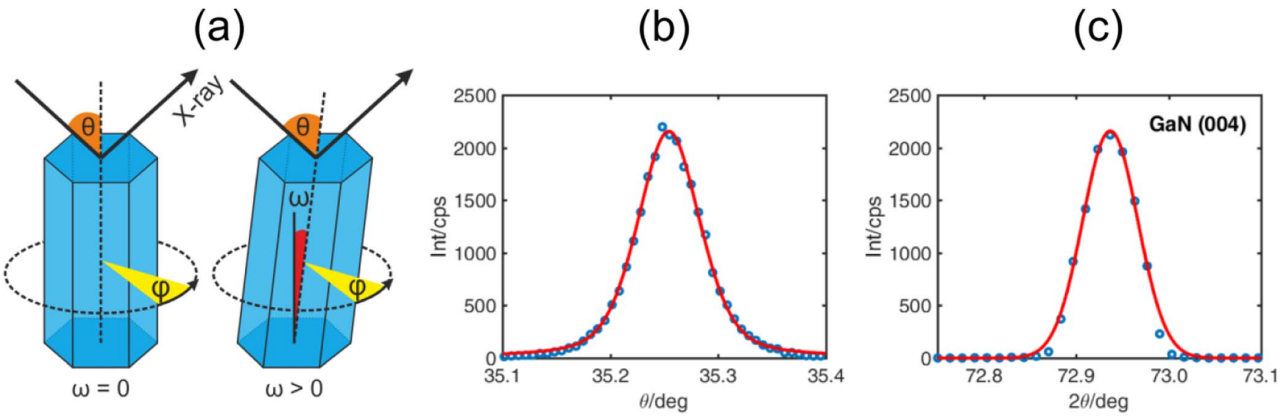

Figure 5. (a) HRXRD measurement geometry for a hexagonal crystal first showing no triclinic lattice distortion $\omega = 90°\text{-}\beta = 0$ and second with $\omega > 0$ measured in dependence of the sample horizontal rotation angle phi φ in a 2*theta, 2θ, geometry. The single crystalline structure of the as-grown GaN crystal is demonstrated by representative rocking curves (b) and Bragg scans (c) of the (004) reflection, where lattice strains can be derived from peak fits (red curve).

the $Q(\theta)$-shift in the maximum peak intensity of the GaN (004) Bragg reflection, Q being the reciprocal lattice vector.

The position of the GaN (004) Bragg reflection was determined to be $2\theta = 72.935°$ and $Q = 4.85$ Å^{-1}, in agreement with the wurtzite-type structure[37] (a = 3.190Å, c = 5.189Å). The respective rocking curve, performed for optimizing the incident angle θ and the 2θ-scan of the GaN (004) reflection is shown in Figures 5b and 5c, respectively. The blue dotted data points were fitted by Voigt-profiles (red curve) with the contribution (Gauss 40%, Lorentzian 60%) to obtain the peak position and full-width at half maxima which are used to derive lattice strains along the crystal c-axis.

For the analysis of the deviation parameter ω representing the triclinic lattice distortion, rocking curves were performed at nine azimuthal rotation angles φ in steps of 30° for the as-grown and etched samples and were evaluated for their intensity maxima peak position as presented in Figure 6a. Both samples show coinciding angular dependence, which is apparent by the superposition of the measurement curves aligning the $\omega = 0$ data points. The deviation of ω with respect to the in-plane orientation is observed to oscillate between −1° and 1° over the measured range having their maxima separated by a 180° rotation in φ which indicates similar results to the lattice distortion $\beta = 89°$ observed with TEM. The respective values of the distortion measured for the as-grown and etched sample at $\phi = 30°$ and $\phi = 210°$ are $\omega_{\text{as-grown}} = 0.9585°$ and $\omega_{\text{etched}} = 0.9917°$, and $\omega_{\text{as-grown}} = -1.0356°$ and $\omega_{\text{etched}} = -1.0360°$, respectively. Therefore an average distortion of $\omega_{\text{as-grown}} = 0.9971°$ and $\omega_{\text{etched}} = 1.0139°$ can be derived for both samples, indeed indicating a structural phenomenon on the larger length scale, which can be described by a triclinic lattice distortion.

Furthermore, lattice strain can be derived from the total reflection position $Q_{(004)}$ and can be resolved with very high precision of up to 10^{-5}, which provides a significant advantage over other methods of evaluating strain. The variation in the $Q_{(004)}$ value is plotted in Figure 6b for the as-grown and etched GaN samples in dependence of the rotation angle φ. The average Q values have been determined to $Q_{\text{as-grown}} = 4.8502 \pm 0.0001$ Å^{-1} and $Q_{\text{etched}} = 4.8493 \pm 0.0006$ Å^{-1} ($c_{\text{as-grown}} = 5.1818 \pm 0.0001$ Å and $c_{\text{etched}} = 5.1828 \pm 0.0006$ Å) which translates into a compressive strain of $\varepsilon_{\text{as-grown}} = -0.118\%$ and $\varepsilon_{\text{etched}} = -0.101\%$ with respect to the literature value of $Q_{(004)} = 4.8444$ Å^{-1} ($c_{(004)} = 5.189$ Å).[37] The presence of residual compressive stress in free standing HVPE grown bulk GaN substrates has been observed before by various techniques such as micro-reflectance spectroscopy,[38,39] HRXRD and photoluminescence spectroscopy.[40] However, the amount of residual compressive strain on the c-axis reported in these studies is significantly smaller (by one order of magnitude) compared to this work. This discrepancy could possibly be explained by the triclinic lattice distortion observed in this work, reasoned by different crystal growth parameters, crystal thickness, and the choice of substrate or intermediate layers to reduce interfacial stresses. Furthermore, electron diffraction experiments by Rao et al. reporting about the triclinic distortion in 4.5 µm thick MOVPE GaN films on sapphire showed a tensile strained c lattice parameter by about 0.2%, which is at least in the same order of magnitude.[36] For the bulk-like GaN films investigated

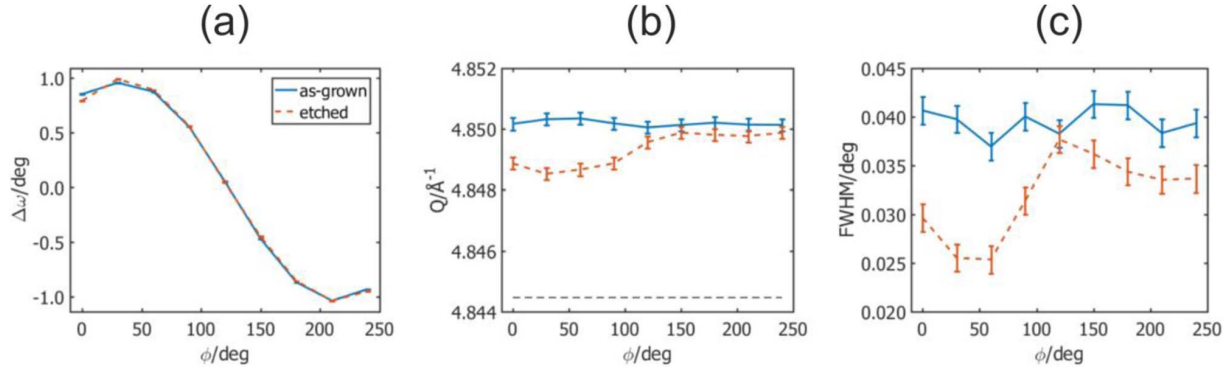

Figure 6. (a) Variation of the deviation parameter omega Δω in dependence of the rotation angle phi φ from HRXRD. The measurements are showing congruent behavior in the boundaries of −1° to 1° for the as-grown and etched samples. (b) Compressive strain $\varepsilon_{\text{as-grown}} = -0.118\%$ and $\varepsilon_{\text{etched}} = -0.101\%$ with respect to the Reference 37 (black dashed line). (c) Full-width at half maximum values of fitted Bragg scans in dependence of the azimuthal rotation. The slightly smaller FHWM width of the etched sample indicates larger coherently diffracted domains which could be attributed to the reduction of defect density after etching.

in this work, the determination of strain from ED pattern, however, seems not to be representative since the information gathered only pictures the first few micrometers and with lower strain precision of just 10^{-3}.

To conclude, next to a monoclinic or triclinic lattice distortion, the amount of residual strain in the HVPE grown crystal was determined by HRXRD to be compressive in *c*-axis direction by about 0.1% for both, the as-grown and etched sample, which slightly tends to relax for the latter.

In Figure 6c the FWHM calculated from the Voigt fits of the Bragg scans is plotted over the azimuthal rotation φ. The mean value of the FWHM is $0.0395 \pm 0.0015°$ for the as-grown and $0.0319 \pm 0.0044°$ for the etched GaN. From the FWHM the size of the coherently diffracting domains can be derived which serves as an indicator for the defect density.[41,42] For the as-grown and etched GaN the mean domain sizes are determined to 111.7 ± 4.3 nm and 140.7 ± 20.8 nm, respectively. In conclusion, the etching process slightly increases the sizes of the coherently diffracting domains, which can be attributed to a reduction in the defect density after etching as evidenced from TEM experiments.

Conclusions

The results of this study demonstrate that the complex 3D nanoarchitectures disclosed by photoelectrochemical etching in HVPE-grown bulk GaN single crystals originate from the spatially modulated electrical conductivity and they prove not to be related to variations of the crystal structure. According to the analysis of the photoluminescence in as-grown and PEC etched samples, the amplitude of spatial modulation of the electrical conductivity in the HVPE-grown GaN is of at least 60%. On the other hand, combining TEM and HRXRD techniques provides a powerful methodological approach to gather structural information on the nanometer to millimeter length scale with high precision. These investigations reveal a distortion of the $P6_3mc$ wurtzite-type structure, indicated by the deviation from the hexagonal symmetry. This deviation varies from 0° to 2° at the nanoscale, while it is of around 1° when averaged over the entire crystal. Furthermore, compressive lattice strain along the crystal *c*-axis derived from peak fits of rocking curves of the (004) reflection is found to be in the order of -0.1% and to be slightly relaxed in PEC-etched samples.

Acknowledgments

The authors acknowledge the German Research Foundation (DFG) under the scheme of the CRC1261 in project A6, the support from the National Agency for Research and Development under the grant #15.817.02.29A, as well as from the European Commission under the Horizon-2020 grant #810652 "NanoMedTwin", and Olaf Magnussen and Joachim Stettner, Kiel University, for access to the X-ray source.

Appendix

Further SEM images showing the GaN surface after subjection to electrochemical and photoelectrochemical etching (S1, S2). Discussion of Piezoforce Microscopy results (S3) and electron diffraction pattern conducted on different positions of the specimen (S4).

ORCID

Eduard Monaico https://orcid.org/0000-0003-3293-8645
Ion Tiginyanu https://orcid.org/0000-0003-0893-0854

References

1. P. Waltereit, W. Bronner, R. Quay, M. Dammann, M. Cäsar, S. Müller, F. Van Raay, R. Kiefer, P. Brückner, J. Kühn, M. Musser, L. Kirste, C. Haupt, W. Pletschen, T. Lim, R. Aidam, M. Mikulla, and O. Ambacher, *Phys. Status Solidi Appl. Mater. Sci.*, **209**, 491 (2012).
2. S. Maroldt, R. Quay, P. Dennler, D. Schwantuschke, M. Musser, M. Dammann, R. Aidam, P. Waltereit, A. Tessmann, and O. Ambacher, *Jpn. J. Appl. Phys.*, **52**, 08JN13 (2013).
3. P. Waltereit, W. Bronner, P. Brückner, M. Dammann, R. Reiner, S. Müller, J. Kühn, M. Musser, R. Quay, M. Mikulla, and O. Ambacher, in: *Int. Conf. Solid State Devices Mater.*, 958 (2013).
4. D. Koyama, A. Barsegyan, and J. Walker, in: *2015 IEEE Int. Conf. Microwaves, Commun. Antennas Electron. Syst.*, (2015).
5. R. Lerner, S. Eisenbrandt, C. Bower, S. Bonafede, A. Fecioru, R. Reiner, and P. Waltereit, in: *Proc. Int. Symp. Power Semicond. Devices ICs*, 451 (2016).
6. P. Waltereit, W. Bronner, R. Quay, M. Dammann, M. Cäsar, S. Müller, R. Reiner, P. Brückner, R. Kiefer, F. Van Raay, J. Kühn, M. Musser, C. Haupt, M. Mikulla, and O. Ambacher, *Semicond. Sci. Technol.*, **28**, 074010 (2013).
7. U. K. Mishra and M. Guidry, in: *Power GaN Devices, Power*, Elec M. Meneghini, G. Meneghesso, and E. Zanoni, (Eds.), p.69, Springer, Switzerland, (2017).
8. M. Shur and R. F. Davis, in: *Sel. Top. Electron. Syst*, Vol. **33**, M. Suhr, Editor, World Scientific, (2004).
9. J. L. B. Walker, *Handbook of RF and Microwave Power Amplifiers*, Cambridge University Press, Cambridge (2011).
10. R. S. Pengelly, S. M. Wood, J. W. Milligan, S. T. Sheppard, and W. L. Pribble, *IEEE Trans. Microw. Theory Tech.*, **60**, 1764 (2012).
11. S. Rajbhandari, J. J. D. McKendry, J. Herrnsdorf, H. Chun, G. Faulkner, H. Haas, I. M. Watson, D. O'Brien, and M. D. Dawson, *Semicond. Sci. Technol.*, **32**, 023001 (2017).
12. T. Kachi, *Jpn. J. Appl. Phys.*, **53**, 100210 (2014).
13. E. L. Piner, *ECS Trans.*, **77**, 95 (2017).
14. S. Keller, H. Li, M. Laurent, Y. Hu, N. Pfaff, J. Lu, D. F. Brown, N. A. Fichtenbaum, J. S. Speck, S. P. Denbaars, and U. K. Mishra, *Semicond. Sci. Technol.*, **29**, 113001 (2014).
15. M. Bockowski, M. Iwinska, M. Amilusik, M. Fijalkowski, B. Lucznik, and T. Sochacki, *Semicond. Sci. Technol.*, **31**, 093002 (2016).
16. R. Doradziński, R. Dwiliński, J. Garczyński, L. P. Sierzputowski, and Y. Kanbara, in: *Technology of Gallium Nitride Crystal Growth*, D. Ehrentraut, E. Meissner, and M. Bockowski, Editors, p. 326, Springer Berlin Heidelberg (2010).
17. S. Suihkonen, S. Pimputkar, S. Sintonen, and F. Tuomisto, *Adv. Electron. Mater.*, **3**, 1600496 (2017).
18. I. Tiginyanu, M. A. Stevens-Kalceff, A. Sarua, T. Braniste, E. Monaico, V. Popa, H. D. Andrade, J. O. Thomas, S. Raevschi, K. Schulte, and R. Adelung, *ECS J. Solid State Sci. Technol.*, **5**(5), P218 (2016).
19. W. Lee, H. J. Lee, S. H. Park, K. Watanabe, K. Kumagai, T. Yao, J. H. Chang, and T. Sekiguchi, *J. Cryst. Growth.*, **351**, 83 (2012).
20. C. Díaz-Guerra, J. Piqueras, V. Popa, A. Cojocaru, and I. M. Tiginyanu, *Appl. Phys. Lett.*, **86**, 1 (2005).
21. V. Popa, I. M. Tiginyanu, V. V. Ursaki, O. Volcius, and H. Morkoç, *Semicond. Sci. Technol.*, **21**, 1518 (2006).
22. R. Lewandowska, J. L. Weyher, J. J. Kelly, L. Konczewicz, and B. Lucznik, *J. Cryst. Growth*, **307**, 298 (2007).
23. B. J. Rodriguez, A. Gruverman, A. I. Kingon, and R. J. Nemanich, *J. Cryst. Growth*, **246**, 252 (2002).
24. T. N. Morgan, *Phys. Rev.*, **139**, A343 (1965).
25. E. Iliopoulos, D. Doppalapudi, H. M. Ng, and T. D. Moustakas, *Appl. Phys. Lett.*, **73**, 375 (1998).
26. R. Dingle and M. Ilegems, *Solid State Commun.*, **9**, 175 (1971).
27. T. Paskova, B. Arnaudov, P. P. Paskov, E. M. Goldys, S. Hautakangas, K. Saarinen, U. Södervall, and B. Monemar, *J. Appl. Phys.*, **98**, 033508 (2005).
28. P. Kozodoy, J. P. Ibbetson, H. Marchand, P. T. Fini, S. Keller, J. S. Speck, S. P. DenBaars, and U. K. Mishra, *Appl. Phys. Lett.*, **73**, 975 (1998).
29. J. Elsner and R. Jones, *Phys. Rev. B - Condens. Matter Mater. Phys.*, **58**, 12571 (1998).
30. S. J. Rosner, E. C. Carr, M. J. Ludowise, G. Girolami, and H. I. Erikson, *Appl. Phys. Lett.*, **70**, 420 (1997).
31. K. Fujito, S. Kubo, H. Nagaoka, T. Mochizuki, H. Namita, and S. Nagao, *J. Cryst. Growth.*, **311**, 3011 (2009).
32. S. T. Kim, Y. J. Lee, D. C. Moon, C. H. Hong, and T. K. Yoo, *J. Cryst. Growth.*, **194**, 37 (1998).
33. B. H. Bairamov, O. Gürdal, A. Botchkarev, H. Morkoç, G. Irmer, and J. Monecke, *Phys. Rev. B.*, **60**, 16741 (1999).
34. A. Vailionis, H. Boschker, W. Siemons, E. P. Houwman, D. H. A. Blank, G. Rijnders, and G. Koster, *Phys. Rev. B.*, **83**, 064101 (2011).
35. Wiley: *International Tables for Crystallography*, Volume A, 5th Edition, Space-Group Symmetry - Theo Hahn, n.d.
36. D. V. Sridhara Rao, K. McLaughlin, M. J. Kappers, and C. J. Humphreys, *Ultramicroscopy*, **109**, 1250 (2009).
37. H. Schulz and K. H. Thiemann, *Solid State Commun.*, **23**, 815 (1977).
38. H. Geng, H. Sunakawa, N. Sumi, K. Yamamoto, A. Atsushi Yamaguchi, and A. Usui, *J. Cryst. Growth*, **350**, 44 (2012).
39. H. Geng, A. A. Yamaguchi, H. Sunakawa, N. Sumi, K. Yamamoto, and A. Usui, *Jpn. J. Appl. Phys.*, **50**, 01AC01 (2011).
40. V. Darakchieva, T. Paskova, P. P. Paskov, B. Monemar, N. Ashkenov, and M. Schubert, *Phys. Status Solidi*, **195**, 516 (2003).
41. B. Heying, X. H. Wu, S. Keller, Y. Li, D. Kapolnek, B. P. Keller, S. P. DenBaars, and J. S. Speck, *Appl. Phys. Lett.*, **68**, 643 (1996).
42. H. Heinke, V. Kirchner, S. Einfeldt, and D. Hommel, *Appl. Phys. Lett.*, **77**, 2145 (2000).

Supporting Information

Modulation of electrical conductivity and lattice distortion in bulk HVPE-grown GaN

Niklas Wolff[a], *Philipp Jordt*[b], *Tudor Braniste*[c], *Veaceslav Popa*[c], *Eduard Monaico*[c], *Veaceslav Ursaki*[c], *Adrian Petraru*[d], *Rainer Adelung*[e], *Bridget M. Murphy*[b,f*]*Lorenz Kienle*[a*] *and Ion Tiginyanu*[c*]

[a] Synthesis and Real Structure, Institute for Materials Science, Kiel University, Kiel 24143, Germany

[b] Institute for Experimental and Applied Physics, Kiel University, Kiel, 24118, Germany

[c] National Center for Materials Study and Testing, Technical University of Moldova, Stefan cel Mare av. 168, MD-2004 Chisinau, Republic of Moldova

[d] Nanoelectronics, Institute for Materials Science, Kiel University, Kiel 24143, Germany

[e] Functional Nanomaterials, Institute for Materials Science, Kiel University, Kiel 24143, Germany

[f] Ruprecht-Haensel Laboratory, Kiel, 24118, Germany

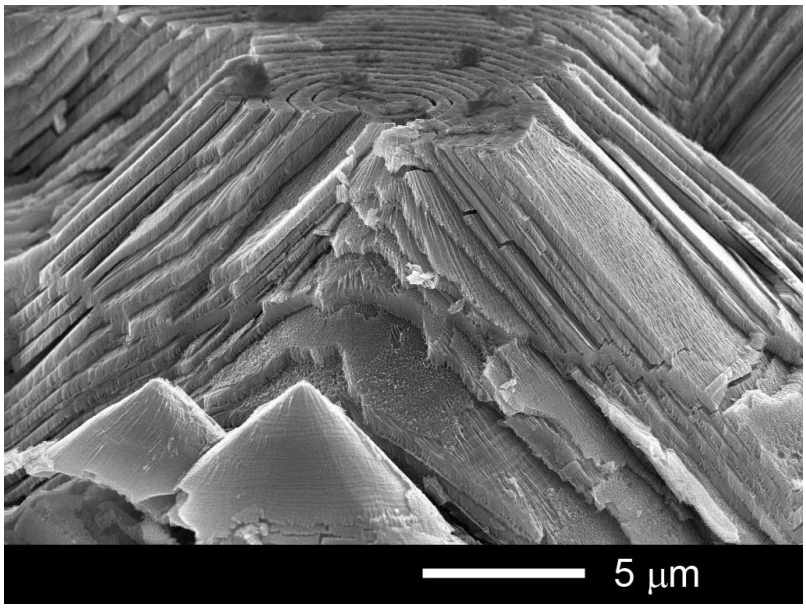

Figure S1: Multilayer conical porous structures formed in bulk HVPE-grown GaN subjected from the top surface (N-face) to electrochemical etching in 0.3 mol. HNO_3 electrolyte under 22 V anodic bias for 20 min. Unlike the PEC etching, in the case of electrochemical etching the anodisation potential was applied between two electrodes. The sample has served as working electrode while a mesh of Pt wire served as counter electrode.

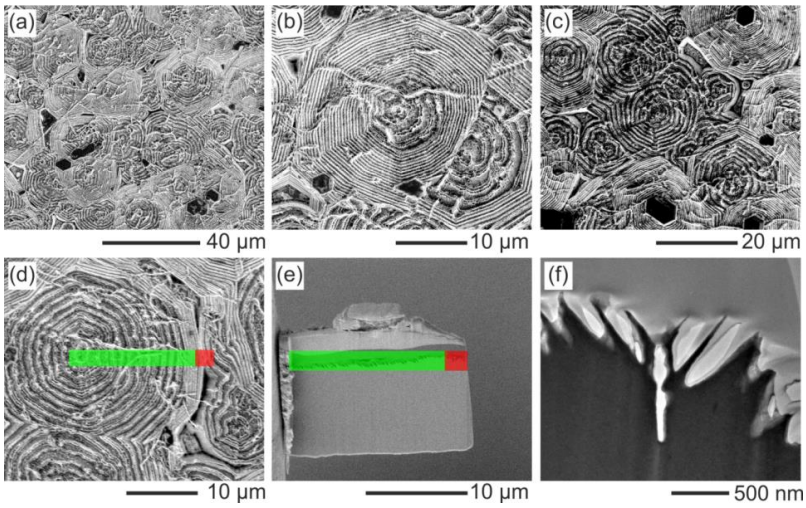

Figure S2: (a-d) SEM images of the bulk GaN surface after photoelectrochemical etching. The colored bar in (d) and (e) highlights the region of a TEM sample prepared by FIB, whereas the red bar indicates the boundary region between two adjacent concentric structures with modulated electrical parameters. (f) TEM image of this boundary region containing one “island” with different polarity as shown in Figure S3. The photoelectrochemical etching produced a straight and deep trench at the “island” in contrast to the inclined etch pits produced at the concentric structures, which is consistent to the peculiarities of the proposed growth scheme in ref. 4.

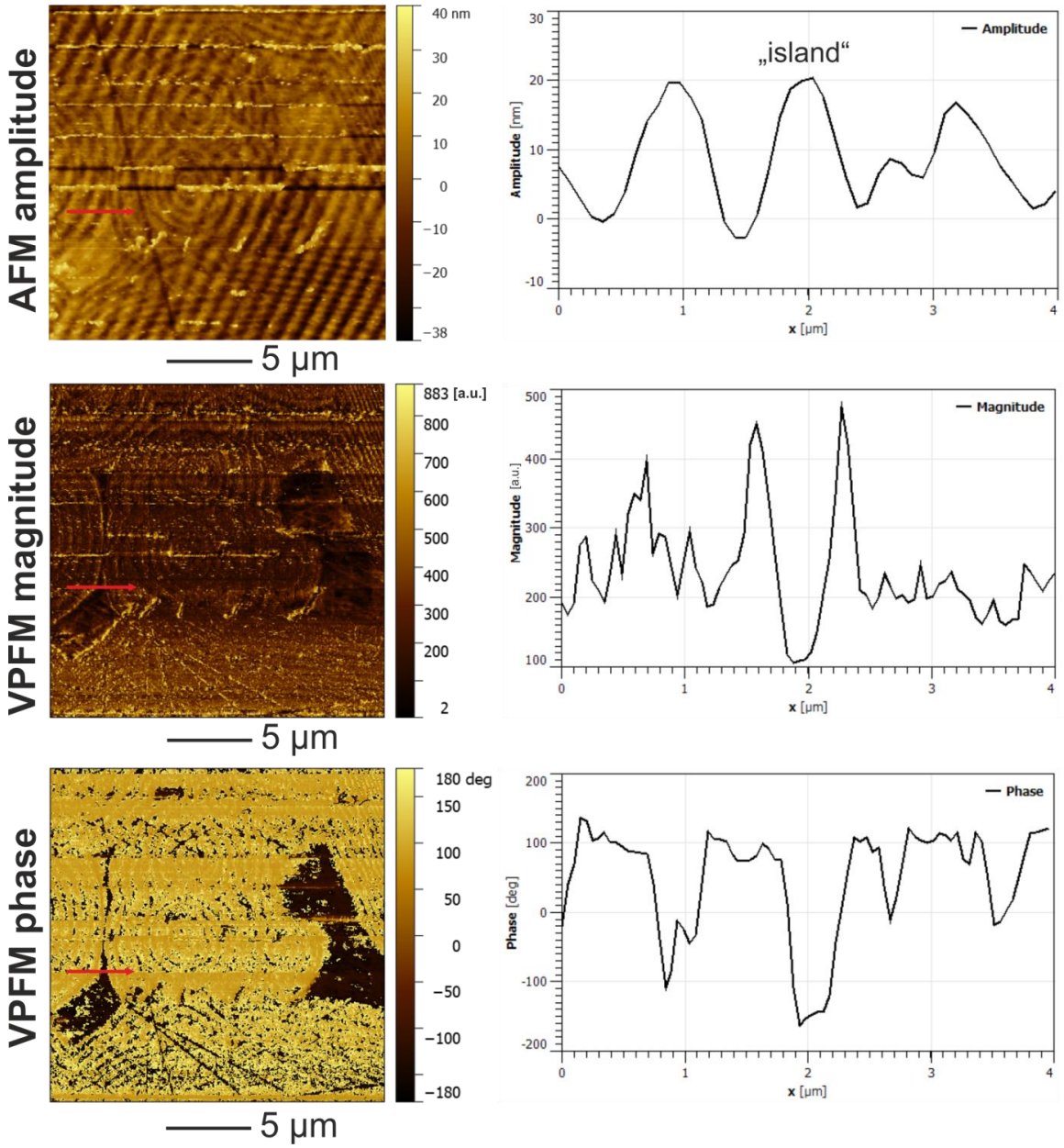

Figure S3: Piezoresponse force microscopy (PFM) measurements of the as grown GaN surface at 247 kHz resonance frequency. AFM topology and the corresponding vertical PFM magnitude and phase signals are displayed. The positions of profiles are indicated by the red arrows. See text for details.

The contact mode AFM image depicts the topology of the surface which is described by circular formations exhibiting alternating rings of different elevation which are occasionally separated by islands. Random oriented scratches, fringe pattern (see the lower right corner) and horizontal measuring artefacts superimpose the image. The topology of the surface is shown in the respective AFM amplitude profile which is taken over the circular structures and bridging the island (see red

arrow). The height difference between the “hill” and “valley” rings and islands is 20 nm peak-to-peak, with hills and islands having roughly the same elevation.

The vertical PFM magnitude image further resembles the topography map but with inverted contrast, therefore an amplification of piezoresponse by the topography can be neglected. The island and hill structures basically show a smaller piezoresponse than the valley structures. A closer inspection of the piezoresponse profile reveals a minimum in magnitude for the island which is bracketed by valley-type rings showing very high piezoresponse at their edges. Additionally, such modulation is also observed in the phase image. Valley-type rings showing larger magnitude in piezoresponse with respect to the hill-type rings exhibit pronounced kinks in the phase (dark contrast in the image and profile). The inversion of the phase signal is also true for the islands, although in contrast to valley-type rings, here the piezoresponse magnitude was observed to be small.

According to theory the piezoelectric response of Ga- and N-face domains will vibrate in-phase and out-of-phase with the modulation voltage, respectively. The pronounced phase difference (more than ~200°) and phase shift can be explained by the experimental setup and capacitive effects between sample and tip, hence only qualitative statements are feasible. However, the small piezoresponse of the island, together with the inversion of the phase signal is a clear indication of a domain with inversed polarity featuring inversion domain boundaries as displayed by the high magnitude regions surrounding the island[1,2].

On the contrary, the modulation of phase and magnitude of the hill- and valley-type rings is believed to have different origin than the inversion of polarity. Moreover, the magnitude and phase could be influenced by several factors which include artefacts of topography, variation of surface charge or piezoactivity, rather than polarization inversion[3]. Please, note that scratches also show the same phase to magnitude correlation like the valley-type rings. In correlation to the real structure, these valley-type rings having smaller lateral dimension coincide with material removed during the PEC etch which can be rationalized from Figure S1. These conical stacked structures are supposed to feature an alternating spatial modulation of dopants[4]. Further, no indication of inversion domain boundaries have been found in the TEM investigation of cross-section through these single crystalline conical structures.

Therefore we conclude from PFM measurements that inversion domains with opposite polarization than the conical structures are formed during the fast growth process, therefore showing a microscale modulation of piezoelectric parameters.

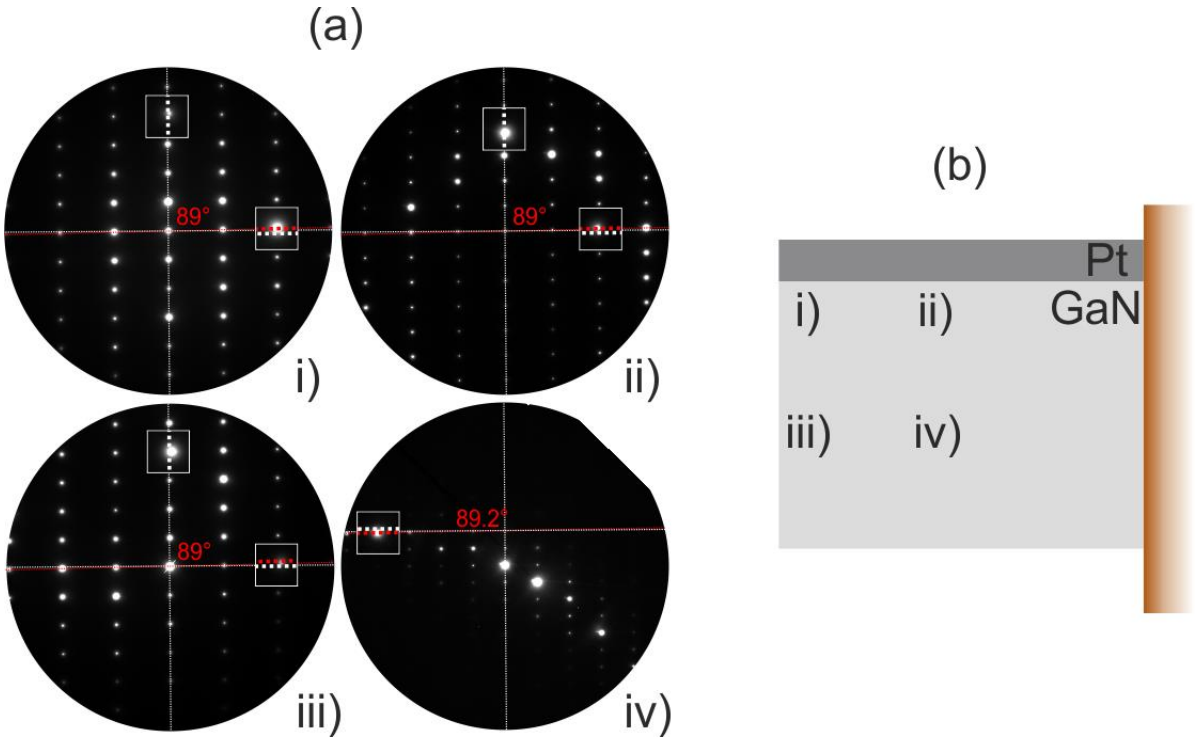

Figure S4: (a) Selected area (diameter of aperture 500 nm) electron diffraction studies screening four positions on the TEM lamella. The specimen was tilted into [2-1-10] orientation for position i) and no further sample tilt was performed during the experiment. The triclinic distortion showing $\beta \approx 89°$ of the wurtzite structure of GaN is observed to be present at all four positions, irrespective the crystalline distortions of the lamella which are apparent from the increasing deviation from the zone axis condition set in i). (b) Sketch of the specimen lamella showing the positions of electron diffraction experiments.

(1) Balke, N.; Maksymovych, P.; Jesse, S.; Herklotz, A.; Tselev, A.; Eom, C.-B.; Kravchenko, I. I.; Yu, P.; Kalinin, S. V. Differentiating Ferroelectric and Nonferroelectric Electromechanical Effects with Scanning Probe Microscopy. *ACS Nano* **2015**, *9* (6), 6484–6492. https://doi.org/10.1021/acsnano.5b02227.

(2) Rodriguez, B. J.; Gruverman, A.; Kingon, A. I.; Nemanich, R. J. Piezoresponse Force Microscopy for Piezoelectric Measurements of III-Nitride Materials. *Journal of Crystal Growth* **2002**, *246* (3), 252–258. https://doi.org/10.1016/S0022-0248(02)01749-9.

(3) Jesse, S.; Mirman, B.; Kalinin, S. V. Resonance Enhancement in Piezoresponse Force Microscopy: Mapping Electromechanical Activity, Contact Stiffness, and Q Factor. *Appl. Phys. Lett.* **2006**, *89* (2), 022906. https://doi.org/10.1063/1.2221496.

(4) Tiginyanu, I.; Stevens-Kalceff, M. A.; Sarua, A.; Braniste, T.; Monaico, E.; Popa, V.; Andrade, H. D.; Thomas, J. O.; Raevschi, S.; Schulte, K.; et al. Self-Organized Three-Dimensional Nanostructured Architectures in Bulk GaN Generated by Spatial Modulation of Doping. *ECS Journal of Solid State Science and Technology* **2016**, *5* (5), P218–P227. https://doi.org/10.1149/2.0091605jss.

FULL PAPER

NANO · MICRO small
www.small-journal.com

Advanced Hybrid GaN/ZnO Nanoarchitectured Microtubes for Fluorescent Micromotors Driven by UV Light

Niklas Wolff, Vladimir Ciobanu, Mihail Enachi, Marius Kamp, Tudor Braniste, Viola Duppel, Sindu Shree, Simion Raevschi, Mariana Medina-Sánchez, Rainer Adelung, Oliver G. Schmidt, Lorenz Kienle, and Ion Tiginyanu**

The development of functional microstructures with designed hierarchical and complex morphologies and large free active surfaces offers new potential for improvement of the pristine microstructures properties by the synergistic combination of microscopic as well as nanoscopic effects. In this contribution, dedicated methods of transmission electron microscopy (TEM) including tomography are used to characterize the complex hierarchically structured hybrid GaN/ZnO:Au microtubes containing a dense nanowire network on their interior. The presence of an epitaxially stabilized and chemically extremely stable ultrathin layer of ZnO on the inner wall of the produced GaN microtubes is evidenced. Gold nanoparticles initially trigger the catalytic growth of solid solution phase $(Ga_{1-x}Zn_x)(N_{1-x}O_x)$ nanowires into the interior space of the microtube, which are found to be terminated by AuGa-alloy nanodots coated in a shell of amorphous GaO_x species after the hydride vapor phase epitaxy process. The structural characterization suggests that this hierarchical design of GaN/ZnO microtubes could offer the potential to exhibit improved photocatalytic properties, which are initially demonstrated under UV light irradiation. As a proof of concept, the produced microtubes are used as photocatalytic micromotors in the presence of hydrogen peroxide solution with luminescent properties, which are appealing for future environmental applications and active matter fundamental studies.

1. Introduction

In the past, intensive research has been performed in the field of photocatalytic materials, predominantly covered by oxides such as TiO_2 and ZnO, oxynitrides or sulfides. These are engineered as single or multiple component nanostructures with potential applications ranging from photoreduction of CO_2, H_2 generation, self-cleaning surfaces, and artificial leaves.[1]

Future trends point to more complex nanoarchitectures by tuning the size, shape, and composition to achieve hierarchically structured nanocomposite photocatalytic semiconductor units.[1]

The fabrication of hollow particles and tubular structures with complex morphologies via template-assisted methods has been demonstrated to come up with exceptional properties for electrochemical energy application.[2] Template-based methods designed toward hollow structures provide high design flexibility and

N. Wolff, M. Kamp, Prof. L. Kienle
Synthesis and Real Structure
Institute for Materials Science
Kiel University
Kaiserstraße 2, 24143 Kiel, Germany
E-mail: lk@tf.uni-kiel.de

V. Ciobanu, Dr. M. Enachi, Dr. T. Braniste, Prof. I. Tiginyanu
National Center for Materials Study and Testing
Technical University of Moldova
Stefan cel Mare 168, Chisinau 2004, Moldova
E-mail: ion.tighineanu@cnstm.utm.md

V. Duppel
Nanochemistry
Max Planck Institute for Solid State Research
Heisenbergstraße 1, 70569 Stuttgart, Germany

The ORCID identification number(s) for the author(s) of this article can be found under https://doi.org/10.1002/smll.201905141.

DOI: 10.1002/smll.201905141

Dr. S. Shree, Prof. R. Adelung
Functional Nanomaterials
Institute for Materials Science
Kiel University
Kaiserstraße 2, 24143 Kiel, Germany

Dr. S. Raevschi
Department of Physics and Engineering
State University of Moldova
Alexei Mateevici Str. 60, Chisinau 2009, Moldova

Dr. M. Medina-Sánchez, Prof. O. G. Schmidt
Institute for Integrative Nanosciences (IIN)
Leibniz IFW Dresden
Helmholtzstraße 20, 01069 Dresden, Germany

Prof. O. G. Schmidt
Material Systems for Nanoelectronics
Chemnitz University of Technology
Reichenhainer Straße 70, 09107 Chemnitz, Germany

Prof. I. Tiginyanu
Academy of Sciences of Moldova
Stefan cel Mare av. 1, Chisinau 2001, Moldova

ADVANCED SCIENCE NEWS
www.advancedsciencenews.com

NANO · MICRO small
www.small-journal.com

control of the final product shape making it one of the most versatile approaches in nanomaterial synthesis.[3] Herein, the concept of "nano casting" is a rigid mechanism;[4] this is deriving a predetermined structure by filling up voids in a mold with the material of choice and subsequent removal of the mold achieving desirable structures even down to the nanometer scale. With this respect, hard templates offer relatively easy and controllable processes resulting in a negative replica of the templates.[5] Commonly, inorganic, ordered porous solids including zeolites,[6] ordered mesoporous structures from silica[5] and carbon,[7] and anodic alumina oxides[8] are used as hard templates and recently metal-organic frameworks[9] have been reviewed for the same application.

The "filling" step is either characterized by coating the outer surfaces followed by selective template removal or by introducing a precursor material inside a porous structure via electrodeposition, galvanic replacement or controllable chemical transformation.[10]

Recently, the coating of zinc oxide (ZnO) microstructures as sacrificial templates raised the interest of the material science community, as ZnO can be easily dissolved in both acid and alkaline solutions making it suitable for producing hollow micro- and nanostructures.[11] Based on this, a variety of hollow structures such as hollow-Si tetrapods,[12] aerographite,[13] tetrapodal self-entangled carbon nanotube tube networks[14] and hollow-GaN tetrapods[15,16] using hydride vapor phase epitaxy (HVPE) for the deposition of GaN have been generated.[17] In this specific, the ZnO template and GaN lattices only show a small in-plane mismatch of 1.9% allowing for strong epitaxy[18] and forming p/n heterojunctions demonstrated useful for optical applications such as UV photodetectors[19] or light emitting diodes.[20]

In this context, another important application of such materials is related to the development of light-driven micromotors having one or 2D structures with high surface to volume fraction.[21] Especially micromotors based on photocatalytic materials such as pure TiO_2 or TiO_2 decorated with Pt, Ag, Au nanodots, or based on microarrays of porous TiO_2 nanotubes have been investigated.[22] Furthermore, using atomic layer deposition, Dong et al.[23] fabricated hybrid ZnO–Pt tubular micromotors with light-enhanced propulsion based on strong photocatalytic properties of ZnO and chemical catalytic properties of Pt. These micromotors, however, did not exhibit on–off capabilities and their chemical stability over time remained undisclosed since ZnO is known to suffer from photocorrosion in an aqueous medium.

Recently, the versatile GaN has attracted interest especially due to its adaptable optical and electrical properties,[24,25] which were also exploited for photocatalysis, suggesting outstanding photocatalytic activity of GaN nanowires (NWs) superior to TiO_2 NWs and even ZnO NWs with chemical stability under harsh acidic conditions.[26] At the same time, GaN is a nontoxic, biocompatible material, which opens wide possibilities for medical applications.

Further radical improvement of GaN electrical, optical, and photocatalytic properties can be achieved by various approaches: tailoring the bandgap energy is possible by 1) the concentration x of co-doping with ZnO forming a solid solution $(Ga_{1-x}Zn_x)(N_{1-x}O_x)$[27] or by 2) tailoring the NW facets by changing the morphology of the NWs from straight to zig-zag.[28] 3) The surface modification with a noble metal cocatalyst[29] demonstrated to improve the visible-light-driven degradation of an organic dye by the factor of 8 with respect to pristine $(Ga_{0.75}Zn_{0.25})(N_{0.75}O_{0.25})$ enhancing the photocurrent response, which is usually associated with localized surface plasmon resonance.[30,31] 4) The reduction of the structure size is believed to further improve the photocatalytic performance.

Hence, the irradiation with designed light sources including wavelengths of the infrared, the visible or UV spectrum could be an efficient energy source for the purpose of achieving directional controlled motion in case of GaN or modified GaN:ZnO tubular microstructures functionalized with a noble metal cocatalyst. Indeed, many research groups focused their efforts on developing chemical micromotors[32] capable of converting, e.g., chemical fuels into self-propelled mechanical motion by catalytic reactions.[33–37] Here, light-driven photocatalytic micromotors[38–40] are one of the most studied due to their excellent propulsion properties. The most commonly known light-induced propulsion mechanisms can be classified into self-diffusiophoretic propulsion,[41] bubble propulsion,[42,43] and self-electrophoretic propulsion.[44]

Their strong propulsion, efficient direction control, and abundant functions hold great promise in a number of potential applications ranging from, e.g., cargo transportation in biomedicine[45–48] to environmental cleaning.[49–54]

However, with decreasing tube diameter, the fluid dynamics in confined volumes like capillaries can either inhibit bubble generation or block the liquid flow. In this context, the development of micromotors based on other propulsion mechanisms, e.g., diffusiophoretic motion, circumvents these issues.[22]

In this contribution, we discuss the synthesis, the morphology, chemical composition, and atomic structure of the hierarchical ordered micro-/nanostructure characterized by TEM analysis using scanning (S)TEM tomography, electron diffraction (ED), high-resolution HRTEM imaging, and energy-dispersive X-ray spectroscopy (EDS). Further, we demonstrate the fluorescent light-driven diffusiophoretic motion of the chemically stable and hierarchical nanostructured micromotors showing switchable on–off characteristics. These micromotors are based on hybrid GaN/ZnO microtubes, the outer surface favoring hydrophobicity and the inner hydrophilic surface being functionalized by solid-solution phase $(Ga_{1-x}Zn_x)(N_{1-x}O_x)$ nanowires (NWs) terminated by cocatalytic AuGa-alloy nanodots.

2. Results and Discussion

2.1. Morphology, Composition, and Structure

Considering the recently demonstrated high chemical stability of ultrathin ZnO layers when interfacing GaN,[15] we propose a novel type of GaN/ZnO microtubes, decorated with Au nanodots. The elaborated technological route consists of the following steps as illustrated in **Figure 1**. First, gold nanodots are deposited by plasma sputtering on the surface of ZnO microneedles exhibiting a gradient of transverse size along their longitudinal axis. Second, the growth of a thin GaN layer

ADVANCED SCIENCE NEWS
www.advancedsciencenews.com

NANO · MICRO small
www.small-journal.com

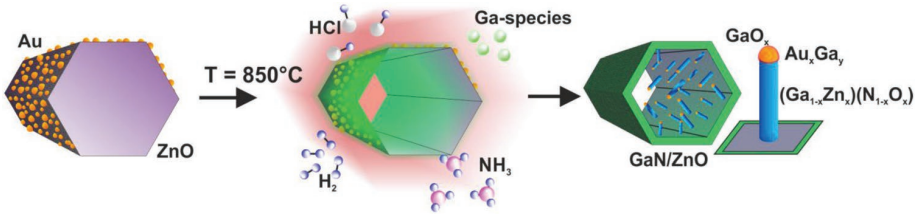

Figure 1. Schematic representation of the synthetic route of GaN/ZnO nanoarchitectured microtubes with an ingrown solid-solution nanowire network. ZnO microwires covered with gold nanoparticles (left image) are subjected to a hydrothermal environment initiating epitaxial growth of GaN while simultaneously etching the ZnO (middle image). The final product of GaN microtubes with a thin ZnO layer chemically stabilized on the inside walls promoting the growth of a nanowire network (right image).

using HVPE is initiated. The process of GaN epitaxial growth is accompanied by the simultaneous hydrothermal removal of ZnO, normally with the exception of an ultrathin ZnO layer which remains at the interface.[15] In the final steps of this process, the Zn- and O-enriched gaseous environment inside the GaN microtubes propagates the growth of NW networks with solid solution phase $(Ga_{1-x}Zn_x)(N_{1-x}O_x)$ composition on the interior wall of the microtubes. The chemical reactions in confined conditions lead to the formation of AuGa-alloyed nanodots enveloped in a shell of amorphous gallium oxide (GaO_x).

The morphology of the ZnO microneedles serving as sacrificial templates and the resulting GaN/ZnO nanoarchitectured microtubes were investigated using a scanning electron microscope (SEM) (see **Figure 2**). The ZnO microneedles were produced with a modified flame transport synthesis[55] (FTS) and possess high aspect ratios of 300–1000 µm in length and ≈1–10 µm of micrometers in diameter (see Figure 2a,b). Uniformly distributed Au nanodots (10 nm) were observed along the microneedles (see Figure 2c). During the epitaxial growth of GaN accompanied by simultaneous ZnO removal, the microneedles are transformed into the GaN/ZnO microtubes with a hexagonal cross-section (see Figure 2d,e). The inner surface of these microtubes with a wall thickness in the ≈30 nm range is decorated by NWs demonstrated to initially grow perpendicular to the $\{\bar{1}100\}$ facets and show straight or kinked structures (see Figure 2f).

Scanning transmission electron microscopy (STEM) was performed to obtain more insights into the composition of different nanostructures on the inner surface of the conical microtubes (**Figure 3**). The template-directed hollow structures synthesized by HVPE produced microtubes and Au dot terminated NWs were observed at the microtubes inner surface (see Figure 3a,b).

Results of the electron diffraction (ED) experiments (Figure 3c) indicate that these GaN/ZnO microtubes grow as single crystals, showing *c*-axis directed growth of the Wurtzite-type structure. The high density of NWs grown inside the hollow microstructures was visualized by a 3D volume reconstruction computed from STEM tomography experiments (see Figure S1 and Movie S1 in the Supporting Information). For this, a sample was tilted over a large angular range along its longitudinal axis using a high angle tilt holder, and the acquired images were combined for a 3D reconstruction (see Figure 3d). A cross-sectional image of this reconstruction is presented with colored isosurfaces of the tube and NWs inside (Figure 3d). The examined GaN/ZnO microtube fragment exhibited a hexagonal

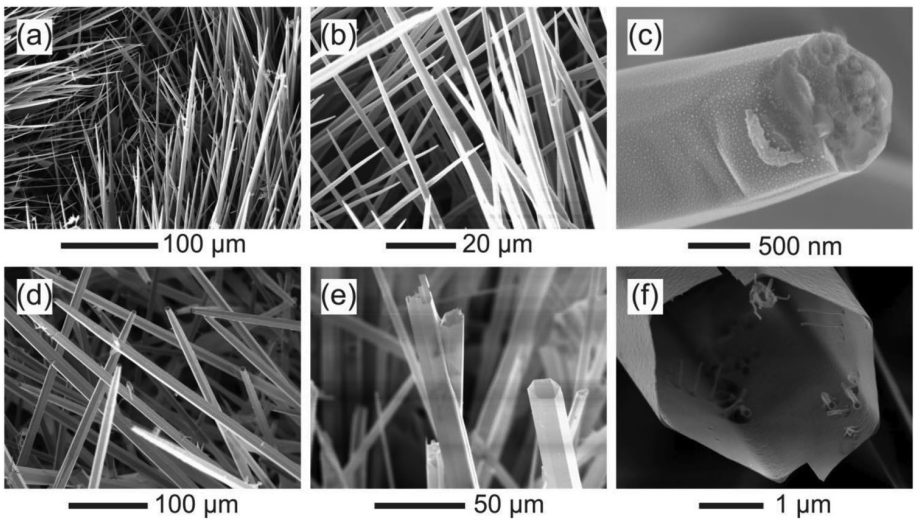

Figure 2. SEM micrographs of a,b) the initial hedgehog-like ZnO microneedles used as templates and c) Au nanodots deposited on ZnO microneedles, d–f) GaN/ZnO microtubes with ingrown NWs.

ADVANCED SCIENCE NEWS
www.advancedsciencenews.com

NANO · MICRO small
www.small-journal.com

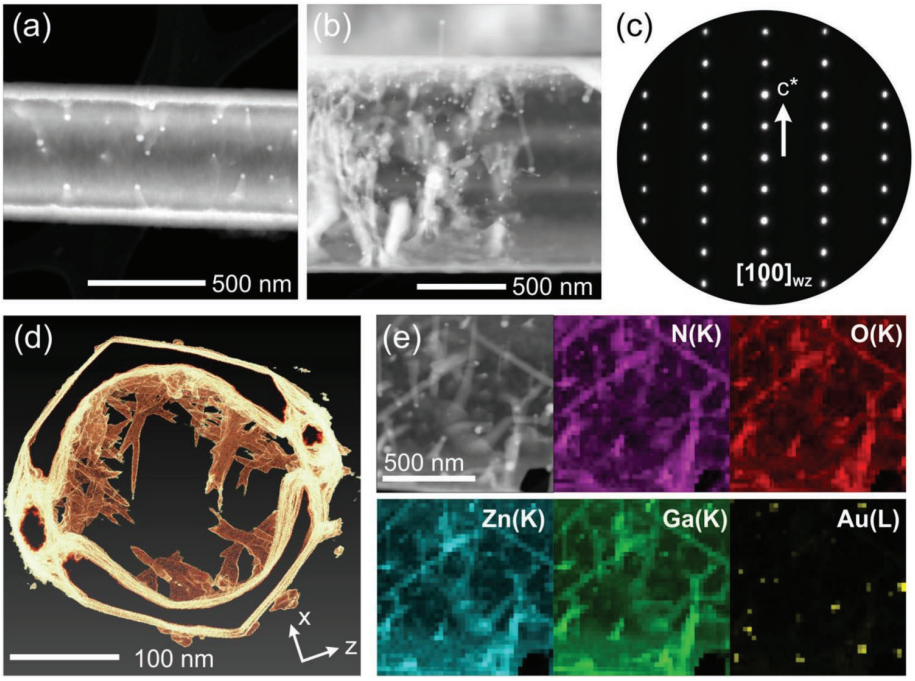

Figure 3. a,b) Scanning TEM images of GaN/ZnO microtubes showing nanowire growth on the inner surface. c) SAED pattern obtained from a GaN/ZnO microtube confirming *c*-axis directed growth in a Wurtzite-type structure. d) Cross-section through the *x*–*z* plane of a 3D tomographic volume reconstruction. e) EDS elemental maps on a sliced microtube colored accordingly for ease of understanding.

cross-section with an outer diameter of ≈300 nm and uniform wall thickness (20–30 nm). The hexagonal shape appears not to be preserved on the inner wall surface. The reconstructed model showed buckled surfaces on the outside and interrupted surfaces on the inside in *z*-direction (*z* being the direction of the electron beam perpendicular to the rotation axis of the *x*–*y* plane), which is explained by a so-called computational missing wedge artifact in that particular direction.[56,57]

Elemental analysis of the characteristic X-rays emitted from a GaN/ZnO microtube fragment was performed via STEM EDS. The superimposed identical spatial distribution of Ga, Zn, N, and O (see Figure 3e) discloses an ultrathin residual layer of ZnO interfacing GaN. This confirms the stability of the ZnO/GaN interface as it was previously reported.[15] Nanowires terminated by Au nanodots were further imaged to propagate into the free space of the tube as visualized in **Figure 4**. In congruence to the SEM micrographs, the NWs shown in the TEM image of Figure 4a grow straight with tapered or needle-shaped morphology, whereas the NWs depicted in the STEM image of Figure 4b show kinks and uniform cylindrical morphology. Such morphological differences of VLS grown NWs are known to be induced by numerous variables in the system describing the static or dynamic local reaction conditions including temperature, the supply rate of reactive species and droplet physics of the catalyst of which an in-depth discussion is provided by Mohammad.[58] Hence, the uncontrolled reaction conditions during the HVPE process and hydrothermal dissolution of ZnO lead to the metal-catalytic VLS growth of NWs of different morphology according to the supposed following reaction schemes[59,60]

$$m\mathrm{Au}^{s} + n\mathrm{GaCl}^{v} + n\mathrm{H}_2^{v} \rightarrow \mathrm{Au}_m\mathrm{Ga}_n^{l} + n\mathrm{HCl}^{v} + \frac{n}{2}\mathrm{H}_2 \quad (1)$$

$$\mathrm{Au}_m\mathrm{Ga}_n^{l} + n\mathrm{NH}_3^{v} \rightarrow m\mathrm{Au}^{s} + n\mathrm{GaN}^{s} + 3n/2\mathrm{H}_2 \quad (2)$$

However, in the Zn and O enriched hydrothermal environment inside the microtubes, the growth of a solid solution phase $(Ga_{1-x}Zn_x)(N_{1-x}O_x)$ is proposed by the EDS analysis on the NWs presented in Figure 4c. In this respect, the elemental distribution maps show the superimposed spatial distribution of X-ray excitations of Ga(K) and Zn(K) edges together with N and O signals.

Further, the EDS analysis proposes that the Au metal catalyst alloyed with Ga is forming intermetallic phases of the binary AuGa system,[61] the alloy being capsulated by a shell of GaO_x. Note that a careful evaluation of the X-ray distribution maps considers the partially overlap of the Zn(K) and Au(L) excitation energies ≈9.60 keV in order to reflect on possible misinterpretation on the signal intensity in the Zn(K) map displayed at the metal catalyst site. Further, the evaluation of the Zn(L) excitation (not shown) reveals partial overlap with Ga(L) excitation. Thus, no conclusive statement can be made on the spatial distribution of Zn at the metal site due to double interference events in the maps shown. However, EDS point measurements did not collect significant intensity of Zn(Kα), concluding that essentially no Zn or only a trace of Zn is alloyed into AuGa (see Figure S2 in the Supporting Information). Additionally, a conclusive statement about the nitrogen distribution has to be taken with care since the signal is smeared out by an increased background induced by the presence of carbon species.

ADVANCED SCIENCE NEWS
www.advancedsciencenews.com

NANO · MICRO small
www.small-journal.com

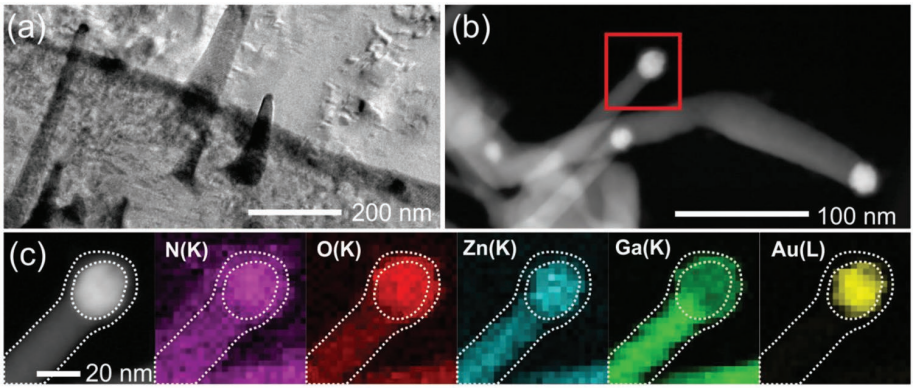

Figure 4. a) TEM image and b) STEM image of NWs grown at the inner surface of the wall. c) STEM EDS elemental maps of metal terminated wires grown at the inner wall surface of GaN/ZnO microtubes. The elemental maps show the distribution of Ga, N, Zn, O, and Au as components of the metal terminated wires.

The averaged concentration of Zn in the solid solution NWs has been determined by numerous EDS point measurements performed on individual NWs. The calculated compositions of $x = 0.12 \pm 0.2$ are very close to single-phase solid solution NWs with $x \approx 0.12$ grown by Han from an Au nanocrystal via a VLS reaction process.[62]

The structure of the solid solution phase $(Ga_{1-x}Zn_x)(N_{1-x}O_x)$ NWs and alloy nanodots was investigated by high-resolution TEM and reciprocal space analysis using fast Fourier transformation (FFT) images and electron diffraction performed also in the precession mode (PED).[63] The real structure of the NWs is characterized by a high density of basal plane defects including polytypic intergrowth and polysynthetic twinning apparent from the TEM investigation shown in **Figure 5**. The structural details of polytypic Wurtzite (WZ) and Zincblende-type (ZB) intergrowth have been described, e.g., by Dick et al.[64] or Caroff et al.[65] For the description the relative positions of Ga- and N-atom $(001)_{WZ}$ bilayers are labeled as A, B, or C. The repetitive hexagonal stacking sequence AB of $(001)_{WZ}$ closed packed planes in growth direction is frequently interrupted by the single or repetitive introduction of a misplaced bilayer C (see Figure 5a). Along the depicted nanostructure, this introduces cubic nanolamellae with single or multiple cubic ABC stacking sequences along $[111]_{ZB}$. The WZ and ZB components are illustrated by the red and blue colors in the high-resolution TEM micrograph associated with the electron diffraction pattern and FFTs given in Figure 5b. The WZ-type lamellae are oriented along $[100]_{WZ}$ and the ZB-type lamellae in $[110]_{ZB}$ zone axis orientation, respectively. The structural heterogeneity can alter the relative orientation of the WZ lamellae attached to both sides of a ZB lamella, particularly, in case of an odd number of layers inside the ZB lamella both WZ lamellae are mirrored to each other, i.e., their stacking sequence changes from AB to AC. More complicated examples of NWs featuring hexagonal-cubic intergrowths are depicted in Figure S3 (Supporting Information).

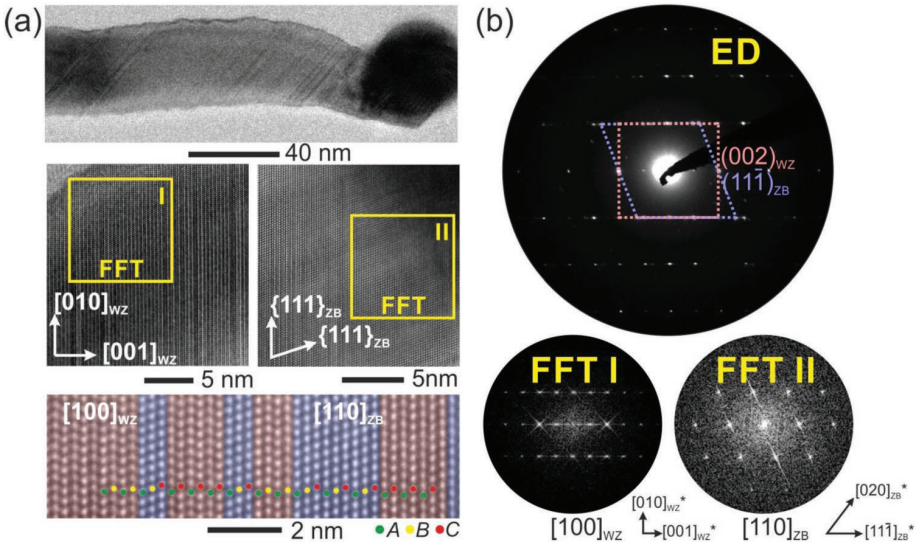

Figure 5. Crystallographic data of a representative $(Ga_{1-x}Zn_x)(N_{1-x}O_x)$ NW. a) High-resolution and b) reciprocal space analysis both reveal a WZ/ZB heterostructure associated with the stacking order of closed packed $\{001\}_{WZ}$ and $\{111\}_{ZB}$ planes along the wires $[001]_{WZ}$ growth direction.

ADVANCED SCIENCE NEWS
www.advancedsciencenews.com

NANO · MICRO small
www.small-journal.com

The WZ/ZB polytypism which is often observed in nanoscale III–V semiconductors is attributed to small differences in the energy landscape. Numerous reports exist about GaN thin films grown on various substrates[66–69] and GaN WZ nanowires[70–73] in which small ZB domains introduce quantum-well like electronic transition states. Hence, the controlled design of the defect structure, growth orientation, and crystal dimensions of heterostructure NWs for purposive application is investigated thoroughly by studying the growth kinetics[64,65] and the influence of the substrate and metal catalyst.

For example, the ability to control the direction of growth has been demonstrated by the choice of the substrate or metal catalyst in VLS or metal-organic chemical vapor deposition (MOCVD) growth environments. For example, Kuykendall used lattice-matched substrates,[74] e.g., (100) $LiAlO_2$ surfaces to grow GaN nanowires along $[1\text{-}10]_{WZ}$ and (111) MgO to achieve $[001]_{WZ}$ directed growth. Further, Au or Ni terminated NWs reported by Kuykendall[75] predominantly show $[210]_{WZ}$ growth, whereas Fe as catalyst leads to the growth along $[100]_{WZ}$.

For the present example of oxynitride solid solution phase heterostructures $(Ga_{1-x}Zn_x)(N_{1-x}O_x)$ with $x = 0.12$, TEM studies on NWs catalytically grown in a VLS process starting from Au particles described crystal growth along $[100]_{WZ}$[62] and intentionally tuning of the crystallographic facets from non-polar to semipolar and polar by controlling temperature and nitridation time.[76]

The structure examination of the present individual single crystal $(Ga_{1-x}Zn_x)(N_{1-x}O_x)$ nanowires in this study revealed growth along the polar $[001]_{WZ}$ and mixed nonpolar $[012]_{WZ}$/$[010]_{WZ}$ crystallographic directions, featuring the formation of kinks. The crystal structure of a kinked NW is further discussed in **Figure 6**. The mechanisms of kink formation and change of growth directions are widely discussed in the literature and can be narrowed down to a perturbation of the trijunction vapor–liquid–solid energies[77] for ZB as well as WZ systems. Hence, the intentional introduction of kinks and switch of the growth direction was reported to be achieved, e.g., by keeping control of the droplet composition,[78] the temperature regime[79] and the growth atmosphere, by regulating the gas pressure or the supply of reactants.[80,81]

In the highly reactive growth environment inside GaN/ZnO microtubes, all those factors possibly take part in multiple kinking events of solid solution NWs. With respect to the nanostructure, the formation of kinks is often accompanied by crystal defects such as stacking faults or twin planes, especially in WZ/ZB heterostructures.[82,83] The kinked NW presented in Figure 6 possesses a large number of stacking faults/twins on the {001}/{111} planes and changes its growth direction from $[010]_{WZ}$ to $[012]_{WZ}$ and back to $[010]_{WZ}$ (red box). We highlight that the crystallographic orientation of $(001)_{WZ}$ planes does not change with respect to the electron beam after the kink but the lamellar stacking faults/twins run down the length of the wire to end at the metal catalyst (green box, Figure 6b).

In fact, the initial control of the supersaturated starting catalyst $Au_{1-x}Ga_x$ has been proven to be an essentially valuable parameter for the growth of unidirectional and pure phase GaAs NWs with minimal defect concentration,[84] hence stable growth conditions could be achieved for operating with a physically stable droplet.[58] Furthermore, the volume of the initial Au droplets does not only determine the NW diameter but also the Ga concentration in the supersaturated droplets differentiating in low-melting-point (AuGa, Au_2Ga, and Au_7Ga_3) and high-melting-point (Au_7Ga_2) catalytic alloys of the binary AuGa system.[61]

In this study, the uncontrolled formation of $Au_{1-x}Ga_x$ binary alloys according to the reaction scheme is supported by the nanoanalytics (see the elemental distribution maps of Au and Ga provided in Figure 4).

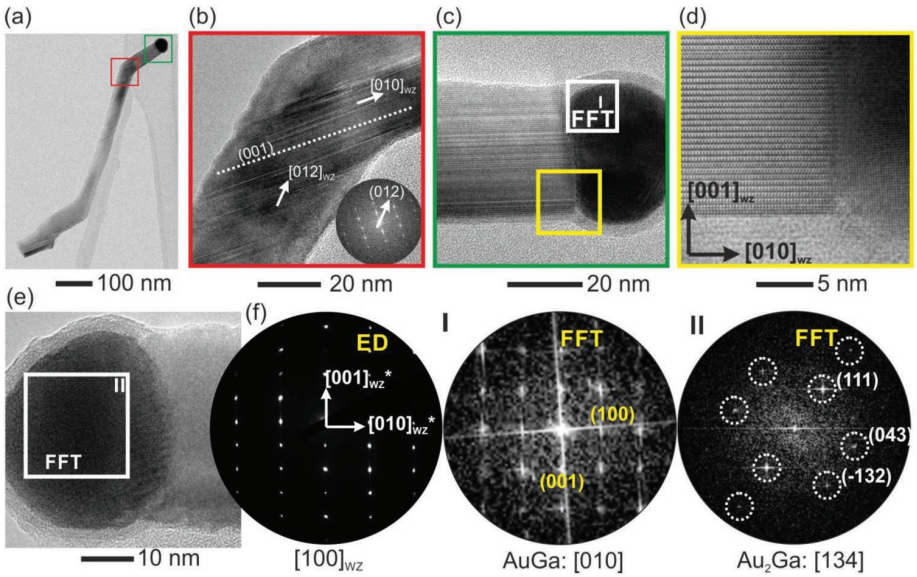

Figure 6. a) Overview image of a kinked NW and b) HRTEM micrograph of the kink region. c–e) HRTEM micrographs showing representative NWs with $Au_{1-x}Ga_x$ catalyst. d) Magnified image shoing the [001]_WZ lattice planes perpendicular to the [010]_WZ growth direction. f) Reciprocal space analysis via electron diffraction from the solid solution NW and FFT from the white framed regions on the $Au_{1-x}Ga_x$ catalyst crystals showing the formation of different AuGa -phases.

ADVANCED SCIENCE NEWS
www.advancedsciencenews.com

NANO · MICRO small
www.small-journal.com

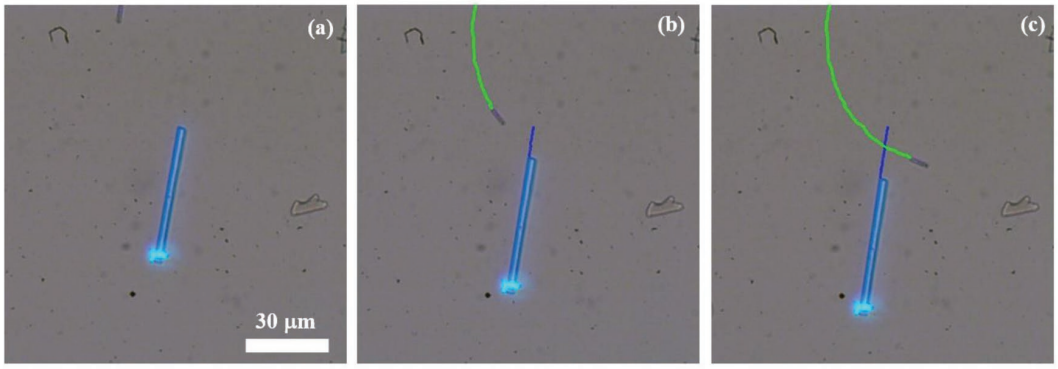

Figure 7. Optical image and corresponding tracking of two microtubes differing essentially in sizes. Motion under UV illumination: a) $t = 0$ s, b) after $t = 5$ s and c) after $t = 9$ s of irradiation. The small microtube is more than four times faster than the big one (5.5 μm s^{-1} compared to 1.4 μm s^{-1}). A 50 W UV power source was used.

Accordingly, the structural characterization via FFTs of HRTEM micrographs illustrated in Figure 6c confirms the existence of the stoichiometric orthorhombic phase AuGa[61] (Figure 6c.I) and the orthorhombic intermetallic γ-phase Au_7Ga_3 (Figure 6c.II), whose structure has been described by Puselj and Schubert in approximation to the Au_2Ga phase.[85] Unfortunately, the direct quantification of the chemical composition of individual catalysts has been restricted by amorphous residues of GaO_x species forming a shell around the alloy observable in Figures 4 and 6b.

2.2. Light-Driven Micromotors

The light-driven motion characteristics of the functionalized nanoarchitectured GaN/ZnO microtubes are demonstrated in aqueous solutions of hydrogen peroxide.

Optical microscopy was utilized to follow two GaN/ZnO microtube-engines operating under UV irradiation (**Figure 7**) and their trajectories were recorded over 9 s (see Movie S2 in the Supporting Information). The investigated microtubes can easily be distinguished by their dimensions, the length and diameter of the larger (smaller) tube are 32 μm (4.6 μm) and 2 μm (0.9 μm), respectively. In order to illustrate the path of the microtubes under UV irradiation, the video files were processed using the ImageJ software. According to the acquired data, the average velocity of the small microtube was ≈5.5 μm s^{-1} while for the larger microtube it was 1.4 μm s^{-1}. The slower velocity of the larger microtube could be assigned to its higher surface area, which results in stronger drag forces in the liquid. Another interesting feature was the blue fluorescence exhibited by the GaN/ZnO microtubes under UV light, which is associated with the presence of a thin ZnO layer on the inner surface of the tube. The UV light-driven motion dynamics can be controlled by the on–off capability of the micromotors. Movie S3 (Supporting Information) shows the abrupt stop of the microtube motion by switching off the UV light accompanied by quenching of the fluorescence. In turn, the motion continues at a steady pace once the UV light was switched on again.

The GaN/ZnO microtubes prepared without gold dots (and thus without the growth of $(Ga_{1-x}Zn_x)(N_{1-x}O_x)$ NWs on the inner surface) do not exhibit light-driven motion in hydrogen peroxide. This control experiment confirms that the presence of metal-dot-terminated NWs inside the GaN/ZnO microtubes plays a major role in creating a strong driving force resulting in the steady motion based on photocatalysis.

The most common propulsion mechanisms of tubular micromotors in hydrogen peroxide are based on bubble formation[36] and diffusiophoresis. Since bubble propulsion is inherent to bigger particles, the dominating mechanism of nanoarchitectured ZnO/GaN micromotor motion can be attributed to diffusiophoresis, which seems to occur mainly at the electrolyte interface with the thin layer of ZnO,[86] in our case decorated by metal-terminated heterogeneous NWs. Until now, ZnO micromotors were considered less applicable, due to the low stability of the material in an aqueous medium, however, the material has a high photocatalytic activity, which makes it promising for environmental applications. In our configuration, the GaN microtubes guarantee high chemical stability of the inner nanometer-thin layer of ZnO, which together with the AuGa-alloy nanodots and heterogeneous NWs accelerate the micromotors via diffusiophoresis generated by the photodegradation of hydrogen peroxide under UV light.

3. Conclusion

Novel hybrid nanoarchitectured GaN/ZnO microtubes with an outer hydrophobic GaN surface and an inner hydrophilic surface of chemically stabilized ZnO decorated by solid solution $(Ga_{1-x}Zn_x)(N_{1-x}O_x)$ NWs, which are terminated by co-catalyst AuGa-alloy nanodots have been developed and characterized extensively by transmission electron microscopy. Our experiments show intense photocatalytic reactions under UV light excitation in the presence of hydrogen peroxide exclusively for decorated microtubes. It has been demonstrated that two microtubes with the lengths of 32 μm and 4.6 μm, and diameters of 2 μm and 0.9 μm, exhibit average velocities of UV-light-driven motion of 1.4 μm s^{-1} and 5.5 μm s^{-1} with switchable on–off capability. The obtained results are in line with literature data arguing that the process of diffusiophoresis could be responsible for the UV-light driven motion of microtubes.

ADVANCED SCIENCE NEWS
www.advancedsciencenews.com

NANO · MICRO small
www.small-journal.com

The GaN/ZnO nanoarchitectured microtubes prove to be very promising for the development of fluorescent micromotors, the fluorescence being generated by the nanoscale-thin ZnO film exhibiting high chemical stability at the interface with GaN. The developed micromotors seem very promising for sensing applications, e.g., by monitoring the fluorescence quenching in the presence of a certain analyte/environment or environmental cleaning by the degradation of organic pollutants by photocatalytic reactions. The presented synthesis approach can be adapted to various morphologies of ZnO microstructures and different metal catalysts, expanding the field of future in-depth studies of architecture-dependent photocatalytic properties with respect to template-based design engineering for device implementation.

4. Experimental Section

Growth Mechanism: In this work, the used hedgehog-like ZnO structures (microneedles) were obtained by a modified flame transport synthesis (FTS) previously reported by Mishra et al.[55] Similar to the FTS process, polyvinyl butane (PVB) and ethanol (purchased from Carl Roth ≥99.8% p.a.) were mixed at a ratio of (2:1). To obtain a bubble-free solution, the mixture was allowed to rest for 14 h. The primary precursor, Zn wire (purchased from Alfa Aesar GmbH & Co KG, Germany) was weighed and dipped into the PVB/ethanol solution. This coated Zn wire was set in a closed ceramic crucible and placed in a muffle furnace, preheated to 500 °C. It was then heated to 950 °C for 20 min. The furnace was cooled to 500 °C before removing the crucible. Once the crucible reached room temperature (20 °C) the ZnO hedgehogs were collected for further experiments. A gold thin film of a few nanometers was deposited on the ZnO microneedles in a Cressington 108 Sputter Coater machine. Subsequently, the samples were exposed to thermal treatment at 300 °C for 1 h in the atmosphere. The thermal treatment leads to the transformation of a continuous Au film into uniformly distributed Au dots. After this decoration step, the ZnO microneedles were used as sacrificial templates for the growth of GaN in an HVPE system. As previously reported,[31] the system is equipped with a four-temperature-zone-heated horizontal reactor, where metallic gallium, ammonia gas and hydrogen chloride gas were used as source materials while hydrogen was used as the carrier gas. The GaCl was formed during the reaction between HCl and Ga in the source zone where the temperature was kept at 850 °C. The formed GaCl was then transported by H_2 gas in the reaction zone where interaction with NH_3 gas at 600 °C for 10 min initiated the nucleation of GaN on the surface of the ZnO microneedles. Then, the temperature was increased up to 850 °C for 10 min to grow a thin GaN layer. In the process of GaN growth, the HCl, NH_3, and H_2 flow rates were equal to 15 500, and 3600 sml min^{-1} (standard mililiters per minute), respectively.

Motion Analysis: To study the motion of the GaN/ZnO microtubes, 10 wt% of H_2O_2 aqueous solution with 1.3 wt% of sodium dodecyl sulfate (SDS) was used. The microtubes were placed in a confined space (cell), specially designed to avoid fluxes associated with solvent evaporation and to provide stable conditions for a reliable analysis of their motion and other related phenomena.

The videos and images of the samples were taken using a Zeiss microscope setup, Zeiss Axio Scope.A1, equipped with a camera, and an EC Plan -Neofluar 40× /0.75 lens. The GaN/ZnO microtubes were irradiated using a 50 W UV light source from the previously mentioned optical microscope.

Structural Characterization: The structural characterization of the GaN/ZnO nanoarchitectured microtubes was performed using the analytical capabilities of transmission electron microscopy. The microscopes used during the study involved a Tecnai F30 STwin (300 kV, field-emission gun, spherical aberration constant C_s = 1.2 mm) and a Philipps CM 30 ST (300 kV, C_s = 1.15 mm). High-resolution TEM and electron diffraction in combination with precession electron diffraction and fast Fourier transform analysis were used to study the crystal structure of the GaN/ZnO microtubes and AuGa-terminated wires. The compositional analysis of the GaN/ZnO microtubes was carried out using energy-dispersive X-ray spectroscopy in combination with TEM and scanning TEM with a high-angle annular dark field detector for imaging. A 3D model of the morphology was computed by STEM tomography using a special single tilt tomography holder to allow for sample tilts in the range of −70° to + 70° minimizing the distortions from the missing wedge. A STEM tomography linear tilt series with a step size of 1° was recorded to compute the reconstruction model, which is based on an algorithm called filtered back projection real space reconstruction.[87,88] The isosurfaces of the volume reconstruction were color-coded to differentiate between the microtubes and wires.

Supporting Information

Supporting Information is available from the Wiley Online Library or from the author.

Acknowledgements

Funding by the German Research Foundation (DFG) within the CRC 1261 is gratefully acknowledged by N.W., M.K., L.K., and V.C., M.E., T.B., R.A., and I.T. acknowledge the support from the Ministry of Education, Culture and Research under the Grant # 15.817.02.29A as well as from the European Commission under the Grant #810652 "NanoMedTwin." S.R. acknowledges the support from the Ministry of Education, Culture, and Research under the Grant #15.817.02.34A. V.C. acknowledges support from the DAAD, Germany, via a research fellowship. N.W. and L.K. acknowledge Prof. Bettina Lotsch for enabling microscope beam time at the Max Planck Institute for Solid State Research.

Conflict of Interest

The authors declare no conflict of interest.

Keywords

hierarchical structures, hybrid materials, photocatalysis, surface modification, transmission electron microscopy

Received: September 9, 2019
Revised: November 13, 2019
Published online:

[1] F. Fresno, R. Portela, S. Suárez, J. M. Coronado, *J. Mater. Chem. A* **2014**, *2*, 2863.
[2] L. Yu, H. B. Wu, X. W. D. Lou, *Acc. Chem. Res.* **2017**, *50*, 293.
[3] A. Huczko, *Appl. Phys. A: Mater. Sci. Process.* **2000**, *70*, 365.
[4] A.-H. Lu, F. Schüth, *Adv. Mater.* **2006**, *18*, 1793.
[5] R. Ryoo, S. H. Joo, S. Jun, *J. Phys. Chem. B* **1999**, *103*, 7743.
[6] T. Kyotani, T. Nagai, S. Inoue, A. Tomita, *Chem. Mater.* **1997**, *9*, 609.
[7] F. Schüth, *Angew. Chem.* **2003**, *115*, 3730.
[8] Q. Wei, Y. Fu, G. Zhang, D. Yang, G. Meng, S. Sun, *Nano Energy* **2019**, *55*, 234.
[9] Z.-X. Cai, Z.-L. Wang, J. Kim, Y. Yamauchi, *Adv. Mater.* **2019**, *31*, 1804903.
[10] H.-H. Li, S.-H. Yu, *Adv. Mater.* **2019**, *31*, 1803503.
[11] Y. K. Mishra, R. Adelung, *Mater. Today* **2018**, *21*, 631.

ADVANCED SCIENCE NEWS
www.advancedsciencenews.com

NANO · MICRO small
www.small-journal.com

[12] I. Hölken, G. Neubüser, V. Postica, L. Bumke, O. Lupan, M. Baum, Y. K. Mishra, L. Kienle, R. Adelung, *ACS Appl. Mater. Interfaces* **2016**, *8*, 20491.
[13] M. Mecklenburg, A. Schuchardt, Y. K. Mishra, S. Kaps, R. Adelung, A. Lotnyk, L. Kienle, K. Schulte, *Adv. Mater.* **2012**, *24*, 3486.
[14] F. Schütt, S. Signetti, H. Krüger, S. Röder, D. Smazna, S. Kaps, S. N. Gorb, Y. K. Mishra, N. M. Pugno, R. Adelung, *Nat. Commun.* **2017**, *8*, 1215.
[15] I. Tiginyanu, T. Braniste, D. Smazna, M. Deng, F. Schütt, A. Schuchardt, M. A. Stevens-Kalceff, S. Raevschi, U. Schürmann, L. Kienle, N. M. Pugno, Y. K. Mishra, R. Adelung, *Nano Energy* **2019**, *56*, 759.
[16] J. Goldberger, R. He, Y. Zhang, S. Lee, H. Yan, H.-J. Choi, P. Yang, *Nature* **2003**, *422*, 599.
[17] T. Detchprohm, K. Hiramatsu, H. Amano, I. Akasaki, *Appl. Phys. Lett.* **1992**, *61*, 2688.
[18] H. J. Fan, F. Fleischer, W. Lee, K. Nielsch, R. Scholz, M. Zacharias, U. Gösele, A. Dadgar, A. Krost, *Superlattices Microstruct.* **2004**, *36*, 95.
[19] C.-H. Chen, S.-J. Chang, S.-P. Chang, M.-J. Li, I.-C. Chen, T.-J. Hsueh, C.-L. Hsu, *Chem. Phys. Lett.* **2009**, *476*, 69.
[20] M.-C. Jeong, B.-Y. Oh, M.-H. Ham, S.-W. Lee, J.-M. Myoung, *Small* **2007**, *3*, 568.
[21] H. Chen, Q. Zhao, X. Du, *Micromachines* **2018**, *9*, 41.
[22] M. Enachi, M. Guix, V. Postolache, V. Ciobanu, V. M. Fomin, O. G. Schmidt, I. Tiginyanu, *Small* **2016**, *12*, 5497.
[23] R. Dong, C. Wang, Q. Wang, A. Pei, X. She, Y. Zhang, Y. Cai, *Nanoscale* **2017**, *9*, 15027.
[24] M. Asif Khan, J. N. Kuznia, J. M. Van Hove, D. T. Olson, S. Krishnankutty, R. M. Kolbas, *Appl. Phys. Lett.* **1991**, *58*, 526.
[25] T. Kawashima, H. Yoshikawa, S. Adachi, S. Fuke, K. Ohtsuka, *J. Appl. Phys.* **1997**, *82*, 3528.
[26] H. S. Jung, Y. J. Hong, Y. Li, J. Cho, Y.-J. Kim, G.-C. Yi, *ACS Nano* **2008**, *2*, 637.
[27] Y. K. Lim, E. W. Keong Koh, Y.-W. Zhang, H. Pan, *J. Power Sources* **2013**, *232*, 323.
[28] B. Ren, X. Zhang, M. Zhao, X. Wang, J. Ye, D. Wang, *AIP Adv.* **2018**, *8*, 015206.
[29] A. Wu, J. Li, B. Liu, W. Yang, Y. Jiang, L. Liu, X. Zhang, C. Xiong, X. Jiang, *Dalton Trans.* **2017**, *46*, 2643.
[30] J. P. Sundararajan, P. Bakharev, I. Niraula, B. A. Fouetio Kengne, Q. MacPherson, M. Sargent, B. Hare, D. N. McIlroy, *Nano Lett.* **2012**, *12*, 5181.
[31] F. Qin, N. Chang, C. Xu, Q. Zhu, M. Wei, Z. Zhu, F. Chen, J. Lu, *RSC Adv.* **2017**, *7*, 15071.
[32] M. Medina-Sánchez, O. G. Schmidt, *Nature* **2017**, *545*, 406.
[33] J. Li, I. Rozen, J. Wang, *ACS Nano* **2016**, *10*, 5619.
[34] W. F. Paxton, S. Sundararajan, T. E. Mallouk, A. Sen, *Angew. Chem., Int. Ed.* **2006**, *45*, 5420.
[35] W. F. Paxton, K. C. Kistler, C. C. Olmeda, A. Sen, S. K. St. Angelo, Y. Cao, T. E. Mallouk, P. E. Lammert, V. H. Crespi, *J. Am. Chem. Soc.* **2004**, *126*, 13424.
[36] A. A. Solovev, Y. Mei, E. B. Ureña, G. Huang, O. G. Schmidt, *Small* **2009**, *5*, 1688.
[37] J. R. Howse, R. A. L. Jones, A. J. Ryan, T. Gough, R. Vafabakhsh, R. Golestanian, *Phys. Rev. Lett.* **2007**, *99*, 048102.
[38] M. Su, V. P. Dravid, *Nano Lett.* **2005**, *5*, 2023.
[39] F. Mou, Y. Li, C. Chen, W. Li, Y. Yin, H. Ma, J. Guan, *Small* **2015**, *11*, 2564.
[40] R. Dong, Y. Cai, Y. Yang, W. Gao, B. Ren, *Acc. Chem. Res.* **2018**, *51*, 1940.
[41] I. Buttinoni, G. Volpe, F. Kümmel, G. Volpe, C. Bechinger, *J. Phys.: Condens. Matter* **2012**, *24*, 284129.
[42] L. Xu, F. Mou, H. Gong, M. Luo, J. Guan, *Chem. Soc. Rev.* **2017**, *46*, 6905.
[43] S. Sanchez, A. N. Ananth, V. M. Fomin, M. Viehrig, O. G. Schmidt, *J. Am. Chem. Soc.* **2011**, *133*, 14860.
[44] R. Dong, Q. Zhang, W. Gao, A. Pei, B. Ren, *ACS Nano* **2016**, *10*, 839.
[45] S. Jeon, S. Kim, S. Ha, S. Lee, E. Kim, S. Y. Kim, S. H. Park, J. H. Jeon, S. W. Kim, C. Moon, B. J. Nelson, J. Kim, S.-W. Yu, H. Choi, *Sci. Rob.* **2019**, *4*, eaav4317.
[46] B. E.-F. de Ávila, P. Angsantikul, J. Li, M. A. Lopez-Ramirez, D. E. Ramírez-Herrera, S. Thamphiwatana, C. Chen, J. Delezuk, R. Samakapiruk, V. Ramez, M. Obonyo, L. Zhang, J. Wang, *Nat. Commun.* **2017**, *8*, 272.
[47] M. Medina-Sánchez, L. Schwarz, A. K. Meyer, F. Hebenstreit, O. G. Schmidt, *Nano Lett.* **2016**, *16*, 555.
[48] S. Balasubramanian, D. Kagan, C.-M. Jack Hu, S. Campuzano, M. J. Lobo-Castañon, N. Lim, D. Y. Kang, M. Zimmerman, L. Zhang, J. Wang, *Angew. Chem., Int. Ed.* **2011**, *50*, 4161.
[49] J. Li, V. V. Singh, S. Sattayasamitsathit, J. Orozco, K. Kaufmann, R. Dong, W. Gao, B. Jurado-Sanchez, Y. Fedorak, J. Wang, *ACS Nano* **2014**, *8*, 11118.
[50] B. Jurado-Sánchez, J. Wang, *Environ. Sci.: Nano* **2018**, *5*, 1530.
[51] L. Wang, A. Kaeppler, D. Fischer, J. Simmchen, *ACS Appl. Mater. Interfaces* **2019**, *11*, 32937.
[52] S. K. Srivastava, M. Guix, O. G. Schmidt, *Nano Lett.* **2016**, *16*, 817.
[53] L. Soler, V. Magdanz, V. M. Fomin, S. Sanchez, O. G. Schmidt, *ACS Nano* **2013**, *7*, 9611.
[54] M. Guix, J. Orozco, M. García, W. Gao, S. Sattayasamitsathit, A. Merkoçi, A. Escarpa, J. Wang, *ACS Nano* **2012**, *6*, 4445.
[55] Y. K. Mishra, S. Kaps, A. Schuchardt, I. Paulowicz, X. Jin, D. Gedamu, S. Freitag, M. Claus, S. Wille, A. Kovalev, S. N. Gorb, R. Adelung, *Part. Part. Syst. Charact.* **2013**, *30*, 775.
[56] S. Bals, S. Van Aert, G. Van Tendeloo, *Curr. Opin. Solid State Mater. Sci.* **2013**, *17*, 107.
[57] P. A. Midgley, M. Weyland, *Ultramicroscopy* **2003**, *96*, 413.
[58] S. N. Mohammad, *Nano Lett.* **2008**, *8*, 1532.
[59] D. Elwell, M. M. Elwell, *Prog. Cryst. Growth Charact.* **1988**, *17*, 53.
[60] V. Gottschalch, G. Wagner, J. Bauer, H. Paetzelt, M. Shirnow, *J. Cryst. Growth* **2008**, *310*, 5123.
[61] C. J. Cooke, W. Hume-Rothery, *J. Less-Common Met.* **1966**, *10*, 42.
[62] W.-Q. Han, Y. Zhang, C.-Y. Nam, C. T. Black, E. E. Mendez, *Appl. Phys. Lett.* **2010**, *97*, 083108.
[63] P. A. Midgley, A. S. Eggeman, *IUCrJ* **2015**, *2*, 126.
[64] K. A. Dick, P. Caroff, J. Bolinsson, M. E. Messing, J. Johansson, K. Deppert, L. R. Wallenberg, L. Samuelson, *Semicond. Sci. Technol.* **2010**, *25*, 024009.
[65] P. Caroff, K. A. Dick, J. Johansson, M. E. Messing, K. Deppert, L. Samuelson, *Nat. Nanotechnol.* **2009**, *4*, 50.
[66] L. López-Conesa, J. A. Pérez-Omil, Ž. Gačević, E. Calleja, S. Estradé, F. Peiró, *Phys. Status Solidi A* **2018**, *215*, 1800218.
[67] A. Trampert, O. Brandt, K. H. Ploog, *Angew. Chem.* **1997**, *109*, 2202.
[68] T. Lei, K. F. Ludwig, T. D. Moustakas, *J. Appl. Phys.* **1993**, *74*, 4430.
[69] B. M. Shi, M. H. Xie, H. S. Wu, N. Wang, S. Y. Tong, *Appl. Phys. Lett.* **2006**, *89*, 151921.
[70] G. Jacopin, L. Rigutti, L. Largeau, F. Fortuna, F. Furtmayr, F. H. Julien, M. Eickhoff, M. Tchernycheva, *J. Appl. Phys.* **2011**, *110*, 064313.
[71] D. Tham, C.-Y. Nam, J. E. Fischer, *Adv. Funct. Mater.* **2006**, *16*, 1197.
[72] M. Heiss, S. Conesa-Boj, J. Ren, H.-H. Tseng, A. Gali, A. Rudolph, E. Uccelli, F. Peiró, J. R. Morante, D. Schuh, E. Reiger, E. Kaxiras, J. Arbiol, A. Fontcuberta i Morral, *Phys. Rev. B* **2011**, *83*, 045303.
[73] J. Arbiol, S. Estradé, J. D. Prades, A. Cirera, F. Furtmayr, C. Stark, Andreas Laufer, M. Stutzmann, M. Eickhoff, M. H. Gass, A. L. Bleloch, F. Peiró, J. R. Morante, *Nanotechnology* **2009**, *20*, 145704.

ADVANCED SCIENCE NEWS
www.advancedsciencenews.com

NANO · MICRO small
www.small-journal.com

[74] T. Kuykendall, P. J. Pauzauskie, Y. Zhang, J. Goldberger, D. Sirbuly, J. Denlinger, P. Yang, *Nat. Mater.* **2004**, *3*, 524.
[75] T. Kuykendall, P. Pauzauskie, S. Lee, Y. Zhang, J. Goldberger, P. Yang, *Nano Lett.* **2003**, *3*, 1063.
[76] J. Li, B. Liu, W. Yang, Y. Cho, X. Zhang, B. Dierre, T. Sekiguchi, A. Wu, X. Jiang, *Nanoscale* **2016**, *8*, 3694.
[77] K. W. Schwarz, J. Tersoff, *Nano Lett.* **2011**, *11*, 316.
[78] J. Wang, S. R. Plissard, M. A. Verheijen, L.-F. Feiner, A. Cavalli, E. P. A. M. Bakkers, *Nano Lett.* **2013**, *13*, 3802.
[79] X. Yang, B. Zhou, C. Liu, Y. Sui, G. Xiao, Y. Wei, X. Wang, B. Zou, *Nano Res.* **2017**, *10*, 2311.
[80] I. R. Musin, M. A. Filler, *Nano Lett.* **2012**, *12*, 3363.
[81] B. Tian, P. Xie, T. J. Kempa, D. C. Bell, C. M. Lieber, *Nat. Nanotechnol.* **2009**, *4*, 824.
[82] F. M. Davidson, D. C. Lee, D. D. Fanfair, B. A. Korgel, *J. Phys. Chem. C* **2007**, *111*, 2929.
[83] R. E. Algra, M. A. Verheijen, M. T. Borgström, L.-F. Feiner, G. Immink, W. J. P. van Enckevort, E. Vlieg, E. P. A. M. Bakkers, *Nature* **2008**, *456*, 369.
[84] N. Han, F. Wang, J. J. Hou, S. Yip, H. Lin, M. Fang, F. Xiu, X. Shi, T. Hung, J. C. Ho, *Cryst. Growth Des.* **2012**, *12*, 6243.
[85] M. Pušelj, K. Schubert, *J. Less-Common Met.* **1974**, *38*, 83.
[86] A. M. Pourrahimi, K. Villa, Y. Ying, Z. Sofer, M. Pumera, *ACS Appl. Mater. Interfaces* **2018**, *10*, 42688.
[87] P. A. Penczek, in *Methods in Enzymology* (Ed.: G. J. Jensen), Academic Press, San Diego, CA **2010**, pp. 1–33.
[88] D. Wolf, A. Lubk, H. Lichte, *Ultramicroscopy* **2014**, *136*, 15.

4.1.5 2D Transition-Metal Dichalcogenides: Few-layer $MoSe_2$

The interest of the materials science community in two dimensional (2D) materials emerged with the successful exfoliation of single layer carbon sheets "graphene" in the year 2004 and led to tremendous research progress in graphene and graphene-like ultrathin 2D nanomaterials and heterostructures, which is impossible to review completely these days.[217], [218] In this broad range of fascinating candidates 2D transition-metal dichalcogenides (TMDs) have emerged showing remarkable properties for a wide range of potential applications in (opto)electronics,[219] flexible devices,[220] energy storage,[221] and field effect transistors for e.g. nonvolatile memory applications[222] to list just a few. Further ground-breaking applications are enabled by the violation of inversion symmetry when downscaling from 3D to 2D materials. That is known to introduce piezoelectricity in TMD sheets as demonstrated for single and odd-numbered MoS_2 layered films[223] and can be generalized to other TMDs and their heterostructures.[224]
One of these TMDs is $MoSe_2$ which crystallizes in a hexagonal lattice (spacegroup: $P6_3mmc$) with two formula units per unit cell and trigonal prismatic coordination of (Mo^{IV}) and pyramidal coordination of (Se^{2-}). The layered structure favors strong in-plane bonding but weak out-of-plane van-der-Waals (vdW) interaction between single layers.[225] A sketch of the structure is shown in Figure 4.2. The weak vdW bonding between single layers results in the in-plane rotational freedom between layers if the bonding forces are very weak and results in vertical aligned domains with identical rotation-symmetric orientated lattices if the bonding forces are strong.
In the following study the magnitude of these interlayer bonding forces was analyzed for an 8-layer $MoSe_2$ film using TEM. The degree of ordering was examined in context of ultralow thermal conductivity for thermoelectric application. The background of the methodological approach is further discussed in addition to the structural investigation performed in the study on **ultralow thermal conductivity of turbostratically disordered $MoSe_2$ ultra-thin films and implication for heterostructures** which was published in Nanotechnology.[7][226]

Instrumentation and Methods

The microscopic plan-view examinations of 8-layer $MoSe_2$ thin films have been performed on a Titan 80-300 TEM with field emission electron source using 300 kV acceleration voltage. Nanobeam electron diffraction (NBED) data was collected on a TitanX 60-300 microscope using a parallel illumination with a 8 nm diameter electron beam at the National Center for Electron Microscopy at Lawrence Berkeley National Lab[8].

Sample Preparation

Cross-section specimens were prepared by focused ion beam (FIB) milling using the FEI Helios 600i Dual-Beam FIB SEM, whereas plan-view specimens were prepared on copper grids by a rupture technique which was developed for layered and disordered misfit compounds.[227]

[7] Reproduced from Nanotechnology 30, 285401 (2019) with the permission of IOP Publishing. The Version of Record is available online at https://doi.org/10.1088/1361-6528/aafea2.

[8] Experiments were conducted in presence of co-author Robert Fischer and operator Christoph Gammer

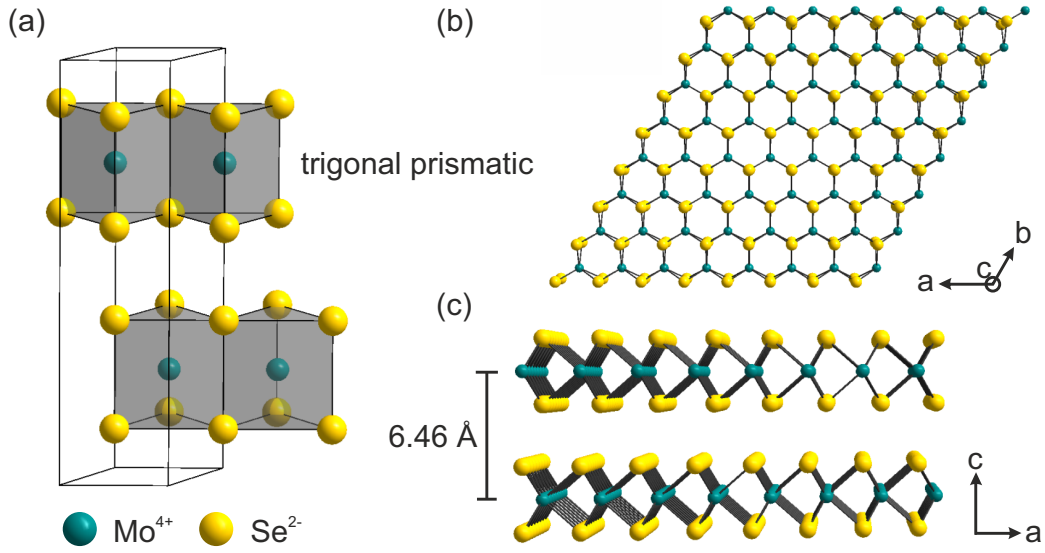

FIGURE 4.2: Schematic representation of the $MoSe_2$ crystal structure. (a) Unit cell with trigonal prismatic Mo-coordination polyhedra (b) top view of a monolayer, (c) lateral view.

The details of this preparation are summarized in Figure 4.3.

Discussion

In case of turbostratically disordered 2D materials like $MoSe_2$ with domain sizes in the range of tens of nanometers, the application of conventional selected area electron diffraction to determine the degree of order is crucial due to the large illumination cross-section which is not adapted to the structure size using conventional apertures with diameters of 250 nm down to 100 nm. The experimental procedure used in this study is sketched in Figure 4.4. On the present material system SAED gives rise to high intensity but smooth diffraction rings having radii corresponding to the interplanar spacing of lattice planes in [0001] zone axis orientation. The homogeneous intensity distribution confined to diffraction rings indicates the in-plane rotational freedom of nanoscale-sized grains. NBED patterns were recorded in STEM mode on a 25x25 grating described by 10 nm stepsize and 8 nm beam diameter. A representative NBED pattern contains enhanced localized information, however is not capable to picture the nanostructural features. These experiments indicate that strong rotational disorder is present but locally order between layers prevails to a certain extend. As an outcome of the TEM experiments in 8-layer $MoSe_2$, local rotational ordering confined to small domains are present as observed using the Fast Fourier Transforms of HRTEM micrographs. The FFT analysis allows for sampling areas as small as 25 nm^2 and therefore to detect rotational variants within the limits of the FFT resolution and its intensity distribution calculated from very small areas. The above argument becomes more clear with the schematic example presented in Figure 4.5, demonstrating showcases of rotational order between single layers. Illustrations of the atomic structure of layered material in cross-section view and schematic hexagon pattern in top view are presented together with examples of FFT patterns extracted from the whole illustrated area. The degree of order is increasing from examples 4.5a to 4.5c. The illustrated scenario in 4.5a depicts complete disorder between the four layers. The reciprocal space data which can be obtained either by NBED or FFT depicts a spot pattern with four distinct orientations of hexagons observed along the [001] direction. Scenario 4.5b depicts two smaller domains

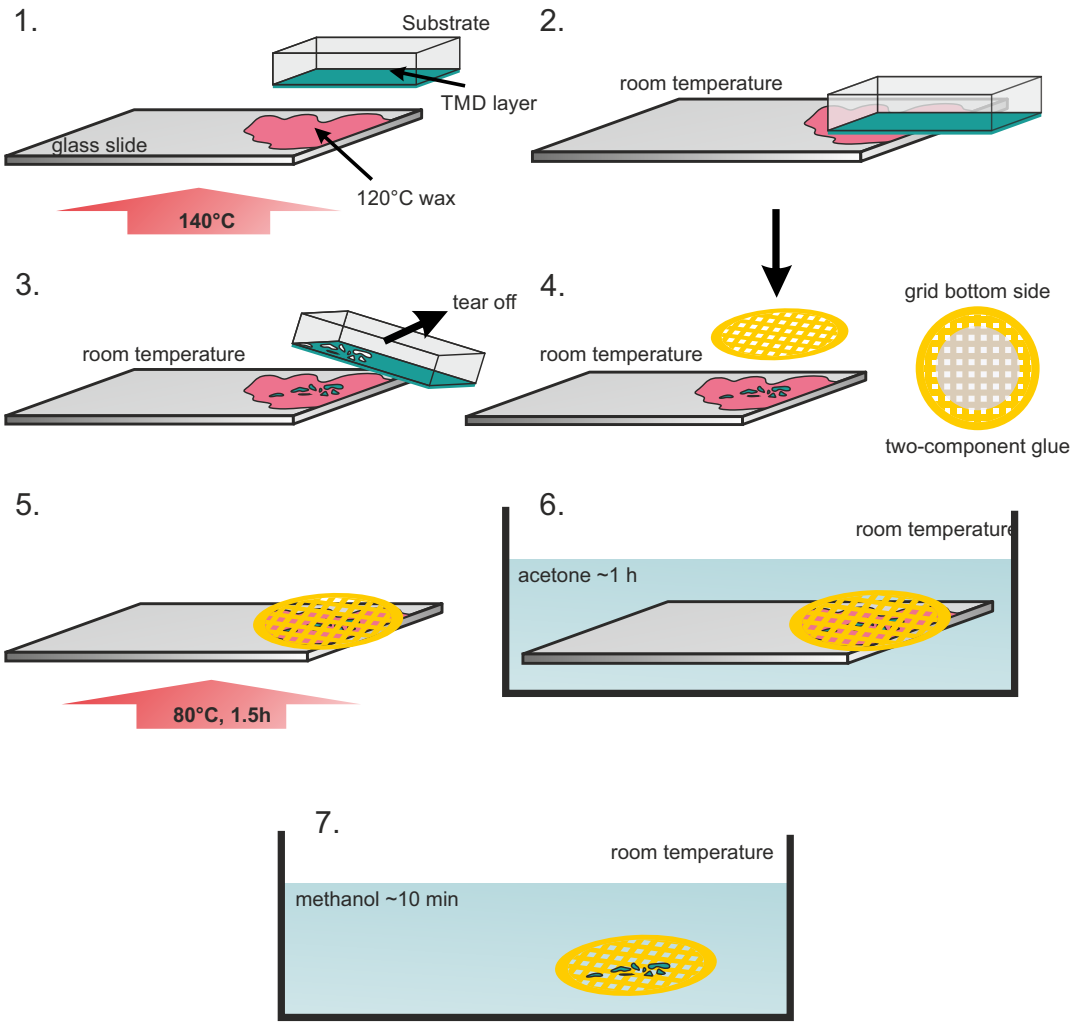

FIGURE 4.3: Preparation recipe of few-layer $MoSe_2$ films on Cu-TEM grids: 1.) Melt the wax (Gatan Mounting Wax (Prod. 623), $T_{melt} = 120\,^{\circ}C$) on a glass slide at $140\,^{\circ}C$ Press the sample into the molten wax. 2.) Let the wax cool down to room temperature. 3.) Tear off the specimen from the glass, parts of the sample will stick to the wax due to the low adhesion forces between single layers or to the substrate. 4.) Apply two-component (VISHAY M-Bond 610, or better non-toxic glues) glue onto one side of a Cu-grid without a carbon film with a sharpened stick or a single hair of a brush. Avoid any glue in the mesh. Place the grid onto the wax at the position where the sample stuck to it. 5.) Let the two-component glue harden at $80\,^{\circ}C$ for 1.5 h. 6.) Put the glass slide with the sample into an acetone bath for 1h to dissolve the wax. 7.) Clean the sample with methanol to remove acetone.

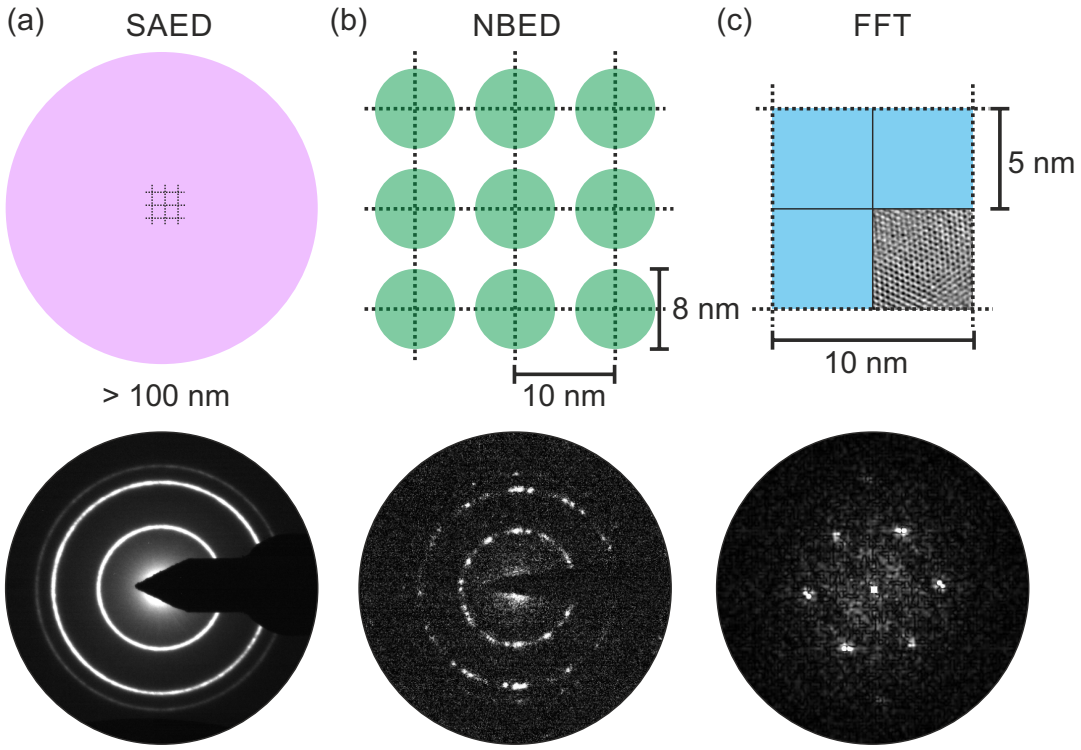

FIGURE 4.4: Degree of rotational disorder in 8-layer $MoSe_2$ films observed using reciprocal space methods with converging real space dimensions: a) SAED, b) NBED, c) FFT. [Taken from [226]]

in which the layers are rotational aligned but the domains have different order with respect to the other. For that case, the NBED technique with its limited spatial resolution is not capable to resolve both single ordered domains but will show a superposition pattern in congruence to the depicted FFT example in top-view. A FFT from a small enough region however can extract information from smaller areas and would be able to resolve both domains as a single hexagon spot pattern as shown in 4.5c. For the latter examples, the real-space information is of course also directly obtained from the phase-contrast HRTEM images. In conclusion, the interpretation of rotational disordered materials is challenging and requires analysis techniques which offer about the identical resolution as the dimensions of the features to investigate. Hence, a FFT analysis which offers the analysis of nanoscale ordered domains in the order of 25 nm^2 was chosen for the investigation of disorder in 8-layer $MoSe_2$ thin films. The FFT analysis is principally congruent to Automated Crystal Orientation Mapping (ACOM)[228] in which NBED pattern are analysed with respect to the crystal orientation and displayed in colored orientation maps, but on a smaller scale. However, in case of a superposition of multiple grains with different rotational order, the ACOM technique is not suitable since it was developed for polycrystalline films with distinct orientation per grain. In this study, a HRTEM micrograph was sectioned into 25 nm^2 squares and the FFTs were calculated and evaluated with respect to the hexagonal shaped [001]-intensity pattern. Immediate inspection of the hexagon patterns resulted in a first conclusion, namely that the hexagon count is often limited to 1-3, which might indicate certain rotational alignment between adjacent layers. Complete disorder would give rise to the superposition of up to 8 patterns on a statistical basis. However, the manual identification of equally rotated hexagons is not prone to human error, since a clear differentiation of the degree of rotation within less than 3° is

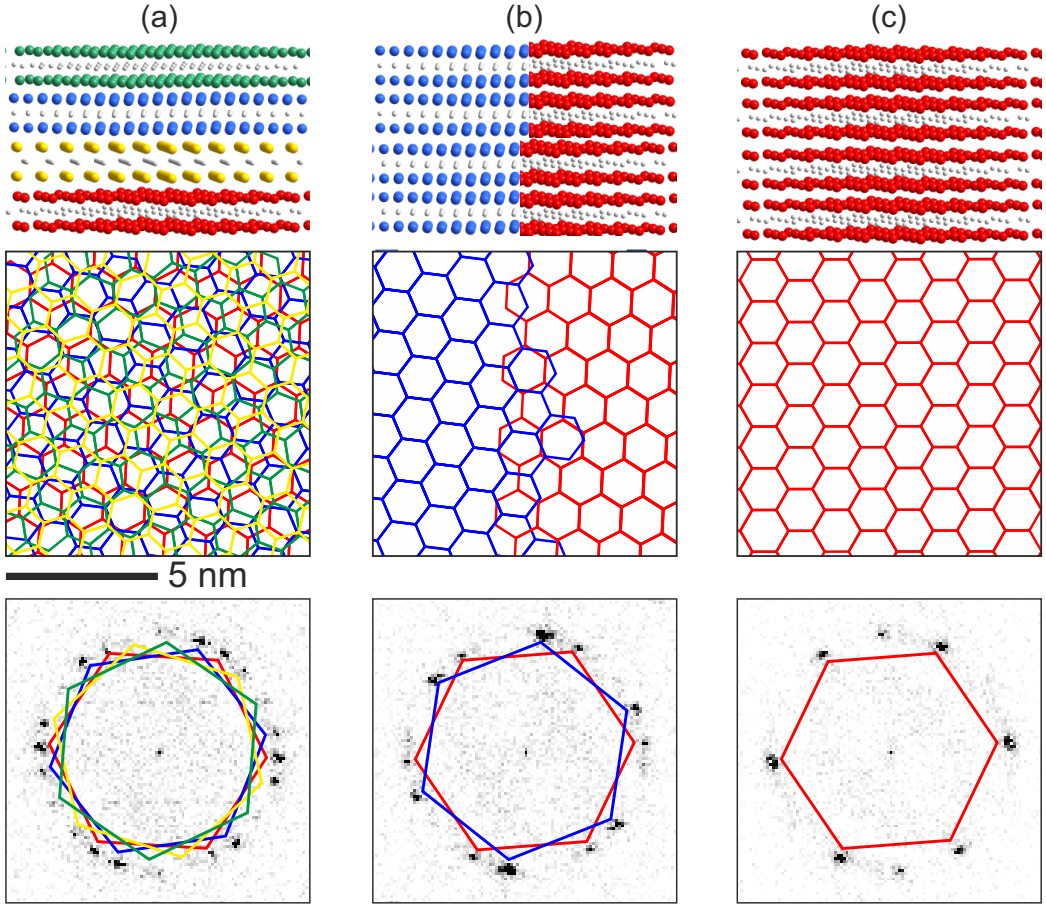

FIGURE 4.5: Showcases of order/disorder phenomena between layers of $MoSe_2$ depicting illustrations of: the atomic structure, superposition pattern arising in HRTEM images and superposition FFTs. Note, the FFT shown in c) partially displays intensity of a second component, since the single domains are smaller than 5 nm x5 nm used for calculating the FFT.

challenging and limited by the FFT resolution. According to the following publication,[226] a representative HRTEM micrograph sectioned into 3x3 FFTs and the color map depicting the amount of rotational aligned intensity spot patterns calculated within one FFT square are presented in Figure 4.6. In this example, the hexagon spot patterns given a green and yellow color were identified in almost all calculated FFTs. Since the corresponding HRTEM phase contrast image does not show clearly separated regions of hexagonal patterned contrast, it is deduced that the green and yellow domains vertically superimpose. The three dimensional component, e.g. the number of rotational aligned layers cannot be retrieved from FFT data due to the influence of various parameters on the image intensity such as the contrast transfer function (CTF) of the microscope.

In summary, the extensive structural characterization presented in our study demonstrates the general rotational misalignment between individual layers, but indicates certain cross-layer ordering on the nanoscale. However, turbostratical disorder creates a very anisotropic environment in the x-y plane for chalcogens in 2D layered dichalcogenides as the chalcogen atom looses its trigonal prismatic coordination compared to bulk crystals implying weak bonding forces in between layers. The loosely bound interface-rich structure invites the incorporation of dopants for electrical property engineering, e.g. bandgap engineering to achieve n- or p-type conduction. Especially in single layers when all atoms contribute to the surface,

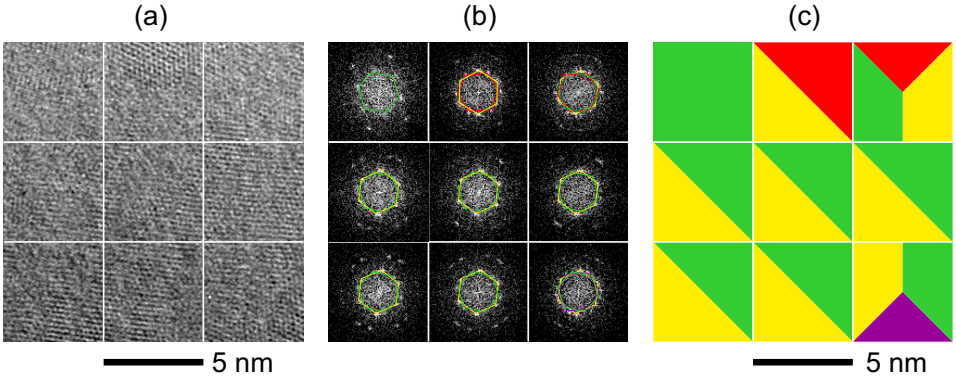

FIGURE 4.6: Example of the FFT mapping procedure. (a) HRTEM micrograph sectioned into 25 nm^2 squares, (b) corresponding FFT showing 1-3 hexagonal intensity pattern and (c) map of vertical rotational aligned domains in 8-layer $MoSe_2$.[Adapted from [226]]

the proper surface modification by dopants and compensating defects implies huge potential for piezoelectric property tuning and application of TMDs in integrated circuits.[229] For example, Niobium doping of $MoSe_2$ on an interstitial site shifts the Fermi energy towards the conduction band resulting in n-type conduction [230] and the curing of native S-vacancies in MoS_2 can increase the piezoelectric coefficient.[231] In this context, state of the art high-resolution imaging methods of STEM in combination with single-atom resolution analytical methods such as EELS will provide a detailed understanding of doping physics with support of computational models.[232], [233]

IOP Publishing Nanotechnology
Nanotechnology 30 (2019) 285401 (9pp) https://doi.org/10.1088/1361-6528/aafea2

Ultralow thermal conductivity of turbostratically disordered $MoSe_2$ ultra-thin films and implications for heterostructures

Erik C Hadland[1], Hyejin Jang[2], Niklas Wolff[3], Robert Fischer[1], Alexander C Lygo[1], Gavin Mitchson[1], Dongyao Li[2], Lorenz Kienle[3], David G Cahill[2] and David C Johnson[1]

[1] Materials Science Institute and Department of Chemistry, University of Oregon, Eugene, OR, United States of America
[2] Department of Materials Science and Engineering and Materials Research Laboratory, University of Illinois at Urbana-Champaign, Urbana, IL, United States of America
[3] Institute for Materials Science, Kiel University, Kiel, Germany

E-mail: davej@uoregon.edu

Received 13 November 2018, revised 28 December 2018
Accepted for publication 15 January 2019
Published 25 April 2019

Abstract

Films containing 8, 16, 24, 32 and 64 $MoSe_2$ layers were synthesized using the modulated elemental reactants method. X-ray reflectivity patterns showed that the annealed films were the targeted number of $MoSe_2$ layers thick with atomically smooth interfaces. In-plane x-ray diffraction (XRD) scans contained only *hk*0 reflections for crystalline $MoSe_2$ monolayers. Specular XRD patterns contained only 00*l* reflections, also indicating that the *hk*0 plane of the $MoSe_2$ layers are parallel to the substrate. Both XRD and electron microscopy techniques indicated that the *hk*0 planes are rotationally disordered with respect to one another, with all orientations equally probable for large areas. The rotational disorder between $MoSe_2$ layers is present even when analyzed spots are within 10 nm of one another. Cross-plane thermal conductivities of 0.07–0.09 W m^{-1} K^{-1} were measured by time domain thermoreflectance, with the thinnest films exhibiting the lowest conductivity. The structural analysis suggests that the ultralow thermal conductivity is a consequence of rotational disorder, which increases the separation between $MoSe_2$ layers. The bonding environment of the Se atoms also becomes significantly distorted from C_{3v} symmetry due to the rotational disorder between layers. This structural disorder efficiently reduces the group velocity of the transverse phonon modes but not that of longitudinal modes. Since rotational disorder between adjacent layers in heterostructures is expected if the constituents have incommensurate lattices, this study indicates that these heterostructures will have very low cross-plane thermal conductivity.

Supplementary material for this article is available online

Keywords: TMDs, molybdenum diselenide, thermal conductivity, heterostructures, rotational disorder, turbostratic disorder

(Some figures may appear in colour only in the online journal)

1. Introduction

In the past decade, van der Waals heterostructures have attracted significant research interest [1–4] due to emergent optoelectronic [5–7] magnetic [8, 9] topological [10–12] and catalytic [13] properties that arise when two or more nanosheets are assembled in a stacked configuration. Depending on the selected constituents, layers can either operate relatively independent of one another [14] or states may be coupled to create novel or modified behavior

[5, 15, 16]. The modular design of heterostructures enables researchers to vary the constituents, layer thicknesses or stacking sequence to tune a targeted property [2]. More recently there have been efforts to understand more precisely how the rotation angle between layers affects properties and gives rise to extended in-plane structural and electronic superlattices (i.e. Moiré lattices). In transition metal dichalcogenide systems, phenomena dependent on rotation angle include carrier lifetime, collection efficiency, band gap and structural modulations [17–21]. These investigations are particularly relevant to nanoelectronics, where the interactions between constituents become more important as interfaces become a larger fraction of devices [22].

While electronic, optical, and structural changes in single layers and heterostructures of van der Waals materials have been widely studied, there has been much less emphasis on thermal properties. Thermal conductivity between dissimilar materials is an important design parameter in many applications, with high thermal conductivity desired for some (heat dissipation in electronics) and low thermal conductivity desired for others (thermoelectric materials). Theoretical and experimental investigations of the in-plane thermal transport properties of monolayers of transition metal dichalcogenides have yielded a range of in-plane thermal conductivity values for MoS_2 and $MoSe_2$ ($\sim$50–100 W m^{-1} K^{-1}) [23–36]. Reported cross-plane thermal conductivities are significantly lower ($\sim$1–4 W m^{-1} K^{-1}), reflecting the weak van der Waals bonding between dichalcogenide layers [37]. There are only a few reports on the interfacial thermal conductance between dichalcogenides and substrates or between dichalcogenides and other 2D materials in heterostructures [38–43]. There are conflicting reports of the thermal conductivity of Bi_2Te_3–Sb_2Te_3 intergrowths [44–46]. These samples were also structurally ill defined, however, and the degree of intermixing of the cations was not defined in the different samples measured [47]. The small number of reports of the thermal conductivity of van der Waals superlattices is mainly due to the synthetic challenges in preparing these structures via epitaxial growth techniques [48].

The weak van der Waals bonding across the interface also creates the opportunity for an arbitrary rotational angle between two constituents in heterostructures, which significantly impacts physical properties including thermal conductivity. Very low thermal conductivity (0.2 W m^{-1} K^{-1}) has been reported for heterostructures with periodic $TiTe_2$–Bi_2Te_3 layers with significant rotational disorder between the constituents [49]. Chiritescu *et al* reported a 30-fold reduction in cross-plane thermal conductivity in WSe_2 compared to bulk single crystal WSe_2 due to significant rotational disorder [50]. Surprisingly, significantly higher cross-plane thermal conductivity has been reported in TMDs with extensive defects and non-planar sheets [51]. Electron microscopy studies of the WSe_2 samples used by Chiritescu also indicated extensive defects and non-planar sheets, raising questions as to the cause of the ultralow thermal conductivity [52]. As we discuss in more detail below, we now believe that these early microscopy results were affected by artifacts created by the methods used to prepare the electron microscopy specimens.

In this work we present the synthesis, in-depth structural characterization, and cross-plane thermal conductivity and speeds of sound analysis of $MoSe_2$ ultra-thin films with targeted thicknesses. Specular x-ray diffraction (XRD) analysis indicates that the films are crystallographically aligned to the substrate and uniform in thickness over a large area ($\sim$2 cm $\times$ 2 cm). The spacing between $MoSe_2$ layers (0.6531 (2) nm) is larger than that reported for the crystalline polymorphs ($\sim$0.646(1) nm) for 2H, 3R, or 4H $MoSe_2$) [53–57]. The measured film thickness is consistent with the targeted integer number of $MoSe_2$ layers. In-plane diffraction reveals only *hk*0 reflections of crystalline $MoSe_2$ and indicates that the $MoSe_2$ grains are randomly orientated with grain sizes on the order of 10–100 nm. The in-plane lattice parameter is consistent with that reported for single crystals and powders of $MoSe_2$ prepared at high temperatures. Cross section high angle annular dark field high-resolution scanning transmission electron microscopy (HAADF HRSTEM) reveals flat and parallel $MoSe_2$ layers with the targeted number of $MoSe_2$ layers. Plan view transmission electron diffraction patterns indicate that the layers are rotationally disordered from one another. Nanobeam electron diffraction (NBED) patterns and Fourier transform analysis of HRTEM micrographs indicate that the orientations of the layers change over a 10 nm length scale. In-plane electrical conductivity measurements show an activated behavior, with activation energy of 0.2 eV. Cross-plane thermal conductivity was evaluated by time domain thermoreflectance (TDTR) and found to be between 0.07 and 0.09 W m^{-1} K^{-1}, which is more than an order of magnitude smaller than previous reports of crystalline $MoSe_2$. Previously, the ultralow thermal conductivity of disordered layered materials has been attributed to the combination of turbostratic disorder and pronounced anisotropy in the elastic constants [58] of the parent crystalline solid. Here, we report experimental evidence that the group velocity of the transverse phonon modes is strongly suppressed in the *z* direction. The suppression of the transverse sound velocity directly reduces the thermal conductivity in the *z* direction and also enhances the anisotropy of the elastic constants which further suppresses heat conduction due to phonon focusing effects [58]. These results show that ultralow cross-plane thermal conductivity can be achieved in a highly periodic $MoSe_2$ array in which interlayer rotational disorder is the salient structural feature.

2. Results and discussion

Samples were prepared by depositing a targeted number of Mo|Se bilayers and annealing the samples at low temperatures to crystalize individual $MoSe_2$ layers and self assemble them into a rotationally disordered stack. Deposition parameters for the modulated elemental precursor were calibrated so that the amount of Mo and Se in a deposited bilayer yielded a 1:2 ratio of the elements. These values were adjusted during this study to yield precursors with varying

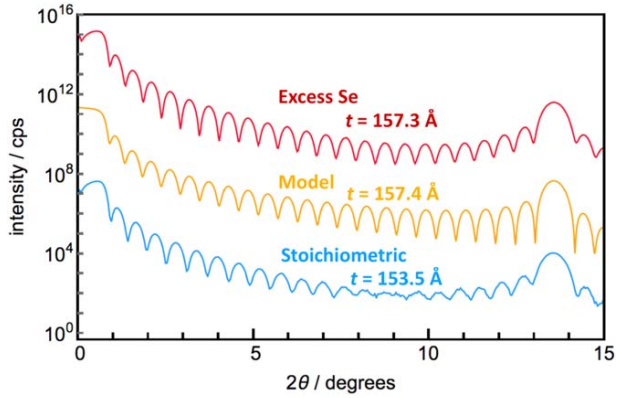

Figure 1. Low-angle reflectivity patterns for two samples designed to form 24 layers of $MoSe_2$. The yellow trace (middle) is a calculated pattern that was used as a comparison for the two experimental patterns (red and blue). The blue (bottom) trace was annealed from a stoichiometric precursor with ∼5% deficiency in Mo, whereas the red trace (top) contained a ∼10% Se excess and the correct amount of Mo to form 24 layers. XRF data indicated that the films after annealing had the same composition.

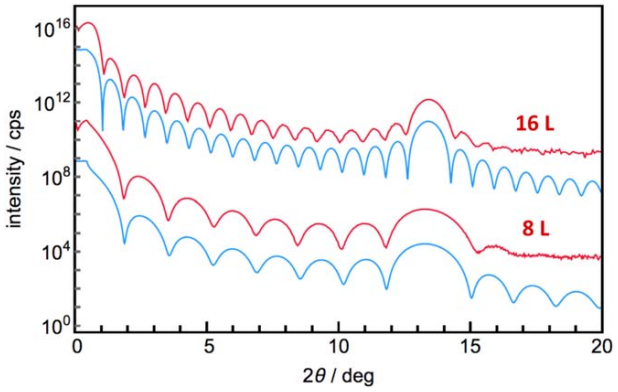

Figure 2. Low-angle reflectivity patterns of 8- and 16-layer $MoSe_2$ films that show strong agreement between the calculated (blue) and experimental (red) traces. The scans are offset for clarity.

amounts of excess Se as this improved the quality of the resulting XRR and XRD patterns. The thickness of the deposited layers was then scaled so the number of atoms in each Mo|Se bilayer matched the number of atoms in a single Se–Mo–Se trilayer of $MoSe_2$ (subsequently called a monolayer). Samples were prepared with a range of total thicknesses by varying the number of Mo|Se bilayers deposited. Samples were annealed at 650 °C for 60 min in a N_2 atmosphere followed by a 60 min anneal at 550 °C in a sealed tube with a Se partial pressure. The specular diffraction patterns of all samples contained only the 00*l* reflections expected for $MoSe_2$ indicating that the $MoSe_2$ planes are parallel to the substrate.

Figure 1 contains both calculated (yellow) and experimental (blue and red) low-angle reflectivity patterns of samples where 24 $MoSe_2$ monolayers were targeted. The patterns contain periodic oscillations called Kiessig fringes, which result from two superimposed phenomena—the interference of scattered x-rays off the top and bottom interfaces of the film and the incomplete destructive interference of the 24 $MoSe_2$ monolayers. The position of the Kiessig fringes at low angles is dominated by the reflectivity of the sample, and their location depends the average total film thickness via Bragg's law corrected for refraction. The position of the Kiessig fringes closer to the 001 Bragg reflection for $MoSe_2$ is dominated by the incomplete destructive interference of the finite size crystal, and their location is related to the number of monolayers and their spacing, which is the *c*-axis lattice parameter. The annealed film from the stoichiometric precursor (blue) was ∼1 nm thinner than the target thickness, leading to a film with less than 24 layers of $MoSe_2$. There is a difference between the thickness calculated from the position of the low-angle Kiessig fringes (between 22 and 23 monolayers) and the higher angle fringes near the Bragg reflection (23 monolayers), indicating that different regions of the film have slightly different thicknesses. The interference between these two areas of the film results in a reduction in the amplitude of the Kiessig fringes between 7° and 10° relative to that in the calculated pattern. Precursors deposited with the correct amount of Mo but a 10%–15% excess of Se form films with Kiessig fringe amplitudes closer to that expected from the calculation; and the excess Se is expelled upon annealing as monitored using x-ray fluorescence spectroscopy (XRF) [59]. The agreement between the experimental (red) and calculated (yellow) reflectivity patterns indicates that this sample contains 24 parallel monolayers, which is consistent with the cross-sectional STEM images discussed later. The samples used in this study were all prepared from precursors with ∼10% excess Se.

Films containing 8–64 monolayers of $MoSe_2$ were prepared by changing the number of Mo|Se bilayers deposited in the precursor. Figure 2 contains the experimental and calculated x-ray reflectivity patterns for 8- and 16-layer structures. The agreement between the experimental (red) traces and calculated (blue) traces demonstrates the ability to prepare films with a targeted number of $MoSe_2$ monolayers over the entire probed area (∼4 cm^2). The Parratt relationship relates the angle to which resolved fringes are observed to how parallel the bottom and top surfaces of the sample are over the probed area [60]. The observation of fringes to $2\theta > 15°$ indicates sub-Angstrom smoothness.

Specular diffraction patterns were collected to determine the out-of-plane structure of the samples. All the observed Bragg maxima (figure 3) can be indexed as the 00*l* series of reflections, indicating that the $MoSe_2$ layers are parallel to the substrate. Rocking curve measurements were done on the 00*l* reflections to measure the extent of preferred alignment, yielding half widths of 1.1° θ. These half widths are significantly narrower than the ∼15° θ reported by Muratore *et al* [51]. The line widths of the reflections broaden as the number of layers decreases and the coherence length becomes limited by the film thickness. *c*-axis lattice parameters were calculated for the different samples (see table 1), yielding an average value of 0.6531(2) nm, which is larger than the individual layer thicknesses calculated from previously reported *c*-axis lattice parameters (0.646(1) nm) for 2H, 3R,

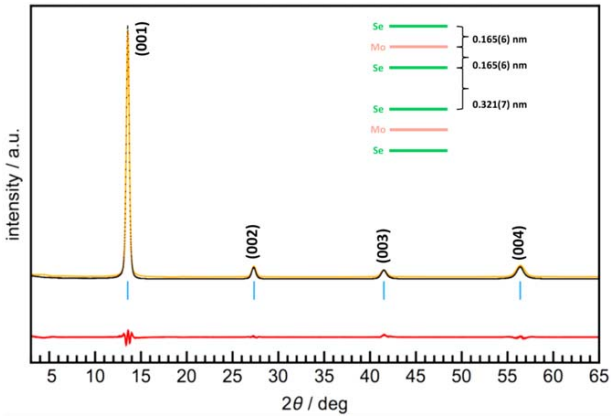

Figure 3. Specular diffraction patterns show only the 00*l* series of Bragg reflections, indicating that $MoSe_2$ nanosheets run parallel to the substrate. The structural refinement shows a slightly increased interplanar distance between Se and Mo planes, which is consistent with other low temperature syntheses. Experimental data points are shown in black, and the refinement is shown in yellow. The residuals are in red.

or 4H $MoSe_2$ prepared by high temperature syntheses [53–57]. We believe that this increased thickness per $MoSe_2$ trilayer is a consequence of the rotational disorder between adjacent $MoSe_2$ layers. Even larger thicknesses per $MoSe_2$ trilayer have been reported for $MoSe_2$ prepared using a variety of low T synthesis techniques [61–63]. The larger thicknesses from these syntheses were not explicitly discussed, but for some approaches may be a consequence of included solvent molecules between the $MoSe_2$ layers.

Rietveld refinement of the specular diffraction pattern of the $MoSe_2$ sample with 64 layers was conducted to gain insight into the cause of the expanded *c*-axis lattice parameter. Figure 3 contains the experimental and calculated diffraction patterns, with a schematic of the refined model inset within the figure. The van der Waals gap from our refined model, taken as the distance between the Se planes in adjacent $MoSe_2$ layers, 0.321(1) nm, is 0.008 nm larger than that reported in the literature for $MoSe_2$ prepared at high temperatures (0.3128 nm). The Se–Mo interatomic distance (0.165(7) nm) is also larger than that reported in the literature for the thermodynamically stable product (0.1615(1) nm). Our XRF analysis indicates that the stoichiometry of all the samples prepared is $MoSe_{1.99(2)}$ [59] indicating that large deviations from stoichiometry (due to Se loss, for example) are not responsible for these differences. The increase in the *c*-lattice parameter is a consequence of both of these distances increasing, which we speculate is caused by the rotational disorder between adjacent $MoSe_2$ layers.

Grazing-incidence XRD was collected to obtain information about the in-plane structure of the samples. All of the patterns contain Bragg maxima that can be indexed as *hk*0 reflections using a hexagonal unit cell (figure 4), consistent with the preferred orientation of $MoSe_2$ layers. The *a*-axis lattice parameters of the different $MoSe_2$ films were determined using LaBail fits of the diffraction patterns. The value obtained, 0.331(1) nm, agrees with literature values for $MoSe_2$, which range from 0.329 nm for $MoSe_2$ prepared at high temperature [54–57] to as low as 3.22 for films prepared at low temperature [7]. The Debye–Scherrer equation was used with line widths obtained from the LaBail fits to obtain an estimate of 10 nm for the in-plane grain sizes [64]. In-plane pole figures indicate that the crystallites are randomly oriented in the *xy*-plane over the $\sim$4 cm^2 analytical area.

Cross-sectional HAADF HRSTEM images were collected to gain additional information about the structure of the $MoSe_2$ layers and their stacking. Figure 5 shows images of the 8- and 24-layer samples, which contain layers of alternating contrast corresponding to the nanosheets (bright) and van der Waals gaps (dark) with the layers parallel to the substrate. The number of Mo|Se layers in the precursors has been retained in the crystalized films, which contain parallel layers and atomically sharp interfaces in agreement with the diffraction data discussed previously. Areas with resolvable zone axes are not frequent and neither are areas with alignment between layers, such as that in the image of the 8-layer sample. This is consistent with the rotational disorder previously reported from other films made via modulated elemental reactant (MER) synthesis and the pole figure measurements discussed earlier. A periodic stacking of the layers observed in the thermodynamically stable bulk phases of $MoSe_2$ is not observed. A non-representative area of the 8-layer film is shown in figure 5 because it contains a rare region where the bottom 2 layers have a [110] orientation while layers 3 and 4 have the [100] axis aligned with the beam. The observed chevron arrangement of the atoms within the $MoSe_2$ nanosheets where the electron beam is aligned down the [100] axis is consistent with trigonal prismatic coordination of the Mo atoms. Layers 5–8 do not show resolvable low index zone axes, indicating that they possess different rotational orientations. Most of the areas viewed in the STEM investigation did not show any, or at most a single layer with a resolvable zone axis. A high density of independent nucleation sites probably causes the rotational disorder between layers during the self-assembly of the precursor. Faster growth along a $MoSe_2$ sheet than heterogeneous nucleation of an adjacent layer at the interface of an existing layer results in the random rotational orientation. Grain sizes within a layer agree with the diffraction estimates using Debye–Scherrer analysis (on the order of $\sim$10 nm).

The HAADF HRSTEM images in figure 5 consist of well-defined planar layers. These images are very different from previously reported HAADF HRSTEM images of WSe_2 made by MER synthesis, where the cross section high-resolution TEM images showed non-planar layers with small in-plane grain sizes [52]. These cross-sectional images of WSe_2 were inconsistent with the reported XRD data on the same sample [50] indicating that the sample was probably damaged during TEM sample preparation.

Plan view HRTEM data and NBED patterns were collected over a 250 $\times$ 250 nm region of the 8-layer sample to obtain information on the local rotational disorder. Figure 6 shows a representative 3 $\times$ 3 grid of these NBED patterns collected with a focused 8 nm electron beam on a square grid with 10 nm between the centers of the electron beam. All of

Nanotechnology **30** (2019) 285401 E C Hadland *et al*

Table 1. Summary of lattice parameters from x-ray diffraction, cross-plane thermal conductivity (Λ), and z-axis longitudinal (C_{33}) and shear (C_{44}) elastic constants for the rotationally disordered $MoSe_2$ films in this study.

# $MoSe_2$ layers	a (nm)	c(nm)	Λ(W m^{-1}K^{-1})	C_{33} (GPa)	C_{44} (GPa)
64	0.3309(5)	0.6532(2)	$0.090^{+0.004}_{-0.002}$	44 ± 3	—
32	0.3313(1)	0.6526(2)	$0.07^{+0.012}_{-0.002}$	32 ± 5	—
24	0.3309(1)	0.6528(5)	$0.07^{+0.02}_{-0.002}$	41 ± 7	—
16	0.3310(1)	0.6536(9)	$0.07^{+0.03}_{-0.004}$	38 ± 8	—
8	0.3308(4)	0.653(1)	—	—	—
≈ 92	—	—	—	33 ± 1	3.0 ± 0.9

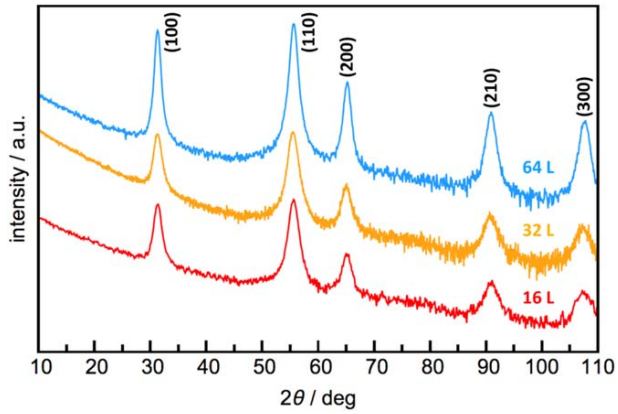

Figure 4. Representative GIXRD patterns of 16-, 32-, and 64-layer films showing only *hk0* reflections due to the preferred orientation of the crystallites.

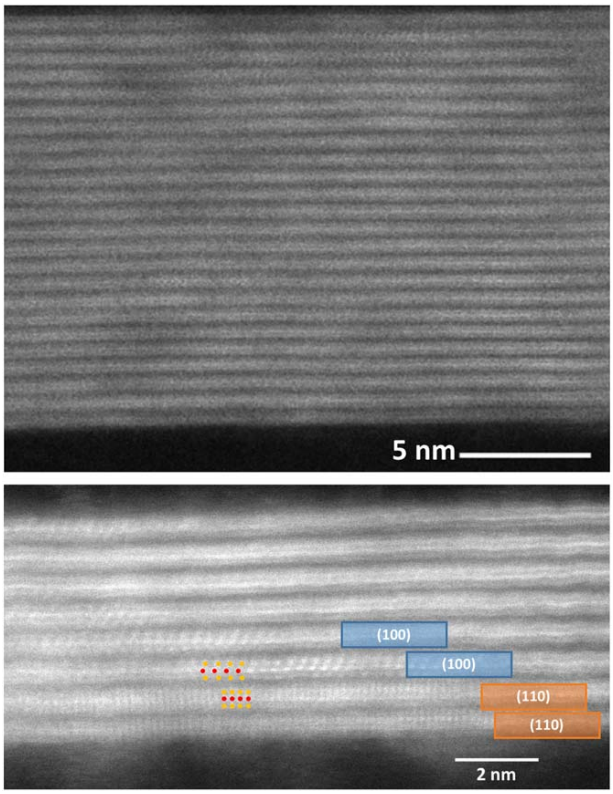

Figure 5. Cross-sectional HAADF-STEM images of 24-layer and 8-layer $MoSe_2$ films. Grain orientations and zone axes are indicated in the shaded boxes, and the arrangement of atoms is shown with red spheres corresponding to Mo atomic columns and gold spheres corresponding to Se atomic columns.

the patterns contain multiple hexagons of varying orientation and intensity, reflecting the local orientations of the hexagonal $MoSe_2$ basal planes. The local orientations change significantly from spot to spot. The grain orientations are randomly distributed and they change intensity independently of one another, consistent with the rotational disorder inferred from the cross section HRSTEM data discussed earlier. If all of the patterns over the 250 × 250 nm area are stacked on top of one another, rings of uniform diffraction intensity are obtained (see SI, available online at stacks.iop.org/NANO/30/285401/mmedia), consistent with the x-ray pole figure experiment discussed earlier. Different grain orientations can be identified in each individual pattern, and are represented by the different color hexagons in the central pattern of figure 6. These orientations were tracked from the central pattern to the adjacent regions. If a specific orientation is still observed, a hexagon of that color is shown. If the orientation is missing in an adjacent region, the hexagon is not shown. While a specific orientation may exist on diffraction patterns collected on adjacent spots, the majority of the orientations change even at this length scale.

Further information about the extent of rotational disorder of the $MoSe_2$ layers on a smaller scale was obtained through the evaluation of fast Fourier transforms (FFTs) taken from 5 × 5 nm^2 region of the HRTEM micrograph depicted in figure 7 and explained in the SI. The rotational disorder of NBED patterns on the larger scale is consistent with the superposition phase contrast visible in figure 7(a). However, confined areas with single rotational alignment could be identified, see, HRTEM contrast and FFT data evaluation showing single hexagon patterns in figures 7(b) and (c), respectively. To show how the orientations of the hexagons vary as a function of location, we created a color coded map of the hexagon orientations (figure 7(d)), similar to the colored hexagons of figure 6. In figure 7(d), the colors refer to specific rotational orientations observed in this area. New orientations appear and rotations from an adjacent square disappear as the FFT area is moved across the image. Specific orientations persist over 10–30 nm length scales, as observed for the sample area examined by NBED. Details of the data evaluation are presented in the supporting material. The changes in grain orientation observed in figure 7 are

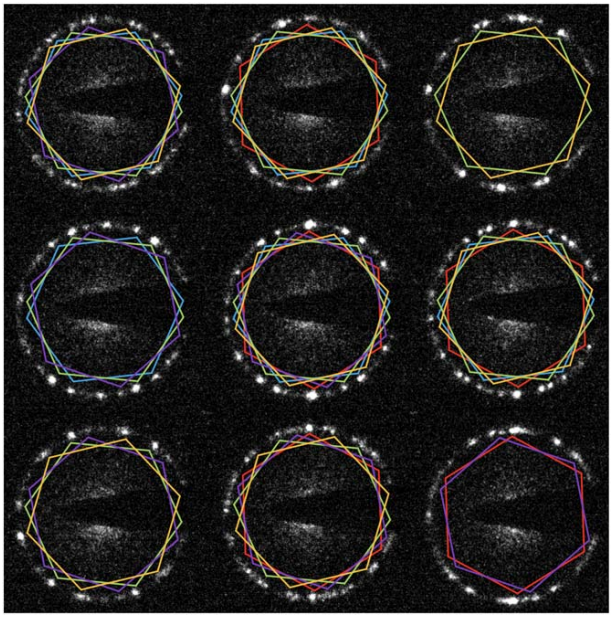

Figure 6. Nanobeam electron diffraction patterns of selected areas of $MoSe_2$ separated by 10 nm. Grain orientations are highlighted by colored hexagons in the central SAED image. If one of these orientations persists in a neighboring SAED image, the color hexagon corresponding to that orientation is superimposed on the image.

consistent with the estimates of the in-plane grain size and illustrate the extensive local rotational disorder between $MoSe_2$ layers on the nanometer scale.

Electrical resistivity was measured at temperatures between 165 and 295 K using the van der Pauw method. The resistivity increased exponentially from 0.83 Ω m at room temperature to 10.7 Ω m at 165 K, indicating that the films are semiconducting. A linear regression of $\ln \rho$ v. T^{-1} (figure 8) yielded an activation energy of ∼0.2 eV over this small temperature range, which is approximately one order of magnitude smaller than the optical band gaps reported for bulk 2H $MoSe_2$ and large-grain monolayer structures [65]. While studies report a narrowing of band gaps in rotationally disordered systems by ∼15% [17] the lower activation energy in our system obtained from the resistivity suggests that we are not observing the intrinsic band gap, but instead we are measuring barriers introduced by the grain boundaries or the activation energy of a defect band [66].

Thermal conductivity measurements were made using the TDTR method [67] on the 16, 24, 32, and 64-layer films with a 80 nm thick aluminum film as an optical transducer sputtered on the $MoSe_2$ films. The 8-layer film was not measurable as it is too thin for the measurement to have enough sensitivity to the thermal conductivity. The thermal model is compared with the measured TDTR data to determine the thermal conductivity of $MoSe_2$ (Λ). Regarding the other parameters of $MoSe_2$ that are needed for the thermal model, we used the heat capacity as 1.89 J K^{-1} cm^{-3} [68]; for the interfacial thermal conductance (G) between Al and $MoSe_2$, we assume the range of G as 100 ± 70 MW m^{-2} K^{-1}. The lower end corresponds to the lowest interfacial thermal conductance of metals and van der Waals materials, i.e. NbV and ReS_2 [68]. The upper end corresponds to the interfacial thermal conductance of Al sputtered on Si thermal oxide. The TDTR signal is most sensitive to Λ of $MoSe_2$ and less sensitive to G, and only the lower end of G affects the fitted Λ. A summary of the thermal conductivity of 16, 24, 32, and 64-layer films is given in table 1. Note that the positive uncertainty of Λ corresponds to G = 30 MW m^{-2} K^{-1} and the negative uncertainty corresponds to G = 170 MW m^{-2} K^{-1}.

The measured cross-plane thermal conductivities, 0.07–0.09 W m^{-1} K^{-1}, are extremely low for a fully dense solid. These values are a factor of 20–50 smaller than what has been reported for bulk dichalcogenides of Mo, W, and Ti for which values ranged from 1.75 W m^{-1} K^{-1} for a purchased single crystal of WSe_2 to 4.7 W m^{-1} K^{-1} for a natural mined single crystal of MoS_2 [35, 37, 50, 51, 69]. Thermal conductivity values for crystals of Mo and W dichalcogenides grown via vapor transport range from a low of 1.2 W m^{-1} K^{-1} for WSe_2 to a high of 3.5 W m^{-1} K^{-1} for $MoSe_2$ [37, 70, 71]. Samples of MoS_2 prepared by annealing Mo films in S vapor have thermal conductivities close to those of bulk crystals [51, 72]. These values are generally in agreement with calculated values [73, 74]. Intercalation has been shown to lower the cross-plane thermal conductivity of dichalcogenides by a factor of 2–3 [69, 72] significantly less than the reduction observed here. Very low cross-plane thermal conductivities have been published for disordered dichalcogenide films prepared by magnetron sputtering, 0.1–0.3 W m^{-1} K^{-1} [51]. Models that accommodate reduced symmetry along z have corroborated that stacking disorder and lattice expansions on the order of 2%–3% can reduce cross-plane thermal conductivity to ∼0.4 W m^{-1} K^{-1} [75].

The longitudinal speed of sound along the z-axis (v_L) of the Al-sputter coated $MoSe_2$ films can be determined by using picosecond acoustics [76]. The longitudinal elastic constant, C_{33}, can be calculated as $C_{33} = \rho v_L^2$, where ρ is the theoretical mass density of $MoSe_2$, 7.0 g cm^{-3}, and is shown in table 1. The C_{33} of 32–44 GPa is comparable to that of other transition metal dichalcogenides, e.g. 52 GPa for MoS_2 bulk [72] and 43 GPa for ReS_2 exfoliated flake [77].

We also determined transverse speed of sound along the z-axis (v_T) via surface acoustic wave measurements [78]. The measurement can be performed in the same setup as TDTR but requires a thicker film with a tuned thickness of Al transducer. Therefore, we used a $MoSe_2$ film prepared by the MER method but of 60 nm thickness (≈92 layers). The sample was coated with 145 nm thick Al. Surface acoustic waves with a wavelength of 700 nm were generated using an elastomeric polydimethylsiloxane phase-shift mask attached onto the sample surface. The shear modulus (C_{44}) was derived from the measured frequency of the surface acoustic waves, from which the transverse speed of sound along the z-axis can be calculated using $C_{44} = \rho v_T^2$.

The shear modulus of the 60 nm thick $MoSe_2$ film is 3.0 ± 0.9 GPa (see table 1). To the best of our knowledge, this is the first experimental data for the shear modulus of a disordered van der Waals material. This value is significantly

Nanotechnology **30** (2019) 285401 E C Hadland *et al*

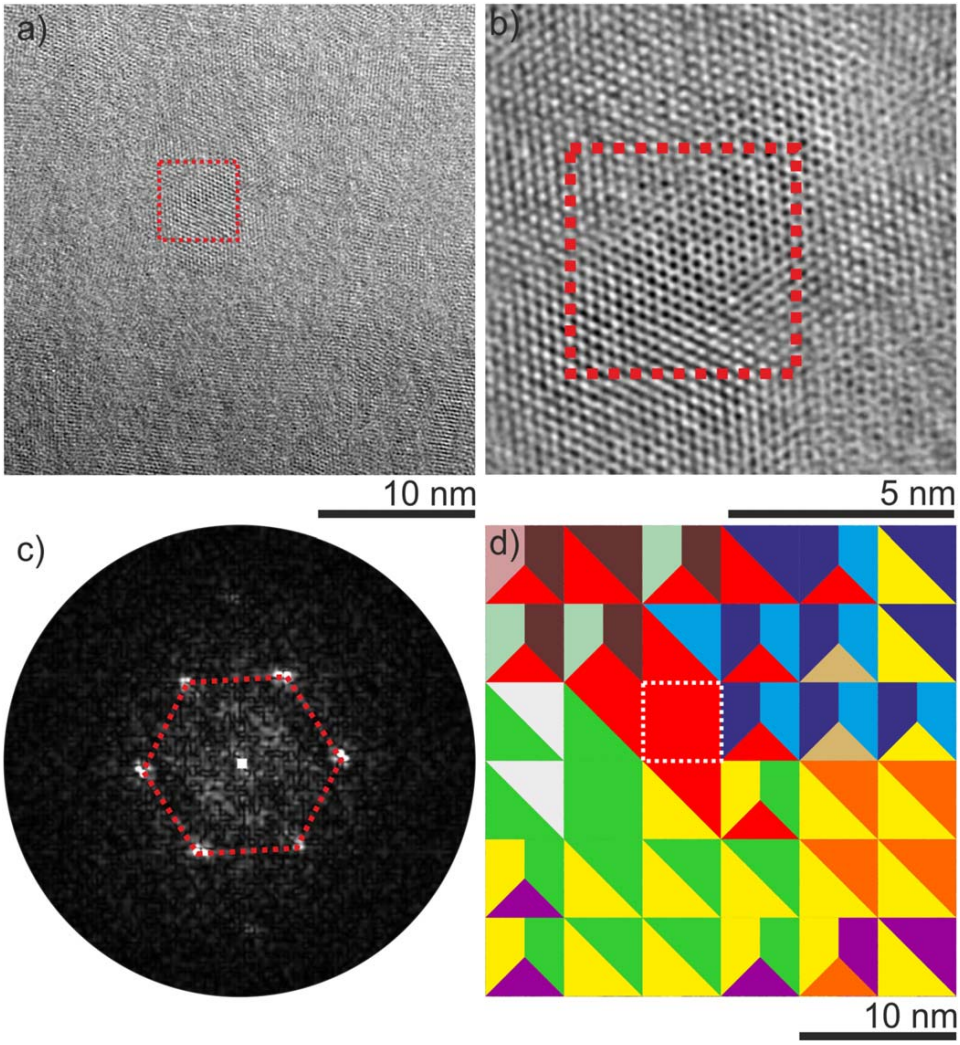

Figure 7. Plan view HRTEM study of the 8-layer $MoSe_2$ sample. (a) HRTEM micrograph showing blurred phase contrast originating from the superposition of rotationally disordered layers. (b) Magnified view of the red box in (a) showing a small area with single rotational alignment, and corresponding FFT pattern (c). (d) Color coded map showing different hexagon orientations extracted from a grid of FFTs from $36 \times 5 \times 5\ nm^2$ square areas. The presentation is limited to the three most prominent rotations.

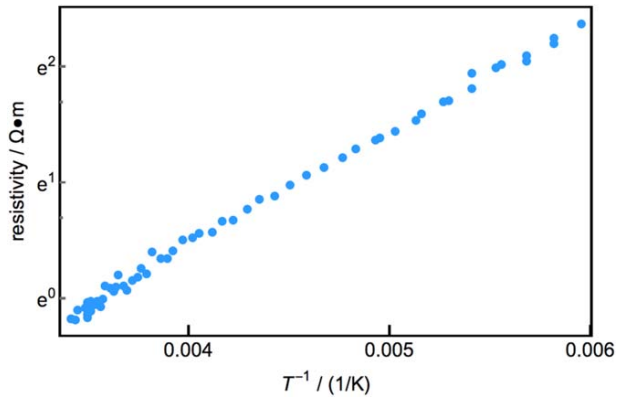

Figure 8. The linear relationship between $\ln\rho$ and T^{-1} indicates that films are semiconducting.

suppressed compared with the bulk counterpart: although direct experimental results are not available, the shear modulus derived from the frequency of Raman-active shear modes is 17–19 GPa for $MoSe_2$ and 19 GPa for MoS_2 [79]. First-principles calculations predict 33 GPa for $MoSe_2$ [80] although we point out that this result is likely to be sensitive to the choice of the functionals used to describe the van der Waals interactions between the layers. The reduced shear modulus implies that the ultralow thermal conductivity of the rotationally disordered $MoSe_2$ films can be partly attributed to the strongly suppressed group velocity of transverse acoustic phonon modes.

Results presented in this study suggest that rotational disorder in otherwise well-defined crystalline systems is sufficient to reduce thermal conductivity to ultralow values. The structural analysis indicates that our films consist of a highly periodic $MoSe_2$ array with flat (non-wavy) monolayers that have in-plane lattice parameters equal to that found in

crystalline $MoSe_2$. The in-plane XRD pole figures show that the layers have a random rotational orientation over the large area probed. The NBED and high-resolution TEM imaging show that this interlayer rotational disorder exists at the nanoscale. The *c*-axis lattice parameter, however, is ~1% larger than that measured in crystalline $MoSe_2$ due to the rotational disorder between the layers.

The ultralow thermal conductivity values reported here are consistent with the cross-plane thermal conductivities reported for WSe_2 and dichalcogenide containing heterostructures prepared using the MER approach with semiconducting rock salt layers, with values ranging from 0.05 to 0.35 $W\,m^{-1}K^{-1}$ [49, 50, 81–84]. From the acoustic measurements, we reveal that the rotational disorder suppresses the group velocity of the transverse phonon modes along the *z*-axis, while that of the longitudinal modes remain intact.

3. Summary

The results presented herein are relevant for researchers investigating the potential use of the novel properties found in van der Waals heterostructures for use in nanoelectronic applications where interfaces between layers are likely to be a large fraction of the active devices. We showed via extensive structural characterization that rotational misalignment between layers creates very anisotropic environment in the *x*–*y* plane for the chalcogen atoms of dichalcogenides, as the chalcogen atom in one layer is no longer sitting in the middle of a triangle of chalcogen atoms from the adjacent layer [85]. This rotational disorder results in extremely low thermal conductivities for a fully dense solid. Similar anisotropic environments are present at the interfaces in van der Waals heterostructures due to the different in-plane lattice parameters of the constituents. Consequently, we expect that van der Waals heterostructures will likely have very low cross-plane thermal conductivities. This will be an important design issue for heterostructures devices that dissipate power and a potential opportunity to obtain high thermoelectric performance in devices operating across the van der Waals interfaces of heterostructures.

Acknowledgments

The authors acknowledge support from the National Science Foundation under grant DMR-1710214 and the German Research Foundation (DFG) under grant CRC1261-A6. We would like to acknowledge the Center for Advanced Materials Characterization in Oregon (CAMCOR) at the University of Oregon. Additionally, we would like to acknowledge the National Center for Electron Microscopy at Lawrence Berkley National Lab and Christoph Gammer for encoding software to acquire the nanobeam electron diffraction data. Work at the Molecular Foundry was supported by the Office of Science, Office of Basic Energy Sciences, of the US. Department of Energy under Contract No. DE-AC02-05CH11231. Thermal conductivity measurements and analysis were carried out in the Frederick Seitz Materials Research Laboratory Central Research Facilities, University of Illinois, and were supported by NSF EFRI-1433467.

ORCID iDs

Erik C Hadland https://orcid.org/0000-0002-2205-4363
Niklas Wolff https://orcid.org/0000-0002-8796-0607

References

[1] Novoselov K S, Mishchenko A, Carvalho A and Castro Neto A H 2016 *Science* **353** 6298
[2] Geim A K and Grigorieva I V 2013 *Nature* **499** 419–25
[3] Hamann D M, Hadland E C and Johnson D C 2017 *Semicond. Sci. Technol.* **32** 93004
[4] Lin Z *et al* 2016 *2D Mater.* **3** 42001
[5] Rivera P *et al* 2015 *Nat. Commun.* **6** 6242
[6] Hong X, Kim J, Shi S-F, Zhang Y, Jin C, Sun Y, Tongay S, Wu J, Zhang Y and Wang F 2014 *Nat. Nanotechnol.* **9** 682–6
[7] Zhou X *et al* 2017 *2D Mater.* **4** 25048
[8] Jiang S, Shan J and Mak K F 2018 *Nat. Mater.* **17** 406–10
[9] Kim H H, Yang B, Patel T, Sfigakis F, Li C, Tian S, Lei H and Tsen A W 2018 *Nano Lett.* **18** 4885–90
[10] Kou L, Wu S-C, Felser C, Frauenheim T, Chen C and Yan B 2014 *ACS Nano* **8** 10448–54
[11] Rajput S, Li Y-Y, Weinert M and Li L 2016 *ACS Nano* **10** 8450–6
[12] Märkl T, Kowalczyk P J, Le Ster M, Mahajan I V, Pirie H, Ahmed Z, Bian G, Wang X, Chiang T-C and Brown S A 2017 *2D Mater.* **5** 11002
[13] Deng D, Novoselov K S, Fu Q, Zheng N, Tian Z and Bao X 2016 *Nat. Nanotechnol.* **11** 218–30
[14] Tongay S *et al* 2014 *Nano Lett.* **14** 3185–90
[15] Ohta T, Robinson J T, Feibelman P J, Bostwick A, Rotenberg E and Beechem T E 2012 *Phys. Rev. Lett.* **109** 186807
[16] Fang H *et al* 2014 *Proc. Natl Acad. Sci. USA* **111** 6198–202
[17] Zhang C, Chuu C-P, Ren X, Li M-Y, Li L-J, Jin C, Chou M-Y and Shih C-K 2017 *Sci. Adv.* **3** e1601459
[18] Liu K *et al* 2014 *Nat. Commun.* **5** 4966
[19] Wang K *et al* 2016 *ACS Nano* **10** 6612–22
[20] Kang J, Li J, Li S S, Xia J B and Wang L W 2013 *Nano Lett.* **13** 5485–90
[21] Heo H *et al* 2015 *Nat. Commun.* **6** 7372
[22] Goyal V and Balandin A A 2012 *Appl. Phys. Lett.* **100** 73113
[23] Hong Y, Zhang J and Zeng X C 2016 *J. Phys. Chem.* C **120** 26067–75
[24] Peng B, Zhang H, Shao H, Xu Y, Zhang X and Zhu H 2016 *RSC Adv.* **6** 5767–73
[25] Kandemir A, Yapicioglu H, Kinaci A, Çağın T and Sevik C 2016 *Nanotechnology* **27** 55703
[26] Norouzzadeh P and Singh D J 2017 *Nanotechnology* **28** 75708
[27] Wang H, Qin G, Li G, Wang Q and Hu M 2017 *2D Mater.* **5** 15022
[28] Jiang J-W, Park H S and Rabczuk T 2013 *J. Appl. Phys.* **114** 64307
[29] Liu X, Zhang G, Pei Q-X and Zhang Y-W 2013 *Appl. Phys. Lett.* **103** 133113
[30] Li W, Carrete J and Mingo N 2013 *Appl. Phys. Lett.* **103** 253103
[31] Gu X and Yang R 2014 *Appl. Phys. Lett.* **105** 131903

[32] Cai Y, Lan J, Zhang G and Zhang Y-W 2014 *Phys. Rev.* B **89** 35438
[33] Yan R, Simpson J R, Bertolazzi S, Brivio J, Watson M, Wu X, Kis A, Luo T, Hight Walker A R and Xing H G 2014 *ACS Nano* **8** 986–93
[34] Sahoo S, Gaur A P S, Ahmadi M, Guinel M J-F and Katiyar R S 2013 *J. Phys. Chem.* C **117** 9042–7
[35] Liu J, Choi G-M and Cahill D G 2014 *J. Appl. Phys.* **116** 233107
[36] Zhang X, Sun D, Li Y, Lee G-H, Cui X, Chenet D, You Y, Heinz T F and Hone J C 2015 *ACS Appl. Mater. Interfaces* **7** 25923–9
[37] Jiang P, Qian X, Gu X and Yang R 2017 *Adv. Mater.* **29** 1701068
[38] Zhang J, Hong Y, Wang X, Yue Y, Xie D, Jiang J, Xiong Y and Li P 2017 *J. Phys. Chem.* C **121** 10336–44
[39] Farahani H, Rajabpour A, Khanaki M and Reyhani A 2018 *Comput. Mater. Sci.* **142** 1–6
[40] Ong Z-Y, Cai Y and Zhang G 2016 *Phys. Rev.* B **94** 165427
[41] Yuan P, Li C, Xu S, Liu J and Wang X 2017 *Acta Mater.* **122** 152–65
[42] Taube A, Judek J, Łapińska A and Zdrojek M 2015 *ACS Appl. Mater. Interfaces* **7** 5061–5
[43] Hong Y, Ju M G, Zhang J and Zeng X C 2018 *Phys. Chem. Chem. Phys.* **20** 2637–45
[44] Venkatasubramanian R, Siivola E, Colpitts T and O'Quinn B 2001 *Nature* **413** 597–602
[45] Touzelbaev M N, Zhou P, Venkatasubramanian R and Goodson K E 2001 *J. Appl. Phys.* **90** 763–7
[46] Winkler M, Liu X, König J D, Kirste L, Böttner H, Bensch W and Kienle L 2012 *J. Electron. Mater.* **41** 1322–31
[47] Hansen A-L, Dankwort T, Winkler M, Ditto J, Johnson D C, Koenig J D, Bartholomé K, Kienle L and Bensch W 2014 *Chem. Mater.* **26** 6518–22
[48] Chen P, Zhang Z, Duan X and Duan X 2018 *Chem. Soc. Rev.* **47** 3129–51
[49] Chiritescu C, Cahill D G, Heideman C, Lin Q, Mortensen C, Nguyen N T, Johnson D, Rostek R and Böttner H 2008 *J. Appl. Phys.* **104** 33533
[50] Chiritescu C, Cahill D G, Nguyen N, Johnson D, Bodapati A, Keblinski P and Zschack P 2007 *Science* **315** 351–3
[51] Muratore C *et al* 2013 *Appl. Phys. Lett.* **102** 81604
[52] Kim S, Zuo J M, Nguyen N T, Johnson D C and Cahill D G 2008 *J. Mater. Res.* **23** 1064–7
[53] Bronsema K D, De Boer J L and Jellinek F 1986 *Z. Anorg. Allg. Chem.* **540** 15–7
[54] Evans B L and Hazelwood R A 1971 *Phys. Status Solidi* **4** 181–92
[55] Kalikhman V L 1983 *Inorg. Mater.* **19** 957–62
[56] Brixner L H 1962 *J. Inorg. Nucl. Chem.* **24** 257–63
[57] Towle L C, Oberbeck V, Brown B E and Stajdohar R 1966 *Science* **154** 895–6
[58] Chen Z and Dames C 2015 *Appl. Phys. Lett.* **107** 193104
[59] Hamann D M, Bardgett D, Cordova D L M, Maynard L A, Hadland E C, Lygo A C, Wood S R, Esters M and Johnson D C 2018 *Chem. Mater.* **30** 6209–16
[60] Wainfan N and Parratt L G 1960 *J. Appl. Phys.* **31** 1331–7
[61] Fan R 2001 *Chem. Mater.* **13** 802–5
[62] Fan C, Yue Q, Yang J, Wei Z, Yang S and Li J 2014 *Appl. Phys. Lett.* **104** 202105
[63] Xenogiannopoulou E *et al* 2015 *Nanoscale* **7** 7896–905
[64] Klug H P and Alexander L E 1974 *X-Ray Diffraction Procedures* 2nd edn (New York: Wiley)
[65] Mann J *et al* 2014 *Adv. Mater.* **26** 1399–404
[66] Kumar S and Schwingenschlögl U 2015 *Chem. Mater.* **27** 1278–84
[67] Cahill D G 2004 *Rev. Sci. Instrum.* **75** 5119–22
[68] Blinder A V, Bolgar A S and Trofimova Z A 1993 *Powder Metall. Met. Ceram.* **32** 234–9
[69] Bhatt R *et al* 2013 *Appl. Phys.* A **111** 465–70
[70] Pisoni A, Jacimovic J, Gaál R, Náfrádi B, Berger H, Révay Z and Forró L 2016 *Scripta Materialia* **114** 48–50
[71] Brixner L H and Teufer G 1963 *Inorg. Chem.* **2** 992–6
[72] Zhu G, Liu J, Zheng Q, Zhang R, Li D, Banerjee D and Cahill D G 2016 *Nat. Commun.* **7** 13211
[73] Wei X, Wang Y, Shen Y, Xie G, Xiao H, Zhong J and Zhang G 2014 *Appl. Phys. Lett.* **105** 103902
[74] Ding Y, Chen M and Xiao B 2016 *RSC Adv.* **6** 7817–28
[75] Erhart P, Hyldgaard P and Lindroth D O 2015 *Chem. Mater.* **27** 5511–8
[76] O'Hara K E, Hu X and Cahill D G 2001 *J. Appl. Phys.* **90** 4852–8
[77] Jang H, Ryder C R, Wood J D, Hersam M C and Cahill D G 2017 *Adv. Mater.* **29** 1700650
[78] Li D, Zhao P, Zhao J-C and Cahill D G 2013 *J. Appl. Phys.* **114** 143102
[79] Kuzuba T and Ishii M 1989 *Phys. Status Solidi* **155** K13–6
[80] Ghosh C K, Sarkar D, Mitra M K and Chattopadhyay K K 2018 *J. Phys. D: Appl. Phys.* **46** 395304
[81] Gunning N S, Feser J, Beekman M, Cahill D G and Johnson D C 2015 *J. Am. Chem. Soc.* **137** 8803–9
[82] Gunning N S, Feser J, Falmbigl M, Beekman M, Cahill D G and Johnson D C 2014 *Semicond. Sci. Technol.* **29** 124007
[83] Heideman C L, Tepfer S, Lin Q, Rostek R, Zschack P, Anderson M D, Anderson I M and Johnson D C 2013 *J. Am. Chem. Soc.* **135** 11055–62
[84] Li Z, Bauers S R, Poudel N, Hamann D, Wang X, Choi D S, Esfarjani K, Shi L, Johnson D C and Cronin S B 2017 *Nano Lett.* **17** 1978–86
[85] Wu X and Luo T 2014 *J. Appl. Phys.* **115** 14901

4.2 Magnetic Materials

Magnetic materials represent the second key component for ME composite magnetic field sensors (Figure 4.7). The magnetic properties of this sensing layer have to meet high demands to translate the weak biomagnetic field signals to the piezoelectric material. These requirements are answered in terms of soft magnetic characteristics describing a low magnetic saturation field strength and a simultaneous high saturation magnetization in connection with decent magnetostrictive coefficients. Amorphous ferromagnetic glasses on the basis of iron and boron e.g. FeCoSiB are suitable materials and readily applied as the magnetic phase material in the ME sensors.[41] However, the amorphous phase is always only a metastable state and external factors such as heat lead to crystallization of Fe and degrade the sensor properties. To show the impact of crystallization of a amorphous FeCoSiB films on the magnetic properties, two magnetic hysteresis curves are schematically displayed in Figure 4.8. In this respect, alternative magnetic material systems have been investigated by TEM which provide thermal stability by using ultra-thin nanolayers of FeCo and TiN or exploiting exchange-bias magnetic multilayer structures composed of FeNi and MnIr to alter the magnetic hysteresis and to pin the magnetic spins in a coupled magnetic material. The results and the specific details of these material investigations are described in the following sections.

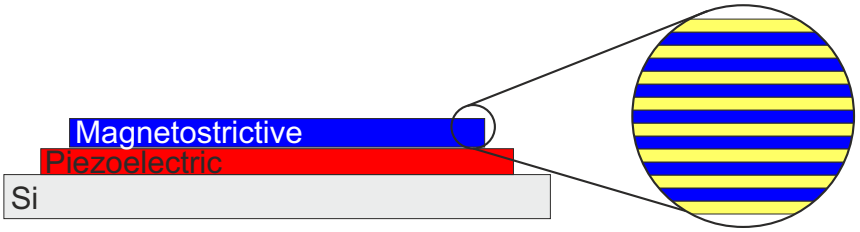

FIGURE 4.7: Schematic ME sensor with focus on the magnetic component, which could be structured in a multilayer geometry.

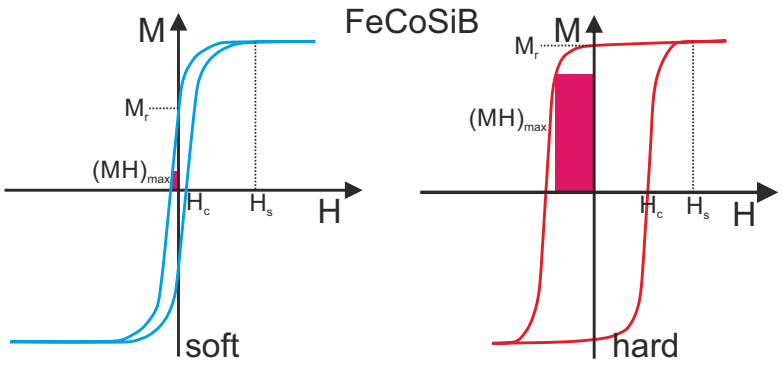

FIGURE 4.8: Illustrations of the magnetic hysteresis of a soft magnetic material (left) such as FeCoSiB and magnetic hardening (right) by crystallization. The coercive and saturation fields H_c, H_s and remanent magnetization M_r as well as the energy product $(MH)_{max}$ are also indicated.

4.2.1 Micro- and Nanostructure of FeCo/TiN Multilayers

The quality factor Q of ME sensors with cantilever beam geometry is an important measure related to the sensor noise and its performance to detect low-frequency magnetic signals. Mathematically, Q can be regarded as a damping coefficient, which is improved by changing the density of the medium from air to vacuum. The Q-factor is demonstrated to be also highly significant for an effective improvement of the LOD of delta-E effect sensor approaches based on the magnetoelastic softening of a magnetostrictive material as discussed in Section 2.2.[63] However, the vacuum encapsulation processes of cantilever ME sensors on wafer level requires elevated temperatures of about 450 °C upon wafer bonding. This is limiting the available temperature budget of each individual functional layer after its deposition. The most concern is focusing on the amorphous FeCoSiB magnetic layer, which is known to crystallize at temperatures above 350 °C resulting in the degradation of the needed soft magnetic properties.[234]

Alternatively, the combination of soft magnetic properties and high temperature stability could be offered by nanostructuring of a material composite. In this respect, the permeability, anisotropy and coercive field of ferromagnetic FeCo alloys is known to be dependent on the grain size.[235] One efficient strategy are multilayer systems in which a 50:50 FeCo alloy is sliced into physically and magnetically decoupled ultra-thin layers by a spacer material. This strategy allows for a targeted tailoring of the magnetic properties providing the ability to control the FeCo grain size by the layer thickness.[236] Choosing a certain thickness of TiN as spacer material serves the purpose for providing temperature stability up to 600 °C and to avoid magnetic coupling between the layers of FeCo. It has been shown for the equiatomic composition of FeCo alloy that magnetic multilayers with TiN as spacer material and FeCo with reducing layer thickness from 5.5 nm to 2.6 nm also reduces the measured coercive field H_c from 1.3 mT to 0.3 mT.[237]

The nanostructure of these multilayer systems was first described in the work of Klever *et al.*[238] and is extended in the study reporting about **heteroepitaxy in ultra-thin FeCo/TiN nanolayer films**.[9] Theoretically, the interface quality is a sensible parameter for the magnitude of saturation magnetostriction λ_S in thin film laminates, which is supposed to deviate from the bulk value $\lambda_s = 53$ ppm[239] due to elastic strain contribution at the interfaces. According to an analytical model, the magnetostriction in ultra-thin layers is described by a function of the lattice distortion t and the alloy composition α, $\lambda_S(t^\alpha)$.[240] For instance, the saturation magnetostriction is strongly dependent on the post annealing treatment and the FeCo layer thickness in FeCo/Ag multilayers varying between $\lambda_s = 53$ ppm - 83 ppm.[239] However, the nanocrystalline FeCo/Ag layers have been described as strongly polycrystalline without the presence of a strong texture, which is present in the FeCo/TiN laminates. In order to study the influence of the individual FeCo and TiN layer thickness on the magnetic properties, in particular the magnitude of magnetostriction, a new set of samples has been deposited at the Karlsruhe Institute of Technology with varying the FeCo or TiN layer thickness.

The structural characterization of a sputter deposited multilayer film featuring 7 monolayers (3 unit cells) of FeCo in a single layer is revealing a columnar grown microstructure with a defined [00l]-texture. The texture is decisive from the superposition of multiple orientations

[9] Submitted to Materials Characterization on January 23, sent to review on February 2, manuscript number MATERIALSCHAR_2020_237.

in the experimental ED pattern shown in Figure 4.9. TEM dark-field imaging is capable to highlight the individual microstructure columns with a large field of view by selecting two prominent reflections of different orientations in the SAED pattern. Markers (yellow and red) highlight the position of the objective aperture set during dark-field imaging experiments. The obtained dark-field images (Figure 4.9 are depicting the columnar arrangement of grains following the [110](red) and [100](yellow) zone axis crystal orientation of the TiN phase with a shared [00l]-rotation axis. The HRSTEM micrographs of Figure 4.10 further display the film's cube-on-cube epitaxy and orientation relationships of the individual [TiN]/[FeCo] lattices: [110]/[100]. To meet the in-plane lattice constants of TiN, the in-plane lattice a_{FeCo} of FeCo is strained by about 5% to match the diagonal lattice constant $\sqrt{2}\,a_{TiN}$ of TiN. According to the HRSTEM data and kinematic simulation of ED pattern, the in-plane expansion of the FeCo lattice introduces a tetragonal distortion by a simultaneous decrease of the out-of-plane parameter resulting in new tetragonal lattice with a = b = 3.0 Å with c $\leqslant$ 2.85 Å. In addition, the layer morphology is highly parallel to the substrate without any significant layer roughness. This is a first apparent difference between the recent deposited film and the film which has been investigated in the attached study. The detailed results of this study are topic of a future publication.

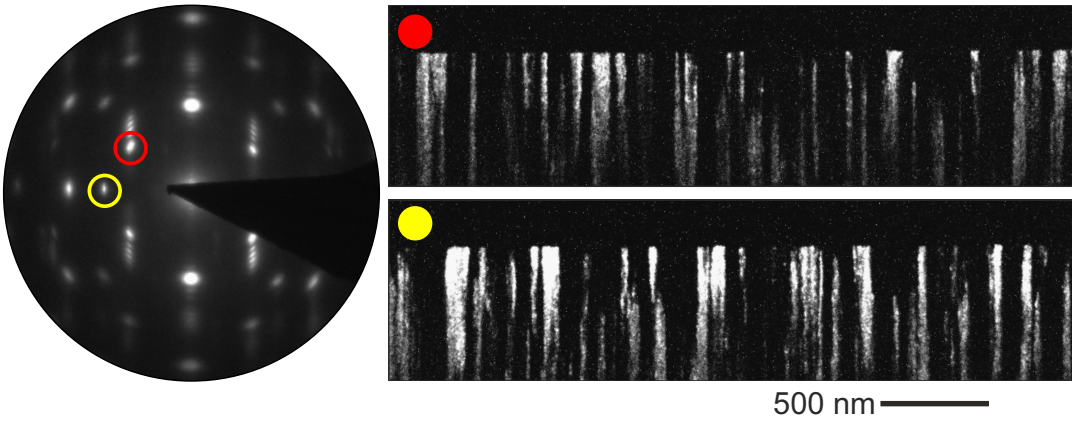

FIGURE 4.9: Electron diffraction pattern and dark-field images showing a columnar microstructure using diffraction intensity stemming from two different crystal orientations as highlighted in the ED pattern.

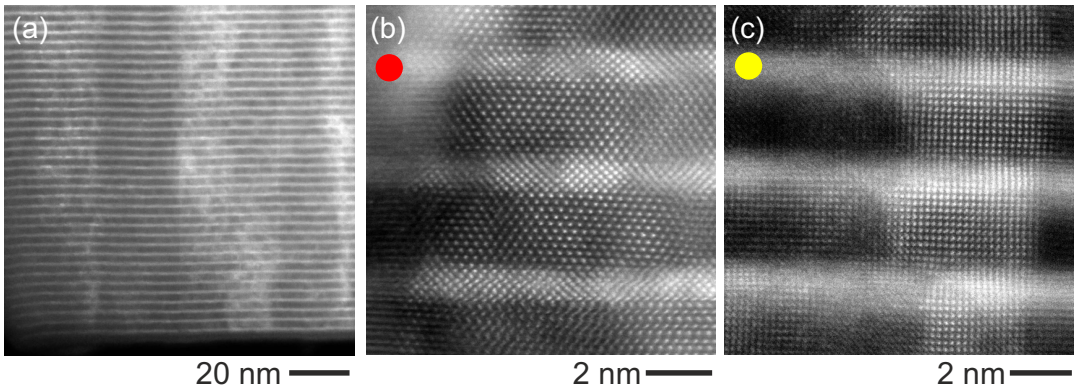

FIGURE 4.10: HRSTEM micrographs showing an (a) overview of the layered structure close to the substrate and lattice structure of grains with (b)[110](red) and (c)[100](yellow) orientation with respect TiN lattice and the orientations mapped in the DF image. The HRSTEM micrographs show the atomic columns with characteristic Z-contrast.

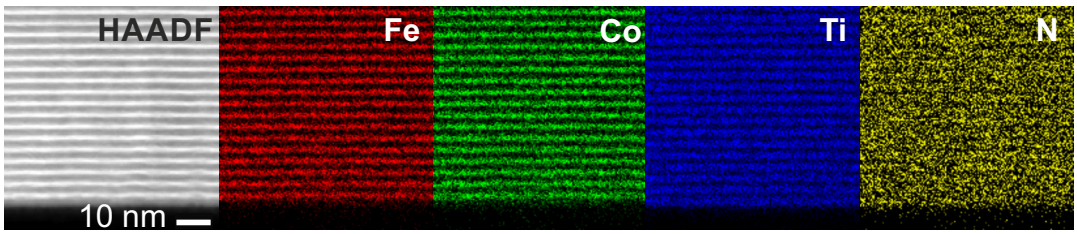

FIGURE 4.11: HRSTEM EDS maps show the chemical integrity of Fe, Co and Ti, N layers after annealing the sample to 500 °C for 1h. The X-ray signal is restricted to the individual nanolayer.

The chemical analysis by EDS in combination with HRSTEM provides elemental mapping with sub-nanometer down to atomic resolution. The EDS study was performed after an annealing procedure at 500 °C to prove the temperature stability of the multilayer system having layer thickness in the nm-regime. The atomic distribution maps are presented in Figure 4.11 and show perfect structural integrity at the mapped region and on the entire film as indicated by overview STEM images.

4.2.2 FeNi/MnIr Exchange Spring Magnetic Multilayers

In the context of ME sensors, the concept of magnetic frequency conversion (MFC) describes the modulation of the resonance frequency to lower frequencies by the application of a small magnetic modulation field. As an extension to the MFC concept, the introduction of an exchange bias (EB) into the magnetostrictive phase has been proven to effectively improve the sensors performance, especially the LOD at low frequency magnetic fields.[241] Exchange biased ME sensors have been realized based on antiferromagnetic/ferromagnetic (AF/FM) multilayers gaining magnetic domain control to further suppress the magnetic noise contributions by domain wall motion.[46], [242] In this respect, possible design configurations have been investigated describing parallel EB (PEB) and anti-parallel EB (APEB) structures on basis of a $MnIr_3$/FeCoSiB heterostructure (see Figure 4.12) with $MnIr_3$ being the AF. Ferromagnetic exchange interaction between the magnetic moments of the FM and the AF sub-lattices close to the AF/FM interface creates a so called unidirectional anisotropy. This triggers the preferable alignment of the magnetic moments in the FM layer in the same direction as the magnetic moments of the AF sub-lattice. In this ferromagnetic alignment of magnetic moments between the AF and FM, the interface moments are frozen resulting in a creation of an internal magnetic field: the exchange bias field H_{EB}. Such effect is equivalent to an application of an additional constant bias field which one can see as a typical shift of the hysteresis loop, as it is illustrated in Figure 4.13a for an idealized case. In comparison to PEB, the APEB-structures demonstrated significant improvement of the noise floor by applying larger magnetic modulation fields.[35] That is reasoned by the elimination of magnetic domain activity to achieve the detection of picotesla magnetic fields as small as LOD $= 60\,\mathrm{pT}/\sqrt{\mathrm{Hz}}$ at 10 Hz.[36]

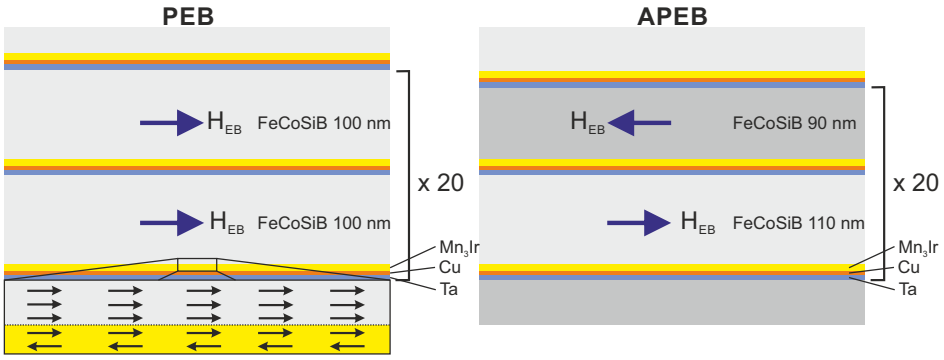

FIGURE 4.12: Schematic drawings of parallel and anti-parallel exchange bias in FeCoSiB/Ta/Cu/Mn_3Ir/FeCoSiB composites. The alignment of magnetic moments is illustrated for zero external magnetic field.

Based on these reports, the future developments on exchange biased ME sensors is considering an exchange spring (ES) concept which should allow for variable biasing.[10] Exchange spring multilayers serve as artificial permanent magnets and combine individual magnetic properties by epitaxial coupling between one hard magnetic phase providing a high coercive field and a soft magnetic phase exhibiting a high magnetic saturation. As a result, the theoretical combination of the individual magnetic hysteresis loops offers new magnetic properties such as an high energy product $(BH)_{max}$ and a reversible demagnetization curve as indicated in Figure 4.13b.[243] In order to establish the desired magnetic exchange properties, it was pointed

[10]The ES concept is proposed for ME sensors by Prof. Dr. Jeffrey McCord and Dr. Dirk Meyners

out that all involved phases must emerge from a common metastable matrix phase to provide crystallographic coherence which is promoting epitaxial coupling. For a properly working ES system, it is therefore evident to precisely control the nanometer-scale layer thickness and the nanostructure in terms of the crystallographic relationship and defects at the interfaces, also with direct imaging techniques such as TEM.[244] Imperfect coupling of both phases results in a pinched hysteresis loops as illustrated in Figure 4.13c, with the width of the hysteresis being dependent on the degree of coupling.[245] Despite hard magnetic systems, also novel ES arrangements focusing on magnetic softness and a large magnetostriction on basis of TbFeCo/YFe multilayers have been realized.[246] In perspective, the targeted design of new magnetostrictive layer stacks including combinations of exchange bias with exchange spring (EB+ES) systems could meet specific sensor requirements. In this context, the following TEM examination was conducted on the structure of a 5 nm/2 nm $(Fe_{19}Ni_{81}/Ir_{23}Mn_{77})_{n=4}$ multilayer deposited on top of a 50 nm magnetic FeCoB thin film. The hard magnetic NiFe exhibits the low magnetostriction of a permalloy is coupled with the antiferromagnetic MnIr to induce a high magnetic anisotropy resulting in an exchange bias.[247] Besides the discussed importance of the nanostructure details of the multilayer, also the amorphous to crystalline structure evolution of the underneath FeCoB layer was in focus of this particular study.

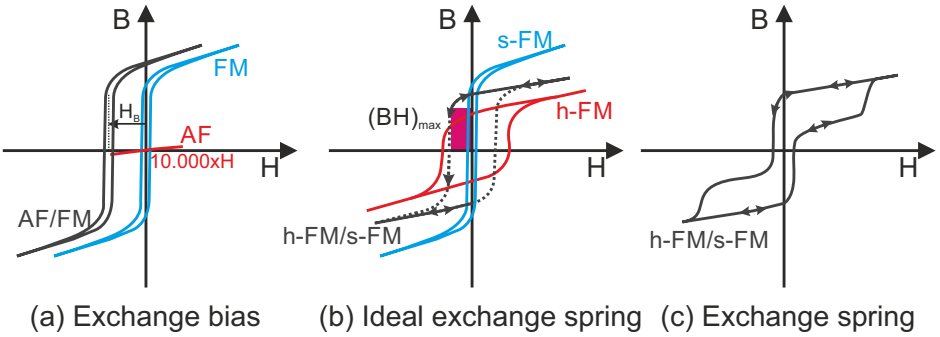

FIGURE 4.13: Schematics of the magnetic hysteresis loops of (a) an exchange bias system, (b) an idealized exchange spring system between an soft FM and hard FM and (c) a more realistic exchange spring system with imperfect coupling. The black color is always representing the resultant loop.

NBED Analysis of $(Fe_{19}Ni_{81}/Ir_{23}Mn_{77})_{n=4}$ Multilayers

The examinations in this study have been performed on the Tecnai F30 instrument installed in Kiel for a basic characterization of the sample and on a probe-corrected Titan^3 G^2 STEM installed at the Leipziger nanoAnalytikum (LenA[11]) for more advanced characterization.
The structural details about the morphology and layer growth were deduced from reciprocal space analysis on converging length scales. First, the selected area electron diffraction (SAED) experiment was conducted using the smallest aperture (⌀250 nm) to obtain averaged structural information about the entire multilayered system. Second, nanobeam electron diffraction (NBED) yields spatial information when scanned across the multilayered system, especially with having a vertical dimension of 30 nm. Meeting the size limitations of the sample, in NBED the electron beam is strongly confined (⌀8 nm) with the condenser lens apparatus. Third, the projection of the atomic structure with relative Z-contrast (4-channel-aSTEM detector) is correlated with reciprocal space data visualized via Fast Fourier Transformation (FFT) images, their inverse (iFFT) implementation and energy-dispersive X-Ray spectroscopy (EDS) to derive fundamental nanoscale structural and chemical information.

Results and Discussion

The chemical and nanoscale structural details about the multilayered $FeNi_3/IrMn_3$ heterostructure deposited onto amorphous FeCoB are discussed in this section. The layered morphology and the distribution of the respective elements are shown by STEM imaging in combination with EDS, the elemental map and elemental profile drawn across the layer sequence are displayed in Figure 4.14. The individual layers of the heterostructure, i.e. their spatial and chemical separation is demonstrated in the STEM-HAADF image shown in Figure 4.14a. Alternating layers with lower and higher Z-contrast correspond to $FeNi_3$ layers and $IrMn_3$, respectively. The EDS elemental map of the identical position confirms chemical separation of individual layers.The elemental profile drawn in Figure 4.14b differentiates between the individual elements superimposed in the elemental map showing the atomic concentration over position. In conclusion of this experiment, there are four alternating layers of $FeNi_3$ (∼4.5 nm) and $IrMn_3$ (∼2.2 nm) which are capped by TaN (∼5 nm) on top and a Ru (∼1 nm) seed layer as spacer to the FeCoB (∼45 nm) film. An evolution of layer roughness is also observed which is initiated by small perturbations on the Ru layer. Concerning the elemental profile, the concentration of Ni is ∼75 at% on average which matches well with the expected stoichiometry of the $FeNi_3$ phase. The concentration of Mn is about ∼60 at% and that of Ir of ∼5 at% summing up to 100 including Fe and Ni contributions. However, this does not indicate chemical mixing but is an artefact of the scan stepsize and in-depth layer roughness. The latter can be reasoned with the vertical dimensions of the $IrMn_3$ layer which are by a factor of ten or more smaller with respect to the sample thickness resulting in a non-negligible factor of stray radiation.
With respect to structure investigation using TEM, ED is the standard technique to obtain structural information averaged from small volumes only limited by the dimensions of the electron beam or a diffraction aperture. The experimental SAED pattern and interpretation based on a kinematic simulation are depicted in Figure 4.15. The SAED pattern indicates a strong <111>-texture along the growth direction. The diffraction intensities are

[11] The HRSTEM, EDS and NBED examinations have been performed by Dr. Ulrich Ross in cooperation with Dr. Andriy Lotnyk.

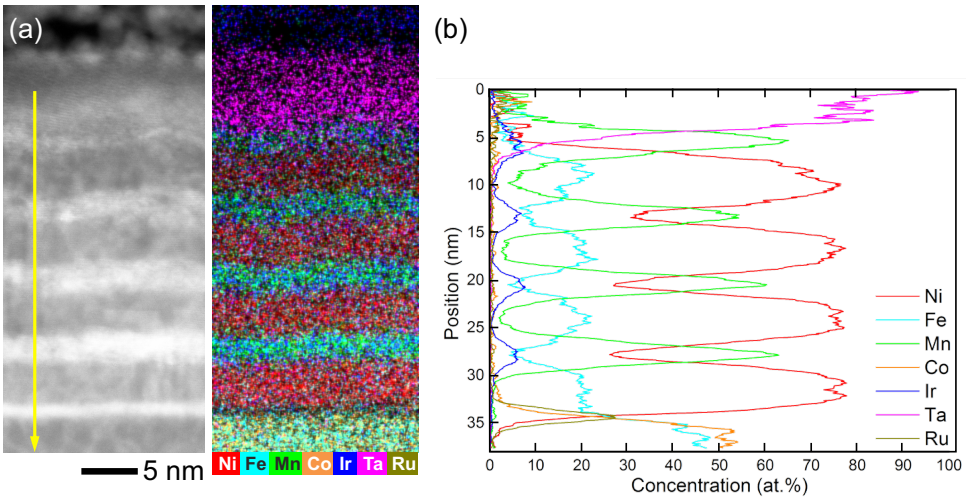

FIGURE 4.14: Spectroscopic analysis of the $FeNi_3/IrMn_3$ heterostructure. a) STEM-HAADF Z-contrast image and element distribution map. b) Element profiles recorded across the heterostructure (yellow arrow).

basically arranged in two sets of cubic spot patterns corresponding to the cubic structures of $FeNi_3$ (spacegroup: Fm-3m) and (Pm-3m) $IrMn_3$. The speckled diffraction rings bear on the nano-polycrystalline Pt protection layer. The {101}-spot patterns are created by the 109.4° in-plane rotation of two <101> oriented lattices, which is further described by twinning on the {111}-planes along the growth direction. Due to the multilayered structure, by chance single reflections show defined splitting along the reciprocal [111]*-direction (see inset in Figure 4.15) which is similar to superlattice reflections observable in epitaxial heterostructure films.[248] Because of the small number of layer repetitions and layer thickness, the reflection splitting is faint but shows evenly spaced intensities which can be translated to the thickness of one repeating unit Λ ~6.6 nm. This number matches quite well to the vertical dimension of a single $NiFe_3/IrMn_3$ building unit. The origin of superlattice reflections is normally reasoned by a coherent in-plane lattice of both components in epitaxial or pseudomorphic grown heterostructures forming one repeating structural unit, the latter often accompanied with an in-plane coherency strain to compensate for the small lattice mismatch. For the present system, the lattice mismatch between the {111}-planes of $FeNi_3$ and $IrMn_3$ is ~6.4%, which would allow for the establishment of pseudomorphism without the accommodation of misfit by misfit dislocations.[249]

The local distribution of the twinned [101]/{111} variants was visualized using HRSTEM micrographs and local iFFT analysis using only relevant frequencies. The recorded HRSTEM images are presented in Figure 4.16a and 4.16b and represent the HAADF Z-contrast image and the corresponding dark-field image simultaneously acquired by collecting electrons under large and smaller scattering angles, respectively. In order to differentiate between the two twin variants two strategies were used. First, the spatial frequencies of the yellow or blue coloured {002}-reflections (see Figure 4.16c) have been chosen exclusively for calculating iFFT images to visualize their origin. Second, the direction of the {002}-planes could be easily identified in the atomically resolved HRSTEM-DF image (see Figure 4.16d). As a result, a colour coded map displaying both twin variants was created showing their distribution in yellow and blue colour as visualized in Figure 4.16b. Obviously, the formation of these twins is not only restricted to the interfaces but is also allowed to randomly switch from one orientation to the

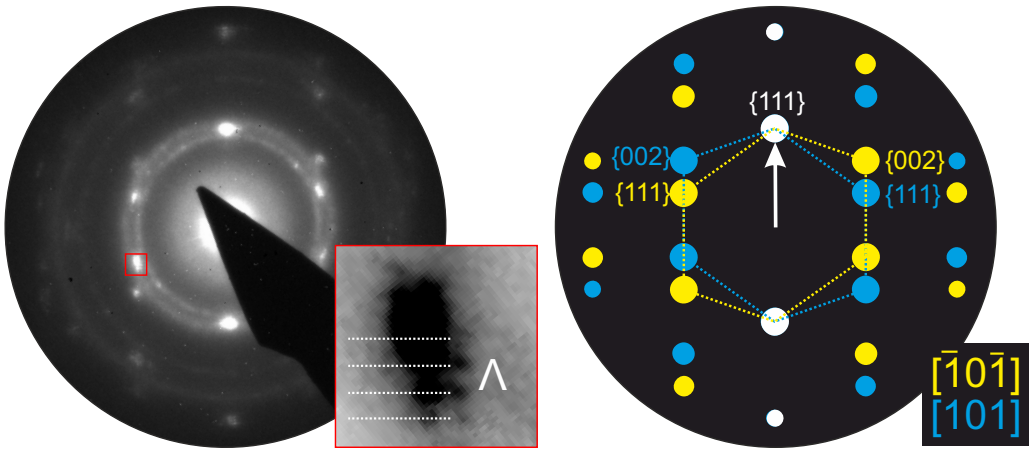

FIGURE 4.15: Experimental SAED pattern (left) and schematic display of main structural reflections (right) based on kinematic simulation. The reflection pattern is constructed by two [101] oriented variants sharing {111} planes. Inset: Reflection splitting with $\Lambda \sim 6.6$ nm.

other within single layers in growth direction. This demonstrates a spatial separation into randomly distributed domains with [101] or [$\bar{1}$0$\bar{1}$] orientation within the multilayer.

These structural features were further investigated by recording NBED patterns across a 200 nm horizontal path as depicted in Figure 4.17. For the experiment, a parallel beam with a diameter of $\sim$ 8 nm was adjusted and a step-width of $\sim$ 6 nm was used to create overlap between subsequent patterns. In detail, the extracted NBED pattern show the contribution of at least four orientations: [101], [112], [213] and [314] which simulated patterns are illustrated in the superposition sketch of Figure 4.17 and in detail in Figure 4.18. Note, that all these orientations are just different representations of the cube with in-plane rotation around the [111]-vector. For each of the depicted NBED pattern, the individual contributions in the confined diffracted volumes are illustrated given a colour code. The number of these individual orientations under the electron beam contributing to the recorded pattern varies between 1 and 3, whereas the described twin variants were only clearly observed within the [101]-orientation. The existence of different domains with certain rotation increments are also visualized by iFFT analysis shown in Figure 4.19. Note here, that the depicted domain does not vertically extend from top to bottom but is embedded into the layer matrix. This further suggests that the crystallographic orientation is free to change its in-plane rotation from monolayer to monolayer, but is most favourable to switch at interfaces due to additional interface energy contributions.

The structure of the soft magnetic film is crucial for application as crystalline filaments change the magnetic uniaxial anisotropy of the film and deteriorate the soft magnetic properties. Therefore, in this sample the structure of the FeCoB thin film was also analyzed with HRTEM and NBED but no deviation from an amorphous state could be detected in the analyzed fraction of the sample. The results of the NBED experiment are summarized in Figure 4.20 showing an overview TEM image of the sample and the 45 nm FeCoB thin film beneath the $FeNi_3/IrMn_3$ heterostructure, the NBED pattern recorded on the FeCoB film and a NBED pattern recorded on the polycrystalline Pt-layer for comparison. The amorphous character of the soft magnetic film can be inferred from this NBED pattern (For further comparison with NBED pattern from amorphous phases the reader is referred to e.g.[250], [251]).

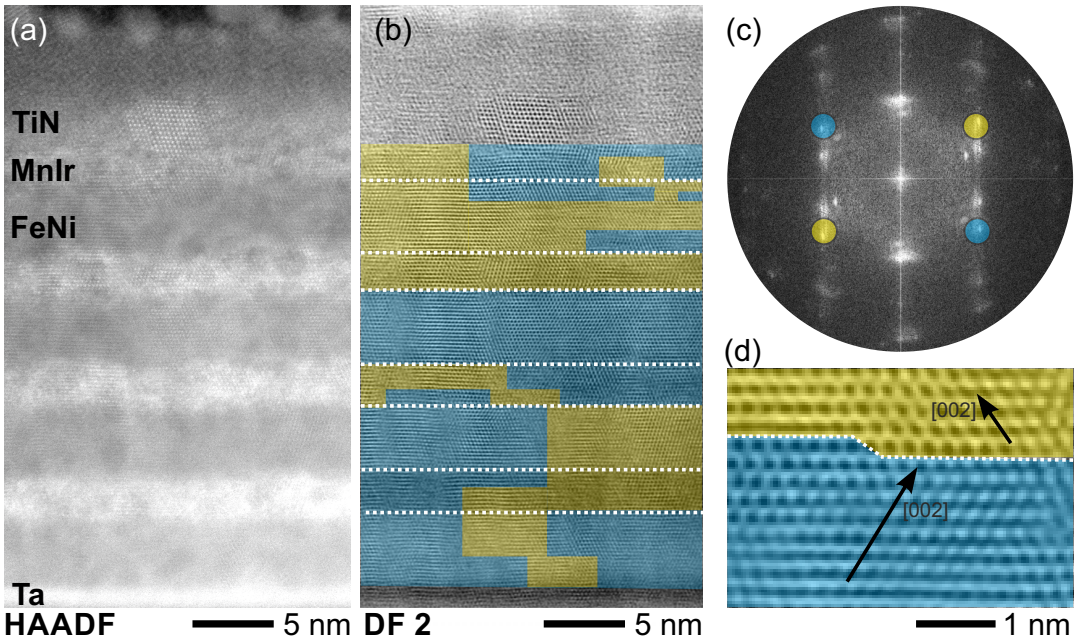

FIGURE 4.16: HRSTEM micrographs recorded with the HAADF and DF detector. (a) HAADF STEM Z-contrast image and (b) dark-field STEM image with interfaces indicated by white dashed lines and a colour scheme illustrating twin variants within single layers and across interfaces. (c) FFT with colored indication of the applied Fourier masks on the {002}-reflections. (d) Magnified HRSTEM DF contrast image showing a twin variant at the NiFe/MnIr interface.

A HRTEM micrograph of the amorphous film structure and its FFT are omitted.

Conclusion

The multilayered $FeNi_3/IrMn_3$ heterostructure has been investigated by electron diffraction methods on two length scales and HRSTEM imaging in combination with chemical analysis via EDS. The results infer the deposition of chemically separated multilayers. The crystallographic examination via HRSTEM and NBED demonstrates a <111>-textured nanostructure of an in-plane epitaxially coupled layer system which is divided into domains of defined in-plane rotation and domain sizes smaller than 20 nm. Further, NBED patterns which were recorded on the FeCoB film indicate an amorphous phase.

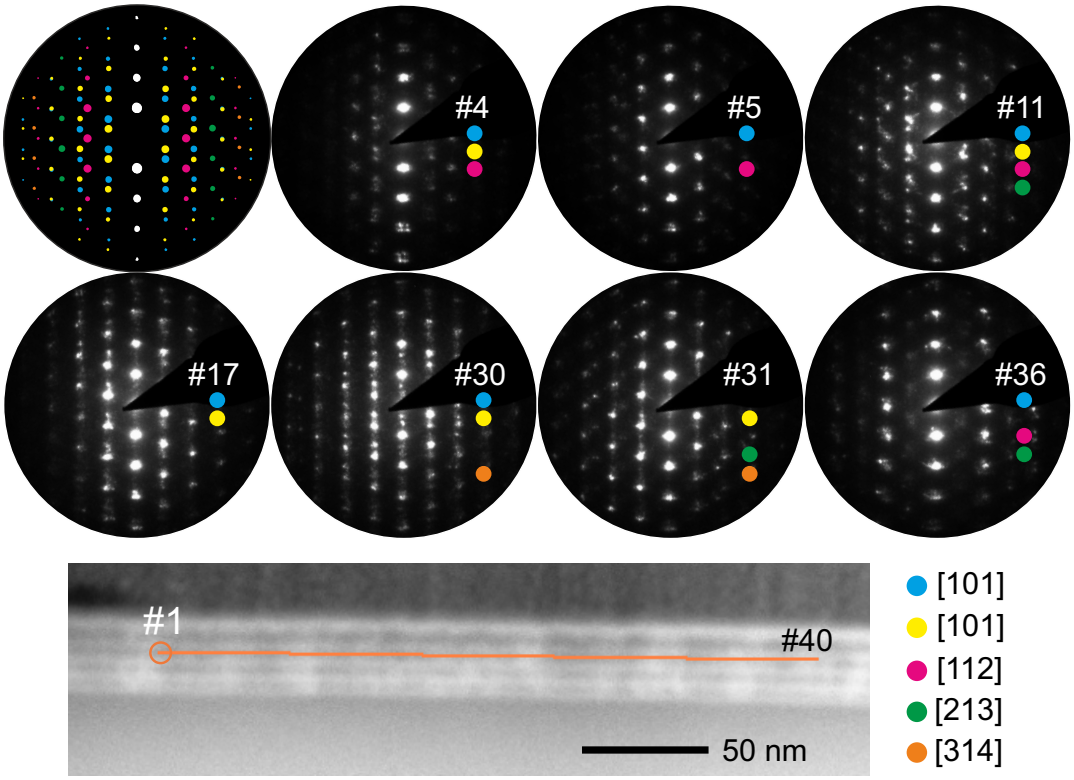

FIGURE 4.17: NBED analysis of the structural heterogeneity along the multilayer. The schematic superposition pattern illustrates the contribution of all observed crystal orientations with a shared in-plane $[11\bar{1}]$ rotation axis (white reflections). Representative NBED pattern of the series obtained along the scan direction presented with colour indicators given for specific crystal orientations.

4.3 Investigation on Composite ME Sensors

The in-depth structural characterization of individual sensor components highlighted in the previous sections is now expanded to more general studies analyzing the microstructure of different ME sensor approaches and geometries. In detail, these are ME sensors in sandwich FeCoSiB/AlN/FeCoSiB geometry (Section 4.3.1) and tunable resonance frequency ME sensors (Section 4.3.2). The presented studies have been performed in collaboration with Erdem Yarar and Sabrina Curtis.

4.3.1 FeCoSiB/AlN/FeCoSiB ME Sensor

The working principle of ME sensors relies on the magnetic field induced transmission of stress from a magnetostrictive material into a piezoelectric material producing a dipole-shift generated measurable output voltage. In this respect, the soft magnetic amorphous FeCoSiB and *c*-axis textured AlN comprises a standard composite combination. In this study, the inverse-bilayer Si/FeCoSiB/AlN geometry was extended by a second FeCoSiB layer on top of AlN creating a sandwich composite.[48] A cross-section STEM image depicting the complete sensor geometry is presented in Figure 4.21 together with detailed microstructure and chemical analysis.

Experimental ED patterns collected at positions (i)-(iii) show the polycrystalline and amorphous microstructure of the AlN and FeCoSiB layers, respectively. However, the ED pattern (i) of the AlN piezoelectric phase only indicate a distinct *c*-axis texture of one larger grain,

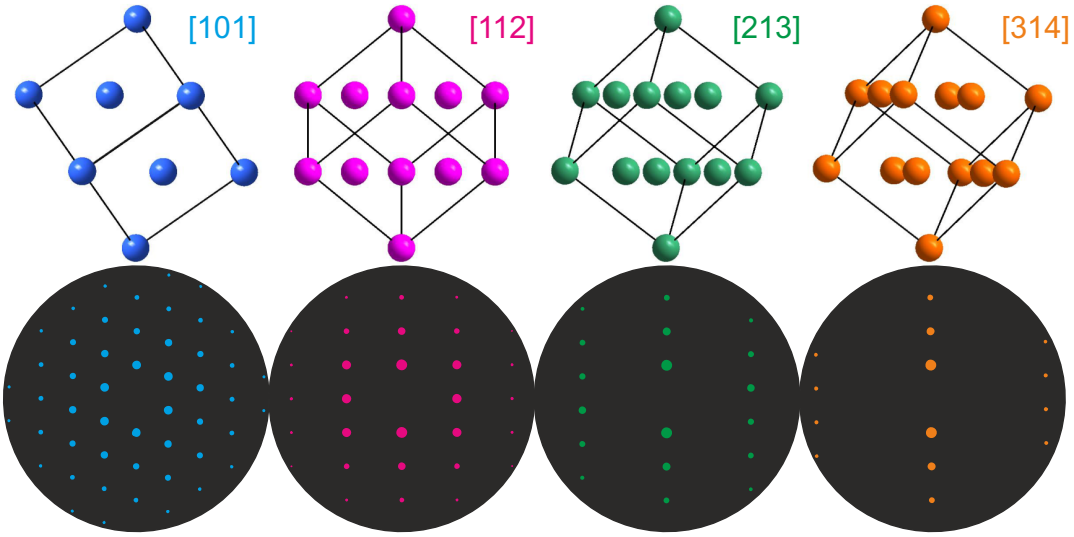

FIGURE 4.18: Crystallographic projections of the $FeNi_3$ unit cell depicted with incremental $(11\bar{1})$ in-plane rotation and corresponding simulated ED pattern.

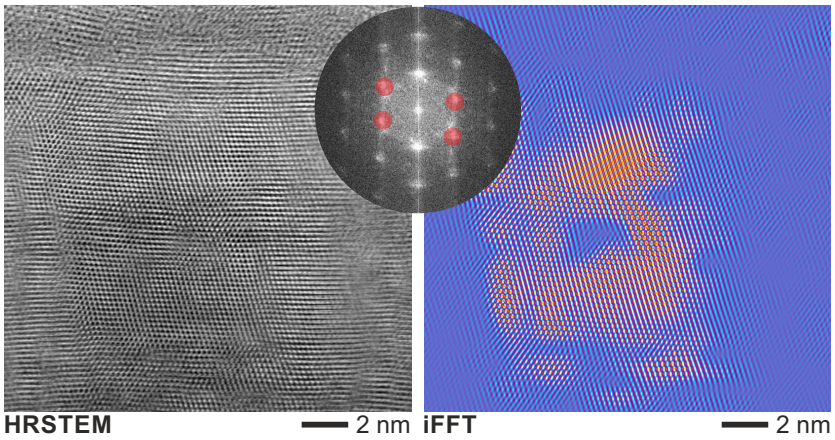

FIGURE 4.19: HRSTEM image, FFT and iFFT image using the spatial frequencies highlighted with the red dots. The red area in the iFFT image represents the origin of spatial frequencies and depicts a single oriented domain in an otherwise oriented matrix.

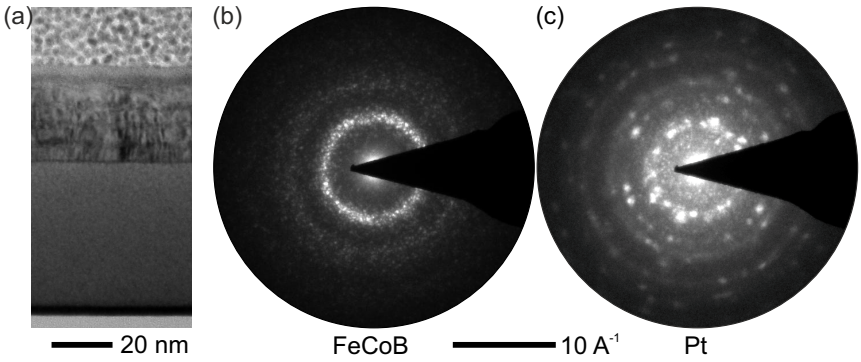

FIGURE 4.20: NBED analysis of FeCoB. (a) Overview TEM image showing the complete layer stack including a 45 nm FeCoB thin film. (b) NBED pattern recorded on the FeCoB film. (c) NBED pattern recorded on the polycrystalline Pt layer to demonstrate the difference between patterns of amorphous and crystalline materials with nanoscale crystals.

but moreover random orientations of smaller grains as visible from the diffraction intensity size and distribution. The described situation is observed to be worse close to the bottom layer at position (ii), showing an increased fraction of randomly distributed diffraction intensity on concentric rings with respect to the {0001}-reflections. The poor *c*-texture of the AlN microstructure should result in a drastically reduced piezoelectric performance which would exclude this specific batch of cantilevers for application in biomagnetic sensing. The obvious reason for the poor AlN quality is directly evidenced by chemical analysis via EDS profiling across the seed layer identifying a single layer of Ta as shown in Figure 4.22. In order to facilitate preferential growth of AlN along the *c*-axis the deposition of a preceding Ta/{111}-Pt seed layer is usually applied. The microstructure of the FeCoSiB layers was evidenced to be amorphous as demonstrated by the pattern shown in (iii). Further, EDS elemental maps of the top electrode (iv) and intermediate AlN/Ta/FeCoSiB interface (v) regions were collected to identify all present layers. According to the EDS maps shown in (iv), a top electrode using the Ta/Mo/Au sequence was deposited onto the FeCoSiB layer. Please note, the Si(K) intensity coinciding with the Ta(L) intensity is due to their similar X-ray energies. However, the unusual choice of Mo instead of Cr as adhesion layer for the Au electrode led to its relieve as apparent from the black space between Mo and Au layer visible in the STEM image. The close-up view onto the Ta electrode in investigation (v) reveals its large surface roughness originating from the rough as-grown AlN surface. Having the FeCoSiB grown onto this rough Ta surface is known to be a decisive factor for putting in additional noise into the system which is contrary to the pursuit of a low LOD. In conclusion, the here characterized sandwich structure ME sensor is not relevant for further investigations, unless its geometry has been refined using a Pt seed layer, electromechanical polishing of the AlN surface and Cr as an adhesion promoter.

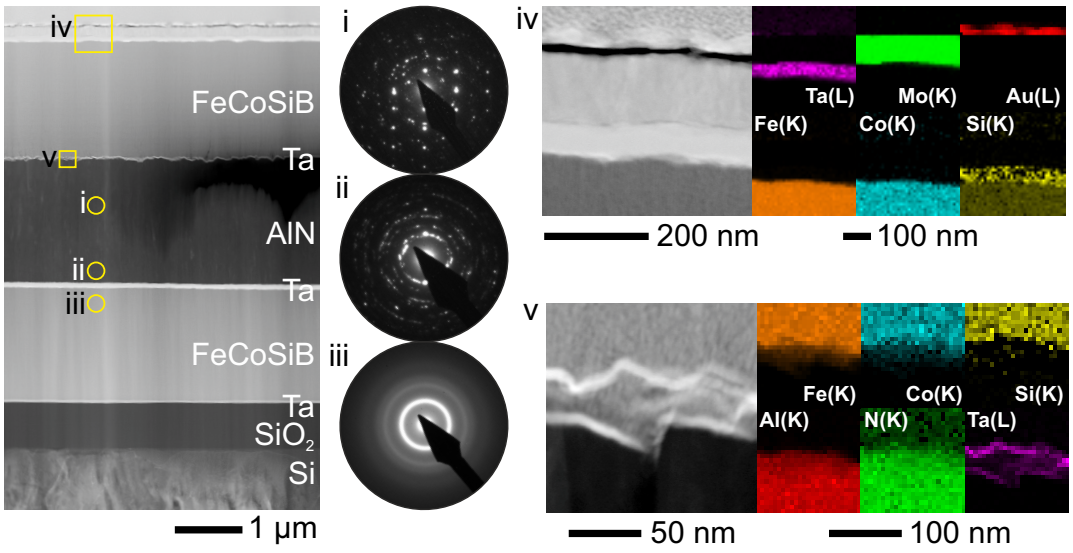

FIGURE 4.21: Cross-section STEM image of the FeCoSiB/AlN/FeCoSiB sandwich ME sensor. (i) ED pattern of AlN obtained within the film, (ii) ED pattern of AlN obtained close to the interface, (iii) ED pattern obtained of FeCoSiB. iv) Elemental maps of the top electrode region and (v) elemental maps of the AlN/Ta/FeCoSiB interface.

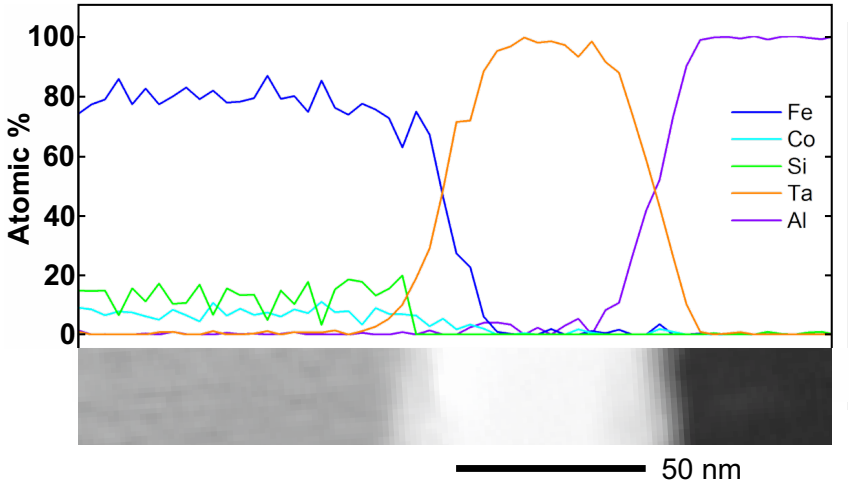

FIGURE 4.22: EDS elemental profile across the FeCoSiB/AlN interface showing a Ta layer but lack of a Pt seed layer.

4.3.2 Tunable Resonance Frequency Shape Memory Alloy ME Sensor

The concept of manipulating the cantilever stiffness to tune the resonance frequency of ME cantilever sensors has been demonstrated.[252] In the reported approach, the martensite-austenite phase transformation of a shape memory alloy (SMA) induces a gradual change of the elastic Young's modulus providing target-oriented modulation of the overall resonance frequency. The ability to operate the sensor at a specific tailored frequency range in resonance might be very interesting for the analysis of stimulated electric fields in an application such as deep brain stimulation. The stimulation frequency of these electrodes usually used for DBS is fixed in the approximate range between 130 and 170 Hz under clinical operation.[253] Hence, the post processed individual tuning of a small band resonance matching to the exact stimulation frequency or multiples would yield high sensor sensitivity for these artificial weak signals.

The process flow for these sensors is described by sputter-deposition of a thick film NiTi 50 µm and the inverse bilayer magnetoelectric composite stack Ta/FeCoSiB/ Ta/Pt/AlN/Pt onto a substrate with removable sacrificial layer. After using photolitography for the structuring process freestanding cantilever sensors with dimensions of 2.5 x 15 mm^2 were released from the substrate by wet etching. The most crucial step in this flow line is the crystallization of the amorphous deposited NiTi to enable phase transformation from martensite to austenite. The crystallization was performed after complete stack deposition using rapid thermal annealing at 450 °C for 30 minutes to impede crystallization of the FeCoSiB and ensure low surface roughness at the NiTi interface. However, a broader magnetic hysteresis suggested that temperature induced changes of the FeCoSiB deteriorated the soft magnetic properties limiting the maximum achievable LOD to 110 $pT/Hz^{1/2}$. To circumvent the limited temperature stability of the amorphous phase FeCoSiB during the annealing to induce crystallization of the shape-memory alloy, fundamental studies on alternative process flows and the resulting device properties have been performed and supported by TEM. The aim of these studies was to investigate the feasible room for improvement of the LOD demonstrated by the first freestanding ME sensor with tunable resonance frequency in the range Δf of 12%. Therefore, in a preparatory study the process flow was re-shaped to deposit an

AlN/FeCoSiB bi-layer geometry onto a NiTiCu SMA gaining the freedom to perform the optimized SMA annealing procedure prior to FeCoSiB deposition. From the perspective of TEM investigation, this study can be split into two parts: (A) Describes the microstructural differences induced upon the choice of annealing parameters. (B) Describes the microstructure of the freestanding and annealed sensor structure. Therefore, the described sensor structures of part (A) will be coined *Si substrate SMA/ME sensors* and the sensor structure of part (B) will be referenced to *freestanding SMA/ME sensor*.

(A) Influence of the annealing procedure on Si substrate SMA/ME sensors

The fabrication of ME sensors onto Si substrates facilitates large mechanical quality factors Q.[63], [254] Hence, the incorporation of ME composites in combination with ultra-low fatigue TiNiCu thin films on Si substrates was the major aim of this work in which the piezoelectric performance of c-textured AlN grown onto different TiNiCu surfaces was investigated. In the first approach Ta/Pt/AlN was grown onto as-deposited amorphous TiNiCu (Sample 1) and in a second approach the TiNiCu thin film was crystallized by RTA at 700 °C for 15 minutes before the deposition of AlN (Sample 2). Both sensor samples have been investigated using TEM and the results are published and discussed in the work about **magnetoelectric composites on ultra-low fatigue TiNiCu shape memory alloy thin-films**.[12]

"The chemical integrity, surface morphology, and interface study of the composites fabricated by the two different approaches are analyzed with STEM Z-contrast images and energy dispersive X-ray spectroscopy. A cross-section image of Sample 1 is shown in Figure 4.23a. The crystalline texture of the AlN film was analyzed by electron diffraction (ED) experiments which show a 5° out-of-plane tilt for the c-axis columnar texture of the (002) AlN film, depicted in Figure 4.23b. Annealing the TiNiCu prior to AlN deposition results in a polycrystalline structure with grains sizes of TiNiCu in the range of 100 nm - 400 nm and of different stoichiometry apparent from the brighter and darker Z-contrast. In order to link these differences in Z-contrast and morphology in the TiNiCu film to the chemical composition, Figure 4.23c shows the EDS profiles along the interface region (yellow arrow) and quantified according to the stoichiometry at each measured data point. The dashed black lines differentiate between grains of different Z-contrast and grain morphology, especially at the 140 nm thick interface region. Following the element profiles from left to right, the high Z-contrast grains of TiNiCu yields the targeted composition of $Ti_{50}Ni_{35}Cu_{15}$. However, upon entering the first low Z-contrast grain the amounts of Ti and Cu increase while Ni decreases yielding an average composition of $Ti_{66}Ni_{14}Cu_{20}$. Close to the interface, the Ni content increases while Cu decreases giving a different average composition of $Ti_{65}Ni_{31}Cu_4$, followed by separate and distinct layers of Ta, Pt and AlN. A detailed characterization of further common precipitates present in TiNiCu films such as Ti_2Cu was not performed in this study. However, for an in-depth discussion of the Ti_2Cu role the reader is referred to [255]. The heterogeneous variation in TiNiCu grain stoichiometry would be problematic for reliable ME sensor operation because the stoichiometry is known to strongly influence the formation enthalpies leading to a degeneracy of transformation temperatures within the film, hence only partial transformations would be observed upon heating to a specific temperature.[256], [257] In comparison, the cross-section and ED pattern of the AlN film of Sample 2 is presented in Figure 4.23d and 4.23e together with the EDS profiles given in Figure 4.23f. The most apparent difference between the two composites is the formation of a 420 nm wide diffusion region expanded over the Ti-enriched and Cu-poor TiNiCu grains at the interface to the bottom Ta/Pt electrode by interdiffusion upon RTA.

This Ti-enriched and Cu-poor interface grain structure (340 nm) is evidenced also at the Si substrate/Ta interface. The ED pattern on the AlN film provides evidence of an

[12]The following marked "text" is an excerpt from a work submitted to the Journal of Materials Research on December 25 2019, manuscript number JMR-2019-1027] Printed with Permission.

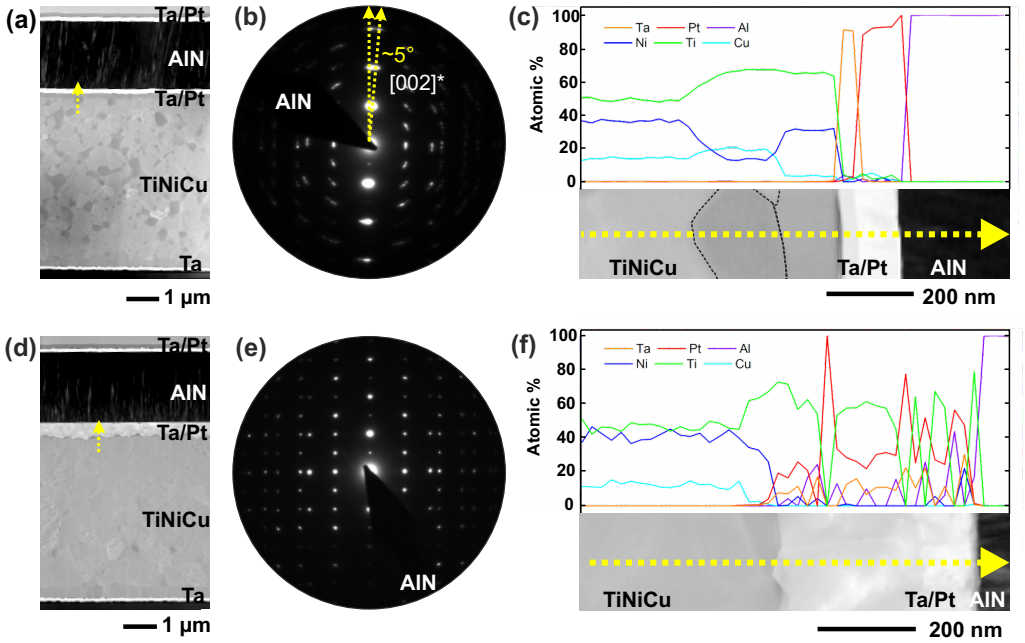

FIGURE 4.23: (a) STEM image showing the cross-section through Sample 1. The yellow arrow labels the position of the EDS profile. (b) ED pattern of the AlN film showing partial out-of-plane tilt of 5° columnar grains. (c) EDS profile showing the quantitative atomic distribution across the interface between AlN and TiNiCu. (d) STEM image showing the cross-section of Sample 2 after RTA. (e) ED pattern of the AlN film. (f) EDS profile showing the quantitative atomic distribution across the interface between AlN and TiNiCu.[Exerpt from a work submitted to the Journal of Materials Research on December 25 2019, manuscript number JMR-2019-1027] Printed with Permission.

excellent c-axis texture without any misalignment in the analyzed area of the film. With respect to the stoichiometry of the SMA film, smaller variations in the Z-contrast images are observed and an average composition of $Ti_{50}Ni_{33}Cu_{17}$ was measured by EDS. However, close to the diffusion region the EDS profiles indicate larger stoichiometric deviance of the TiNiCu composition compared to the average composition. Here, it is assumed that Ti diffused into the Ta/Pt layers, breaking up the electrode structure. As a result, Ni (∼40 at.%) accumulated in the intermediate interface region with respect to the average film stoichiometry. The transformation from the martensite phase (room temperature) into the austenite (120 °C) phase was probed by *in situ* heating experiments collecting diffraction information at room and high temperature for both samples. These results are further discussed in Figure 4.27."[13] Additional analyses via EDS detected low amounts of oxygen accompanied with the AlN thin film, which influence will be referred to in the discussions.

"The average structural transformation of the TiNiCu film was investigated by heating the samples *in situ* to temperatures above the austenite finish temperature $A_f = 69\,°C$ which was determined for these films. The results are presented in Figure 4.24 showing the ED patterns and rotational average plots of the intensity distribution at room temperature and at 120 °C, respectively. The phase transformation from the martensite into the parent austenite phase is evidenced for both films by smoothing of the ED patterns and the profiles. The low symmetry orthorhombic B19 phase is transformed into the high symmetry cubic B2 austenite phase; thereby the number of reflections is significantly reduced. Former studies on the phase transformation mechanism in Ti-rich TiNiCu films revealed Ti-rich nano-precipitates embedded in the alloy matrix to serve as epitaxial misfit strain mediators between the B19 and B2 phases.[258] These precipitates promote the transformation upon temperature cycling by epitaxial stabilization of a B2 transition layer, even in the martensite stable regime. Indeed, chemical variations in the form of Cu-enriched precipitates were evidenced in the present films. More details on the microstructure of Ti-rich TiNiCu films can be found elsewhere.[255] Hence, despite the presence of precipitate phases the *in situ* analysis demonstrated the transformation of the active martensite to the austenite phase for both Samples 1 and 2."[14]

[13] Excerpt of a work submitted to Journal of Materials Research on December 25 2019, manuscript number JMR-2019-1027. Printed with Permission.

[14] Excerpt of a work submitted to Journal of Materials Research on December 25 2019, manuscript number JMR-2019-1027. Printed with Permission.

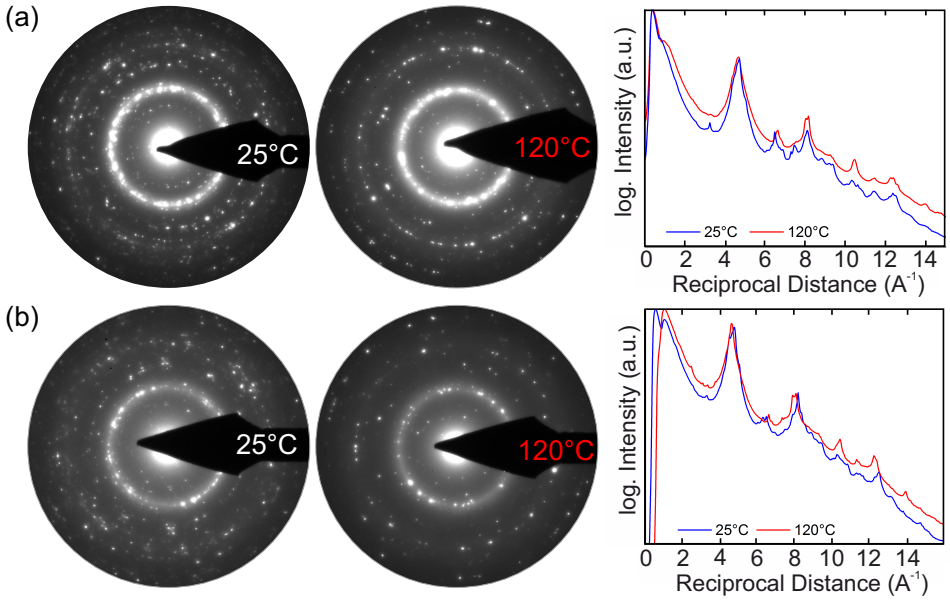

FIGURE 4.24: Electron diffraction pattern and according rotational average intensity plots of TiNiCu recorded at room temperature and 120 °C. (a) Sample with AlN deposited onto crystallized TiNiCu. (b) Sample with AlN desposited onto amorphous TiNiCu. The rotational average intensity plots clarify the induced transformation from the martensite to austenite phase.[Extracted from a work submitted to to Journal of Materials Research on December 25 2019, manuscript number JMR-2019-1027] Printed with Permission.

(B) Microstructure of freestanding SMA/ME sensor

In this study, one freestanding cantilever ME SMA based sensor with a TiNiCu/Ta /Pt/AlN/Ta/Pt/Ta/FeCoSiB/Ta layer sequence was investigated by analytical TEM on the Tecnai F30 instrument. Electron diffraction was used to determine the phase of TiNiCu and crystalline texture of AlN in combination with EDS to probe the average and nanoscale composition of individual layers.

For the freestanding sensor AlN/FeCoSiB was deposited onto amorphous TiNiCu and the complete sensor stack was released and annealed at 500 °C for 15 minutes to crystallize the SMA. This short time and rather low temperature should prevent interdiffusion phenomena and keep the exposition to higher temperatures of the FeCoSiB film as short as possible. To ensure a smooth interface for the FeCoSiB layer a second Ta layer was deposited onto the Pt top electrode. An overview STEM image of the freestanding sample geometry is depicted in Figure 4.25 also indicating the positions of EDS nanoprobe analyses (i) mapping the elemental distribution at the Ta/Pt/Ta/FeCoSiB electrode and (ii) disclosing the quantified atomic composition along the bottom TiNiCu/Ta/Pt interface. First, these analyses demonstrate the chemical integrity of all functional layers during all deposition and structuring steps as well as temperature treatments. Second, the quantified EDS element profiles reveal a homogeneous TiNiCu stoichiometry up to the Ta interface in good agreement with the intended average composition of TiNiCu. This result is different compared to observations on *Si substrate SMA/ME sensors* showing an interface layer with only 5 at% of Cu.

The high-resolution TEM investigation shown in Figure 4.26 also revealed a structural difference of the TiNiCu phase at the interface region to the Ta electrode. In comparison to the granular interface structure of the *Si substrate SMA/ME sensors*, the *freestanding SMA/ME sensor* possesses a not-crystallized but still amorphous interface evidenced by the respective

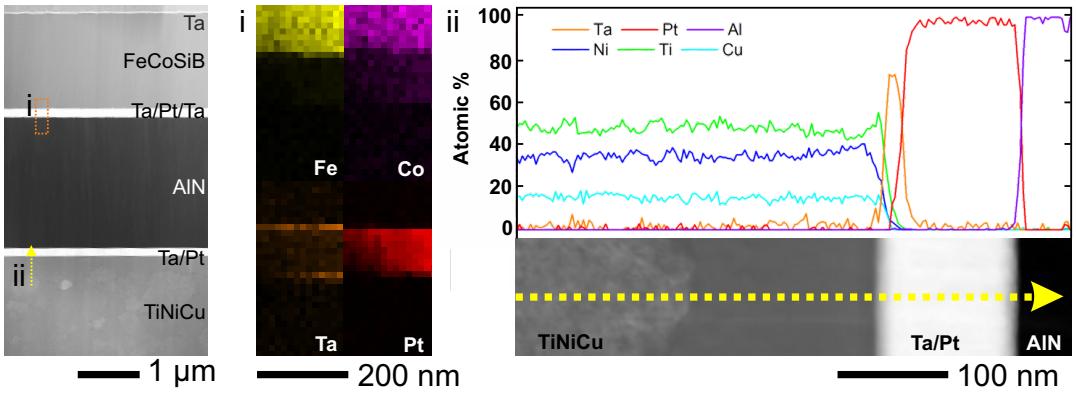

FIGURE 4.25: Cross-section STEM image showing the freestanding ME sensor geometry and chemical analysis. i) EDS elemental maps (orange frame) verifying the Ta/Pt/Ta/FeCoSiB layer sequence. ii) EDS elemental profile across the interface TiNiCu/Ta/Pt/AlN (yellow arrow in the preceding STEM image) showing a constant elemental composition of Ti:Ni:Cu at the Ta interface region.

FFT image of Figure 4.26a. The ED experiment shows a non-textured polycrystalline pattern which fits very nicely to the structure of the austenite B2 phase (see Figure 4.26b). The inset rotational average intensity plot offers indices of the lattice planes according to the cubic B2 phase. The functional AlN film exhibits the intended *c*-axis textured growth, which was observed in both the HRTEM/FFT and ED experiments displayed in Figure 4.26. However, the EDS analysis revealed moderate oxygen contamination up to 4 at% as well as in the *Si substrate SMA/ME sensors*. The FeCoSiB layer is evidenced by the presented ED pattern to be not affected with respect to crystallization by the short annealing procedure.

Discussion on SMA/ME sensors

In the following, the thermodynamics and reaction kinetics of the TiNiCu crystallization process by rapid thermal annealing will be briefly discussed and translated to the observation of a diffusion Ti/Ta/Pt layer.

Rapid thermal annealing uses intense heat radiation from a quartz lamp to produce high heating rates and little temperature profiles at the sample position. In the presented studies, the amorphous TiNiCu phase was crystallized at temperatures of $T_a = 700\,^{\circ}C$ and at minimum of $T_a = 500\,^{\circ}C$ for 15 minutes the latter matching with the crystallization temperature of TiNiCu. The choice of annealing temperature was observed to have an impact on the crystallization behaviour of the amorphous TiNiCu phase. In amorphous films annealed at significantly higher temperature than T_{cryst}, the crystallization is expected to start within the film. The crystallization proceeds independent from interface nucleation and is expected to be finished within <20 seconds under consideration of grain growth mechanisms which are creating stress fields in the amorphous matrix.[259], [260] For the rest of the time diffusion processes dominate resulting in growth or dissolution of various precipitates in the TiNiCu matrix in dependence of time and temperature, which is know to affect the transformation temperatures of the alloy.[261], [262] In case of high-temperature annealing a layer of Ti-enriched and Cu-poor grains with different grain morphology is established at the interfaces of the Ta-adhesion layer and Ta-electrode layer, whereas for low-temperature annealing an amorphous layer could be traced at the Ta-electrode interface. This gives hint that the

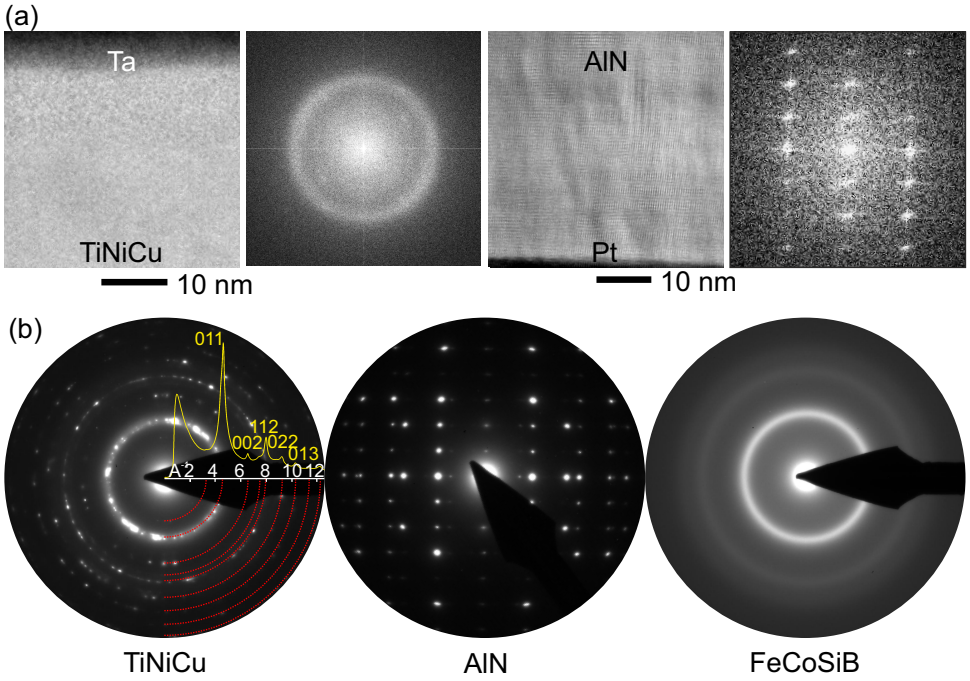

FIGURE 4.26: Structure analysis of functional layers and at the Pt/AlN and Ta/TiNiCu interfaces. (a) High-resolution TEM micrographs and inset FFT images showing the excellent AlN *c*-axis texture at the Pt interface (top) and an amorphous TiNiCu layer close to the Ta interface. (b) Electron diffraction experiments displaying the polycrystalline character of the TiNiCu in its austenite B2 phase with inset showing the rotational average intensity profile and ED pattern showing amorphous phase FeCoSiB and highly *c*-axis textured polycrystalline AlN.

crystallization happens randomly in the center of the film to the interfaces. A possible explanation for the Cu-poor grains at the Ta-interface is the consumption of Cu by precipitation of Cu-enriched grains within the film as evidenced in this investigation. The presence of these precipitates might be related to (i) small variation in the film composition, (ii) temperature dependent stress fields during crystallization or (iii) thermodynamic considerations at elevated temperatures. Note, no Cu-enriched precipitates have been observed in films annealed at $T_a = 500\,^{\circ}C$. However, in these films the amorphous interface could possibly also result from (i) the major bending stress or (ii) due to the low crystallization temperatures, the 40 µm thick film was not fully crystallized in the given time up to the interfaces, where interface energies also contribute to the crystallization process. Further, for films annealed at elevated temperatures, the martensite-austenite transformation could be observed during *in situ* TEM heating experiments, while the low-temperature annealed film was observed to be already in its austenite B2 phase at room temperature. This indicates that the martensite transformation temperatures are shifted below room temperature, reasoning the presence of the austenite phase after cooling down from annealing at $T_a = 500\,^{\circ}C$. Indeed, this observation is congruent to DSC measurements performed by Sabrina Curtis pointing out the direct influence of the annealing temperature on the transformation temperatures. In detail the transformation temperatures measured in dependence of the annealing temperatures are: $T_a = 500\,^{\circ}C$: $M_s = 21.9\,^{\circ}C$, $M_f = 14.9\,^{\circ}C$ and $A_s = 31.5\,^{\circ}C$, $A_f = 39.7\,^{\circ}C$ and for $T_a = 700\,^{\circ}C$: $M_s = 52.4\,^{\circ}C$, $M_f = 50.3\,^{\circ}C$ and $A_s = 63.5\,^{\circ}C$ and $A_f = 68.8\,^{\circ}C$. Second, in temperature sensitive materials, the transformation can also be triggered by ion or electron beam irradiation via Joule heating during sample preparation or TEM examination.[263], [264]

Heat might also be the decisive factor for the formation of a diffusion region at the TiNiCu/Ta/Pt interface in the *Si substrate SMA/ME sensor* annealed at $T_a = 700\,^{\circ}C$. Note, no diffusion was observed in films annealed at $T_a = 500\,^{\circ}C$ for 15 minutes. "The formation of a diffusion region is sketched in Figure 4.27 resembling simplified experimental EDS concentration profile data. Herein, the stages of the envisioned diffusion process at the TiNiCu/Ta/Pt interface are depicted under following assumptions: (Top) Situation after rapid crystallization, $t < 20\,s$. A Cu-poor and Ti-enriched interface region is formed immediately (blue box). Such interface morphology was observed at the substrate side Ta-adhesion layer in both investigated sensors after 15 minutes of annealing. (Bottom) Situation after diffusion originated from the grains at the interface resulting in a mixed poly-crystalline region under complete dissolution of the electrode structure. The complete interpretation of diffusion in a multicomponent system with only two sets of data is not possible. In the following, a coarse idea of the diffusion processes along the following lines and boundary conditions is presented. TiNiCu crystallizes immediately, as the annealing temperature of $700\,^{\circ}C$ is exceeding significantly the crystallization temperature of $500\,^{\circ}C$.[260] From TEM investigations it is clear that all layers are polycrystalline with lateral grain sizes of around 200 nm in the TiNiCu alloy due to crystallization and around 10 nm and 100 nm in Ta and Pt layers during sputter deposition (grain size of the order of the film thickness). This setup is regarded as interdiffusion experiment in a multicomponent alloy with fine grain size. To discuss this, thermodynamics (i.e. attractive and repulsive interactions of the up to five components, possible intermetallic phase formation, solubility limits) as well as kinetics (tracer and chemical diffusion in the bulk as well as grain boundary diffusion) has to be taken into account. We start by estimating the diffusivities needed. Using the well-known parabolic growth law [265]:

$$x = 2\sqrt{D(T) \cdot t}$$

with t = 15 min. and x = 100 nm being roughly half of the length of the diffusion zone (see Fig. 4.27) results in diffusivities of the order of $10^{-18} m^2/s$ needed to explain the change of the concentration profiles. However it is not clear, whether bulk or grain boundary diffusion is dominant the latter being orders of magnitude faster than the former. No data for grain boundary diffusion is available for this system.[266] Bulk diffusivities can be estimated from data collections on diffusion couples depending on matrix and diffusing element.[265] Calculations result in diffusivities between $4.2x10^{-21} m^2/s$ for Fe in Ta and $5.6x10^{-21} m^2/s$ for Al in Ta (according to tables in [267]). These values for bulk diffusivity are much too small compared to the needed $10^{-18} m^2/s$. However, it has to be stressed that grain boundary diffusion might occur as well and is three to five orders of magnitude larger than the bulk values calculated here.[265], [266], [268] Thus from kinetic and diffusion point of view, such concentration profiles as in Figure 4.27 are possible.

To understand the sequence of processes and the shape of the concentration profiles in detail the thermodynamics of the binary systems serve acceptable approximation to estimate solubility limits an thermodynamic effects (thermodynamic factor of diffusion [265]) in multiple phase systems. The binary phase diagrams for the present systems offer the following information: {Ti-Ta}: Good solubility with two intermetallic phases (IPs).[269] {Ta-Pt}: Little solubility and a large number of IPs.[270]
{Ti-Pt}: little solubility with large number of IPs.[271] {Ni-Ta}: medium solubility and large number of IPs.[272] {Cu-Ta}: no solubility.[273] Based on the good solubility of Ti in Ta and

the small grain size of the Ta-layer, it is expected that first the 10 nm Ta barrier is dissolved by interdiffusion via grain boundary diffusion. Then, without an intact Ta barrier, Ta and Pt start to diffuse towards the boundary of the Ti-enriched interface layer, while Ta also diffuses into the Pt-layer. Formation of binary or ternary Ti-Ta-Pt phases having no solubility of Ni, causes an enrichment of Ni towards the matrix. Cu is also driven away from the interface due to the low solubility of Ta and Cu. Note, the exact nature of phases formed within this diffusion region and the respective grain sizes have not been determined and are assumed to be strongly heterogeneous.

In summary, it is consistent with kinetics and phase diagrams that first crystallization occurs, then dissolution of the Ta barrier via grain boundary diffusion and then grain boundary diffusion of Ta and Pt into the remaining matrix driving Ni and Cu away from the interface."[15]

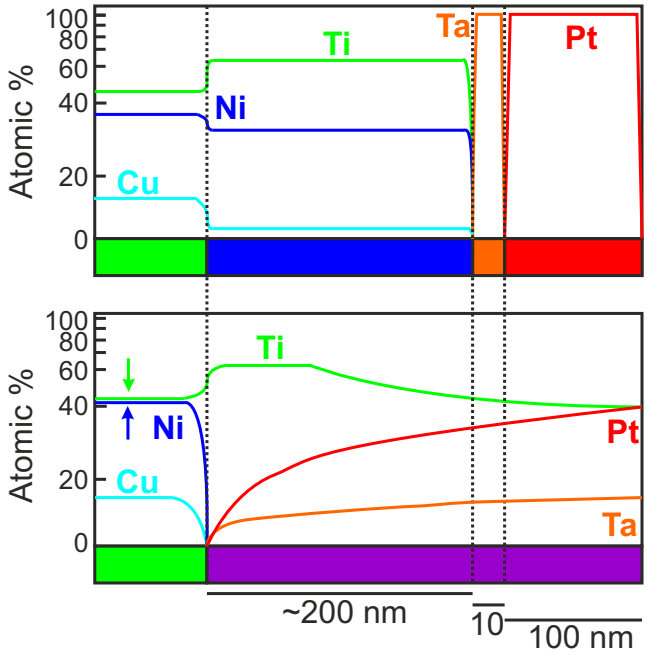

FIGURE 4.27: Simplified sketch of the experimental element profiles at the TiNiCu/Ta/Pt interface. (Top) Situation after rapid crystallization, no diffusion took place and a Cu-poor and Ti-enriched interface layer is established. (Bottom) Situation after diffusion, Ti diffuses towards the Pt layer and Ta, Pt diffuse towards the TiNiCu matrix. Green box: TiNiCu matrix, blue box: Cu-poor and Ti-rich crystal interface, orange box: Ta-layer, red box: Pt-layer, violet box: diffusion region.[Extracted from a work submitted to Journal of Materials Research on December 25 2019, manuscript number JMR-2019-1027. Printed with Permission.]

[15]Excerpt of a work submitted to Journal of Materials Research on December 25 2019, manuscript number JMR-2019-1027. Printed with Permission.

Conclusion

The presented investigations on two kinds of SMA/ME sensors revealed remaining issues with the AlN and TiNiCu material. In both the Si substrate SMA/ME sensors as well as the *freestanding SMA/ME sensor* oxygen contamination of AlN was detected. Oxygen contamination in the AlN lattice produce point defects which are described as isolated Al vacancies or extended defects leading to the inversion of piezoelectric polarity.[274] Further, the AlN grain size as well as the electromechanical coupling factor k^2 is reported to be affected by oxygen contamination.[275] For the application of AlN in ME or SAW sensors, a high quality in both structural and electromechanical properties is inevitable for achieving the desired low LOD in the sub-pT regime required for biomedical application. Further, structural discrepancies from an ideal TiNiCu/Ta interface were identified basically in all samples. For example, in the *Si substrate SMA/ME sensors* a granular interface morphology with different stoichiometry compared to the TiNiCu matrix was probed and its chemical instability was shown in contact with a Ta/Pt electrode interface upon RTA treatment. In the *freestanding SMA/ME sensors* a layer of remaining amorphous TiNiCu was observed at the Ta interface, which does not contribute to the shape memory performance and can be regarded as "dead volume". Thus it might negatively effect the overall change in mechanical stiffness possibly resulting in a limited range of possible resonance frequency shifts of the cantilever sensor. In addition, long time factors such as fatigue behavior have to be taken into account.

Chapter 5

Sensors for Breath Monitoring

The detection of gaseous species in air is an important issue in the field of environmental sensing which includes safety applications i.e. detecting toxic compounds, chemical warfare agents or explosives exceeding certain concentration limits. But also the detection of organic species in the human odor becomes seemingly more interesting in terms of medical application. This chapter concentrates on the specific detection of hydrogen gas and acetone vapors related to human healthcare. The human breath contains a mixture of a plethora of gaseous molecules such as oxygen, nitrogen, water, hydrogen, hydrogen sulfide, methane, carbon monoxide, carbon dioxde, nitric oxide and further volatile organic compounds (VOCs) such as acetone or ethanol which do play important role in biological systems. The detection of these molecules can be used to monitor specific microbiological metabolism in the colon produced by intestinal bacteria and informs about a humans health condition. Hence, breath sensors can revolutionize medical diagnostics by providing a platform for on-demand detection and monitoring of health parameters in a noninvasive and personalized fashion.[276]
In the following sections, the focus is on the materials studies for the development of sensors with high selectivity and high sensitivity to hydrogen molecules and acetone vapors. Usual materials of choice are n-type and p-type metal oxide (MOx) semiconductors. N-type MOx semiconductors play an important role due to their response to large changes in resistance when gas molecules interact with the surface. The resulting change in conductivity is highly sensitive to the composition of the gas and provides the ability to detect subtle changes in concentration down to the ppm limit.[277] In this respect, intrinsic n-type semiconductors such as SnO_2 and ZnO micro- and nanostructures show high potential for gas sensing applications, since their sensor performance can be modified, e.g. by the design of morphology or exposed crystal facets,[85], [195], [278] and surface functionalization with metal or metal oxide nanoparticles (NPs) offering a high surface-to-volume ratio.[88], [193] On the other side, the mechanisms of p-type MOx such as Fe- and Cu-oxides have been demonstrated to be sensitive to volatile organic compounds and their response to acetone will be discussed.[279]

5.1 Hydrogen Detection

The analysis of the amount of breath hydrogen reflects on the carbohydrate fermentation by anaerobic bacteria in the colon and could be an important biomarker for a patients gastrointestinal health condition.[280] In this context, the orocecal transit time (OCCT) which is defined as "the time from lactulose ingestion to a sustained increase of over 5 ppm above fasting levels in the end-expiratory hydrogen concentration".[281] In clinical diagnostics, the OCCT is an important measure for the change in hydrogen gas concentration in the breath over time and is a direct indicator with respect to bacterial overgrowth or malabsorption being the trigger for abdominal symptoms.[282], [283] Also, the effectiveness or possible side effects of certain drugs can be monitored helping with the drug decision and diagnosis of lactose intolerance has been shown feasible.[284]

However, there are quite some challenges to the interpretation of the measured data. The amount of hydrogen gas in the breath is typically low in the parts per million regime and the average baseline is still unclear as the hydrogen level might also dependent on the type of diet, gender or age.[280] The small amount of breath hydrogen sets up certain requirements on the sensor characteristics and the sensor material. Typically, gas sensors can be compared according to their performance by the following quantities: gas response, which is the ratio of the measured resistance of the analyte gas mixture to the resistance measured in air R_{gas}/R_{air} or vice versa dependent on n- or p-type semiconductor; selectivity to other molecules in the analyte gas mixture, described by the selectivity factor which is the ratio of the individual gas responses; the optimum operation temperature and response dynamics describing the response time τ_r being the amount of time to reach 90% of the final indication and the recovery time τ_d being the time the system needs to approach 10% of the preceding response after exposure to air; as well as the limit of detection describing the amount of analyte gas in the gas mixture which gives a quantifiable and selective gas response. Therefore, the sensor device and choice of material should offer a good cross selectivity to other gas molecules, a low limit of detection and a high uncertainty, especially at low concentration in the ppm regime.

There is an immense amount of concepts for hydrogen sensors on the market.[285] One important group for breath analysis techniques combines gas chromatography with solid-state MOx sensors in electronic noses that are highly sensitive to specific gases at low consumption costs and short times of analysis. Next to n-type semiconductor SnO_2 and TiO_2,[286], [287] microstructures of ZnO are interesting materials due to the possibility to produce them in various morphology by a change of process parameters.[190] Furthermore, surface functionalization with noble metal or metal oxide NPs is widely known to achieve significant improvement of the sensor performance. In this respect, the high affinity of H_2 to Pd is readily exploited resulting in ultra-high sensor response characteristics.[288]–[291]

The focus of the attached studies was on the fabrication of single structure gas sensors using nanowire (NW) and tetrapod (T) geometries of ZnO. Functionalized ZnO structures have been analyzed to investigate the impact of the type of surface functionalization on the sensor characteristics. The attached contributions report on $ZnAl_2O_4$-functionalized ZnO tetrapod

structures[198][1] and Au-modified ZnO nanowires.[197][2] In the first study, the structure investigations by TEM supported the manuscript by identification of the $ZnAl_2O_4$ spinel-type phase NPs, the size distribution of these particles and the specific crystallographic relationships between the ZnO and $ZnAl_2O_4$ lattice. No orientation relationship has been identified in the case of Au NPs on ZnO.

The individual sensor characteristics are presented and compared with similar studies in Table 5.1. Further comparison to sensor data of similar studies reported in the literature can be found in the referenced studies. The selected studies demonstrate sensitivity to hydrogen at room temperature (RT) with respect to other VOCs in the gas mixture and still reasonable gas responses larger than 1, which can be increased by elevated temperatures, as well as the limit of detection and response dynamics. This temperature dependence is described by the improved adsorption and oxidizing reaction kinetics of gas molecules on the ZnO surface due to a larger resulting charge transfer from the NPs to the ZnO by the formation of heterojunctions, e.g. Schottky-contacts. The geometry such as the diameter of the device nanostructure displays a crucial quantity for the sensor performance due to the modulation of the conduction channel width and free surface area.[292], [293] The effect of the structure morphology[195] on the gas response was evidenced in ZnO nanostructures modified with $ZnAl_2O_4$ NPs on the surface showing an increased value of 2 for a tetrapod structure with respect to a NW structure. Further, improved hydrogen sensing performance could be achieved by the deposition of Au NPs onto ZnO NWs showing a gas response of 7.5 at RT for about 7% of covered surface by Au. Together with a low limit of detection of 1 ppm, response dynamics in the regime of some minutes and the growth of samples in a one-step process would enable Au:ZnO based sensors for application in hydrogen gas breath analysis even at room temperature operation. As demonstrated in these studies, the sensing characteristics of single structure devices can be further improved by tuning the operation temperature with respect to the target gas or by using NW networks.[293] However, Pd-based ZnO sensors using Pd NPs as catalyst show significant better performance of the single structure.[294]

As a conclusion one has to keep in mind, that these are fundamental studies demonstrating the improvement of hydrogen gas sensing performance on the example of single NW structures to study effects of structure size, geometry and functionalization. The implementation of such single structures into real devices for mass-production, however, is not practicable. Therefore, the implementation of semiconducting MOx thin films is readily established and tentative for future flexible sensing devices without the requirement of heating.[295] Further, the effect of relative humidity, which is as high as 80-90% in human breath has to be analyzed and taken into account, since the ambient water molecules could have significant influence on the gas sensor performance.[296]

[1] Reprinted with permission from Phys. Status Solidi A 2018, 215, 1700772 published by © 2018 WILEY-VCH Verlag GmbH Co. KGaA, Weinheim

[2] Reprinted with permission from ACS Appl. Mater. Interfaces 2019, 11, 32115-32126, © 2019, American Chemical Society

TABLE 5.1: Sensor characteristics of single structure sensors to hydrogen gas

Material	**Diameter / nm**	**Concentration / ppm**	**Gas Response***	$T_{operation}/^{\circ}C$	$\tau_r \vert \tau_d$ / **s**	**Limit of Detection / ppm**
$ZnAl_2O_4$: ZnO NW[198]**	400	100	1.15	RT	190|280	90
$ZnAl_2O_4$: ZnO NW[198]**	400	100	3.3	100	45|80	5
$ZnAl_2O_4$: ZnO – T[198]**	400	100	2	RT	30|60	10
Au : ZnO NW[197]**	120	100	7.5	RT	180|320	1
Au : ZnO NWnetwork[293]**	-	100	40	RT	-|-	1
PdO : ZnO(Pd) film[87]**	-	125	11	150	40|30	3
Pd : ZnO NW[290]	100	100	400	RT	-|-	-
Pd : ZnO NW[294]	160	100	13100	RT	6.4|7.4	0.015

*All sensor characteristics have been measured in a gas mixture with air of 30-40% relative humidity

** Publication with Co-Authorship

ORIGINAL PAPER
Hydrogen Sensors
physica status solidi a
www.pss-a.com

$ZnAl_2O_4$-Functionalized Zinc Oxide Microstructures for Highly Selective Hydrogen Gas Sensing Applications

Mathias Hoppe, Oleg Lupan, Vasile Postica, Niklas Wolff, Viola Duppel, Lorenz Kienle, Ion Tiginyanu, and Rainer Adelung**

In this work, a simple method of $ZnAl_2O_4$-functionalization of ZnO microstructures is presented. The different characterization methods (structural, chemical, and micro-Raman) demonstrated the presence of only ZnO and $ZnAl_2O_4$ crystalline phases. $ZnAl_2O_4$ nano-crystallites grow on the surfaces of ZnO 3D microstructures having diameters of 50–100 nm and with high density. Transmission electron microscopy (TEM) and high-resolution TEM (HRTEM) results clearly show $ZnAl_2O_4$ crystallites functionalizing zinc oxide tetrapod arms. The individual structures (microwires (MWs) and three-dimensional (3D) tetrapods (Ts)) are integrated into functional devices, suitable for gas sensing applications. All devices show excellent hydrogen gas selectivity at relatively low operating temperature in the range of 25–100 °C. The highest gas sensing performances are obtained based on individual $ZnAl_2O_4$-functionalized ZnO tetrapods ($ZnAl_2O_4$/ZnO-T, with an arm diameter (D) of ≈400 nm) and a response of ≈2 at 25 °C to 100 ppm of hydrogen gas (H_2), while a $ZnAl_2O_4$/ZnO-MW ($D \approx 400$ nm) shows only a response of ≈1.1. The Al-doped ZnO MW ($D \approx 400$ nm) without $ZnAl_2O_4$ elaborated in another work, chosen only for comparison reason, shows no response up to 800 ppm H_2 gas concentration. A gas sensing mechanism is proposed for a single $ZnAl_2O_4$/ZnO-T microstructure based sensor. The obtained results on $ZnAl_2O_4$/ZnO-T-based devices is superior to many reported performances of other individual metal oxide nanostructures with much lower diameter, showing promising results for room temperature H_2 gas sensing applications.

1. Introduction

Hydrogen is considered to be the perfect fuel candidate for the 21st century, among its high heat of combustion (≈142 kJ g^{-1}) and wide flammable range (≈5–75%) it is also one of the cleanest energy carriers. The combustion product of hydrogen is only water, which is free from contamination, thus this reaction is eco-friendly and termed "green." However, H_2 gas is tasteless, colorless, and odorless referring to a dangerous character as it cannot be detected by human beings. Therefore, the rapid and accurate H_2 gas detection even to small concentrations is necessary to be realized by miniaturized portable nano-devices. In this context, ZnO micro- and nano-structures are excellent candidates for gas sensing applications.[1] However, pristine ZnO has a low selectivity to specific gaseous species such as hydrogen gas.[2,3] Therefore, different methods to improve the selectivity were reported, such as doping or functionalization with Pd,[4,5] the formation of different types of hetero-junctions,[6,7] etc. However, the surface functionalization of ZnO nano- and micro-structures with oxide spinel compounds to enhance the sensing properties was less reported to date and needs further exploration. The formation reactions of oxide spinel compounds AB_2O_4-based on Zn are easily accessible by the calcination of ZnO and other metal oxides (Al_2O_3, In_2O_3, SnO_2, TiO_2, etc.).[8,9]

Oxide spinel compounds AB_2O_4 are ceramics that have a wide range of versatile applications due to many interesting properties and the large family of materials.[8,10,11] Different types of oxide spinel compounds are known to be important sensing materials for the detection of reducing and oxidizing gases, as well as water vapors.[12–15] For example, Li et al.[16] reported that the gas response of $ZnFe_2O_4$-decorated ZnO composites to 100 ppm acetone was about three times higher than that of undecorated ZnO microspheres. Guan et al.[17] demonstrated that $ZnAl_2O_4$ inside the calcined sample acts as a catalyst to accelerate the response and recovery behaviors in ethanol sensing of ZnO. Wongchoosuk et al.[18] developed a photo-stimulated electronic nose based on ZnO—$ZnAl_2O_4$ and ZnO—Zn_2TiO_4 core–shell

M. Hoppe, Prof. O. Lupan, N. Wolff, Prof. L. Kienle, Prof. Dr. R. Adelung
Institute for Materials Science
Kiel University
Kaiserstr. 2, 24143, Kiel, Germany
E-mail: ollu@tf.uni-kiel.de; oleg.lupan@mib.utm.md; ra@tf.uni-kiel.de

Prof. O. Lupan, V. Postica, Prof. I. Tiginyanu
Department of Microelectronics and Biomedical Engineering
Technical University of Moldova
168 Stefan cel Mare Av., MD-2004 Chisinau
Republic of Moldova

V. Duppel
Max Planck Institute for Solid State Research
Heisenbergstr. 1, 70569 Stuttgart, Germany

The ORCID identification number(s) for the author(s) of this article can be found under https://doi.org/10.1002/pssa.201700772.

DOI: 10.1002/pssa.201700772

ADVANCED SCIENCE NEWS
www.advancedsciencenews.com

physica status solidi a
www.pss-a.com

nanowires that work at room temperature for detecting toxic gases. Thus, it is demonstrated that functionalization with spinel compounds can efficiently enhance the gas sensing properties of ZnO.

From all oxide spinel compounds, zinc aluminate ($ZnAl_2O_4$) holds great promise due to the peculiar arrangement of its cations in the spinel structure which lead to a better mobility of the charge carriers.[19] $ZnAl_2O_4$ is a wide bandgap semiconductor (3.8 eV) and crystallizes at ambient pressure in a diamond-type cubic spinel structure with the space-group $Fd\bar{3}m$ (227).[11,20] Its characteristics make it extremely attractive as catalyst, high temperature- and mechanical-resistant material, thermal and optical control coating for spacecrafts and other applications. Also Zn and Al are relatively inexpensive materials. However, as was mentioned earlier, only few results were reported on the gas sensing properties of $ZnAl_2O_4$, as well as on $ZnAl_2O_4$-functionalized ZnO nano- and micro-structures.[7,17,21] The $ZnAl_2O_4$ and ZnO composites are mainly synthesized by high doping of ZnO with Al or Al_2O_3 and further extended calcination time.[7,22]

Herein, we present a simple method for the growth of small and homogenously distributed $ZnAl_2O_4$ crystals with a diameter of 50–100 nm on the surface of ZnO nano- and micro-structures using aluminum acetate basic hydrate. In this work, the gas sensing properties such as selectivity to hydrogen gas and the operating temperature of this approach are discussed and compared to sensors based on $ZnAl_2O_4$ polycrystalline clusters on ZnO tetrapod networks, reported in our previous works.[7,23]

The functionalization of ZnO-T networks with $ZnAl_2O_4$ demonstrated an improved H_2 gas sensing response by a factor of 5.[7] However, the diameter of the $ZnAl_2O_4$ polycrystalline clusters was in the micrometric range (up to 10 μm) which results in a low number of heterojunctions. Therefore, the essential improvement in the sensing properties compared to pristine ZnO-T networks was hard to achieve. In this work we try to overcome this issue by the growth of nanoscopic crystals of $ZnAl_2O_4$ directly on the surface of the ZnO-T networks. This promotes a considerable increase in the sensing properties of individual structures due to the larger amount of $ZnAl_2O_4$/ZnO heterojunctions and increased charge transfer. Thus, the enhanced modulation of the conduction channel width can be achieved due to additional electron depletion regions formed at the interface of these materials. Additionally, nanoscopic materials can be more active and selective as catalysts compared to microscopic or even larger particles.[24]

2. Experimental Section

Starting from ZnO-T material the aluminum acetate basic hydrate (Alfa Aesar, A11620) was mixed in ratios (2:0.5; 2:1.0; 2:1.5) in a glass beaker filled with diluted ethanol (45 ml) as mixing agent. This suspension was then stirred for 10 min at 500 rpm. To evaporate the ethanol, the beaker was placed on a hot plate set to 80 °C for approximately 12 h. The dry powder was then put in a crucible and placed in a muffle oven for 6 h at a temperature of 500 °C to get rid of the organic residues. Finally, the powder was pressed into a cylindrical shape (diameter: 5 mm, height: 4 mm) to a resulting density of 1 g cm^{-3}. At last, the tablets underwent a calcination procedure at 1150 °C for 5 h. The pristine ZnO microstructures used in this work were synthesized by the flame transport synthesis (FTS) approach; detailed characterizations are presented in our previous works.[25,26]

The scanning electron microscopy (SEM), micro-Raman, and X-ray diffraction (XRD) measurements were performed as was reported previously.[27] Micro-Raman spectra were recorded at 20 °C on a Raman WITec Alpha 300R spectrometer in a backscattering configuration interfaced with a digital photometer and a data acquisition monitor processor. A 532 nm line from a Nd-YAG laser was used for off-resonance excitation with less than 4 mW power at the sample. The instrument was calibrated to the same accuracy using silicon standard. Transmission electron microscopy (TEM) studies on the morphology, chemical composition via energy dispersive X-ray (EDX) spectroscopy and crystal orientation analysis were conducted on two microscopes: (1) a Philips CM 30 ST operating with a LaB_6 cathode at 300 kV for electron diffraction experiments; and (2) a FEI Tecnai F30 (300 kV, EDAX detector system) for chemical mapping. Selected-area electron diffraction (SAED) experiments were performed by inserting an aperture as small as 100 nm in diameter into the optical axis to select individual crystals followed by tilting into a highly symmetric zone axis orientation for ZnO, e.g., $[2\bar{1}\bar{1}0]_{ZnO}$. Precession electron diffraction (PED) was enabled by a Digistar device to reduce dynamical effects and to increase the information limit.

Single nanosensor devices based on individual $ZnAl_2O_4$-functionalized ZnO microstructures (from samples with a (ZnO):(aluminum acetate ratio) of 2:1) were fabricated using a procedure described by Lupan et al.[28–31] in a FIB/SEM system by contacting individual structures with different morphologies and from different types of samples with a Pt complex to Au/Cr pads of the chip. The influence of the $ZnAl_2O_4$ content on the gas sensing properties of individual $ZnAl_2O_4$-functionalized ZnO microstructures will be presented in another forthcoming work.

In order to investigate the influence of the operating temperature on the gas sensing properties of individual structures, gas sensing measurements were performed in the range of 25 °C (RT) −100 °C. The ambient relative humidity (RH) was 30–40 %. The following gases and vapors were used for the investigation of sensing properties of the fabricated devices: hydrogen gas (H_2), methane gas (CH_4), ethanol (C_2H_5OH), acetone (CH_3COCH_3), and ammonia (NH_3) vapors. More details on the gas sensing measurements are presented in our recent works.[32,33] All electrical measurements were performed using a Keithley 2400 source meter. The gas response was defined as the ratio of current under exposure to tested gas and in air ($S_{gas} = I_{gas}/I_{air}$). The response and recovery times are defined as the necessary times to reach or recover 90% of full response.[34]

3. Results and Discussion

3.1. Characterization of $ZnAl_2O_4$-Functionalized Zinc Oxide Structures

Figure 1 shows scanning electron microscopy (SEM) images of $ZnAl_2O_4$-functionalized zinc oxide microstructures obtained for

ADVANCED SCIENCE NEWS
www.advancedsciencenews.com

physica status solidi a
www.pss-a.com

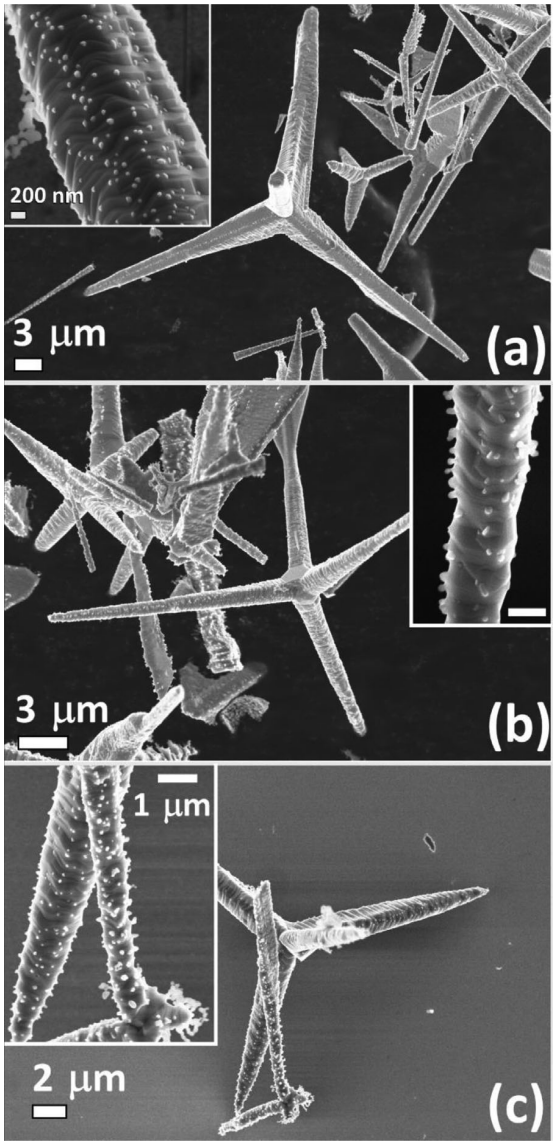

Figure 1. SEM images with general view and surface morphology (in inset of each figure) of $ZnAl_2O_4$- functionalized ZnO-T networks with ZnO:Al-acetate ratio: (a) 2:0.5; (b) 2:1.0 (scale bar in inset is 500 nm); and (c) 2:1.5.

the initial mixing ratios of ZnO to aluminum acetate of 2:0.5; 2:1.0, and 2:1.5. A gradual increase in the density of the nanoscopic particles on the surface of the ZnO microstructures can be observed along with a higher ZnO:Al-acetate ratio. The diameter of single particles varies from 50 to 100 nm and can agglomerate to chain-like structures as observed with increasing the ZnO-T to aluminum acetate ratio (see Figure 1 and Supporting Information Figure S1). Note that the diameter of the nanoscopic particles seems not to depend on the content of aluminum acetate in the synthesis. The influence of the ZnO:Al-acetate ratio used in the synthesis on the stoichiometry of the obtained networks is described in the supporting information (see Supporting Information Figures S1 and S2 and Table S1).

3.2. Structural Properties

In order to investigate the structure of nanocrystals on the surface of the ZnO-Ts an X-ray diffraction (XRD) analysis was performed. XRD patterns in the angular range of 31–39° are presented in **Figure 2**a for pristine ZnO-T and $ZnAl_2O_4$-functionalized ZnO-T networks for simplicity. For pristine ZnO-T networks the three major reflections located at 31.80, 34.45, and 36.30° are assigned to the (1 0 –1 0), (0 0 0 2), and (1 0 –1 1) crystal facets, respectively (PDF card # 36–1451). In the case of $ZnAl_2O_4$-functionalized ZnO-T networks, two additional reflections with lower intensity at 31.25 and 36.80° were observed, which are attributed to the (2 2 0) and (3 1 1) crystal facets of $ZnAl_2O_4$ with cubic spinel structure (PDF card # 05–0669).[35] Neither reflections corresponding to other phases of Zn and Al nor other impurities (not shown) were observed. Thus, we can conclude that the nanocrystals on the surface of ZnO-T are purely $ZnAl_2O_4$.

The morphology of the $ZnAl_2O_4$ crystals was further examined via TEM as depicted in **Figure 3**. The bright field

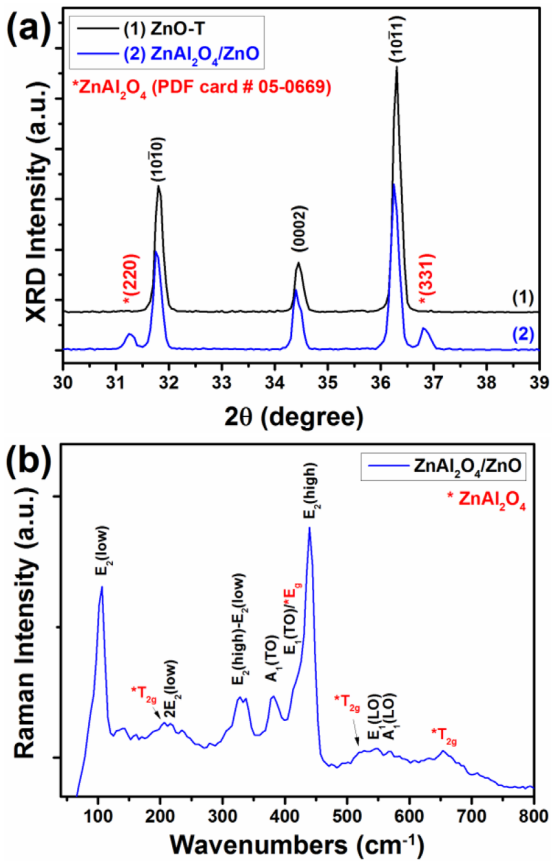

Figure 2. a) XRD patterns of ZnO-T and nanoparticles-$ZnAl_2O_4$-functionalized ZnO-T networks. b) Room temperature Raman spectrum of nanoparticles-$ZnAl_2O_4$-functionalized ZnO-T networks.

ADVANCED SCIENCE NEWS
www.advancedsciencenews.com

physica status solidi a
www.pss-a.com

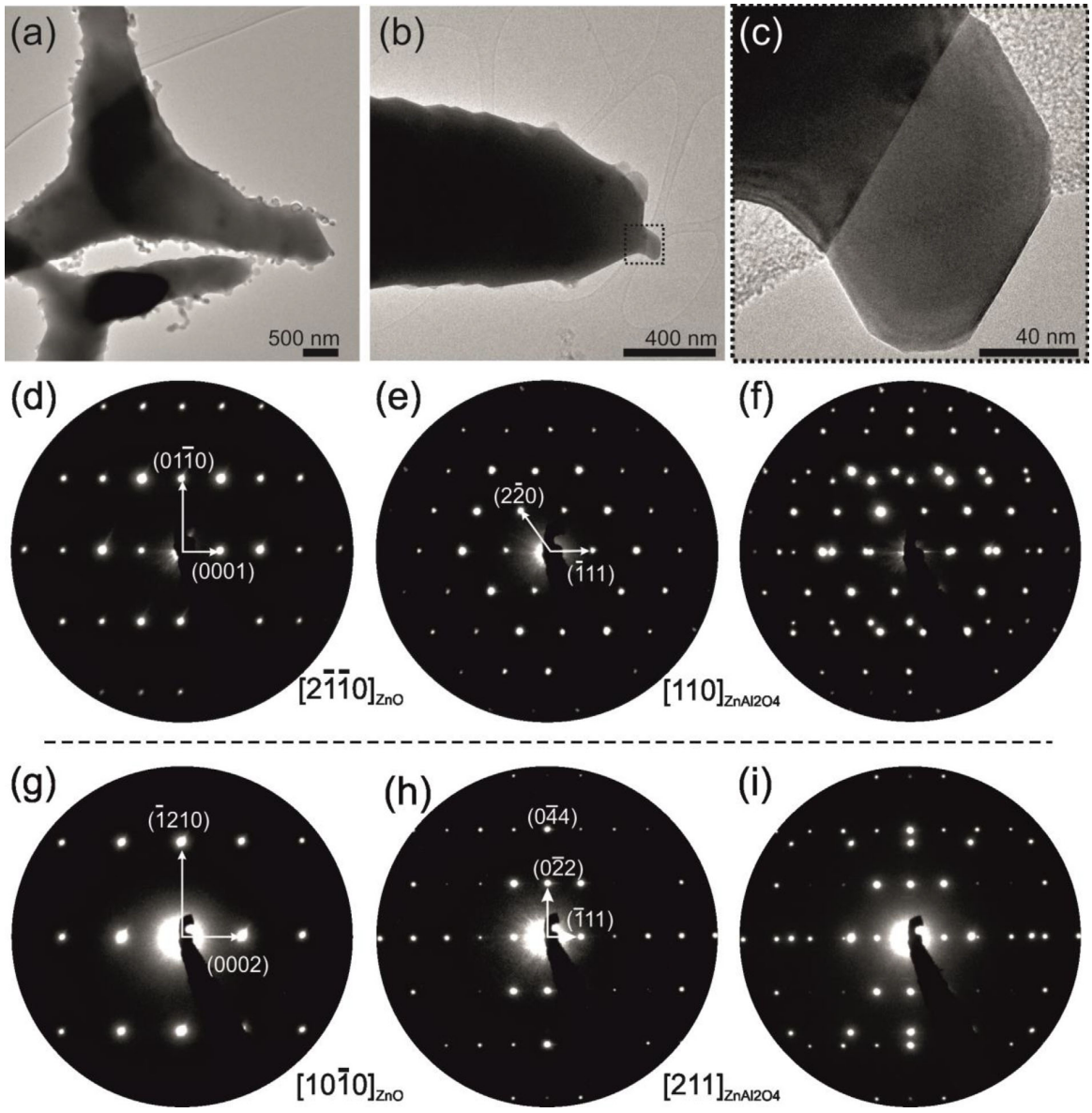

Figure 3. a–c) TEM bright field images of $ZnAl_2O_4$ decorated ZnO tetrapods. Electron diffraction tilting experiments were performed on the crystal depicted in (c). d and e) Single crystal SAED pattern of: (d) ZnO tilted into $[2\bar{1}\bar{1}0]$ orientation, (e) the [110] cubic pattern according to $ZnAl_2O_4$, and (f) the superposition PED pattern. g and h) Single crystal SAED pattern of (g) ZnO tilted into $[10\bar{1}0]$, (h) the [211] pattern according to $ZnAl_2O_4$, and (i) the superposition PED pattern from which epitaxial relationships can be obtained. See text for details.

images (a–c) show the $ZnAl_2O_4$-functionalized ZnO tetrapods at different magnifications. From Figure 3b it is apparent that the growth origins from specific facets of the ZnO crystal, which is further examined by electron diffraction experiments.

After tilting the ZnO crystal into $[2\bar{1}\bar{1}0]_{ZnO}$ (d–f) and $[10\bar{1}0]_{ZnO}$ (g–i) zone axis orientation, selected area electron diffraction (SAED), and precession electron diffraction (PED) experiments were conducted on individual $ZnAl_2O_4$ single crystals grown at the side and top faces of a tetrapod arm framed in (b) and magnified in (c). The SAED pattern depicted in (d) and (e) show single crystal patterns of the $[2\bar{1}\bar{1}0]_{ZnO}$ and aligned $[110]_{ZnAl2O4}$ zone axis orientation together with the superposition PED pattern (f). To observe all epitaxial relationships directly, the ZnO crystal was tilted into $[10\bar{1}0]_{ZnO}$ and SAED patterns of the individual components ZnO (g) and $ZnAl_2O_4$ (h) were recorded in addition to the superposition PED pattern shown in (i). The latter superposition pattern allows the determination of epitaxial relationships of $ZnAl_2O_4$ ($\bar{1}11$) grown onto ZnO(0001) as follows: $[\bar{1}2\bar{1}0]_{ZnO} \parallel [\bar{2}20]_{ZnO}$ and $[\bar{1}0\bar{1}0]_{ZnO} \parallel [211]_{ZnAl_2O_4}$. This crystallographic relationship is

ADVANCED SCIENCE NEWS
www.advancedsciencenews.com

physica status solidi a
www.pss-a.com

also reported for structurally equal systems of wurtzite ZnO or GaN grown onto spinel $MgAl_2O_4(111)$.[36,37] Chemical analyses via TEM-energy dispersive X-ray (EDX) spectra were performed from pure ZnO and $ZnAl_2O_4$ individually. The chemical composition of the crystal depicted in Figure 3c was determined to agree well with the nominal stoichiometric composition of $ZnAl_2O_4$ (Zn:15.6 Al:25.6 O:58.8 at.%), however, the ZnO EDX spectra showed no sign of Al intensity. Thereby, a homogenous Al doping of the ZnO bulk larger than 0.3 at.% is ruled out, which is about the detection limit of the EDX detector. Further, mapping of the chemical distribution is presented in Supporting Information Figure S3. The distinct separation between Al signals of the nanocrystal and the tetrapod arm reasons no further intermixing upon calcination. Localized shallow Al surface doping cannot be evidenced with the EDX method.

3.3. Micro-Raman Study

The room temperature Raman spectrum of $ZnAl_2O_4$-functionalized ZnO-T networks is presented in Figure 2b. The high intensity peaks at 105 and 439 cm^{-1} can be attributed to $E_2(low)$ and $E_2(high)$ modes of ZnO, respectively.[38] The other peaks at 215, 332, 381, 408 cm^{-1} and the broad peak at 580 cm^{-1} can be attributed to 2 $E_2(low)$ second-order mode, $E_2(low) - E_2(high)$ multi-phonon scattering, $A_1(TO)$, $E_1(TO)$, and $A_1(TO) + E_1(TO)$ (superposition) modes of ZnO.[39,40] In the Raman spectrum additional peaks were also observed. The phonon modes at the Γ point of spinel $ZnAl_2O_4$ are classified as follows[11]:

$$\Gamma = A_{1g} + E_g + T_{1g} + 3T_{2g} + 2A_{2u} + 2E_u + 4T_{1u} + 2T_{2u} \quad (1)$$

where A_{1g}, E_g, and $3T_{2g}$ modes are Raman active and $4T_{1u}$ are infrared (IR) active. Thus the additional peaks at 200, 518, and 653 cm^{-1} observed in the Raman spectrum can be attributed to spinel $ZnAl_2O_4$ T_{2g} vibrational modes.[11] Also, the superposition of the E_g mode at 427 cm^{-1} can occur with $E_1(TO)$ and E_2(high) modes of ZnO. Nasr et al.[41] also observed the additional peaks at 414 and 654 cm^{-1} in the Raman spectrum of $ZnO/ZnAl_2O_4$ multi co-centric nanotubes.

3.4. Devices Based on Individual $ZnAl_2O_4$-Functionalized ZnO Microstructures and Tetrapods

Figure 4 shows SEM images of fabricated devices for the investigations performed in this work. A SEM image of a ZnO MW used in our previous approach in functionalizing ZnO surfaces with large $ZnAl_2O_4$ polycrystalline clusters (further denoted as ZnO:Al MW) and integrated in sensor was shown in Ref. [42]. Figure 4a show SEM images of a $ZnAl_2O_4$-functionalized ZnO MW (produced by the procedure in this work, which will be referred to as $ZnAl_2O_4$/ZnO MW). The diameter of both structures (ZnO:Al MW and $ZnAl_2O_4$/ZnO MW) is ≈400 nm. In the case of the ZnO:Al MW a layered morphology is observed, which was demonstrated to be very efficient for the enhancement of the surface-to-volume ratio of MWs.[7,34,43] This leads to a higher gas response due to a higher amount of adsorbed oxygen species.[44] In the case of the $ZnAl_2O_4$/ZnO MW, the well distributed $ZnAl_2O_4$ nanocrystals along the MW can be spotted easily, while the diameter of nanocrystals varies from 10 to 50 nm (see Figure 4a). Because the diameter is the main parameter which determines the performances of individual devices,[45] these two devices with practically the same diameter will be used in order to compare the reported two methods.

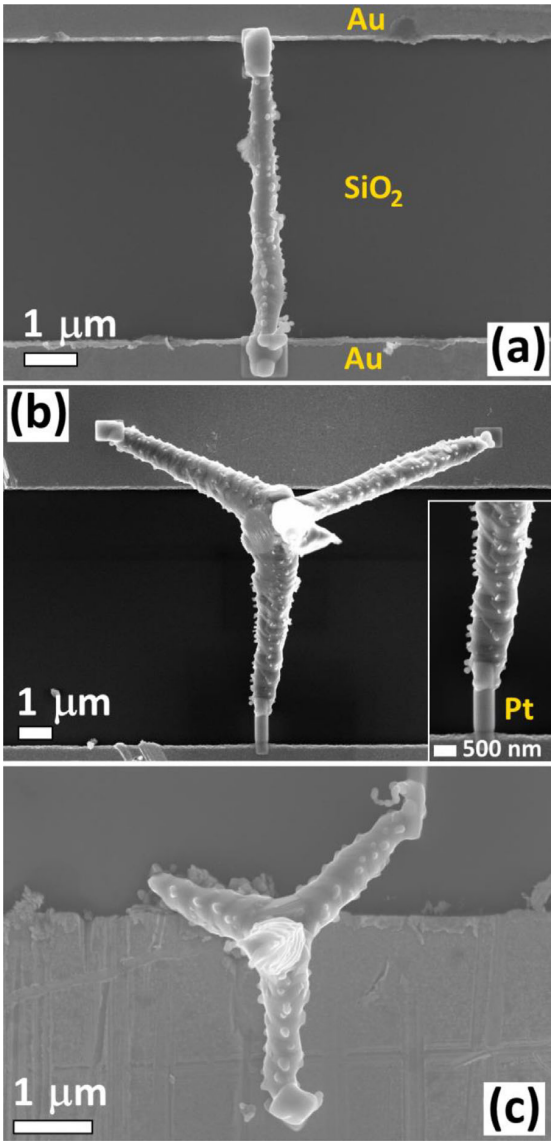

Figure 4. SEM images of the fabricated devices based on a: (a) $ZnAl_2O_4$/ZnO MW; (b) $ZnAl_2O_4$/ZnO-T (D1) – bigger tetrapod; and (c) $ZnAl_2O_4$/ZnO-T (D2) – smaller tetrapod.

Figure 4b and c show SEM images of $ZnAl_2O_4$-functionalized ZnO tetrapods with different diameters and lengths of arms. In the case of Figure 4b the diameter of the arm is

ADVANCED SCIENCE NEWS
www.advancedsciencenews.com
physica status solidi a
www.pss-a.com

≈1.6 μm at the base and ≈800 nm at the tip. The length of the arm is ≈7 μm. This device will be denoted as $ZnAl_2O_4$/ZnO-T (D1). The tetrapod from Figure 4c is much smaller. The arm diameter is ≈600 nm at the base and ≈400 nm at the tip (which is comparable with the diameter of the MWs). The length of the arm is ≈1.2 μm. This device will be denoted as $ZnAl_2O_4$/ZnO-T (D2). These two tetrapods will be used to compare the morphology influence of $ZnAl_2O_4$-functionalized ZnO structures on the gas response. Supporting Information Figure S4 shows the current–voltage (*I*–*V*) characteristics of these devices at 25 °C (room temperature, RT), 50 and 100 °C in the −3 *V* to +3 *V* range. All devices show a non-linear *I*–*V* characteristic which is indicative of the formation of non-symmetrical Schottky barriers at the Pd/ZnO interface of structures at both ends.[46]

3.5. Gas Sensing Properties of Individual ZnO:Al and $ZnAl_2O_4$-Functionalized ZnO MWs

First, we will compare the gas sensing properties of the devices based on MWs, i.e., the ZnO:Al MW and the $ZnAl_2O_4$/ZnO MW in order to find out which method for modification of ZnO material leads to the best results. The ZnO:Al MW samples were synthesized as was reported in a previous work.[23] **Figure 5a** shows the gas response to 800 ppm of the tested gases and vapors versus the operating temperature for both devices. As can be observed, no gas response to gaseous methane, ethanol, acetone, and ammonia vapors was detected, demonstrating the high selectivity to H_2 gas (see also Supporting Information Figure S5a). At 25, 50, and 100 °C the gas response to 800 ppm of H_2 gas is 1.1, 1.8, and 7.1 for the ZnO:Al MW and 2.5, 4.7, and 8.5 for the $ZnAl_2O_4$/ZnO MW, respectively (see Figure 5a). The increase in the response of metal oxide structures at increasing operating temperatures is well known and can be explained based on increased thermal energy, which becomes high enough to overcome the activation energy barrier for the reaction of gas molecules with adsorbed oxygen species.[47] In general, the gas response dependence on the operating temperature has a bell shape,[48] but in order to protect the sensor structures from eventual current spikes due to the exposure to high concentrations of reducing gases, we limited the maximum operating temperature to 100 °C.

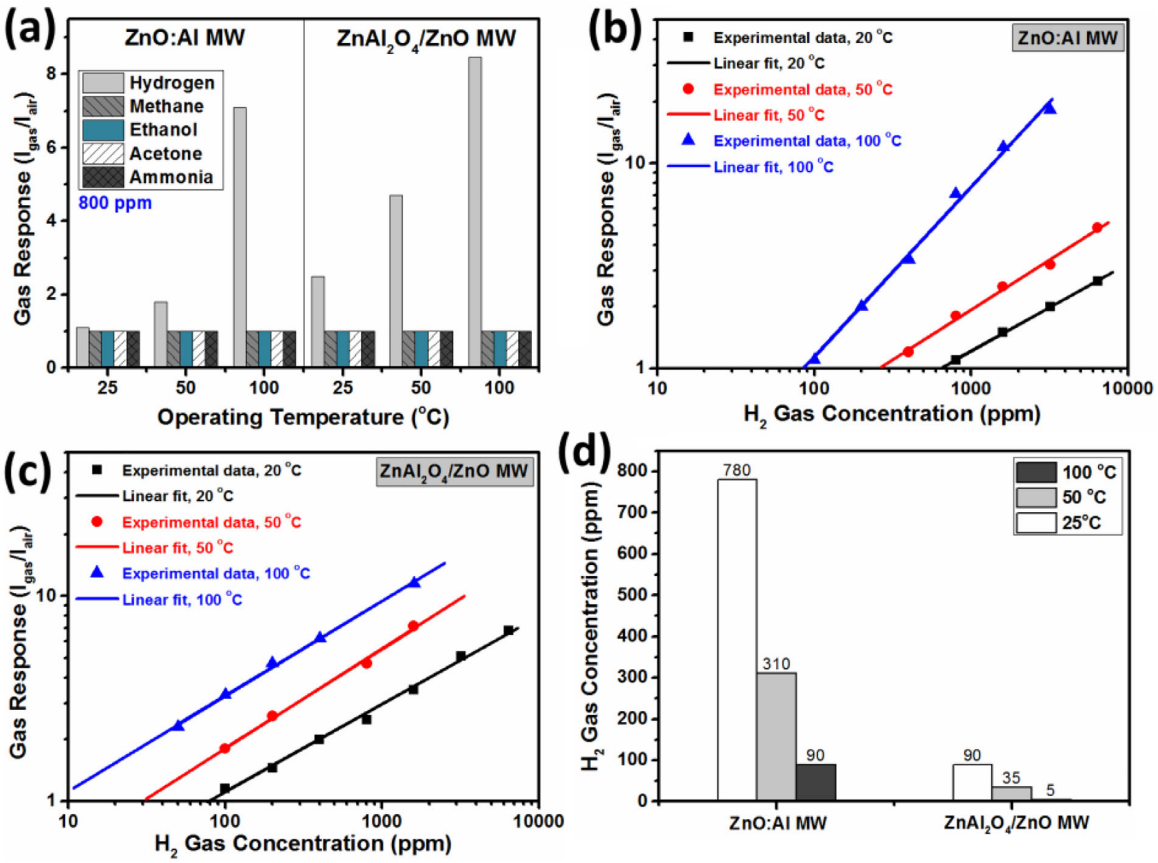

Figure 5. a) Gas response of ZnO:Al and $ZnAl_2O_4$/ZnO MWs to 800 ppm of different gases and vapors versus the operating temperature. Gas response versus H_2 gas concentration at different operating temperatures for the: (b) ZnO:Al MW, and (c) $ZnAl_2O_4$/ZnO MW. d) The calculated theoretical detection limit to H_2 gas versus operating temperature.

ADVANCED SCIENCE NEWS
www.advancedsciencenews.com

physica status solidi a
www.pss-a.com

Next, we exposed the ZnO:Al and $ZnAl_2O_4$/ZnO MWs to a wide range of H_2 gas concentrations (from 100 to 6400 ppm) at different operating temperatures. The results are presented in Figure 5b and c for the ZnO:Al and $ZnAl_2O_4$/ZnO MW, respectively, as well as in Supporting Information Table S2. Both samples showed a power law relationship to the varied H_2 gas concentration.[27] At RT, only the $ZnAl_2O_4$/ZnO MW showed a detectable gas response of 1.15–100 ppm of H_2 gas, while the ZnO:Al MW showed a detectable response starting from 800 ppm (response of 1.1). By increasing the operating temperature to 50 °C, the lowest detectable concentration was decreasing to 400 ppm (response = 1.2) and only by increasing the operating temperature to 100 °C it was possible to detect 100 ppm of H_2 using the ZnO:Al MW (response of 1.1). Generally, at RT and 50 °C the $ZnAl_2O_4$/ZnO MW showed a higher H_2 gas response compared to ZnO:Al MW (see Figure 5b and c). Also, it needs to be mentioned that the RT gas response of 1.15–100 ppm of H_2 of $ZnAl_2O_4$/ZnO MW is higher compared to an individual ZnO nanorod,[49] a ZnO NW with 200 nm diameter,[1] a MoO_3 nanobelt with 150 nm diameter[29] and a SnO_2 NW.[50]

To further evaluate the performances of the investigated devices, the theoretical detection limit (DL) was estimated from Figure 5b and c, as was reported in detail by Dua et al. and Lu et al., i.e. using *signal*/(*noise ratio*)^2.[51,52] The estimated results are presented in Figure 5d and Supporting Information Table S3. In the case of the ZnO:Al MW for 25, 50, and 100 °C the theoretical DLs are 780, 310, and 90 ppm, respectively, while for the $ZnAl_2O_4$/ZnO MW much lower values of 350, 90, and 5 ppm, respectively were obtained. Thus, the $ZnAl_2O_4$/ZnO MW demonstrates the potential ability to detect much lower concentrations of hydrogen gas.

The response and recovery times belong to the next group of important parameters which determine the performances of gas sensors. Figures 6 and 7 show the dynamic gas response of the ZnO:Al MW and $ZnAl_2O_4$/ZnO MW to different concentrations of H_2 at different operating temperatures, respectively. The calculated response and recovery times are presented in Supporting Information Table S4 showing that the values are decreasing by increasing the concentration of H_2 gas, as well as operating temperature. This proves that the typical concentration- and temperature-dependent surface reactions rate of metal oxides.[53] In general, the $ZnAl_2O_4$/ZnO MW shows faster response and recovery times compared to the ZnO:Al MW. For example, to the exposure of a H_2 gas concentration of 800 ppm, at 25 °C operating temperature the response and recovery times for the $ZnAl_2O_4$/ZnO MW are 120 and 160 s, respectively, while for the ZnO:Al MW the response time is 200 s and the recovery time is longer than 500 s (see Supporting Information Table S4).

In comparison to the ZnO:Al MW, the $ZnAl_2O_4$-functionalized ZnO MW shows a higher gas response at 25 and 50 °C operating temperatures for a wide range of H_2 concentrations. The $ZnAl_2O_4$/ZnO MW also shows a much lower experimental and theoretical detection limit to hydrogen gas, as well as faster response and recovery times. Thus, the $ZnAl_2O_4$/ZnO structures are more favorable for gas sensing applications. This also supports the conclusions from previous works related to Fe_2O_3 nanoparticles (NPs)-functionalization of individual ZnO microstructures.[34,42,44] Therefore, only $ZnAl_2O_4$-functionalized structures with different morphologies will be investigated in the following, namely MW and tetrapods with different dimensions. The study will be mainly focused on RT as operating temperature, because it is a more attractive setting and allows for the exclusion of micro-heaters and thermometer plates from the fabrication process for the final gas sensor structures. This essentially reduces the technological steps and the complexity of the device.

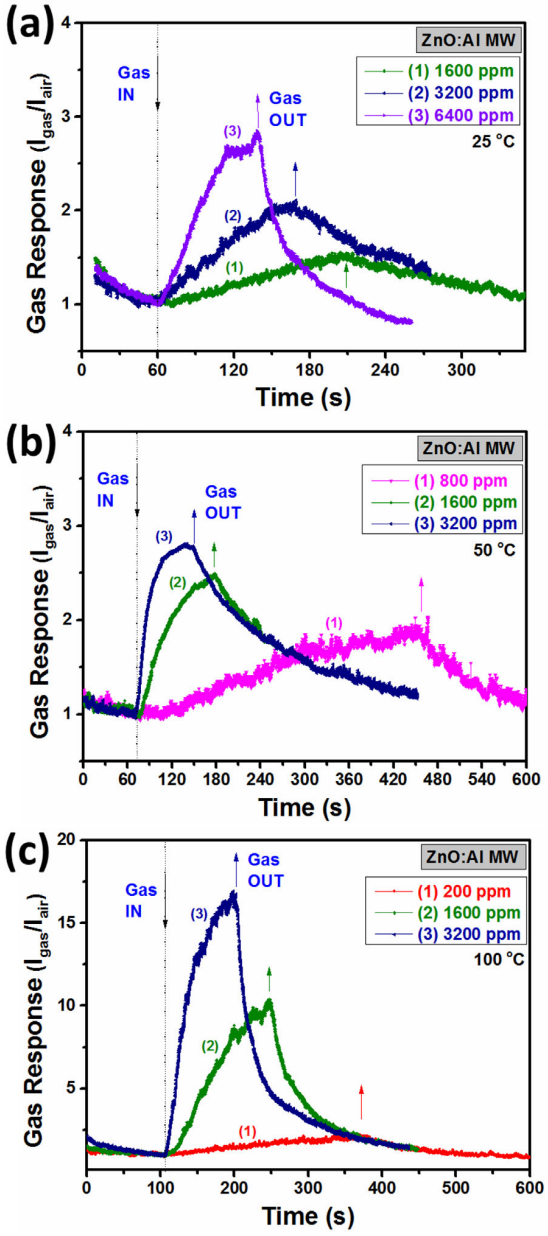

Figure 6. Dynamic gas response versus time of ZnO:Al MW for different H_2 gas concentrations at: (a) 25 °C; (b) 50 °C; and (c) 100 °C.

ADVANCED SCIENCE NEWS
www.advancedsciencenews.com

physica status solidi a
www.pss-a.com

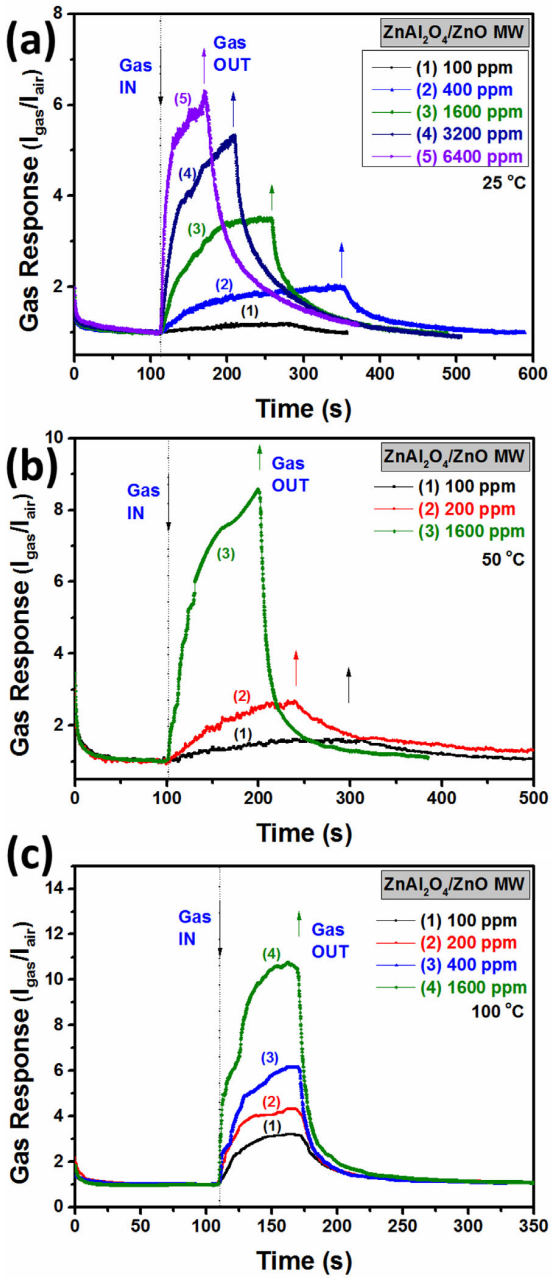

Figure 7. Dynamic gas response versus time of $ZnAl_2O_4$/ZnO MW for different H_2 gas concentrations at: (a) 25 °C; (b) 50 °C; and (c) 100 °C.

3.6. Influence of the Morphology on the Sensing Properties of $ZnAl_2O_4$-Functionalized ZnO Structures

To study the morphologic influence on the gas sensing properties, the two already mentioned $ZnAl_2O_4$-functionalized ZnO-T sensors will be investigated, namely $ZnAl_2O_4$/ZnO-T (D1) – the bigger tetrapod and $ZnAl_2O_4$/ZnO-T (D2) – the smaller tetrapod. As in the case of MWs, the $ZnAl_2O_4$-functionalized ZnO-Ts showed an excellent selectivity to H_2 gas (see Supporting Information Figure S5c and d and **Figure 8**a), i.e., there was no response to other tested gases and vapors. The gas response versus concentration of H_2 gas for devices based on tetrapods is presented in Figure 8b and Supporting Information Table S2. At RT the gas response to 100 ppm H_2 is 1.3 and 2 for $ZnAl_2O_4$/ZnO-T (D1) and $ZnAl_2O_4$/ZnO-T (D2), respectively, which is higher than the 1.15 for $ZnAl_2O_4$/ZnO MW. The gas response of device D2 is also higher than the values reported for individual CeO_2 NW,[54] CuO NW,[55] TeO_2 NW,[56] as well as pristine ZnO-T.[31,57]

The calculated theoretical detection limit for H_2 gas at 25 °C operating temperature is 35 and 10 ppm for D1 and D2, respectively (see Supporting Information Table S3). Taking into account that the leg diameters of tetrapod D1 are higher (≈800 nm) compared to the diameter of the $ZnAl_2O_4$-functionalized MW (≈400 nm) and the leg diameters of the tetrapod D2 (≈400 nm), reveals that the use of individual tetrapods is more favorable for gas sensing applications because the calculated values for the theoretical DL are much smaller than for the $ZnAl_2O_4$/ZnO MW.

Figure 8c and d show the dynamic gas response of devices D1 and D2 to different concentrations of H_2 gas at 25 °C operating temperature, respectively. The calculated response and recovery times are presented in Supporting Information Table S4. As can be observed, the device D2 showed the fastest response and recovery times, especially at 25 °C. This is more observable from **Figure 9**, generally the $ZnAl_2O_4$-functionalized ZnO structures show faster response and recovery times. For example, at 25 °C operating temperature the response and recovery times to 800 ppm of H_2 gas for D2 are ≈23 and ≈36 s, respectively, while for ZnO:Al MW they are 200 and >500 s, respectively.

Table 1 lists the results on H_2 gas sensing of individual structures of metal oxides from different publications in order to compare them with our results. As can be observed, our results are superior to many of the reported data, although the diameter of the structures is much lower than in our case. This demonstrates the high efficiency of $ZnAl_2O_4$ functionalization of ZnO microstructures for high performance gas sensing applications.

3.7. Gas Sensing Mechanism Proposed for Developed $ZnAl_2O_4$/ZnO-T-Functionalized Structures

The basic gas sensing mechanism of individual structures can be rationalized in terms of the existing models of ionosorption.[61,59] At temperatures lower than 150–200 °C on the surface of metal oxides (the temperature range used for the study in this work) mainly molecular species of oxygen (O_2), which capture a free electron at a surface state $\left(O_2(g) \rightarrow O_2(ad) + e^- \rightarrow O_2^-(ad)\right)$ are adsorbed.[7,31,61] In the case of individual structures this will lead to the formation of an electron depleted region at the surface, while the internal conduction channel will be narrowed. Under exposure to H_2 gas the following reaction will take place: $2H_2(g) + O_2^-(ad) \rightarrow 2H_2O + e^-$.[1,60] As a result, the two hydrogen molecules react with double ionized oxygen species and produce two H_2O molecules with the release of one electron in the metal oxide. This will lead to a narrowing of the electron

ADVANCED SCIENCE NEWS
www.advancedsciencenews.com
physica status solidi a
www.pss-a.com

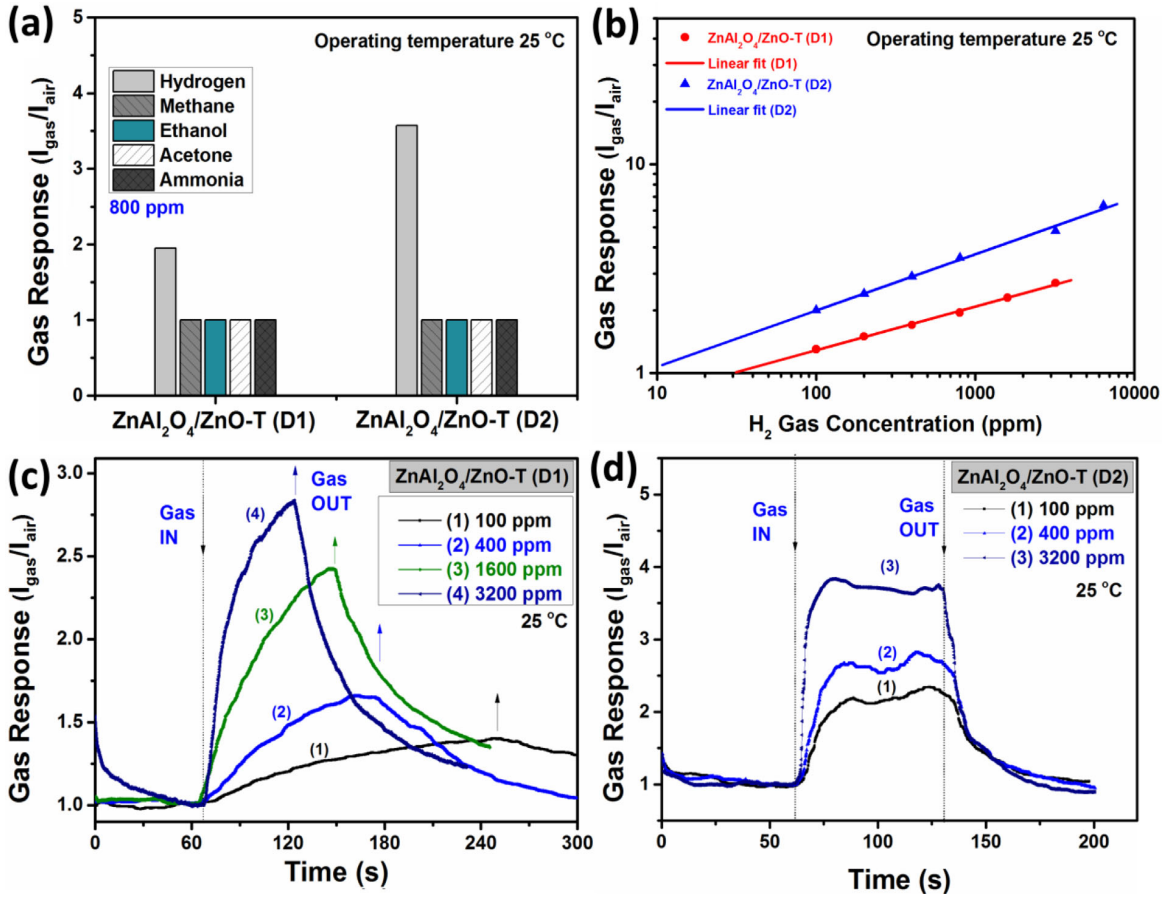

Figure 8. a) Gas response of ZnO:Al and $ZnAl_2O_4$/ZnO MWs – based sensors to 800 ppm of different gases and vapors at 25 °C operating temperature. b) Gas response versus H_2 gas concentration at different operating temperatures for $ZnAl_2O_4$/ZnO-T (D1) – bigger tetrapod and $ZnAl_2O_4$/ZnO-T (D2) – smaller tetrapod based sensors. Dynamic gas response versus time of: (c) $ZnAl_2O_4$/ZnO-T (D1); and (d) $ZnAl_2O_4$/ZnO-T (D2) for different H_2 gas concentrations at 25 °C.

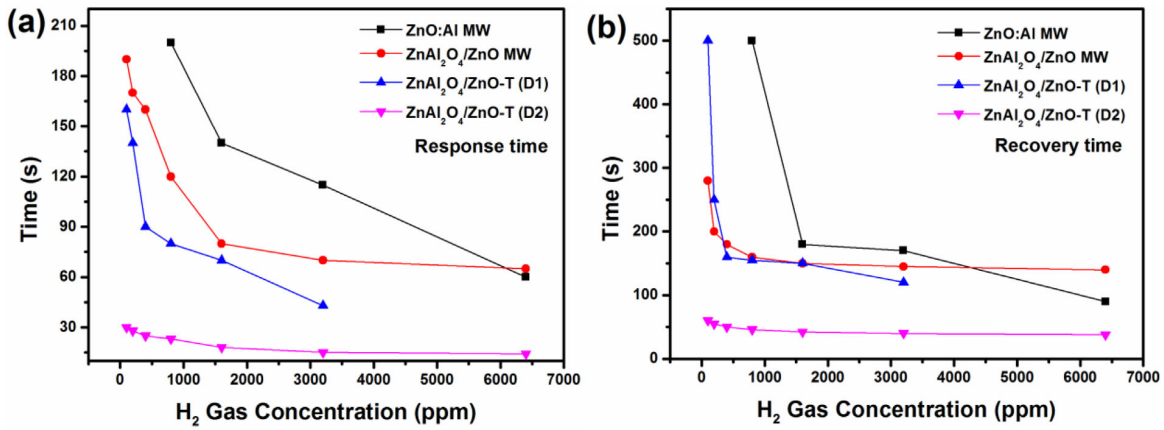

Figure 9. The calculated: (a) response and (b) recovery times to different concentrations of H_2 gas at 25 °C operating temperature of ZnO:Al, $ZnAl_2O_4$/ZnO MWs and $ZnAl_2O_4$/ZnO-T – based sensors.

ADVANCED SCIENCE NEWS
www.advancedsciencenews.com

physica status solidi a
www.pss-a.com

Table 1. Summary of the hydrogen gas sensors based on individual metal oxide structures.

Type of individual metal oxide structure	Diameter (nm)	H_2 conc. (ppm)	Gas response (R_g/R_a)[a] or (R_a/R_g)[b]	Operating temp. (°C)	Response time (s)	Recovery time (s)
Pt/CeO_2 NW[54]	–	200	≈1.5[b]	RT	–	–
CuO NW[55]	50–100	500	≈1.75[a]	RT	–	–
Fe_2O_3 NW[58]	≈ 100	200	≈3.2[b]	RT	–	–
TeO_2 NW[56]	30–40	5000	≈1.3[b]	RT	100	250
SnO_2 Nanobelt[50]	–	20 000	≈1.6[b]	RT	220	220
ZnO NW[49]	–	100	≈1.04[b]	RT	30–40	≈100
ZnO-T[31]	≈300	100	≈1.06[b]	RT	≈30	≈60
ZnO:Ag NW[59]	≈250	100	≈1.6[b]	RT		
ZnO:Cd NW[60]	≈200	100	≈1.5[b]	RT	14	11
$ZnAl_2O_4$/ZnO-T (This work)	**≈400**	**100**	**≈2[b]**	**RT**	**30**	**60**

[a] Gas response for *p*-type semiconducting oxides. [b] Gas response for *n*-type semiconducting oxides. [c] Denotes a value approximated from a graphical plot. Bold values represent data from the current work.

depletion region and a widening of the conduction channel, i.e., an increase in the electrical current or a decrease in the resistance of the individual microstructure.

The detailed H_2 gas sensing mechanism of an individual ZnO NW including energy band diagrams was proposed in our previous work,[59] as well as for an individual ZnO tetrapod.[34] Thus, the main gas sensing mechanism in the case of individual structures is the modulation of the electron depletion region, respective of the conduction channel under exposure to reducing or oxidizing gases.[34] Therefore, the structure diameter plays a major role for the gas sensing performances.[45] It was experimentally demonstrated that the lower the diameter, the higher the gas response which can be obtained based on individual metal oxide nanostructures.[45,62] This can be explained based on the higher modulation of the conduction channel width in the case of a lower nanostructure diameter, especially when the radius is comparable to the Debye length.[60] This accounts for the poor gas sensing performances of the ZnO:Al MW with D ≈400 nm, since the modulation is not so significant, thus the gas response is relatively low. The previous calculations showed that the electron depletion region width can be estimated to ≈35 nm (for pristine ZnO),[59] which is much lower compared to the radius of the ZnO:Al MW (≈200 nm). Thus, a change of the electrical current flow through the channel, i.e., the gas response value, is minimal in the case of such large individual structures integrated to gas sensors.

However, it does not explain the excellent selectivity to H_2 gas of the devices under consideration in our current work. By analyzing all fabricated devices, it can be observed that the main electrical characteristic is the formation of a double Schottky contact at the interface of the material with Pt complex contacts (see Supporting Information Figure S4). The Schottky contacts based on Pd or Pt with ZnO are known to be contributing significantly to hydrogen gas response.[43,63,64] Therefore, the formation of Schottky contacts based on Pd or Pt due to the high catalytic effect of such noble metals can induce the H_2 sensing properties, too, for such materials as carbon nanotubes (CNTs) and Si, which normally are not sensible to H_2 gas at room temperature.[65–67] The detailed gas sensing mechanism with representation of the energy band diagram for individual structures with single and double Schottky contacts was presented in our previous works.[43,45,59,65]

In its turn, this does not explain the higher gas sensing performances of individual $ZnAl_2O_4$-functionalized ZnO structures. Thus, we can propose that the main factor, compared to ZnO:Al MW, is the presence of $ZnAl_2O_4$ nanocrystals on the surface of ZnO. As $ZnAl_2O_4$ is known to be a good catalytic material with low surface acidity, high thermal and chemical stability for synthesis, dehydrogenation, hydrogenation, dehydration, isomerization and combustion processes.[20,68] DFT calculations showed that $ZnAl_2O_4$/ZnO-T are excellent hybrid networks with respect to gas sensing, since the $ZnAl_2O_4$ functionalized ZnO(0001) surfaces demonstrate strong interaction with numerous different gases.[7] In a previous work the excessive addition of $ZnAl_2O_4$ microparticles to ZnO-T-$ZnAl_2O_4$ hybrid networks resulted in an enhanced CH_4 gas response.[7] Therefore, it can be concluded that in our case the addition of $ZnAl_2O_4$ nanocrystals does not lead to enhanced catalytic reactions at the investigated operating temperatures, because no response to CH_4 was observed.

Therefore, the enhancement in the response can be explained based on the free electrons and holes transfer and the separation according to the energy band diagram of the $ZnAl_2O_4$/ZnO heterostructure. In general, the formation of *n*-*n* and *n*-*p* heterojunctions is known to be very efficient for enhanced gas sensing performances.[7,33,69] **Figure 10**a shows the schematic illustration of a device based on an individual $ZnAl_2O_4$/ZnO-T, while Figure 10b and c shows the schematic illustration of the hydrogen sensing mechanism proposed for a $ZnAl_2O_4$/ZnO heterostructure. The detailed energy band diagram was drawn in a previous paper[7] on the basis of the data from Ref. [70], where the conduction band discontinuity (ΔE_C) is 0.83 eV. Due to type II energy band alignment (staggered type), which is very efficient for electron and hole

ADVANCED SCIENCE NEWS
www.advancedsciencenews.com
physica status solidi a
www.pss-a.com

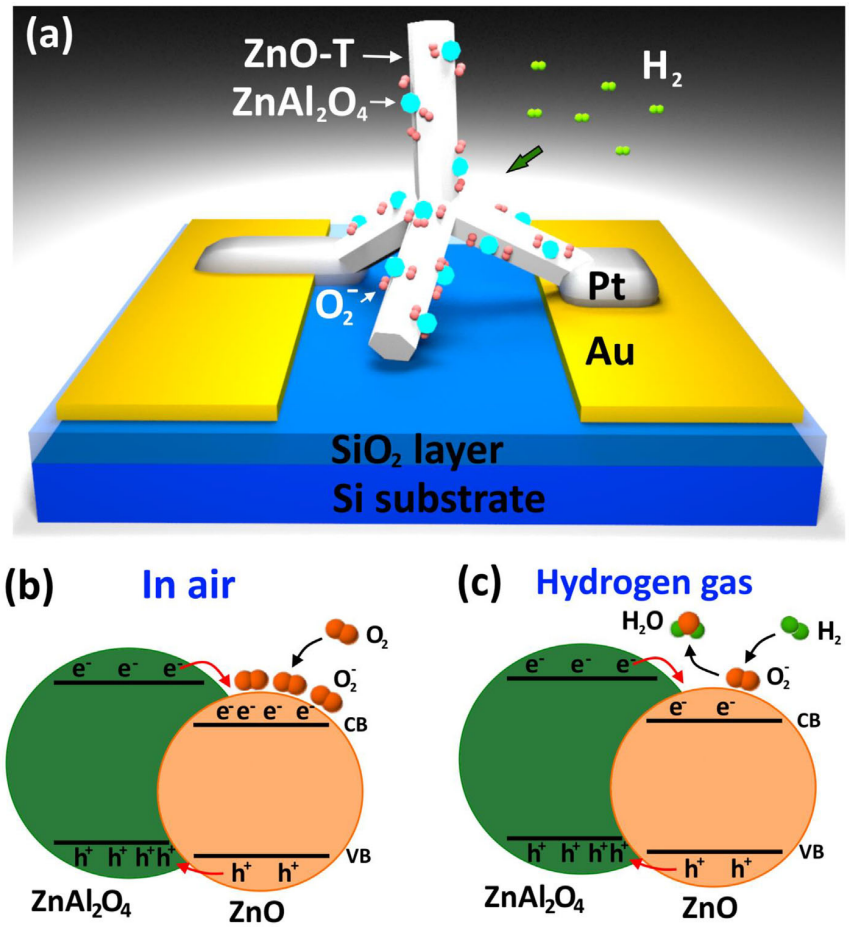

Figure 10. a) Schematic illustration of a $ZnAl_2O_4$/ZnO-T (D2) device. Schematic illustration of hydrogen sensing mechanism for $ZnAl_2O_4$/ZnO heterostructure: (b) under ambient air; and (c) under hydrogen gas. At the surface of ZnO functionalized with $ZnAl_2O_4$ more oxygen molecules are adsorbed, leading to a higher modulation in resistance (charge transfer) of individual structures after exposure to hydrogen gas molecules.

separation.[7] Thus, an electron flow will take place from $ZnAl_2O_4$ nanocrystals to ZnO microstructures, causing a higher concentration of free-electrons in the ZnO material surrounding nanocrystals. This will lead to a higher oxygen coverage of the ZnO microstructure surfaces in air, especially in the areas around the $ZnAl_2O_4$ nanocrystals (Figure 10b), leading to a higher concentration of free-electrons, thus enhancing surface reactions of the gas absorption when the sensor is exposed to H_2 gas (Figure 10c) will take place, respectively improving the gas response value and shortening the response time due to a larger quantity of charge transfer at the surface.[7,69,70] Thus, our proposed sensing mechanism indicates that the presence of $ZnAl_2O_4$ can promote the adsorption of gas molecules on the ZnO surface due to free charge transfer from $ZnAl_2O_4$ to ZnO and accelerate the oxidizing processes, which can explain the faster response and recovery time of the $ZnAl_2O_4$-functionalized samples.[14,17] The promotion of surface reactions involving adsorption, dissociation, and the ionization of oxygen by the presence of different metal oxides nanoparticles, such as NiO and In_2O_3, was observed by other authors, too.[71,72]

In general, the higher gas response of the $ZnAl_2O_4$/ZnO tetrapodal structure compared to the MW (with practically the same diameter) can be explained based on the presence of an internal junction at the tetrapod base,[73,74] which, combined with the free-standing arm of the tetrapod, adds additional modulation of electrical current through the device under exposure to gaseous species.[75] However, only very few information on the physical and electrical properties of the ZnO tetrapod core is present in the literature and no veridical conclusions can be made at this stage to explain in detail the corresponding gas sensing mechanism (using the presented data). Thus it represents an interesting subject for further studies and will be investigated in another forthcoming paper.

4. Conclusion

The $ZnAl_2O_4$-surface functionalization of ZnO structures from aqueous solutions was successfully realized. The $ZnAl_2O_4$ crystals grow with a diameter of 50–100 nm and a high density on the surface of ZnO. Based on the individual $ZnAl_2O_4$/ZnO

ADVANCED SCIENCE NEWS
www.advancedsciencenews.com

physica status solidi a
www.pss-a.com

structures with different morphologies, mainly MWs and tetrapods were used to fabricate devices, which were tested to different gases and operating temperatures. All devices showed an excellent selectivity to H_2 gas and the main conclusions of the obtained data are as follows:

- The individual $ZnAl_2O_4$/ZnO MW shows higher gas sensing performances compared to an individual ZnO:Al MW with a comparable diameter (≈400 nm), demonstrating the efficiency of $ZnAl_2O_4$-functionalization of ZnO;
- The $ZnAl_2O_4$/ZnO-T tetrapodal structures (with a leg diameter of ≈400 nm) show a more enhanced response compared to the $ZnAl_2O_4$/ZnO MW. The $ZnAl_2O_4$/ZnO tetrapod (D2) showed a gas response of 2 at room temperature to 100 ppm, which is higher compared to 1.15 of $ZnAl_2O_4$/ZnO MW, as well as to many reports on H_2 gas sensors based on different metal oxides individual nanostructures with much lower diameter.

A gas sensing mechanism was proposed for an individual $ZnAl_2O_4$/ZnO structure based sensor. Therefore, this work demonstrates promising results for nanoparticles-$ZnAl_2O_4$-functionalized ZnO microstructures for highly selective hydrogen gas sensing applications at room temperature.

Supporting Information

Supporting Information is available from the Wiley Online Library or from the authors.

Acknowledgements

Dr. Lupan acknowledges the Alexander von Humboldt Foundation for the research fellowship for experienced researchers 3-3MOL/1148833 STP at the Institute for Materials Science, Kiel University, Germany. This research was partly supported by the project Institutional 45inst-15.817.02.29A funded by the Government of the Republic of Moldova. Katrin Brandenburg is acknowledged for her help in the proof-reading of the manuscript. Authors from Kiel University acknowledge the support from German Research Foundation (DFG) under the scheme SFB 1261, TP ((A05, RA) & (A06, LK)) and FOR 2093, TP A2 & B2.

Conflict of Interest

The author declares no conflict of interest.

Keywords

functionalization, hybrid, hydrogen sensors, $ZnAl_2O_4$, ZnO tetrapod

Received: October 13, 2017
Revised: January 10, 2018
Published online: February 14, 2018

[1] O. Lupan, V. V. Ursaki, G. Chai, L. Chow, G. A. Emelchenko, I. M. Tiginyanu, A. N. Gruzintsev, A. N. Redkin, *Sens. Actuators B* **2010**, *144B*, 56.
[2] L.-J. Bie, X.-N. Yan, J. Yin, Y.-Q. Duan, Z.-H. Yuan, *Sens. Actuators B* **2007**, *126B*, 604.
[3] C. S. Rout, S. Hari Krishna, S. R. C. Vivekchand, A. Govindaraj, C. N. R. Rao, *Chem. Phys. Lett.* **2006**, *418*, 586.
[4] S. Basu, A. Dutta, *Sens. Actuators B* **1994**, *22B*, 83.
[5] O. Lupan, V. Postica, F. Labat, I. Ciofini, T. Pauporté, R. Adelung, *Sens. Actuators B* **2018**, *254B*, 1259.
[6] S. Mridha, D. Basak, *Semicond. Sci. Technol.* **2006**, *21*, 928.
[7] O. Lupan, V. Postica, J. Gröttrup, A. K. Mishra, N. H. de Leeuw, J. F. C. Carreira, J. Rodrigues, N. Ben Sedrine, M. R. Correia, T. Monteiro, V. Cretu, I. Tiginyanu, D. Smazna, Y. K. Mishra, R. Adelung, *ACS Appl. Mater. Interfaces* **2017**, *9*, 4084.
[8] H. Jin Fan, M. Knez, R. Scholz, K. Nielsch, E. Pippel, D. Hesse, M. Zacharias, U. Gosele, *Nat. Mater* **2006**, *5*, 627.
[9] C. Wang, B.-Q. Xu, X. Wang, J. Zhao, *J. Solid State Chem.* **2005**, *178*, 3500.
[10] M. Liu, Z. Rong, R. Malik, P. Canepa, A. Jain, G. Ceder, K. A. Persson, *Energy Environ. Sci.* **2015**, *8*, 964.
[11] S. López, A. H. Romero, P. Rodríguez-Hernández, A. Muñoz, *Phys. Rev. B* **2009**, *79B*, 214103.
[12] G. Lu, N. Miura, N. Yamazoe, *J. Mater. Chem.* **1997**, *7*, 1445.
[13] N.-S. Chen, X.-J. Yang, E.-S. Liu, J.-L. Huang, *Sens. Actuators B* **2000**, *66B*, 178.
[14] X. Niu, W. Du, W. Du, *Sens. Actuators B* **2004**, *99B*, 405.
[15] Z. Chen, C. Lu, *Sens. Lett.* **2005**, *3*, 274.
[16] X. Li, C. Wang, H. Guo, P. Sun, F. Liu, X. Liang, G. Lu, *ACS Appl. Mater. Interfaces* **2015**, *7*, 17811.
[17] M.-Y. Guan, D.-M. Xu, Y.-F. Song, Y. Guo, *Sens. Actuators B* **2013**, *188B*, 1148.
[18] C. Wongchoosuk, K. Subannajui, C. Wang, Y. Yang, F. Guder, T. Kerdcharoen, V. Cimalla, M. Zacharias, *RSC Adv.* **2014**, *4*, 35084.
[19] H. Dixit, N. Tandon, S. Cottenier, R. Saniz, D. Lamoen, B. Partoens, *Phys. Rev. B* **2013**, *87B*, 174101.
[20] Y. Wang, K. Wu, *J. Am. Chem. Soc.* **2005**, *127*, 9686.
[21] S. D. Kapse, F. C. Raghuwanshi, V. D. Kapse, D. R. Patil, *Curr. Appl. Phys.* **2012**, *12*, 307.
[22] J.-S. Na, Q. Peng, G. Scarel, G. N. Parsons, *Chem. Mater.* **2009**, *21*, 5585.
[23] J. Gröttrup, I. Paulowicz, A. Schuchardt, V. Kaidas, S. Kaps, O. Lupan, R. Adelung, Y. K. Mishra, *Ceram. Int.* **2016**, *42*, 8664.
[24] C. T. Campbell, S. C. Parker, D. E. Starr, *Science* **2002**, *298*, 811.
[25] Y. K. Mishra, G. Modi, V. Cretu, V. Postica, O. Lupan, T. Reimer, I. Paulowicz, V. Hrkac, W. Benecke, L. Kienle, R. Adelung, *ACS Appl. Mater. Interfaces* **2015**, *7*, 14303.
[26] Y. K. Mishra, S. Kaps, A. Schuchardt, I. Paulowicz, X. Jin, D. Gedamu, S. Wille, O. Lupan, R. Adelung, *KONA Powder Part. J.* **2014**, *31*, 92.
[27] V. Cretu, V. Postica, A. K. Mishra, M. Hoppe, I. Tiginyanu, Y. K. Mishra, L. Chow, N. H. de Leeuw, R. Adelung, O. Lupan, *J. Mater. Chem. A* **2016**, *4A*, 6527.
[28] O. Lupan, G. Chai, L. Chow, *Microelectron. J.* **2007**, *38*, 1211.
[29] O. Lupan, V. Cretu, M. Deng, D. Gedamu, I. Paulowicz, S. Kaps, Y. K. Mishra, O. Polonskyi, C. Zamponi, L. Kienle, V. Trofim, I. Tiginyanu, R. Adelung, *J. Phys. Chem. C* **2014**, *118C*, 15068.
[30] O. Lupan, V. Postica, V. Cretu, N. Wolff, V. Duppel, L. Kienle, R. Adelung, *Phys. Status Solidi RRL* **2016**, *10*, 260.
[31] O. Lupan, L. Chow, G. Chai, *Sens. Actuators, B* **2009**, *141B*, 511.
[32] O. Lupan, V. Postica, M. Mecklenburg, K. Schulte, Y. K. Mishra, B. Fiedler, R. Adelung, *J. Mater. Chem. A* **2016**, *4A*, 16723.
[33] O. Lupan, V. Cretu, V. Postica, O. Polonskyi, N. Ababii, F. Schütt, V. Kaidas, F. Faupel, R. Adelung, *Sens. Actuators B* **2016**, *230B*, 832.
[34] O. Lupan, V. Postica, J. Gröttrup, A. K. Mishra, N. H. de Leeuw, R. Adelung, *Sens. Actuators B* **2017**, *245B*, 448.
[35] Z. Fang, S. Zheng, W. Peng, H. Zhang, Z. Ma, S. Zhou, D. Chen, J. Qiu, *J. Am. Ceram. Soc.* **2015**, *98*, 2772.

ADVANCED SCIENCE NEWS
www.advancedsciencenews.com

physica status solidi a
www.pss-a.com

[36] C. J. Sun, J. W. Yang, Q. Chen, M. A. Khan, T. George, P. Chang-Chien, S. Mahajan, *Appl. Phys. Lett.* **1996**, *68*, 1129.
[37] Y. Chen, S. Hong, H. Ko, M. Nakajima, T. Yao, Y. Segawa, *Appl. Phys. Lett.* **2000**, *76*, 245.
[38] F. Decremps, J. Pellicer-Porres, A. M. Saitta, J.-C. Chervin, A. Polian, *Phys. Rev. B* **2002**, *65B*, 092101.
[39] R. Cuscó, E. Alarcón-Lladó, J. Ibáñez, L. Artús, J. Jiménez, B. Wang, M. J. Callahan, *Phys. Rev. B* **2007**, *75B*, 165202.
[40] V. Postica, I. Hölken, V. Schneider, V. Kaidas, O. Polonskyi, V. Cretu, I. Tiginyanu, F. Faupel, R. Adelung, O. Lupan, *Mater. Sci. Semicond. Process.* **2016**, *49*, 20.
[41] M. Nasr, R. Viter, C. Eid, F. Warmont, R. Habchi, P. Miele, M. Bechelany, *RSC Adv.* **2016**, *6*, 103692.
[42] J. Gröttrup, V. Postica, D. Smazna, M. Hoppe, V. Kaidas, Y. K. Mishra, O. Lupan, R. Adelung, *Vacuum* **2017**, *146*, 492.
[43] V. Postica, J. Gröttrup, R. Adelung, O. Lupan, A. K. Mishra, N. H. de Leeuw, N. Ababii, J. F. C. Carreira, J. Rodrigues, N. B. Sedrine, M. R. Correia, T. Monteiro, V. Sontea, Y. K. Mishra, *Adv. Funct. Mater.* **2017**, *27*, 1604676.
[44] J. Gröttrup, V. Postica, N. Ababii, O. Lupan, C. Zamponi, D. Meyners, Y. K. Mishra, V. Sontea, I. Tiginyanu, R. Adelung, *J. Alloys Compd.* **2017**, *701*, 920.
[45] O. Lupan, V. Postica, N. Wolff, O. Polonskyi, V. Duppel, V. Kaidas, E. Lazari, N. Ababii, F. Faupel, L. Kienle, R. Adelung, *Small* **2017**, *13*, 1602868.
[46] Z. L. Wang, J. Song, *Science* **2006**, *312*, 242.
[47] J. F. Chang, H. H. Kuo, I. C. Leu, M. H. Hon, *Sens. Actuators B* **2002**, *84B*, 258.
[48] G. Sakai, N. Matsunaga, K. Shimanoe, N. Yamazoe, *Sens. Actuators B* **2001**, *80B*, 125.
[49] O. Lupan, G. Chai, L. Chow, *Microelectron. Eng.* **2008**, *85*, 2220.
[50] L. L. Fields, J. P. Zheng, Y. Cheng, P. Xiong, *Appl. Phys. Lett.* **2006**, *88*, 263102.
[51] V. Dua, S. P. Surwade, S. Ammu, S. R. Agnihotra, S. Jain, K. E. Roberts, S. Park, R. S. Ruoff, S. K. Manohar, *Angew. Chem. Int. Ed.* **2010**, *49*, 2154.
[52] J. Li, Y. Lu, Q. Ye, M. Cinke, J. Han, M. Meyyappan, *Nano Lett.* **2003**, *3*, 929.
[53] N. Minh Vuong, D. Kim, H. Kim, *Sci. Rep.* **2015**, *5*, 11040.
[54] L. Liao, H. X. Mai, Q. Yuan, H. B. Lu, J. C. Li, C. Liu, C. H. Yan, Z. X. Shen, T. Yu, *J. Phys. Chem. C* **2008**, *112C*, 9061.
[55] L. Liao, Z. Zhang, B. Yan, Z. Zheng, Q. L. Bao, T. Wu, C. M. Li, Z. X. Shen, J. X. Zhang, H. Gong, J. C. Li, T. Yu, *Nanotechnol.* **2009**, *20*, 085203.
[56] C. Yan, B. Huy Le, D. J. Kang, *J. Mater. Chem. A* **2014**, *2*, 5394.
[57] L. Chow, O. Lupan, G. Chai, *Phys. Status Solidi B* **2010**, *247B*, 1628.
[58] L. Liao, Z. Zheng, B. Yan, J. X. Zhang, H. Gong, J. C. Li, C. Liu, Z. X. Shen, T. Yu, *J. Phys. Chem. C* **2008**, *112C*, 10784.
[59] O. Lupan, V. Cretu, V. Postica, M. Ahmadi, B. R. Cuenya, L. Chow, I. Tiginyanu, B. Viana, T. Pauporté, R. Adelung, *Sens. Actuators B* **2016**, *223B*, 893.
[60] O. Lupan, L. Chow, T. Pauporté, L. K. Ono, B. Roldan Cuenya, G. Chai, *Sens. Actuators B* **2012**, *173*, 772.
[61] N. Barsan, U. Weimar, *J. Electroceram.* **2001**, *7*, 143.
[62] M. Tonezzer, N. V. Hieu, *Sens. Actuators B* **2012**, *163B*, 146.
[63] F. Favier, E. C. Walter, M. P. Zach, T. Benter, R. M. Penner, *Science* **2001**, *293*, 2227.
[64] S. N. Das, J. P. Kar, J.-H. Choi, T. I. Lee, K.-J. Moon, J.-M. Myoung, *J. Phys. Chem. C* **2010**, *114C*, 1689.
[65] V. Postica, F. Schütt, R. Adelung, O. Lupan, *Adv. Mater. Interfaces* **2017**, *4*, 1700507.
[66] Y. M. Wong, W. P. Kang, J. L. Davidson, A. Wisitsora, K. L. Soh, *Sens. Actuators B* **2003**, *93B*, 327.
[67] K. Skucha, Z. Fan, K. Jeon, A. Javey, B. Boser, *Sens. Actuators, B* **2010**, *145B*, 232.
[68] J. Okal, M. Zawadzki, *Appl. Catal. A* **2013**, *453A*, 349.
[69] D. R. Miller, S. A. Akbar, P. A. Morris, *Sens. Actuators B* **2014**, *204B*, 250.
[70] X. Zhao, L. Wang, X. Xu, X. Lei, S. Xu, F. Zhang, *AIChE J.* **2012**, *58*, 573.
[71] H.-J. Kim, H.-M. Jeong, T.-H. Kim, J.-H. Chung, Y. C. Kang, J.-H. Lee, *ACS Appl. Mater. Interfaces* **2014**, *6*, 18197.
[72] H.-R. Kim, K.-I. Choi, K.-M. Kim, I.-D. Kim, G. Cao, J.-H. Lee, *Chem. Comm.* **2010**, *46*, 5061.
[73] M. C. Newton, S. Firth, P. A. Warburton, *Appl. Phys. Lett.* **2006**, *89*, 072104.
[74] Y. Gu, J. Zhou, W. Mai, Y. Dai, G. Bao, Z. L. Wang, *Chem. Phys. Lett.* **2010**, *484*, 96.
[75] Y. Cui, U. Banin, M. T. Björk, A. P. Alivisatos, *Nano Lett.* **2005**, *5*, 1519.

ACS APPLIED MATERIALS & INTERFACES

Research Article

Cite This: ACS Appl. Mater. Interfaces 2019, 11, 32115−32126

www.acsami.org

Low-Temperature Solution Synthesis of Au-Modified ZnO Nanowires for Highly Efficient Hydrogen Nanosensors

Oleg Lupan,*[,†,‡,§] Vasile Postica,[§] Niklas Wolff,[∥] Jun Su,[⊥] Frédéric Labat,[⊥] Ilaria Ciofini,*[,⊥] Heather Cavers,[‡] Rainer Adelung,*[,‡] Oleksandr Polonskyi,[#] Franz Faupel,[#] Lorenz Kienle,[∥] Bruno Viana,[†] and Thierry Pauporté*[,†]

[†]Institut de Recherche de Chimie Paris-IRCP, Chimie ParisTech, PSL Université, rue Pierre et Marie Curie 11, 75231 Paris Cedex 05, France

[‡]Functional Nano Materials, Institute for Materials Science, Faculty of Engineering, Kiel University, str. Kaiserstraße 2, D-24143 Kiel, Germany

[§]Center for Nanotechnology and Nanosensors, Department of Microelectronics & Biomedical Engineering, Technical University of Moldova, Stefan Cel Mare Av. 168, MD 2004 Chisinau, Republic of Moldova

[∥]Institute for Materials Science, Synthesis and Real Structure, Christian Albrechts University Kiel, str. Kaiserstraße 2, D-24143 Kiel, Germany

[⊥]i-CLeHS, Chimie ParisTech, PSL University, rue Pierre et Marie Curie nr. 11, 75231 Paris Cedex 05, France

[#]Faculty of Engineering, Chair for Multicomponent Materials, Christian-Albrechts University of Kiel, str. Kaiserstraße nr. 2, D-24143 Kiel, Germany

Supporting Information

ABSTRACT: In this research, the low-temperature single-step electrochemical deposition of arrayed ZnO nanowires (NWs) decorated by Au nanoparticles (NPs) with diameters ranging between 10 and 100 nm is successfully demonstrated for the first time. The AuNPs and ZnO NWs were grown simultaneously in the same growth solution in consideration of the $HAuCl_4$ concentration. Optical, structural, and chemical characterizations were analyzed in detail, proving high crystallinity of the NWs as well as the distribution of Au NPs on the surface of zinc oxide NWs demonstrated by transmission electron microscopy. Individual Au NPs-functionalized ZnO NWs (Au-NP/ZnO-NWs) were incorporated into sensor nanodevices using an focused ion bean/scanning electron microscopy (FIB/SEM) scientific instrument. The gas-sensing investigations demonstrated excellent selectivity to hydrogen gas at room temperature (RT) with a gas response, I_{gas}/I_{air}, as high as 7.5−100 ppm for Au-NP/ZnO-NWs, possessing a AuNP surface coverage of ∼6.4%. The concentration of $HAuCl_4$ in the electrochemical solution was observed to have no significant impact on the gas-sensing parameters in our experiments. This highlights the significant influence of the total Au/ZnO interfacial area establishing Schottky contacts for the achievement of high performances. The most significant performance of H_2 response was observed for gas concentrations higher than 500 ppm of H_2 in the environment, which was attributed to the surface metallization of ZnO NWs during exposure to hydrogen. For this case, an ultrahigh response of about 32.9 and 47 to 1000 and 5000 ppm of H_2 was obtained, respectively. Spin-polarized periodic density functional theory calculations were realized on Au/ZnO bulk and surface-functionalized models, validating the experimental hypothesis. The combination of H_2 gas detection at RT, ultralow power consumption, and reduced dimensions makes these micro-nanodevices excellent candidates for hydrogen gas leakage detection, including hydrogen gas monitoring (less than 1 ppm).

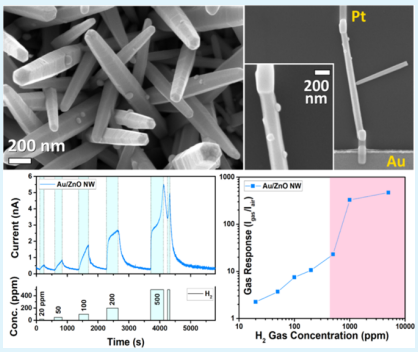

KEYWORDS: *Au-modified ZnO NW, gas sensor, nanosensor, hydrogen, electrochemical deposition*

1. INTRODUCTION

During the last decade, the synthesis of new nanomaterials for a wide range of applications, such as high-performance gas sensors, nanosensors, biosensors, photocatalysis, electronics, optoelectronics, and so forth, has been in the focus of extensive and intense studies from the scientific community.[1] In such a context, ZnO nano- and micro-structures are ideal building blocks for high-performance hybrid nanomaterials as they possess superior electrical, optical, and sensing properties and can be synthesized by numerous cost-effective synthesis

Received: May 17, 2019
Accepted: August 6, 2019
Published: August 6, 2019

DOI: 10.1021/acsami.9b08598
ACS Appl. Mater. Interfaces 2019, 11, 32115−32126

ACS Applied Materials & Interfaces Research Article

methods.[2−7] Another essential advantage of ZnO is the possibility to fabricate a broad range of one-dimensional, two-dimensional, and three-dimensional morphologies in a controlled manner.[2,8,9] Great attention has been paid to one-dimensional nanostructures, such as nanorods, nanowires (NWs), nanotubes, nanospikes, and nanobelts, as they are excellent candidates for the fabrication of devices based on individual structures with unique optical and sensing properties.[10−12] It was demonstrated that surface reactions (adsorption/desorption of gaseous species) have a large influence on the electrical transport properties in individual nanostructures,[12] which is extremely advantageous for fabrication of more sensitive gas nanosensors that are able to operate at room temperature (RT).[13,14]

Different methods were used in order to improve the selectivity and response of these gas nanosensors, such as doping,[15] surface modification with noble metal nanoparticles (NPs),[13,14] or with transition-metal oxides,[16,17] as well as the design of Schottky contacts.[18] In this context, the surface deposition of gold NPs on the ZnO nanostructures for the formation of Au-NP//ZnO structures is very attractive for high-performance gas sensors and UV photodetectors.[19−22] For example, Liu et al. designed an UV photodetector based on a single ZnO NW modified with Au NPs that showed increased improvement of the device performance.[21] At the same time, to the best of our knowledge, no data on gas detection performances of a single ZnO NW decorated with gold NPs have been reported in the literature yet. Thus, it is highly important to study the gas detection performances of individual Au-NP/ZnO nanostructures/NWs, which is the main aim of our research presented in the current study.

Herein, one report on a single-step electrochemical functionalization of the surface of ZnO NW arrays with Au NPs for the fabrication of nanodevices with highly selective gas-sensing applications, where Au-NP nucleation, growth, and deposition were realized in the same approach as the ZnO NW synthesis. An individual ZnO NW decorated with Au-NPs was integrated into the nanosensor device employing a FIB/scanning electron microscopy (SEM) double beam instrument. This approach proves the possibility to fabricate micro- and nanodevices with highly selective and sensitive hydrogen gas detection properties, even at RT. We also observed that water vapor has a lower impact on the gas detection properties of a single Au-NP/ZnO-NW, which is essential for practical applications in normal ambient conditions.

2. EXPERIMENTAL SECTION

2.1. Growth of AuNP/ZnO NW Arrays. The synthesis of AuNP/ZnO-NW arrays was performed by electrochemical deposition in a classical electrochemical cell with three electrodes,[15,23−25] employing a glass substrate covered with F-doped SnO_2 [fluorine doped tin oxide (FTO), 10 Ω/□] polycrystalline films as a working electrode. The growth solution was made of zinc chloride ($ZnCl_2$) at 0.20 mM, a KCl-supporting electrolyte with a concentration of 0.1 M, and oxygen bubbling continuously at the saturation level.[23] The concentration of $HAuCl_4$ (Sigma-Aldrich, >99.9%) in the growth solution was varied from 0.1 to 2.0 μM to investigate the effect on the growth of ZnO NW arrays with Au-NPs. Upon deposition, the FTO substrate was rotated at a speed of 300 rpm (constant).[15,23,24] The electrodeposition was performed at 85 or 90 °C at constant applied potential, as indicated further for each sample investigated in this work, employing an Autolab PGSTAT30 galvanostat/potentiostat controlled by the software GPES Autolab.[23] More details are presented in previous works.[15,23,24,26]

2.2. Material Characterization and Computational Details. The ZnO NWs decorated with Au-NPs have been examined with methods of transmission electron microscopy (TEM). The samples were prepared by scratching the deposit onto a lacey carbon//copper grid and placing it into a double-tilt TEM holder. Structural analysis was performed by using FEI Tecnai F30 G^2 STwin working at 301 kV, assembled with a gun field emission. Selected area electron diffraction patterns (SAED) were measured employing apertures as low as 250 nm in diameter. The obtained SAED patterns were figured out with the Digital Micrograph (from Gatan, Inc.) analysis software. For the chemical analysis via energy-dispersive X-ray (EDX) spectroscopy, a detector with Si/Li (in EDAX System) was employed. Images from the scanning (S) TEM Z-contrast were registered by employing a detector with high-angle annular dark field (HAADF).

X-ray photoelectron spectroscopy (XPS, Omicron Nano-Technology GmbH) was employed for the characterization of the surface of deposited Au-NP/ZnO-NW samples in order to reveal the chemical composition of the sample surface. All the spectra were charge-referenced after the measurements using the aliphatic carbon peak (285.0 eV) with the help of CasaXPS software.

The nanodevices based on single NWs were designed following a technological approach developed by Lupan et al.[15,27] The gas-sensing studies were realized at RT (~25 °C) and under normal ambient air (relative humidity of ~25%), following the procedure reported in previous works.[15,28] The electrical studies were continuously measured and collected using a computer-controlled Keithley2400 sourcemeter through LabVIEW software (from National Instruments) by applying 1 V bias voltage.[28] The gas response (S) was calculated as the current ratio under exposure to gas (I_{gas}) versus current when the sample was exposed to ambient air (I_{air}), that is, $S = I_{gas}/I_{air}$. The detection limit was theoretically calculated using the method proposed by Dua et al. using a signal/(noise)^2 ratio.[29]

All details on the computational part, density functional theory (DFT) modeling, and selection of the surface models based on experimental evidences are given in the Supporting Information (S1 and S2 Texts, respectively).

3. RESULTS AND DISCUSSION

3.1. Growth of Samples. Figure S1a presents the first voltammetry cycles registered on the FTO glass in the zinc oxide electrodeposition complex with different $HAuCl_4$ concentrations: (a) 0.6; (b) 1.0; and (c) 2.0 μM. The electrochemical bath was made of $ZnCl_2$ at 0.2 mM, a KCl supporting electrolyte at 0.1 M, and oxygen (100%) at the saturation level.[23] As can be seen, a small rise in the cathodic electrical current appears at above −0.4, −0.3, and −0.22 V for samples with $HAuCl_4$ concentrations of 0.6, 1.0, and 2.0 μM, respectively. This reduction peak was seen by Argoubi et al. in the experiments of electrochemical reduction of Au(III) on the top of electrodes with screen-printed carbon.[30] Therefore, it can be attributed to the reduction of Au.[30] The cathodic wave appears at above −0.8, −0.8, and −0.75 V, respectively, with further increase of the negative-going scan (see Figure S1a), and can be attributed to the reduction of Zn^{2+} to the metal Zn.[26] The slight increase in the measured current density is observed with increasing $HAuCl_4$ concentrations, which might indicate that Au-ions act as the electrocatalyst for the electrochemical reaction ($O_2 + 2H_2O + 4e^- \rightarrow 4OH^-$).[23] Based on these curves, the values of constant potential for the deposition of samples were determined (see Table S1).

The chronoamperometry curves, measured while the electrode with the FTO glass substrate was rotated at 300 rpm, are shown in Figure S1b. It is observed from this figure that the deposition current density sharply decreases in the initial period and gradually stabilizes. One can be assigned to the process of nucleation of ZnO NWs and Au NPs. Taking

DOI: 10.1021/acsami.9b08598
ACS Appl. Mater. Interfaces 2019, 11, 32115−32126

ACS Applied Materials & Interfaces Research Article

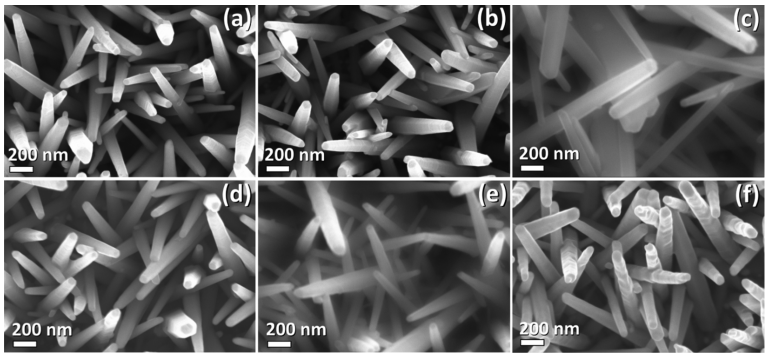

Figure 1. SEM images of Au-modified ZnO NWs grown using different concentrations of $HAuCl_4$ in the electrolyte: (a) 0.3; (b) 0.6; (c) 0.75; (d) 1.0; (e) 1.5; and (f) 2.0 μM.

into account the current density values for pure zinc oxide NW arrays and by adding $HAuCl_4$ to the growth solution, a significant increase in the growth cathodic current density is obtained, which was also published for Ag:ZnO NWs[23] and Pd/ZnO NWs.[14] Thus, we believe that the Au-NPs decorating the deposited ZnO NWs serve as good electrocatalysts for the electrochemical reactions.

3.2. Morphological and Structural Properties. Figure 1a–f presents SEM images of Au-NP/ZnO NW arrays grown using different concentrations of $HAuCl_4$ in the electrolyte solution: (a) 0.3; (b) 0.6; (c) 0.75; (d) 1.0; (e) 1.5; and (f) 2.0 μM. All samples are composed of arrays of free-standing ZnO NWs. The diameters of the NWs vary in the range of 100–200 nm (see Figure S2). With increasing $HAuCl_4$ concentration, essentially the size of the NWs did not change, according to our experimental observations (see Figures 1 and S2). While unmodified ZnO NW arrays are vertically oriented,[23] the Au-NP-decorated ZnO NWs are tilted from the vertical direction with increased surface texture (see Figure 1). This effect increases with the $HAuCl_4$ concentration, which indicates more difficultly with the nucleation of the NWs and that the NW growth starts at the same point and forms flower-like architectures, which were also observed for Ag-doped ZnO NWs grown by the same approach.[23] It is necessary to mention that at higher magnifications, Au-NPs deposited on the zinc oxide NW surface could be observed (see red circles in Figure S3). These clusters are described in more details, using TEM measurements, in the following. The cathodic electrodeposition of Au NPs from the dissolved precursor can be described by the following equation[31]

$$AuCl_4^- + 3e^- \leftrightarrow Au^0 + 4Cl^- \quad (1)$$

In the case of samples grown using 2.0 μM of $HAuCl_4$, a deformation of the NW morphology can be observed as well as a lack of Au-NPs (see Figures 1f and S4). In this case, the applied potential was −0.951 V versus the SCE (saturated calomel electrode). The rugged surface structure could be due to the formation of native defects, for example vacancies, during crystal growth in the solution, which can migrate to the surface and contribute to indentation of the surface. This effect was also observed for Pd-modified ZnO NW arrays[14] as well as for Cl- and Sb-doped ZnO NW arrays.[32,33] However, the samples grown at −0.65 V versus SCE showed no deformation on the surface of the NWs while Au-NPs were observed on their surface (see Figure S5). This could be tentatively described by the fact that the lower applied bias of −0.65 V versus SCE is closer to the kinetic regime of gold deposition (−0.51 V vs SCE in the case of $HAuCl_4$), as was determined using current–potential curves by Wijnhoven et al.[34]

X-ray diffraction (XRD) $\theta/2\theta$ investigations were performed to investigate the influence of the $HAuCl_4$ concentration on the crystallinity of the Au-NP/ZnO-NW arrays. Figure 2a shows the XRD data in the 10–90° 2θ range with 0.02° scanning step for Au-NP/ZnO-NW arrays, grown using different concentrations of $HAuCl_4$ (0.0, 0.3, 1.5, and 2.0 μM). Reflections at 31.79°, 34.44°, 36.28°, 47.65°, 56.63°, 62.88°, and 72.54° were assigned to the planes (1 0 0), (0 0 2), (1 0 1), (1 0 2), (1 1 0), (1 0 3), and (0 0 4) of wurtzite ZnO (PDF card # 36-1451), while reflections noted with red "*" were assigned to SnO_2 (i.e., to the FTO substrate), according to PDF card # 01-077-0488.[24]

To investigate the influence of doping on the crystallinity of the zinc oxide NWs, the intensity of the (0 0 2) and (1 0 1) reflections was monitored (see Figure 2b). A slight decrease in the diffraction peak intensity for (0 0 2) and (1 0 1) planes was observed, corresponding to an increase in the $HAuCl_4$ concentration up to 2.0 μM. The ionic radii of Zn and Au are $r(Zn^{2+})$ = 0.074 nm and $r(Au^{3+})$ = 0.085 nm, respectively.[35] Therefore, the Au incorporation in the ZnO lattice should lead to an expansion of the lattice, shifting the XRD diffraction peaks.[35] However, in our case no detectable shift in the position of the (0 0 2) and (1 0 1) reflections, with the $HAuCl_4$ concentration, was observed (see Figure 2b). Moreover, additional low intensity peaks were observed for Au-NP/ZnO-NW arrays at 38.17° and 44.42°, which can be assigned to cubic Au with the $Fm\bar{3}m$ space group (a = 4.0786 Å, PDF card # 03-065-2870, see Figure 2c).[20] The weak reflections of Au indicate that only a small amount of gold on the nanometer scale is present.[20] These reflections increase in intensity with increasing $HAuCl_4$ concentration (see Figure 2c). Therefore, one can conclude that the Au-NPs are deposited on the surface of ZnO NWs during the process of electrochemical deposition and that likely no significant doping occurs.[14] This could be due to the low solubility of Au in ZnO,[9,36] and only a few works have reported on Au-doped ZnO with evident proof.[35]

Figure 3a,b shows the experimental results of the TEM investigations of the sample grown using 2.0 μM $HAuCl_4$ at −0.65 V versus SCE. Figure 3a shows a scanning transmission electron microscopy (STEM) HAADF image of ZnO microcrystals decorated with Au nanodots which were observed ranging from 10 to 100 nm in size. An EDX elemental map (Figure 3b) of the area within the red frame correlates the high

DOI: 10.1021/acsami.9b08598
ACS Appl. Mater. Interfaces 2019, 11, 32115–32126

ACS Applied Materials & Interfaces Research Article

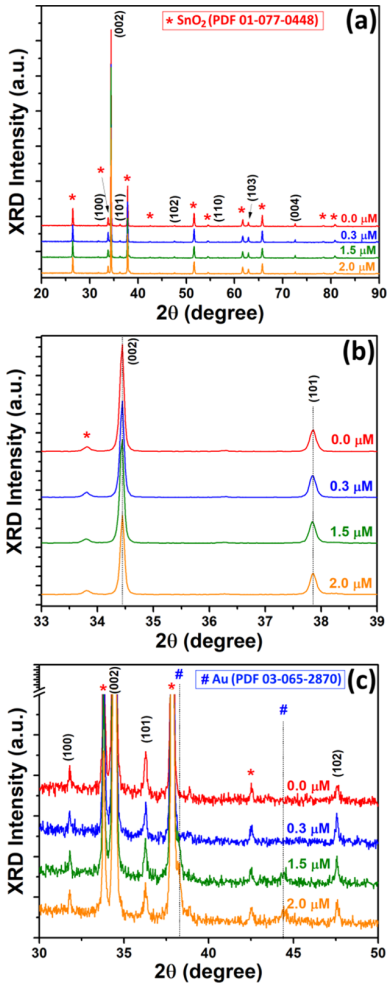

Figure 2. (a) XRD patterns of the Au-modified ZnO NW arrays grown using different concentrations of $HAuCl_4$ in the electrolyte. (b) Position of (0 0 2) and (1 0 1) peaks for Au-modified ZnO NW arrays. (c) Demonstration of peaks with low relatively intensity which correspond to Au.

Z-contrast positions with X-ray signals denoted to the Au M-shell. The electron diffraction pattern depicted in Figure 3c shows the superposition of structural reflections of the ZnO crystal in $[2\bar{1}\bar{1}0]$ orientation, and reflection spots originate from the (1 1 1) and (0 0 2) planes of face-centered cubic gold, with d = 0.231 nm and d = 0.201 nm, respectively.[37] No systematic orientation relationship between the ZnO and the Au lattice could be identified. For the Au nanodots, multiple twinning[38] as well as an amorphous shell coating the nanodot could be evidenced by high-resolution imaging.

3.3. EDX and XPS Studies of the Au-NP/ZnO-NWs.

Analysis by EDX spectroscopy on a Zeiss SEM has been performed to give a rough estimate about the molar Au content in the NW arrays grown in the presence of increasing $HAuCl_4$ concentration. The obtained results are presented in Table S1. The molar ratio between gold and zinc in the Au-NP/ZnO-NWs increased once the $HAuCl_4$ concentration in the bath was increased and was comparable with the ratio present in the deposition bath. Two samples of Au-NP/ZnO-NW arrays, grown using the addition of 0.6 and 0.9 μM of $HAuCl_4$ to the ZnO NW growth solution, were investigated by using XPS. Figure 4a presents a survey spectrum of a typical Au-NP/ZnO-NW array grown using a solution containing 0.6 μM of $HAuCl_4$. The following elements were detected: C, O, Zn, and Au, and the relative atomic concentrations are shown below the spectrum. Generally, the deposition process does not contain carbon, and so carbon is not expected to be present in the films. However, because the samples were exposed to ambient air and no surface cleaning was made before XPS characterization, the carbon observed can be attributed to adventitious carbon resulting from exposure to the ambient atmosphere.[39] The presence of the adventitious carbon (285.0 eV) allowed us to use it as a reference for energy calibration. Detailed deconvolution of the C-1s spectrum (Figure 4b) shows that in addition to the adventitious carbon, there are also two peaks present at 286.7 and 289.4 eV, corresponding to CO and CO_2, respectively.[39]

Au-NP/ZnO-NW arrays grown using solutions with 0.6 and 0.9 μM of $HAuCl_4$ contain around 0.4 and 0.6 at % of Au, respectively, as revealed by XPS analysis. This is slightly lower in comparison to the data measured using EDX (see Table S1). High-resolution XPS spectra of Au-4d are demonstrated in Figure 4c. The XPS peaks observed at 352.26 and 334.72 eV may be attributed to metallic Au and are in high agreement with the XPS results published in the specialized literature.[40,41] As will be discussed later, samples containing different concentrations of gold demonstrate different gas sensing behaviors. In Figure 4d, the high-resolution spectrum of the O-1s core level is depicted. To get more insight into the chemical composition of the specimen surface, the higher resolution O-1s spectrum was deconvoluted using several components, following the proposed structure suggested in ref 42. The resulted fitting is depicted in Figure 4d, and it contains the following three main components: ZnO (530.4 eV),

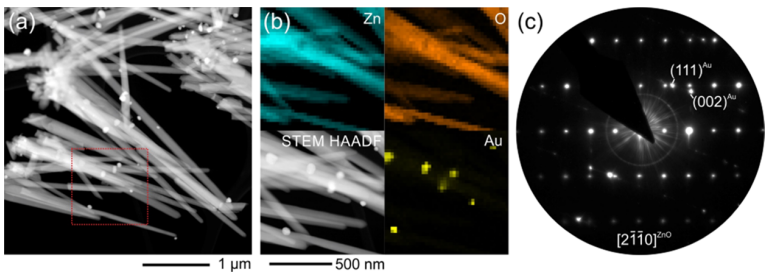

Figure 3. Structural and chemical analysis with TEM. (a) STEM dark field image of ZnO nano- and microwires faceted with gold nanodots (samples grown using 2.0 μM of $HAuCl_4$ at −0.65 V vs SCE). (b) STEM EDX elemental mapping of the red framed area in (a) depicting Au nanodots on ZnO. (c) Electron diffraction pattern of ZnO in $[2\bar{1}\bar{1}0]$ orientation superimposing with reflections of Au.

DOI: 10.1021/acsami.9b08598
ACS Appl. Mater. Interfaces 2019, 11, 32115−32126

ACS Applied Materials & Interfaces Research Article

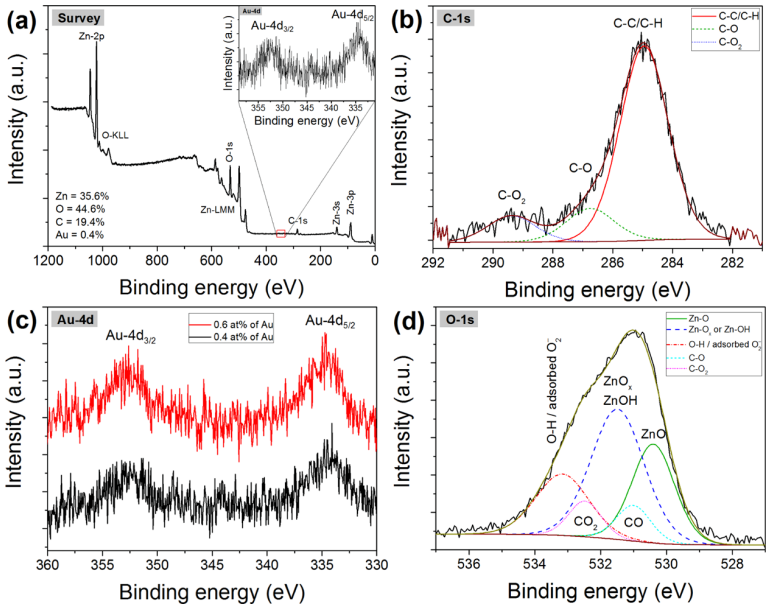

Figure 4. XPS spectra of Au-NP/ZnO-NW arrays grown using different concentrations of $HAuCl_4$: (a) survey spectrum of a sample grown using 0.6 μM; (b) high resolution of the C-1s peak; (c) high-resolution spectra of Au-4d peaks for two samples grown using 0.6 and 0.9 μM; (d) high resolution of the O-1s peak.

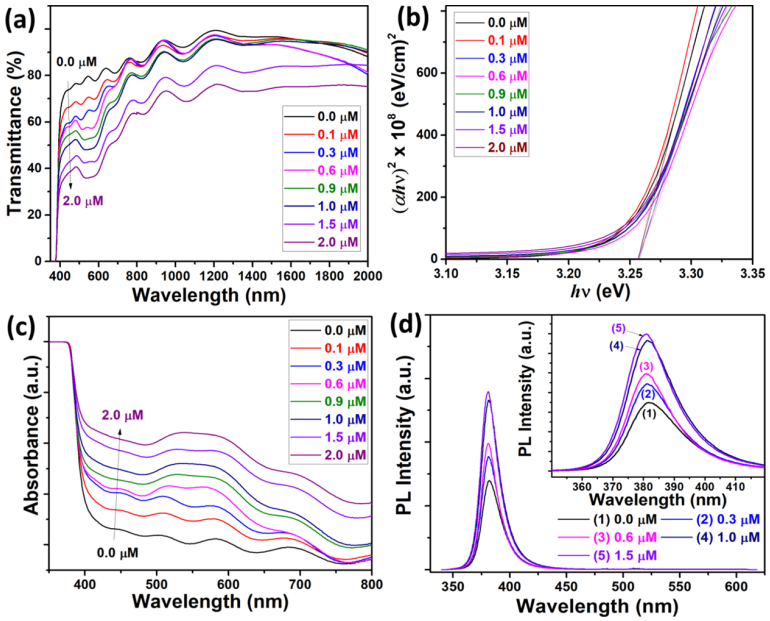

Figure 5. (a) Transmission spectra; (b) plot of $(\alpha h\nu)^2$ vs photon energy ($h\nu$); (c) absorbance spectra; and (d) PL spectra at room temperature for Au-modified ZnO NW arrays grown using different concentrations of $HAuCl_4$. In the inset, the PL spectra for the NBE peak are presented.

defective $Zn(OH)_2$ (531.5 eV) or ZnO_x, and OH groups or adsorbed oxygen (533.2 eV).[14,42] Additionally, two smaller peaks located at 531.0 and 532.5 eV were attributed to adventitious CO and CO_2, respectively.[14,42]

3.4. Optical Properties of the Au-NP/ZnO-NWs. It was demonstrated that defects in ZnO can greatly affect the gas-sensing properties.[43,44] In this case, the measurements of optical properties can provide useful information related to defects in ZnO NWs. Figure 5a shows UV−visible transmission spectra of the Au-NP-modified ZnO NW arrays electrodeposited using various concentrations of $HAuCl_4$ in the growth solution. While unmodified ZnO NW arrays are highly transparent in the near-IR region (close to 100%), by adding $HAuCl_4$ to the growth solution, a decrease in transparency for the entire UV−visible spectrum can be observed. No detectable shift of the band-edge, corresponding to an increase in the $HAuCl_4$ concentration, was observed. The optical band gap (E_g) was accomplished from the intercept of $(\alpha h\nu)^2$ versus $h\nu$—photon energy (see Figure 5b). It can be observed that no modifications in the value of E_g (~3.26 eV) are induced by an increase in the $HAuCl_4$ concentration.

DOI: 10.1021/acsami.9b08598
ACS Appl. Mater. Interfaces 2019, 11, 32115−32126

ACS Applied Materials & Interfaces Research Article

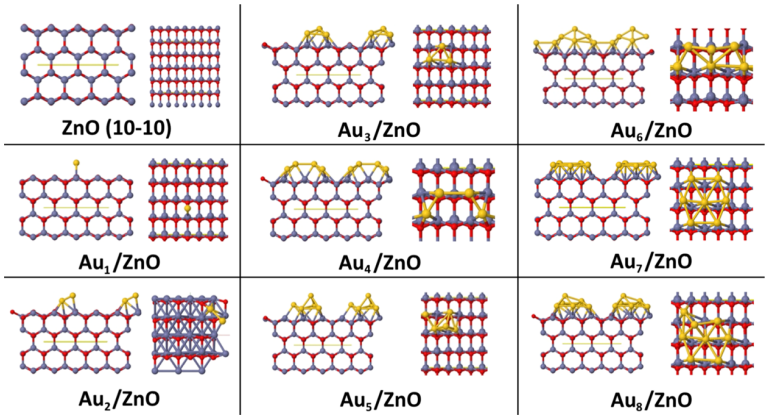

Figure 6. Side and top views of the unit cells of a pure ZnO (10−10) surface with 8 layers and of Au_n/ZnO (10−10) with n ranging from 1 to 8. Red, gray, and yellow balls correspond to O, Zn, and Au atoms, respectively. The unit cell is shown as solid yellow lines.

Therefore, no evidence of doping was seen in these experiments.

The presence of Au-NPs in the Au-NP/ZnO-NW arrays was further demonstrated by the UV−vis absorption spectra. Figure 5c shows the absorbance spectra of Au-NP/ZnO-NW arrays electrodeposited using several different concentrations of $HAuCl_4$ in the growth solution. The gradual increase in the peak intensity at ∼540 nm with higher concentration of $HAuCl_4$ is observed (see Figure 5c), which is attributed to the surface plasmon resonance of Au NPs,[3,45] demonstrating the successful surface modification of ZnO NWs with Au NPs.

The photoluminescence (PL) spectra recorded at RT for Au-NP/ZnO-NW arrays, grown using different concentrations of $HAuCl_4$ in the growth solution, are presented in Figure 5d. Visible emission was not detected, which is associated to bulk and surface defects, either for the unmodified ZnO NWs or Au-NP/ZnO-NWs, demonstrating that the synthesized NW arrays possess a good structural quality, even with a growth temperature of about 90 °C.[23] Position changes of the near-band edge (NBE) emission peak were not observed, corresponding to an increase in the $HAuCl_4$ concentration (see Figure 5d). However, a gradual increase in the intensity of the NBE emission with an increase in the $HAuCl_4$ concentration was detected. The emission is enhanced by Au as the surface is higher, despite stronger reabsorption at the wavelengths of the ZnO emission. As the absorbance increases with the $HAuCl_4$ concentration as presented in Figure 5c, this unexpected enhancement of the UV emission may be attributed to the big interfacial coupling between the gold NPs (metal) and the zinc oxide NWs (semiconducting oxide) as observed in ref 45, where Au surface electrons are transferred to the zinc oxide NWs, leading to an increase in the electron density in the conduction band (CB) of ZnO resulting in an increased recombination rate.[45]

3.5. Theoretical Insights into the Structural and Electronic Modifications due to Doping. From the above discussions, Au-doping in the bulk of zinc oxide NW arrays was not evidenced; however, surface modification of Au-NP/ZnO-NWs was highlighted. To shed light on possible Au/ZnO nanostructures involved, we present experimental−computational data realized on models of Au-doped bulk ZnO wurtzite and adsorption of Au clusters of various sizes on the clean (pure) ZnO (10−10) surface, as an example of functionalization of such surface. As previously performed for the bulk case of Ag[23] and Pd,[14] calculations have also been made on: (i) pure ZnO, and (ii) doped ZnO with inserted Au (Au_i) at a 1.85 at % doping amount to gain insight into the effect of the Au insertion into the wurtzite bulk structure on the electronic properties. The unit cell of the inserted Au:ZnO system is presented in Figure S6, and respective band structures are illustrated in Figure S7, along with the obtained data in Table S2.

Computed shortest distances between Au and O (d_1 to d_6, see Table S2) indicate that when Au is inserted in the ZnO lattice, a highly distorted octahedron around Au can be evidenced, with distances ranging between 2.37 and 3.94 Å. The a and b wurtzite lattice vectors are slightly increased (+0.4%), while the c lattice vector is decreased of about −1.6%. According to the data presented in Figure S7 and Table S2, it is evident that the zinc oxide band gap decreases upon insertion of Au, with at least 1.10 eV. Gold mainly contributes through 5d orbitals at the upper levels of the valence band (VB) and at the lower levels of the CB, with bands possessing very low dispersion, indicating an approximately atomic-like character. The lack of a shallow level at the bottom of the CB illustrates that p-type conduction is not obtained in such a case, however, as already outlined for Pd-[14] or Ag-[23] doping.

Adsorption of Au_n nanoclusters (n is between 1 to 8) on a bulk ZnO (10−10) surface[17,30] has also been computed (see Figure 6). More detailed discussions on the models for functionalized surfaces are included in the Supporting Information Text S2.

According to the data collected in Table S3, from the Supporting Information, the negative adsorption energies obtained indicate the stable adsorption of the Au_n clusters in all the cases investigated, with Au_6 showing the largest adsorption energy, probably due to the favorable bonding between adjacent clusters from one periodic cell to the other. In particular, while Au atoms of small clusters tend to occupy bridge sites between Zn and O surface atoms, in larger clusters, Au atoms tend to occupy hollow sites with a clear *hcp* motif obtained for the Au_7 and Au_8 clusters. In addition, larger clusters tend to spread on the ZnO substrate, as evidenced by the d_{Au-Au} distances reported in Table S3, which increase from the smallest to the largest clusters. Both bonding to surface Zn and O atoms can be evidenced, the shortest distances involving surface O atoms. A charge transfer from the Au_n cluster to the ZnO substrate can also be evidenced, the Au_n cluster being

DOI: 10.1021/acsami.9b08598
ACS Appl. Mater. Interfaces 2019, 11, 32115−32126

ACS Applied Materials & Interfaces Research Article

positively charged, with a charge value close to +1, as already highlighted in the case of the adsorption of Au_9/TiO_2 (001),[46] for instance. Computed band gaps globally decrease upon increasing the size of the adsorbed Au_n cluster, and all reported band gaps are lower than that of the clean ZnO (10−10) surface (3.88 eV). From Figure S8, Supporting Information, weakly interacting Au_{5d} levels contribute anyhow to the decreasing of the band gap commented above for the functionalized surface. Shallow levels can be observed in all cases, both at the upper levels of the VB and at the lower levels of the CB. Together with the charge transfer mentioned above, this clearly outlines that the NP size strongly influences the ZnO electronic structure, with very different reactivity of the functionalized ZnO substrate possible, depending on the size of the chosen NP.

3.6. Gas Nanosensors Based on Individual Au-NP/ZnO-NWs. The nanosensor devices based on single Au-NP/ZnO-NWs were designed and assembled following the technological approach developed by Lupan et al.[15,47] The Au-NP/ZnO-NWs were removed from the NW arrays grown on the original substrate via sonication in ethanol. In order to obtain a lower density of NWs on the chip for next integration into the device, the transport to an intermediate SiO_2 (300 nm) on a Si substrate (SiO_2/Si) was used.[14] Next, the dispersion was diluted further to decrease the density of NWs on the substrate and for further transfer on a special designed chip with preliminary patterned Au/Cr electrical pads using a direct contact technique and a gentle rubbing few times in order to decrease the density and good distribution of NWs on the chip. Finally, the NWs were contacted to the Au/Cr electrical pads with the Pt complex in SEM/FIB by maskless localized patterning feature, forming the Au/Pt/ZnO:Au/Pt/Au structure. The schematic presentation of the device connection is illustrated in Figure S9. Figure 7a demonstrates the typical image of the device developed from a single Au-NP/ZnO-NW. From the inset in Figure 7a, the Au-NPs can be observed on the ZnO NW surface. The typical current−voltage (I−V) characteristic of a device based on an individual Au-NP/ZnO-NW is presented in Figure 7b. The nonlinear and asymmetrical I−V curves indicate the creation of double-Schottky contacts, which was observed for all samples. The formation of double-Schottky contacts is due to the higher work function of Pt (ϕ = 6.11 eV) contacts compared to the electron affinity of a ZnO NW (E_a = 4.21 eV).[14,15] The asymmetry of I−V curves can be a result of the different contact barriers, the different area of contacts, and the barrier height.[11,12,18]

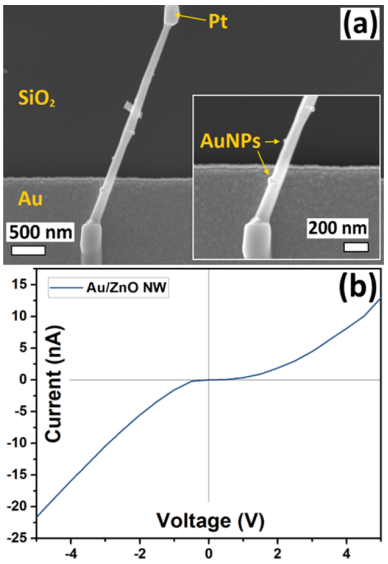

Figure 7. (a) Typical SEM image of a device based on an individual Au-NP/ZnO-NW. In the inset, the zoomed region with Au NPs attached on the surface of the ZnO NW is presented. (b) Room-temperature current−voltage characteristic of the device.

Figure S11a presents the gas response to 100 ppm of H_2 gas for individual ZnO NWs grown using different concentrations of $HAuCl_4$. It is necessary to mention that no Au NPs were observed on the surface of these NWs. Also, for these ZnO NWs, the diameter is 120 ± 10 nm to study only the potential influence of the NW growth in different concentrations of $HAuCl_4$. The results from Figure S11a demonstrate that the concentration of $HAuCl_4$ does not significantly influence the gas response of individual ZnO NWs. This can be attributed to the fact that the ZnO NWs are not doped with Au nor show large amounts of structural defects. Therefore, we conclude that the main parameter, that is important for the improvement of the gas response, is the number of Au NPs on the surface of individual NWs, that is, the surface ratio of nanoscale Schottky contacts to the pristine ZnO surface.

To achieve a considerable increase in gas response by surface-modification of the ZnO NWs with Au NPs, a gas-sensing mechanism is proposed, which is attributed to both the electronic and chemical sensitization.[48] Figure 8 demonstrates

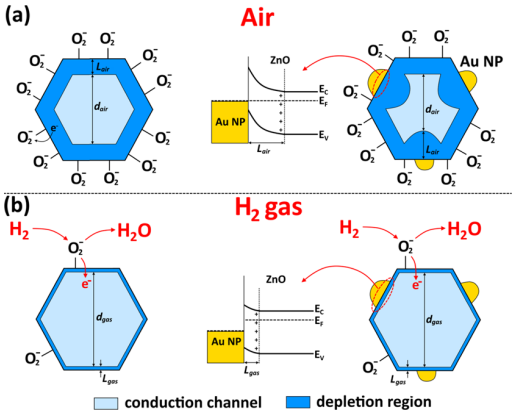

Figure 8. Tentatively proposed gas-sensing mechanism for an individual ZnO and Au-NP/ZnO-NW: (a) under exposure in ambient air; and (b) under exposure in H_2 gas.

the proposed gas-sensing mechanism of the developed devices based on single Au NP-modified ZnO NWs. Under exposure in ambient air at RT, the oxygen species are adsorbed on the top surface of the ZnO NWs by capturing free electrons from the conduction band (E_C)[13,15,48]

$$O_2 + e^- \rightarrow O_2^-{}_{(ad)} \quad (2)$$

This reduction conducts to the formation of a region with higher electrical resistivity than the conductive core at the surface of the ZnO NW (see Figure 8a).[13,15] The width of the depleted region with electrons was noted with L_{air}, while the diameter of the channel, where conduction takes place, was noted as d_{air} (see Figure 8a). Because of operation/function at

DOI: 10.1021/acsami.9b08598
ACS Appl. Mater. Interfaces 2019, 11, 32115−32126

ACS Applied Materials & Interfaces Research Article

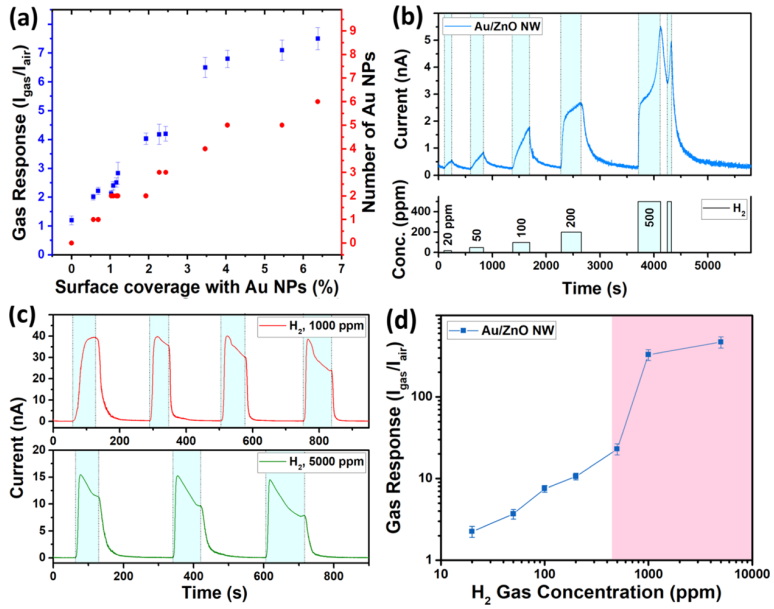

Figure 9. (a) Measured gas response vs the Au NPs surface coverage of an individual Au-NP/ZnO-NW (with diameter of 120 ± 10 nm and grown in various solutions of $HAuCl_4$) calculated from SEM images. The number of Au NPs for each individual Au-NP/ZnO-NW is also presented to show the minor influence of the shear amount of Au NPs on the gas response. (b) Dynamic gas response to different concentrations of H_2 gas, (c) the multiple exposures to 1000 and 5000 ppm of H_2 gas, and (d) the dependence of the gas response on H_2 gas concentrations for an individual Au-NP/ZnO-NW (with ~6.4% AuNPs coverage). The error bars represent the standard deviation between the three measurements in the gas-sensing testing of the same sensors.

RT, the chemical sensitization effect, described above, is considerably reduced, that is, adsorption of more oxygen species occurs via the "spillover effect", which was observed at high operating temperatures (thermally activated event, >200 °C).[49] In the case of RT conditions, the electronic sensitization is a dominant factor, which can greatly influence the electrical transport through the conduction channel. Because of higher work function of Au ($q\phi_{Au}$ = 5.1 eV) compared to electron affinity of ZnO ($q\chi_{ZnO}$ = 4.5 eV), the electrons will flow from ZnO to Au NPs,[50−52] which results in the formation of a Schottky barrier at the Au NP/ZnO NW interface and a depletion region (L_{air}), as indicated in Figure 8a. Das et al. calculated the barrier height of 0.40−0.42 eV for the Au/ZnO Schottky diode based on individual NW, using the temperature-dependent current−voltage measurement and XPS study.[53] The energy band diagram of the Au/ZnO interface is presented in Figure S10 (see Figure 8a).[13,19,22,48] As a result, the Schottky barrier formation leads to an essential size decrease of the conduction channel (d_{air}) (see Figure 8a).[13,19,22,48]

Under exposure to H_2 gas, the hydrogen molecules are oxidized by the adsorbed oxygen species as follow[15,54]

$$H_2 + \frac{1}{2}O_{2\,(ad)}^{-} \rightarrow H_2O + \frac{1}{2}e^{-} \quad (3)$$

The electrons released after these surface reactions will contribute to the narrowing of the electron depletion region or a widening of the conduction channel (see Figure 8b). Because of the exothermic nature of the reaction (1.8 kcal mol^{-1}), the water molecules desorb quickly from the surface.[54] In the studied case with Au-NP/ZnO-NWs, the modulation of the conduction channel diameter could be larger, which will lead to a greater change in current flowing through the conduction channel and in a higher gas response (see Figure 8b).[13,15] Therefore, the formation of nanoscale Schottky barriers is an efficient step to highly improve the detection properties of individual nanostructures such as NWs. In this respect, works on AuNP/ZnO nanorod structures by Shingange et al.[55] and Hosseini et al.[56] demonstrate that a narrow size distribution of Au-NPs with diameters ranging between 5 and 15 nm and a uniform surface coverage yields the highest response at RT to H_2 or H_2S gas. Kim et al. used the same strategy, that is, the surface functionalization of ZnO NWs but with the Pt and Pd NPs for the detection of toluene and benzene using the self-heating mode.[50] Also, the electron-beam irradiation was used in the case of Pd-loaded ZnO nanofibers in order to decrease the work function of ZnO and to increase the value of barrier height between Pd and ZnO, resulting in higher gas response to hydrogen gas.[51]

Figure 9a shows the behavior of the measured gas response to 100 ppm of H_2 gas for individual Au-NP/ZnO-NWs, integrated in nanosensors, versus the ratio of the Schottky contact area formed by Au NPs on the ZnO to the uncovered ZnO surface. This ratio is further called the "Au NP surface coverage" and is determined from SEM images. The coverage was calculated by $(S_{NP} \times 100\%)/S_{NW}$, where S_{NP} is the Schottky contact area formed by Au-NPs (calculated as πr^2, with r the radius of the Au-NP approximated as half-spheres) on the top surface of the ZnO NW, and S_{NW} is the surface of the zinc oxide NWs (calculated as $2\pi rh$, where h and r are the length and radius of the NW). The gas response was investigated at RT under 1 V applied bias voltage, in order to reduce the self-heating effect.[15] All chosen NWs possess diameters of 120 ± 10 nm in order to study only the effects of the Schottky contact area. As expected, the gas response to hydrogen gas increased with the percentage of the Au-covering surface. The number of Au-NPs follows the same tendency as the gas response, demonstrating that the surface coverage of

DOI: 10.1021/acsami.9b08598
ACS Appl. Mater. Interfaces 2019, 11, 32115−32126

ACS Applied Materials & Interfaces Research Article

the Au-NPs is an essential factor in order to achieve a higher gas response. Further, the H_2 gas response for individual Au-NP/ZnO-NWs with ~0.0, ~1.1, ~2.2, ~4.0, and ~6.4% Au-NPs coverage is 1.2, 2.4, 4.2, 6.8 and 7.5, respectively. The gas response at RT to different vapors of volatile organic compounds (VOCs, concentration of 100 ppm) is presented in Figure S11b,c. As it is shown, the gas response to VOC vapors such as acetone, ethanol, *n*-butanol, 2-propanol, and methanol is lower than 1.1, demonstrating the high selectivity of Au-NP/ZnO-NWs to hydrogen gas at RT. This high selectivity of H_2 is also characteristic for unmodified ZnO NWs,[15,54] therefore, no change in the selectivity of individual NWs was observed with addition of Au-NPs, but a considerable increase in the gas response was induced (by a factor of 6.25). To conclude, it is believed that an even larger increase in the gas response to hydrogen gas could be achieved by a larger surface coverage density of smaller Au-NPs and a narrower size distribution, regarding this and previous studies.

Figure 9b shows the gas response of one individual Au-NP/ZnO-NW (0.9 μM $HAuCl_4$ and ~6.4% Au-NPs coverage) to various concentrations of H_2 gas (in the range of 20−500 ppm). The gas response value to 20, 50, 100, and 200 ppm is 2.25, 3.7, 7.5, and 10.6, respectively. Under exposure to relatively higher concentrations of 500 ppm, a rapid increase in the current value can be observed. A second short pulse of 500 ppm of H_2 gas was applied, and the same effect was observed (see Figure 9b). Figure 9c presents the gas response to 1000 and 5000 ppm of H_2 gas, which is ~329 and ~470, respectively. One can see from Figure 9b that the stabilization of the current during exposure to hydrogen gas is slow, as well as the recovery, resulting in a "saw-tooth"-like response which indicates a slow saturation rate and may be assigned to the charge accumulation and quite slow recovery rate of a NW which operates at RT.[57] The increase and further decrease in current after introducing into the test chamber with higher concentrations of hydrogen gas (>500 ppm, see Figure 9c) can be attributed to the competition of two main mechanisms involved in the gas-sensing process, namely the surface metallization (which will be further discussed in detail) and the adsorption/desorption of the gas species on the surface of the sensor.[57] Therefore, the individual Au-NPs/ZnO NW needs time to get a stabilized response after exposure to relatively low or high concentrations of H_2 gas.

The dependence of the gas response to the concentration of H_2 gas is presented in Figure 9d. The error bars represent the deviation through the three measurements in the gas-sensing experiments of the same sensors. In the gas concentration region of 20−200 ppm, the gas response is according to a power law relationship: $S \propto p_{H_2}^{\beta}$, where $\beta = 0.72$ is the slope of the dependence curve.[58,59] In the case of gas concentrations higher than 500 ppm, a considerable increase in the response can be observed. The theoretical detection limit of ~1 ppm was estimated using the ratio signal/(noise)^2, as was published by Dua et al.[29]

Such a sharp increase in the response for gas concentrations higher than 500 ppm (pink region) can be explained using the semiconductor-to-metal transition of the zinc oxide NW surface, which takes place in the presence of hydrogen gas molecules.[60] The same effect was also observed for ultrathin CuO NWs,[61] ZnO nanofibers,[62,63] and ZnO−SnO_2 composite nanofibers.[64] In the presence of hydrogen, the surface of ZnO will take on a metallic character. This is due to the fact that the 4*s* orbital of Zn in ZnO is occupied by one electron ($4s^1$), and when hydrogen gas adsorbs on the surface, this orbital becomes fully occupied ($4s^2$), causing a metallization of the ZnO on the surface.[60,65,66] As shown in the results, in the presence of H_2 gas the hydrogen molecules will adsorb on the top surface of the ZnO NW ($H_{2(ad)} \rightarrow 2H^+ + 2e^-$), and the region with surface depletion of ZnO (resulting from the adsorption of oxygen molecules) will be narrowed and a thin metallic Zn (ϕ_{Zn} = 4.3 eV) layer will be formed (Zn ($4s^1$) + e^- → Zn ($4s^2$), see Figure 10a,b).[60] This process will drastically

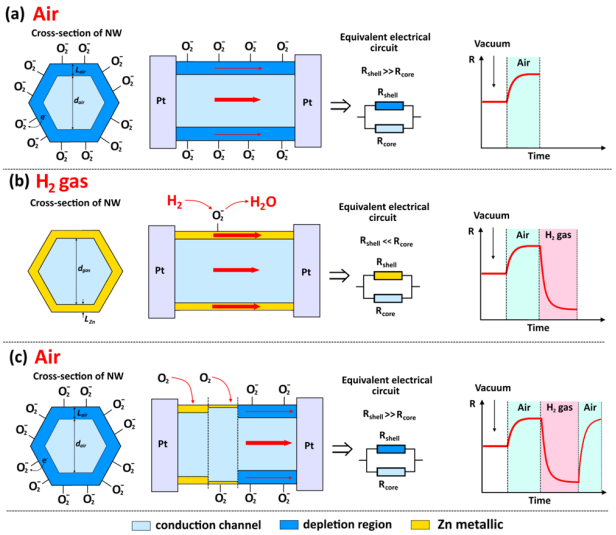

Figure 10. Tentatively proposed gas-sensing mechanism involving surface metallization for an individual ZnO NW: (a) under exposure in ambient air; (b) under exposure in H_2 gas with surface metallization; and (c) under exposure in ambient air with oxidation of metallic Zn and formation of a surface depletion region.

lower the resistance between the Pt contacts, leading to a considerable increase in current of the device (which was observed in Figure 8b). When the hydrogen gas is evacuated from the test chamber, the metallic Zn layer will be converted back to ZnO $\left(\frac{1}{2}O_{2(g)} + Zn_{(s)} \rightarrow ZnO_{(s)}\right)$, returning the current value to its original baseline (see Figure 10c).[60]

However, it is necessary to point out that surface metallization occurs at relatively high temperatures because of the necessity of high energy for the reduction of metal oxides.[62−64] In our case, the gas sensing is performed at RT by applying a bias voltage of 1 V to reduce the self-heating influence. However, the Joule heating of an individual Au-NPs/ZnO-NW integrated into the device is inevitable due to a high increase in current of the device at testing to high concentrations of hydrogen gas (see Figure 9b). Thus, we believe that the locally generated high temperature at testing to high concentrations of hydrogen gas is responsible for the surface metallization of the NW.[67]

Table S4 demonstrates the results of hydrogen gas sensing of single structures of metal oxides and other materials from literature to compare with the current results. One can see that our observations are better than many of the reported data. Another important factor are the fast response and recovery (~10 s) at exposure to high concentrations of H_2 gas (5000 ppm), which is attributed to the semiconductor-to-metal surface transition process under H_2 and leads to an enhanced

DOI: 10.1021/acsami.9b08598
ACS Appl. Mater. Interfaces 2019, 11, 32115−32126

ACS Applied Materials & Interfaces Research Article

hydrogen response at concentrations higher than 500 ppm. This allows for its use in the fabrication of rapid detectors for hydrogen gas leakages. Because of its ease of fabrication and its various applications, the use of liquid/gaseous H_2 has been extended in various fields such as petroleum transformation, hydrogenation processes, soldering, cryogenic cooling, or chemical substances production.[68] Under normal atmospheric conditions, gaseous H_2 leakage in air can lead to a hazardous atmosphere easily ignited for H_2 concentrations between 4% (lower explosive limit) and 74.5% (upper explosive limit)—at RT and pressure.[68,69] Thus, the fast detection of hydrogen leakage is very important for safety purposes and is one of the major safety concerns in different fields because of the small ignition energy of only 0.02 mJ and large velocity of flame propagation.[70]

4. CONCLUSIONS

In this work, the one-step electrochemical deposition of Au-NP-modified ZnO nanowire arrays is reported. The optical, structural, and chemical studies were realized in detail, demonstrating high crystallinity of the NW arrays, and that doping of the NWs with Au does not occur according to these results. The growth of Au NPs, with diameters varying from 10 to >100 nm on the top surface of the ZnO NWs, was observed with TEM. Individual Au-NP/ZnO-NWs were integrated into sensor devices showing promising hydrogen gas sensing properties, that is, a high gas response of ∼7.5 to 100 ppm at RT and an excellent selectivity against selected alcohols and ketones. It was observed that a higher gas response can be achieved by using the individual Au-NP/ZnO-NWs with a larger coverage of Au NPs on the surface (in the case of NPs the gas response is ∼7.5). At high concentrations of H_2 gas, a great increase in the gas response was observed, which could be due to surface metallization of the ZnO NW, resulting in ultra-high responses of 329 and 470 for 1000 and 5000 ppm of H_2. Such devices are ideal candidates for detection of hydrogen gas leakages with very-low power consumption and the possibility of RT operation. DFT computations realized on Au-doped ZnO bulk and surface-functionalized models help and validate the model proposed based on the experimental findings.

■ ASSOCIATED CONTENT

Supporting Information

The Supporting Information is available free of charge on the ACS Publications website at DOI: 10.1021/acsami.9b08598.

First voltammetry cycles measured on the FTO glass substrate in the zinc oxide electrodeposition liquids with different $HAuCl_4$ concentrations, SEM images of Au-modified ZnO NW arrays grown using different concentrations of $HAuCl_4$ in electrolyte solution, SEM images at higher magnification of Au-modified ZnO NW arrays grown using 0.3 μM of $HAuCl_4$ in electrolyte solution in order to show the presence of NPs on the surface of the NWs, side view of the unit cell of doped ZnO wurtzite from computational studies, computed structures of the bands, total, and orbital-projected density of states for ZnO and Au-doped ZnO bulk systems, computed structures of the bands, entire, and projected density for states of pure ZnO (10−10) and Au_n/ZnO (10−10) with n ranging from 1 to 8, schematic illustration of the connection of the individual Au-NPs/ZnO NW into the device, gas response of individual ZnO NWs (without Au NPs on the surface) with a diameter of 120 ± 10 nm versus the concentration of $HAuCl_4$ used for the growth of NWs, computed lattice parameters (a, b, and c in Å and α, β, and γ in degrees), computed adsorption energies per Au atom (E_{ads}, in eV), electronic band gaps (E_{gap}^{α} and E_{gap}^{β}, in eV), and top of VB energies (E_{VB}^{α} and E_{VB}^{β}, in eV), along with charge transfer from the Au_n clusters to ZnO (Δq, in lel) for the pure ZnO (10−10) surface and the different Au_n/ZnO (10−10) systems considered, and summary of the hydrogen gas sensors based on a single structure of semiconductor oxides and other materials (PDF)

■ AUTHOR INFORMATION

Corresponding Authors

*E-mail: ollu@tf.uni-kiel.de, oleg.lupan@mib.utm.md (O.L.).
*E-mail: ilaria.ciofini@chimieparistech.psl.eu (I.C.).
*E-mail: ra@tf.uni-kiel.de (R.A.).
*E-mail: thierry.pauporte@chimieparistech.psl.eu (T.P.).

ORCID

Oleg Lupan: 0000-0002-7913-9712
Oleksandr Polonskyi: 0000-0001-5013-0944
Franz Faupel: 0000-0003-3367-1655

Notes

The authors declare no competing financial interest.

■ ACKNOWLEDGMENTS

Dr. Lupan gratefully acknowledges PSL Universite, Chimie-ParisTech for the invited professor position and CNRS Council for constant support as expert researcher at Chimie ParisTech IRCP, Paris, France. This investigation was partially financially supported by the German Research Foundation (DFG—Deutsche Forschungsgemeinschaft) under the schemes SFB1261 and FOR2093. Dr. Lupan acknowledges the Alexander von Humboldt Foundation for the research fellowship for experienced researchers 3-3MOL/1148833 STP at the Institute for Materials Science, Kiel University, Germany. This research was partly supported by the Technical University of Moldova. I.C., F.L. and J.S. would like to thank the HPC resources of TGCC made possible by GENCI (Grand Equipement National de Calcul Intensif) within the project A0050810135. Katrin Brandenburg is acknowledged for her help in the proof-reading of the manuscript. J.S. gratefully acknowledges the China Scholarship Council (grant number 201706150081) for PhD funding.

■ REFERENCES

(1) Franklin, A. D. Nanomaterials in Transistors: From High-Performance to Thin-Film Applications. *Science* **2015**, *349*, aab2750.
(2) Mishra, Y. K.; Adelung, R. ZnO Tetrapod Materials for Functional Applications. *Mater. Today* **2018**, *21*, 631−651.
(3) Li, P.; Wei, Z.; Wu, T.; Peng, Q.; Li, Y. Au−ZnO Hybrid Nanopyramids and Their Photocatalytic Properties. *J. Am. Chem. Soc.* **2011**, *133*, 5660−5663.
(4) Özgür, Ü.; Alivov, Y. I.; Liu, C.; Teke, A.; Reshchikov, M. A.; Doğan, S.; Avrutin, V.; Cho, S.-J.; Morkoç, H. A Comprehensive Review of ZnO Materials and Devices. *J. Appl. Phys.* **2005**, *98*, 041301.
(5) Katoch, A.; Kim, J.-H.; Kim, S. S. TiO_2/ZnO Inner/Outer Double-Layer Hollow Fibers for Improved Detection of Reducing Gases. *ACS Appl. Mater. Interfaces* **2014**, *6*, 21494−21499.

DOI: 10.1021/acsami.9b08598
ACS Appl. Mater. Interfaces 2019, 11, 32115−32126

(6) Katoch, A.; Kim, J.-H.; Kwon, Y. J.; Kim, H. W.; Kim, S. S. Bifunctional Sensing Mechanism of SnO_2−ZnO Composite Nanofibers for Drastically Enhancing the Sensing Behavior in H_2 Gas. *ACS Appl. Mater. Interfaces* **2015**, *7*, 11351−11358.
(7) Choi, S.-W.; Katoch, A.; Sun, G.-J.; Kim, J.-H.; Kim, S.-H.; Kim, S. S. Dual Functional Sensing Mechanism in SnO_2−ZnO Core−Shell Nanowires. *ACS Appl. Mater. Interfaces* **2014**, *6*, 8281−8287.
(8) Wang, Z. L. Zinc Oxide Nanostructures: Growth, Properties and Applications. *J. Phys.: Condens. Matter* **2004**, *16*, R829.
(9) Pearton, S. J.; Norton, D. P.; Ip, K.; Heo, Y. W.; Steiner, T. Recent Advances in Processing of ZnO. *J. Vac. Sci. Technol., B* **2004**, *22*, 932−948.
(10) Huang, M. H.; Mao, S.; Feick, H.; Yan, H.; Wu, Y.; Kind, H.; Weber, E.; Russo, R.; Yang, P. Room-Temperature Ultraviolet Nanowire Nanolasers. *Science* **2001**, *292*, 1897.
(11) Li, Q. H.; Wan, Q.; Liang, Y. X.; Wang, T. H. Electronic Transport Through Individual ZnO Nanowires. *Appl. Phys. Lett.* **2004**, *84*, 4556−4558.
(12) Li, Q. H.; Liang, Y. X.; Wan, Q.; Wang, T. H. Oxygen Sensing Characteristics of Individual ZnO Nanowire Transistors. *Appl. Phys. Lett.* **2004**, *85*, 6389−6391.
(13) Kolmakov, A.; Klenov, D. O.; Lilach, Y.; Stemmer, S.; Moskovits, M. Enhanced Gas Sensing by Individual SnO_2 Nanowires and Nanobelts Functionalized with Pd Catalyst Particles. *Nano Lett.* **2005**, *5*, 667−673.
(14) Lupan, O.; Postica, V.; Adelung, R.; Labat, F.; Ciofini, I.; Schürmann, U.; Kienle, L.; Chow, L.; Viana, B.; Pauporté, T. Functionalized Pd/ZnO Nanowires for Nanosensors. *Phys. Status Solidi RRL* **2017**, *12*, 1700321.
(15) Lupan, O.; Cretu, V.; Postica, V.; Ahmadi, M.; Roldan Cuenya, B.; Chow, L.; Tiginyanu, I.; Viana, B.; Pauporté, T.; Adelung, R. Silver-Doped Zinc Oxide Single Nanowire Multifunctional Nanosensor with a Significant Enhancement in Response. *Sens. Actuators, B* **2016**, *223*, 893−903.
(16) Lupan, O.; Postica, V.; Gröttrup, J.; Mishra, A. K.; de Leeuw, N. H.; Adelung, R. Enhanced UV and Ethanol Vapour Sensing of a Single 3-D ZnO Tetrapod Alloyed with Fe_2O_3 Nanoparticles. *Sens. Actuators, B* **2017**, *245*, 448−461.
(17) Kuang, Q.; Lao, C.-S.; Li, Z.; Liu, Y.-Z.; Xie, Z.-X.; Zheng, L.-S.; Wang, Z. L. Enhancing the Photon- and Gas-Sensing Properties of a Single SnO_2 Nanowire Based Nanodevice by Nanoparticle Surface Functionalization. *J. Phys. Chem. C* **2008**, *112*, 11539−11544.
(18) Hu, Y.; Zhou, J.; Yeh, P.-H.; Li, Z.; Wei, T.-Y.; Wang, Z. L. Supersensitive, Fast-Response Nanowire Sensors by Using Schottky Contacts. *Adv. Mater.* **2010**, *22*, 3327−3332.
(19) Gogurla, N.; Sinha, A. K.; Santra, S.; Manna, S.; Ray, S. K. Multifunctional Au-ZnO Plasmonic Nanostructures for Enhanced UV Photodetector and Room Temperature NO Sensing Devices. *Sci. Rep.* **2014**, *4*, 6483.
(20) Guo, J.; Zhang, J.; Zhu, M.; Ju, D.; Xu, H.; Cao, B. High-Performance Gas Sensor Based on ZnO Nanowires Functionalized by Au Nanoparticles. *Sens. Actuators, B* **2014**, *199*, 339−345.
(21) Liu, K.; Sakurai, M.; Liao, M.; Aono, M. Giant Improvement of the Performance of ZnO Nanowire Photodetectors by Au Nanoparticles. *J. Phys. Chem. C* **2010**, *114*, 19835−19839.
(22) Zheng, Z. Q.; Wang, B.; Yao, J. D.; Yang, G. W. Light-Controlled C_2H_2 Gas Sensing Based on Au-ZnO Nanowires with Plasmon-Enhanced Sensitivity at Room Temperature. *J. Mater. Chem. C* **2015**, *3*, 7067−7074.
(23) Pauporté, T.; Lupan, O.; Zhang, J.; Tugsuz, T.; Ciofini, I.; Labat, F.; Viana, B. Low-Temperature Preparation of Ag-Doped ZnO Nanowire Arrays, DFT Study, and Application to Light-Emitting Diode. *ACS Appl. Mater. Interfaces* **2015**, *7*, 11871−11880.
(24) Lupan, O.; Pauporté, T.; Chow, L.; Viana, B.; Pellé, F.; Ono, L. K.; Roldan Cuenya, B.; Heinrich, H. Effects of Annealing on Properties of ZnO Thin Films Prepared by Electrochemical Deposition in Chloride Medium. *Appl. Surf. Sci.* **2010**, *256*, 1895−1907.
(25) Lupan, O.; Pauporté, T. Hydrothermal Treatment for the Marked Structural and Optical Quality Improvement of ZnO Nanowire Arrays Deposited on Lightweight Flexible Substrates. *J. Cryst. Growth* **2010**, *312*, 2454−2458.
(26) Pauporté, T.; Bataille, G.; Joulaud, L.; Vermersch, F. J. Well-Aligned ZnO Nanowire Arrays Prepared by Seed-Layer-Free Electrodeposition and Their Cassie−Wenzel Transition after Hydrophobization. *J. Phys. Chem. C* **2010**, *114*, 194−202.
(27) Lupan, O.; Chai, G.; Chow, L. Fabrication of ZnO Nanorod-Based Hydrogen Gas Nanosensor. *Microelectron. J.* **2007**, *38*, 1211−1216.
(28) Lupan, O.; Postica, V.; Mecklenburg, M.; Schulte, K.; Mishra, Y. K.; Fiedler, B.; Adelung, R. Low Powered, Tunable and Ultra-Light Aerographite Sensor for Climate Relevant Gas Monitoring. *J. Mater. Chem. A* **2016**, *4*, 16723−16730.
(29) Dua, V.; Surwade, S. P.; Ammu, S.; Agnihotra, S. R.; Jain, S.; Roberts, K. E.; Park, S.; Ruoff, R. S.; Manohar, S. K. All-Organic Vapor Sensor Using Inkjet-Printed Reduced Graphene Oxide. *Angew. Chem., Int. Ed.* **2010**, *49*, 2154−2157.
(30) Argoubi, W.; Saadaoui, M.; Ben Aoun, S.; Raouafi, N. Optimized Design of a Nanostructured SPCE-Based Multipurpose Biosensing Platform Formed by Ferrocene-Tethered Electrochemically-Deposited Cauliflower-Shaped Gold Nanoparticles. *Beilstein J. Nanotechnol.* **2015**, *6*, 1840−1852.
(31) Song, Y.; Ma, Y.; Wang, Y.; Di, J.; Tu, Y. Electrochemical Deposition of Gold−Platinum Alloy Nanoparticles on an Indium Tin Oxide Electrode and Their Electrocatalytic Applications. *Electrochim. Acta* **2010**, *55*, 4909−4914.
(32) Liang, J. K.; Su, H. L.; Kuo, C. L.; Kao, S. P.; Cui, J. W.; Wu, Y. C.; Huang, J. C. A. Structural, Optical and Electrical Properties of Electrodeposited Sb-Doped ZnO Nanorod Arrays. *Electrochim. Acta* **2014**, *125*, 124−132.
(33) Wang, F.; Seo, J.-H.; Li, Z.; Kvit, A. V.; Ma, Z.; Wang, X. Cl-Doped ZnO Nanowires with Metallic Conductivity and Their Application for High-Performance Photoelectrochemical Electrodes. *ACS Appl. Mater. Interfaces* **2014**, *6*, 1288−1293.
(34) Wijnhoven, J. E. G. J.; Zevenhuizen, S. J. M.; Hendriks, M. A.; Vanmaekelbergh, D.; Kelly, J. J.; Vos, W. L. Electrochemical Assembly of Ordered Macropores in Gold. *Adv. Mater.* **2000**, *12*, 888−890.
(35) Sahu, D.; Panda, N. R.; Acharya, B. S.; Panda, A. K. Enhanced UV Absorbance and Photoluminescence Properties of Ultrasound Assisted Synthesized Gold Doped ZnO Nanorods. *Opt. Mater.* **2014**, *36*, 1402−1407.
(36) Lee, E.-C.; Chang, K. J. Possible p-Type Doping with Group-I Elements in ZnO. *Phys. Rev. B: Condens. Matter Mater. Phys.* **2004**, *70*, 115210.
(37) Morris, M. C.; McMurdie, H. F.; Evans, E. H.; Paretzkin, B.; Degrbot, J. H. Standard X-ray Diffraction Powder Patterns: Section 13-Data for 58 Substances. *Interim Report National Bureau of Standards*; Institute for Materials Research: Washington, DC, 1976.
(38) Johnson, C. L.; Snoeck, E.; Ezcurdia, M.; Rodríguez-González, B.; Pastoriza-Santos, I.; Liz-Marzán, L. M.; Hÿtch, M. J. Effects of Elastic Anisotropy on Strain Distributions in Decahedral Gold Nanoparticles. *Nat. Mater.* **2007**, *7*, 120.
(39) Greczynski, G.; Hultman, L. C 1s Peak of Adventitious Carbon Aligns to the Vacuum Level: Dire Consequences for Material's Bonding Assignment by Photoelectron Spectroscopy. *ChemPhysChem* **2017**, *18*, 1507−1512.
(40) Tian, Y.; Tatsuma, T. Mechanisms and Applications of Plasmon-Induced Charge Separation at TiO_2 Films Loaded with Gold Nanoparticles. *J. Am. Chem. Soc.* **2005**, *127*, 7632−7637.
(41) Moulder, J. F.; Chastain, J. *Handbook of X-ray Photoelectron Spectroscopy: A Reference Book of Standard Spectra for Identification and Interpretation of XPS Data*; Physical Electronics Division, Perkin-Elmer Corporation, 1992.
(42) Lupan, O.; Chow, L.; Ono, L. K.; Cuenya, B. R.; Chai, G.; Khallaf, H.; Park, S.; Schulte, A. Synthesis and Characterization of Ag- or Sb-Doped ZnO Nanorods by a Facile Hydrothermal Route. *J. Phys. Chem. C* **2010**, *114*, 12401−12408.

DOI: 10.1021/acsami.9b08598
ACS Appl. Mater. Interfaces 2019, 11, 32115−32126

(43) Ahn, M.-W.; Park, K.-S.; Heo, J.-H.; Park, J.-G.; Kim, D.-W.; Choi, K. J.; Lee, J.-H.; Hong, S.-H. Gas Sensing Properties of Defect-Controlled ZnO-Nanowire Gas Sensor. *Appl. Phys. Lett.* **2008**, *93*, 263103.
(44) Li, L. M.; Du, Z. F.; Wang, T. H. Enhanced Sensing Properties of Defect-Controlled ZnO Nanotetrapods Arising from Aluminum Doping. *Sens. Actuators, B* **2010**, *147*, 165−169.
(45) Wang, X.; Kong, X.; Yu, Y.; Zhang, H. Synthesis and Characterization of Water-Soluble and Bifunctional ZnO−Au Nanocomposites. *J. Phys. Chem. C* **2007**, *111*, 3836−3841.
(46) Jiang, Z.-Y.; Zhao, Z.-Y. Density Functional Theory Study on the Metal−Support Interaction Between a Au_9 Cluster and an Anatase TiO_2(001) Surface. *Phys. Chem. Chem. Phys.* **2017**, *19*, 22069−22077.
(47) Lupan, O.; Postica, V.; Marx, J.; Mecklenburg, M.; Mishra, Y. K.; Schulte, K.; Fiedler, B.; Adelung, R. Individual Hollow and Mesoporous Aero-Graphitic Microtube Based Devices for Gas Sensing Applications. *Appl. Phys. Lett.* **2017**, *110*, 263109.
(48) Yamazoe, N. New Approaches for Improving Semiconductor Gas Sensors. *Sens. Actuators, B* **1991**, *5*, 7−19.
(49) Chang, C.-M.; Hon, M.-H.; Leu, I.-C. Outstanding H_2 Sensing Performance of Pd Nanoparticle-Decorated ZnO Nanorod Arrays and the Temperature-Dependent Sensing Mechanisms. *ACS Appl. Mater. Interfaces* **2013**, *5*, 135−143.
(50) Kim, J.-H.; Lee, J.-H.; Park, Y.; Kim, J.-Y.; Mirzaei, A.; Kim, H. W.; Kim, S. S. Toluene- and benzene-selective gas sensors based on Pt- and Pd-functionalized ZnO nanowires in self-heating mode. *Sens. Actuators, B* **2019**, *294*, 78−88.
(51) Kim, J.-H.; Mirzaei, A.; Woo Kim, H.; Kim, S. S. Combination of Pd loading and electron beam irradiation for superior hydrogen sensing of electrospun ZnO nanofibers. *Sens. Actuators, B* **2019**, *284*, 628−637.
(52) Park, W. I.; Yi, G.-C.; Kim, J.-W.; Park, S.-M. Schottky nanocontacts on ZnO nanorod arrays. *Appl. Phys. Lett.* **2003**, *82*, 4358−4360.
(53) Das, S. N.; Choi, J.-H.; Kar, J. P.; Moon, K.-J.; Lee, T. I.; Myoung, J.-M. Junction properties of Au/ZnO single nanowire Schottky diode. *Appl. Phys. Lett.* **2010**, *96*, 092111.
(54) Lupan, O.; Chow, L.; Pauporté, T.; Ono, L. K.; Roldan Cuenya, B.; Chai, G. Highly Sensitive and Selective Hydrogen Single-Nanowire Nanosensor. *Sens. Actuators, B* **2012**, *173*, 772−780.
(55) Shingange, K.; Tshabalala, Z. P.; Ntwaeaborwa, O. M.; Motaung, D. E.; Mhlongo, G. H. Highly Selective NH_3 Gas Sensor Based on Au Loaded ZnO Nanostructures Prepared Using Microwave-Assisted MethodHighly selective NH 3 gas sensor based on Au loaded ZnO nanostructures prepared using microwave-assisted method. *J. Colloid Interface Sci.* **2016**, *479*, 127−138.
(56) Hosseini, Z. S.; Mortezaali, A.; Iraji zad, A.; Fardindoost, S. Sensitive and Selective Room Temperature H_2S Gas Sensor based on Au Sensitized Vertical ZnO Nanorods with Flower-Like Structures. *J. Alloys Compd.* **2015**, *628*, 222−229.
(57) Chan, N. Y.; Zhao, M.; Huang, J.; Au, K.; Wong, M. H.; Yao, H. M.; Lu, W.; Chen, Y.; Ong, C. W.; Chan, H. L. W.; Dai, J. Highly Sensitive Gas Sensor by the $LaAlO_3/SrTiO_3$ Heterostructure with Pd Nanoparticle Surface Modulation. *Adv. Mater.* **2014**, *26*, 5962−5968.
(58) Volanti, D. P.; Felix, A. A.; Orlandi, M. O.; Whitfield, G.; Yang, D.-J.; Longo, E.; Tuller, H. L.; Varela, J. A. The Role of Hierarchical Morphologies in the Superior Gas Sensing Performance of CuO-Based Chemiresistors. *Adv. Funct. Mater.* **2013**, *23*, 1759−1766.
(59) Choi, Y.-H.; Kim, D.-H.; Hong, S.-H.; Hong, K. S. H_2 and C_2H_5OH Sensing Characteristics of Mesoporous p-Type CuO Films Prepared via a Novel Precursor-Based Ink Solution Route. *Sens. Actuators, B* **2013**, *178*, 395−403.
(60) Katoch, A.; Choi, S.-W.; Kim, H. W.; Kim, S. S. Highly Sensitive and Selective H_2 Sensing by ZnO Nanofibers and the Underlying Sensing Mechanism. *J. Hazard. Mater.* **2015**, *286*, 229−235.
(61) Lupan, O.; Postica, V.; Ababii, N.; Hoppe, M.; Cretu, V.; Tiginyanu, I.; Sontea, V.; Pauporté, T.; Viana, B.; Adelung, R. Influence of CuO Nanostructures Morphology on Hydrogen Gas Sensing Performances. *Microelectron. Eng.* **2016**, *164*, 63−70.
(62) Kim, J.-H.; Mirzaei, A.; Woo Kim, H.; Wu, P.; Kim, S. S. Design of Supersensitive and Selective ZnO-Nanofiber-Based Sensors for H_2 Gas Sensing by Electron-Beam Irradiation. *Sens. Actuators, B* **2019**, *293*, 210−223.
(63) Abideen, Z. U.; Kim, H. W.; Kim, S. S. An Ultra-Sensitive Hydrogen Gas Sensor Using Reduced Graphene Oxide-Loaded ZnO Nanofibers. *Chem. Commun.* **2015**, *51*, 15418−15421.
(64) Katoch, A.; Abideen, Z. U.; Kim, H. W.; Kim, S. S. Grain-Size-Tuned Highly H_2-Selective Chemiresistive Sensors Based on ZnO−SnO_2 Composite Nanofibers. *ACS Appl. Mater. Interfaces* **2016**, *8*, 2486−2494.
(65) Xu, H.; Fan, W.; Rosa, A. L.; Zhang, R. Q.; Frauenheim, T. Hydrogen and Oxygen Adsorption on ZnO Nanowires: A First-Principles Study. *Phys. Rev. B: Condens. Matter Mater. Phys.* **2009**, *79*, 073402.
(66) Wang, Y.; Meyer, B.; Yin, X.; Kunat, M.; Langenberg, D.; Traeger, F.; Birkner, A.; Wöll, C. Hydrogen Induced Metallicity on the ZnO {10-10} Surface. *Phys. Rev. Lett.* **2005**, *95*, 266104.
(67) Prades, J. D.; Jimenez-Diaz, R.; Hernandez-Ramirez, F.; Barth, S.; Cirera, A.; Romano-Rodriguez, A.; Mathur, S.; Morante, J. R. Ultralow Power Consumption Gas Sensors Based on Self-Heated Individual Nanowires. *Appl. Phys. Lett.* **2008**, *93*, 123110.
(68) Bévenot, X.; Trouillet, A.; Veillas, C.; Gagnaire, H.; Clément, M. Hydrogen Leak Detection Using an Optical Fibre Sensor for Aerospace Applications. *Sens. Actuators, B* **2000**, *67*, 57−67.
(69) Okazaki, S.; Nakagawa, H.; Asakura, S.; Tomiuchi, Y.; Tsuji, N.; Murayama, H.; Washiya, M. Sensing Characteristics of an Optical Fiber Sensor for Hydrogen Leak. *Sens. Actuators, B* **2003**, *93*, 142−147.
(70) Sumida, S.; Okazaki, S.; Asakura, S.; Nakagawa, H.; Murayama, H.; Hasegawa, T. Distributed Hydrogen Determination with Fiber-Optic Sensor. *Sens. Actuators, B* **2005**, *108*, 508−514.

DOI: 10.1021/acsami.9b08598
ACS Appl. Mater. Interfaces 2019, 11, 32115−32126

5.2 Acetone Detection

Diabetes mellitus (DM) is a chronic metabolic disorder resulting from insulin deficiency and affects about 1/11 (463 million) adults (20-79 years) of the human population according to the 2019 diabetes atlas of the international diabetes-federation (IDF).[297] The report further forecasts an increase in positive diagnosis up to 700 million by the year 2045 and yet further assumes a large estimated number of unreported cases in the hundred millions of undiagnosed indisposition in adults. The metabolic disorder is accompanied with elevated amounts of sugar and ketone bodies such as acetone in the blood, which is easy to measure. Hence, all current therapies for diabetes are based on glucose-control. Acetone is derived from oxidation of non-esterified fatty acids during the ketone metabolism and leaves the human body through the blood, urine, sweat and exhaled breath. In this way, despite by conventional and reliable blood analysis, monitoring acetone species in breath offers huge potential. The correlation of the breath acetone concentration with the blood-sugar concentration[298] turn breath acetone into an important and qualitatively known biomarker for diagnostics and monitoring of DM. Therefore, the analysis of diabetic-breath acetone concentration offers a cheap, comfortable, non-invasive and portable alternative for daily quantitative monitoring of blood-sugar levels which conventionally requires the use of blood tests by punctuation or is monitored by implantable glucose sensors.[299] Breath acetone levels in healthy people are subject to variations $\leqslant 1\,\mathrm{ppm}$ and are elevated to around 2 ppm in diabetic patients[300] setting the benchmark for the sensitivity of the kind of measurement technique.

In this respect established but expensive and stationary techniques such as gas chromatography, solid-phase microextraction or mass spectrometry techniques all provide highly selective and sensitive analysis of VOCs.[301] Chemoresistive sensors of semiconducting metal oxides which change their resistance upon exposure to certain molecules interacting on its surface are promising for the development of non-invasive and portable monitoring devices of the diabetic condition in everyday use at home. In this respect, a variety of MOx materials have been investigated concerning their sensor characteristics with respect to acetone detection as summarized in Table 5.2. For instance, very low detection limits in the low ppb regime could be achieved by stabilization of the ferroelectric $\varepsilon - WO_3$ phase by co-doping with Cr[302] or Si[303] to clearly distinguish between acetone levels in the breath of healthy or diabetic patients by a difference of about 40% in gas response. However, investigations at large relative humidity (RH) which is a relevant factor for human breath investigations demonstrated a significant decrease of the sensor response by 68% in humid environment. In this respect, reports on SnO_2 NWs coated with carbon nanotubes (CNT) demonstrated a RH dependent decrease of the response by a factor of 4.6 at 85 % RH.[304]
To overcome these limitations moisture resistant acetone breath sensors based on $Pt@In_2O_3$ core-shell NWs coated with a molecular sieve of mesoporous silica (SBA-15) were developed. The introduced coating demonstrated the stability of the gas response over the full range of relative humidity and proved its application by the clear separation of test patients into groups of healthy people and people with diabetes by their breath acetone level within seconds.[305]

The Fe_2O_3/Fe_3O_4 networks and single Fe_2O_3 NW structures presented in the attached

study[292][3] demonstrated a very high gas response of 125 for the network and 14.6 to a standard of 100 ppm at operating temperature of 250 °C and RT, respectively. HRTEM and ED studies were capable to identify both iron oxide phases present in the grown NW networks and the spike geometry of the Fe_2O_3 NW structures was described by tilting experiments. Further, structural peculiarities related to a symmetry reduction which is commonly observed in nanostructures of hematite phase Fe_2O_3 are identified and described also within the second attached study. In there, Fe_2O_3 NW networks have been fabricated together with CuO NW in a novel 3D-printing process.[306][4] Chemical characterization was performed using EELS and EFTEM methods and the structure of CuO NWs was observed showing polysynthetic twinning and structural intergrowth. The response to acetone gas was analyzed to be relatively small only showing an increase of 50% in response to 100 ppm and 14% to 1 ppm, but demonstrated the application to concentrations as low as 0.5 ppm suitable for sensor devices which can be printed on flexible substrates to be integrated into wearable electronics.

[3]Reprinted with permission from small 2017, 13, 1602868 published by © 2017 WILEY-VCH Verlag GmbH Co. KGaA, Weinheim

[4]Reprinted with permission from Nanoenergy 2020, 70, 104420 published by ©2020 Elsevier

TABLE 5.2: Sensor characteristics by exposure to acetone vapor.

Material	**Gas Response**	**Concentration / ppm**	$T_{opt}/^{\circ}C$	$\tau_r\|\tau_d$ / **s**	**Detection Limit / ppb**	**Relative Humidity**
$Cr:\varepsilon-WO_3$ [302]	0.5	2.0	400	<10|-	200	0%
$Si:\varepsilon-WO_3$ [303]	4.63	0.6	400	340|354	20	0%
$Si:\varepsilon-WO_3$ [303]	<2 |>3.2	<0.9 | >1.8	400	78|84	20	90%
$CNT:SnO_2$ NWs [304]	550	2.5	200	120|780	500	0%
$CNT:SnO_2$ NWs [304]	120	2.5	200	-|-	500	85%
$Pt@In_2O_3(+SBA-15)$ NWs [305]	2.5 | 6.2	<0.9 | >1.8	320	14|16	10	0-100%
ZnO nanorods [307]	30	100	300	5|15	1000	0%
Fe_2O_3 NW network [292]*	125	100	250	8|7	250	30%
Fe_2O_3 single NW (D = 25 nm) [292]*	14.6	100	RT	16|50	20	30%
CuO/Fe_2O_3 network [306]*	1.5	100	300	14|>50	500	30%
CuO/Fe_2O_3 network [306]*	1.14	1	300	11|10	500	30%

* Publication with Co-Authorship

Localized Synthesis of Iron Oxide Nanowires and Fabrication of High Performance Nanosensors Based on a Single Fe_2O_3 Nanowire

Oleg Lupan, Vasile Postica, Niklas Wolff, Oleksandr Polonskyi, Viola Duppel, Victor Kaidas, Eugen Lazari, Nicolai Ababii, Franz Faupel,* Lorenz Kienle,* and Rainer Adelung**

A *composed morphology of iron oxide microstructures covered with very thin nanowires (NWs) with diameter of 15–50 nm has been presented. By oxidizing metallic Fe microparticles at 255 °C for 12 and 24 h, dense iron oxide NW networks bridging prepatterned Au/Cr pads are obtained. X-ray photoelectron spectroscopy studies reveal formation of α-Fe_2O_3 and Fe_3O_4 on the surface and it is confirmed by detailed high-resolution transmission electron microscopy and selected area electron diffraction (SAED) investigations that NWs are single phase α-Fe_2O_3 and some domains of single phase Fe_3O_4. Localized synthesis of such nano- and microparticles directly on sensor platform/structure at 255 °C for 24 h and reoxidation at 650 °C for 0.2–2 h, yield in highly performance and reliable detection of acetone vapor with fast response and recovery times. First nanosensors on a single α-Fe_2O_3 nanowire are fabricated and studied showing excellent performances and an increase in acetone response by decrease of their diameter was developed. The facile technological approach enables this nanomaterial as candidate for a range of applications in the field of nanoelectronics such as nanosensors and biomedicine devices, especially for breath analysis in the treatment of diabetes patients.*

Prof. O. Lupan, N. Wolff, Dr. O. Polonskyi, V. Kaidas, Prof. F. Faupel, Prof. L. Kienle, Prof. R. Adelung
Faculty of Engineering
Institute for Materials Science
Christian-Albrechts Universität zu Kiel
Kiel University
Kaiserstr. 2, D-24143 Kiel, Germany
E-mail: ollu@tf.uni-kiel.de, oleg.lupan@mib.utm.md; ff@tf.uni-kiel.de; lk@tf.uni-kiel.de; ra@tf.uni-kiel.de
Prof. O. Lupan, V. Postica, E. Lazari, N. Ababii
Department of Microelectronics and Biomedical Engineering
Technical University of Moldova
168 Stefan cel Mare Av., MD-2004 Chisinau, Republic of Moldova
V. Duppel
Max Planck Institute for Solid State Research
Heisenbergstrasse 1, D-70569 Stuttgart, Germany

DOI: 10.1002/smll.201602868

1. Introduction

Due to high stability under ambient conditions[1–3] and high catalytic activity in the dehydrogenation reaction and the ring-opening reaction of hydrocarbon,[4] α-Fe_2O_3 (hematite) nanostructures have been studied more extensively as sensing material for gas sensor applications[5,6] than other Fe oxides, such as Fe_3O_4 (magnetite) and FeO (wustite). Fe_3O_4 is known to be a very low-cost and nontoxic transition metal oxide[7,8] which has been widely used as anode material for lithium-ion batteries due to high electronic conductivity,[8,9] for controlled drug delivery and biomedical imaging applications due to biocompatibility and superparamagnetic properties,[2,10] cathode catalyst for fuel cells,[11] etc. However, it was less studied as gas sensing material,[12] especially as α-Fe_2O_3 and Fe_3O_4 mixed phases or heterostructures.[13]

On the other hand, the use of nanowire (NW) networks as sensing materials is a very efficient way to improve the gas sensing capabilities of the sensors, which have been demonstrated for SnO_2 NWs,[14] CuO NWs,[15,16] ZnO NWs,[17,18] and ZnO tetrapods,[19] as well as for a single NW.[18] NWs of metal oxides are perfect candidates for superior gas sensing, due to specific mechanisms which strongly depend on the very high porosity and surface-to-volume ratio of the nanomaterials.[15,16,20] Inspired by these promising results in the field of sensing devices, our group has focused on the exploration of gas sensing properties for another important metal oxide nanomaterial, namely, iron oxide in order to fabricate sensors highly selective to volatile organic compounds (VOCs).[21] Acetone being a highly inflammable VOC is widely used in industry, i.e., in medicine as biomarker for diabetes,[22] biomedical, and cosmetic applications.[23] When it is exposed to the air, it very quickly evaporates and can produce explosions and flash fire. Thus, it is very important to rapidly detect the acetone vapors, especially in industry and also in house environment. It is important to mention that many of the commonly used household products can contain acetone. However, a device structure based on iron oxide NW networks and the possibility of the locally synthesized sensing material, exhibiting superior properties were not communicated to date. Also, it is well known that the main advantage of gas sensors based on individual nanostructures of metal oxides is the possibility of efficient detection of gaseous species at room temperature.[16,18,24,25] However, the very few works are reported on gas sensing properties of individual Fe_2O_3 nanostructures,[26] while on acetone vapor sensing we did not find any report. Thus, from fundamental point of view and taking into account the rapid progress of nanotechnologies, it is very important to investigate the gas sensing properties of single nanostructures of Fe_2O_3, especially with very thin diameter.

In this paper, we report on the properties of iron oxide nanowire networks grown by an oxidation process in ambient air at relatively low temperature (255 °C), using metallic Fe microparticles as a starting material. By a previously reported method,[16] the Fe metal microparticles can be placed directly onto the substrate with prepatterned Au electrodes by drop casting and further exposure to controlled oxidation processes in air. Thus, minimal numbers of technological steps to locally fabricate a final device structure based on oxidized Fe microparticles covered with iron oxide NWs are necessary, which will definitely decrease its final cost. Such a novel composed morphology avoids agglomeration of nanostructures leading to high porosity of the samples and better device operation. A subsequent reoxidation process resulted in the higher performance sensing characteristics for selective and highly sensitive detection of acetone vapor at an operating temperature of 250 °C with high stability, repeatability, and full recovery to the initial baseline. The very high porosity and surface-to-volume ratio of the sensing material lead to fast diffusion and oxidation of analyte gas, resulting in excellent rapidity with minimum response time of the sensor. The single NWs of Fe_2O_3 with different diameters down to ≈25 nm were integrated into devices resulting in the highly efficient acetone nanosensors with high response and rapidity, capable to work at room temperature. Also, the size-dependent gas sensing properties were investigated.

2. Results and Discussions

2.1. Morphological Studies of Iron Oxide Networks

Figure 1 shows scanning electron microscope (SEM) images of Fe microparticles oxidized in ambient air at 255 °C during 6 h (a) and 12 h (b), as well as, for 24 h at lower and higher magnifications (c,d). The heating rate was fixed at 40 °C min^{-1} in our experiments.[16] The longest time of oxidation leads to highest density of NWs on the surface of microparticles and agglomeration of Fe microparticles (see Figure S1a–d,

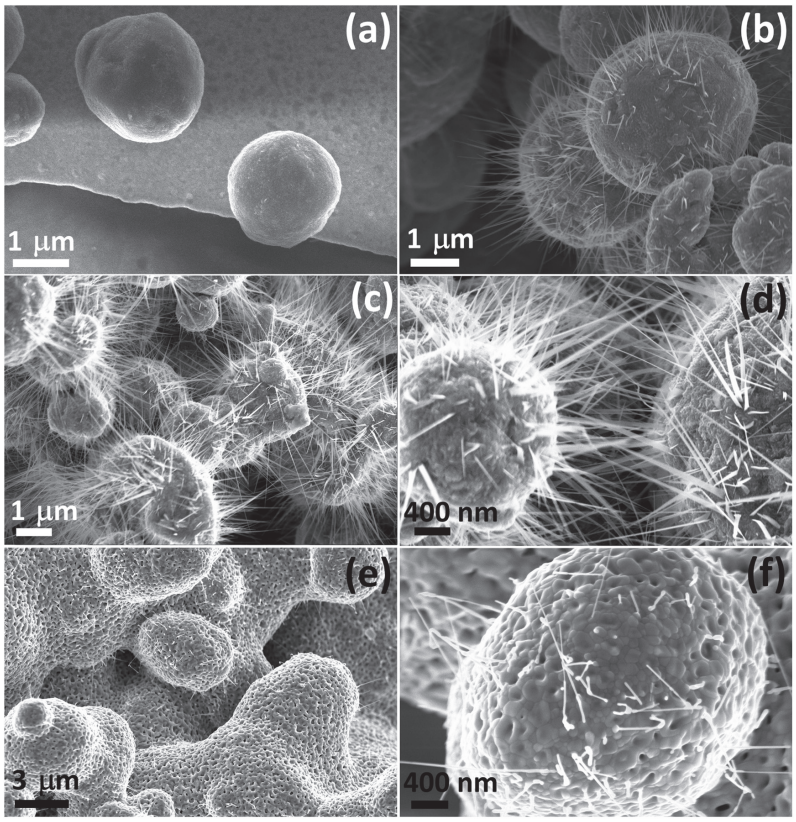

Figure 1. SEM images of Fe microparticles oxidized in ambient air at 255 °C for a) 6 h; b) 12 h; and c,d) 24 h at higher and lower magnifications for demonstration of nanowires interconnection. SEM images of reoxidized microparticles (initially annealed at 255 °C for 24 h) at 650 °C for 2 h at e) lower and f) higher magnification, respectively.

Supporting Information). In case of 6 h duration of oxidation, no growth of NWs on the entire surface was observed (see Figure 1a), while for 12 and 24 h of oxidation (see Figure 1b–d) an increasing density of the NWs was obtained. The diameters of the NWs of 15–50 nm are related for both sets of samples, however, the length of synthesized NWs is up to about 3 and 10 μm for 12 and 24 h of annealing, respectively. The lengths (L) of the NWs are dependent on the synthesis duration (t) of the oxidation process by the following relation $L = At^{0.5-x}$, where the power is close to 0.5 indicating that the growth rate is controlled by the diffusive supply of iron.[27] A reoxidation process was also performed to investigate the properties of NW networks for annealing at higher temperatures of 650 °C for 0.2–2 h. Experimental results are presented in Figure 1e,g and Figure S1e–h (Supporting Information), which clearly demonstrate an essential reduction in density of NWs on the surface of microparticles and coalescence between microparticles. Figure S1a,h (Supporting Information) shows the essential differences of oxidized and reoxidized microparticles more clearly. Additionally, the formation of nanopores can be observed (with diameters in the range of 30–100 nm, see Figure S1e–h, Supporting Information) on the surface of reoxidized at 650 °C and interconnected microparticles. By contrast, samples oxidized at 255 °C for 12 and 24 h, just show nanograins on the surface of the microparticles (Figure S1d, Supporting Information). In conclusion, a highly porous iron oxide layer is formed, which is very important/interesting for gas sensing applications and fundamental studies, too. However, the optimal technological conditions for annealing to yield the more dense iron oxide NW networks were 24 h at 255 °C in air.[16]

2.2. Structural and Chemical Properties of Iron Oxide Nanowires

The growth of α-Fe_2O_3 NWs by oxidation of Fe metal has been explained by relaxation of comprehensive stress generated at the α-Fe_2O_3/Fe_3O_4 interface.[3] Nanopores, as discussed above, are formed only during a reoxidation process (at 650 °C for 2 h) of oxidized Fe microparticles in air. From the significant change of volume due to the formation of oxide stress is generated, especially at the FeO/Fe interface, which is consistent with other results.[3] To confirm the presence of three phases of iron oxide, namely, Fe_2O_3, Fe_3O_4, and FeO, X-ray difffraction (XRD), X-ray photoelectron spectroscopy (XPS), and transmission electron microscopy (TEM) measurements were performed. The structure of oxidized Fe microparticles was first investigated by XRD measurements. For oxidized Fe microparticles at 255 °C (6, 12, and 24 h) some of the diffraction patterns can be assigned to metallic Fe in addition to peaks of iron oxide (not shown), originating from unoxidized Fe microparticles remained at the middle or bottom of the deposited layer, leading to lower resistance of the device structure (in order of 100 Ω, see Figure S2, Supporting Information). Thus, such structures demonstrated no essential gas response and were excluded for further gas sensing studies. However, the reoxidizing process at 650 °C during 20–120 min completely oxidizes the Fe microparticles (Figures S2 and S3, Supporting Information) and results in gradual reduction of the NW density (Figure 1; Figure S1, Supporting Information).

Survey XPS spectra (see Figure S4, Supporting Information) of the oxidized iron microparticles are dominated by the presence of Fe, O, and C peaks. The presence of carbon (C-1s signal at 285 eV) is due to exposure of samples in ambient air before investigations and is the result of surface contamination. A high resolution XPS spectrum of Fe-2p peak of the sample oxidized at 255 °C in 24 h and then reoxidized at 650 °C in air is represented in **Figure 2**a. Two distinct peaks can be observed, at binding energies (BE) of 711.2 eV for Fe-$2p_{3/2}$ and 724.8 eV for Fe-$2p_{1/2}$ with spin–orbit split energy difference of around 13.6 eV, which is characteristic for α-Fe_2O_3 structures.[28] The respective corresponding shake-up satellites located at around 719.0 and 733.0 eV (indicated by arrows in Figure 2a) support the presence of α-Fe_2O_3 compounds in the film.[29,30] However, in TEM, high-resolution TEM (HRTEM), and XRD investigations, Fe_3O_4 and FeO phases were also detected beside α-Fe_2O_3 phase. Thus, in order to make the situation about structural properties more clear, the Fe-$2p_{3/2}$ peak was deconvoluted into three peaks to

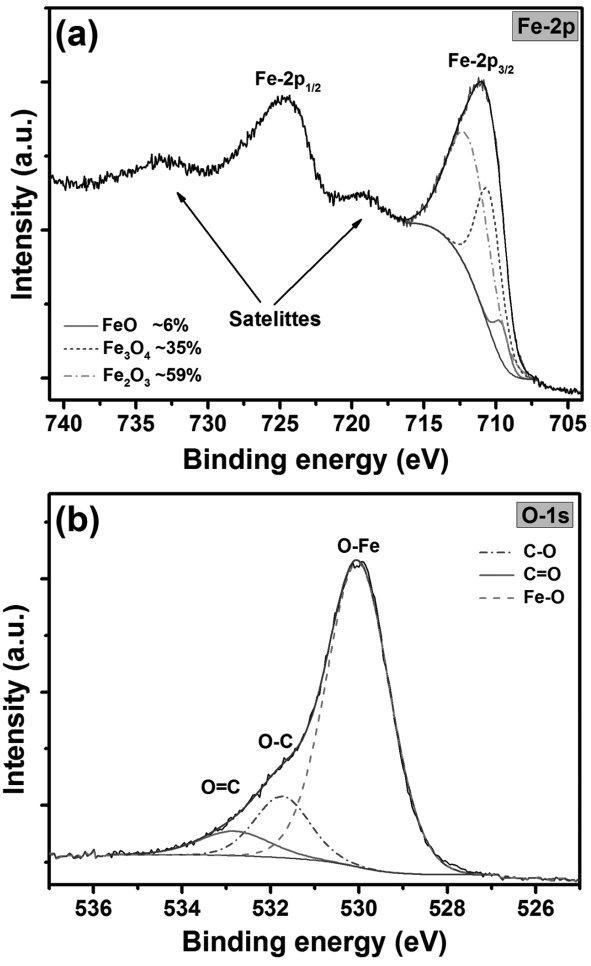

Figure 2. a) Fe-2p and b) O-1s XPS spectra of Fe microparticles oxidized in ambient air at 255 °C for 24 h and then reoxidized at 650 °C.

obtain the iron oxides ratio for the analyzed sample.[29,30] The deconvoluted components were assigned to FeO (709.6 eV), Fe_3O_4 (710,5 eV), and α-Fe_2O_3 (711.9 eV) iron oxide phases, respectively (see Figure 2a).[3,29,31] Resulted iron oxides ratio in oxidized sample is 6% FeO/35% Fe_3O_4/59% Fe_2O_3. As one can see, the lowest amount of the iron oxide phase is for FeO, what can be also indirectly approved by absence of a strong respective satellite normally located at around 715.5 eV (for Fe-$2p_{3/2}$ peak).[32] The very low amount or absence at all of the FeO phase was also confirmed by other techniques (XRD and TEM). The respective O-1s high resolution peak of the same sample, what is typical for α-Fe_2O_3 and Fe_3O_4, is presented in Figure 2b. This asymmetric peak is fitted by three components in Figure 2. The main BE peak is situated at around 530.0 eV, and corresponds to the formation of Fe−O bonds on the sample surface.[3,33] Other peaks at 531.61 and 533.21 eV were attributed to chemisorbed and dissociated oxygen species or OH and also to carbon contamination of the surface.[3,29,30,33]

Two apparent morphologies and iron oxide phases could be examined via TEM on NWs from samples oxidized at 255 °C (see **Figure 3**): (1) single crystalline NWs showing a discontinuous contrast perpendicular to their longitudinal axis (Figure 3a) and (2) polycrystalline wires with crystal sizes in the range of 5–10 nm at their tips (Figure 3c). Common features of iron oxide nanostructures are twin defects along the growth direction.[34] Since such defects were not apparently visible, the morphology of the single crystalline NWs was analyzed via high angle tilting experiments in the range from –60° to +60° (see Figure S6, Supporting Information).

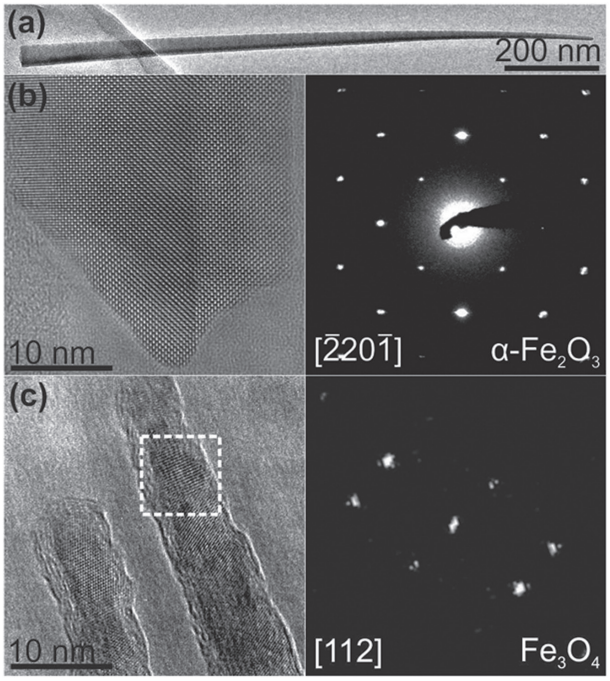

Figure 3. a) TEM bright field image exemplifying the morphology of single crystalline α-Fe_2O_3 nanowires. b) HRTEM image and corresponding SAED pattern of the tip of a hematite type wire like the one shown in a). c) Tips of polycrystalline magnetite phase nanowires with FFT.

No apparent planar defects could be observed for any wire under investigation. However, the morphology of the respective nanowire can be described as a razorblade structure with a very thin cross-section of <10 nm and a thicker part in the range of 10–20 nm. Otherwise, from Figure 3a and HRTEM images a nearly flat triangle could be assumed for cross-sectional geometry. Such nanostructures are of high interest for fundamental studies too.

To obtain information about their crystal structure, HRTEM and electron diffraction (ED) studies on both types of morphologies were conducted. The polycrystalline NWs, which are less frequently observed, could be assigned to the Fe_3O_4 phase according to fast Fourier transformed (FFT) images. By performing deliberate tilting series into different zone axis orientations and recording SAED patterns, the single crystalline NWs could be attributed to a modified α-Fe_2O_3 structure. However, discrepancies between the experimental and calculated (kinematic approximation) ED patterns of the hematite structure were identified, see Figure S7 (Supporting Information). These deviations can be grouped into two sets of reflections occurring in addition to those expected for the hematite structure. Note that multiple scattering phenomena for the production of these anomalies can be excluded via precession electron diffraction (PED) analyses (cf. the Experimental Section) which show these additional intensities strongly excited. The first set of reflections (h-h0l, l = 2*n* + 1, 000l, l = 3*n*) (Figure S7a, Supporting Information) which we observed here for the zones [2-1-10] and [10-31] could be explained by a reduction in symmetry from the trigonal space group of hematite (*R*-3, details of crystallographic anomalies are beyond the scope of this paper and will be presented elsewhere[35]). The second set of reflections (Figure S7b, Supporting Information) we encountered more frequently, e.g., for the zones [40-41], [10-10], [4-1-31], and [42-6-1]. Such reflections were already observed in a diffraction study on twinned bladelike platelets[36] and reconfirmed in our group. These reflections are explainable as intersection points of elongated relrods (in consequence of planar defects) and the Ewald sphere.[37]

2.3. Gas Sensing Properties of Iron Oxide Nanowire Networks

As mentioned above, only reoxidized iron oxide samples were selected for gas sensing measurements. All response curves demonstrated a typical bell shape form (**Figure 4**a) and the optimal operating temperature for ethanol vapor, ammonia (NH_3) vapor, and hydrogen (H_2) gas is 300 °C, while for acetone vapor it is 250 °C, with high gas response $S_{acetone} \approx 125$. At the same operating temperature the other gas responses are 24, 18.8, and 2.9 for ethanol vapor, NH_3 vapor, and H_2 gas, respectively (see Figure 4b). Thus, resulted selectivity factors for acetone at 250 °C are $S_{acetone}/S_{EtOH} \approx 5.2$, $S_{acetone}/S_{NH3} \approx 6.7$, $S_{acetone}/S_{H2} \approx 32$, hence our samples were showing quite good selectivity to acetone vapors in the performed experiments.

Figure 4c shows the dynamic gas response to 5–100 ppm of acetone. As can be observed, the sensor showed stable sensing with good repeatability and complete recovery to

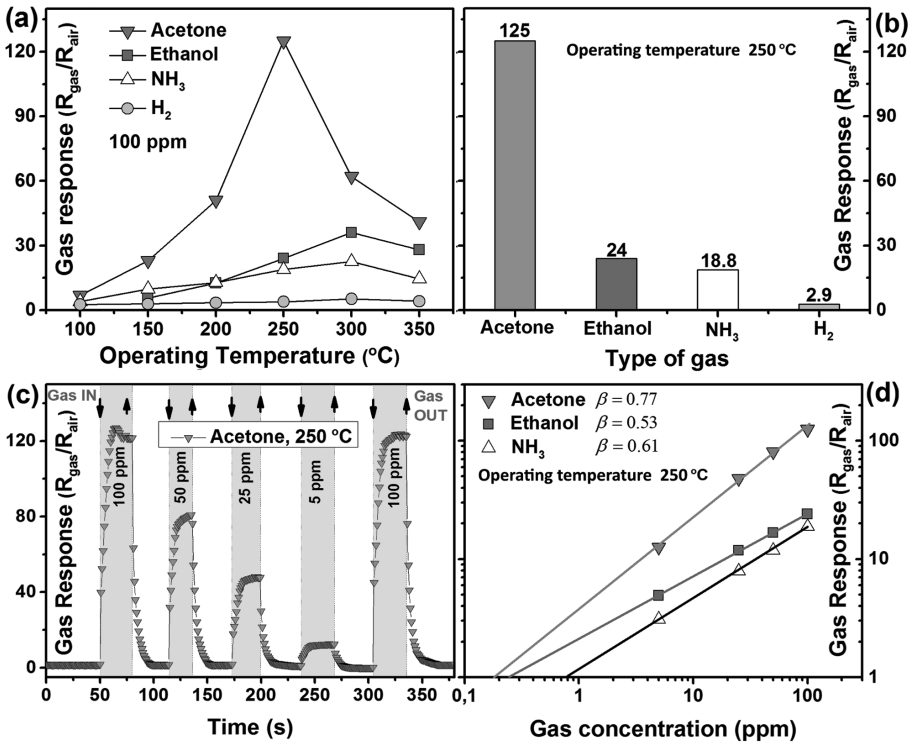

Figure 4. a) Gas response of iron oxide nano- and microstructures versus operating temperature for acetone vapor, ethanol vapor, NH_3 vapor, and H_2 gas (all 100 ppm). b) Gas response at 250 °C operating temperature of iron oxide nano- and microstructures versus analyte types. c) Dynamic response at 250 °C to 5–100 ppm acetone of iron oxide nano- and microstructures. d) Gas response versus concentration of tested gases.

the initial electrical baseline. The calculated gas response ($S_{acetone}$) is 13, 48, 81, and 125 for 5, 25, 50, and 100 ppm of acetone, respectively. The last 100 ppm pulse of acetone was applied to demonstrate excellent repeatability of the sensor structure. The response and recovery time (defined as necessary time to reach 90% variation in resistance of the maximal response to tested gas) of the sensor at operating temperature of 250 °C is about 8 and 7 s, respectively. Such relatively fast response of the sensors (see **Table 1**) can be attributed to the high porosity of the sensing material, which facilitates rapid diffusion and oxidation of analyte gas with adsorbed oxygen species on the iron oxide surface.[15,17,19,20] The recovery time of the sensors is the same quite fast, due to fast adsorption, dissociation, and ionization of oxygen species.[16,18–20] All tested sensor structures were fabricated in a similar way and demonstrated p-type gas response (increase in an electrical resistance value upon exposure to analyte reducing gas), and will be discussed later in the next section.

Figure 4d shows the gas response dependence on concentration of acetone, ethanol (EtOH), and NH_3 vapor, in order to calculate the lowest detection limit (LDL) of the sensor structures. Using $R_{gas}/R_{air} > 1.2$ criterion[45] the calculated LDL values are about 0.25, 0.33, and 0.95 ppm, for acetone, EtOH, and NH_3 vapor, respectively. A sub-ppm LDL value was demonstrated which is characteristic for sensing material with high surface-to-volume ratio and which is very important for specific gas sensing applications. Calculated slopes are also demonstrated in the inset of Figure 4d.

2.4. Nanosensors Based on a Single Fe_2O_3 Nanowire and Its Performances

To avoid the disadvantage of Fe_2O_3 NW networks, i.e., low resistance due to presence of metallic Fe, we fabricated several sets of nanodevices on a single nanostructure. Each nanosensor consists of a single Fe_2O_3 NW with varying diameters (from 20 to 50 nm), in order to investigate the influence of diameter on gas sensing properties. The technological procedure for fabrication of single NW nanosensors was reported by Lupan et al. in previous works.[16,18,24] Fe_2O_3 NWs were released from oxidized nanoparticles (see **Figure 5**a), followed by a transfer to a SiO_2/Si substrate with prepatterned Au/Cr electrodes for dispersion to a lower concentration (see Figure 5b) and integration into a device by Pt contacts nanodeposition of Pt contacts at both ends of the NW (see Figure 5c).[16,24] The current–voltage characteristic of fabricated devices based on a single NW with different diameters is presented in Figure S8 (Supporting Information), showing a formation of double Schottky contacts for all investigated devices. SEM images of nanosensors with different diameters are presented in Figure S9 (Supporting Information). It is important to mention that such nanostructures were integrated and studied individually in premiere in the current work and it opens a new field for fundamental and applicative studies of a single Fe_2O_3 nanowire.

Figure 5d shows the gas response at room temperature (RT ≈ 24 °C) to acetone versus diameter (D) of Fe_2O_3 NW.

Table 1. Summary of the acetone sensors based on iron oxide and other metal oxide nanostructures.

Morphology and properties of sensing material	Gas and conc. [ppm]	Type of response	Gas response (R_g/R_a)[a] or (R_a/R_g)[b]	Operating temp. [°C]	Response time [s]	Recovery time [s]
$ZnO/ZnFe_2O_4$[38]	Acetone, 100	n-type	16.8	250	1	33
$ZnFe_2O_4$ hollow microspheres[39]	Acetone, 20	n-type	11.3	200	14	407
Zn-doped γ-Fe_2O_3 nanopowders[6]	Acetone, 1000	n-type	45	270	5	34
Fe_3O_4/Fe_2O_3 NPs[13]	Acetone, 200	p-type	≈5.5[c]	500	–	–
α-Fe_2O_3 film[40]	Ethanol, 300	p-type	≈5[c]	300	–	–
Cu-doped WO_3 fibers[41]	Acetone, 20	n-type	≈7	300	5	20
Au/In_2O_3 inverse opal[42]	Acetone, 5	n-type	≈42	340	≈11	14
ZnO nanorod thin film[43]	Acetone, 50	n-type	≈15	300	5	15
Ni-doped SnO_2 nanofibers[44]	Acetone, 50	n-type	≈46	340	7	30
Fe_2O_3/Fe_3O_4 microparticle networks (this work)	Acetone, 100	p-type	69	250	9	8
Single Fe_2O_3 NW ($D \approx 25$ nm) (this work)	Acetone, 100	n-type	14.6	24 (RT)	16	50

[a]Gas response for p-type semiconducting oxides; [b]Gas response for n-type semiconducting oxides; [c]Denotes a value approximated from a graphical plot.

The typical increase in response by decrease of NW diameter can be observed.[24,46] Gas response increase from ≈2.6 to ≈14.6 by decrease D from ≈50 to ≈25 nm. The decrease in response by increase in D value can be explained as follows. As was mentioned, the gas response was defined as ratio of resistance in air and upon exposure to analyte reducing gas (R_{air}/R_{gas}). Taking into account that the resistance of surface electrons in the depleted region with width L_D is very high, these values can be defined as resistance of the conduction channel[47]

$$R_{air} = \frac{\rho L}{\pi r_{air}^2} = \frac{\rho L}{\pi\left(D/2 - L_{D(air)}\right)^2} \quad (1)$$

$$R_{gas} = \frac{\rho L}{\pi r_{gas}^2} = \frac{\rho L}{\pi\left(D/2 - L_{D(gas)}\right)^2} \quad (2)$$

where ρ is the Fe_2O_3 NW resistivity, L is the length of NW, r_{air} and r_{gas} is the radius of the conduction channel in the air and upon exposure to reducing gas, respectively. $L_{D(air)}$ and $L_{D(gas)}$ denote the extent of the surface electron depleted region in the air and upon exposure to reducing gas, respectively. Further, the gas response can be written as

$$S = \frac{R_{air}}{R_{gas}} = \left(\frac{D/2 - L_{D(gas)}}{D/2 - L_{D(air)}}\right)^2 \quad (3)$$

The $L_{D(air)}$ = 20 nm value was estimated (see Text S1, Supporting Information. Thus, the flat band situation is highly possible ($L_{D(air)} \rightarrow D/2$) for NWs with $D < 40$ nm.[18,47,48] Thus, for Fe_2O_3 NWs with $D < 40$ nm the R_{air} is very low, and by decrease of NW diameter the further reduction of R_{air} can be obtained, which leads to the increase in gas response.[16,18,47,48] Figure S8 (Supporting Information) depicts that current values upon exposure in air at room temperature increasing with larger NW diameter.

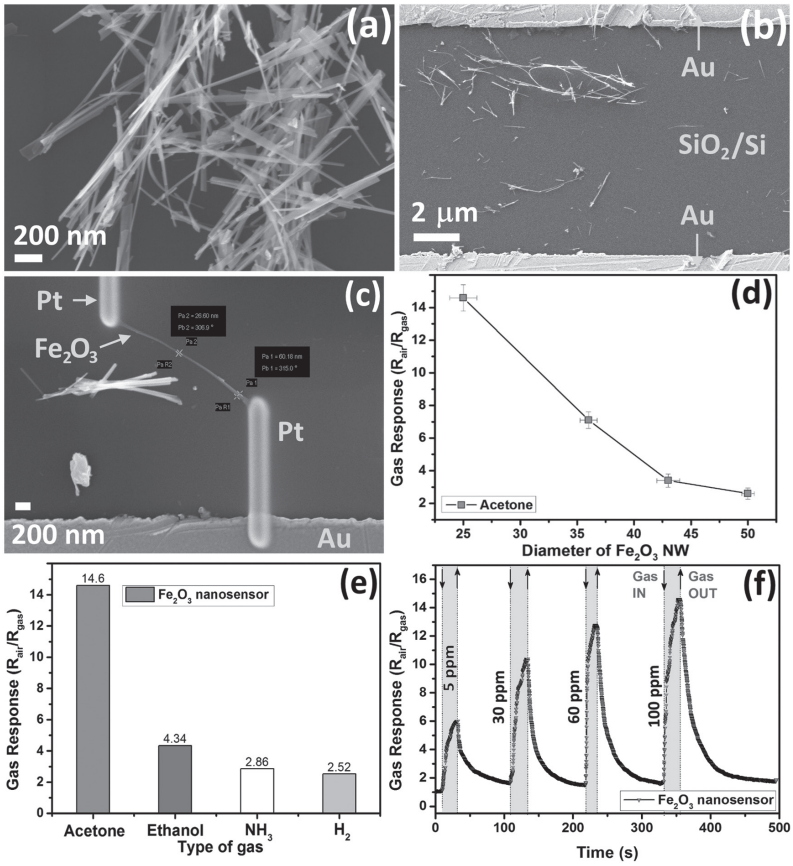

Figure 5. SEM images of the Fe_2O_3 nanowires after releasing from the initial substrate and a) transferred to an intermediate SiO_2/Si substrate; and b) dispersion to a lower concentration. c) SEM image of the fabricated nanosensor based on a single Fe_2O_3 nanowire with $D \approx 25$ nm. d) Gas response to 100 ppm acetone vapor versus diameter of Fe_2O_3 nanowire. e) Gas response for different reducing gases of nanosensor based on a single Fe_2O_3 nanowire with $D \approx 25$ nm. f) Dynamic response at room temperature to 1–100 ppm acetone vapor.

To investigate the selectivity of Fe_2O_3 NWs, the gas sensing measurements were also performed to other tested gases (see Figure 5e). Resulted selectivity factors for acetone at RT are $S_{acetone}/S_{EtOH} \approx 3.3$, $S_{acetone}/S_{NH3} \approx 5.1$, $S_{acetone}/S_{H2} \approx 5.8$, hence the fabricated nanosensors were showing quite good selectivity to acetone vapors in performed experiments as in the case of networks. Further, to investigate rapidity of nanosensors the dynamic response was evaluated. Figure 5e shows gas response upon exposure to different concentrations of acetone vapor (from 1 to 100 ppm). The calculated response and recovery times are 16 and 50 s, respectively. The LDL ≈ 0.02 ppm was calculated using the same procedure as for networks (Figure 4d). This value is lower than for networks and is comparable with some of the best results reported in literature.[49] The main reason can be higher surface-to-volume ratio of the single structure leading to improved influence of surface reactions onto properties of NW. [16,18,24,48]

A typical analogue-type gradual change in the resistance observed only for Fe-metal microparticles oxidized at 255 °C is presented in Figure S10a,b (Supporting Information) and is referred to memristive switching. More details are presented therein.

2.5. Gas Sensing Mechanism

α-Fe_2O_3 is known to be a *n*-type semiconductor with a band gap of 2.2 eV.[40] As was mentioned, the iron oxide networks demonstrated p-type gas response behavior, i.e., increase in an electrical resistance value upon exposure to analyte reducing gas (see Figure 4c), while single Fe_2O_3 NWs demonstrated n-type gas response behavior, i.e., decrease in an electrical resistance value upon exposure to analyte reducing gas (see Figure 5f). Such unusual p-type behavior of n-type α-Fe_2O_3 and half-metal Fe_3O_4 is a consequence of interesting electrical and conduction properties of iron oxides.[5,13,50] A similar new physical effect[13] can be explained by reduction of half-metallic conduction of Fe_3O_4 due to released electrons after oxidation of acetone molecules.[6,39] For example, Capone et al. observed that Fe_3O_4/γ-Fe_2O_3 nanoparticles with one monolayer showed *p*-type gas response and were attributed to an enhancement of half-metallic conduction.[13] Another explanation could be the inversion of α-Fe_2O_3 from *n*-type to *p*-type due to a strong adsorption of oxygen species which can produce *p*-type behavior,[40,50,51] this is more probable due to the very high surface-to-volume ratio and porosity of the samples. Gurlo et al. observed a *p*- to *n*-transition of α-Fe_2O_3 thick films induced by a change in the gas concentration and the operating temperature and was attributed to an inversion layer at the surface of the film.[52] Lee et al. also attributed *p*-type conductivity of α-Fe_2O_3 NW to strong surface adsorption owing to the oxygen vacancies and the high surface-to-volume ratio.[51] It is well known that at higher temperatures (between 150 and 400 °C) the molecular oxygen dissociates to atomic oxygen (see **Figure 6**a)[19,53,54]

$$O_2(\text{ads}) + e^- \leftrightarrow O_2^-(\text{ads}) \quad (4)$$

$$O_2^-(\text{ads}) \leftrightarrow 2O^-(\text{ads}) \quad (5)$$

Due to strong adsorption of oxygen species the surface energy band bending is enough to determine a *p*-type surface conductivity of oxidized microparticles (see Figure 6a), which was also demonstrated experimentally by Gurlo et al.[52] It is known that conduction in *p*-type semiconducting oxides occurs on surfaces of nanostructures, through the created hole accumulation layer (HAL, see Figure 6a).[20] Thus, the surface structure of microparticles and NWs, has main impact[16,20] while the internal structure is less significant. Hence, investigations in detail of the internal structure are not required for this study and will be fundamentally studied in our coming works.

During exposure to acetone vapors the following reaction takes place with releasing the electrons to the conduction band (see Figure 6b)[42]

$$CH_3COCH_3(g) + 8O^-(\text{ads}) \rightarrow 3CO_2 + 3H_2O + 8e^- \quad (6)$$

In results, the number of holes from surface HAL layer is reduced by electron-hole recombination leading to decrease in band bending and respective to the increase in resistance of surface layer due to lower number of holes (see Figure 6b).[55]

The *n*-type gas response single Fe_2O_3 NWs can be explained based on the absence of Fe_3O_4 phase and Fe_3O_4/Fe_2O_3 heterojunctions. Another factor is operation at different conditions, i.e., different adsorbed oxygen species are present on the NWs surface as result of operation at room temperature.[53] It is well known that in the temperature range from RT to ≈150 °C oxygen (O_2) is adsorbed onto surface of semiconducting oxides in its nondissociatively molecular form.[18,19,53]

This phenomena leads to a different reactivity of the oxide surface to analyte gas and different coverage with oxygen species.[18,19,53,54] Thus, it seems to be that at room temperature no inversion at the surface of Fe_2O_3 NW takes place.[40,51,52] Taking into account the formation of Schottky barriers (SB) at both ends of NW, such high response at room temperature can be explained based on modulation of SB height (ϕ_{SB}) by adsorption/desoprtion of gaseous species at the Schottky contact (see Figure 6c,d), which is known to be very sensitive to surface reactions.[56] Wei and co-workers demonstrated that an increase in ϕ_{SB} by adsorption of the oxygen at the Schottky contact area can lead to more than one order of magnitude of electrical current reduction.[56] The gas mechanism of devices based on Schottky contacts was reported in previous work in detail.[57] Thus, during exposure to ambient air, the ϕ_{SB} will increase ($\phi_{SB} + \Delta$, see Figure 6c) due to adsorption of oxygen species at the Schottky contact region (Equation (6)),[56] leading to considerable decrease in the current through the conduction channel. During exposure to acetone vapors, the adsorbed oxygen at the Schottky contact region is consumed by oxidation of acetone molecules and the SB height decreases ($\phi_{SB} + \Delta - \Delta'$, see Figure 6d), leading to the increase of current value through the conduction channel.[56]

Table 1 shows the gas sensing properties of sensors based on iron oxide and compared with other metal oxide nanostructures, in order to observe performances of the

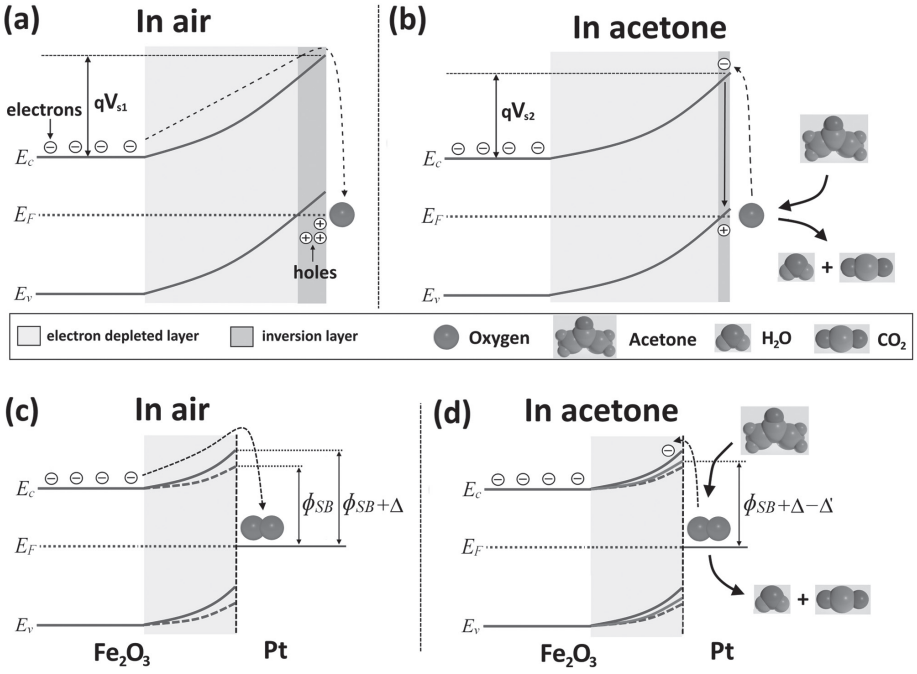

Figure 6. Schematic illustration of acetone sensing mechanism based on energy band diagrams for iron oxide nano- and microstructures. a) During exposure in air the oxygen atoms are adsorbed on the surface of iron oxide and extract electrons forming an electron depleted layer. By a strong adsorption the inversion layer can be formed at the surface, leading to p-type surface conduction. The height of the formed surface potential barrier is noted as qV_{s1}. b) During exposure in acetone vapors the acetone molecules are oxidized to H_2O and CO_2 molecules by releasing electrons to conduction band, which recombine with holes from the surface layer leading to narrowing of the inversion layer and decrease of the potential barrier (qV_{s2}). Schematic illustration of acetone sensing mechanism for devices based on a single Fe_2O_3 NW. c) During exposure in air the oxygen molecules are adsorbed at the Schottky contact region and extract electrons giving rise to Schottky barrier (SB) height $\phi_{SB} + \Delta$. b) During exposure in acetone vapors the SB height decreases due to oxygen molecule consumption $\phi_{SB} + \Delta - \Delta'$.

developed sensor structures with one which are the best results reported in literature. As can be observed, our sensor structures demonstrate a high gas response with excellent rapidity at operating temperature comparable to other results. The gas sensing properties of the nanosensor based on a single Fe_2O_3 NW is complicated to compare with other acetone sensors based on single structures due to absence of reports in literature.

3. Conclusion

Successful localized growth of iron oxide nanowire networks by thermal oxidation at relatively low temperature (255 °C) in air was demonstrated in premiere. Integration of single Fe_2O_3 NWs into nanodevices showed excellent acetone sensing properties at room temperature. Several nanodevices based on a single NW with different diameters, showing an increase in acetone response by decrease of diameter were investigated. The lowest diameter studied in this work was ≈25 nm showing the $R_{air}/R_{gas} \approx 24.6$ to 100 ppm of acetone and a very low detection limit of 20 ppb, indicating an excellent potential for sensitive and highly selective sensor applications based on nanosensors. The *p*-type behavior of *n*-type α-Fe_2O_3 and half-metal Fe_3O_4 can be a consequence of interesting/new electrical and conduction properties of mixed phases of iron oxides.

The fabrication method of iron oxide networks is facile and requires minimum technological steps, which can be extended to large-scale fabrication and simple device integration. The highest aspect ratio of the NWs was obtained for 24 h oxidation time at 255 °C, leading to growth of very thin NW with diameters in the range of 15–50 nm. Using Fe microparticles as initial source-material, highly porous networks were obtained. XPS results demonstrated the formation of three different iron oxide phases, namely, FeO, Fe_3O_4, and α-Fe_2O_3 on the surface of iron microparticles after thermal annealing in air at relatively low temperature. XPS reveal the majority formation of α-Fe_2O_3 on the surface and it was confirmed by detailed HRTEM studies that NWs are single phase α-Fe_2O_3. Integration of such nano- and microparticles in a sensor structure, yield high performance and reliable detection of acetone vapor with fast response and recovery times after reoxidizing process at 650 °C during 0.2–2 h. High repeatability and complete recovery of the resistance to its initial electrical baseline after exposure to analyte gas at operating temperature of 250 °C, demonstrated excellent potential for the fabrication of reliable and robust nano- and microsensors. Such an advanced material with high repeatability and complete recovery to the initial baseline can serve as potential candidate for the fabrication of efficient acetone sensors for biomedical applications, diabetes monitoring, and memristive devices. Considering that acetone is highly flammable and a very dangerous reagent, we consider that the

current work is a great step forward in the applicative field of nanoscience and nanoengineering.

4. Experimental Section

SEM, XRD, and XPS investigations were performed as reported previously.[15] Surface characterization of Fe-oxide samples was performed by XPS (Omicron Nanotechnology GmbH). The samples were measured after preparation and exposure to atmosphere. No additional surface cleaning under vacuum conditions was performed in this case. An X-ray source with Al anode operating at a power of 240 W was utilized. Spectra were recorded with pass energies of 100 eV (survey) and 30 eV (high-resolution spectra). All XPS spectra were charge-referenced to the aliphatic carbon at 285.0 eV. Detailed structural investigations in real and reciprocal space by TEM were performed on three microscopes: (1) A Philips CM 30 ST microscope (LaB_6 cathode, 300 kV) for HRTEM and ED studies, equipped with a spinning star device enabling precession (P)ED analysis. The PED patterns recorded on thin samples were known to suppress multiple scattering very well.[58] (2) An FEI Tecnai F30 G^2 STwin (FEG cathode, 300 kV) for HRTEM and (3) a JEOL JEM-2100 (LaB_6 cathode, 200 kV) equipped with a tomography holder for large angle tilting experiments. The specimens were prepared by scratching the nanostructures onto a lacey carbon/copper grid. Iron oxide NW networks were synthesized by an oxidation approach in ambient air of metallic Fe microparticles (99.99% from Aldrich) with diameter of 1–10 μm on a glass substrate with prepatterned Au/Cr (170 nm/10 nm) pads, for further structural and gas sensing measurements. The prepatterned substrate structure with external electrodes for electrical connections was presented in a previous work.[16] Discussion on the advantage of the synthesis method is presented in Table S1 (Supporting Information), and can be described by very low oxidation temperature, direct integration of sensing material onto substrate for electrical investigations, antiagglomeration properties of the NWs forming 3D interconnected structures, and independence of sophisticated and expensive vacuum systems.

The current–voltage characteristics of the iron oxide-based device structures were performed by a conventional two-point DC method. Iron oxide-based sensors were tested to four types of reducing gases/vapor, namely, EtOH, NH_3, and H_2 at operating temperatures in the range of 100–300 °C, with stepwise increase of 50 °C. More technological and technical details of the sensor structure fabrication have been reported by Lupan et al.[16] To obtain thermal stabilization, the sensor structure was placed in the test chamber at necessary operating temperature for 30 min prior to gas sensing measurements. The relative humidity (RH) was measured by a standard hygrometer and amounted to about 30% RH. All details on gas sensing experiments and other measurements are presented in our previous works.[20,56,59]

Supporting Information

Supporting Information is available from the Wiley Online Library or from the author.

Acknowledgements

This research was sponsored in part by the German Research Foundation (DFG) under the schemes FOR 2093 & PAK 902 (KI 1263/14-1 & AD 183/12-1). Prof. Lupan acknowledges the Alexander von Humboldt Foundation for the research fellowship for experienced researchers (3-3MOL/1148833 STP) at the Institute for Materials Science, University of Kiel, Germany. This research was in part supported by the Project Institutional (Project No. 45inst-15.817.02.29A) funded by the Government of the Republic of Moldova.

[1] a) J. Lian, K. Anggara, M. Lin, Y. Chan, *Small* **2014**, *10*, 667; b) G. Liu, J. Gao, H. Ai, X. Chen, *Small* **2013**, *9*, 1533.
[2] D. Ling, T. Hyeon, *Small* **2013**, *9*, 1450.
[3] L. Yuan, Y. Wang, R. Cai, Q. Jiang, J. Wang, B. Li, A. Sharma, G. Zhou, *Mater. Sci. Eng., B* **2012**, *177*, 327.
[4] A. Yu, J. Qian, H. Pan, Y. Cui, M. Xu, L. Tu, Q. Chai, X. Zhou, *Sens. Actuators, B* **2011**, *158*, 9.
[5] J. Chen, L. Xu, W. Li, X. Gou, *Adv. Mater.* **2005**, *17*, 582.
[6] Z. Jing, *Mater. Sci. Eng., A* **2006**, *441*, 176.
[7] S. M. Hussain, K. L. Hess, J. M. Gearhart, K. T. Geiss, J. J. Schlager, *Toxicol. In Vitro* **2005**, *19*, 975.
[8] P. L. Taberna, S. Mitra, P. Poizot, P. Simon, J. M. Tarascon, *Nat. Mater.* **2006**, *5*, 567.
[9] W.-M. Zhang, X.-L. Wu, J.-S. Hu, Y.-G. Guo, L.-J. Wan, *Adv. Funct. Mater.* **2008**, *18*, 3941.
[10] Y. Deng, D. Qi, C. Deng, X. Zhang, D. Zhao, *J. Am. Chem. Soc.* **2008**, *130*, 28.
[11] Z.-S. Wu, S. Yang, Y. Sun, K. Parvez, X. Feng, K. Müllen, *J. Am. Chem. Soc.* **2012**, *134*, 9082.
[12] Z. Ai, K. Deng, Q. Wan, L. Zhang, S. Lee, *J. Phys. Chem. C* **2010**, *114*, 6237.
[13] S. Capone, M. G. Manera, A. Taurino, P. Siciliano, R. Rella, S. Luby, M. Benkovicova, P. Siffalovic, E. Majkova, *Langmuir* **2014**, *30*, 1190.
[14] I. Paulowicz, V. Hrkac, S. Kaps, V. Cretu, O. Lupan, T. Braniste, V. Duppel, I. Tiginyanu, L. Kienle, R. Adelung, Y. K. Mishra, *Adv. Electron. Mater.* **2015**, *1*, 1500081.
[15] O. Lupan, V. Postica, N. Ababii, M. Hoppe, V. Cretu, I. Tiginyanu, V. Sontea, T. Pauporté, B. Viana, R. Adelung, *Microelectron. Eng.* **2016**, *164*, 63.
[16] O. Lupan, V. Postica, V. Cretu, N. Wolff, V. Duppel, L. Kienle, R. Adelung, *Phys. Status Solidi RRL* **2016**, *10*, 260
[17] L. Chow, O. Lupan, H. Heinrich, G. Chai, *Appl. Phys. Lett.* **2009**, *94*, 163105.
[18] O. Lupan, V. Cretu, V. Postica, M. Ahmadi, B. R. Cuenya, L. Chow, I. Tiginyanu, B. Viana, T. Pauporté, R. Adelung, *Sens. Actuators, B* **2016**, *223*, 893.
[19] Y. K. Mishra, G. Modi, V. Cretu, V. Postica, O. Lupan, T. Reimer, I. Paulowicz, V. Hrkac, W. Benecke, L. Kienle, R. Adelung, *ACS Appl. Mater. Interfaces* **2015**, *7*, 14303.
[20] O. Lupan, V. Cretu, V. Postica, N. Ababii, O. Polonskyi, V. Kaidas, F. Schütt, Y. K. Mishra, E. Monaico, I. Tiginyanu, *Sens. Actuators, B* **2016**, *224*, 434.
[21] D. Zhang, A. Liu, H. Chang, B. Xia, *RSC Adv.* **2015**, *5*, 3016.
[22] a) A. M. Diskin, P. Španěl, D. Smith, *Physiol. Meas.* **2003**, *24*, 107; b) P. R. Galassetti, B. Novak, D. Nemet, C. Rose-Gottron, D. M. Cooper, S. Meinardi, R. Newcomb, F. Zaldivar, D. R. Blake, *Diabetes Technol. Ther.* **2005**, *7*, 115.
[23] C. Turner, P. Španěl, D. Smith, *Physiol. Meas.* **2006**, *27*, 321.
[24] O. Lupan, V. Cretu, M. Deng, D. Gedamu, I. Paulowicz, S. Kaps, Y. K. Mishra, O. Polonskyi, C. Zamponi, L. Kienle, V. Trofim, I. Tiginyanu, R. Adelung, *J. Phys. Chem. C* **2014**, *118*, 15068.

[25] a) L. Chow, O. Lupan, G. Chai, H. Khallaf, L. K. Ono, B. Roldan Cuenya, I. M. Tiginyanu, V. V. Ursaki, V. Sontea, A. Schulte, *Sens. Actuators, A* **2013**, *189*, 399; b) G. Y. Chai, O. Lupan, E. V. Rusu, G. I. Stratan, V. V. Ursaki, V. Şontea, H. Khallaf, L. Chow, *Sens. Actuators, A* **2012**, *176*, 64; c) I. Hölken, G. Neubüser, V. Postica, L. Bumke, O. Lupan, M. Baum, Y. K. Mishra, L. Kienle, R. Adelung, *ACS Appl. Mater. Interfaces* **2016**, *8*, 20491; d) O. Lupan, V. Postica, M. Mecklenburg, K. Schulte, Y. K. Mishra, B. Fiedler, R. Adelung, *J. Mater. Chem. A* **2016**, *4*, 16723.
[26] L. Liao, Z. Zheng, B. Yan, J. X. Zhang, H. Gong, J. C. Li, C. Liu, Z. X. Shen, T. Yu, *J. Phys. Chem. C* **2008**, *112*, 10784.
[27] P. M. Rao, X. Zheng, *Nano Lett.* **2009**, *9*, 3001.
[28] a) S. Al Khabouri, S. Al Harthi, T. Maekawa, Y. Nagaoka, M. E. Elzain, A. Al Hinai, A. D. Al-Rawas, A. M. Gismelseed, A. A. Yousif, *Nanoscale Res. Lett.* **2015**, *10*, 1; b) C. O. Chey, A. Masood, A. Riazanova, X. Liu, K. V. Rao, O. Nur, M. Willander, *J. Nanomater.* **2014**, *2014*, 222; c) W.-G. Zhang, B. Lu, L.-Q. Zhang, J.-G. Lu, M. Fang, K.-W. Wu, B.-H. Zhao, Z.-Z. Ye, *Thin Solid Films* **2011**, *519*, 6624.
[29] A. Abidov, B. Allabergenov, J. Lee, H.-W. Jeon, S.-W. Jeong, S. Kim, *Int. J. Mater., Mech. Manuf.* **2013**, *1*, 294.
[30] T. Yamashita, P. Hayes, *Appl. Surf. Sci.* **2008**, *254*, 2441.
[31] a) T. Fujii, F. M. F. de Groot, G. A. Sawatzky, F. C. Voogt, T. Hibma, K. Okada, *Phys. Rev. B* **1999**, *59*, 3195; b) P. Mills, J. L. Sullivan, *J. Phys. D: Appl. Phys.* **1983**, *16*, 723.
[32] P. C. J. Graat, M. A. J. Somers, *Appl. Surf. Sci.* **1996**, *100–101*, 36.
[33] J. Ouyang, J. Pei, Q. Kuang, Z. Xie, L. Zheng, *ACS Appl. Mater. Interfaces* **2014**, *6*, 12505.
[34] R. Wang, Y. Chen, Y. Fu, H. Zhang, C. Kisielowski, *J. Phys. Chem. B* **2005**, *109*, 12245.
[35] D. Gedamu, V. Hrkac, unpublished work.
[36] R. L. Tollman, E. A. Gulbransen, *J. Electrochem. Soc.* **1968**, *115*, 770.
[37] C. Cayron, M. Den Hertog, L. Latu-Romain, C. Mouchet, C. Secouard, J. L. Rouviere, E. Rouviere, J. P. Simonato, *J. Appl. Crystallogr.* **2009**, *42*, 242.
[38] X. Li, C. Wang, H. Guo, P. Sun, F. Liu, X. Liang, G. Lu, *ACS Appl. Mater. Interfaces* **2015**, *7*, 17811.
[39] X. Zhou, X. Li, H. Sun, P. Sun, X. Liang, F. Liu, X. Hu, G. Lu, *ACS Appl. Mater. Interfaces* **2015**, *7*, 15414.
[40] A. Gurlo, M. Sahm, A. Oprea, N. Barsan, U. Weimar, *Sens. Actuators, B* **2004**, *102*, 291.
[41] X. Bai, H. Ji, P. Gao, Y. Zhang, X. Sun, *Sens. Actuators, B* **2014**, *193*, 100.
[42] R. Xing, Q. Li, L. Xia, J. Song, L. Xu, J. Zhang, Y. Xie, H. Song, *Nanoscale* **2015**, *7*, 13051.
[43] Y. Zeng, T. Zhang, M. Yuan, M. Kang, G. Lu, R. Wang, H. Fan, Y. He, H. Yang, *Sens. Actuators, B* **2009**, *143*, 93.
[44] J. P. Cheng, B. B. Wang, M. G. Zhao, F. Liu, X. B. Zhang, *Sens. Actuators, B* **2014**, *190*, 78.
[45] I.-S. Hwang, S.-J. Kim, J.-K. Choi, J.-J. Jung, D. J. Yoo, K.-Y. Dong, B.-K. Ju, J.-H. Lee, *Sens. Actuators, B* **2012**, *165*, 97.
[46] M. Tonezzer, N. V. Hieu, *Sens. Actuators, B* **2012**, *163*, 146.
[47] F. Hernandez-Ramirez, J. D. Prades, A. Tarancon, S. Barth, O. Casals, R. Jimenez-Diaz, E. Pellicer, J. Rodriguez, J. R. Morante, M. A. Juli, S. Mathur, A. Romano-Rodriguez, *Adv. Funct. Mater.* **2008**, *18*, 2990.
[48] O. Lupan, L. Chow, T. Pauporté, L. K. Ono, B. R. Cuenya, G. Chai, *Sens. Actuators, B* **2012**, *173*, 772.
[49] M. Righettoni, A. Tricoli, S. E. Pratsinis, *Chem. Mater.* **2010**, *22*, 3152.
[50] Z. Fan, X. Wen, S. Yang, J. G. Lu, *Appl. Phys. Lett.* **2005**, *87*, 013113.
[51] Y.-C. Lee, Y.-L. Chueh, C.-H. Hsieh, M.-T. Chang, L.-J. Chou, Z. L. Wang, Y.-W. Lan, C.-D. Chen, H. Kurata, S. Isoda, *Small* **2007**, *3*, 1356.
[52] A. Gurlo, N. Bârsan, A. Oprea, M. Sahm, T. Sahm, U. Weimar, *Appl. Phys. Lett.* **2004**, *85*, 2280.
[53] A. Gurlo, *ChemPhysChem* **2006**, *7*, 2041.
[54] V. Postica, I. Hölken, V. Schneider, V. Kaidas, O. Polonskyi, V. Cretu, I. Tiginyanu, F. Faupel, R. Adelung, O. Lupan, *Mater. Sci. Semicond. Process.* **2016**, *49*, 20.
[55] V. Cretu, V. Postica, A. K. Mishra, M. Hoppe, I. Tiginyanu, Y. K. Mishra, L. Chow, N. H. De Leeuw, R. Adelung, O. Lupan, *J. Mater. Chem. A* **2016**, *4*, 6527.
[56] a) Y. Hu, J. Zhou, P.-H. Yeh, Z. Li, T.-Y. Wei, Z. L. Wang, *Adv. Mater.* **2010**, *22*, 3327; b) T.-Y. Wei, P.-H. Yeh, S.-Y. Lu, Z. L. Wang, *J. Am. Chem. Soc.* **2009**, *131*, 17690.
[57] V. Postica, J. Gröttrup, R. Adelung, O. Lupan, A. K. Mishra, N. H. De Leeuw, N. Ababii, J. F. C. Carreira, J. Rodrigues, N. B. Sedrine, M. R. Correia, T. Monteiro, V. Sontea, Y. K. Mishra, *Adv. Funct. Mater.* **2016**, *27*, 1604676.
[58] R. Vincent, P. A. Midgley, *Ultramicroscopy* **1994**, *53*, 271.
[59] V. V. Ursaki, O. I. Lupan, L. Chow, I. M. Tiginyanu, V. V. Zalamai, *Solid State Commun.* **2007**, *143*, 437.

Received: August 27, 2016
Revised: December 16, 2016
Published online: February 10, 2017

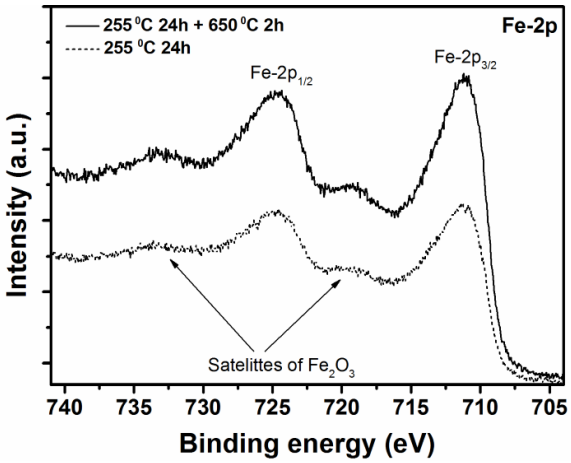

Figure S5. Fe-2p XPS spectra of Fe microparticles oxidized in ambient air at 255 °C in 24 h and then re-oxidized at 650 °C for 2 h.

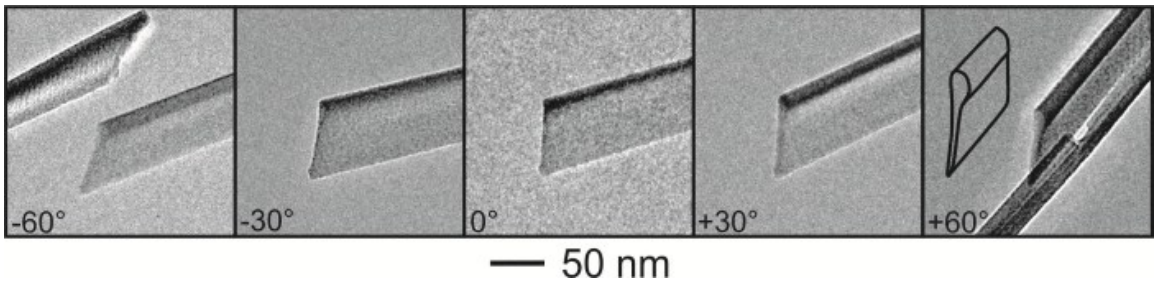

Figure S6. High angle tilting experiment from -60° to +60° shows a razorblade like morphology of iron oxide nanostructures.

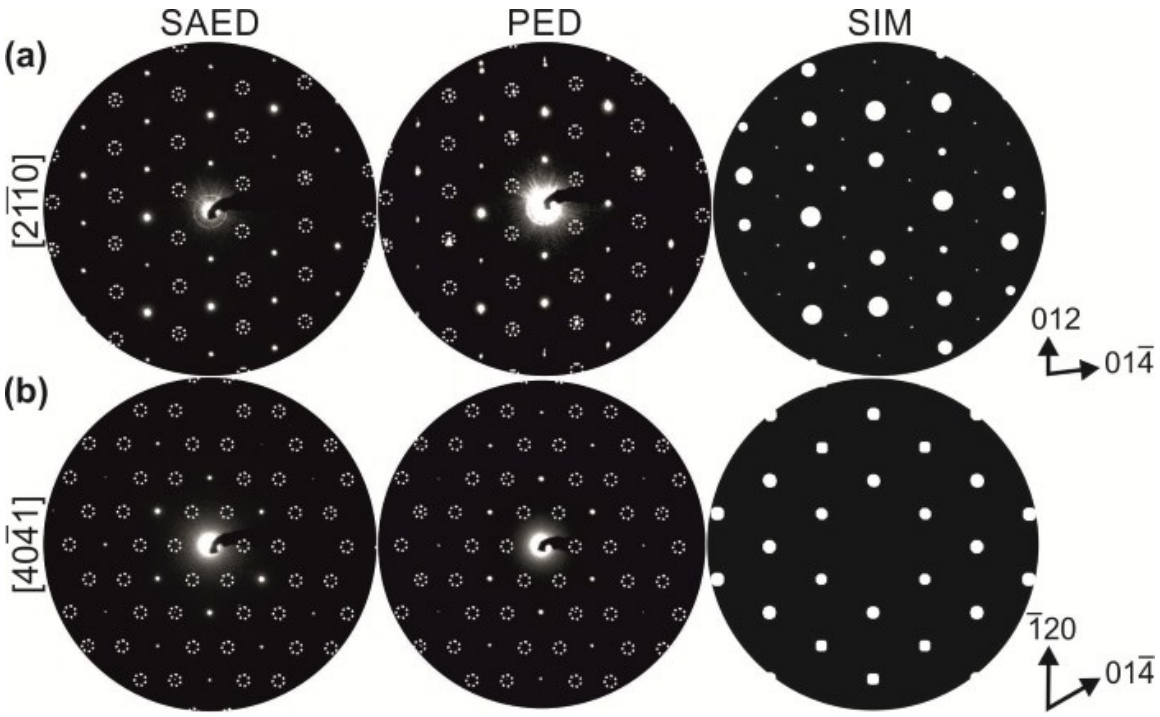

Figure S7. ED studies showing essentially two types of reflections which are not consistent with the original hematite structure (white circles). (a) Reflections based on a symmetry reduction of space-group R-3*c* to R-3 and according simulation of the modified hematite structure. The reflection condition for the *000l* reflections changes from $l = 6n$ (R-*3c*) to $l = 3n$ (R-*3*) and for the *h-h0l* reflections the additional condition $l = 2n+1$ is set up. (b) Reflections generated by the degeneracy and elongation of relrods due to nano-sized planar defects and extreme thin dimensions.

Nano Energy 70 (2020) 104420

Contents lists available at ScienceDirect

Nano Energy

journal homepage: http://www.elsevier.com/locate/nanoen

Facile fabrication of semiconducting oxide nanostructures by direct ink writing of readily available metal microparticles and their application as low power acetone gas sensors

Leonard Siebert [a], Niklas Wolff [b], Nicolai Ababii [c], Maik-Ivo Terasa [a], Oleg Lupan [a,c,**], Alexander Vahl [d], Viola Duppel [e], Haoyi Qiu [a], Maik Tienken [a], Mattia Mirabelli [a], Victor Sontea [c], Franz Faupel [d], Lorenz Kienle [b], Rainer Adelung [a,*]

[a] Chair for Functional Nanomaterials, Institute for Materials Science, Kiel University, Kaiserstr. 2, D-24143, Kiel, Germany
[b] Chair for Synthesis and Real Structure, Institute for Materials Science, Kiel University, Kaiserstr. 2, D-24143, Kiel, Germany
[c] Department of Microelectronics and Biomedical Engineering, Center for Nanotechnology and Nanosensors, Technical University of Moldova, 168 Stefan cel Mare Av., MD-2004, Chisinau, Republic of Moldova
[d] Chair for Multicomponent Materials, Institute for Materials Science, Kiel University, Kaiserstr. 2, D-24143, Kiel, Germany
[e] Nanochemistry, Max Planck Institute for Solid State Research, Heisenbergstr. 1, D-70569, Stuttgart, Germany

ARTICLE INFO

Keywords:
Direct ink writing
Cu–Fe deposition
Heterojunction
Fe_2O_3–$CuO/Cu_2O/Cu$
Gas sensing
Transmission electron microscopy

ABSTRACT

In this work, a facile two-step fabrication and characterization of printed acetone sensors based on mixed semiconducting metal oxides is introduced. The devices are fabricated by Direct Ink Writing metal microparticle (MP) stripes of commercially available pure iron and copper particles onto the surface of a glass substrate, forming a bridging multi-phase semiconducting oxide net by subsequent thermal annealing. The open, highly porous bridging structures consist of heterojunctions which are interconnected via non-planar $CuO/Cu_2O/Cu$ nanowires and Fe_2O_3/Fe nanospikes. Morphological, vibrational, chemical and structural studies were performed to investigate the contact-forming Fe_2O_3–CuO nanostructures on the surface of the MPs. The power consumption and the gas sensing properties showed selectivity to acetone vapor at an operating temperature of around 300 °C with a high gas response of about 50% and the lowest operating power of around 0.26 μW to a concentration of 100 ppm of acetone vapor. The combination of the possibility of acetone vapor detection, the controllable size and geometry and their low power make these printed structures important candidates for next developments of accessible detection devices, as well as acetone vapor monitoring (even below 1 ppm). The printing of MPs in general paves the way for a new generation of printed different devices, even in "home-made" conditions, for a manifold of applications tailored by the composition and geometry of the printed MP stripes, enabled through the simplicity and versatility of the fabrication method.

1. Introduction

The increased demand towards individual devices in the Internet-of-Things (IoT) era with selected and often special sets of properties requires both sophisticated multipurpose materials as well as new methods to fabricate devices out of these materials.

Multifunctional materials, including semiconducting oxides of both n- and p-type conductivity with tunable properties are highly demanded in most semiconductor-powered devices. Producing such hybrid materials however is often demanding with respect to shape and size control on a macroscopic level. Standard techniques include vacuum deposition, controlling the shape in 2D through a manifold of microfabrication techniques, all of them requiring costly and energy consuming clean room technology. A more facile technological approach to produce hybrid systems in all three spatial dimensions as well as highly complex geometries is required.

Especially direct ink writing (DIW), a subset of additive manufacturing (AM), also known as 3D-printing, as mentioned in

* Corresponding author.
** Corresponding author.
E-mail addresses: ollu@tf.uni-kiel.de, oleg.lupan@mib.utm.md (O. Lupan), ra@tf.uni-kiel.de (R. Adelung).

https://doi.org/10.1016/j.nanoen.2019.104420
Received 20 November 2019; Received in revised form 19 December 2019; Accepted 19 December 2019
Available online 3 January 2020

different works, enables time and cost effective fabrication of state-of-the-art structures and systems with different levels of complexity for applications in many major fields of technology [1–5]. Such applications range from biomedical devices, mechanical parts and functional to electronic and sensor applications [2,5,6]. The decisive benefits include high flexibility in the design of both the geometry and the desired materials paired with the simplicity of the respective additive manufacturing technique. Pairing these qualities with the wide assortment of treatment and fabrication methods from materials science leads to an ever increasing popularity of 3D-printing processes manufacturing novel devices.

As one important subset, 3D-printed electronics range from fully integrated electronics to sensor applications, e.g., to be used in the field of breath analysis to diagnose and monitor diabetes mellitus [7,8] or strain sensors [9]. This holds true especially for DIW, where rheologically optimized inks can be combined with micro- and nanoparticles to achieve specific functionalities. These systems can even outperform classic microfabrication techniques [9,10], eliminating the necessity for clean room technology such as photolithography, exposure to ultraviolet radiation or sophisticated etching processes. Beyond that, the 3D-printing technology offers potential to integrate complex shaped semiconducting metal oxide-based materials directly onto circuit boards of standardized portable devices, e.g., for medical application. Additional treatment steps can be used to refine certain qualities of the as-printed devices, like their base resistance or their sensitivity towards outside stimuli.

As an application example, a facile fabrication of portable sensors based on the chemiresistive effect for breath analysis is highly demanded by both the medical industry and patients suffering from diabetes.

Conventional tests of blood glucose levels suffer from inaccuracies by the individual fat loss rate, health condition and diet [7,8] in contrast to the concentration of breath acetone which is < 1 ppm for healthy individuals, while it ranges from >2 ppm to even 1250 ppm for patients with diabetic ketoacidosis [11–13]. This biological fingerprint motivates the use of acetone as a biological marker for reliable diagnosis and monitoring of diabetic conditions over breath analysis rather than testing the blood glucose level with pain for the patient. The increasing number of registered diagnoses with diabetes [14] and the amount of people suffering from anxiety of venipuncture [15] motivate the development of direct and gentle medical diagnostic pathways [16–19].

Possible candidates for sensing acetone vapors include ZnO and single component iron oxide and copper oxide nanostructures [10, 20–22], but mixed oxides of copper and iron were not studied extensively so far. Their chemical and physical properties, especially related to interfacial phenomena, can be improved by forming hybrid structures of p- and n-type semiconducting oxides. These nanocomposites in such a combination are important for fundamental studies and for practical advanced applications in portable sensor devices [18,19].

In this contribution, we report on printed low power, functional nanomaterial nets consisting of nanowires and nanospikes bridging microparticles (MP) of $CuO/Cu_2O/Cu$ and Fe_2O_3/Fe heterojunctions made by combining DIW with thermal annealing.

The fabricated printed mixed metal oxide networks will be presented with respect to acetone vapor sensors featuring a flexible design concept proving this approach to be highly attractive for the near future.

2. Materials and methods

2.1. Ink fabrication and DIW

The fabrication steps of the acetone sensor devices are depicted in Fig. 1. The first step is the production of a rheologically optimal ink containing the respective materials (Fig. 1a). Copper and iron microparticles as well as 96 vol% ethanol were purchased from Sigma Aldrich, polyvinylbutyral (PVB) was kindly supplied by Kuraray. The mean particle diameter for the copper and iron microparticles were 15–25 and 45–60 µm, respectively.

The mixing ratios of the final ink were 3:1:1 (ethanol:PVB:metals) by weights and the metal MPs were mixed in a 1:1 ratio by weights. The ink was prepared by sonicating the metal particles with the Ethanol for 3 min with a Bandelin Sonoplus HD 4100 ultrasonic rod at 30% power. The PVB was then added and the solution was stirred, until it became homogeneous. The ink was filled into a 30 cm^3 polypropylene cartridge (Fig. 1a) and left over night before printing. The cartridge was then loaded into a custom built direct ink writing setup. For printing a tapered nozzle with a diameter of 0.58 mm was used and samples with various layer heights were printed on standard glass slides (Fig. 1b, 25 mm $\times$ 75 mm) at a speed of around 0.4 $mm^3\ s^{-1}$. Each line had a height of 0.1 mm and a width of 0.6 mm.

After the printing step, the samples were dried for 24 h at room temperature to evaporate all of the ethanol remaining.

After drying, the printed devices were rapidly annealed in a series of annealing steps at both 425 °C and 650 °C in air at a heating rate of 40 °C s^{-1} and kept at this temperature for varying time lengths (Fig. 1c). This leads to the formation of a net of nanowires and nanospikes between the particles as well as completing the oxidation inside of the MPs, leading to a higher base resistance. After cooling down, multiple meandering gold contacts (Fig. 1d) (thickness ~170 nm) were sputtered onto each sample using a sputtering mask. This is done for contacting and the samples were cut down into individual sensors. Each sensor is made of two interdigitating electrodes with a gap size of 1 mm. The utilization of gold was done to enable reliable testing of the gas sensing and low power qualities of the sensors. To completely obviate the need for vacuum technology, one can fabricate an all printed device. The contacts may be made from conducting inks containing materials like graphene, CNTs, silver flakes or conducting polymers like PEDOT:PSS [41].

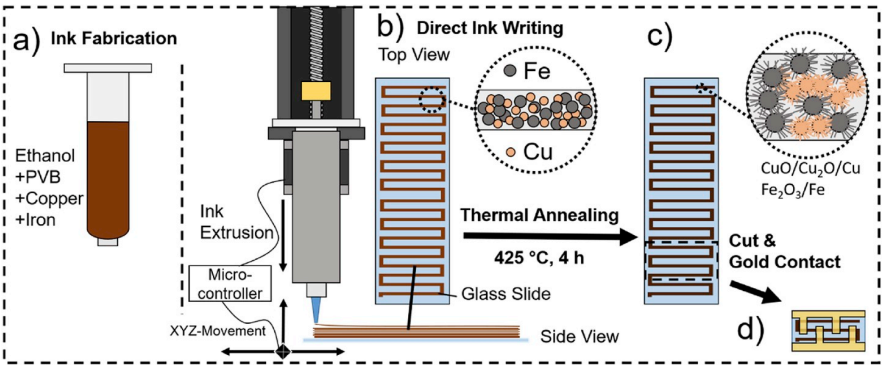

Fig. 1. Schematic sensor fabrication process: (a) ink fabricated by mixing copper and iron microparticles in ethanol, stirring in PVB until homogeneous, then the ink is filled into the printer cartridge; (b) direct ink writing via piston-driven syringe pumps in a 3D-printing setup. Layer by layer building of meandering copper-iron stripes. (c) The glass slide with the printed object is placed in an oven at air at 425 °C for 4 h where the metal oxide nanostructures form. (d) Single sensor devices are gold coated and then cut for further electrical and sensor investigations.

2.2. Morphological, chemical and Real Structure characterization

The samples geometry and morphology was investigated by using digital camera and scanning electron microscopy (SEM) REM-ZEISS (7 kV, 10 μA). The analysis of the chemical composition of the specimens was done by energy dispersive X-ray (EDX) spectroscopy. Micro-Raman investigations were realized at room temperature with a WITec system in a backscattering configuration. The Nd:YAG laser power was less than 4 mW at the printed samples, which were examined with a Nd:YAG laser, $\lambda_{ex} = 532$ nm and for each spectrum 10 accumulations at an integration time of 10 s were taken. The measurements on a 25 μm × 25 μm scanning area, 50 points per line, and 50 lines per image were conducted on the sample surface to visualize the heterojunction net.

An integral characterization was performed by an X-ray powder diffraction (XRD) Seifert 3000 TT unit operating at 40 kV and 40 mA, with CuKα1 radiation ($\lambda = 1.540598$ Å) [23].

Three sensor samples of the $CuO/Cu_2O/Cu$ Fe_2O_3/Fe system were investigated by X-ray photoelectron spectroscopy (XPS, Omicron Nano-Technology GmbH), operating with an Al-anode at a power of 240 W. Main peaks were measured with a 25 eV pass energy. The recorded spectra were charge referenced to the aliphatic carbon C-1s peak at 284.9 eV (atmospheric contamination) and the software "CasaXPS" in version 2.3.16 [24,25].

Analytical methods of transmission electron microscopy (TEM) have been performed on a Tecnai F30 microscope equipped with an EDAX Si–Li drift detector for chemical analysis via energy dispersive X-ray spectroscopy (EDX) and a Gatan Imaging Filter (GIF) unit for collecting electron energy-loss spectra (EELS) and energy-filtered (EF)TEM images. For these TEM sample preparation, iron oxide and copper oxide nanostructures were scratched off the substrate and transferred to a carbon lacey film of a gold grid. Energy-loss spectra were collected on both type of oxides using the oxygen K-edge feature beginning at 532 eV and the $L_{3,2}$ edges located at 708 eV (Fe) and 931 eV (Cu). The inelastic background was subtracted with the EELS plug-in for the Digital-Micrograph software and individual spectra were corrected by an energy shift according to the position instability of the zero-loss peak (ZLP). The electron energy loss spectra were collected with an energy resolution of about 3 eV full-width at half maxima of the ZLP. Additional local crystallographic information was collected using precession electron diffraction (PED) performed on a Philipps CM 30 ST microscope.

By contacting the gold layers on the printed samples the gas response was obtained as the ratio $\Delta R/R_{air}$, where R_{air} and R_{gas} and $\Delta R = R_{gas} - R_{air}$, are the electrical resistances of the sensor structures in ambient air (R_{air}) and under exposure to VOCs or gas (R_{gas}), respectively [26,27]. This ratio is different for the chemical composition and the concentration of the respective species in air. The VOC species sensing performances were investigated by a two-probe method after mounting sensors inside a test chamber connected to gas flow instrumentation. The test gases were permanently circulated through the test chamber at a flow rate of 110 sccm. Details on the sensing experiments can be found in our previous works [23,26].

3. Results

3.1. Morphology of the printed sensors

In Fig. 2a the photograph of the printed devices based on Cu–Fe-MPs on a standard glass substrate (25 mm × 75 mm) used for further research is presented. Additionally, sputtered gold contacts, subdividing the glass slide into multiple individual sensor devices can be observed in Fig. 2b. Digital as well as scanning electron microscopy (SEM) micrographs of the meandering stripes and the interdigitated gold contacts are displayed in Fig. 2c and d.

It is pointed out, that the direct print of the stripes onto a glass substrate offers the potential application as flexible and free-standing precursor stripes by gently detaching them from the glass substrate. The detachment occurs after gold deposition and before thermal annealing. The stripes still contain the elemental iron and copper particles as well as the polymer binder, meaning they are not suited for sensing in this state. In this state the detached stripes could be potentially used for conformal attachment of the sensor on curved surfaces. The structures presented in Fig. 3 show the directly printed and semi-detached freestanding stripes produced by breaking away the glass slide on one side.

The morphological details of the interpenetrated Fe_2O_3–CuO NWs bridging the $CuO/Cu_2O/Cu$ and Fe_2O_3/Fe microparticles are presented in Fig. 4 by showing SEM micrographs obtained at multiple steps of magnification (increasing magnification from (a) to (d)). The morphologies of the individual species are described as flake-like spikes and long nanowires both in the range of just a few tens of nanometers, which are made of Fe_2O_3 and CuO, respectively. A peculiarity of this printed microstructure is the occasional touching of these two nanostructures, which is inferred from the SEM micrographs (Fig. 4c and d).

A more detailed view onto both the $CuO/Cu_2O/Cu$ and Fe_2O_3

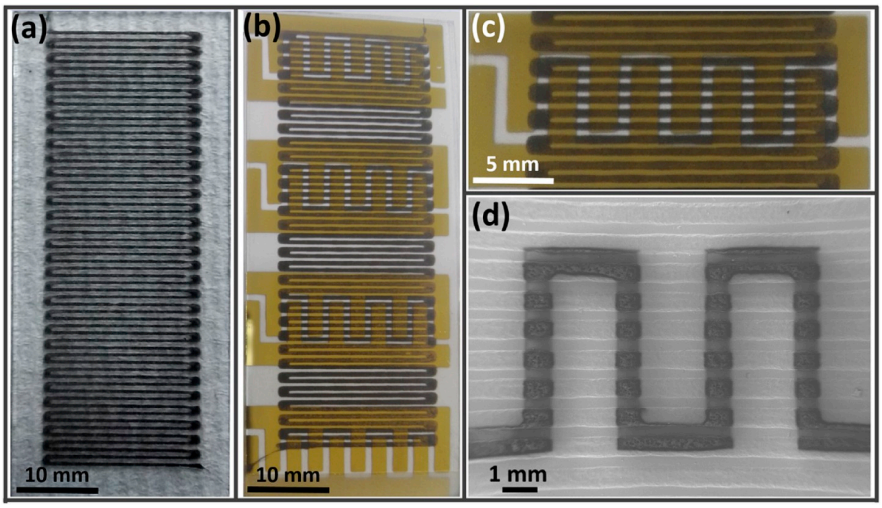

Fig. 2. Photograph of meandering printed stripes based on Cu–Fe-MPs on glass slide used for further research: (a) representative sample after printing and prior to gold deposition; (b) sample divided into individual sensors by interdigitating gold contacts; (c) the back side of a sensor element in higher magnification. (d) The SEM micrograph of the sensor element from (c).

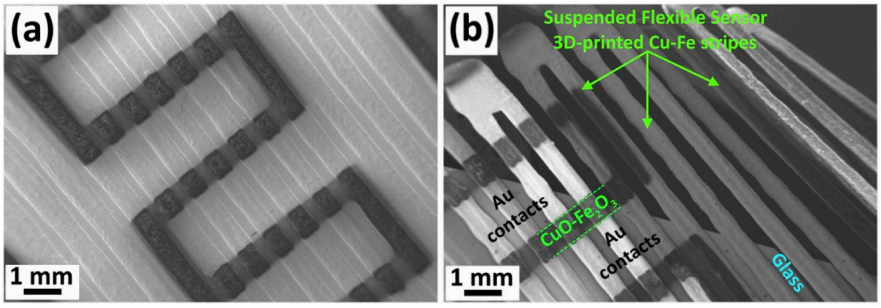

Fig. 3. SEM micrograph of the sensor element printed Cu–Fe mixed MPs: (a) on glass with Au contacts on top (brighter area); (b) suspended on the glass slide edge of flexible sensor printed Cu–Fe stripes with Au contacts on top.

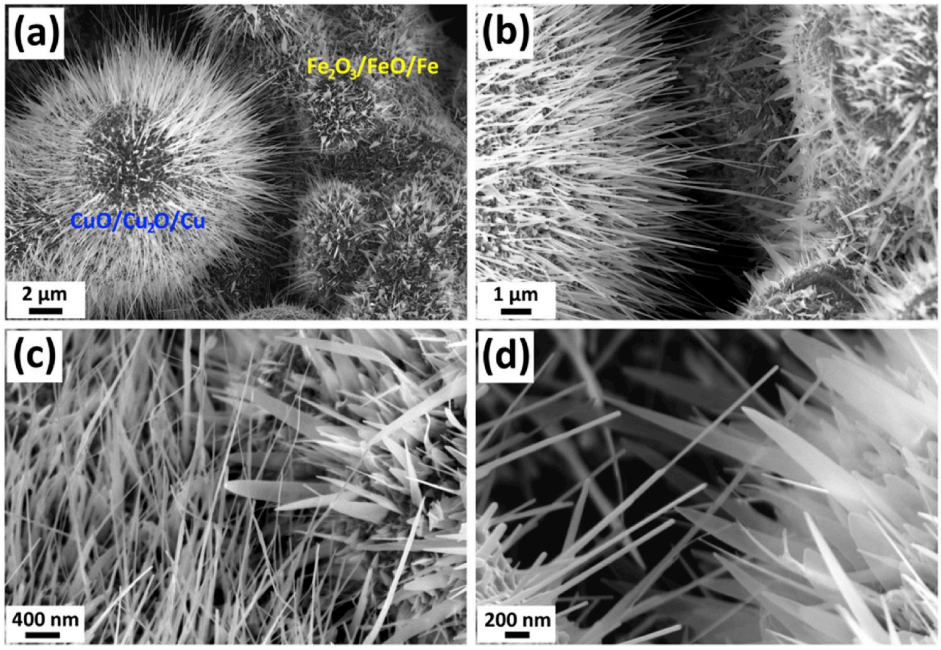

Fig. 4. SEM micrograph of the printed Cu–Fe mixed MP stripes forming $CuO/Cu_2O/Cu$ and Fe_2O_3/Fe junction contacts: (a) lower magnification of the spike-covered MPs; (b–d) higher magnification of the area between the printed microparticles with CuO/Cu_2O nanowires and Fe_2O_3 nanospikes bridging the MPs. The thinner CuO/Cu_2O can clearly be distinguished from the broader Fe_2O_3 nanoparticles.

nanostructures is presented in the SEM images included in Fig. S1 and Fig. S2. Also, a morphological comparison is presented for samples annealed with different temperature ramping. As seen in Fig. 4 and the Supporting Figs. S1 and S2, the nanostructures arrange in an open, readily accessible net-like microstructure, which is hard to achieve for planar thin film structures fabricated by standard techniques. For most gas sensors the accessibility (e.g. by high porosity) of the structures is important [23,24], since the active surface area is increased and the gas diffusion is easier resulting in an enhanced gas response. The high free volume of these structures paired with the macroscopic design freedom shows that 3D printing approaches like these will become more important for various technological applications, including gas sensors. In particular, the co-existence of p- and n-type semiconducting oxides are expected to improve the selectivity and sensitivity to weakly reactive gas species.

3.2. *Crystalline structure of the nanowire/nanospike-covered microparticles*

A detailed structural analysis of Fe and Cu particles, both before and after thermal annealing respectively as well as one sample of a mixed powder after thermal annealing was performed via XRD. The results suggest that primitive cubic Cu_2O, as well as CuO in its monoclinic structure have formed from oxidation of metallic Cu in its face-centered cubic structure. Additionally, the only Fe-related species observed for the iron containing samples was Fe_2O_3. When heated at 425 °C for 4 h leftover metallic phases can be observed in the diffractograms. The samples that were re-heated at 650 °C for 2 h, did not show any metallic remains in the diffractograms, indicating a complete oxidation of the samples. Details on the results as well as the respective diffractograms can be found in the Supporting Information (Fig. S3).

In order to verify the findings from XRD studies, additional Raman spectra on the printed stripes were made and are presented in Fig. 5.

Due to the high sensitivity of Micro-Raman, it can be used extensively for surface investigations of the formed nanostructures. Fig. 5a shows micro-Raman spectra at room temperature for the printed structures finished by thermal annealing: (1) nanowire $CuO/Cu_2O/Cu$; (2) nanowire $CuO/Cu_2O/Cu$ - nanospike Fe_2O_3/Fe; and (3) nanospike Fe_2O_3/Fe in the range of 100–1000 cm^{-1}. The presence of CuO as Tenorite and Cu_2O as Cuprite on the MPs as well as the existence of

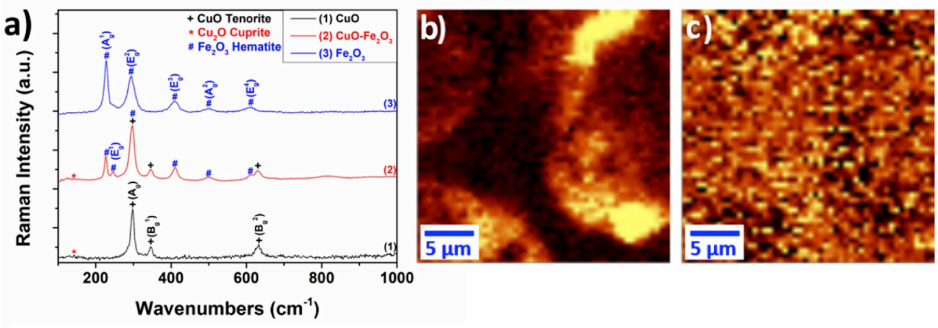

Fig. 5. Raman spectra of the 3D-printed stripes: (a) spectrum (1) nanowire-covered $CuO/Cu_2O/Cu$; curve (2) nanowire $CuO/Cu_2O/Cu$ - nanospike Fe_2O_3/Fe; and curve (3) nanospike Fe_2O_3/Fe. Filtered Raman images of Fe_2O_3/Fe - $CuO/Cu_2O/Cu$ heterojunction nets in terms of: (b) mode A1g (227 cm^{-1}) corresponding to α-Fe_2O_3 (Hematite); and (c) mode B^1_g (345 cm^{-1}) corresponding to CuO (Tenorite).

α-Fe_2O_3 (Hematite) was confirmed by the detected vibrational modes. The details on the Raman modes are described in the Supporting Information.

3.3. XPS, chemical analysis

The XPS spectra of three sensor sample sets with different compositions are compared in Fig. 6. The structures are either based on MPs of Cu (black line), Fe (blue line) or mixed Cu and Fe (red line) oxides. In the overview spectra (Fig. 6a) the elements Cu, Fe, O, Na and C were identified. The presence of Cu, Fe and partially O originates from the printed structures after thermal annealing whereas the signal related to carbon stems from surface contamination by atmospheric carbon (e.g. from carbohydrates) [26,28]. Accordingly, adventitious carbon (high resolution spectrum of C-1s line in Fig. 6b) was used to correct charging effects. The signal corresponding to Na is a result of the glass substrate, on which the sensor stripes were deposited, and the heat treatment step [29]. The peak position of the C-1s line was used in order to correct charging by referencing to 285.0 eV.

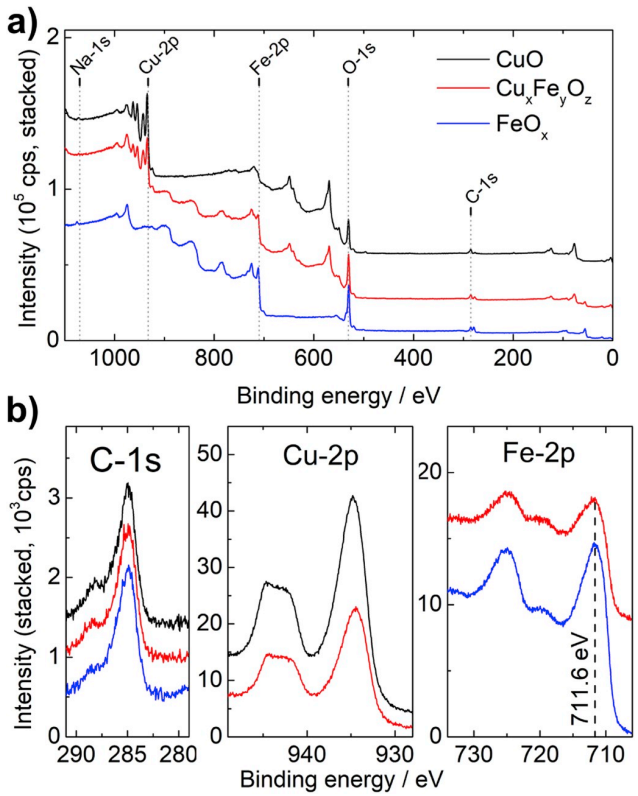

Fig. 6. XPS spectra of the mixed metal oxide sensors: (a) overview spectra; (b) high resolution spectra of C-1s, Cu-$2p_{3/2}$ and Fe-2p lines.

The high resolution spectra of the Cu-$2p_{3/2}$ and Fe-2p lines are shown in Fig. 6b. The Cu-$2p_{3/2}$ line reveals clear satellite peaks in case of the Cu and mixed metal sensor structures. The satellite peaks are shifted to higher binding energies with respect to the peak position of the Cu-$2p_{3/2}$ line. The observation of satellite peaks is commonly regarded as signature for the presence of Cu^{2+} (in CuO) [24,30,31]. Accordingly, this Cu signal arising in all spectra and samples can be attributed to the presence of CuO.

A close look at the Fe-2p lines indicates different signal strengths of Fe in the different sensor structures. In case of the Fe and the mixed sensor structures the presence of Fe is clearly identified. The corresponding peak position of the Fe-$2p_{3/2}$ line is located around 711.6 eV, which indicates the presence of Fe^{3+} in Fe_2O_3 (typically located between 710.4 eV and 711.6 eV) rather than Fe^{2+} in FeO (between 709.3 eV and 710.6 eV) or metallic Fe (between 706.5 eV and 707.7 eV) [28,30].

In conclusion, the mixed metals sensor nanostructure contains mostly CuO as well as Fe_2O_3. The quantification based on the XPS high resolution spectra reveals a Cu/Fe ratio of roughly 1.4.

3.4. Real Structure analysis of the nanospikes/nanowires

Transmission electron microscopy investigations on the structure and chemical details were performed on the CuO nanowires and Fe_2O_3 nanospikes having the described morphologies (cf. Fig. 4) shown in the STEM image of Fig. 7a.

Despite from their geometry, a direct identification of copper and iron containing nanostructures was enabled by using EFTEM using electrons from the L-loss features to create element specific contrast images. The superimposed and colored EFTEM images are depicted in Fig. 7b. EELS was used for the identification of the metal oxidation state and oxide phases present at three positions labeled A, B and C in Fig. 7a. The respective core-loss signals of the oxygen-K edge and Fe-, Cu-L edges including their near-edge fine structures (ELNES) are presented in Fig. 6c–f and are compared with standard references [32]. For the Cu-oxide nanowire (label A) the ELNES resembles very well the one of the reference for Cu^{2+} present in the CuO phase [32,33] and for the Fe-oxide nanospikes (label B and C) excellent coincidence is observed with Fe^{3+} present in Hematite Fe_2O_3. Small differences in the ELNES between the experimental signals and the reference spectra concerning the low intensity missing third feature around 550 eV may be related to the presence of oxygen vacancies [34].

Further, ED experiments were performed on the structures labeled A and C to validate the results of the spectroscopic measurements on a

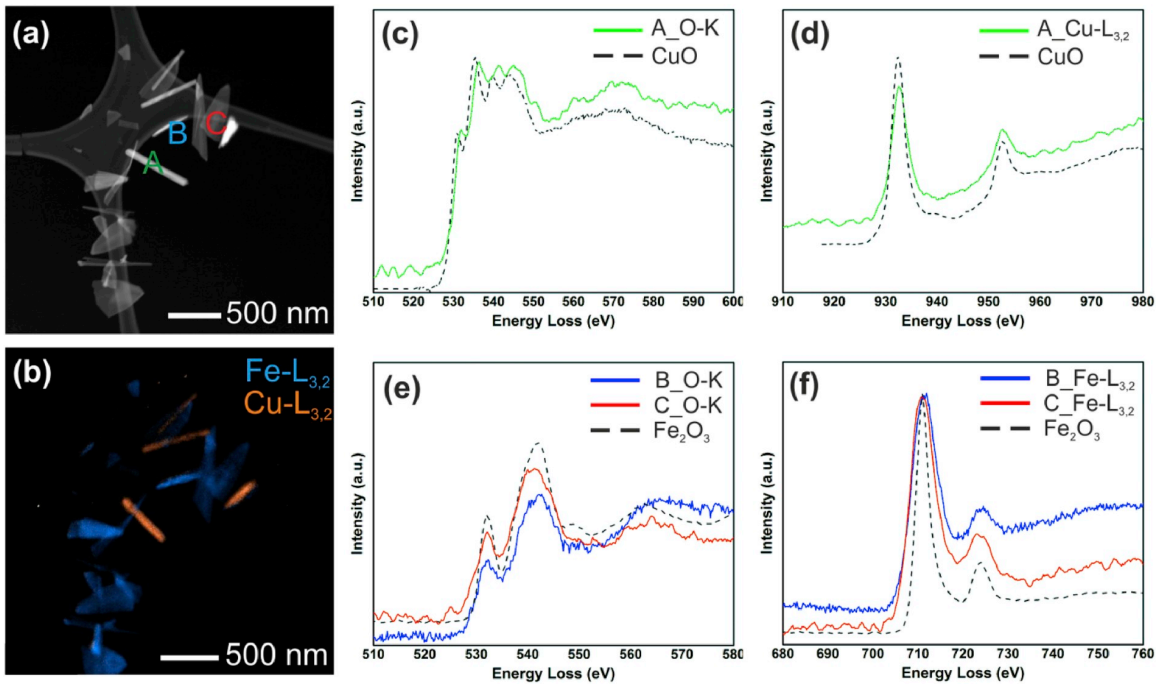

Fig. 7. Spectroscopic analyses of inelastic scattered electrons in the TEM. (a) Scanning TEM image; positions of EELS measurements are indicated with capital letters A-C. (b) EFTEM map showing the spatial distribution of Fe and Cu core loss signals. Please note, that there is a small offset of the stage tilt between images (a) and (b). (c) Core loss features of oxygen and Cu (d). (e) Core loss features of oxygen and Fe (f).

single point with crystallographic data. These investigations are summarized showing a ZLP filtered image in Fig. 8a including indicators for the positions of the virtual diffraction aperture. The experimental and simulated ED pattern of the positions A and C are depicted in Figs. 7b and 8c. Indeed, the ED patterns shown in Fig. 8b and c are assigned to the [101] zone axis pattern of monoclinic CuO and the [110] pattern of trigonal Fe_2O_3, coinciding with the EELS results. The ED pattern of the CuO nanowire presented in (b) shows diffuse streaks along the reciprocal [11-1]* direction, an effect which arises due to structural disorder. Structural peculiarities of CuO nanowires showing defects such as stacking faults, polysynthetical twinning or intergrowth of two CuO components are further demonstrated in Fig. S4 of the Supporting Information. With respect to Fe_2O_3 pattern (c) additional reflections arise in discrepancy to the trigonal space group of Hematite *R*-3*c* (yellow circles). In congruence to previous studies on iron oxide nanowires [21] a modified Hematite structure with space group R-3 (Ilmenite-type structure) may rationalize these reflections in a kinematic simulation. The reduced space group symmetry is interrelated to the elimination of the zonal reflection condition, i.e., for the 00l reflections the condition $l = 6n$ (*R*-3*c*) changes to $l = 3n$ (*R*-3), and for the h-hl reflections the condition $l = 2n$ (*R*-3*c*) is broken. For the interpretation of the ED pattern a pure kinematic approach is insufficient since dynamic scattering effects can be strongly significant. However, double diffraction is ruled out as an explanation for these yellow circled reflections (cf. Fig. 8c) because of the low thickness of the specimen and former precession electron diffraction experiments excluding such effects [21,35]. Since no indication for impurities were traced with EDX (not shown) on the nanospike (label C), the symmetry reduction may be rationalized with local ordering of oxygen vacancies, which are known to incorporate into Hematite nanostructures [34,36]. High-resolution TEM is capable to provide evidence on possible vacancy ordering or local structure variations. A representative HRTEM micrograph is presented in Fig. 8d together with a Fast Fourier Transformation (FFT) pattern. The interpretation of several FFT pattern calculated at different positions on the Fe_2O_3 nanospike (label C) suggest local strain variations most feasible

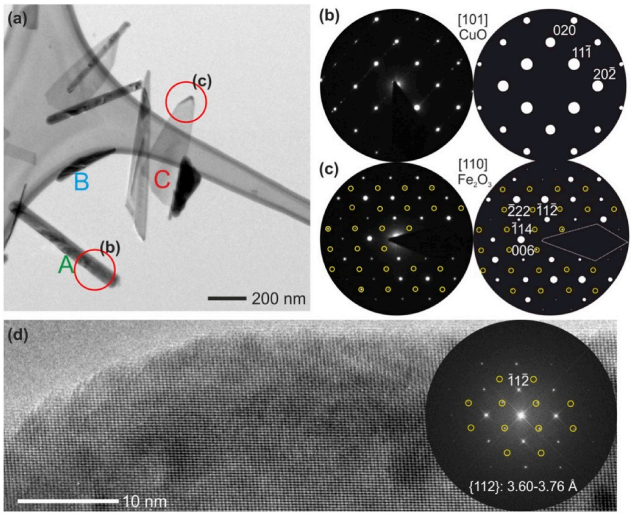

Fig. 8. (a) TEM bright-field image showing the respective oxide nanostructures with indication of the locations for electron diffraction experiments and high-resolution imaging. (b) Electron diffraction pattern of monoclinic CuO in [101] orientation and simulated pattern. Scattered intensities along the reciprocal [11-1]* direction indicate planar defects parallel to the growth direction. (c) Electron diffraction pattern of a Fe_2O_3 nanospike in [110] orientation. Reflections marked with yellow circles appear in deviation from the ideal Hematite structure and are explainable by a reduction in symmetry. (d) High-resolution TEM micrograph and FFT analysis from the area highlighted as region (c). The evaluation of local FFT pattern shows a variation of the {112} lattice parameter (standard: 3.68 Å) in the range between 3.60 and 3.76 Å, indicating a locally strained environment.

from the range of d-spacings 3.60–3.76 Å measured for the {-11-2} planes (in Hematite 3.68 Å).

In conclusion, the TEM study demonstrates the growth of defect-rich CuO nanowires and Fe_2O_3 nanospikes, described with a modified Hematite-type structure which is possibly based on ordering of oxygen vacancies.

3.5. Gas sensing properties

The plot in Fig. 9a shows the gas response to various volatile organic compound (VOC) gases (acetone, ethanol, 2-propanol and n-butanol) with 100 ppm gas concentration for printed sensor structures based on $CuO/Cu_2O/Cu$ - Fe_2O_3/Fe. These samples were thermally annealed at 425 °C for 4 h with a ramp of about 40 °C/min to grow nanowire-nanospike nets and re-heated at 650 °C for 1 h to increase its electrical resistance. From Fig. 9 we can see that at all operating temperatures (OPTs) the printed sensor structures are selective to acetone vapor and the optimal OPT is 300 °C with a gas response to 100 ppm of about 50%.

Fig. 9b shows the typical dynamic response curves of the printed stripes exposed to 100 ppm of acetone in air. The response is about 50% with response and recovery/decay times of $\tau_r = 14.4$ s and $\tau_d > 50$ s, respectively.

For a series of VOC vapor concentration (0.5–1000 ppm), see Fig. S6 of the Supporting Information.

In Fig. 9c the current-voltage (I–V) characteristics for $CuO/Cu_2O/Cu–Fe_2O_3/Fe$ printed sample sets are depicted at different operating temperatures. From Fig. 9c it can be seen that from room temperature up to 250 °C there is a non-linear current-voltage relation, indicating the dominance of an energy barrier-driven conductivity effect. Possible candidates for the room temperature conductivity could be a Poole-Frenkel or a Trap Assisted Tunneling effect. At higher temperatures the I–V-characteristics become ohmic, which means that the remaining series resistance is dominating the resistivity. The high current values can be explained based on the non-oxidized Fe and Cu micro-particles at the central or bottom parts [21].

For a more detailed characterization of the acetone sensing properties of the printed sensors, the plot in Fig. 10a shows the gas response to acetone vapor (100 ppm and 1000 ppm). At OPTs of 300 °C, 325 °C and 350 °C gas responses at 100 ppm are about 50%, 37% and 35%, respectively, and at a concentration of 1000 ppm the measured gas responses were about 50%, 52% and 53%, respectively.

Gas sensors are typically selective towards one gas but still show reactivity towards other gas species. This can lead to an unclear evaluation when mixed atmospheres are investigated with one sensor type. A means to correctly detect specific gases is by using multiple sensors in one platform and by cross-correlating their signals to find a specific compound. These preliminary results hint at a good selectivity for acetone. A good selectivity for a compound at a certain temperature can be used to create a sensor array with multiple sensors kept at different temperatures, where a linear combination of each signal enables the identification of a specific compound in a gas mixture.

In Fig. 10b the gas response versus concentration of acetone vapors is represented from 0.5 ppm to 1000 ppm at OPT of 300 °C. From Fig. 10 one can see that at low concentrations, the response is quite high and increasing with the concentration. The respective gas responses at 0.5, 1.0, 5.0 and 10 ppm, are, 12%, 14%, 15% and 16%. For more details on selectivity for low concentrations see Fig. S6 of the Supporting Information.

Fig. 10c shows the dynamic response at OPT of 300 °C to 1, 10 and 100 ppm acetone vapors. As can be seen, at lower vapor concentrations the value of the practical response does not change significantly, thus obtaining the values at 1, 10 and 100 ppm gas concentration of about 14%, 16% and 50%, respectively, and the response/recovery times of $\tau_r = 11.1$ s, 11.6 s, 14.4 s and $\tau_d = 10.33$ s, 11.9 s, >50 s, respectively.

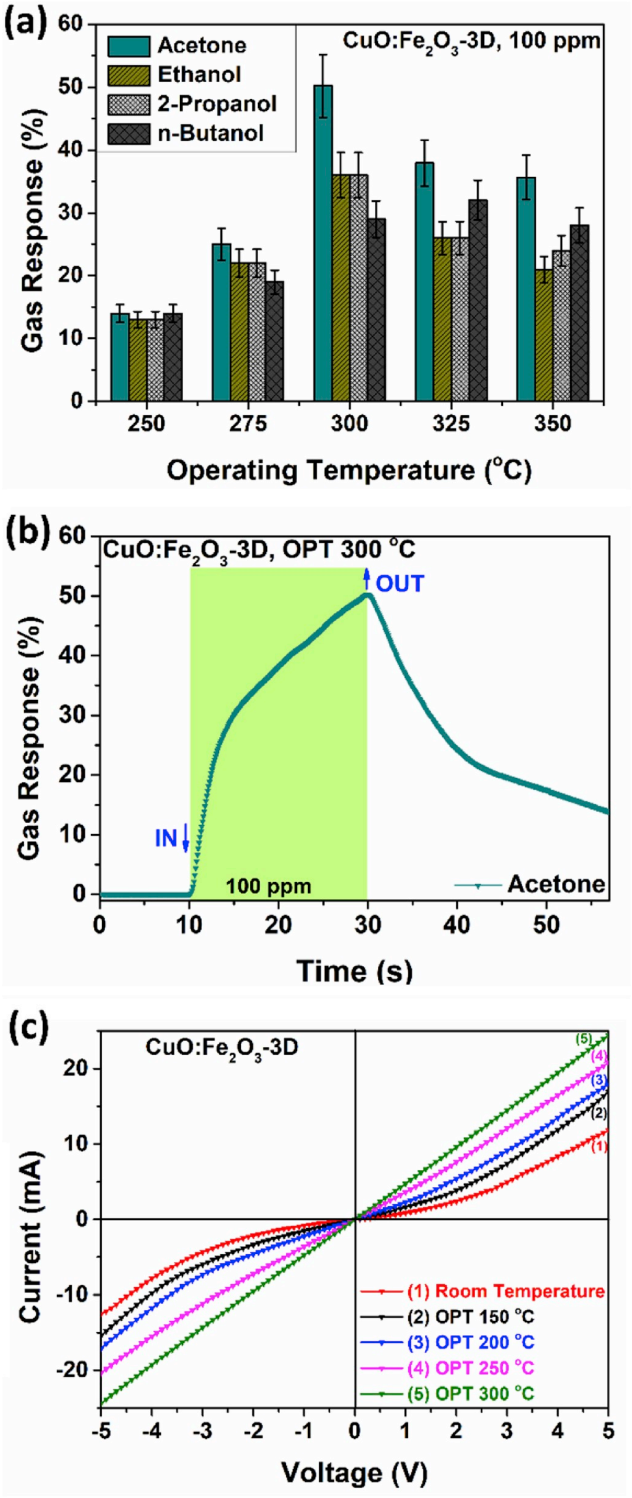

Fig. 9. (a) Gas response to various gases (100 ppm) versus operating temperature for the printed sensors based on $CuO/Cu_2O/Cu$ - Fe_2O_3/Fe after thermal annealing at 425 °C for 4 h. (b) Dynamic response to 100 ppm of acetone vapor of the same sensor. (c) I/V-characteristics for different operating temperatures for the $CuO/Cu_2O/Cu$ - Fe_2O_3/Fe sensors.

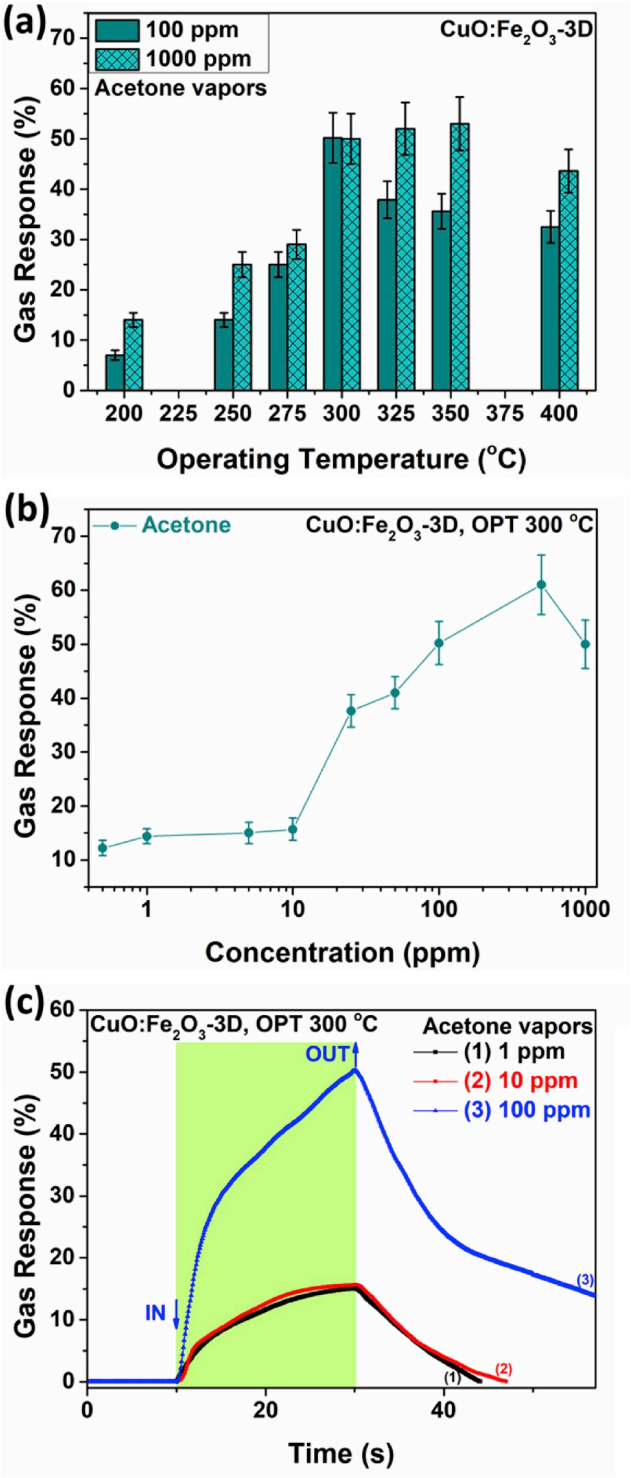

Fig. 10. (a) Gas response to acetone vapor (100 ppm and 1000 ppm) for the printed sensors measured at OPT from 200 °C to 400 °C. (b) Concentration dependency of the gas response for the printed sensors at an operating temperature of 300 °C (c) Dynamic response at OPT of 300 °C to 1, 10 and 100 ppm of acetone vapor.

3.6. Power consumption

By increasing the time and temperature of the thermal annealing, the level of oxidation of the MPs can be tailored, which can lead to the removal of electrical shortcut, increasing the sensitivity while lowering the power consumption.

In Fig. 11a the dependence of the power consumption and the response to acetone versus type of thermal annealing for printed samples of CuO:Fe_2O_3-3D is represented. The samples were treated in the following way: #1: 425 °C for 4 h; #2: 425 °C for 8 h; #3: 425 °C for 4 h and 650 °C for 1 h; #4: 425 °C for 4 h and 650 °C for 3 h.

It is observed that as the temperature and time of treatment increase, the power consumption decreases, and the highest value of the gas response is for the thermal annealing # 3, which included a 4-h treatment at 425 °C followed by a shorter 650 °C treatment. This indicates that for the correct formation of the nanowire and nanospike nets, a long duration of lower temperatures is necessary, which is in good agreement with the current model of the NW formation [37]. Additional heating at 650 °C leads to a much higher base resistance, which coincides with a higher gas response. This effect is likely caused by complete oxidation of the microparticles, forcing the current through the nanowires and nanospikes, while not changing their structure and therefore their conductivity mode. This can also be observed from the characterization, where Fig. S3 in the supporting information shows the XRD diffractogram of samples only heated once at 425 °C for 4 h. This sample shows a significant amount of remaining elemental copper and iron. When re-heated at 650 °C for 2 h no more elemental phases are visible in the diffractogram, further strengthening the hypothesis of a more complete oxidation in this second heating step. The complete oxidation is likely due to higher diffusion rates of oxygen into the metal microparticles at these elevated temperatures.

There is a trade-off however between the gas response and the power consumption, when the duration of the treatment at 650 °C is increased in time. The gas response lowers, which shows that the temperature also has an influence on the structure and the mode of conductivity of the NWs, which is not beneficial for the surface sensitive gas sensing mechanism proposed in the following section.

The possibility to tailor the quality of the sensors by simple thermal annealing adds an additional degree of freedom in designing electronic devices like the acetone vapor sensor presented here.

Fig. 11b shows the dependence of the power consumption and the response to acetone versus operating temperature of CuO:Fe_2O_3-3D samples. It can be seen that the operating temperature of OPT 300 °C leads to the highest response of ~50% with the power consumption of around 0.26 μW, which represents the optimal operating temperature for the developed devices. This is most likely due to the processes established on the NW surfaces during the experiment, which is proposed as a model in the following section. This calculation however does not include the necessary operation temperature and the corresponding power consumption. This issue has to be addressed in further iterations of such sensor systems by integrating a current-driven heating into the nanowires by employing high voltages and thermally insulating the substrate underneath. This could be realized by printing porous SiO_2 nanoparticles as an insulating layer. Another option would be to find a composition of nanowire covered particles and the corresponding conductivity modes that would alleviate the necessity of a higher operation temperature altogether.

The long-term stability of metal oxide semiconductors is also often discussed. Typically, sensors of this kind do not show any significant sensor drift in individual measurements, but drift can occur over longer durations of operation. While metal oxide semiconductors do not easily fail and are very robust, they need re-calibration after some time to account for this kind of thermal drift [42].

In summary, this concept of manufacturing allows for many different new concepts for such sensors and can easily be adopted, hinting at much more potential for developing a sensor with the desired properties.

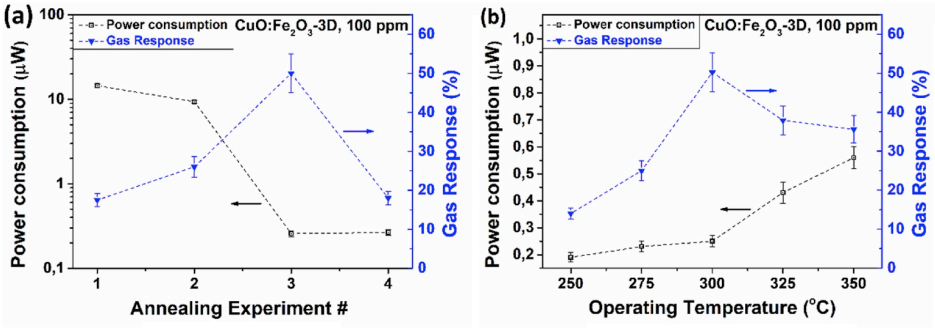

Fig. 11. (a) Dependence of the power consumption and the response to acetone versus type of thermal annealing for samples of CuO:Fe_2O_3-3D; (b) Dependence of the power consumption and the response to acetone versus operating temperature of CuO:Fe_2O_3-3D samples.

4. Proposed gas sensing mechanism

The proposed gas sensing mechanism is based on physico-chemical reactions on the sensor surface, which take place at different operating temperatures [38,39]. Under exposure to air oxygen species are adsorbed on the surface of CuO nanowires and ionized in dependence of the operating temperature. For example, at temperatures around 200–250 °C, O^- is formed in the following manner [22,38]:

$$\frac{1}{2}O_2(g) \rightarrow O^-(ad) + h^+ \quad (1)$$

Besides O^-, depending on the OPT, also O_2^- and O^{2-} can be formed. The consequence for the mechanism is the same, as all ions will take up electrons leading to the accumulation of positively charged holes.

The negative charge will promote the formation of a hole accumulation layer (HAL) in the CuO nanowires acting as a conduction channel. The size of this conduction channel critically depends on the temperature, since the amount of adsorbed oxygen ions sinks with increasing temperature, resulting in an increase in sensitivity towards the concentration of the adsorbed gas molecules. After exposure to acetone vapor, the acetone molecules react with the adsorbed O^- and the HAL width will decrease, increasing the electrical resistance again. The proposed reactions facilitating the detection will be done as follows [22,38].

$$CH_3COCH_3(gas) + O^{2-} + h^+ \rightarrow CH_3CO + CH_3O^- \quad (2)$$

$$CH_3CO \rightarrow CH_3 + CO \quad (3)$$

$$CO + O^{2-} + 2h^+ \rightarrow CO_2 \quad (4)$$

For Fe_2O_3, the opposite mechanism as for CuO is proposed, where under exposure to air the reaction towards adsorbed oxygen is the reduction in conductivity via the formation of a depletion layer at the Fe_2O_3 surface a lightly doped n-type semiconductor oxide following manner [21,40]:

$$O_2(gas) + 2e^- \rightarrow 2O^-(ad) \quad (5)$$

but after exposure to acetone vapor, gas molecules will react with the chemisorbed oxygen ions at the Fe_2O_3 nanospikes surface to form CO_2 and H_2O according to the following equation [21,40]:

$$CH_3COCH_3(gas) + 8O^-(ad) \rightarrow 3CO_2 + 3H_2O + 8e^- \quad (6)$$

Both of these mechanisms will lead to a p-n-junction formation at the interface of the CuO NWs and the Fe_2O_3 nanospikes, where at some connections, an additional resistance will be in place due to insufficient contacting between the two materials. When a p-n-junction at the interfaces between the p-type CuO and the n-type Fe_2O_3 is formed, a depletion region WD1 and an accumulation region WA1 will be present with the exposure of atmospheric O_2 (see Fig. S10 from the Supporting Information). The introduction of acetone leads to a reduction in both the accumulation layer of the CuO, as well as the depletion layer in Fe_2O_3. Additionally, acetone adsorbed at the interface between CuO and Fe_2O_3 increases the contact resistance. This might lead to an increase in the potential barrier at the interface of the two materials (see Fig. S10 from the Supporting Information), making the junctions resistance higher. An increase in resistance of the CuO will then lead to an increase in the overall resistance. Both Fe_2O_3 and CuO are responsive to VOCs, so in order to maximize the effect of the junctions, the number of junctions has to be maximized. The density of iron is slightly higher than that of iron and the average particle size of the iron is larger. The amount of particles in contact when mixed in a 1:1 wt ratio should be approximately equal. A higher tendency towards one particle system will change the mechanism more to the pure particle system and will not lead to a higher sensitivity based on the junction effect.

Aside from this, the increase of the operation temperature leads to both an increase in the intrinsic charge carrier concentrations for both materials and therefore an increased conductivity, as well as it provides more energy for crossing the potential barriers at the interface between the two materials.

5. Summary and outlook

A facile 3D-printing based fabrication of otherwise clean room dependent structures made of mixed metal microparticles for gas sensing applications was demonstrated for the first time. Printed Cu and Fe MPs with diameters of 45–60 µm and 15–25 µm, respectively, were mixed and the MPs formed bridging non-planar CuO/Cu_2O/Cu - Fe_2O_3/Fe nanostructures after thermal annealing at 425 °C for 4 h in air. The contacts touching at the interface between the particles showed a highly open porous structure, which is beneficial for gas sensing applications. Morphological, vibrational, chemical and structural investigations were performed in detail. The TEM study demonstrates the growth of defect rich CuO nanowires and Fe_2O_3 nanospikes, described with a modified Hematite structure which is possibly based on ordering of oxygen vacancies. The gas sensing measurements showed excellent selectivity to acetone vapor at an operating temperature of 300 °C with high gas response of 50%–100 ppm which occurred after an additional annealing step of 650 °C for 1 h. The power consumption was low at 0.26 µW. The combination of the possibility of fast acetone vapor detection and controllable size and geometry, makes these devices ideal candidates for fast detection, as well as acetone vapor monitoring (down to 1 ppm).

More generally the mixing of easily obtained metal micro particles, their macroscopic alignment in real sensor devices via printing and their interplay in the gas sensing opens new ways for other such sensor systems. This demonstration represents the ground work for 3D-printing of semiconducting oxides of both types' n- and p-conductivity with tunable properties as an alternative for clean room technology and microfabrication.

Declaration of conpeting interest

The authors declare that they have no known competing financial interests or personal relationships that could have appeared to influence the work reported in this paper.

Acknowledgements

This work was financially supported by the German Research Foundation (DFG) via the research unit FOR 2093 “Memristive devices for neuronal systems” through project A2, as well as within the CRC1261, gratefully acknowledged by NW and LK. LK thanks Prof. Bettina Lotsch from the Max Planck Institute for Solid State Research for enabling additional TEM measurements. Additional funding was provided under the project “Hot End” (grant number: 16KN021247), by the Federal ministry for Economic Affairs and Energy. This research was sponsored in part by the NATO Science for Peace and Security Programme (SPS) under grant G5634, “Advanced Electro-Optical Chemical Sensors” AMOXES. Dr. Oleg Lupan acknowledges the Alexander von Humboldt Foundation for the research fellowship for experienced researchers 3-3MOL/1148833 STP at the Institute for Materials Science, Kiel University, Germany. The authors would like to thank J. Bahr for the technical assistance and Prof. Tiginyanu for fruitful scientific discussions.

Appendix A. Supplementary data

Supplementary data to this article can be found online at https://doi.org/10.1016/j.nanoen.2019.104420.

References

[1] E. MacDonald, R. Wicker, Multiprocess 3D printing for increasing component functionality, Science 353 (2016), aaf2093, https://doi.org/10.1126/science.aaf2093.
[2] J.J. Schwartz, A.J. Boydston, Multimaterial actinic spatial control 3D and 4D printing, Nat. Commun. 10 (2019) 791, https://doi.org/10.1038/s41467-019-08639-7.
[3] M. Nadgorny, A. Ameli, Functional polymers and nanocomposites for 3D printing of smart structures and devices, ACS Appl. Mater. Interfaces 10 (2018) 17489–17507, https://doi.org/10.1021/acsami.8b01786.
[4] T.D. Ngo, A. Kashani, G. Imbalzano, K.T.Q. Nguyen, D. Hui, Additive manufacturing (3D printing): a review of materials, methods, applications and challenges, Compos. B Eng. 143 (2018) 172–196, https://doi.org/10.1016/j.compositesb.2018.02.012.
[5] Y. Xu, X. Wu, X. Guo, B. Kong, M. Zhang, X. Qian, S. Mi, W. Sun, The boom in 3D-printed sensor technology, Sensors 17 (2017) 1166, https://doi.org/10.3390/s17051166.
[6] G.I. Peterson, M.B. Larsen, M.A. Ganter, D.W. Storti, A.J. Boydston, 3D-Printed mechanochromic materials, ACS Appl. Mater. Interfaces 7 (2015) 577–583, https://doi.org/10.1021/am506745m.
[7] V. Saasa, T. Malwela, M. Beukes, M. Mokgotho, C.-P. Liu, B. Mwakikunga, Sensing technologies for detection of acetone in human breath for diabetes diagnosis and monitoring, Diagnostics 8 (2018) 12, https://doi.org/10.3390/diagnostics8010012.
[8] D. Smith, P. Španěl, A.A. Fryer, F. Hanna, G.A.A. Ferns, Can volatile compounds in exhaled breath be used to monitor control in diabetes mellitus? J. Breath Res. 5 (2011), 022001 https://doi.org/10.1088/1752-7155/5/2/022001.
[9] M.T. Rahman, R. Moser, H.M. Zbib, C.V. Ramana, R. Panat, 3D printed high performance strain sensors for high temperature applications, J. Appl. Phys. 123 (2018), 024501, https://doi.org/10.1063/1.4999076.
[10] L. Siebert, O. Lupan, M. Mirabelli, N. Ababii, M.-I. Terasa, S. Kaps, V. Cretu, A. Vahl, F. Faupel, R. Adelung, 3D-Printed chemiresistive sensor array on nanowire CuO/Cu2O/Cu heterojunction nets, ACS Appl. Mater. Interfaces 11 (2019) 25508–25515, https://doi.org/10.1021/acsami.9b04385.
[11] J.C. Anderson, Measuring breath acetone for monitoring fat loss: review, Obesity 23 (2015) 2327–2334, https://doi.org/10.1002/oby.21242.
[12] Z. Wang, C. Wang, Is breath acetone a biomarker of diabetes? A historical review on breath acetone measurements, J. Breath Res. 7 (2013), 037109, https://doi.org/10.1088/1752-7155/7/3/037109.
[13] C. Wang, A. Mbi, M. Shepherd, A study on breath acetone in diabetic patients using a cavity ringdown breath analyzer: exploring correlations of breath acetone with blood glucose and glycohemoglobin A1C, IEEE Sens. J. 10 (2010) 54–63, https://doi.org/10.1109/JSEN.2009.2035730.
[14] W.R. Rowley, C. Bezold, Y. Arikan, E. Byrne, S. Krohe, Diabetes 2030: insights from yesterday, today, and future trends, Popul. Health Manag. 20 (2017) 6–12, https://doi.org/10.1089/pop.2015.0181.
[15] J.H. Simmons, K.K. McFann, A.C. Brown, A. Rewers, D. Follansbee, R.E. Temple-Trujillo, G.J. Klingensmith, Reliability of the diabetes fear of injecting and self-testing questionnaire in pediatric patients with type 1 diabetes, Diabetes Care 30 (2007) 987–988, https://doi.org/10.2337/dc06-1553.
[16] D. Guo, D. Zhang, N. Li, L. Zhang, J. Yang, in: D. Zhang, M. Sonka (Eds.), Diabetes Identification and Classification by Means of a Breath Analysis System BT - Medical Biometrics, Springer Berlin Heidelberg, Berlin, Heidelberg, 2010, pp. 52–63.
[17] D. Zhang, D. Guo, K. Yan, A breath analysis system for diabetes screening and blood glucose level prediction, in: D. Zhang, D. Guo, K. Yan (Eds.), Breath Anal. Med. Appl., Springer Singapore, Singapore, 2017, pp. 259–279, https://doi.org/10.1007/978-981-10-4322-2_14.
[18] C. Sun, G. Maduraiveeran, P. Dutta, Nitric oxide sensors using combination of p- and n-type semiconducting oxides and its application for detecting NO in human breath, Sens. Actuators B Chem. 186 (2013) 117–125, https://doi.org/10.1016/j.snb.2013.05.090.
[19] C. Turner, C. Walton, S. Hoashi, M. Evans, Breath acetone concentration decreases with blood glucose concentration in type I diabetes mellitus patients during hypoglycaemic clamps, J. Breath Res. 3 (2009), 046004, https://doi.org/10.1088/1752-7155/3/4/046004.
[20] O. Lupan, V. Postica, J. Gröttrup, A.K. Mishra, N.H. de Leeuw, J.F.C. Carreira, J. Rodrigues, N. Ben Sedrine, M.R. Correia, T. Monteiro, V. Cretu, I. Tiginyanu, D. Smazna, Y.K. Mishra, R. Adelung, Hybridization of zinc oxide tetrapods for selective gas sensing applications, ACS Appl. Mater. Interfaces 9 (2017) 4084–4099, https://doi.org/10.1021/acsami.6b11337.
[21] O. Lupan, V. Postica, N. Wolff, O. Polonskyi, V. Duppel, V. Kaidas, E. Lazari, N. Ababii, F. Faupel, L. Kienle, R. Adelung, Localized synthesis of iron oxide nanowires and fabrication of high performance nanosensors based on a single Fe2O3 nanowire, Small 13 (2017) 1602868, https://doi.org/10.1002/smll.201602868.
[22] S. Park, H. Kheel, G.-J. Sun, T. Ko, W.I. Lee, C. Lee, Acetone gas sensing properties of a multiple-networked Fe2O3 -functionalized CuO nanorod sensor, J. Nanomater. 2015 (2015) 1–6, https://doi.org/10.1155/2015/830127.
[23] N. Ababii, M. Hoppe, S. Shree, A. Vahl, M. Ulfa, T. Pauporté, B. Viana, V. Cretu, N. Magariu, V. Postica, V. Sontea, M.-I. Terasa, O. Polonskyi, F. Faupel, R. Adelung, O. Lupan, Effect of noble metal functionalization and film thickness on sensing properties of sprayed TiO2 ultra-thin films, Sensors Actuators A Phys 293 (2019) 242–258, https://doi.org/10.1016/j.sna.2019.04.017.
[24] J.F. Moulder, J. Chastain, Handbook of X-ray Photoelectron Spectroscopy: A Reference Book of Standard Spectra for Identification and Interpretation of XPS Data, Illustrate, Physical Electronics Division, Perkin-Elmer Corporation, 1992. https://books.google.md/books?id=A_XGQgAACAAJ.
[25] A. Vahl, J. Dittmann, J. Jetter, S. Veziroglu, S. Shree, N. Ababii, O. Lupan, O. C. Aktas, T. Strunskus, E. Quandt, R. Adelung, S.K. Sharma, F. Faupel, The impact of O2/Ar ratio on morphology and functional properties in reactive sputtering of metal oxide thin films, Nanotechnology 30 (2019) 235603, https://doi.org/10.1088/1361-6528/ab0837.
[26] O. Lupan, V. Cretu, V. Postica, O. Polonskyi, N. Ababii, F. Schütt, V. Kaidas, F. Faupel, R. Adelung, Non-planar nanoscale p – p heterojunctions formation in ZnxCu1−xOy nanocrystals by mixed phases for enhanced sensors, Sens. Actuators B Chem. 230 (2016) 832–843, https://doi.org/10.1016/j.snb.2016.02.089.
[27] M. Hoppe, N. Ababii, V. Postica, O. Lupan, O. Polonskyi, F. Schütt, S. Kaps, L. F. Sukhodub, V. Sontea, T. Strunskus, F. Faupel, R. Adelung, (CuO-Cu2O)/ZnO:Al heterojunctions for volatile organic compound detection, Sens. Actuators B Chem. 255 (2018) 1362–1375, https://doi.org/10.1016/j.snb.2017.08.135.
[28] O. Lupan, L. Chow, T. Pauporté, L.K. Ono, B. Roldan Cuenya, G. Chai, Highly sensitive and selective hydrogen single-nanowire nanosensor, Sens. Actuators B Chem. 173 (2012) 772–780, https://doi.org/10.1016/j.snb.2012.07.111.
[29] O. Lupan, V. Cretu, V. Postica, N. Ababii, O. Polonskyi, V. Kaidas, F. Schütt, Y. K. Mishra, E. Monaico, I. Tiginyanu, V. Sontea, T. Strunskus, F. Faupel, R. Adelung, Enhanced ethanol vapour sensing performances of copper oxide nanocrystals with mixed phases, Sens. Actuators B Chem. 224 (2016) 434–448, https://doi.org/10.1016/j.snb.2015.10.042.
[30] Y. Shimizu, T. Maekawa, Y. Nakamura, M. Egashira, Effects of gas diffusivity and reactivity on sensing properties of thick film SnO2-based sensors, Sens. Actuators B Chem. 46 (1998) 163–168, https://doi.org/10.1016/S0925-4005(97)00247-5.
[31] N. Pauly, S. Tougaard, F. Yubero, Determination of the Cu 2p primary excitation spectra for Cu, Cu2O and CuO, Surf. Sci. 620 (2014) 17–22, https://doi.org/10.1016/j.susc.2013.10.009.
[32] O. Lupan, V. Postica, V. Cretu, N. Wolff, V. Duppel, L. Kienle, R. Adelung, Single and networked CuO nanowires for highly sensitive p-type semiconductor gas sensor applications, Phys. Status Solidi Rapid Res. Lett. 10 (2016) 260–266, https://doi.org/10.1002/pssr.201510414.
[33] J.P. Ngantcha, M. Gerland, Y. Kihn, A. Rivière, Correlation between microstructure and mechanical spectroscopy of a Cu-Cu2O alloy between 290 K and 873 K, Eur. Phys. J. Appl. Phys. 29 (2005) 83–89, https://doi.org/10.1051/epjap:2004200.
[34] T. Li, H. Feng, Y. Wang, C. Wang, W. Zhu, L. Yuan, G. Zhou, Formation of modulated structures induced by oxygen vacancies in α-Fe2O3 nanowires, J. Cryst. Growth 498 (2018) 10–16, https://doi.org/10.1016/j.jcrysgro.2018.05.031.
[35] P.A. Midgley, A.S. Eggeman, Precession electron diffraction – a topical review, IUCrJ 2 (2015) 126–136, https://doi.org/10.1107/S2052252514022283.
[36] Z. Chen, U. Cvelbar, M. Mozetič, J. He, M.K. Sunkara, Long-range ordering of oxygen-vacancy planes in α-Fe2O3 nanowires and nanobelts, Chem. Mater. 20 (2008) 3224–3228, https://doi.org/10.1021/cm800288y.

Cu_2O, but also appears peaks at A^1_g (227 cm^{-1}), E^1_g (246 cm^{-1}), E^2_g (297 cm^{-1}), E^3_g (408 cm^{-1}), A^2_g (498 cm^{-1}) and E^4_g (612 cm^{-1}), which are associated to α-Fe_2O_3 (Hematite) [20,21]. Intensity maps created by filtering the Raman modes A^1_g (227 cm^{-1}) and B^1_g (345 cm^{-1}) shown in Figure 4b-c illustrate the local distribution of the α-Fe_2O_3 (Hematite) and the CuO (Tenorite) phases represented by high intensity in Figure 4b and Figure 4c, respectively.

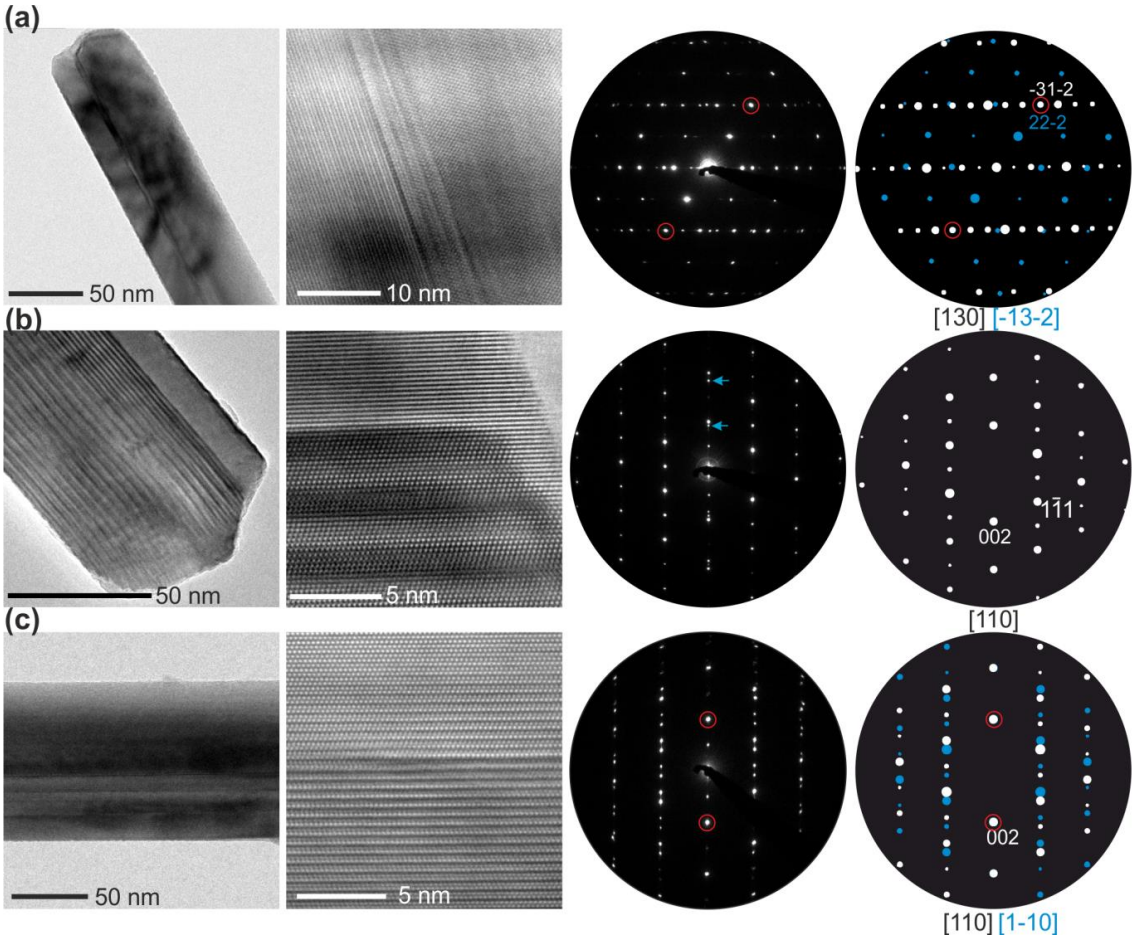

Figure S4. Structure of CuO nanowires: TEM image, high-resolution micrograph, precession electron diffraction pattern, simulation (from left to right). (a) Edge-on view onto an intergrowth boundary of - (31-2) and (22-2) planes of a two component CuO

nanowire. (b) Moirée contrast established by the superposition of two different orientated lattices due to structural intergrowth. The blue arrows in the PED pattern indicate the reflections belonging to a low order zone axis orientation of the second component. (c) Polysynthetic twinning on the (002) planes is observed parallel to the nanowire growth direction.

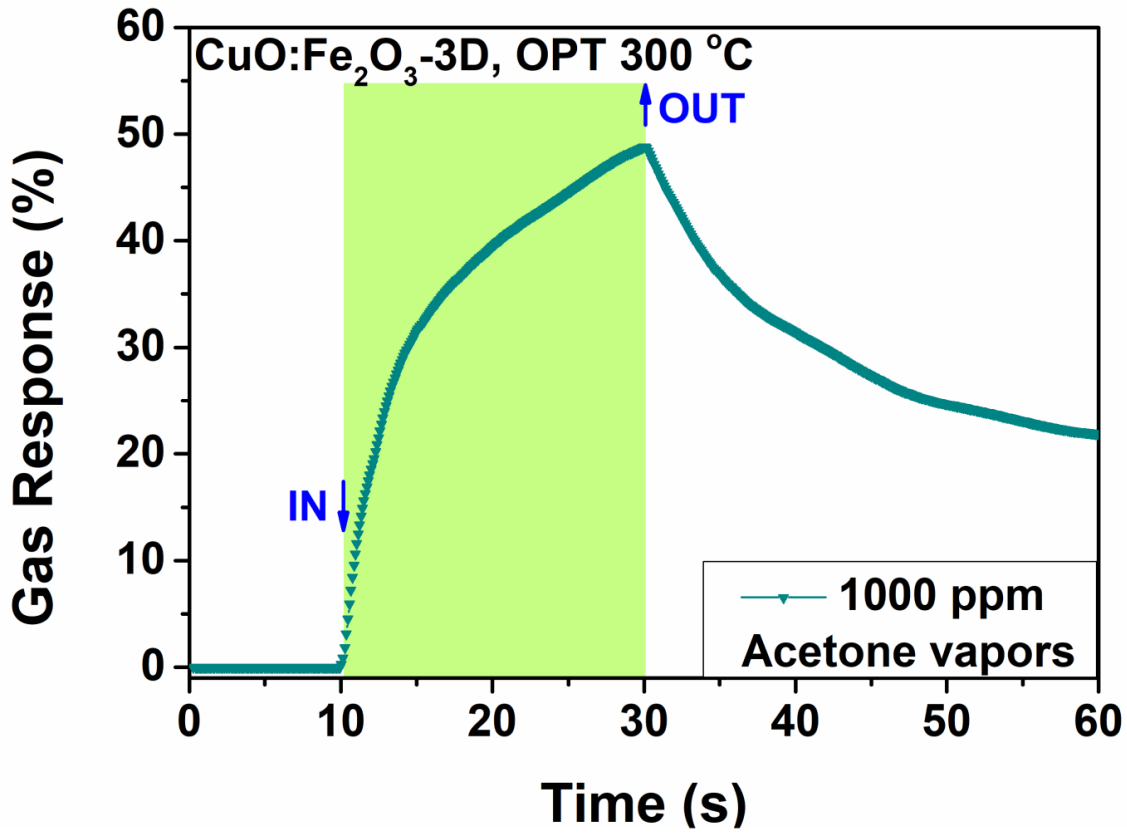

Figure S5. Dynamic response to 1000 ppm of acetone vapors of $CuO/Cu_2O/Cu$ and Fe_2O_3/Fe based sensor structure.

Chapter 6

Summary and Outlook

In the scope of this thesis, several material systems have been analyzed by transmission electron microscopy. In the first topical area, the samples are related to the framework of magnetoelectric composites for sensing biomagnetic fields and are divided into three groups:

1. Piezoelectric materials,
2. Magnetic materials,
3. Magnetoelectric sensors.

These studies are published in peer reviewed journals and have been discussed in Chapter 4 *Materials for Magnetoelectric Sensors*.
In a second topical area, the samples are related to the framework of detection of chemical species in gaseous atmosphere. The published articles are discussed in context of *Sensors for Breath Monitoring* in Chapter 5 and belong to two groups:

1. Hydrogen detection,
2. Acetone detection.

The results obtained in the first topical area highlight the fundamental research and further development of the piezoelectric and magnetostrictive phases to improve the sensitivity of ME sensors to small biomagnetic fields. The studies have been motivated in context of their specific application in cantilever-type ME or piezotronic-based ME sensors.
The results conclusively showed that the piezoelectric performance of AlN thin films is successfully improved by alloying Sc into the wurtzite-type structure up to $x_{Sc} = 0.43$, which is regarded as onset for the cubic phase transition. The piezoelectric properties were improved, such as the longitudinal piezoelectric coefficient $d_{33,f} = 15.7\,\mathrm{pm/V}$, the transverse thin film piezoelectric coefficient $e_{31,f} = 3.16\,\mathrm{C/m^2}$ by a factor of three and the dielectric permittivity by a factor of 2 at $x_{Sc} = 0.36$.[167], [169] The development of a lithographic compliant sputter deposition process was supported by structural investigations using TEM. Out-of-plane misoriented grains were identified to reduce the longitudinal piezoelectric film response and their density was reduced by changing the substrate and deposition geometry. The destabilization of the wurtzite-type structure was observed for high Sc concentrations evidencing the presence of the cubic phase. The discovery of ferroelectricity in these alloys could pave the way for new interesting design applications by replacing AlN in ME sensors. Here, conventional cantilever designs and SAW sensors will potentially benefit from this new development. However, a microscopy investigation of the introduced polarization inversion has not been feasible so far, but such experiments will be addressed using dedicated microscopes and techniques which require rarely available equipment.

Thin films of BCZT exhibit high effective piezo-coefficients and their crystal symmetry at the MPB was evidenced to be tetragonal with spacegroup P4*mm*.[185] A complicated defect structure was identified in BCZT and was described by supercell modeling. In addition, domains of cation ordering phenomena were identified, which might be related to the relaxor properties, but their complete description was not feasible with atomically resolved EDS and EELS methods due to the partial overlap of the analyzed energy levels. However, the implementation of BCZT thin films in ME sensor devices seems not viable with the commonly used fabrication processes. This is due to a high deposition temperature of 800 °C which is excluding the deposition of the magnetic layer in advance and the pulsed laser deposition method which is not compliant with standard MEMS processes on wafer level.

Piezotronic based ME sensors might have the potential to outperform magnetic or electric modulated ME sensor concepts if noise sources could be identified and reduced regarding the crystal quality and the semiconductor-metal interface. Various micro- and nanostructure morphologies of semiconductor ZnO[194] and GaN[209], [216] have been analyzed and lattice defects such as twins or inelastic deformations of the crystal structure have been identified using the combination of XRD and TEM. In case of ZnO nanostructures, a theoretic structure model of the observed twin interfaces was set up to discuss the nanostructure of these microneedles. Several strategies to improve the electric properties of ZnO microwires by doping or surface functionalization with metal and metal oxide nanoparticles have been subject of different studies. In case of Ga-doping, the ZnO surface was functionalized with gallium oxide species which showed large improvement in the conductivity of the ZnO microneedles, but no piezotronic measurements have been performed to study its impact.[193] In contrary, the surface functionalization with e.g. Au nanocrystals increases the intrinsic resistance by local space charge regions established at the ZnO/Au Schottky contacts and is modulated under external stimuli with gaseous species adsorbing on the ZnO surface which is rather beneficial for gas sensing (refer to **Chapter 5**).[197] The measurement of strain at such ZnO/Au interfaces showed neglectable lattice strains in the few surface layers of the ZnO lattice. GaN substrates grown by HVPE show intrinsic concentrically arranged electrical modulations originating from impurities and dislocation defects. Here, by means of polarization force microscopy the inversion of polarization direction could be evidenced at these electronic defect structures. Further, the valuable combination of electron diffraction and X-ray diffraction quantified an inelastic lattice deformation of the $P6_3mc$ wurtzite-type structure as a result of the rapid growth technique. In addition, complex hollow morphologies of GaN tubes with grown nanowhiskers on the interior walls have been analyzed with respect to their structure and composition. STEM tomography was applied to obtain a three-dimensional model of the nanostructure. The GaN walls of such micro- and nanotubes grow epitaxial onto a ZnO substrate and chemically stabilize ultra-thin layers of this ZnO after an hydrothermic etch.

The practical application of an *in situ* straining platform which is usable with a conventional heating holder for the TEM was demonstrated.[153] The conducted experiments describe tensile tests on a ZnO entangled tetrapodal network observing elastic deformations of individual tetrapod arms and on a nanocrystalline Au film observing the evolution of polycrystalline texture with applied strain. More robust designs of the presented concept could potentially be used for designing *in situ* electromechanical measurement experiments or to investigate the deformation characteristics in two-dimensional materials. If the dimensions of a material are reduced new properties could arise since the spacious confinement enhances

the significance of structure related properties or defects to e.g. the electronic structure, determining the electric and optical properties. One class of materials in which downscaling to 2D introduces a measurable in-plane piezoelectric effect are few-layer TMDs such as $MoSe_2$. Here, the interlayer bonding strength in 8-layer $MoSe_2$ films by a weak van der Waals-type bonding was analyzed by plan-view TEM and a FFT study to investigate the degree of order between layers on the nanoscale promoting an ultra-low thermal conductivity across the layers.[226]

Materials for the magnetostrictive phase of the ME sensors usually are amorphous Fe-based metallic glasses. To analyze and evaluate changes in the short-range order after thermal treatment a novel technique based on nanobeam electron diffraction was tested and applied (Section 3.3). By performing a hyperspectral analysis this 4D STEM technique allows to display small differences in the atomic environment by mapping them out with nanometer resolution. In the FeCoSiB film such differences in the radial distribution function could be evidenced close to interfaces and by local changes in the chemical environment.
The micro- and nanostructure of magnetostrictive mulitlayers of FeCo/TiN with fairly high temperature stability up to 600 °C have been studied using aberration corrected HRTEM and HRSTEM. Structural models have been designed on basis of the atomic scale observations to describe the average structure information obtained by electron diffraction experiments. In this respect, geometric phase analysis has been useful to demonstrate and analyze the epitaxial strain resulting in pseudomorphic in-plane and out-of-plane lattice deformation of the FeCo unit cell.This lattice deformation results in the nanostabilization of tetragonal distorted variants of FeCo which can modify the targeted magnetic properties of the film. In perspective of potential future exchange-bias designs, the FeNi/MnIr layer system used in the exchange spring concept was subject of a microscopy study concentrating on HRSTEM and nanobeam electron diffraction. The investigation demonstrated that the layers grow columnar, twinning occurs within layers and at interfaces and that grains with different rotation along a common [001] axis can be found inside a differently oriented matrix.

TEM studies on composites for ME sensors have been conducted in detail on a new sensor concept based on the delta-E effect.That relies on frequency tuning of the resonance by an shape memory alloy substrate TiNiCu, which changes its elastic modulus depending on the volume ratio of martensite to austenite phase. Here, the microstructure of the whole sensor stack was investigated for two different annealing processes and interdiffusion of the TiNiCu/Ta/Pt interface was observed and described by theoretic assumptions based on thermodynamics and kinetics. The studies have been compared with freestanding structures in which the Si substrate was dissolved. Here, a layer of amorphous TiNiCu was evidenced at the interfaces to the Ta-electrodes which is unable to contribute to the shape memory properties.

To proceed the development of low noise and high sensitive ME sensors for biomedical diagnostics further research on the individual sensor approaches, the signal processing and device integration have to be performed together with materials research. The development of AlScN which will be exploited in upcoming sensors is a direct product of material research and its understanding is supported by analytical methods such as TEM and XRD. The sensor integration of AlScN films can potentially outperform AlN-based sensor concepts in terms of sensitivity and has to be experimentally confirmed. This example demonstrates that materials research is necessary even at advanced stages of sensor development and that new approaches such as the SAW-sensor or the piezotronic read out should be explored to

investigate their fundamental noise limits. The presented methods of transmission electron microscopy can support materials research in the most fundamental way of understanding the materials nanostructure in relation to its properties. In this respect, the presented 4D STEM RDF mapping technique will be further exploited to analyze the impact of temperature on the chemical environment in amorphous magnetostrictive films of FeCoSiB used as single layer or exchange bias system in nearly all ME sensor approaches. Of high interest is the Boron distribution which will be mapped out by EFTEM in connection with spatially resolved EELS data.
Additionally, fundamental research on the TMD materials for application in piezotronic based devices will be supported by structural investigation of their response to strain by design of a special functional grid geometry introducing torsion. However, all material studies should be accompanied by the support of experimental sensor data to relate the macroscopic function to the individual materials contribution.

To conclude, the recently achieved sensitivity and frequency bandwidth of the developed ME sensor approaches is displayed in Figure 6.1. The present level of sensitivity does not display the capability of the ME sensors to be suitable at the moment for the envisioned medical applications. But the promising results displayed in this graph provide chance for further improvement by optimizing the measurement parameters, the materials and the signal processing routines. On the material side, TEM can be used to study temperature induced short-range order phenomena in amorphous ferromagnets, structural defects, strain and atomic structure at interfaces and direction of polarization, as described in this thesis. So far, the electrically modulated ME sensors reach the highest sensitivity over a broad frequency regime and are on the onset of biomagnetic signals form the heart. If further development can gain one to two orders of magnitude with this approach and also with the SAW or delta-E effect approaches the application of biomagnetic measurements in MCG and DBS are feasible. Until now, a heart rate monitoring of the strongest R-wave of the QRS-complex of the human heart is practicable.[308]

For the development of sensors for medical monitoring via the breath, several studies have been presented on selected materials for hydrogen as well as acetone detection. The medical need and application has been reviewed, e.g. the relevance for diabetic patients to measure their blood glucose level which is related to the breath acetone. In this regard, the surface functionalization of ZnO has been studied by TEM and the influence on the hydrogen gas sensing properties was tested.[197], [198] The major critical aspect of these studies is the direct observation of the interface between the ZnO structure and the grown nanocrystals which requires precise sample tilting into specific zone axis conditions. For acetone sensing, iron and copper oxides have been studied with TEM and their defect structure was described evaluating PED data. A new ink writing technique to directly write those oxides on a glass slides or flexible substrates was demonstrated with cooperation partners.[292], [306] Further improvement of the breath sensors with regard to their targeted gas sensing application can be obtained with research putting the focus on the type of surface functionalization. For example, ZnO materials functionalized with Pd-species showed high performances to hydrogen gas whereas functionalization with Au resulted in excellent selectivity. So future research might be directed towards multicomponent surface functionalizations, where a major role is denoted to chemical and structural analysis. In perspective to new materials, layered

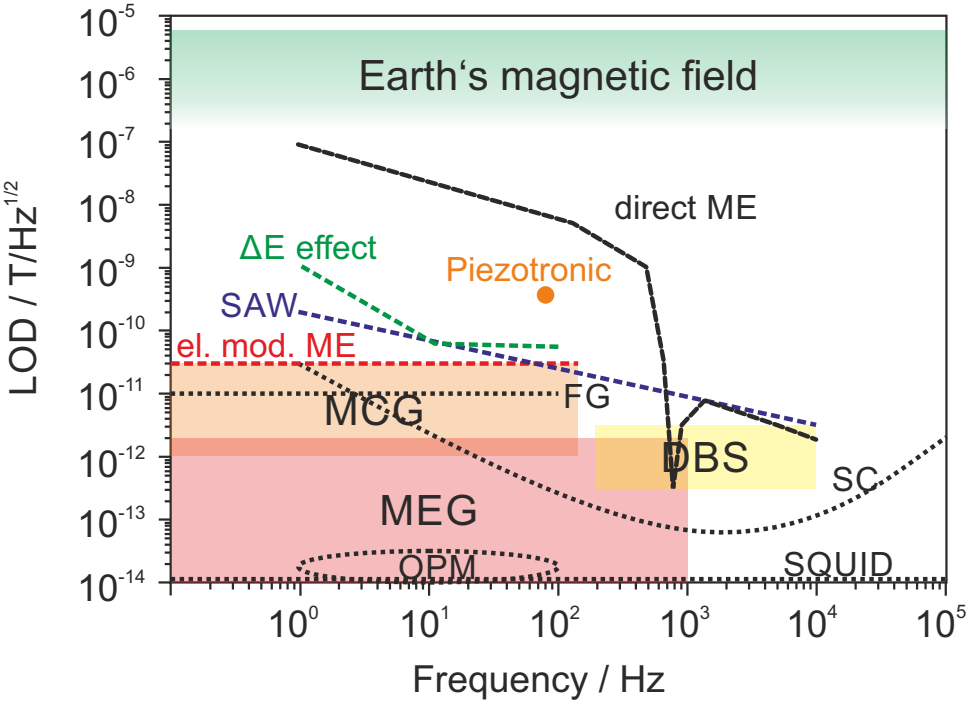

FIGURE 6.1: Schematic showing the magnetic sensitivity as a function of frequency for various biomedical applications and the detection limits of common magnetometers and ME sensor approaches. (Biomedical application: *MCG = magnetocardiography, MEG = magnetoencephalography, DBS = deep brain stimulation.* Magnetometers: *SQUID = superconducting quantum interference devices, OPM = optically pumped magnetometer, FG = fluxgate, SC = search coil*) ME sensors: *direct ME[22], SAW = surface acoustic wave[58], electric modulated ME[54],* ΔE – effect[36], [68]

TMDs have demonstrated their gas sensing capabilities to ammonium or nitric oxides as well providing small limits of detection and high gas responses.[309] However, the gas sensing field of TMDs is still a black box and offers endless opportunities for the materials scientists to investigate their response to different analyte gases. Herein, the role of the material itself, the number of single layers, the architecture of TMD layered composites, intentionally or unintentionally produced defects, intercalation of foreign atoms and hybridization with metal oxides on the surface are not investigated yet.

Bibliography

[1] W. Einthoven, "Die galvanometrische Registrirung des menschlichen Elektrokardiogramms, zugleich eine Beurtheilung der Anwendung des Capillar-Elektrometers in der Physiologie", *Pflügers Archiv European Journal of Physiology*, vol. 99, no. 9, pp. 472–480, 1903.

[2] S. S. Barold, "Willem Einthoven and the birth of clinical electrocardiography a hundred years ago", *Cardiac electrophysiology review*, vol. 7, no. 1, pp. 99–104, 2003.

[3] J. Zimmerman, P. Thiene, and J. Harding, "Design and operation of stable rf-biased superconducting point-contact quantum devices, and a note on the properties of perfectly clean metal contacts", *Journal of Applied Physics*, vol. 41, no. 4, pp. 1572–1580, 1970.

[4] D. Cohen, E. A. Edelsack, and J. E. Zimmerman, "Magnetocardiograms taken inside a shielded room with a superconducting point-contact magnetometer", *Applied Physics Letters*, vol. 16, no. 7, pp. 278–280, 1970.

[5] D. Cohen, "Magnetoencephalography: Detection of the brain's electrical activity with a superconducting magnetometer", *Science*, vol. 175, no. 4022, pp. 664–666, 1972.

[6] P. Ripka, "Advances in fluxgate sensors", *Sensors and Actuators A: Physical*, vol. 106, no. 1-3, pp. 8–14, 2003.

[7] C. Coillot, J. Moutoussamy, R. Lebourgeois, S. Ruocco, and G. Chanteur, "Principle and performance of a dual-band search coil magnetometer: A new instrument to investigate fluctuating magnetic fields in space", *IEEE Sensors Journal*, vol. 10, no. 2, pp. 255–260, 2009.

[8] T. M. Tierney, N. Holmes, S. Mellor, J. D. López, G. Roberts, R. M. Hill, E. Boto, J. Leggett, V. Shah, M. J. Brookes, *et al.*, "Optically pumped magnetometers: From quantum origins to multi-channel magnetoencephalography", *NeuroImage*, 2019.

[9] I. Kominis, T. Kornack, J. Allred, and M. V. Romalis, "A sub-femtotesla multichannel atomic magnetometer", *Nature*, vol. 422, no. 6932, pp. 596–599, 2003.

[10] T. Kornack, S. Smullin, S.-K. Lee, and M. V. Romalis, "A low-noise ferrite magnetic shield", *Applied physics letters*, vol. 90, no. 22, p. 223 501, 2007.

[11] L. Lu, J. Shang, Z. Pan, and Y. Ji, "Chip-scale SERF atomic magnetometer without magnetic shield", in *2017 IEEE 67th Electronic Components and Technology Conference (ECTC)*, IEEE, 2017, pp. 1900–1905.

[12] A. Gusarov, D. Levron, E. Paperno, R. Shuker, and A. B.-A. Baranga, "Three-dimensional magnetic field measurements in a single SERF atomic-magnetometer cell", *IEEE Transactions on Magnetics*, vol. 45, no. 10, pp. 4478–4481, 2009.

[13] J. Clarke and A. I. Braginski, *The SQUID handbook*. Wiley Online Library, 2004, vol. 1.

[14] Y. Liu, J. Guo, A. Yu, Y. Zhang, J. Kou, K. Zhang, R. Wen, Y. Zhang, J. Zhai, and Z. L. Wang, "Magnetic-induced-piezopotential gated MoS_2 field-effect transistor at room temperature", *Advanced Materials*, vol. 30, no. 8, p. 1 704 524, 2018.

[15] M. Fiebig, "Revival of the magnetoelectric effect", *Journal of Physics D: Applied Physics*, vol. 38, no. 8, R123, 2005.

[16] W. Eerenstein, N. Mathur, and J. F. Scott, "Multiferroic and magnetoelectric materials", *nature*, vol. 442, no. 7104, p. 759, 2006.

[17] W. Borchardt-Ott, *Kristallographie*. Springer, 2002, vol. 5.

[18] F. Martin, P. Muralt, M.-A. Dubois, and A. Pezous, "Thickness dependence of the properties of highly c-axis textured AlN thin films", *Journal of Vacuum Science & Technology A: Vacuum, Surfaces, and Films*, vol. 22, no. 2, pp. 361–365, 2004.

[19] D. M. Kim, C.-B. Eom, V. Nagarajan, J. Ouyang, R. Ramesh, V. Vaithyanathan, and D. G. Schlom, "Thickness dependence of structural and piezoelectric properties of epitaxial $Pb_(Zr_{0.52}Ti_{0.48})O_3$ films on Si and $SrTiO_3$ substrates", *Applied physics letters*, vol. 88, no. 14, p. 142 904, 2006.

[20] L. Lian and N. R. Sottos, "Effects of thickness on the piezoelectric and dielectric properties of lead zirconate titanate thin films", *Journal of Applied Physics*, vol. 87, no. 8, pp. 3941–3949, 2000.

[21] J. Zhao, H. Lu, J. Sun, and B. Shen, "Thickness dependence of piezoelectric property of ultrathin $BiFeO_3$ films", *Physica B: Condensed Matter*, vol. 407, no. 12, pp. 2258–2261, 2012.

[22] E. Yarar, V. Hrkac, C. Zamponi, A. Piorra, L. Kienle, and E. Quandt, "Low temperature aluminum nitride thin films for sensory applications", *AIP Advances*, vol. 6, no. 7, p. 075 115, 2016.

[23] K.-I. Park, S. Xu, Y. Liu, G.-T. Hwang, S.-J. L. Kang, Z. L. Wang, and K. J. Lee, "Piezoelectric $BaTiO_3$ thin film nanogenerator on plastic substrates", *Nano letters*, vol. 10, no. 12, pp. 4939–4943, 2010.

[24] C. Guo, H. Zou, S. Pu, M. Li, and J. Cao, "Polarity determination of ferroelectric $LiNbO_3$ crystals and $BiFeO_3$ thin films by the convergent beam electron diffraction technique", *Materials Characterization*, vol. 61, no. 9, pp. 859–865, 2010.

[25] N. Ledermann, P. Muralt, J. Baborowski, S. Gentil, K. Mukati, M. Cantoni, A. Seifert, and N. Setter, "{1 0 0}-textured, piezoelectric $Pb(Zr_xTi_{1-x})O_3$ thin films for MEMS: Integration, deposition and properties", *Sensors and Actuators A: Physical*, vol. 105, no. 2, pp. 162–170, 2003.

[26] N. Sama, C. Soyer, D. Remiens, C. Verrue, and R. Bouregba, "Bottom and top electrodes nature and PZT film thickness influence on electrical properties", *Sensors and Actuators A: Physical*, vol. 158, no. 1, pp. 99–105, 2010.

[27] S. Marauska, R. Jahns, C. Kirchhof, M. Claus, E. Quandt, R. Knöchel, and B. Wagner, "Highly sensitive wafer-level packaged MEMS magnetic field sensor based on magnetoelectric composites", *Sensors and Actuators A: Physical*, vol. 189, pp. 321–327, 2013.

[28] M. Akiyama, T. Kamohara, K. Kano, A. Teshigahara, Y. Takeuchi, and N. Kawahara, "Enhancement of piezoelectric response in scandium aluminum nitride alloy thin films prepared by dual reactive co-sputtering", *Advanced Materials*, vol. 21, no. 5, pp. 593–596, 2009.

[29] A. Piorra, A. Petraru, H. Kohlstedt, M. Wuttig, and E. Quandt, "Piezoelectric properties of $0.5(Ba_{0.70}Ca_{0.3}TiO_3)$–$0.5[Ba(Zr_{0.2}Ti_{0.8})O_3]$ ferroelectric lead-free laser deposited thin films", *Journal of Applied Physics*, vol. 109, no. 10, p. 104 101, 2011.

[30] C. Koops, S. Hrkac, M. Abes, P. Jordt, J. Stettner, A. Petraru, H. Kohlstedt, V. Hrkac, N. Wolff, L. Kienle, *et al.*, "Elastic coupling at epitaxial multiferroic interfaces: In situ X-ray studies of electric field induced strain", in *International Conference on Nanotechnologies and Biomedical Engineering*, Springer, 2019, pp. 187–191.

[31] Y. Wang, D. Gray, D. Berry, J. Gao, M. Li, J. Li, and D. Viehland, "An extremely low equivalent magnetic noise magnetoelectric sensor", *Advanced Materials*, vol. 23, no. 35, pp. 4111–4114, 2011.

[32] E. Quandt, S. Stein, and M. Wuttig, "Magnetic vector field sensor using magnetoelectric thin-film composites", *IEEE transactions on magnetics*, vol. 41, no. 10, pp. 3667–3669, 2005.

[33] J. Ryu, A. V. Carazo, K. Uchino, and H.-E. Kim, "Magnetoelectric properties in piezoelectric and magnetostrictive laminate composites", *Japanese Journal of Applied Physics*, vol. 40, no. 8R, p. 4948, 2001.

[34] S. Hrkac, M. Abes, C. Koops, C. Krywka, M. Müller, S. Kaps, R. Adelung, J. McCord, E. Lage, E. Quandt, *et al.*, "Local magnetization and strain in single magnetoelectric microrod composites", *Applied Physics Letters*, vol. 103, no. 12, p. 123 111, 2013.

[35] M. Jovičević Klug, L. Thormählen, V. Röbisch, S. Toxværd, M. Höft, R. Knöchel, E. Quandt, D. Meyners, and J. McCord, "Antiparallel exchange biased multilayers for low magnetic noise magnetic field sensors", *Applied Physics Letters*, vol. 114, no. 19, p. 192 410, 2019.

[36] S. Salzer, V. Röbisch, M. Klug, P. Durdaut, J. McCord, D. Meyners, J. Reermann, M. Höft, and R. Knöchel, "Noise limits in thin-film magnetoelectric sensors with magnetic frequency conversion", *IEEE Sensors Journal*, vol. 18, no. 2, pp. 596–604, 2017.

[37] A. t. Clark and H. Belson, "Giant room-temperature magnetostrictions in $TbFe_2$ and $DyFe_2$", *Physical Review B*, vol. 5, no. 9, p. 3642, 1972.

[38] D. Forester, C. Vittoria, J. Schelleng, and P. Lubitz, "Magnetostriction of amorphous Tb_xFe_{1-x} thin films", *Journal of Applied Physics*, vol. 49, no. 3, pp. 1966–1968, 1978.

[39] F. Schatz, M. Hirscher, M. Schnell, G. Flik, and H. Kronmüller, "Magnetic anisotropy and giant magnetostriction of amorphous TbDyFe films", *Journal of applied physics*, vol. 76, no. 9, pp. 5380–5382, 1994.

[40] E. Quandt and A. Ludwig, "Giant magnetostrictive multilayers", *Journal of applied physics*, vol. 85, no. 8, pp. 6232–6237, 1999.

[41] H. Greve, E. Woltermann, H.-J. Quenzer, B. Wagner, and E. Quandt, "Giant magnetoelectric coefficients in $(Fe_{90}Co_{10})_{78}Si_{12}B_{10}$-AlN thin film composites", *Applied Physics Letters*, vol. 96, no. 18, p. 182 501, 2010.

[42] R. O'handley, "Magnetostriction of ferromagnetic metallic glasses", *Solid State Communications*, vol. 21, no. 12, pp. 1119–1122, 1977.

[43] J. Lou, R. Insignares, Z. Cai, K. S. Ziemer, M. Liu, and N. X. Sun, "Soft magnetism, magnetostriction, and microwave properties of FeGaB thin films", *Applied Physics Letters*, vol. 91, no. 18, p. 182 504, 2007.

[44] T. Nan, Y. Hui, M. Rinaldi, and N. X. Sun, "Self-biased 215MHz magnetoelectric NEMS resonator for ultra-sensitive DC magnetic field detection", *Scientific reports*, vol. 3, p. 1985, 2013.

[45] J. Lou, M. Liu, D. Reed, Y. Ren, and N. X. Sun, "Giant electric field tuning of magnetism in novel multiferroic FeGaB/Lead Zinc Niobate–Lead Titanate (PZN-PT) heterostructures", *Advanced Materials*, vol. 21, no. 46, pp. 4711–4715, 2009.

[46] E. Lage, C. Kirchhof, V. Hrkac, L. Kienle, R. Jahns, R. Knöchel, E. Quandt, and D. Meyners, "Exchange biasing of magnetoelectric composites", *Nature materials*, vol. 11, no. 6, p. 523, 2012.

[47] M. Jovičević Klug, *Methodological reduction of magnetically induced noise in magnetic multilayers for sensor applications*, 2019.

[48] E. Yarar, S. Salzer, V. Hrkac, A. Piorra, M. Höft, R. Knöchel, L. Kienle, and E. Quandt, "Inverse bilayer magnetoelectric thin film sensor", *Applied Physics Letters*, vol. 109, no. 2, p. 022 901, 2016.

[49] S. Pawar, A. Kumar, K. Singh, and D. Kaur, "High magnetoelectric coupling in Si-integrated AlN/NiMnIn thin film double layers at room temperature", *Applied Physics Letters*, vol. 113, no. 24, p. 242 902, 2018.

[50] J. Zhai, S. Dong, Z. Xing, J. Li, and D. Viehland, "Giant magnetoelectric effect in metglas/polyvinylidene-fluoride laminates", *Applied Physics Letters*, vol. 89, no. 8, p. 083 507, 2006.

[51] C.-S. Park, A. Khachaturyan, and S. Priya, "Giant magnetoelectric coupling in laminate thin film structure grown on magnetostrictive substrate", *Applied Physics Letters*, vol. 100, no. 19, p. 192 904, 2012.

[52] C. Cibert, J. Zhu, G. Poullain, R. Bouregba, J. More-Chevalier, and A. Pautrat, "Magneto-electric coupling in $Tb_{0.3}Dy_{0.7}Fe_2/Pt/PbZr_{0.56}Ti_{0.44}O_3$ thin films deposited on $Pt/TiO_2/SiO_2/Si$ substrate", *Applied Physics Letters*, vol. 102, no. 2, p. 022 906, 2013.

[53] R. Jahns, H. Greve, E. Woltermann, E. Quandt, and R. Knöchel, "Sensitivity enhancement of magnetoelectric sensors through frequency-conversion", *Sensors and Actuators A: Physical*, vol. 183, pp. 16–21, 2012.

[54] P. Hayes, M. J. Klug, S. Toxværd, P. Durdaut, V. Schell, A. Teplyuk, D. Burdin, A. Winkler, R. Weser, Y. Fetisov, *et al.*, "Converse magnetoelectric composite resonator for sensing small magnetic fields", *Scientific reports*, vol. 9, no. 1, pp. 1–10, 2019.

[55] P. Hayes, V. Schell, S. Salzer, D. Burdin, E. Yarar, A. Piorra, R. Knöchel, Y. Fetisov, and E. Quandt, "Electrically modulated magnetoelectric AlN/FeCoSiB film composites for DC magnetic field sensing", *Journal of Physics D: Applied Physics*, vol. 51, no. 35, p. 354 002, 2018.

[56] R. Jahns, S. Zabel, S. Marauska, B. Gojdka, B. Wagner, R. Knöchel, R. Adelung, and F. Faupel, "Microelectromechanical magnetic field sensor based on Δ-E effect", *Applied Physics Letters*, vol. 105, no. 5, p. 052 414, 2014.

[57] B. Gojdka, R. Jahns, K. Meurisch, H. Greve, R. Adelung, E. Quandt, R. Knöchel, and F. Faupel, "Fully integrable magnetic field sensor based on delta-E effect", *Applied Physics Letters*, vol. 99, no. 22, p. 223 502, 2011.

[58] A. Kittmann, P. Durdaut, S. Zabel, J. Reermann, J. Schmalz, B. Spetzler, D. Meyners, N. X. Sun, J. McCord, M. Gerken, *et al.*, "Wide band low noise love wave magnetic field sensor system", *Scientific reports*, vol. 8, no. 1, p. 278, 2018.

[59] C. Tu, Z.-Q. Chu, B. Spetzler, P. Hayes, C.-Z. Dong, X.-F. Liang, H.-H. Chen, Y.-F. He, Y.-Y. Wei, I. Lisenkov, *et al.*, "Mechanical-resonance-enhanced thin-film magnetoelectric heterostructures for magnetometers, mechanical antennas, tunable RF inductors, and filters", *Materials*, vol. 12, no. 14, p. 2259, 2019.

[60] J. Gröttrup, S. Kaps, J. Carstensen, D. Smazna, Y. K. Mishra, A. Piorra, C. Kirchhof, E. Quandt, and R. Adelung, "Piezotronic-based magnetoelectric sensor: Fabrication and response", *physica status solidi (a)*, vol. 213, no. 8, pp. 2208–2215, 2016.

[61] M. Mintken, M. Schweichel, S. Schröder, S. Kaps, J. Carstensen, Y. K. Mishra, T. Strunskus, F. Faupel, and R. Adelung, "Nanogenerator and piezotronic inspired concepts for energy efficient magnetic field sensors", *Nano energy*, vol. 56, pp. 420–425, 2019.

[62] A. Ludwig and E. Quandt, "Optimization of the Delta-E effect in thin films and multilayers by magnetic field annealing", *IEEE transactions on magnetics*, vol. 38, no. 5, pp. 2829–2831, 2002.

[63] B. Spetzler, C. Kirchhof, J. Reermann, P. Durdaut, M. Höft, G. Schmidt, E. Quandt, and F. Faupel, "Influence of the quality factor on the signal to noise ratio of magnetoelectric sensors based on the delta-E effect", *Applied Physics Letters*, vol. 114, no. 18, p. 183 504, 2019.

[64] P. Durdaut, J. Reermann, S. Zabel, C. Kirchhof, E. Quandt, F. Faupel, G. Schmidt, R. Knöchel, and M. Höft, "Modeling and analysis of noise sources for thin-film magnetoelectric sensors based on the delta-E effect", *IEEE Transactions on Instrumentation and Measurement*, vol. 66, no. 10, pp. 2771–2779, 2017.

[65] N. Weigman, "Barkhausen effect in magnetic thin films: Experimental noise spectra", *Applied physics*, vol. 12, no. 2, pp. 157–161, 1977.

[66] C. Tsang and S. Decker, "The origin of barkhausen noise in small permalloy magnetoresistive sensors", *Journal of Applied Physics*, vol. 52, no. 3, pp. 2465–2467, 1981.

[67] B. Spetzler, E. V. Golubeva, C. Müller, J. McCord, and F. Faupel, "Frequency dependency of the Delta-E effect and the sensitivity of delta-e effect magnetic field sensors", *Sensors*, vol. 19, no. 21, p. 4769, 2019.

[68] S. Zabel, J. Reermann, S. Fichtner, C. Kirchhof, E. Quandt, B. Wagner, G. Schmidt, and F. Faupel, "Multimode delta-E effect magnetic field sensors with adapted electrodes", *Applied Physics Letters*, vol. 108, no. 22, p. 222 401, 2016.

[69] B. Spetzler, C. Kirchhof, E. Quandt, J. McCord, and F. Faupel, "Magnetic sensitivity of bending-mode Delta-E-effect sensors", *Physical Review Applied*, vol. 12, no. 6, p. 064 036, 2019.

[70] Y. Zhang, Y. Liu, and Z. L. Wang, "Fundamental theory of piezotronics", *Advanced Materials*, vol. 23, no. 27, pp. 3004–3013, 2011.

[71] P. Voyles, D. Muller, J. Grazul, P. Citrin, and H.-J. Gossmann, "Atomic-scale imaging of individual dopant atoms and clusters in highly n-type bulk Si", *Nature*, vol. 416, no. 6883, p. 826, 2002.

[72] N. Shibata, S. Findlay, S. Azuma, T. Mizoguchi, T. Yamamoto, and Y. Ikuhara, "Atomic-scale imaging of individual dopant atoms in a buried interface", *Nature materials*, vol. 8, no. 8, pp. 654–658, 2009.

[73] I. Tiginyanu, T. Braniste, D. Smazna, M. Deng, F. Schütt, A. Schuchardt, M. A. Stevens-Kalceff, S. Raevschi, U. Schürmann, L. Kienle, *et al.*, "Self-organized and self-propelled aero-GaN with dual hydrophilic-hydrophobic behaviour", *Nano energy*, vol. 56, pp. 759–769, 2019.

[74] C. Kirchhof, M. Krantz, I. Teliban, R. Jahns, S. Marauska, B. Wagner, R. Knöchel, M. Gerken, D. Meyners, and E. Quandt, "Giant magnetoelectric effect in vacuum", *Applied Physics Letters*, vol. 102, no. 23, p. 232 905, 2013.

[75] G. Korotcenkov, "Metal oxides for solid-state gas sensors: What determines our choice?", *Materials Science and Engineering: B*, vol. 139, no. 1, pp. 1–23, 2007.

[76] N. Yamazoe, G. Sakai, and K. Shimanoe, "Oxide semiconductor gas sensors", *Catalysis Surveys from Asia*, vol. 7, no. 1, pp. 63–75, 2003.

[77] N. Yamazoe, "New approaches for improving semiconductor gas sensors", *Sensors and Actuators B: Chemical*, vol. 5, no. 1-4, pp. 7–19, 1991.

[78] C. Xu, J. Tamaki, N. Miura, and N. Yamazoe, "Grain size effects on gas sensitivity of porous SnO_2-based elements", *Sensors and Actuators B: Chemical*, vol. 3, no. 2, pp. 147–155, 1991.

[79] N. Yamazoe and K. Shimanoe, "Receptor function and response of semiconductor gas sensor", *Journal of sensors*, vol. 2009, 2009.

[80] S. Kurtin, T. McGill, and C. Mead, "Fundamental transition in the electronic nature of solids", *Physical Review Letters*, vol. 22, no. 26, p. 1433, 1969.

[81] V. E. Henrich and P. A. Cox, *The surface science of metal oxides*. Cambridge university press, 1996.

[82] G. Korotcenkov, V. Brinzari, V. Golovanov, and Y. Blinov, "Kinetics of gas response to reducing gases of SnO_2 films, deposited by spray pyrolysis", *Sensors and Actuators B: Chemical*, vol. 98, no. 1, pp. 41–45, 2004.

[83] D. Kohl, "The role of noble metals in the chemistry of solid-state gas sensors", *Sensors and Actuators B: Chemical*, vol. 1, no. 1-6, pp. 158–165, 1990.

[84] G. Korotcenkov, V. Brinzari, J. R. Stetter, I. Blinov, and V. Blaja, "The nature of processes controlling the kinetics of indium oxide-based thin film gas sensor response", *Sensors and Actuators B: Chemical*, vol. 128, no. 1, pp. 51–63, 2007.

[85] V. Hrkac, N. Wolff, V. Duppel, I. Paulowicz, R. Adelung, Y. K. Mishra, and L. Kienle, "Atomic structure and crystallography of joints in SnO_2 nanowire networks", *Applied Microscopy*, vol. 49, no. 1, p. 1, 2019.

[86] V. Hrkac, L. Kienle, S. Kaps, A. Lotnyk, Y. K. Mishra, U. Schuermann, V. Duppel, B. V. Lotsch, and R. Adelung, "Superposition twinning supported by texture in ZnO nanospikes", *Journal of Applied Crystallography*, vol. 46, no. 2, pp. 396–403, 2013.

[87] O. Lupan, V. Postica, M. Hoppe, N. Wolff, O. Polonskyi, T. Pauporté, B. Viana, O. Majérus, L. Kienle, F. Faupel, *et al.*, "PdO/PdO_2 functionalized ZnO: Pd films for lower operating temperature H_2 gas sensing", *Nanoscale*, vol. 10, no. 29, pp. 14 107–14 127, 2018.

[88] O. Lupan, N. Wolff, V. Postica, T. Braniste, I. Paulowicz, V. Hrkac, Y. K. Mishra, I. Tiginyanu, L. Kienle, and R. Adelung, "Properties of a single $SnO_2 : Zn_2SnO_4$–functionalized nanowire based nanosensor", *Ceramics International*, vol. 44, no. 5, pp. 4859–4867, 2018.

[89] H. Tan, J. Verbeeck, A. Abakumov, and G. Van Tendeloo, "Oxidation state and chemical shift investigation in transition metal oxides by EELS", *Ultramicroscopy*, vol. 116, pp. 24–33, 2012.

[90] C. Wang, L. Yin, L. Zhang, D. Xiang, and R. Gao, "Metal oxide gas sensors: Sensitivity and influencing factors", *Sensors*, vol. 10, no. 3, pp. 2088–2106, 2010.

[91] L. Zhu, W. Zeng, and Y. Li, "A non-oxygen adsorption mechanism for hydrogen detection of nanostructured SnO_2 based sensors", *Materials Research Bulletin*, vol. 109, pp. 108–116, 2019.

[92] M. E. Franke, T. J. Koplin, and U. Simon, "Metal and metal oxide nanoparticles in chemiresistors: Does the nanoscale matter?", *small*, vol. 2, no. 1, pp. 36–50, 2006.

[93] H. S. Kang, J. S. Kang, S. S. Pang, E. S. Shim, and S. Y. Lee, "Variation of light emitting properties of ZnO thin films depending on post-annealing temperature", *Materials Science and Engineering: B*, vol. 102, no. 1-3, pp. 313–316, 2003.

[94] K. Wang, Y. Chang, L. Lv, and Y. Long, "Effect of annealing temperature on oxygen vacancy concentrations of nanocrystalline CeO_2 film", *Applied Surface Science*, vol. 351, pp. 164–168, 2015.

[95] A. Heilig, N. Barsan, U. Weimar, and W. Göpel, "Selectivity enhancement of SnO_2 gas sensors: Simultaneous monitoring of resistances and temperatures", *Sensors and Actuators B: Chemical*, vol. 58, no. 1-3, pp. 302–309, 1999.

[96] O. Lupan, V. Ursaki, G. Chai, L. Chow, G. Emelchenko, I. Tiginyanu, A. Gruzintsev, and A. Redkin, "Selective hydrogen gas nanosensor using individual ZnO nanowire with fast response at room temperature", *Sensors and Actuators B: Chemical*, vol. 144, no. 1, pp. 56–66, 2010.

[97] D. B. Williams and C. B. Carter, "The transmission electron microscope", in *Transmission electron microscopy*, Springer, 1996, pp. 3–17.

[98] C. B. Carter and D. B. Williams, *Transmission electron microscopy: Diffraction, imaging, and spectrometry*. Springer, 2016.

[99] B. Fultz and J. M. Howe, *Transmission electron microscopy and diffractometry of materials*. Springer Science & Business Media, 2012.

[100] H. Müller, S. Uhlemann, P. Hartel, and M. Haider, "Advancing the hexapole C_s-corrector for the scanning transmission electron microscope", *Microscopy and Microanalysis*, vol. 12, no. 6, pp. 442–455, 2006.

[101] J. Friedel, *Dislocations: International series of monographs on solid state physics*. Elsevier, 2013, vol. 3.

[102] C. Woodward, "First-principles simulations of dislocation cores", *Materials Science and Engineering: A*, vol. 400, pp. 59–67, 2005.

[103] M. J. Hÿtch, J.-L. Putaux, and J.-M. Pénisson, "Measurement of the displacement field of dislocations to 0.03 å by electron microscopy", *Nature*, vol. 423, no. 6937, p. 270, 2003.

[104] W. Shockley and J. Bardeen, "Energy bands and mobilities in monatomic semiconductors", *Physical Review*, vol. 77, no. 3, p. 407, 1950.

[105] Y. Sun, S. Thompson, and T. Nishida, "Physics of strain effects in semiconductors and metal-oxide-semiconductor field-effect transistors", *Journal of Applied Physics*, vol. 101, no. 10, p. 104 503, 2007.

[106] C. Kuo, S. Vong, R. Cohen, and G. Stringfellow, "Effect of mismatch strain on band gap in III-V semiconductors", *Journal of Applied Physics*, vol. 57, no. 12, pp. 5428–5432, 1985.

[107] S. Nakamura, "GaN growth using GaN buffer layer", *Japanese Journal of Applied Physics*, vol. 30, no. 10A, p. L1705, 1991.

[108] C. A. Broderick, S. Jin, I. P. Marko, K. Hild, P. Ludewig, Z. L. Bushell, W. Stolz, J. M. Rorison, E. P. O'Reilly, K. Volz, *et al.*, "$GaAs_{1-x}Bi_x/GaN_yAs_{1-y}$ type-II quantum wells: novel strain-balanced heterostructures for GaAs-based near-and mid-infrared photonics", *Scientific reports*, vol. 7, p. 46 371, 2017.

[109] A. R. Adams, "Strained-layer quantum-well lasers", *IEEE Journal of Selected Topics in Quantum Electronics*, vol. 17, no. 5, pp. 1364–1373, 2011.

[110] P. Sundgren, J. Berggren, P. Goldman, and M. Hammar, "Highly strained InGaAs/ GaAs multiple quantum-wells for laser applications in the 1200–1300 nm wavelength regime", *Applied Physics Letters*, vol. 87, no. 7, p. 071 104, 2005.

[111] R. Hartman and A. Hartman, "Strain-induced degradation of GaAs injection lasers", *Applied Physics Letters*, vol. 23, no. 3, pp. 147–149, 1973.

[112] L. Wang, S. Liu, Z. Zhang, X. Feng, L. Zhu, H. Guo, W. Ding, L. Chen, Y. Qin, and Z. L. Wang, "2D piezotronics in atomically thin zinc oxide sheets: Interfacing gating and channel width gating", *Nano Energy*, vol. 60, pp. 724–733, 2019.

[113] I. Robinson and R. Harder, "Coherent X-ray diffraction imaging of strain at the nanoscale", *Nature materials*, vol. 8, no. 4, p. 291, 2009.

[114] F. Pfeiffer, "X-ray ptychography", *Nature Photonics*, vol. 12, no. 1, pp. 9–17, 2018.

[115] A. Béché, J. Rouvière, J. Barnes, and D. Cooper, "Strain measurement at the nanoscale: Comparison between convergent beam electron diffraction, nano-beam electron diffraction, high resolution imaging and dark field electron holography", *Ultramicroscopy*, vol. 131, pp. 10–23, 2013.

[116] F. Hüe, M. Hÿtch, H. Bender, F. Houdellier, and A. Claverie, "Direct mapping of strain in a strained silicon transistor by high-resolution electron microscopy", *Physical review letters*, vol. 100, no. 15, p. 156 602, 2008.

[117] D. Cooper, C. Le Royer, A. Béché, and J.-L. Rouvière, "Strain mapping for the silicon-on-insulator generation of semiconductor devices by high-angle annular dark field scanning electron transmission microscopy", *Applied physics letters*, vol. 100, no. 23, p. 233 121, 2012.

[118] D. Su and Y. Zhu, "Scanning moiré fringe imaging by scanning transmission electron microscopy", *Ultramicroscopy*, vol. 110, no. 3, pp. 229–233, 2010.

[119] S. Kim, S. Lee, Y. Oshima, Y. Kondo, E. Okunishi, N. Endo, J. Jung, G. Byun, S. Lee, and K. Lee, "Scanning moiré fringe imaging for quantitative strain mapping in semiconductor devices", *Applied Physics Letters*, vol. 102, no. 16, p. 161 604, 2013.

[120] M. Hÿtch, F. Houdellier, F. Hüe, and E. Snoeck, "Nanoscale holographic interferometry for strain measurements in electronic devices", *Nature*, vol. 453, no. 7198, p. 1086, 2008.

[121] F. Hüe, M. Hÿtch, F. Houdellier, H. Bender, and A. Claverie, "Strain mapping of tensile strained silicon transistors with embedded $Si_{1-y}C_y$ source and drain by dark-field holography", *Applied Physics Letters*, vol. 95, no. 7, p. 073 103, 2009.

[122] M. Hÿtch, C. Gatel, F. Houdellier, E. Snoeck, and K. Ishizuka, "Darkfield electron holography for strain mapping at the nanoscale", *Microscopy and Analysis*, vol. 26, pp. 6–10, 2012.

[123] Z. Zhang, X. Qi, and X. Duan, "Direct determination of the polarization direction of domains in $BaTiO_3$ single crystal", *Applied physics letters*, vol. 89, no. 24, p. 242 905, 2006.

[124] A. Béché, J. Rouvière, L. Clément, and J. Hartmann, "Improved precision in strain measurement using nanobeam electron diffraction", *Applied physics letters*, vol. 95, no. 12, p. 123 114, 2009.

[125] J.-L. Rouviere, A. Béché, Y. Martin, T. Denneulin, and D. Cooper, "Improved strain precision with high spatial resolution using nanobeam precession electron diffraction", *Applied Physics Letters*, vol. 103, no. 24, p. 241 913, 2013.

[126] F. Hofmann, E. Tarleton, R. J. Harder, N. W. Phillips, P.-W. Ma, J. N. Clark, I. K. Robinson, B. Abbey, W. Liu, and C. E. Beck, "3D lattice distortions and defect structures in ion-implanted nano-crystals", *Scientific reports*, vol. 7, p. 45 993, 2017.

[127] S. Kim, Y. Kondo, K. Lee, G. Byun, J. Jung Kim, S. Lee, and K. Lee, "Quantitative measurement of strain field in strained-channel-transistor arrays by scanning moiré fringe imaging", *Applied Physics Letters*, vol. 103, no. 3, p. 033 523, 2013.

[128] M. Hÿtch, E. Snoeck, and R. Kilaas, "Quantitative measurement of displacement and strain fields from HREM micrographs", *Ultramicroscopy*, vol. 74, no. 3, pp. 131–146, 1998.

[129] I. Orue, M. Fdez-Gubieda, F. Plazaola, and J. Barandiarán, "Influence of the short-range order on the magnetic properties of metallic glasses", *Journal of Physics: Condensed Matter*, vol. 10, no. 17, p. 3807, 1998.

[130] A. Hindmarch, A. Rushforth, R. Campion, C. Marrows, and B. Gallagher, "Origin of in-plane uniaxial magnetic anisotropy in CoFeB amorphous ferromagnetic thin films", *Physical Review B*, vol. 83, no. 21, p. 212 404, 2011.

[131] A. Garcia-Arribas, M. Fdez-Gubieda, I. Orue, J. Barandiarán, J. Herreros, and F. Plazaola, "Correlation between structure and magnetic behavior of Fe-P amorphous alloys", *Physical Review B*, vol. 52, no. 17, p. 12 805, 1995.

[132] M. Treacy, J. Gibson, L. Fan, D. Paterson, and I. McNulty, "Fluctuation microscopy: A probe of medium range order", *Reports on Progress in Physics*, vol. 68, no. 12, p. 2899, 2005.

[133] C. Koch and S. Garofalini, "Determining the radial pair-distribution function within intergranular amorphous films by numerical nanodiffraction", *Ultramicroscopy*, vol. 106, no. 4-5, pp. 383–388, 2006.

[134] K. Ganesh, M. Kawasaki, J. Zhou, and P. J. Ferreira, "D-STEM: A parallel electron diffraction technique applied to nanomaterials", *Microscopy and Microanalysis*, vol. 16, no. 5, pp. 614–621, 2010.

[135] X. Mu, D. Wang, T. Feng, and C. Kübel, "Radial distribution function imaging by STEM diffraction: Phase mapping and analysis of heterogeneous nanostructured glasses", *Ultramicroscopy*, vol. 168, pp. 1–6, 2016.

[136] X. Mu, S. Neelamraju, W. Sigle, C. T. Koch, N. Toto, J. C. Schön, A. Bach, D. Fischer, M. Jansen, and P. A. van Aken, "Evolution of order in amorphous-to-crystalline phase transformation of MgF_2", *Journal of Applied Crystallography*, vol. 46, no. 4, pp. 1105–1116, 2013.

[137] D. Cockayne and D. McKenzie, "Electron diffraction analysis of polycrystalline and amorphous thin films", *Acta Crystallographica Section A: Foundations of Crystallography*, vol. 44, no. 6, pp. 870–878, 1988.

[138] D. J. Cockayne, "The study of nanovolumes of amorphous materials using electron scattering", *Annu. Rev. Mater. Res.*, vol. 37, pp. 159–187, 2007.

[139] P. Longo, "The use of MLLS fitting approach to resolve overlapping edges in the EELS spectrum at the atomic level", *DigitalMicrograph EELS Analysis User's Guide*, 2003.

[140] C. Wang, T. Feng, D. Wang, X. Mu, M. Ghafari, R. Witte, A. Kobler, C. Kübel, Y. Ivanisenko, H. Gleiter, *et al.*, "Low temperature structural stability of $Fe_{90}Sc_{10}$ nanoglasses", *Materials Research Letters*, vol. 6, no. 3, pp. 178–183, 2018.

[141] S. Zhou, B. Dong, J. Qin, D. Li, S. Pan, X. Bian, and Z. Li, "The relationship between the stability of glass-forming Fe-based liquid alloys and the metalloid-centered clusters", *Journal of Applied Physics*, vol. 112, no. 2, p. 023 514, 2012.

[142] M. Legros, D. Gianola, and C. Motz, "Quantitative in situ mechanical testing in electron microscopes", *MRS bulletin*, vol. 35, no. 5, pp. 354–360, 2010.

[143] M. Mačković, T. Przybilla, P. Herre, S. Romeis, J. Paul, E. Barthel, J. Teisseire, N. Schrenker, W. Peukert, and E. Spiecker, "In situ compression experiments of fused silica pillars in the TEM and SEM", in *European Microscopy Congress 2016: Proceedings*, Wiley Online Library, 2016, pp. 296–297.

[144] E. Spiecker, T. Przybilla, J. Guénolé, A. Prakash, E. Bitzek, Z. Xie, P. Schweizer, M. Mačković, B. Winter, F. Niekiel, *et al.*, "Combined in situ mechanical testing and scale-bridging 3D analysis of nanoporous gold", 2017.

[145] V. Samaee, R. Gatti, B. Devincre, T. Pardoen, D. Schryvers, and H. Idrissi, "Dislocation driven nanosample plasticity: New insights from quantitative in-situ TEM tensile testing", *Scientific reports*, vol. 8, no. 1, p. 12 012, 2018.

[146] V. Samaeeaghmiyoni, H. Idrissi, J. Groten, R. Schwaiger, and D. Schryvers, "Quantitative in-situ TEM nanotensile testing of single crystal Ni facilitated by a new sample preparation approach", *Micron*, vol. 94, pp. 66–73, 2017.

[147] S. Gupta and O. N. Pierron, "MEMS based nanomechanical testing method with independent electronic sensing of stress and strain", *Extreme Mechanics Letters*, vol. 8, pp. 167–176, 2016.

[148] Y. Wang, L. Gao, S. Fan, W. Zhou, X. Li, and Y. Lu, "3D printed micro-mechanical device (MMD) for in situ tensile testing of micro/nanowires", *Extreme Mechanics Letters*, vol. 33, p. 100 575, 2019.

[149] J. Kacher, T. Zhu, O. Pierron, and D. E. Spearot, "Integrating in situ TEM experiments and atomistic simulations for defect mechanics", *Current Opinion in Solid State and Materials Science*, 2019.

[150] S. Kaps, S. Bhowmick, J. Grottrup, V. Hrkac, D. Stauffer, H. Guo, O. L. Warren, J. Adam, L. Kienle, A. M. Minor, *et al.*, "Piezoresistive response of quasi-one-dimensional ZnO nanowires using an in situ electromechanical device", *Acs Omega*, vol. 2, no. 6, pp. 2985–2993, 2017.

[151] B. Xiang, L. Wang, G. Liu, and A. M. Minor, "Electromechanical probing of Li/Li_2Co_3 core/shell particles in a TEM", *Journal of The Electrochemical Society*, vol. 160, no. 3, A415–A419, 2013.

[152] S. Pak, J. Lee, Y.-W. Lee, A.-R. Jang, S. Ahn, K. Y. Ma, Y. Cho, J. Hong, S. Lee, H. Y. Jeong, *et al.*, "Strain-mediated interlayer coupling effects on the excitonic behaviors in an epitaxially grown MoS_2/WS_2 van der Waals heterobilayer", *Nano letters*, vol. 17, no. 9, pp. 5634–5640, 2017.

[153] U. Schürmann, C. Chluba, N. Wolff, D. Smazna, R. L. de Miranda, P. Junker, R. Adelung, E. Quandt, and L. Kienle, "Functional NiTi grids for in situ straining in the TEM", *Ultramicroscopy*, vol. 182, pp. 10–16, 2017.

[154] R. Lima de Miranda, C. Zamponi, and E. Quandt, "Micropatterned freestanding superelastic TiNi films", *Advanced Engineering Materials*, vol. 15, no. 1-2, pp. 66–69, 2013.

[155] ——, "Method for producing a medical functional element comprising a self-supporting lattice structure", *Acandis GmbH and Co KG / United States Patent*, vol. US008758636B2, 2014.

[156] R. Hugo, H. Kung, J. Weertman, R. Mitra, J. Knapp, and D. Follstaedt, "In-situ TEM tensile testing of DC magnetron sputtered and pulsed laser deposited Ni thin films", *Acta Materialia*, vol. 51, no. 7, pp. 1937–1943, 2003.

[157] A. Kobler, A. Kashiwar, H. Hahn, and C. Kübel, "Combination of in situ straining and ACOM TEM: A novel method for analysis of plastic deformation of nanocrystalline metals", *Ultramicroscopy*, vol. 128, pp. 68–81, 2013.

[158] A. Kobler, C. Brandl, H. Hahn, and C. Kübel, "In situ observation of deformation processes in nanocrystalline face-centered cubic metals", *Beilstein journal of nanotechnology*, vol. 7, no. 1, pp. 572–580, 2016.

[159] M. Samayoa, M. A. Haque, and P. Cohen, "Focused ion beam irradiation effects on nanoscale freestanding thin films", *Journal of Micromechanics and Microengineering*, vol. 18, no. 9, p. 095 005, 2008.

[160] K. F. Murphy, L. Y. Chen, and D. S. Gianola, "Effect of organometallic clamp properties on the apparent diversity of tensile response of nanowires", *Nanotechnology*, vol. 24, no. 23, p. 235 704, 2013.

[161] V. Röbisch, S. Salzer, N. O. Urs, J. Reermann, E. Yarar, A. Piorra, C. Kirchhof, E. Lage, M. Höft, G. U. Schmidt, *et al.*, "Pushing the detection limit of thin film magnetoelectric heterostructures", *Journal of Materials Research*, vol. 32, no. 6, pp. 1009–1019, 2017.

[162] Y. Saito, H. Takao, T. Tani, T. Nonoyama, K. Takatori, T. Homma, T. Nagaya, and M. Nakamura, "Lead-free piezoceramics", *Nature*, vol. 432, no. 7013, pp. 84–87, 2004.

[163] O. Zywitzki, T. Modes, S. Barth, H. Bartzsch, and P. Frach, "Effect of scandium content on structure and piezoelectric properties of AlScN films deposited by reactive pulse magnetron sputtering", *Surface and Coatings Technology*, vol. 309, pp. 417–422, 2017.

[164] S. Zhang, D. Holec, W. Y. Fu, C. J. Humphreys, and M. A. Moram, "Tunable optoelectronic and ferroelectric properties in Sc-based III-nitrides", *Journal of applied physics*, vol. 114, no. 13, p. 133 510, 2013.

[165] K. R. Talley, S. L. Millican, J. Mangum, S. Siol, C. B. Musgrave, B. Gorman, A. M. Holder, A. Zakutayev, and G. L. Brennecka, "Implications of heterostructural alloying for enhanced piezoelectric performance of (Al,Sc)N", *Physical Review Materials*, vol. 2, no. 6, p. 063 802, 2018.

[166] M. Uehara, H. Shigemoto, Y. Fujio, T. Nagase, Y. Aida, K. Umeda, and M. Akiyama, "Giant increase in piezoelectric coefficient of AlN by Mg-Nb simultaneous addition and multiple chemical states of Nb", *Applied Physics Letters*, vol. 111, no. 11, p. 112 901, 2017.

[167] S. Fichtner, N. Wolff, F. Lofink, L. Kienle, and B. Wagner, "AlScN: A III-V semiconductor based ferroelectric", *Journal of Applied Physics*, vol. 125, no. 11, p. 114 103, 2019.

[168] W. Wang, P. M. Mayrhofer, X. He, M. Gillinger, Z. Ye, X. Wang, A. Bittner, U. Schmid, and J. Luo, "High performance AlScN thin film based surface acoustic wave devices with large electromechanical coupling coefficient", *Applied Physics Letters*, vol. 105, no. 13, p. 133 502, 2014.

[169] S. Fichtner, N. Wolff, G. Krishnamurthy, A. Petraru, S. Bohse, F. Lofink, S. Chemnitz, H. Kohlstedt, L. Kienle, and B. Wagner, "Identifying and overcoming the interface originating c-axis instability in highly Sc enhanced AlN for piezoelectric micro-electromechanical systems", *Journal of Applied Physics*, vol. 122, no. 3, p. 035 301, 2017.

[170] M. Hambe, S. Wicks, J. Gregg, and V. Nagarajan, "Creation of damage-free ferroelectric nanostructures via focused ion beam milling", *Nanotechnology*, vol. 19, no. 17, p. 175 302, 2008.

[171] H. Lichte, M. Reibold, K. Brand, and M. Lehmann, "Ferroelectric electron holography", *Ultramicroscopy*, vol. 93, no. 3-4, pp. 199–212, 2002.

[172] C.-L. Jia, S.-B. Mi, K. Urban, I. Vrejoiu, M. Alexe, and D. Hesse, "Atomic-scale study of electric dipoles near charged and uncharged domain walls in ferroelectric films", *Nature materials*, vol. 7, no. 1, p. 57, 2008.

[173] M. J. Polking, M.-G. Han, A. Yourdkhani, V. Petkov, C. F. Kisielowski, V. V. Volkov, Y. Zhu, G. Caruntu, A. P. Alivisatos, and R. Ramesh, "Ferroelectric order in individual nanometer-scale crystals", *Nature materials*, vol. 11, no. 8, p. 700, 2012.

[174] S. Priya and S. Nahm, *Lead-free piezoelectrics*. Springer Science & Business Media, 2011.

[175] R. E. Cohen, "Origin of ferroelectricity in perovskite oxides", *Nature*, vol. 358, no. 6382, p. 136, 1992.

[176] B. Noheda, D. Cox, G. Shirane, J. Gonzalo, L. Cross, and S. Park, "A monoclinic ferroelectric phase in the $Pb(Zr_{1-x}Ti_x)O_3$ solid solution", *Applied physics letters*, vol. 74, no. 14, pp. 2059–2061, 1999.

[177] H. Fu and R. E. Cohen, "Polarization rotation mechanism for ultrahigh electromechanical response in single-crystal piezoelectrics", *Nature*, vol. 403, no. 6767, p. 281, 2000.

[178] M. Ahart, M. Somayazulu, R. Cohen, P. Ganesh, P. Dera, H.-k. Mao, R. J. Hemley, Y. Ren, P. Liermann, and Z. Wu, "Origin of morphotropic phase boundaries in ferroelectrics", *Nature*, vol. 451, no. 7178, p. 545, 2008.

[179] W. Li, Z. Xu, R. Chu, P. Fu, and G. Zang, "Polymorphic phase transition and piezoelectric properties of $(Ba_xCa_{1-x})(Ti_{0.9}Zr_{0.1})O_3$ lead-free ceramics", *Physica B: Condensed Matter*, vol. 405, no. 21, pp. 4513–4516, 2010.

[180] Z. Zhao, X. Li, H. Ji, Y. Dai, and T. Li, "Microstructure and electrical properties in Zn-doped $(Ba_{0.85}Ca_{0.15})(Ti_{0.9}Zr_{0.1})O_3$ piezoelectric ceramics", *Journal of Alloys and Compounds*, vol. 637, pp. 291–296, 2015.

[181] B. P. Burton, E. Cockayne, and U. V. Waghmare, "Correlations between nanoscale chemical and polar order in relaxor ferroelectrics and the lengthscale for polar nanoregions", *Physical Review B*, vol. 72, no. 6, p. 064 113, 2005.

[182] R. Cohen, "Materials science: Relaxors go critical", *Nature*, vol. 441, no. 7096, p. 941, 2006.

[183] S. Vakhrushev and S. Shapiro, "Direct evidence of soft mode behavior near the burns temperature in the $PbMg_{1/3}Nb_{2/3}O_3$ relaxor ferroelectric", *Physical Review B*, vol. 66, no. 21, p. 214 101, 2002.

[184] G. Burns and F. Dacol, "Crystalline ferroelectrics with glassy polarization behavior", *Physical Review B*, vol. 28, no. 5, p. 2527, 1983.

[185] A. Piorra, V. Hrkac, N. Wolff, C. Zamponi, V. Duppel, J. Hadermann, L. Kienle, and E. Quandt, "$(Ba_{0.85}Ca_{0.15})(Ti_{0.9}Zr_{0.1})O_3$ thin films prepared by PLD: Relaxor properties and complex microstructure", *Journal of Applied Physics*, vol. 125, no. 24, p. 244 103, 2019.

[186] Z. L. Wang, "From nanogenerators to piezotronics—A decade-long study of ZnO nanostructures", *MRS bulletin*, vol. 37, no. 9, pp. 814–827, 2012.

[187] T. Frömling, R. Yu, M. Mintken, R. Adelung, and J. Rödel, "Piezotronic sensors", *MRS Bulletin*, vol. 43, no. 12, pp. 941–945, 2018.

[188] L. Zhu and Z. L. Wang, "Progress in piezotronics and piezo-phototronics of quantum materials", *Journal of Physics D: Applied Physics*, vol. 52, no. 34, p. 343 001, 2019.

[189] Z. L. Wang, "ZnO nanowire and nanobelt platform for nanotechnology", *Materials Science and Engineering: R: Reports*, vol. 64, no. 3-4, pp. 33–71, 2009.

[190] Y. K. Mishra, S. Kaps, A. Schuchardt, I. Paulowicz, X. Jin, D. Gedamu, S. Freitag, M. Claus, S. Wille, A. Kovalev, *et al.*, "Fabrication of macroscopically flexible and highly porous 3D semiconductor networks from interpenetrating nanostructures by a simple flame transport approach", *Particle & Particle Systems Characterization*, vol. 30, no. 9, pp. 775–783, 2013.

[191] V. Karpina, V. Lazorenko, C. Lashkarev, V. Dobrowolski, L. Kopylova, V. Baturin, S. Pustovoytov, A. J. Karpenko, S. Eremin, P. Lytvyn, *et al.*, "Zinc oxide–analogue of gan with new perspective possibilities", *Crystal Research and Technology: Journal of Experimental and Industrial Crystallography*, vol. 39, no. 11, pp. 980–992, 2004.

[192] C. Park, S. Zhang, and S.-H. Wei, "Origin of p-type doping difficulty in ZnO: The impurity perspective", *Physical Review B*, vol. 66, no. 7, p. 073 202, 2002.

[193] D. Smazna, N. Wolff, S. Shree, F. Schütt, Y. Mishra, L. Kienle, and R. Adelung, "Enhancing the conductivity of ZnO micro-and nanowire networks with gallium oxide", in *2017 IEEE 7th International Conference Nanomaterials: Application & Properties (NAP)*, IEEE, 2017, 01FNC07–1.

[194] N. Wolff, V. Hrkac, J. J. Ditto, V. Duppel, Y. K. Mishra, D. C. Johnson, R. Adelung, and L. Kienle, "Crystallography at the nanoscale: Planar defects in ZnO nanospikes", *Journal of applied crystallography*, vol. 52, no. 5, 2019.

[195] I. Paulowicz, V. Postica, O. Lupan, N. Wolff, S. Shree, A. Cojocaru, M. Deng, Y. K. Mishra, I. Tiginyanu, L. Kienle, *et al.*, "Zinc oxide nanotetrapods with four different arm morphologies for versatile nanosensors", *Sensors and Actuators B: Chemical*, vol. 262, pp. 425–435, 2018.

[196] V. Postica, I. Paulowicz, O. Lupan, F. Schütt, N. Wolff, A. Cojocaru, Y. K. Mishra, L. Kienle, and R. Adelung, "The effect of morphology and functionalization on uv detection properties of ZnO networked tetrapods and single nanowires", *Vacuum*, vol. 166, pp. 393–398, 2019.

[197] O. Lupan, V. Postica, N. Wolff, J. Su, F. Labat, I. Ciofini, H. Cavers, R. Adelung, O. Polonskyi, F. Faupel, *et al.*, "Low-temperature solution synthesis of Au-modified ZnO nanowires for highly efficient hydrogen nanosensors", *ACS Applied Materials & Interfaces*, vol. 11, no. 35, pp. 32 115–32 126, 2019.

[198] M. Hoppe, O. Lupan, V. Postica, N. Wolff, V. Duppel, L. Kienle, I. Tiginyanu, and R. Adelung, "$ZnAl_2O_4$-functionalized zinc oxide microstructures for highly selective hydrogen gas sensing applications", *physica status solidi (a)*, vol. 215, no. 7, p. 1 700 772, 2018.

[199] R. F. Davis, "III-V nitrides for electronic and optoelectronic applications", *Proceedings of the IEEE*, vol. 79, no. 5, pp. 702–712, 1991.

[200] B. J. Baliga, "Gallium nitride devices for power electronic applications", *Semiconductor Science and Technology*, vol. 28, no. 7, p. 074 011, 2013.

[201] T. J. Flack, B. N. Pushpakaran, and S. B. Bayne, "GaN technology for power electronic applications: A review", *Journal of Electronic Materials*, vol. 45, no. 6, pp. 2673–2682, 2016.

[202] Z. Zhao, X. Pu, C. Han, C. Du, L. Li, C. Jiang, W. Hu, and Z. L. Wang, "Piezotronic effect in polarity-controlled GaN nanowires", *Acs Nano*, vol. 9, no. 8, pp. 8578–8583, 2015.

[203] Z. L. Wang, "Progress in piezotronics and piezo-phototronics", *Advanced Materials*, vol. 24, no. 34, pp. 4632–4646, 2012.

[204] L. Liu and J. H. Edgar, "Substrates for gallium nitride epitaxy", *Materials Science and Engineering: R: Reports*, vol. 37, no. 3, pp. 61–127, 2002.

[205] M. Sun, Y. Zhang, X. Gao, and T. Palacios, "High-performance GaN vertical fin power transistors on bulk GaN substrates", *IEEE Electron Device Letters*, vol. 38, no. 4, pp. 509–512, 2017.

[206] T. Paskova, D. A. Hanser, and K. R. Evans, "GaN substrates for III-nitride devices", *Proceedings of the IEEE*, vol. 98, no. 7, pp. 1324–1338, 2009.

[207] A. Usui, H. Sunakawa, A. Sakai, and A. A. Yamaguchi, "Thick GaN epitaxial growth with low dislocation density by hydride vapor phase epitaxy", *JAPANESE JOURNAL OF APPLIED PHYSICS PART 2 LETTERS*, vol. 36, pp. L899–L902, 1997.

[208] I. Tiginyanu, M. A. Stevens-Kalceff, A. Sarua, T. Braniste, E. Monaico, V. Popa, H. D. Andrade, J. O. Thomas, S. Raevschi, K. Schulte, *et al.*, "Self-organized three-dimensional nanostructured architectures in bulk GaN generated by spatial modulation of doping", *ECS Journal of Solid State Science and Technology*, vol. 5, no. 5, P218–P227, 2016.

[209] N. Wolff, P. Jordt, T. Braniste, V. Popa, E. Monaico, V. Ursaki, A. Petraru, R. Adelung, B. M. Murphy, L. Kienle, *et al.*, "Modulation of electrical conductivity and lattice distortions in bulk HVPE-grown GaN", *ECS Journal of Solid State Science and Technology*, vol. 8, no. 8, Q141–Q146, 2019.

[210] K. Kim, W. R. Lambrecht, and B. Segall, "Electronic structure of GaN with strain and phonon distortions", *Physical Review B*, vol. 50, no. 3, p. 1502, 1994.

[211] P.-R. Huang, Y. He, C. Cao, and Z.-H. Lu, "Impact of lattice distortion and electron doping on $\alpha - MoO_3$ electronic structure", *Scientific reports*, vol. 4, p. 7131, 2014.

[212] M. Dragoman, I. Tiginyanu, D. Dragoman, A. Dinescu, T. Braniste, and V. Ciobanu, "Learning mechanisms in memristor networks based on GaN nanomembranes", *Journal of Applied Physics*, vol. 124, no. 15, p. 152 110, 2018.

[213] Y. S. Zhou, R. Hinchet, Y. Yang, G. Ardila, R. Songmuang, F. Zhang, Y. Zhang, W. Han, K. Pradel, L. Montès, *et al.*, "Nano-Newton transverse force sensor using a vertical GaN nanowire based on the piezotronic effect", *Advanced Materials*, vol. 25, no. 6, pp. 883–888, 2013.

[214] C.-H. Wang, W.-S. Liao, N.-J. Ku, Y.-C. Li, Y.-C. Chen, L.-W. Tu, and C.-P. Liu, "Effects of free carriers on piezoelectric nanogenerators and piezotronic devices made of GaN nanowire arrays", *Small*, vol. 10, no. 22, pp. 4718–4725, 2014.

[215] R. Yu, L. Dong, C. Pan, S. Niu, H. Liu, W. Liu, S. Chua, D. Chi, and Z. L. Wang, "Piezotronic effect on the transport properties of GaN nanobelts for active flexible electronics", *Advanced Materials*, vol. 24, no. 26, pp. 3532–3537, 2012.

[216] N. Wolff, V. Ciobanu, M. Enachi, M. Kamp, T. Braniste, V. Duppel, S. Shree, S. Raevschi, M. Medina-Sánchez, R. Adelung, *et al.*, "Advanced hybrid GaN/ZnO nanoarchitectured microtubes for fluorescent micromotors driven by UV light", *Small*, vol. 16, no. 2, p. 1 905 141, 2019.

[217] K. S. Novoselov, A. K. Geim, S. V. Morozov, D. Jiang, Y. Zhang, S. V. Dubonos, I. V. Grigorieva, and A. A. Firsov, "Electric field effect in atomically thin carbon films", *science*, vol. 306, no. 5696, pp. 666–669, 2004.

[218] P. Chen, Z. Zhang, X. Duan, and X. Duan, "Chemical synthesis of two-dimensional atomic crystals, heterostructures and superlattices", *Chemical Society Reviews*, vol. 47, no. 9, pp. 3129–3151, 2018.

[219] K. F. Mak and J. Shan, "Photonics and optoelectronics of 2D semiconductor transition metal dichalcogenides", *Nature Photonics*, vol. 10, no. 4, p. 216, 2016.

[220] L. Gao, "Flexible device applications of 2D semiconductors", *Small*, vol. 13, no. 35, p. 1 603 994, 2017.

[221] S. M. Oh, S. B. Patil, X. Jin, and S.-J. Hwang, "Recent applications of 2D inorganic nanosheets for emerging energy storage system", *Chemistry–A European Journal*, vol. 24, no. 19, pp. 4757–4773, 2018.

[222] S. Bertolazzi, P. Bondavalli, S. Roche, T. San, S.-Y. Choi, L. Colombo, F. Bonaccorso, and P. Samorı, "Nonvolatile memories based on graphene and related 2D materials", *Advanced Materials*, vol. 31, no. 10, p. 1 806 663, 2019.

[223] W. Wu, L. Wang, Y. Li, F. Zhang, L. Lin, S. Niu, D. Chenet, X. Zhang, Y. Hao, T. F. Heinz, *et al.*, "Piezoelectricity of single-atomic-layer MoS_2 for energy conversion and piezotronics", *Nature*, vol. 514, no. 7523, p. 470, 2014.

[224] S. Yu, Q. Rice, B. Tabibi, Q. Li, and F. J. Seo, "Piezoelectricity in WSe_2/MoS_2 heterostructure atomic layers", *Nanoscale*, vol. 10, no. 26, pp. 12 472–12 479, 2018.

[225] P. B. James and M. Lavik, "The crystal structure of $MoSe_2$", *Acta Crystallographica*, vol. 16, no. 11, pp. 1183–1183, 1963.

[226] E. C. Hadland, H. Jang, N. Wolff, R. Fischer, A. C. Lygo, G. Mitchson, D. Li, L. Kienle, D. G. Cahill, and D. C. Johnson, "Ultralow thermal conductivity of turbostratically disordered $MoSe_2$ ultra-thin films and implications for heterostructures", *Nanotechnology*, 2019.

[227] I. Häusler, R. Atkins, M. Falmbigl, S. P. Rudin, W. Neumann, and D. C. Johnson, "Insights from STEM and NBED studies into the local structure and growth mechanism of misfit layered compounds prepared using modulated reactants", *Zeitschrift für Kristallographie-Crystalline Materials*, vol. 230, no. 1, pp. 45–54, 2015.

[228] E. Rauch and M. Véron, "Automated crystal orientation and phase mapping in TEM", *Materials Characterization*, vol. 98, pp. 1–9, 2014.

[229] R. Hinchet, U. Khan, C. Falconi, and S.-W. Kim, "Piezoelectric properties in two-dimensional materials: Simulations and experiments", *Materials Today*, vol. 21, no. 6, pp. 611–630, 2018.

[230] N. Onofrio, D. Guzman, and A. Strachan, "Novel doping alternatives for single-layer transition metal dichalcogenides", *Journal of Applied Physics*, vol. 122, no. 18, p. 185 102, 2017.

[231] S. A. Han, T.-H. Kim, S. K. Kim, K. H. Lee, H.-J. Park, J.-H. Lee, and S.-W. Kim, "Point-defect-passivated MoS_2 nanosheet-based high performance piezoelectric nanogenerator", *Advanced Materials*, vol. 30, no. 21, p. 1 800 342, 2018.

[232] Y.-C. Lin, D. O. Dumcenco, H.-P. Komsa, Y. Niimi, A. V. Krasheninnikov, Y.-S. Huang, and K. Suenaga, "Properties of individual dopant atoms in single-layer MoS_2: Atomic structure, migration, and enhanced reactivity", *Advanced materials*, vol. 26, no. 18, pp. 2857–2861, 2014.

[233] J. Hong, C. Jin, J. Yuan, and Z. Zhang, "Atomic defects in two-dimensional materials: From single-atom spectroscopy to functionalities in opto-/electronics, nanomagnetism, and catalysis", *Advanced Materials*, vol. 29, no. 14, p. 1 606 434, 2017.

[234] V. Hrkac, E. Lage, G. Köppel, J. Strobel, J. McCord, E. Quandt, D. Meyners, and L. Kienle, "Amorphous FeCoSiB for exchange bias coupled and decoupled magnetoelectric multilayer systems: Real-structure and magnetic properties", *Journal of Applied Physics*, vol. 116, no. 13, p. 134 302, 2014.

[235] G. Herzer, "Grain structure and magnetism of nanocrystalline ferromagnets", *IEEE Transactions on Magnetics*, vol. 25, no. 5, pp. 3327–3329, 1989.

[236] X. Liu and A. Morisako, "Soft magnetic properties of FeCo films with high saturation magnetization", *Journal of Applied Physics*, vol. 103, no. 7, 07E726, 2008.

[237] C. Klever, M. Stüber, H. Leiste, E. Nold, K. Seemann, S. Ulrich, H. Brunken, A. Ludwig, C. Thede, and E. Quandt, "Multifunctional FeCo/TiN multilayer thin films with combined magnetic and protective properties", *Advanced Engineering Materials*, vol. 11, no. 12, pp. 969–975, 2009.

[238] C. Klever, K. Seemann, M. Stüber, S. Ulrich, H. Brunken, A. Ludwig, and H. Leiste, "Epitaxially stabilized TiN/(Ti,Fe,Co)N multilayer thin films in (pseudo-) fcc crystal structure by sequential magnetron sputter deposition", *Journal of Physics D: Applied Physics*, vol. 43, no. 39, p. 395 406, 2010.

[239] T. Lafford, M. Gibbs, and C. Shearwood, "Magnetic, magnetostrictive and structural properties of iron-cobalt/silver multilayers", *Journal of magnetism and magnetic materials*, vol. 132, no. 1-3, pp. 89–94, 1994.

[240] H. Fukuzawa, Y. Kamiguchi, K. Koi, H. Iwasaki, and M. Sahashi, "Saturation magnetostriction of an ultrathin CoFe free-layer on double-layered underlayers", *Journal of applied physics*, vol. 91, no. 5, pp. 3120–3124, 2002.

[241] V. Röbisch, E. Yarar, N. Urs, I. Teliban, R. Knöchel, J. McCord, E. Quandt, and D. Meyners, "Exchange biased magnetoelectric composites for magnetic field sensor application by frequency conversion", *Journal of Applied Physics*, vol. 117, no. 17, 17B513, 2015.

[242] S. Salzer, P. Durdaut, V. Röbisch, D. Meyners, E. Quandt, M. Höft, and R. Knöchel, "Generalized magnetic frequency conversion for thin-film laminate magnetoelectric sensors", *IEEE Sensors Journal*, vol. 17, no. 5, pp. 1373–1383, 2016.

[243] E. F. Kneller and R. Hawig, "The exchange-spring magnet: A new material principle for permanent magnets", *IEEE Transactions on Magnetics*, vol. 27, no. 4, pp. 3588–3560, 1991.

[244] E. E. Fullerton, J. Jiang, and S. Bader, "Hard/soft magnetic heterostructures: Model exchange-spring magnets", *Journal of Magnetism and Magnetic Materials*, vol. 200, no. 1-3, pp. 392–404, 1999.

[245] J. P. Prieto-Ruiz, F. M. Romero, H. Prima-Garcıa, and E. Coronado, "Exchange coupling in an electrodeposited magnetic bilayer of prussian blue analogues", *Journal of Materials Chemistry C*, vol. 3, no. 42, pp. 11 122–11 128, 2015.

[246] N. Duc, D. H. Giang, and N. Chau, "Novel exchange-spring configuration for excellent magnetic and magnetostrictive softness", *Journal of magnetism and magnetic materials*, vol. 290, pp. 800–803, 2005.

[247] A. Kohn, A. Kovács, R. Fan, G. McIntyre, R. Ward, and J. Goff, "The antiferromagnetic structures of irmn$_3$ and their influence on exchange-bias", *Scientific reports*, vol. 3, p. 2412, 2013.

[248] J. Jiang, X. Pan, W. Tian, C. Theis, and D. Schlom, "Abrupt $PbTiO_3/SrTiO_3$ superlattices grown by reactive molecular beam epitaxy", *Applied Physics Letters*, vol. 74, no. 19, pp. 2851–2853, 1999.

[249] K. L. Chopra, "Metastable thin film epitaxial structures", *physica status solidi (b)*, vol. 32, no. 2, pp. 489–507, 1969.

[250] H. Han, H. Choi, S. Mhin, Y.-R. Hong, K. M. Kim, J. Kwon, G. Ali, K. Y. Chung, M. Je, H. N. Um, *et al.*, "Advantageous crystalline-amorphous phase boundary for enhanced electrochemical water oxidation", *Energy & Environmental Science*, 2019.

[251] W. Wu, S. Chen, J. Zhai, X. Liu, T. Lai, S. Song, and Z. Song, "Multi-level storage and ultra-high speed of superlattice-like $Ge_{50}Te_{50}/Ge_8Sb_{92}$ thin film for phase-change memory application", *Nanotechnology*, vol. 28, no. 40, p. 405 206, 2017.

[252] V. Röbisch, A. Piorra, R. Lima de Miranda, E. Quandt, and D. Meyners, "Frequency-tunable nickel-titanium substrates for magnetoelectric sensors", *AIP Advances*, vol. 8, no. 12, p. 125 320, 2018.

[253] G. Deuschl and Y. Agid, "Subthalamic neurostimulation for parkinson's disease with early fluctuations: Balancing the risks and benefits", *The Lancet Neurology*, vol. 12, no. 10, pp. 1025–1034, 2013.

[254] S. Zabel, C. Kirchhof, E. Yarar, D. Meyners, E. Quandt, and F. Faupel, "Phase modulated magnetoelectric delta-Eeffect sensor for sub-nano tesla magnetic fields", *Applied Physics Letters*, vol. 107, no. 15, p. 152 402, 2015.

[255] T. Dankwort, J. Strobel, C. Chluba, W. Ge, V. Duppel, M. Wuttig, E. Quandt, and L. Kienle, "Martensite adaption through epitaxial nanotransition layers in TiNiCu shape memory alloys", *Journal of Applied Crystallography*, vol. 49, no. 3, pp. 1009–1015, 2016.

[256] H. Gu, L. Bumke, C. Chluba, E. Quandt, and R. D. James, "Phase engineering and supercompatibility of shape memory alloys", *Materials Today*, vol. 21, no. 3, pp. 265–277, 2018.

[257] J. Frenzel, A. Wieczorek, I. Opahle, B. Maaß, R. Drautz, and G. Eggeler, "On the effect of alloy composition on martensite start temperatures and latent heats in ni–ti-based shape memory alloys", *Acta Materialia*, vol. 90, pp. 213–231, 2015.

[258] C. Chluba, W. Ge, R. L. de Miranda, J. Strobel, L. Kienle, E. Quandt, and M. Wuttig, "Ultralow-fatigue shape memory alloy films", *Science*, vol. 348, no. 6238, pp. 1004–1007, 2015.

[259] X. Wang and J. J. Vlassak, "Crystallization kinetics of amorphous niti shape memory alloy thin films", *Scripta Materialia*, vol. 54, no. 5, pp. 925–930, 2006.

[260] H.-J. Lee, H. Ni, D. T. Wu, and A. G. Ramirez, "Grain size estimations from the direct measurement of nucleation and growth", *Applied Physics Letters*, vol. 87, no. 12, p. 124 102, 2005.

[261] P. Surbled, C. Clerc, B. Le Pioufle, M. Ataka, and H. Fujita, "Effect of the composition and thermal annealing on the transformation temperatures of sputtered TiNi shape memory alloy thin films", *Thin Solid Films*, vol. 401, no. 1-2, pp. 52–59, 2001.

[262] C. Chluba, H. Ossmer, C. Zamponi, M. Kohl, and E. Quandt, "Ultra-low fatigue quaternary TiNi-based films for elastocaloric cooling", *Shape Memory and Superelasticity*, vol. 2, no. 1, pp. 95–103, 2016.

[263] M. Ishimaru, I. V. Afanasyev-Charkin, and K. E. Sickafus, "Ion-beam-induced spinel-to-rocksalt structural phase transformation in mgal 2 o 4", *Applied Physics Letters*, vol. 76, no. 18, pp. 2556–2558, 2000.

[264] K. Yin, Y. Xia, Z. Liu, J. Yin, and L. Sun, "Electron-beam induced phase transformation in β-ag2se thin films", *physica status solidi (a)*, vol. 209, no. 1, pp. 135–138, 2012.

[265] H. Mehrer, *Diffusion in solids: fundamentals, methods, materials, diffusion-controlled processes*. Springer Science & Business Media, 2007, vol. 155.

[266] I. Kaur, W. Gust, and Y. Mishin, *Fundamentals of grain and interphase boundary diffusion*. Wiley Chichester, 1995.

[267] G. Neumann and C. Tuijn, *Self-diffusion and impurity diffusion in pure metals: handbook of experimental data*. Elsevier, 2011, vol. 14.

[268] T. Tisone and J. Drobek, "Diffusion in thin film Ti–Au, Ti–Pd, and Ti–Pt couples", *Journal of Vacuum Science and Technology*, vol. 9, no. 1, pp. 271–275, 1972.

[269] J. L. Murray, "The Ta-Ti (Tantalum-Titanium) system", *Bulletin of Alloy Phase Diagrams*, vol. 2, no. 1, pp. 62–66, 1981.

[270] R. Waterstrat, "Analysis of selected alloys in the systems Cr-Pd, Cr-Ru, V-Pd and Ta-Pt", *Journal of the Less Common Metals*, vol. 80, no. 1, P31–P36, 1981.

[271] J. L. Murray, "The Pt-Ti (Platinum-Titanium) system", *Bulletin Of Alloy Phase Diagrams*, vol. 3, no. 3, pp. 329–335, 1982.

[272] J. Larson, R. Taggart, and D. Polonis, "Ni_8Ta in nickel-rich Ni-Ta alloys", *Metallurgical and Materials Transactions B*, vol. 1, no. 2, pp. 485–489, 1970.

[273] P. Subramanian and D. Laughlin, "The Cu-Ta (copper-tantalum) system", *Bulletin of alloy phase diagrams*, vol. 10, no. 6, pp. 652–655, 1989.

[274] J. Harris, R. Youngman, and R. Teller, "On the nature of the oxygen-related defect in aluminum nitride", *Journal of Materials Research*, vol. 5, no. 8, pp. 1763–1773, 1990.

[275] L. Vergara, M. Clement, E. Iborra, A. Sanz-Hervás, J. G. Lopez, Y. Morilla, J. Sangrador, and M. Respaldiza, "Influence of oxygen and argon on the crystal quality and piezoelectric response of AlN sputtered thin films", *Diamond and related materials*, vol. 13, no. 4-8, pp. 839–842, 2004.

[276] A. T. Guntner, S. Abegg, K. Konigstein, P. A. Gerber, A. Schmidt-Trucksass, and S. E. Pratsinis, "Breath sensors for health monitoring", *ACS sensors*, vol. 4, no. 2, pp. 268–280, 2019.

[277] K. Wetchakun, T. Samerjai, N. Tamaekong, C. Liewhiran, C. Siriwong, V. Kruefu, A. Wisitsoraat, A. Tuantranont, and S. Phanichphant, "Semiconducting metal oxides as sensors for environmentally hazardous gases", *Sensors and Actuators B: Chemical*, vol. 160, no. 1, pp. 580–591, 2011.

[278] I. Paulowicz, V. Hrkac, S. Kaps, V. Cretu, O. Lupan, T. Braniste, V. Duppel, I. Tiginyanu, L. Kienle, R. Adelung, *et al.*, "Three-dimensional SnO_2 nanowire networks for multifunctional applications: From high-temperature stretchable ceramics to ultraresponsive sensors", *Advanced Electronic Materials*, vol. 1, no. 8, p. 1 500 081, 2015.

[279] O. Lupan, V. Postica, V. Cretu, N. Wolff, V. Duppel, L. Kienle, and R. Adelung, "Single and networked CuO nanowires for highly sensitive p-type semiconductor gas sensor applications", *physica status solidi (RRL)–Rapid Research Letters*, vol. 10, no. 3, pp. 260–266, 2016.

[280] W. Shin, "Medical applications of breath hydrogen measurements", *Analytical and bioanalytical chemistry*, vol. 406, no. 16, pp. 3931–3939, 2014.

[281] E. Resmini, A. Parodi, V. Savarino, A. Greco, A. Rebora, F. Minuto, and D. Ferone, "Evidence of prolonged orocecal transit time and small intestinal bacterial overgrowth in acromegalic patients", *The Journal of Clinical Endocrinology & Metabolism*, vol. 92, no. 6, pp. 2119–2124, 2007.

[282] I. Andalib, H. Shah, B. S. Bal, T. R. Shope, F. C. Finelli, and T. R. Koch, "Breath hydrogen as a biomarker for glucose malabsorption after Roux-en-Y gastric bypass surgery", *Disease markers*, vol. 2015, 2015.

[283] F. Castiglione, G. D. V. Blanco, A. Rispo, G. Petrelli, G. Amalfi, A. Cozzolino, I. Cuccaro, and G. Mazzacca, "Orocecal transit time and bacterial overgrowth in patients with Crohn's disease", *Journal of clinical gastroenterology*, vol. 31, no. 1, pp. 63–66, 2000.

[284] D. L. Swagerty, A. D. Walling, and R. M. Klein, "Lactose intolerance", *American family physician*, vol. 65, no. 9, pp. 1845–1860, 2002.

[285] T. Hübert, L. Boon-Brett, G. Black, and U. Banach, "Hydrogen sensors–a review", *Sensors and Actuators B: Chemical*, vol. 157, no. 2, pp. 329–352, 2011.

[286] B. Wang, L. Zhu, Y. Yang, N. Xu, and G. Yang, "Fabrication of a SnO_2 nanowire gas sensor and sensor performance for hydrogen", *The Journal of Physical Chemistry C*, vol. 112, no. 17, pp. 6643–6647, 2008.

[287] Z. Li, Z. Yao, A. A. Haidry, T. Plecenik, L. Xie, L. Sun, and Q. Fatima, "Resistive-type hydrogen gas sensor based on TiO_2: A review", *International Journal of Hydrogen Energy*, vol. 43, no. 45, pp. 21 114–21 132, 2018.

[288] Y. Im, C. Lee, R. P. Vasquez, M. A. Bangar, N. V. Myung, E. J. Menke, R. M. Penner, and M. Yun, "Investigation of a single Pd nanowire for use as a hydrogen sensor", *Small*, vol. 2, no. 3, pp. 356–358, 2006.

[289] F. Favier, E. C. Walter, M. P. Zach, T. Benter, and R. M. Penner, "Hydrogen sensors and switches from electrodeposited palladium mesowire arrays", *Science*, vol. 293, no. 5538, pp. 2227–2231, 2001.

[290] O. Lupan, V. Postica, F. Labat, I. Ciofini, T. Pauporté, and R. Adelung, "Ultra-sensitive and selective hydrogen nanosensor with fast response at room temperature based on a single Pd/ZnO nanowire", *Sensors and Actuators B: Chemical*, vol. 254, pp. 1259–1270, 2018.

[291] A. Kolmakov, D. Klenov, Y. Lilach, S. Stemmer, and M. Moskovits, "Enhanced gas sensing by individual SnO_2 nanowires and nanobelts functionalized with Pd catalyst particles", *Nano Letters*, vol. 5, no. 4, pp. 667–673, 2005.

[292] O. Lupan, V. Postica, N. Wolff, O. Polonskyi, V. Duppel, V. Kaidas, E. Lazari, N. Ababii, F. Faupel, L. Kienle, *et al.*, "Localized synthesis of iron oxide nanowires and fabrication of high performance nanosensors based on a single Fe_2O_3 nanowire", *Small*, vol. 13, no. 16, p. 1 602 868, 2017.

[293] O. Lupan, V. Postica, T. Pauporte, B. Viana, M.-I. Terasa, and R. Adelung, "Room temperature gas nanosensors based on individual and multiple networked Au-modified ZnO nanowires", *Sensors and Actuators B: Chemical*, vol. 299, p. 126 977, 2019.

[294] O. Lupan, V. Postica, R. Adelung, F. Labat, I. Ciofini, U. Schürmann, L. Kienle, L. Chow, B. Viana, and T. Pauporté, "Functionalized Pd/ZnO nanowires for nanosensors", *physica status solidi (RRL)–Rapid Research Letters*, vol. 12, no. 1, p. 1 700 321, 2018.

[295] S. M. Kim, H. J. Kim, H. J. Jung, J.-Y. Park, T. J. Seok, Y.-H. Choa, T. J. Park, and S. W. Lee, "High-performance, transparent thin film hydrogen gas sensor using 2D electron gas at interface of oxide thin film heterostructure grown by atomic layer deposition", *Advanced Functional Materials*, vol. 29, no. 7, p. 1 807 760, 2019.

[296] V. I. Gaman, N. K. Maksimova, A. V. Almaev, and N. V. Sergeychenko, "Effect of humidity on characteristics of hydrogen sensors based on nanocrystalline SnO_2 thin films with various catalysts", in *Key Engineering Materials*, Trans Tech Publ, vol. 683, 2016, pp. 353–357.

[297] P. Saeedi, I. Petersohn, P. Salpea, B. Malanda, S. Karuranga, N. Unwin, S. Colagiuri, L. Guariguata, A. A. Motala, K. Ogurtsova, *et al.*, "Global and regional diabetes prevalence estimates for 2019 and projections for 2030 and 2045: Results from the international diabetes federation diabetes atlas", *Diabetes research and clinical practice*, vol. 157, p. 107 843, 2019.

[298] C. Tassopoulos, D. Barnett, and T. R. Fraser, "Breath-acetone and blood-sugar measurements in diabetes", *The Lancet*, vol. 293, no. 7609, pp. 1282–1286, 1969.

[299] J. Y. Lucisano, T. L. Routh, J. T. Lin, and D. A. Gough, "Glucose monitoring in individuals with diabetes using a long-term implanted sensor/telemetry system and model", *IEEE Transactions on Biomedical Engineering*, vol. 64, no. 9, pp. 1982–1993, 2016.

[300] C. Wang, A. Mbi, and M. Shepherd, "A study on breath acetone in diabetic patients using a cavity ringdown breath analyzer: Exploring correlations of breath acetone with blood glucose and glycohemoglobin A1C", *IEEE Sensors Journal*, vol. 10, no. 1, pp. 54–63, 2009.

[301] V. Saasa, T. Malwela, M. Beukes, M. Mokgotho, C.-P. Liu, and B. Mwakikunga, "Sensing technologies for detection of acetone in human breath for diabetes diagnosis and monitoring", *Diagnostics*, vol. 8, no. 1, p. 12, 2018.

[302] L. Wang, A. Teleki, S. E. Pratsinis, and P. Gouma, "Ferroelectric WO_3 nanoparticles for acetone selective detection", *Chemistry of Materials*, vol. 20, no. 15, pp. 4794–4796, 2008.

[303] M. Righettoni, A. Tricoli, and S. E. Pratsinis, "Si : WO_3 sensors for highly selective detection of acetone for easy diagnosis of diabetes by breath analysis", *Analytical chemistry*, vol. 82, no. 9, pp. 3581–3587, 2010.

[304] S. Salehi, E. Nikan, A. A. Khodadadi, and Y. Mortazavi, "Highly sensitive carbon nanotubes–SnO_2 nanocomposite sensor for acetone detection in diabetes mellitus breath", *Sensors and Actuators B: Chemical*, vol. 205, pp. 261–267, 2014.

[305] W. Liu, L. Xu, K. Sheng, X. Zhou, B. Dong, G. Lu, and H. Song, "A highly sensitive and moisture-resistant gas sensor for diabetes diagnosis with $Pt@In_2O_3$ nanowires and a molecular sieve for protection", *NPG Asia Materials*, vol. 10, no. 4, p. 293, 2018.

[306] L. Siebert, N. Wolff, N. Ababii, M.-I. Terasa, O. Lupan, A. Vahl, V. Duppel, H. Qiu, M. Tienken, M. Mirabelli, *et al.*, "Facile fabrication of semiconducting oxide nanostructures by direct ink writing of readily available metal microparticles and their application as low power acetone gas sensors", *Nano Energy*, p. 104 420, 2020.

[307] Y. Zeng, T. Zhang, M. Yuan, M. Kang, G. Lu, R. Wang, H. Fan, Y. He, and H. Yang, "Growth and selective acetone detection based on ZnO nanorod arrays", *Sensors and Actuators B: Chemical*, vol. 143, no. 1, pp. 93–98, 2009.

[308] J. Reermann, P. Durdaut, S. Salzer, T. Demming, A. Piorra, E. Quandt, N. Frey, M. Höft, and G. Schmidt, "Evaluation of magnetoelectric sensor systems for cardiological applications", *Measurement*, vol. 116, pp. 230–238, 2018.

[309] E. Lee, Y. S. Yoon, and D.-J. Kim, "Two-dimensional transition metal dichalcogenides and metal oxide hybrids for gas sensing", *ACS sensors*, vol. 3, no. 10, pp. 2045–2060, 2018.

Appendix A

Permissions

Whenever the materials studies included within this thesis have been published in peer reviewed journals, this has been indicated accordingly to the granted permissions by each of the following licence and permission grants provided by the respective journals.

JOHN WILEY AND SONS LICENSE
TERMS AND CONDITIONS

Dec 16, 2019

This Agreement between Technical Faculty, Christian-Albrechts-University Kiel -- Niklas Wolff ("You") and John Wiley and Sons ("John Wiley and Sons") consists of your license details and the terms and conditions provided by John Wiley and Sons and Copyright Clearance Center.

License Number	4730681052164
License date	Dec 16, 2019
Licensed Content Publisher	John Wiley and Sons
Licensed Content Publication	Small
Licensed Content Title	Localized Synthesis of Iron Oxide Nanowires and Fabrication of High Performance Nanosensors Based on a Single Fe2O3 Nanowire
Licensed Content Author	Rainer Adelung, Lorenz Kienle, Franz Faupel, et al
Licensed Content Date	Feb 10, 2017
Licensed Content Volume	13
Licensed Content Issue	16
Licensed Content Pages	10

Type of use	Dissertation/Thesis
Requestor type	Author of this Wiley article
Format	Print and electronic
Portion	Full article
Will you be translating?	No
Title of your thesis / dissertation	Transmission Electron Microscopy on Advanced Functional Nanomaterials and their relation to medical application: Biomagnetic Sensing and Breath Monitoring
Expected completion date	Mar 2020
Expected size (number of pages)	1
Requestor Location	Technical Faculty, Christian-Albrechts-University Kiel Kaiserstrasse 2 Kiel, other 24143 Germany Attn: Technical Faculty, Christian-Albrechts-University Kiel
Publisher Tax ID	EU826007151
Total	0.00 EUR
Terms and Conditions	

TERMS AND CONDITIONS

This copyrighted material is owned by or exclusively licensed to John Wiley & Sons, Inc. or one of its group companies (each a"Wiley Company") or handled on behalf of a society with

JOHN WILEY AND SONS LICENSE TERMS AND CONDITIONS

Oct 09, 2019

This Agreement between Technical Faculty, Christian-Albrechts-University Kiel -- Niklas Wolff ("You") and John Wiley and Sons ("John Wiley and Sons") consists of your license details and the terms and conditions provided by John Wiley and Sons and Copyright Clearance Center.

License Number	4684690485905
License date	Oct 09, 2019
Licensed Content Publisher	John Wiley and Sons
Licensed Content Publication	physica status solidi (a) applications and materials science
Licensed Content Title	ZnAl2O4-Functionalized Zinc Oxide Microstructures for Highly Selective Hydrogen Gas Sensing Applications
Licensed Content Author	Rainer Adelung, Ion Tiginyanu, Lorenz Kienle, et al
Licensed Content Date	Feb 14, 2018
Licensed Content Volume	215
Licensed Content Issue	7
Licensed Content Pages	13
Type of use	Dissertation/Thesis
Requestor type	Author of this Wiley article
Format	Print and electronic
Portion	Full article
Will you be translating?	No
Title of your thesis / dissertation	Transmission Electron Microscopy on Advanced Functional Nanomaterials and their relation to medical application: Biomagnetic Sensing and Breath Monitoring
Expected completion date	Mar 2020
Expected size (number of pages)	1
Requestor Location	Technical Faculty, Christian-Albrechts-University Kiel Kaiserstrasse 2 Kiel, other 24143 Germany Attn: Technical Faculty, Christian-Albrechts-University Kiel
Publisher Tax ID	EU826007151
Total	0.00 EUR
Terms and Conditions	

TERMS AND CONDITIONS

This copyrighted material is owned by or exclusively licensed to John Wiley & Sons, Inc. or one of its group companies (each a"Wiley Company") or handled on behalf of a society with which a Wiley Company has exclusive publishing rights in relation to a particular work

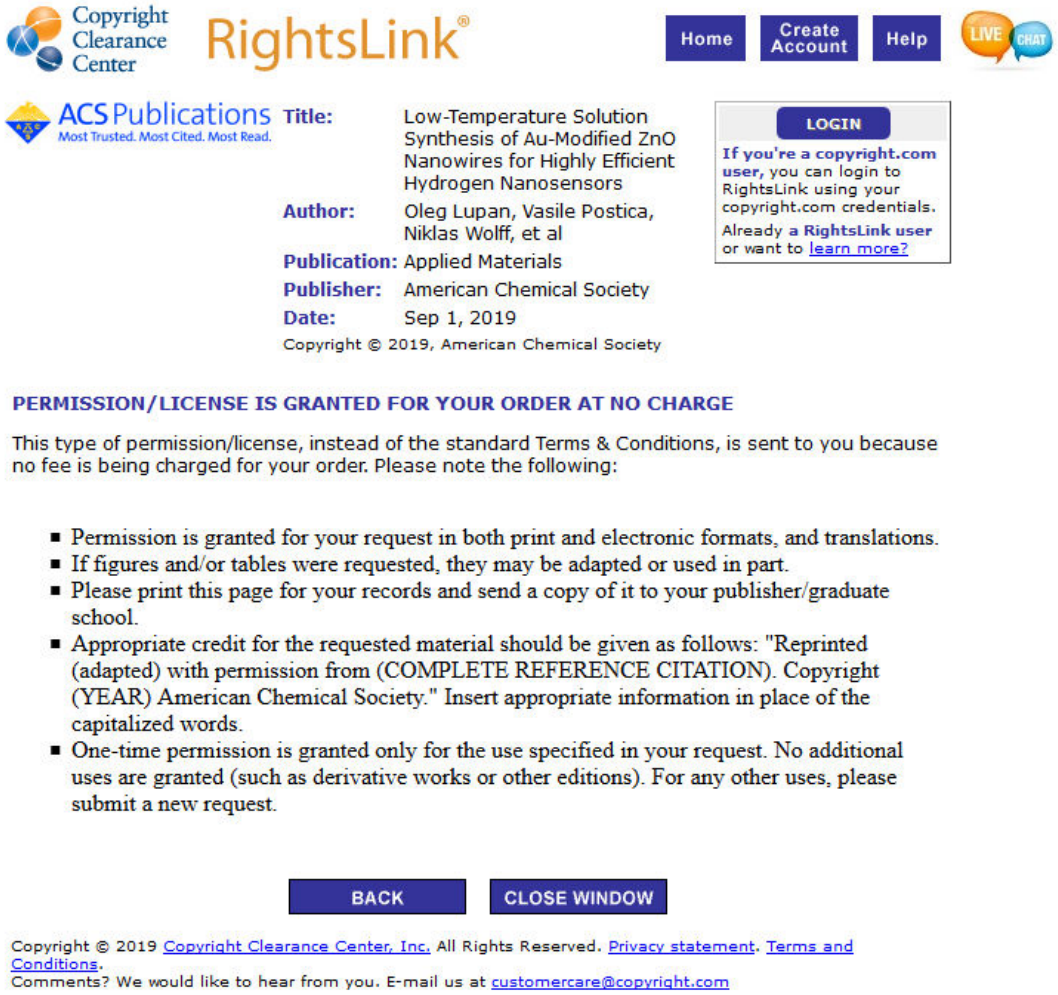

FIGURE A.1: American Chemical Society (ACS)

REUSING AIP PUBLISHING CONTENT

Permission from AIP Publishing is required to:

- republish content (e.g., excerpts, figures, tables) if you are not the author
- modify, adapt, or redraw materials for another publication
- systematically reproduce content
- store or distribute content electronically
- copy content for promotional purposes

To request permission to reuse AIP Publishing content, use RightsLink® for the fastest response or contact AIP Publishing directly at rights@aip.org and we will respond within one week:

For RightsLink, use Scitation to access the article you wish to license, and click on the Reprints and Permissions link under the TOOLS tab. (For assistance click the "Help" button in the top right corner of the RightsLink page.)

To send a permission request to rights@aip.org, please include the following:

- Citation information for the article containing the material you wish to reuse
- A description of the material you wish to reuse, including figure and/or table numbers
- The title, authors, name of the publisher, and expected publication date of the new work
- The format(s) the new work will appear in (e.g., print, electronic, CD-ROM)
- How the new work will be distributed and whether it will be offered for sale

Authors do **not** need permission from AIP Publishing to:

- quote from a publication (please include the material in quotation marks and provide the customary acknowledgment of the source)
- reuse any materials that are licensed under a Creative Commons CC BY license (please format your credit line: "Author names, Journal Titles, Vol.#, Article ID#, Year of Publication; licensed under a Creative Commons Attribution (CC BY) license.")
- reuse your own AIP Publishing article in your thesis or dissertation (please format your credit line: "Reproduced from [FULL CITATION], with the permission of AIP Publishing")
- reuse content that appears in an AIP Publishing journal for republication in another AIP Publishing journal (please format your credit line: "Reproduced from [FULL CITATION], with the permission of AIP Publishing")
- make multiple copies of articles–although you must contact the Copyright Clearance Center (CCC) at www.copyright.com to do this

FIGURE A.2: American Institute of Physics (AIP)

Can I use material from my Elsevier journal article within my thesis/dissertation? –

As an Elsevier journal author, you have the right to Include the article in a thesis or dissertation (provided that this is not to be published commercially) whether in full or in part, subject to proper acknowledgment; see the Copyright page for more information. No written permission from Elsevier is necessary.

This right extends to the posting of your thesis to your university's repository provided that if you include the published journal article, it is embedded in your thesis and not separately downloadable.

FIGURE A.3: ELSEVIER

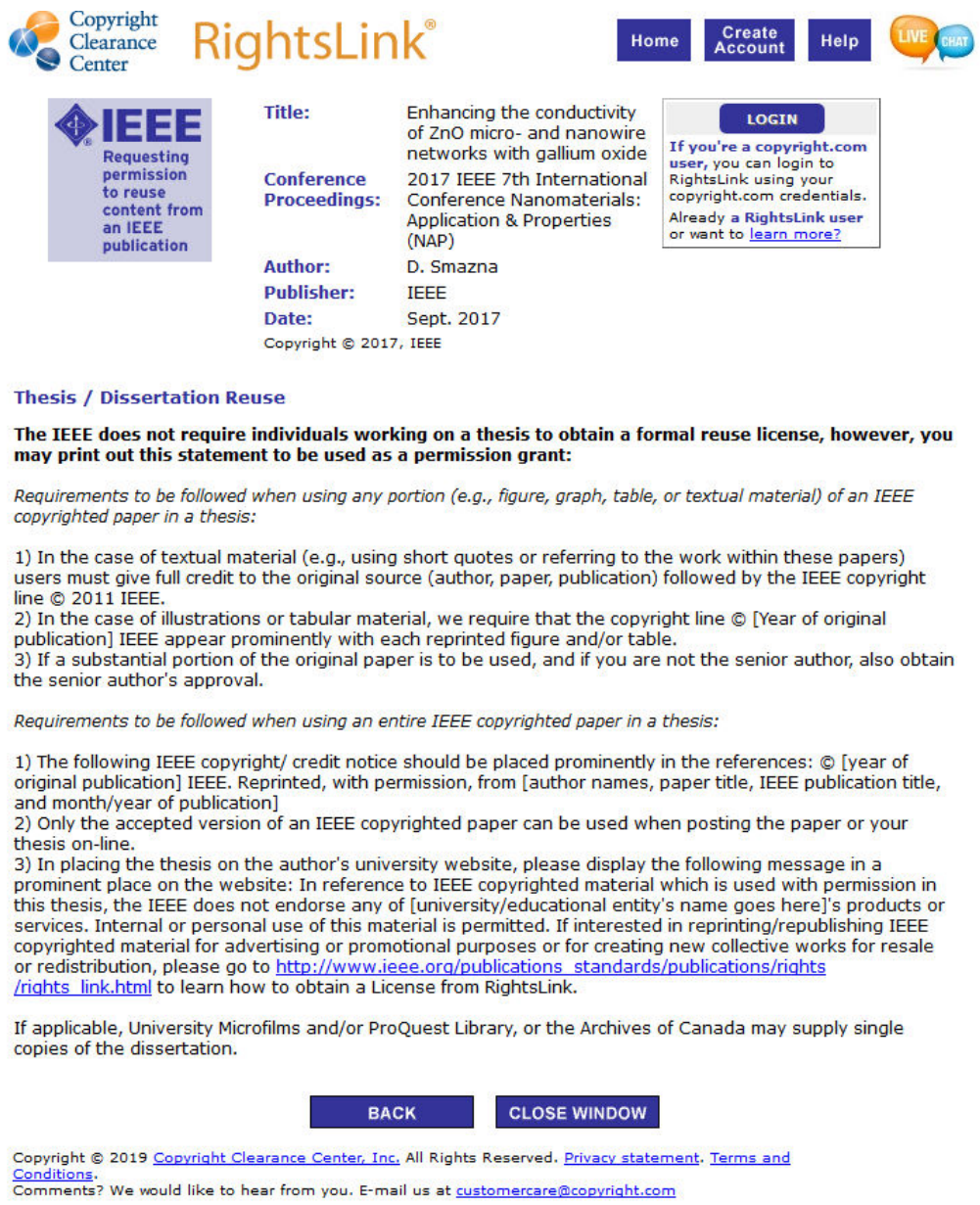

Copyright Clearance Center RightsLink®

Home | Create Account | Help | LIVE CHAT

IEEE Requesting permission to reuse content from an IEEE publication

Title: Enhancing the conductivity of ZnO micro- and nanowire networks with gallium oxide

Conference Proceedings: 2017 IEEE 7th International Conference Nanomaterials: Application & Properties (NAP)

Author: D. Smazna

Publisher: IEEE

Date: Sept. 2017

Copyright © 2017, IEEE

LOGIN

If you're a copyright.com user, you can login to RightsLink using your copyright.com credentials.

Already a RightsLink user or want to learn more?

Thesis / Dissertation Reuse

The IEEE does not require individuals working on a thesis to obtain a formal reuse license, however, you may print out this statement to be used as a permission grant:

Requirements to be followed when using any portion (e.g., figure, graph, table, or textual material) of an IEEE copyrighted paper in a thesis:

1) In the case of textual material (e.g., using short quotes or referring to the work within these papers) users must give full credit to the original source (author, paper, publication) followed by the IEEE copyright line © 2011 IEEE.
2) In the case of illustrations or tabular material, we require that the copyright line © [Year of original publication] IEEE appear prominently with each reprinted figure and/or table.
3) If a substantial portion of the original paper is to be used, and if you are not the senior author, also obtain the senior author's approval.

Requirements to be followed when using an entire IEEE copyrighted paper in a thesis:

1) The following IEEE copyright/ credit notice should be placed prominently in the references: © [year of original publication] IEEE. Reprinted, with permission, from [author names, paper title, IEEE publication title, and month/year of publication]
2) Only the accepted version of an IEEE copyrighted paper can be used when posting the paper or your thesis on-line.
3) In placing the thesis on the author's university website, please display the following message in a prominent place on the website: In reference to IEEE copyrighted material which is used with permission in this thesis, the IEEE does not endorse any of [university/educational entity's name goes here]'s products or services. Internal or personal use of this material is permitted. If interested in reprinting/republishing IEEE copyrighted material for advertising or promotional purposes or for creating new collective works for resale or redistribution, please go to http://www.ieee.org/publications_standards/publications/rights/rights_link.html to learn how to obtain a License from RightsLink.

If applicable, University Microfilms and/or ProQuest Library, or the Archives of Canada may supply single copies of the dissertation.

BACK | CLOSE WINDOW

Copyright © 2019 Copyright Clearance Center, Inc. All Rights Reserved. Privacy statement. Terms and Conditions.
Comments? We would like to hear from you. E-mail us at customercare@copyright.com

FIGURE A.4: IEEE

IOPscience Journals Books Publishing Support Search Publishing support

Publishing Support

May I include the Final Published Version of the article in my research thesis or dissertation?

Upon transfer of copyright, IOP and/or the copyright owner grants back to authors a number of rights. These include the right to include the Final Published Version of the article in your research thesis or dissertation. Please include citation details and, for online use, a link to the Version of Record. IOP's permission will be required for commercial use of an article published as part of your thesis. IOP does not allow ProQuest to publish or sell the article as part of your dissertation.

FIGURE A.5: IOP Publishing

Appendix B

Contributions/Eigenanteil

My own contributions are categorized and ranked according to the criteria:
Conceptualization, Methodology/Measurements, Data Analysis, Visualization, Writing-Draft, Review/Editing.

The following table lists all contributions in chronological order and is divided into first- and co-author publications. An estimate of the own contribution to each category is given in percentages.

Mein Anteil eingebrachter Publikationen wird anhand dieser Kriterien bewertet: **K**onzeptionierung, **D**atenerhebung/Messungen, **A**uswertung,
Visualisierung, **T**exterstellung-Draft, **R**ezension und Überarbeitung.

Die folgende Tabelle listet alle eingebrachten Publikationen chronologisch und sortiert nach Erst- oder Ko-Autorschaft auf und gibt eine Einschätzung des Eigenanteils in Prozentzahlen ab.

Diese Bewertung erfolgt rein subjektiv und spiegelt nicht zwangsläufig die Leistung meiner Ko-Autoren wider.

Konzeptionierung, **D**atenerhebung/Messungen, **A**uswertung, **V**isualisierung, **T**exterstellung, **R**ezension/Überarbeitung

Publikation	K	D	A	V	T	R
N. Wolff, P. Jordt, J. Jetter, H. Vogt, A. Lotnyk, K. Seemann, S. Ulrich, E. Quandt, B. M. Murophy, L. Kienle, Heteroepitaxy in ultra-thin FeCo/TiN Nanolayer Films, sent to review by *Materials Characterization* (02.02.2020)	100	75	75	80	90	60
N. Wolff, V. Ciobanu, M. Enachi, M. Kamp, T. Braniste, V. Duppel, S. Shree, S. Raevchi, M. Medina-Sánchez, R. Adelung, O. Schmidt, I. Tiginyanu, L. Kienle: Advanced Hybrid GaN/ZnO nano-Architectured Microtubes for fluorescent Micromotors driven by UV-light, *Small* 16, 1905141 (2019)	70	50	80	70	80	60
N. Wolff, V. Hrkac, J. J. Ditto, V. Duppel, Y. K. Mishra, D. C. Johnson, R. Adelung, L. Kienle: Crystallography at the nanoscale, planar defects in ZnO nanospikes. *J. Appl. Cryst.* 52. 1009-1015 (2019).	100	20	100	100	80	70
N. Wolff, P. Jordt, T. Braniste, V. Popa, E. Monaico, V. Ursaki, A. Petraru, R. Adelung, B. M. Murphy, L. Kienle, I. Tiginyanu: Modulation of Electrical Conductivity and Lattice Distortions in Bulk HVPE-Grown GaN. *ECS J. Solid State Sci. Technol.* 8, 141–146 (2019).	40	50	50	50	70	40
S. Curtis, **N. Wolff**, D. Dengiz, H. Lewitz, J. Jetter, L. Bumke, E. Yarar, L. Thormählen, L. Kienle, D. Meyners, E. Quandt: MAgnetoelectric Composites on Ultra-Low Fatigue TiNiCu Shape Memory Alloy Thin-Films. Submitted to *Journal of Materials Research* (25.12.2019).	10	20	20	10	20	20
L. Siebert, **N. Wolff**, N. Ababii, M.-I. Teresa, O. Lupan, A. Vahl, V. Duppel, H. Qiu, M. Tienken, M. Mirabelli, V. Sontea, F. Faupel, L. Kienle, R. Adelung: Facile Fabrication of Semiconducting Oxide Nanostructures by Direct Ink Writing of Readily Available Metal Microparticles and their Application as Low Power Acetone Gas Sensors, *Nano Energy.* 70, 104420 (2020).	10	15	15	15	15	40
E. C. Hadland, H. Jang, **N. Wolff**, R. Fischer, A. C. Lygo, G. Mitchson, D. Li, L. Kienle, D. G. Cahill, D. C. Johnson, Ultralow Thermal Conductivity of Turbostratically Disordered $MoSe_2$ Ultra-thin Films and Implications for Heterostructures. *Nanotechnology*. 30, 285401 (2019).	20	20	20	25	20	10
S. Fichtner, **N. Wolff**, F. Lofink, L. Kienle, B. Wagner, AlScN: A III-V Semiconductor based Ferroelectric. *Journal of Applied Physics.* 125, 114103 (2019).	0	10	10	10	10	10
O. Lupan, V. Postica, **N. Wolff**, J. Su, F. Labat, I. Ciofini, H. Cavers, R. Adelung, O. Polonskyi, F. Faupel, L. Kienle, B. Viana, T. Pauporté: Low-Temperature Solution Synthesis of Au-Modified ZnO Nanowires for Highly Efficient Hydrogen Nanosensors. *ACS Appl. Mater. Interfaces.* 11, 32115–32126 (2019).	0	10	20	20	10	60
A. Piorra, V. Hrkac, **N. Wolff**, C. Zamponi, V. Duppel, J. Hadermann, L. Kienle, E. Quandt: $(Ba_{0.85}Ca_{0.15})(Ti_{0.9}Zr_{0.1})O_3$ Thin Films prepared by PLD: Relaxor Properties and Complex Microstructure. *Journal of Applied Physics*. 125, 244103 (2019).	70	0	15	40	30	70
O. Lupan, V. Postica, **N. Wolff**, O. Polonskyi, V. Duppel, V. Kaidas, E. Lazari, N. Ababii, F. Faupel, L. Kienle, R. Adelung: Localized Synthesis of Iron Oxide Nanowires and Fabrication of High Performance Nanosensors Based on a Single Fe_2O_3 Nanowire. *Small*. 13, 1602868 (2017).	10	20	30	20	15	40
S. Fichtner, **N. Wolff**, G. Krishnamurthy, A. Petraru, S. Bohse, F. Lofink, S. Chemnitz, H. Kohlstedt, L. Kienle, B. Wagner: Identifying and Overcoming the Interface Originating c-axis Instability in Highly Sc Enhanced AlN for Piezoelectric Micro-electromechanical Systems. *Journal of Applied Physics*. 122, 035301 (2017)	20	20	20	20	15	20

Publikation	K	D	A	V	T	R
D. Smazna, **N. Wolff**, S. Shree, F. Schuett, Y. K. Mishra, L. Kienle, R. Adelung: Enhancing the Conductivity of ZnO Micro- and Nanowire Networks with Gallium Oxide. *in Proceedings of the 2017 IEEE 7th International Conference Nanomaterials: Application & Properties* (nap), A. D. Pogrebnjak, V. Novosad, P. Zukowski, S. I. Protsenko, Y. Shabelnyk, Eds. (IEEE, New York, 2017), p. UNSP 01FNC07 (2017).	30	40	40	40	25	30
U. Schürmann, C. Chluba, **N. Wolff**, D. Smazna, R. Lima de Miranda, P. Junker, R. Adelung, E. Quandt, L. Kienle: Functional NiTi grids for in situ straining in the TEM. *Ultramicroscopy*. 182, 10–16 (2017).	0	15	0	10	0	20

_____ _____

Niklas Wolff Prof. Dr. Lorenz Kienle